Citation for published version:
Johnston, DN & Plummer, A (eds) 2007, Power Transmission and Motion Control (PTMC 2007). Centre for Power Transmission and Motion Control, Bath, UK.

Publication date:
2007

Document Version
Publisher's PDF, also known as Version of record

Link to publication

University of Bath

General rights
Copyright and moral rights for the publications made accessible in the public portal are retained by the authors and/or other copyright owners and it is a condition of accessing publications that users recognise and abide by the legal requirements associated with these rights.

Take down policy
If you believe that this document breaches copyright please contact us providing details, and we will remove access to the work immediately and investigate your claim.

Download date: 12. May. 2019

Power Transmission and Motion Control

Power Transmission and Motion Control

(PTMC 2007)

Edited by

Dr D N Johnston
Workshop Organiser

Professor A R Plummer
Director

Centre for Power Transmission and Motion Control
University of Bath, UK

Copyright © With The Centre for Power Transmission and Motion Control

British Library Cataloguing in Publication Data

A catalogue record for this book is available from the British Library

All rights reserved. No part of this publication or the information contained herein may be reproduced, stored in a retrieval system, or transmitted in any form or by any means, electronic, mechanical, by photocopying, recording or otherwise, without written prior permission from the publisher. Although all care is taken to ensure the integrity and quality of this publication and the information herein, no responsibility is assumed by the publishers nor the author for any damage to property or persons as a result of operation or use of this publication and/or the information contained herein.

Printed by:
Hadleys Ltd
13 Winstanley Way, Basildon, Essex SS14 3BP, United Kingdom
Tel: +44 (0) 1268 533121
Fax: +44 (0) 1268 286879
www.hadleyprint.com
e-mail: enquiries@hadleyprint.com

ISBN 978-0-86197-140-4

Printed in Great Britain

Front cover picture: Pressure distribution on a screw-centrifugal pump
Back cover picture: CFD model of fuel injector

Contents

Preface **xi**

Condition Monitoring and Fault Diagnosis

On-line condition monitoring of a radial LSHT motor in a pulp washer application 15
(T Huvila, E Mäkinen, Tampere University of Technology, Finland)

Fault diagnosis of pneumatic systems 27
(S Fritz, H Murrenhoff, University of Aachen, Germany)

Self-organising maps for change detection in hydraulic systems 41
(A Zachrison, M Sethson, Linköping University, Sweden)

Detection of cylinder and valve leakage in hydraulic position servo 53
(E Mäkinen, T Virvalo, Tampere University of Technology, Finland)

Pressure based fault detection and diagnosis of a digital valve system 67
(L Siivonen, M Linjama, M Huova, Tampere University of Technology, Finland)

Pumps: Modelling, Performance and Noise

A simulation study to reduce noise of compact power-split-drive transmissions 83
(R Klop, K Williams, D Dyminski, M Ivantysynova, Purdue University, USA)

Flow pulsation reduction for variable displacement motors using cross-angle 103
(L Ericson, J Ölvander, J-O Palmberg, Linköping University, Sweden)

High-frequency axial vibration in a combined pump unit with gear stage 117
(M Gasparov, A Kruchkov, L Rodionov, E Shakhmatov, Samara State Aerospace University, Russia)

Tribological simulation of a hydrostatic swash plate bearing in an axial piston pump 129
(A Wohlers, H Murrenhoff, University of Aachen, Germany)

Modelling

Modelling and measurement of the compliance and friction losses of screwjack electromechanical actuators 145
(W Karam, J-C Mare, Laboratoire de Génie Mécanique, France)

Numerical analysis of the hydraulic circuit of a commercial common rail diesel fuel injection system 159
(P Beierer, K Huhtala, M Vilenius, Tampere University of Technology, Finland)

Experimental study on the use of a dynamic neural network for modelling a variable load sensing pump 175
(L Li, D Bitner, R Burton, G Schoenau, University of Saskatchewan, Saskatoon, Canada)

Modelling, simulation and identification of the electro-hydraulic speed governors for Kaplan turbines by AMESim 189
(N Vasiliu, C Calinoui, D Vasiliu, University Politehnica of Bucharest, Romania)

The full vehicle simulation – a virtual test environment for mobile hydraulic systems 201
(A Schumacher, H-H Harms, Technical University of Braunschweig, Germany)

A Fourier-Galerkin-Newton method for period nonlinear transmission line problems 217
(H Kogler, Linz Centre of Mecatronics GmbH, Austria, B Manhartsgruber, R Haas, Johannes Kepler University, Austria)

Applications

Optimized pace drive concept for glass panel conveyors 231
(D Prust, H Murrenhoff, University of Aachen, Germany)

Electric hydrostatic drive – a concept for the clamping unit of a high-speed injection moulding machine 245
(S Räcklebe, S Helduser, Technical University of Dresden, Germany)

Energy storing and recovering in loading and unloading cycles of forward loader 255
(T Virvalo, Tampere University of Technology, Finland, W Sun, Zhejiang University, China)

An electropneumatic control and actuation system for the vanes of the variable geometry turbine of a turbocharged diesel engine 269
(A Almondo, GM Powertrain Europe, Italy, G Jacazio, Politecnico di Torino, Italy)

Systems and Control

Metering poppet valve system control 283
(C Harvey, O Cline, R Fales, University of Missouri-Columbia, USA)

On stability and dynamic characteristics of hydraulic drives with distributed vales 297
(M Linjama, M Vilenius, Tampere University of Technology, Finland)

Pressure tracking control for a self-energizing hydraulic brake 315
(M Liermann, C Stammen, H Murrenhoff, University of Aachen, Germany)

Independent force control of pneumatic McKibben actuators using the multiplexing technique 331
(V Jouppila, A Ellman, Tampere University of Technology, Finland)

Fluid Dynamics and Noise

Vibroacoustic load reduction in hydro mechanical systems by use of flow oscillation dampers 351
(E Shakhmatov, A Kruchkov, A Prokofiev, V Sverbilov, Samara State Aerospace University, Russia)

A new method for power steering hose assembly design and acoustic optimisation by means of time domain hydraulic line simulation models 367
(H Baum, FLUIDON GmbH, Germany, M Hofmann, Continental Contitech Fluid Technology, France)

Numerical simulation of pulsating flow in resonator hose based on measured data of wave speed 383
(I-Y Lee, M-G Kang, J-W Kim, Pukyong National University, Korea)

High Performance Valves

Dynamical performance of a fast magnetorheological (MR) valve 399
(J Kostamo, E Kostamo, J Kajaste, M Pietola, Helsinki University of Technology, Finland)

Design optimization of a special relief valve with response surface methodology 413
(P Casoli, A Vacca, University of Parma, Italy)

A proposal to compare electro-pneumatic continuous control valves: required main characteristics 431
(S Sesmet R de Giorgi, E Bideaux D Thomasset, Ampere, France, D Hubert ASCO-Joucomatic, France, J Lecerf, CETIM, France)

Flow characteristics measurement of large valves 449
(B Manhartsgruber, Johannes Kepler University, Austria, B Winkler, Linz Centre of Mechatronics GmbH, Austria)

Authors' Index 459

Preface

The 2007 Power Transmission and Motion Control Symposium took place on 12-14 September. It was co-sponsored by the Network of Fluid Power Centres in Europe (FPCE), and is the 20th in the series held annually at the University of Bath. The events have always attracted an international audience, and this time the authors originated from 11 countries. Twenty-nine fully refereed papers were presented with particular emphasis on advances in hydraulic and pneumatic systems and components. The event included a visit to Brunel's historic ship, the SS Great Britain.

Without the continued support and enthusiasm of authors, reviewers, delegates and staff, it would not be possible to sustain such a long-running and successful series of events. Heartfelt thanks are due to all who have contributed. Special thanks are due to Dan Clifford, Jane Phippen and Barbara Terry for their considerable assistance in compiling the material for this book, and for organizing and ensuring the smooth running of the event. We are also grateful for the support from Hadleys Ltd.

Professor A R Plummer *Director*
Dr D N Johnston, *Symposium Organiser*
Centre for Power Transmission and Motion Control
Bath, September 2007

ptmc
The Centre for
Power Transmission
and Motion Control

FPCE
NETWORK OF FLUID POWER
CENTRES IN EUROPE

Condition Monitoring and Fault Diagnosis

ON-LINE CONDITION MONITORING OF A RADIAL LSHT MOTOR IN A PULP WASHER APPLICATION

Timo Huvila and Esa Mäkinen
Tampere University of Technology, Finland

ABSTRACT

In this paper a case study of condition monitoring of a hydraulic motor is presented. Studied motors are low speed, high torque (LSHT) hydraulic motors that are used at a pulp mill to drive pulp washers.

An index number for estimating the condition of the motor at different temperatures and pressure conditions is introduced. The index is based on measured leakage flow, pressures and temperatures at a given point and comparing the calculated values with a known reference point.

The thermodynamic monitoring method is well suited for this kind of measurement since it doesn't significantly affect the machine's normal operation. This paper will take a look at the general principles of realising such measurements and their feasibility in this research.

1. INTRODUCTION

The initial objective for this research was to gain more information about the condition of the hydraulic motors that drive pulp washers. The motors power a crucial part of pulp making process. Thus an unexpected failure in one of the motors will result in considerable capital loss as the process will have to be stopped. Also the value of a motor is substantial. For these reasons monitoring of the motors is important and - if done successfully – can result in saved capital both in maintenance costs and most importantly in downtime costs.

Several different monitoring methods have been applied to such motors in the past. The low rotating speed of the motors has produced challenges in finding a suitable and reliable

---

Power Transmission and Motion Control 2007 Edited by Dr D N Johnston and Professor A R Plummer
© With The Centre for Power Transmission and Motion Control

monitoring means. Vibration measurements at low speeds are not easy to implement as they are designed to measure vibrations at higher speeds of rotation.

Acoustic methods have also been tested, mainly SPM (Shock Pulse Method). This method is normally applied in monitoring rolling bearings. The advantage is that SPM can be also used at slow speeds to some extent. However it is rather sensitive to all disturbing sources. A hydraulic motor like the ones studied here has numerous separately moving parts and sliding surfaces that make it difficult to actually get accurate results with SPM. [4] Scheduled measurements have been undertaken on the hydraulic system every six months by the maintenance personnel.

The mill wanted to get a different view to the problem. It is possible that a better understanding of the motors' condition could be achieved by continuously measuring the hydraulics associated quantities. Constructing a life cycle model or establishing a prediction of operational reliability of a machine is becoming increasingly important in the process industry. Long term measurements are necessary in order to get sufficient data to make decisions concerning the possible life time of a machine. The aim of the research is the implementation of a life cycle model for the measured motors in the future.

2. STUDIED MOTORS

The motors studied here drive the pulp washers in a pulp mill. Low rotating speed and fluctuating high load are characteristics for this application. In a washer, the pulp is loaded between the washer drum and cylinder surrounding it. The pulp travels through different compartments as the washer drum rotates. These compartments are separated by sealing mechanisms. Finally the washed pulp –cake- is removed from the drum's surface. The structure of the compartments and the loading of the pulp results in periodically fluctuating friction and torque value, resulting in oscillations of working pressure. There are two motors for each washer drum and both are supplied by a same pump via a closed hydraulic circuit.

The studied motor is of radial the piston type with internal flow channels. The motors are of Marathon type manufactured by Hägglunds Drives, having a cam ring that piston driven cam rollers are acting against, producing an axial torsional moment. The rotating speed of the motors in a particular case was 2 rpm on average. Each motor has additional flushing flow trough their housing. This flushing function is needed for the motors that are used in applications with high loads and helps to control the temperature of the housing. This cooling flow makes the monitoring of the motor more complicated since additional flow exits the housing together with the internal leakage. The flushing can be stopped for a short period of time by manually turning a valve. The manufacturer of the motor states the maximum allowed leakage flow to be 5 litres per minute, although this value is of course highly dependant on pressure and viscosity circumstances. Next a short description of realised measurement system is given.

3. MEASUREMENT SYSTEM

The quantities that were included in the measurements were chosen firstly to gain as much information as possible and secondly to keep the measurement system as simple as possible. One design aspect was that the instrumentation had to be easily transferred and refitted from a motor to another. The cost of the measurement instrumentation was kept low in order to provide data at affordable cost. The measurements were carried out using two measuring units. One unit was moved between several motors while the other one was used to measure one motor continuously. This way it was possible to both get long term data and also to measure possible differences between motors. The data acquisition was centralized using a CAN-bus between the two measurement units. The system can be expanded by adding additional units. Different sensors were used for measuring the values that indicate the motor's performance and working point. The measured quantities are listed in Table 1.

Table 1. Used measurement channels in condition control of the motors.

Measurement location	Quantity	Unit
Work line in	Pressure	bar
Work line out	Pressure	bar
Leakage line	Pressure	bar
Work line in	Temperature	°C
Work line out	Temperature	°C
Leakage line	Temperature	°C
Flushing line	Temperature	°C
Return line	Contamination	ISO
Leakage line	Flow	l/min
Return line	Water activity	-----
Ambient	Temperature	°C

Continuous measurement was carried out for all channels except for the leakage line flow. The flow could not be measured continuously since the pressure of the motor housing increased close to the maximum value recommended by the manufacturer because of the pressure loss created by the flow sensor. Also the additional flushing flow had to be manually shut down during the actual leakage flow measurement. The particle contamination was monitored using new low-cost optical particle counters. The water activity of the oil was measured on one of the motors. Water activity is a number that describes the ability of the oil to keep water from separating from oil.

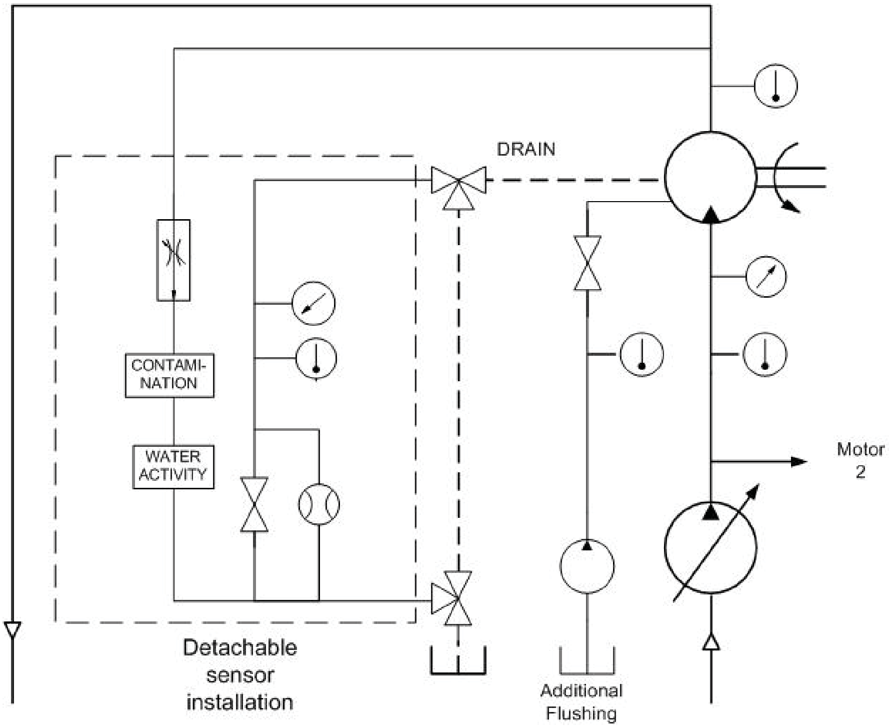

Figure 1. Sensor installation in condition monitoring of the motor.

Figure 1 shows the sensor arrangement used in the condition monitoring. The layout was developed and changed during the measurement period and all the sensors were not simultaneously attached.

The initial idea was to simply monitor the measured values and determine the trends since the motors were assumed to be working at constant conditions and loads. During the measurement it was soon discovered that conditions were changing so much that spotting the trends straight from the data could not be done reliably. Also the interactions between different quantities were found to be complex.

4. ANALYSING THE LEAKAGE FLOW OF THE MOTORS

There are different leakage flows in a hydraulic motor during its operation. Internal leakage is the term for leakage that occurs typically in the mechanism that divides the oil flow to the displacement devices that is the distributor valve. Leakage takes place between the main oil lines. External leakage on the other hand usually takes place at the piston – cylinder mechanism where the oil escapes to the motor housing trough gaps between piston and cylinder. [3] This external flow is vented from the motor casing via a separate drain line. The flow rate in the drain line can be measured with a flowmeter.

The amount of external leakage in the motor can be used to assess the condition of the motor. The clearances between pistons and cylinders increase as the mechanical parts loose material from their surfaces over time. The pressurised oil in the cylinders flows through the clearances between the pistons and cylinder surfaces to the motor housing. This produces a flow in the drain line, which can be measured by using a flow sensor.

The amount of the leakage flow depends on several factors. The pressure difference over the clearance is the most dominant component. The viscosity of the oil which is highly dependant on temperature is another factor that strongly determines the actual flow rate. The pressure difference- mainly the working pressure- is not constant. Also the temperature of the oil changes over time. This makes the comparison of flow rates difficult since the momentary conditions are seldom identical over time. Similar difficulties have been reported by Byington. [2] The third factor that considerably contributes to the amount of oil flowing through the cylinder clearances is the motion of the piston and thus the rotational speed of the motor. In this specific case the speeds of individual motors are constant and therefore the rotational speed of the motor makes the comparison simpler.

In this particular case, the additional flushing of the motor housing prevented continuous measurement of the actual leakage flow since the flushing had to be manually shut down during measurements. This led to the situation in which the data was even more rarely measured at comparable working conditions. As a result the obtained flow rate data was rather inconsistent. Therefore an index number was calculated to make it easier to compare the actual amount of the leakage at different pressure and temperature conditions.

The calculation for the number was based on following assumptions:

1) The flow in the piston-cylinder clearance is laminar. This assumption is well justified since the clearances are small and viscosity of the oil is high. Also the flow rate is very low.

2) The leakage takes place over a symmetric annular slit.

Knowing the actual construction and dimensions of the clearances is not necessary when performing the calculation. This can be stated when comparing similar components. The physical dimensions of the clearances are compressed into one coefficient that describes the possible changes in a motor's leakage characteristic. The formula of the flow in the symmetric annular slit was applied and the coefficient *L* was calculated as shown below:

$$Q_L = \frac{\pi \cdot d \cdot h^3}{12 \cdot \mu \cdot l} \cdot \Delta p \qquad (1)$$

where Q_L is leakage flow rate
d is the inner diameter of the slit
h is the radial clearance of the slit
l is the axial length of the slit
μ is the dynamic viscosity of the oil

The dynamic viscosity can be converted to kinematic viscosity:

$$\nu = \mu \cdot \rho \qquad (2)$$

where ν is the kinematic viscosity of the oil
ρ is the density of the oil

By combining the two formulae above and merging the constants that describe the physical dimensions of the slit to a constant L we get the following result:

$$L = \frac{Q_L \cdot \nu}{\Delta p} \qquad (3)$$

Theoretically, if each motor was identical the coefficient L would be the same for every motor atsimilar working conditions. Thus if the working conditions of two motors are the same but the coefficient L differs, we can assume that the physical characteristics of a particular motor have changed.

To be able to compare acquired results at different working conditions, a reference value has to be integrated into the calculations.

The reference point was chosen to represent typical values during pulp washers operation. The pressure value was $p_r = 200\ bar$ and the viscosity of the oil $\nu_r = 90\ cSt$ which corresponds to an oil temperature of $50°C$.

$$L_r = \frac{Q_L \cdot \left(\dfrac{\nu}{\nu_r} \right)}{\left(\dfrac{\Delta p}{\Delta p_r} \right)} \tag{4}$$

This formula was applied to the measurement data and relative leakage index L_r was calculated for the motors during several measurements. Some of the obtained results are presented below in Figure 2. As a comparison, the absolute leakage flow rate measurements are presented in Figure 3.

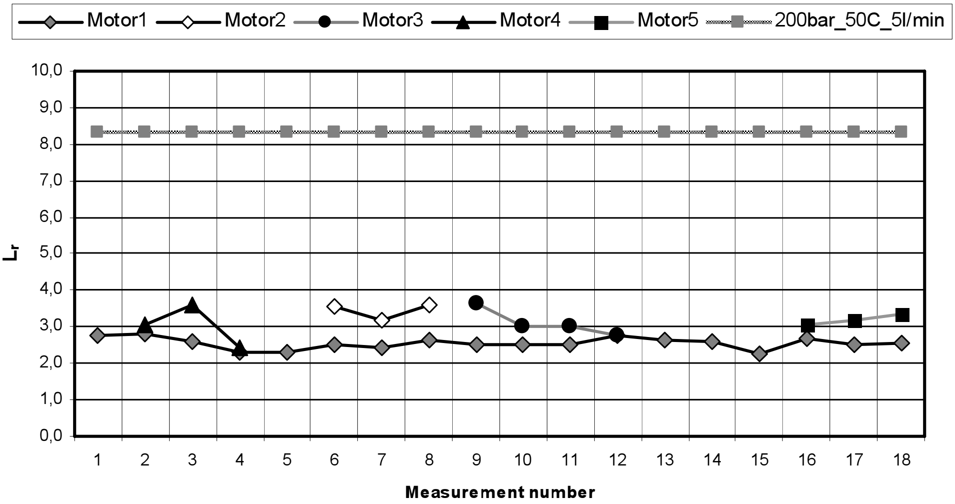

Figure 2. Relative leakage index at different measurement times.

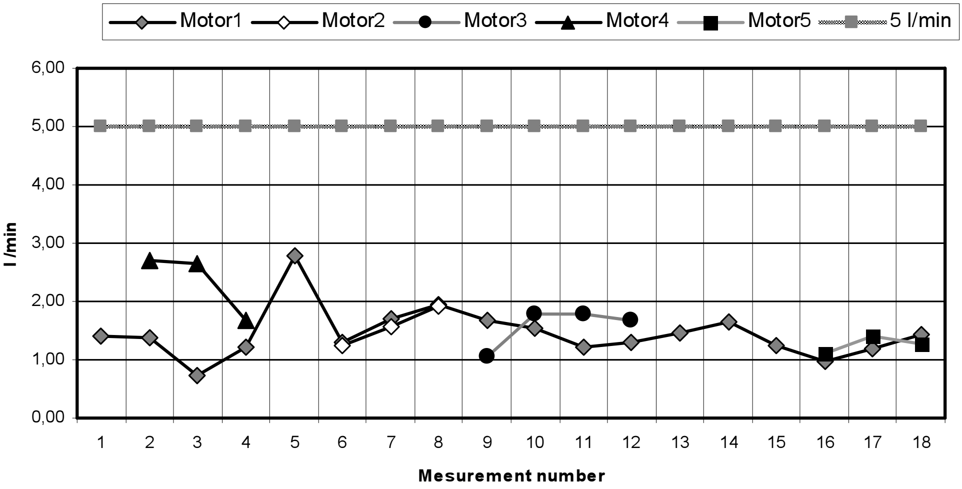

Figure 3. Absolute leakage flow rates.

Motor number 1 was measured continuously while the other measurement unit was circulated between the other motors. The measurements were executed over an 18 month period.

It can be seen, that the absolute flow rates (Fig.3) are more oscillatory compared to calculated numbers (Fig.2). Following the trends of leakage flow can be done more conveniently using the calculated values and setting alarm limits is easier because the index numbers L_r are more consistent. Of course the absolute flow values have to be also observed to make sure that calculated values are reliable. During the measurement period no significant changes or differences in leakage flow rates were observed.

5. FEASIBILITY STUDY OF THERMODYNAMIC MONITORING METHOD

A considerable amount of power is transmitted through the motors that drive the pulp washer drums. Ideally all hydraulic energy supplied to the motor is transferred to torque and angular velocity at the motor shaft. In reality some hydraulic energy is needed to overcome the mechanical and hydraulic losses that exist in the motor. Mechanical losses are created mainly by friction between moving parts. Hydraulic losses are generated mainly by the internal friction of the oil which is determined by viscosity and pressure losses. According to [3] following the hydromechanical losses are dominant in radial piston motors: Friction between piston and cylinder, rolling friction in piston roller - cam ring interaction, friction in radial shaft seals, pressure drop as the fluid flows through the motor and inertia losses of moving parts.

Heat is created due to the mechanical and hydraulic losses during operation. The amount of this dissipation power can be estimated through thermodynamic examination.[6] The efficiency of the motor is a strong indicator of its condition. By monitoring the dissipation power the over all efficiency level can be estimated. The main point of interest is in monitoring the amount of mechanical losses since they indicate the actual level of wear more accurately.

One noteworthy advantage of thermodynamic monitoring is that it can be realised with only little disturbance to the normal operation of a motor. That is important in this case, where the studied motors are in operation continuously. As a downside, the thermodynamic method is considered to be rather slow to react to malfunctions. In other words, some serious failure might have already taken place at the point where the increase of dissipated power will be observed. Thus this method is better suited for monitoring of wear that increases gradually during a longer period of time rather than for detection of acute faults.

In this paper the feasibility of a method for performing thermodynamic estimation of dissipation power is discussed for a particular application. Some interesting research has been done on this subject by Pomierski [5,6] A thermodynamic condition control system for a hydrostatic transmission has been developed. In this case the interest lies primarily at the motor as a component instead of the whole hydrostatic transmission. The ideas presented by Pomierski can also be implemented to the monitoring a single component with a few modifications. In Figure 4 the heat flows of the motor are shown. The interface for examination is chosen so that only the motor is located inside. The idea is that the possible changes in heat balance can be tracked down to the motor itself. Flow number 1 is the main input flow, 2 is the out coming main flow, 3 is the additional flushing of the housing. Flow 4 is the leakage line. There is also some heat flow Φ_∞ through the housing of the motor straight to the environment, namely the air surrounding the motor.

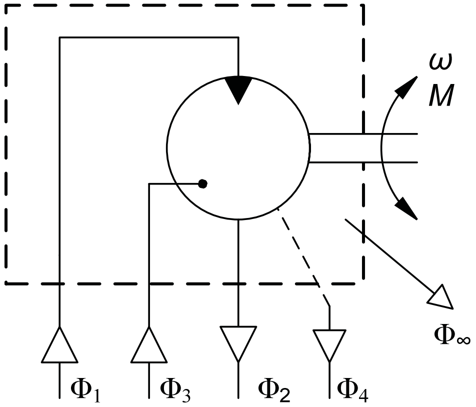

Figure 4. Heat flows during operation.

To calculate each oil-related heat flow component one has to obtain the mass flows and temperatures from all flow lines together with the specific heat capacity of the oil. The heat flow through the motor housing must be estimated based on the temperature of the environment and the surface area of the housing. Also the torque and angular velocity of the motor has to be known to rate the load of the motor.

Heat flow for each oil line can be calculated by using the mass flow and temperature of the oil and the energy equation for open systems found in literature. Research [7] has been undertaken on estimating the efficiency of water pumps using the thermodynamic approach. In this study it was noticed that the temperature rise caused by the change in enthalpy was very small. For incompressible liquids enthalpy is solely a function of temperature. Heat flows are defined by individual mass flows, their temperatures and the specific heat capacity of the oil.

The estimation of the mass flows in the working lines has to be done based on the rotational speed of the motor. This can be done by using the rotational speed and the displacement of the motor per radian. Flow sensors, such as turbine meters, can not be used in main lines since mounting them would mean that the whole process would have to be shut down. Also the pressure losses of such sensors would create significant reduction in efficiency over a long period of time.

The calculation of heat flux through the motor housing to environment has to be based on empiric perception since accurate evaluation of the coefficient for substitute heat penetration would require extensive laboratory tests which are not possible with the particular motors in this study. Because the aim is to make comparisons between similar motors, it is sufficient to use similar coefficients that are close enough to reality when calculating the heat flux to the environment.

The idea is that the difference between the combined heat flux going into the motor and the total heat flux leaving the motor is due the increase of thermal energy as the motor runs. This rise in thermal energy represents the amount of dissipated energy in motor.

The load acting on the motor has to be estimated in order to evaluate the current power level. Knowing the load level is crucial when comparing the amount of dissipation energy at different load conditions.

Load estimation has to be done based on the working pressure and rotational speed of the washer. More accurate result would be obtained by using a torque sensor to measure the actual load. In this case such a sensor can not be used. Therefore, the moment created by the motors has to be evaluated from pressure values of the work line.

6. CONCLUSIONS

In this paper a case study of condition monitoring of a low speed hydraulic motor in a pulp washer application has been presented. Two different approaches have been proposed. One is based on monitoring the level of motor external leakage flow. This method has been tested in reality and results are promising. A longer measurement time is required to verify the actual feasibility of the method.

The other method concentrates on monitoring heat currents over the motors. The aim is to evaluate the amount of dissipation energy during a motor's operation. Testing the thermodynamic method in practice is currently beginning and no real-life results exist so far. By recognising changes in either one of these indicators, drawing conclusions about the condition of the motors is more attainable.

In the future, the utilisation of both of these methods is studied in order to develop better tools for condition monitoring of low speed hydraulic motors.

7. REFERENCES

[1] Balawender, A., Pomierski, W. ”The Microprocessor System for Monitoring a Closed Circuit Hydrostatic Transmission”, Proceedings, The Fourth Scandinavian Conference on Fluid Power. Tampere. Finland. 1995.

[2] Byington,C.S., Watson,M., Edwards,D., Dunkin,B. ”In-Line Monitoring System For Hydraulic Pumps and Motors” , IEEE Aerospace Conference Proceedings, 2003.

[3] Dahlén, L., Olson,H. ”A Study of Lubricated Contacts in a Radial Piston Hydraulic Motor”, The Eight Scandinavian International Conference on Fluid Power, SICFP'03. Tampere. Finland. 2003.

[4] Miettinen, J. Anderson, P. “Acoustic Emission of Rolling Bearings Lubricated with Contaminated Grease”. Tribology International. Volume 33, Issue 11. November 2000.

[5] Pomierski, W. ”Condition Monitoring of Hydrostatic Transmission by Using the Volumetric Loss Method”. Proceedings, The Sixth Scandinavian International Conference on Fluid Power, SICFP'99. Tampere. Finland. 1999.

[6] Pomierski, W. “Condition Monitoring Thermodynamic Method for Testing Hydrostatic Transmissions in Non-Steady State of Working Conditions”. Proceedings, The Seventh Scandinavian International Conference on Fluid Power, SICFP'01. Linköping. Sweden. 2001.

[7] Thorne, E.W., Neal, A.N. “Pump Efficiency Testing by the Thermodynamic Method- An Independent View”, Proceedings of the Institution of Mechanical Engineers. Part A. Journal of power and energy, IMechE. 2000.

Fault Diagnosis of Pneumatic Systems

S FRITZ and **H MURRENHOFF**
Institute for Fluid Power Drives and Controls, RWTH-Aachen University, Aachen, Germany

ABSTRACT

Online-diagnosis can help to avoid costs by predictable maintenance, using the full lifespan of the pneumatic elements and easy-to-use localization of faults in complex systems in case of damage. Starting from an industrial application –a welding gun of an automobile manufacturer's welding facility– the paper will show the main forms of wear and their consequences to the pneumatic process. These faults are integrated into a simulation model of the whole pneumatic system based on the DSH*plus* simulation tool for fluid power systems. Mathematical functions use only the present sensor signals of the system control in specific time ranges and yield so-called features for the fault diagnosis. Classification of these calculated features to faults is done by a weighted feature-fault matrix.

1 INTRODUCTION

Pneumatic driven, electrical controlled systems are used throughout all fields of production and automation technology. Most of these systems run 24 hours a day in order to achieve maximum machine productivity. As a result, the failure of an individual component often leads to long, expensive downtimes for the whole device. So far, preventive maintenance work in fixed intervals has been carried out to replace all pneumatic elements which would cause a system breakdown if the element failed. The maintenance intervals are scheduled to be so short that many of the pneumatic components are far away from the end of their life cycles. Therefore condition monitoring can help here to decrease costs by time-effective usage of the built-in components. The complete range of sensor signals and drive

Power Transmission and Motion Control 2007 Edited by Dr D N Johnston and Professor A R Plummer
© With The Centre for Power Transmission and Motion Control

commands of the pneumatic cylinders and valves is available due to the electric control of the system. So these signals can additionally be used for the diagnosis of the elements. In addition, these local diagnosis results can be transferred to the central control. Here, a diagnosis routine can summarize the local diagnosis, perform a ‘global health-analysis’ of all pneumatic subsystems installed in the plant and provide information about the components’ conditions. Finally, this information can be used for a time and cost-efficient condition-based maintenance. The goal of the presented work is to built up a diagnosis method, which generates information about the components’ condition by using all available sensor signals. In addition, it has to be clarified if and how additional sensors can optionally increase the quality of the diagnosis. **Figure 1** gives a survey about the planned concept.

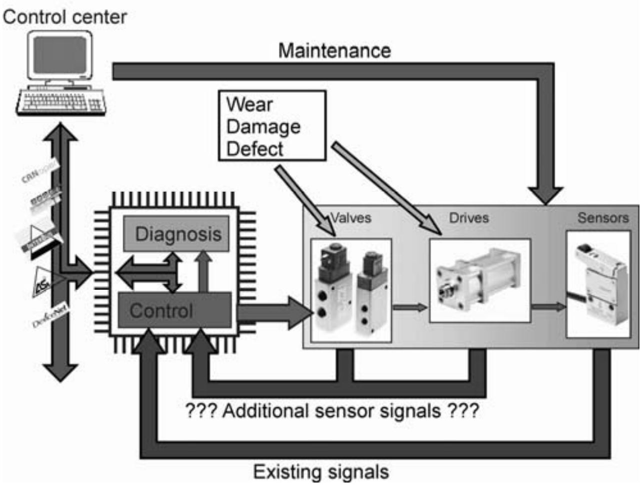

Figure 1: Integrating system diagnosis into the control concept

2 PNEUMATIC SYSTEM OF A WELDING GUN

A pneumatic driven welding gun of a vehicle body welding system (**Figure 2**) used throughout the automotive industry was selected in order to examine the functional capability of the developed diagnostic functions under practical conditions. The actuators in these welding guns are predominantly operated pneumatically. These systems are therefore characterized by a variety of different valves, cylinders and sensors as can be found in other pneumatic systems. To perform the welding task, the welding gun runs in different modes. First, the gun will be moved to the automobile body by the robot arm. Then the welding cylinder runs the prestroke to close the gun. After this, the balancing cylinder is activated and the welding stroke is closed for pressing the welding tips against the body sheets. When welding pressure is reached, the welding current flows –the body sheets are welded. After welding is completed the welding cylinder opens for welding stroke and the robot arm moves the gun to the next welding tip to perform. When all welding points are set, for instance after setting 20 welding points, the welding gun opens for prestroke and the welding process is finished.

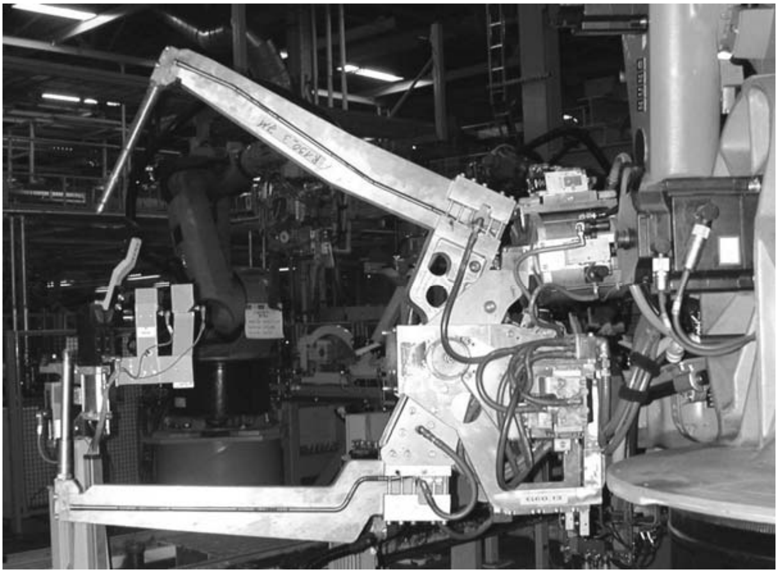

Figure 2: Welding system with welding guns (Tuenkers, Ford)

The circuit diagram in **Figure 3** shows the various types of valves and actuators which will be used in pneumatic driven welding guns. The welding cylinder is constructed as a four-position cylinder to perform prestroke and welding stroke. It is steered by two electrically controlled, pneumatically piloted 5/2-way valves for conducting high air flow rates. The position of the cylinder's prestroke-piston is checked by proximity switches that are capable of withstanding the electromagnetic field produced during welding. According to the case of operation and the gun's construction the welding stroke part of the cylinder is monitored by a differential pressure switch or two pressure sensors. This signal is used by the welding controller to conclude to the welding force for switching the welding current. Together with the valve to perform an outgoing of the welding stroke the balancer is activated. So, both cylinder chambers of the balancer are pressurized. This works like a flexible air cushion, if one welding tip is in contact with the sheet during the close motion of the welding stroke. Due to the absence of sensors in the balancers' circuit, the diagnosis focuses on the welding cylinder and its supporting valves.

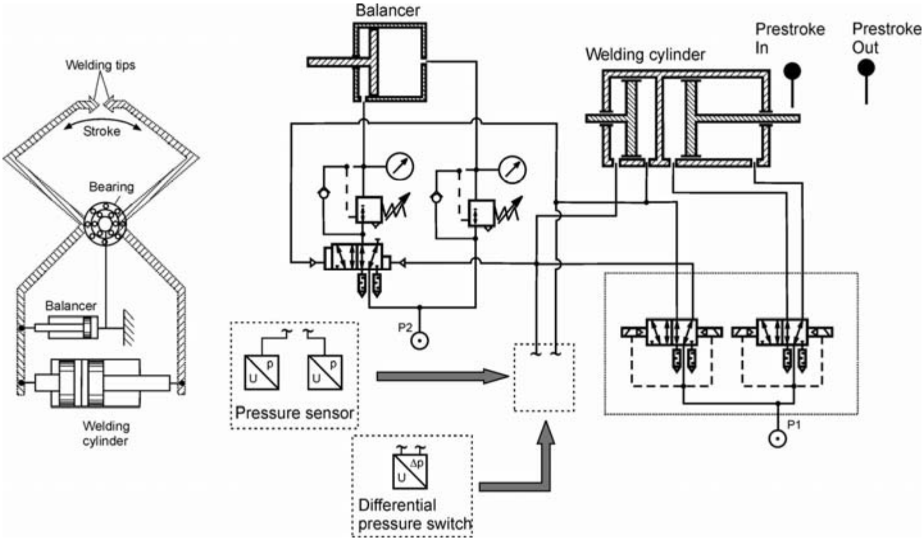

Figure 3: Scheme of a pneumatic driven welding gun and circuit diagram of the pneumatic components

3 FORMS OF WEAR AND THEIR CONSEQUENCES

In the industrial environment, wear of the actuators of a pneumatic driven welding gun are primarily caused by dirt –slag particles typically produced during welding operations- affecting the sealing and guide elements of the cylinder. A further reason for increasing wear in the pneumatic cylinders is the gun's changing orientation in space and thereby changing working loads of the cylinder. At least, the usage of non-specified lubricants leads to chemical decomposition of the used sealing material (2). The following **Figure 4** illustrates typical forms of wear, which can be detected on piston and housing. In general, faults and damage encountered in welding cylinders occur in the vicinity of the rod guide and seal, as well as the piston seals. This leads to a change of friction and an augmentation of leakage of the pneumatic drive. The change in frictional behavior and both internal and external leakage will be perceived by the service staff as a change in the run-out time of the piston. If the leakage rises to higher values, the differential pressure required for a proper welding operation no longer reaches the optimal value. Apart from the changes in these process variables, the system also consumes more compressed air. To prevent cost-intensive plant downtimes in case of an unexpected gun defect, the car manufacturers have to keep an identical welding gun in stock for a fast gun replacement. A diagnostic system would therefore also reduce the cost-intensive storage of spare parts to the bare essentials.

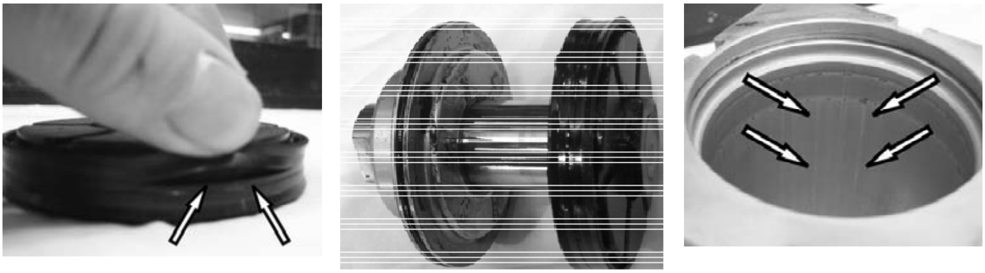

Figure 4: Typical wear of components of pneumatic cylinders taken out of the industrial service; left: Broken seal; middle: Contaminated lubricant by dirt right: Grooves in the cylinder's housing

Figure 5 depicts the main effects of wear at pneumatic cylinders and valves. If the welding tongs have been in storage for a longer period, the slide occasionally becomes jammed in the valve sleeve. Due to the 24-hour usage of the valves, increasing wear at the sealing elements is detected. Hence, a change in the friction level and an augmentation of leakage is expectable. Further damage occurs on the outside of the housing as the result of the robotically guided welding guns colliding during a test run. Furthermore, valve solenoids often break away, causing the component to fail as a result of the hostile industrial environment. Welding guns used in automated systems set the joining weld spots at a high rate. The impact of the welding tips on sheet metal gives rise to major stresses on the mechanical joining between cylinder pistons and welding tips. Increasing gradual wear in the bearings and articulated elements –referred to as play in the connected kinematics– detrimentally affects the process characteristics to a noticeable extent. Monitoring the pneumatic parameters and the electrical signals from the proximity switched can make an important contribution towards localizing such faults. A survey of owners of welding guns brought the certainty that wear occurring in the valves compared to wear in the cylinders is negligibly small. So, diagnosis of the pneumatic cylinder has to be the main goal.

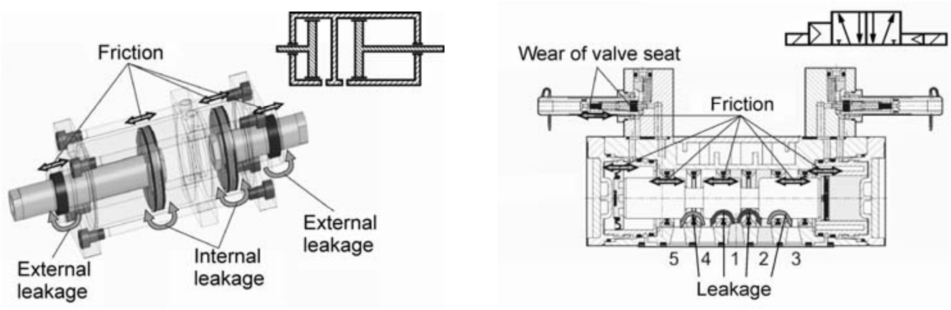

Figure 5: Forms of wear at the welding cylinder and the pneumatic 5/2-way valves

The most significant faults occurring in pneumatic systems are summarized in **Table 1** and **Table 2**. For example, increasing friction in the pneumatic actuator or the coupled mechanics leads to a higher pressure difference during motion of the cylinder's piston. Less pressure can be used for acceleration of the piston and the coupled mechanics. With respect to a fault-free state, the cycle time decreases. Depending on the integrated sensors these consequence of fault can be detected with more or less accuracy. Internal leakage leads to an augmentation of the cycle time, too. But there is also a decrease of the pressure difference during the welding procedure, while the piston of the welding stroke's part is in the maximum outgoing position. Here, proximity switches can be used to sense the additional time for piston's motion, while the pressure sensors can detect the pressure loss during welding. Friction and internal leakage are two different effects on stroke time and pressure built-up, which can be used for the exact diagnosis of the two faults. A diagnosis system with minimum sensor equipment like proximity switches is incapable of doing this exact fault recognition.

Table 1: Faults at the pneumatic cylinder and their consequence for the dynamics of the process which will be recognized by sensors

Component	Fault	Consequence	Effect	Available sensors/signals	Upgraded configuration of sensors (Optional)
Cylinder	Internal leakage	Increase of cycle time	Slower in-/outgoing of piston	Control pulse of valves	Displacement sensor
				Signal of proximity switch	
			Reduced pressure built-up	Signal of differential pressure switch	
				Signal of pressure sensor	
		Increase of air-consumption	Loss of air due to leakage		Volume flow sensor
		Reduced welding-pressure in front limit of travel	Persistent existence of leakage-massflow	Signal of differential pressure switch	
				Signal of pressure sensor	
	External leakage	Increased retraction-time	Leakage-massflow cannot be used for pressure build-up	Control pulse of valves	Displacement sensor
				Signal of proximity switch	
				Signal of differential pressure switch	
				Signal of pressure sensor	
		Decreased time for outgoing motion	Raised exhaust diameter in consequence of leakage	Control pulse of valves	Displacement sensor
				Signal of proximity switch	
				Signal of differential pressure switch	
				Signal of pressure sensor	
		Increased air-consumption while retracting	Loss of air due to leakage		Volume flow sensor
		Reduced holding-pressure in rear limit of travel	Persistent existence of leakage-massflow	Signal of differential pressure switch	
				Signal of pressure sensor	
	Fricition	Augmentation of cycle time	Slower in-/outgoing of piston	Control pulse of valves	Displacement sensor
				Signal of proximity switch	
			Max. pressure difference cannot be used for acceleration of piston	Signal of differential pressure switch	
				Signal of pressure sensor	
		Traversing at changed level of pressure-difference		Signal of pressure sensor	
	Play	Step in motion	Piston starts motion unloaded; then load is escalated		High-resolution pressure sensor signal
					Displacement sensor
					Proximity sensor with continous signal

Table 2: Faults at the pneumatic valve and their consequence for the dynamics of the process which will be recognized by sensors

Component	Fault	Consequence	Effect	Available sensors/signals	Upgraded configuration of sensors (Optional)
Valve	Leakage	Increase of cycle time	Loss of air due to leakage; lost air is missing for pressure build-up	Control pulse of valves	Displacement sensor
				Signal of proximity switch	High-resolution pressure sensor signal
				Signal of differential pressure switch	
		Increase of air-consumption			Volume flow sensor
	Friction	Increase of cycle time	Delay of pressurize and venting procedure in the cylinderchambers		High-resolution pressure sensor signal
					Proximity sensor with continous signal
	Wear of seat	Increased lift of anchor of magnet	Changed characteristic curve of current and voltage		High-resolution current and voltage signal

4 SIMULATION MODEL

A simulation model of the welding gun's pneumatic system can be seen in **Figure 6**. It is created on the software platform DSH*plus* (1) and will be used for the investigation of the developed diagnosis methods (see 5). Here, friction will be pictured by an external, velocity dependent force. Internal and external leakage of the welding cylinder will be modeled by adjustable restrictors. Play in the force line between the piston and the coupled mass is realized by a special element. All pneumatic elements of the real welding gun like four-position cylinder and 5/2-way valve are considered. Elements for the proximity switch and the differential pressure switch were built. Last but not least, a controller was set up, to emulate the functionality of a welding gun controller under real conditions. With respect to the different designs of the welding guns' pneumatic system, pressure sensors are integrated, too. A diagnosis module based upon the software MATLAB/Simulink generates an online diagnosis state using only the sensor signals and steering commands for the valves, which are used by the welding controller. Due to the alternative usage of pressure sensors instead of a differential pressure switch the diagnosis module can utilize their signals for diagnosis, too.

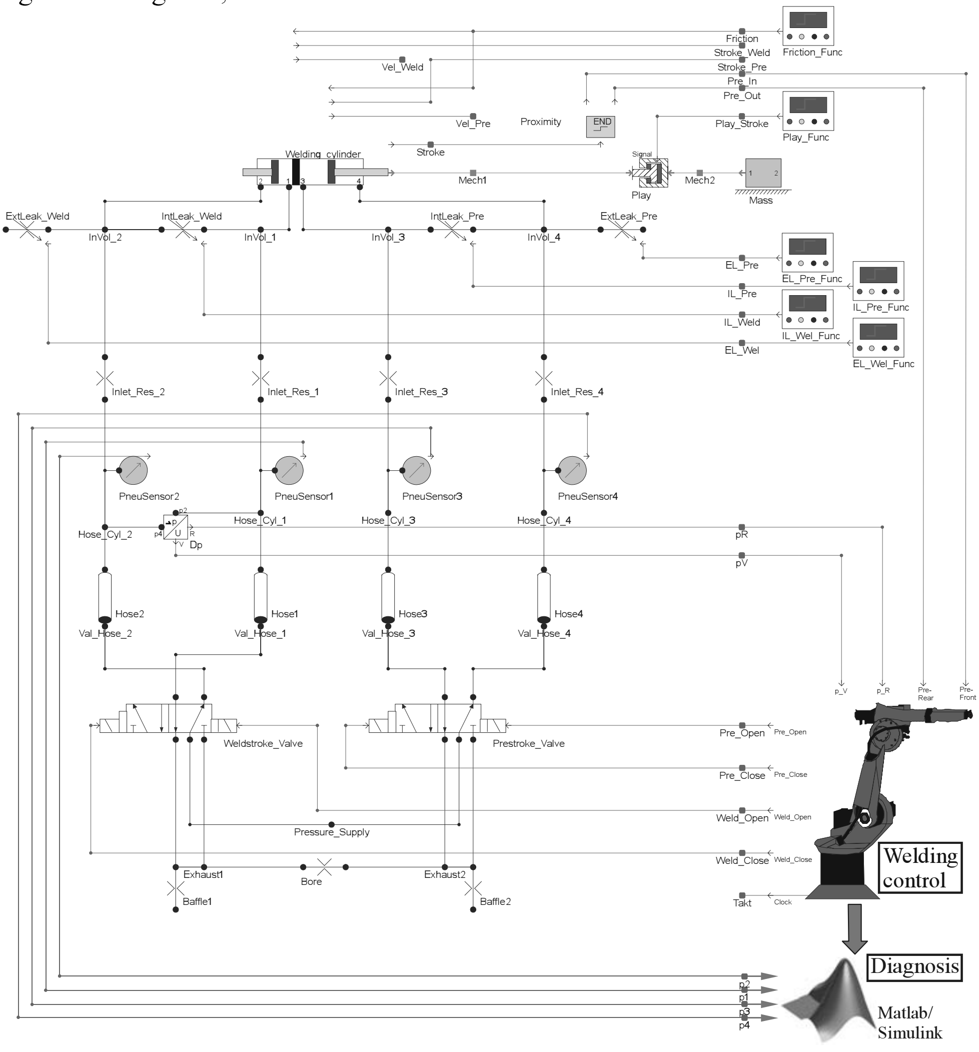
Friction
Friction_Func
Stroke_Weld
Stroke_Pre
Vel_Weld
Pre_In
Pre_Out
Vel_Pre
Proximity
END
Play_Stroke
Play_Func
Stroke
Welding_cylinder
2
1
3
4
Mech1
Signal
Play
Mech2
1
2
Mass
ExtLeak_Weld
IntLeak_Weld
IntLeak_Pre
ExtLeak_Pre
InVol_2
InVol_1
InVol_3
InVol_4
EL_Pre
EL_Pre_Func
IL_Pre
IL_Pre_Func
IL_Weld
IL_Wel_Func
EL_Wel
EL_Wel_Func
Inlet_Res_2
Inlet_Res_1
Inlet_Res_3
Inlet_Res_4
PneuSensor2
PneuSensor1
PneuSensor3
PneuSensor4
p2
p4
p
U
R
V
Dp
Hose_Cyl_2
Hose_Cyl_1
Hose_Cyl_3
Hose_Cyl_4
pR
pV
Hose2
Hose1
Hose3
Hose4
Val_Hose_2
Val_Hose_1
Val_Hose_3
Val_Hose_4
p_V
p_R
Pre-Rear
Pre-Front
Weldstroke_Valve
Prestroke_Valve
Pre_Open
Pre_Open
Pre_Close
Pre_Close
Weld_Open
Weld_Open
Pressure_Supply
Weld_Close
Weld_Close
Welding control
Exhaust1
Bore
Exhaust2
Baffle1
Baffle2
Takt
Clock
Diagnosis
p2
p1
p3
p4
Matlab/ Simulink

Figure 6: DSH*plus* simulation model of the pneumatic driven welding gun

5 MATHEMATICAL METHODS FOR FAULT DIAGNOSIS

First step in a signal based online condition monitoring (OCM) is the definition of features from the measured sensor signals. The mathematical process of feature generation describes an information compressing method. Here, sensor signals will be linked and calculated together in a way to get fault-dependent information. **Figure** 7 shows the characteristics of the valve signals (Close welding gun / Open welding gun) and the differential pressure switch (Welding pressure reached / Open pressure reached) which will be used for feature generation. The clocked characteristics of the chamber pressures are shown, too. During specific time ranges, these signals will be additionally used for feature generation.

5.1 Features

For example, the times for piston's running out Δt_{Out} and running in Δt_{In} are defined as the time difference between the rising edge of the valve steering signal and the rising edge of the differential pressure switch signal. Referenced to their values in the fault free state, these leads to the features F_1 and F_2.

$$F_1 = \frac{\Delta t_{Out}}{\Delta t_{Out}\big|_{Ref}} \qquad F_2 = \frac{\Delta t_{In}}{\Delta t_{In}\big|_{Ref}}$$

Because of the clocked scanning of the signals by the time T, the temporal resolution of the above defined features is very bad. Therefore additional features with less dependency on time are needed. Due to the moving piston in the housing the chamber pressures change dynamically (5). The characteristics of these chamber pressures are used for detecting deviations due to faults. So, the features F_3 and F_5 are defined, which describes the minimum pressure during the piston's out-run (F_3) and in-run (F_5). The dynamics of the piston depends on the chamber pressures driving it. Hence, the features F_4 and F_6 are formulated, which define the pressure differences when the minimum chamber pressures are reached.

$$F_3 = \frac{p_{1;Out,Min}}{p_{1;Out,Min}\big|_{Ref}} \qquad F_4 = \frac{\Delta p_{p1;Out,Min}}{\Delta p_{p1;Out,Min}\big|_{Ref}}$$

$$F_5 = \frac{p_{2;In,Min}}{p_{2;In,Min}\big|_{Ref}} \qquad F_6 = \frac{\Delta p_{p2;In,Min}}{\Delta p_{p2;In,Min}\big|_{Ref}}$$

According to the piston dynamics the features F_7 and F_8 stand for the time between the controls' steering signal and the minimum chamber pressure.

$$F_7 = \frac{\Delta t_{Out,2}}{\Delta t_{Out,2}\big|_{Ref}} \qquad F_8 = \frac{\Delta t_{In,2}}{\Delta t_{In,2}\big|_{Ref}}$$

When the piston is completely out or in four additional features can be obtained by evaluating the averaged pressures in the cylinder chambers. This leads to the features F_9 to F_{10}:

$$F_9 = \frac{p_{1,Avg}}{p_{1,Avg}\big|_{Ref}} = \frac{\dfrac{\sum_n T \cdot p_1}{\Delta t_{Wel}}}{\left.\dfrac{\sum_n T \cdot p_1}{\Delta t_{Wel}}\right|_{Ref}} \qquad F_{10} = \frac{\Delta p_{Wel,Avg}}{\Delta p_{Wel,Avg}\big|_{Ref}} = \frac{\dfrac{\sum_n T \cdot (p_2 - p_1)}{\Delta t_{Wel}}}{\left.\dfrac{\sum_n T \cdot (p_2 - p_1)}{\Delta t_{Wel}}\right|_{Ref}}$$

$$F_{11} = \frac{p_{2,Avg}}{p_{2,Avg}\big|_{Ref}} = \frac{\dfrac{\sum_n T \cdot p_2}{\Delta t_{Motion}}}{\left.\dfrac{\sum_n T \cdot p_2}{\Delta t_{Motion}}\right|_{Ref}} \qquad F_{12} = \frac{\Delta p_{Motion,Avg}}{\Delta p_{Motion,Avg}\big|_{Ref}} = \frac{\dfrac{\sum_n T \cdot (p_2 - p_1)}{\Delta t_{Motion}}}{\left.\dfrac{\sum_n T \cdot (p_2 - p_1)}{\Delta t_{Motion}}\right|_{Ref}}$$

Finally, four features (F_{13} to F_{16}) are created, which stand for the time averaged pressure differences and pressure ratios during the motion of the piston. The hatched area in Figure 7 depicts this. Referenced these values to the fault-free state yields:

$$F_{13} = \frac{Rp_{Out,Avg}}{Rp_{Out,Avg}\big|_{Ref}} \qquad F_{14} = \frac{\Delta p_{Out,Avg}}{\Delta p_{Out,Avg}\big|_{Ref}}$$

$$F_{15} = \frac{Rp_{In,Avg}}{Rp_{In,Avg}\big|_{Ref}} \qquad F_{16} = \frac{\Delta p_{In,Avg}}{\Delta p_{In,Avg}\big|_{Ref}}$$

Written in vector form leads to:

$$\vec{F} = \left[F_1, F_2, \ldots, F_N\right]^T \text{ with } N = 16$$

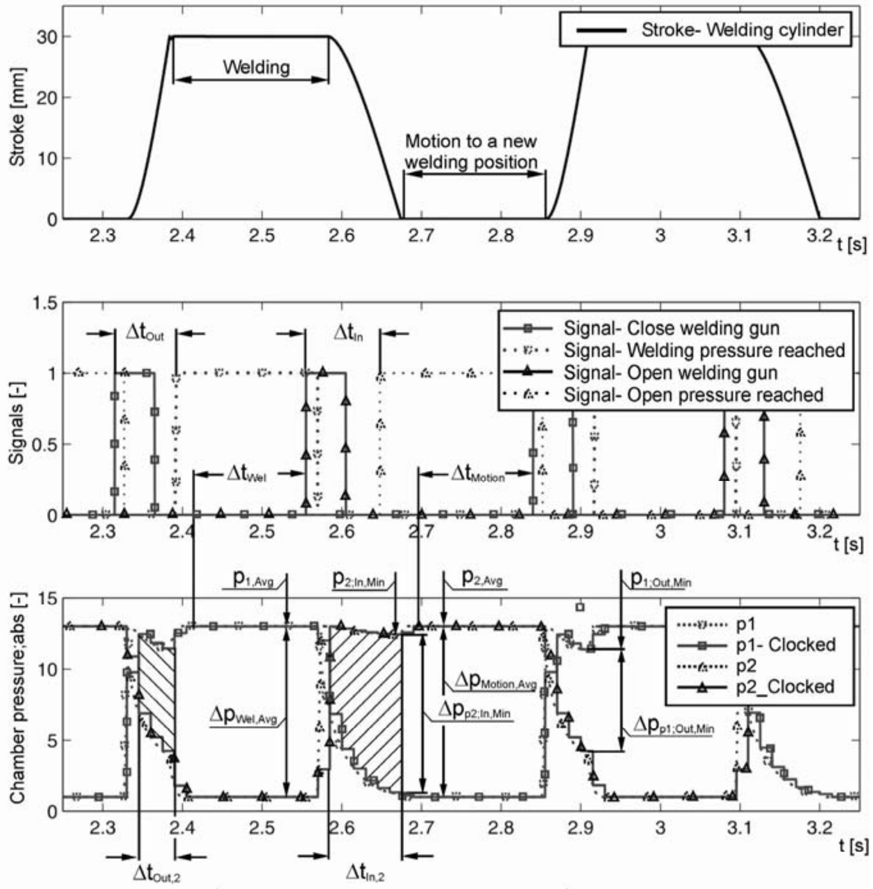

$$Rp_{Out,Avg} = \frac{\sum_{n} T\cdot\left(p_1 / p_2\right)\Big|_{\Delta t_{Out,2}}}{\Delta t_{Out,2}} \qquad Rp_{In,Avg} = \frac{\sum_{n} T\cdot\left(p_2 / p_1\right)\Big|_{\Delta t_{In,2}}}{\Delta t_{In,2}}$$

$$\Delta p_{Out,Avg} = \frac{\sum_{n} T\cdot\left(p_1 - p_2\right)\Big|_{\Delta t_{Out,2}}}{\Delta t_{Out,2}} \qquad \Delta p_{In,Avg} = \frac{\sum_{n} T\cdot\left(p_2 - p_1\right)\Big|_{\Delta t_{In,2}}}{\Delta t_{In,2}}$$

Figure 7: Time differences and chamber pressures for feature generation

5.2 Classification

One of the main problems in OCM of technical systems is the classification process. In general, classification describes the allocation of the generated features to system affecting faults. Here, neural networks are applied in practical examples (4), (5), (8). Other classification methods (Bayes,…) use the statistical distribution of the generated features for fault detection. Analytical methods like Support-Vector-Machines (SVM) interpret the feature vector as a point in a n-dimensional fault-space (3).

One goal of the work described here is to realize a system which runs parallel to the robot's welding control with low numerical effort. It has to be simple in use and has to generate a current health-state of the system in a harsh industrial environment. A method to classify the online calculated features to faults is given with modified polynomial-classifiers (6). This method has advantages due to the simple usage, the low numerical effort and the possibility to model complex physical relationships with respect to the order *o* of the used polynomials. In the frame of this work this algorithm is not only used to detect the fault in general (i.e. internal Leakage, Friction,…), but to generate an ongoing fault-condition value.

With respect to the main faults present in a pneumatic system and the coupled mechanics (f_1: External Leakage, f_2: Internal leakage, f_3: Friction) the mathematical model for polynomial order *o* = 1 and *o* = 2 reads as follows:

- First order; *o* = 1: $[f_1, f_2, f_3]^T = A_{ij;1} \cdot [1, F_1, F_2, \ldots, F_N]$ with $N = 16$

- Second order; *o* = 2: $[f_1, f_2, f_3]^T = A_{ij;2} \cdot [1, F_1, F_2, \ldots, F_N, F_1^2, F_1F_2, \ldots, F_N^2]$ with $N = 16$

The matrix A_{ij} is called 'feature-fault matrix', according to the relationship between a given feature pattern $\vec{F}$ and the system affecting faults $\vec{f}$. In a first approach, these two polynomials are tested for feature-fault classification in pneumatic systems. Therefore it is necessary to train the matrix A_{ij} with a number *n* of well-known fault-feature combinations. Here, more fault-feature combinations may be used than for the solution of A_{ij} are needed. In practice, a least-squares algorithm is used to determine the polynomial coefficients with minimum error.

$$G = \frac{1}{n}\left(\vec{f} - A_{ij}\vec{F}\right)^T \cdot \left(\vec{f} - A_{ij}\vec{F}\right) \rightarrow Min$$

5.3 Results of classification

The following **Figure 8** and **Figure 9** depict the results of the classification process via the polynomial classifier. The process shown here consists of 20 welding points (20 times out- and in-going of the cylinder's piston) and is adapted from a welding procedure of the underbody sheet metal. To get a significant diagnosis result, the faults were activated in the simulation model stepwise. In the real industrial environment, damages occur much slower. In the time range between 0 and 3,3 s fault-free state prevails. This time range is used for referencing the feature equations (Chapter 5.1). After the fault free state, a second range (3,3 to 6,6 s) with 50% fault effect and a full developed fault range (6,6 s till end) are added. As shown in Figure 8, the detected fault follows the adjusted wear-phenomena in a satisfactory manner. Only little classification errors (<10%) at high fault-rate can be seen. One can notice that, shortly after the faults are changed stepwise, wrong classification results are identified or classification errors increase. According to the non-fully defined feature vector in case of a stepwise change of the fault, the classification-error increases. After one complete stroke the feature vector is completely filled with information of the actual fault state. Hence, classification errors decrease and detected fault is in common with the pre-set damage. As can be seen, the 1st order classifier is less adequate to detect 'pure' low internal leakage. Here, features became predominant, which are not linear-dependent to the proposed faults.

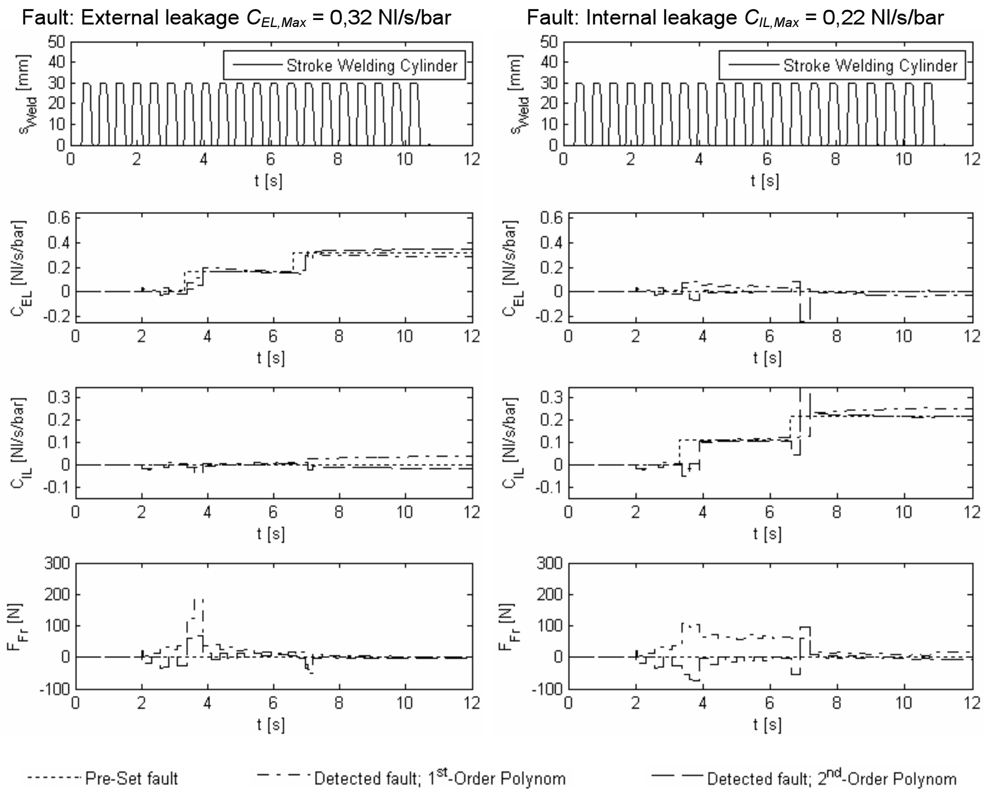
Fault: External leakage $C_{EL,Max}$ = 0,32 Nl/s/bar

Fault: Internal leakage $C_{IL,Max}$ = 0,22 Nl/s/bar

Figure 8: Classification results of the faults 'external leakage' and 'internal leakage'

Figure 9 depicts the classification results for an increasing additional load in form of friction in the cylinder and the coupled mechanics. Here, classification error in friction is less than 8%. The general characteristics of the adjusted faults were detected well. Additionally, the wear effects external leakage, internal leakage and friction are successively brought into the simulation (Figure 9, right). As can be seen, the method is able to differentiate between the different faults and provide the operator a permanent actualized characteristic of the system's health state.

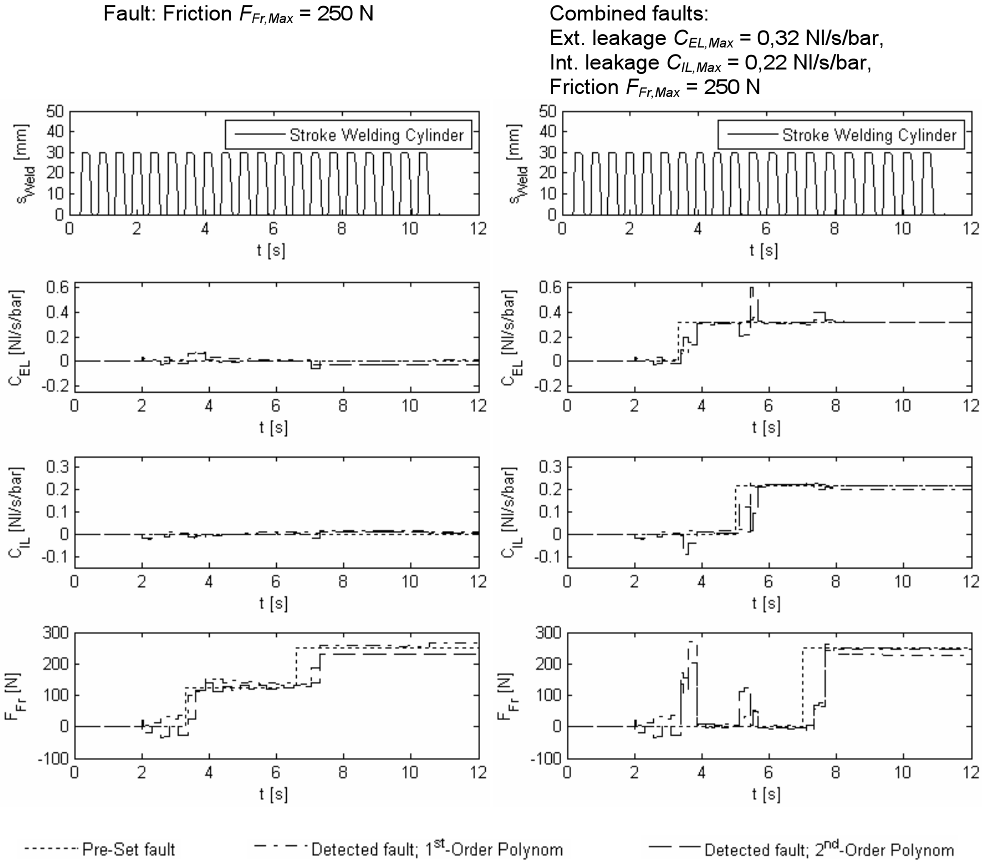

Fault: Friction $F_{Fr,Max}$ = 250 N

Combined faults:
Ext. leakage $C_{EL,Max}$ = 0,32 Nl/s/bar,
Int. leakage $C_{IL,Max}$ = 0,22 Nl/s/bar,
Friction $F_{Fr,Max}$ = 250 N

Figure 9: Classification results of the fault 'friction' and a combined fault situation

6 CONCLUSIONS

On-off pneumatic systems play an important role in the wide range of fully automated production technology. Most of these air driven systems were involved in cost intensive processes, like the above presented welding gun of an automobile manufacturer. Today, preventive maintenance is state-of-the-art. A real online diagnosis system for switching pneumatic devices is still missing. Here, the signal based condition monitoring system described above represents a first approach. In a first step to occurring fault in the pneumatic system of a welding gun were examined and transferred to a simulation model. First results were used to train the feature-fault matrix A_{ij} of the polynomial classifier. Both first order and second order classification polynomials have shown good agreement between the adjusted damage and the detected faults. Nevertheless, the results of the 2nd order classifier are more precise. It has to be taken into account the low quality of the clocked sensor signals and the absence of a continuous position sensor. The verification of the proposed algorithm with test stand results and real process data will be the next step in the research project.

ACKNOWLEDGEMENT

The work described in this article is performed during the research project "Diagnostic potential in pneumatic systems" commissioned by the Research Committee for Mechanical Engineering (*Forschungskuratorium Maschinenbau e.V.*) and the Research Foundation for Fluid Technology (*Forschungsfonds Fluidtechnik*) within the VDMA (*Verband Deutscher Maschinen- und Anlagenbau* - German Engineering Federation). Thanks go to the participating companies and their representatives in the industrial working group accompanying the project for their support.

REFERENCES

(1)	Anon.	DSHplus Handbook, Fluidon GmbH, Aachen, Germany, 2004
(2)	Anon.	Schadensatlas- Dichtsysteme für fluidtechnische Anwendungen, Verband Deutscher Maschinen- und Anlagenbau, Frankfurt, Germany, 2002
(3)	Chen, H. X. Chua, P. S. K. Lim, G. H.	Feature Extraction, Optimization and Classification by Second Generation Wavelet and Support Vector Machine for Fault Diagnosis of Water Hydraulic Power Systems, International Journal of Fluid Power 7, No. 2, 39-52, 2006
(4)	Crowther, W. J. Edge, K. A. Burrows, C. R. Atkinson, R. M. Woollons, D. J.	Fault diagnosis of a hydraulic actuator circuit using neural networks - an output vector space classification approach, Proc IMechE, Part 1, vol 212, 57-68, 1998
(5)	Isermann, R.	Fault-Diagnosis Systems, Springer-Verlag, Berlin, Germany, 2006
(6)	Murrenhoff, H.	Grundlagen der Fluidtechnik, Teil 2: Pneumatik, 2nd edition, RWTH Aachen, Shaker Verlag, 2006
(7)	Schürmann, J.	Polynomklassifikatoren für die Zeichenerkennung, Oldenbourg Verlag, Munich, Germany, 1977
(8)	Vidqvist, V. Hiirsalmi, M.	Data Mining Enhancement in Model Based Classifiers of a Hydraulic Cylinder Drive, Proceedings of 4th FPNI-Phd Symposium, Sarasota, 2006

Self-Organising Maps for Change Detection in Hydraulic Systems

A. Zachrison and M. Sethson
Department of Management and Engineering, Linköping University, Sweden

ABSTRACT

Not only system builders, but also component manufacturers are interested in supplying the customer with a condition monitoring system. However, the component manufacturer has the potential problem that he/she does not know how and in what system the component will be used. Thus, only detection of unknown faults/system changes becomes viable in the general case.

This paper exemplifies the combined use of a sub-set of a-priori system knowledge with a data driven, feature based neural network, viz. the self-organising map.

1 INTRODUCTION

In this paper, we take on the view of the valve manufacturer and his/her desire to deliver a condition monitoring aid. Assuming no knowledge of the hydraulic system, how might a data driven approach to condition monitoring look and what performance can be achieved? Further, such an assumption makes it hard to draw any specific conclusions about what fault has occurred. Thus, the focus is on detection of changes in the component and system, rather than the combined task of detection and identification.

The detection of unknown faults in a pneumatic system using self-organising maps, SOMs, is discussed in [1] and a similar discussion of known faults can be found in [2]. The first paper discusses condition monitoring from a component manufacturer's, the cylinder, point of view. This manufacturer does not know how the cylinder is to be used and under what conditions, but still wants to deliver a condition monitoring aid. The second paper adds the discussion about classification/identification of certain faults in the system, while retaining the ability to detect unknown faults or changes to the system.

1.1 Approaches to change detection

In this work, the focus is on detection of unknown faults or system changes. Two approaches to this problem will be discussed, together with their respective advantages and disadvantages. The first approach looks at the sampled data in the time domain and filters out samples with a value outside a normal envelope. Thus, using this approach, samples where a large

Power Transmission and Motion Control 2007 Edited by Dr D N Johnston and Professor A R Plummer
© With The Centre for Power Transmission and Motion Control

step is taken in the signals will not be used. However, this has proven to be useful to find certain faults. This method, apart from the addition of the extra filtering step, is similar to the one used in [1].

The second approach is to estimate the parameters of a standard linear "confection" model [3], an ARX model, and use these estimated parameters as features. It can be argued, see section 4.5, that a reasonable choice of ARX model can be made, even though the valve manufacturer does not know anything about the complete and final system.

The paper is structured as follows. The experimental system is described in section 2. Subsequent sections contain a brief introduction to SOMs (section 3) and different ways to use the SOM for condition monitoring are discussed in section 4, where the main ideas in this work are also presented. In section 5 the results are presented and a discussion and conclusion follow in sections 6 and 7.

2 TEST SYSTEM AND DATA

2.1 Test setup

A hydraulic position servo, see figure 1, is used as the test object. A servo valve is used to control the symmetric cylinder. Three position sensors are used, one measuring the system pressure and the other two the chamber pressures. A linear position sensor is mounted in the cylinder. The servo valve also measures the spool position.

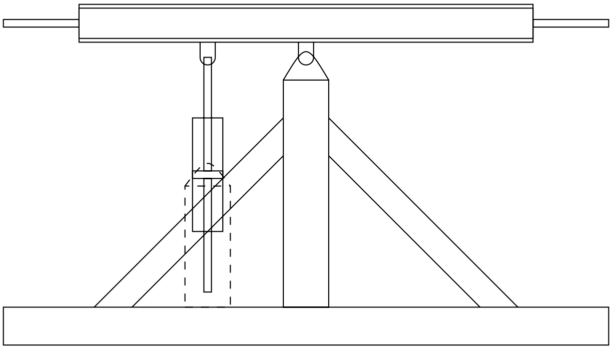

Figure 1: The test system. The cylinder support is shown by dashed lines.

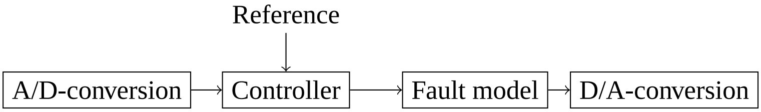

Figure 2: The structure of the implementation of the control and fault simulation. The control signal from the controller is passed through a fault model, where a possible offset to and filtering of the signal is applied.

Two symptoms of faults have been studied in this work: an offset of the spool and a decrease in the bandwidth of the valve. These faults have been applied between the output from the controller and the D/A-converter, see figure 2. The simulated faults and the corresponding fault levels are listed in table 1. The offset is calculated as a percentage of the maximum valve opening (control signal for the simulated fault) and for the bandwidth the percentage of the degradation of bandwidth of the valve is shown. Both single faults and double faults are simulated in the test rig. Thus, all possible 25 combinations from table 1 are used for the study.

Table 1: The fault modes and the fault levels used.

Fault	Fault levels				
Offset in spool	0%	0.5%	1%	1.5%	2%
Bandwidth	0%	5 %	10%	15%	20 %

The decrease in the bandwidth of the valve is simulated by letting the command signal, for the faulty cases, pass through a low pass filter with the cut-off frequency set to $\omega_{v,X\%} = (1-X\%)\omega_{v,n}$, with X% taken from table 1. The nominal bandwidth of the valve is here denoted $\omega_{v,n}$.

The test system itself, neglecting the dynamics of the much (7–10 times) faster servo valve, has a bandwidth of

$$\omega_h = \sqrt{\frac{4\beta_e A_p^2}{V_t M_t}} \approx 79.9\,\text{rad/s} \approx 12.8\,\text{Hz} \tag{1}$$

This also assumes a centred piston (equal chamber volumes). β_e is the effective bulk modulus, A_p the piston area, V_t the total chamber volume, and M_t the total mass load of the system.

2.2 Training data

As the work is performed from the point of view of the valve manufacturer, only the signals that could be available in the valve have been used, that is the command signal, $x_{v,ref}$, the spool position, x_v, and the load pressure, p_L. Thus, the training data for the time series monitoring, see section 4.4, is one of the following three sets:

$$[x_v, p_L, x_{v,ref}] \tag{2}$$

$$[x_{v,ref}, p_L] \tag{3}$$

$$[x_{v,ref}, x_v] \tag{4}$$

The performance of all sets of features is evaluated in section 5.1. The evaluations of the effect of different filtering levels and scaling of the features in (2)– (4) are not discussed.

In the second approach, the combination of SOM and an ARX model, only the second set, (3), has been used. However, here the parameters of an ARX model have been estimated and then the estimated parameters, (5), are used as the training features.

$$[a_1, a_2, b_1, b_2] \tag{5}$$

The ARX-model is defined as, [3]:

$$A(q)p_L(t) = B(q)x_{v,ref}(t-n_k)+e(t) \tag{6}$$

$$\text{with } A(q) = 1+a_1q^{-1}+a_2q^{-2}+\ldots+a_{n_a}q^{-n_a} \tag{7}$$

$$B(q) = b_1+b_2q^{-1}+\ldots+b_{n_b}q^{-n_b} \tag{8}$$

with n_a and n_b being the length of the polynomials, n_k the delay between $x_{v,ref}$ and p_L, and $e(t)$ white noise.

In both approaches, the choice of what measured signals to use will greatly influence what faults can be detected. For instance, in the case of (3), it will hardly be possible to depict that a fault has occurred specifically in the valve and not in the system.

3 SELF-ORGANISING MAPS

Self-organising (feature) maps, SOMs, are a special kind of neural network first presented by Kohonen; see for instance [4, 5].

The SOM works by approximating the probability distribution of the input vectors by its neurons' weight vectors. As such, it accumulates knowledge during training and this knowledge is distributed in the same areas as the input vectors. This allows the SOM implementation to maintain a record of well-known regions in the input domain, and distinguish these from unknown, novel inputs.

In [6] two ways of using the SOM for condition monitoring are discussed: the quantisation error method, q.e., and the forbidden area method. The quantisation error is a measure of the misfit of the input vector compared to the stored knowledge in the SOM and is primarily used when the SOM is trained using only non-faulty data. In the forbidden area method, faulty data are included in the training set; these faulty data will create one or more areas in the SOM lattice that corresponds to these faults. By keeping track of the winning neuron in the lattice, this can be used to classify the current state as faulty.

The inherent suitability for parallelisation of the SOM-algorithm has been used by e.g. [7] and [8]. This property allows an easy distributed implementation or a direct implementation in for example an FPGA.[1]

3.1 SOM algorithm

The use of the SOM can generally be divided into three phases, of which the last two are used while training the SOM. These three phases (described by Haykin [9]) are: the competitive process, the cooperative process and the adaptive process. The first and last steps are illustrated in the following sections.

3.1.1 Competitive process

The output layer of the SOM is a competitive layer, where the best matching (winning) neuron is selected. The competitive process consists of

$$i(\vec{x}) = \arg\min_j \|\vec{x}-\vec{w}_j\|, \qquad j = 1,2,\ldots l \tag{9}$$

---

[1] Field Programmable Gate Array

where $\vec{x}$ is the training vector to be matched, $\vec{w}_j$ the weight vector of neuron j, and l the number of neurons in the lattice. The winning (best matching) neuron is denoted i.

3.1.2 Adaptive process

The standard learning rule is

$$\vec{w}_j(n+1) = \vec{w}_j(n) + \eta(n)h_{j,i}(n)(\vec{x} - \vec{w}_j(n)) \tag{10}$$

where n is the stimuli iteration, $\eta(n)$ the time-dependent learning-rate parameter, and $h_{j,i}(n)$ the neighbourhood function, often chosen as a Gaussian function that shrinks as time passes. The learning-rate parameter will make the neurons learn fast in the beginning, when the lattice is untrained; at the same time, the neurons closer to the best matching neuron will learn more compared to the rest. The winning neuron, i, will always have $h_{j,i}(n) \equiv 1$.

4 CONDITION MONITORING

4.1 Classification based monitoring

One problem in condition monitoring with classification based algorithms is when the decision areas overlap. A fictitious illustration is found in Figure 3. Two choices exist, either try to overcome the problem or try to accept it. To overcome the problem, a careful study and then selection of features is needed; however, it is still possible that the problem can not be fully coped with. The second alternative, to accept the problem also requires a fundamental knowledge of the application domain; otherwise it is hardly possible to motivate such a choice. This choice might be reasonable if the system is expected to be working in a cycle that will introduce significant differences between the two working states during parts of the cycle. Then it could be argued that given knowledge of this, the repeatedly mis-/unclassified points can be disregarded. In the case of unknown faults, this problem is avoided as no classification can be performed. In some cases, another solution might be to move to the use of support vector machines, [10], as they can improve the separability of classes.

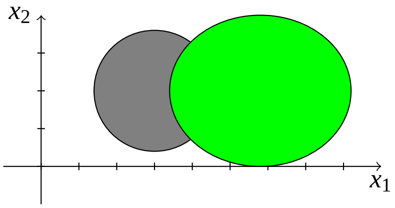

Figure 3: A fictitious example showing a problem for fault classification algorithms. Similar measurements (features) are found in both classes; the decision areas thus overlapp.

4.2 Unknown faults

The standard measure for detection of unknown faults/system states, when working with SOMs is the quantisation error, q.e.:

$$\text{q.e.} = ||\vec{x} - \vec{w}_i|| \tag{11}$$

with $\vec{w}_i$ determined according to (9). Thus, the q.e. is a measure of the misfit of the test vector, $\vec{x}$, compared to the knowledge stored in the SOM. This misfit is calculated in the feature space, using the scaled features.

4.3 General adaption and detection algorithm

Figure 4 is an illustration of the complete procedure, as it could be implemented by the valve manufacturer. First the length of the sequence is determined, which could be automated. Afterwards, possible filtering and scaling of the signals are performed. In the time-based monitoring, the signals are scaled and sample times with extreme signal values are discarded according to the dashed lines in figure 5. The filtering limits and scale factors could also be automated, partly by studying the mean and variance of the signals.

Unsupervised training of the SOM is then performed according to the algorithm in section 3.1. The change detection is then performed on the trained SOM. Due to the variability of the quantisation error, post-filtering is suggested. Examples of suggested post-filters are a low-pass filter, a floating mean or, as was used in this work, the mean of a working cycle.

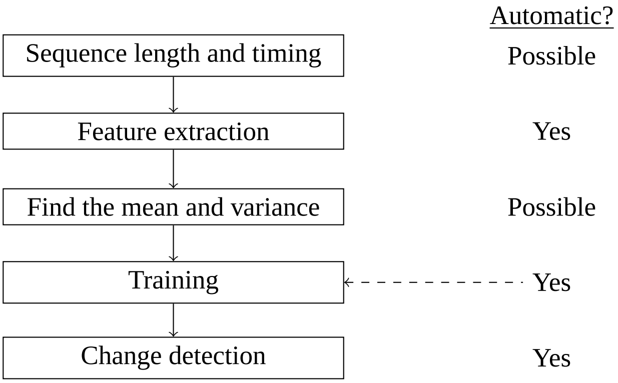

Figure 4: The complete procedure for training, adaption and condition monitoring. Whether the different parts are done automatically or if it is possible to perform them automatically is also shown. The mean and variance are only calculated for the time-series approach.

4.4 Time series monitoring

Large values are filtered out as shown in figure 5. As a consequence the monitoring will be focused around the “normal” levels of the measured signals. Such filtering can easily be automated by studying the nature of the signals together with their mean and variance.

Another benefit of this filtering will be that all signals will be more evenly distributed between their respective minimum and maximum and thus even better suited for the SOM. A drawback might be that faults showing as large peaks or too large an offset could potentially be almost completely filtered out. Hence, a check is needed of how large the set of discarded samples is compared to the total set available. It might also possibly be more difficult to find faults showing as changes in the bandwidth of the system.

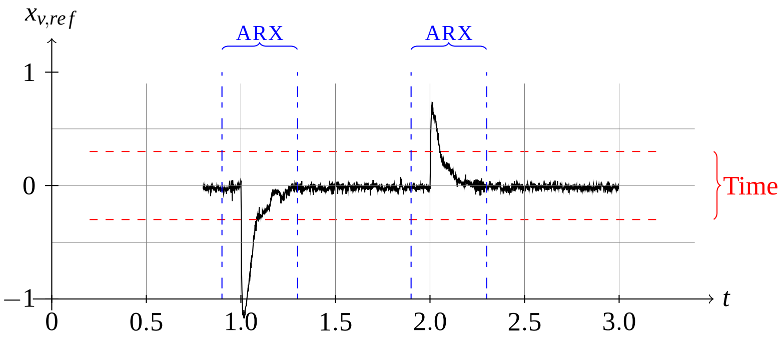

Figure 5: The effect of the approaches. The dashed line depicts the signals that are kept after filtering in the time series approach, where large signals are truncated. The dash-dotted lines depict which parts of the signal will dominate the ARX parameter estimations, as it is here that the excitation of the system occurs.

4.5 Tracking of dynamic parameters

In the second investigated approach, the coefficients of an ARX (2,2) model are estimated and stored in a small SOM. As the coefficients of the ARX model should be more stable throughout a working cycle, the SOM lattice can be made smaller compared to the size of the lattice as used in the approach in section 4.4 and previously in [1, 2].

The idea here resembles the one in [11], although done in the opposite direction. In [11] a small SOM is trained using the time-series data and an AR model is fitted to the trained weight vectors. This AR-model is the used as the basis for the control of the system.

In general, most mechanical systems can at some level be modelled as a spring and mass system, i.e. a 2nd order system. Even if more frequencies are added, due to a more complex system, a 2nd order model will often catch the dominant frequency/ies of the system. Hence, a good choice of model order for an arbitrary system would be a 2nd order system, if no knowledge of the system is available. An example of the identification of such a model used to increase the damping can be found in [12].

In this particular case, a model from $x_{v,ref}$ to p_L can be shown to be of 2nd order. An SOM with 16 neurons is trained using ARX parameters estimated from normal state data. As the monitoring here is based on the measured signals $x_{v,ref}$ and p_L, the monitoring includes changes to the system and not only the valve. The same type and order of model is valid for a large class of systems, but would not, however, it would not work for all systems. The results from the test cases are discussed in section 5.2.

Here again, the question of how to size the SOM lattice arises. In general, the SOM lattice could here be made much smaller, with only a few neurons. If the system is working over a larger set of operating points, the result might be that several models (different coefficients of the same model) are needed to cover the complete working cycle. As a result, the SOM would need to be made larger. Assuming that the SOM is trained over a specific time period, during which it is assumed that no faults exist, this could be handled by letting the SOM grow if the winning neuron is too far away (in the feature space) from the current input vector.

There have been several versions of the growing self-organising map in literature, see for instance [13]. This is currently not implemented.

5 RESULTS

To evaluate the detection capabilities of the different sets of sensor signals, as well as the two approaches to choose features, the results are evaluated for all levels of both of the two single faults and all combinations thereof. Thus, 25 test cases are available, including the normal state case.

5.1 Time series monitoring

By working according to the scheme in section 4.4, the following results were achieved. In table 2 the mean q.e. taken over one cycle for the large feature vector and all tested combinations of faults is shown. In tables 3 and 4 the mean q.e. for the feature vectors according to (3) and (4), respectively, is shown.

As can be seen, all feature vectors allow the detection of the single offset fault in the valve. The current scaling of the feature vectors made the first two, (2) and (3), increase the mean q.e. between 3.3 and 6.5 times, while the feature vector consisting of $x_{v,ref}$ and x_v increased between 2.6 and 3.8 times. Thus, somewhat surprisingly, it turned out to be more important to include the load pressure than the measured valve position to find the offset fault.

It is much more difficult to detect the single bandwidth fault. The normal mean q.e. increases about 1.23–1.72 times for feature vector (2), 1.20–1.74 times for (3), and 1.24–2.56 times for (4). This fault is thus difficult to detect for all tested feature vectors.

5.2 Tracking of dynamic parameters

An example of the quantisation error when using the SOM trained using ARX parameters estimated from one cycle is shown in table 5. The same results are shown normalised with the q.e. for a normal cycle in table 6. Hence, in this table values close to 1 indicate an unchanged system. As can be seen from these tables, the ARX modelling quite easily detects the change caused by the bandwidth fault.

One important point to remember is that these results are single values (although calculated over one cycle), whereas those in section 5.1 are calculated for each sample in one cycle and then averaged over the cycle in the table.

6 DISCUSSION

Condition monitoring is an important part of a system, not least when the aim is to reduce maintenance costs. A complete overview of the system is important in order to create a good condition monitoring *and* fault diagnosis system. However, there is also interest in more generic change detection appliances, both from component manufacturers lacking the system overview, but also occasionally from system builders, both for new systems and as add-ons to older systems.

When designing condition monitoring systems, the decision as to what principle the monitoring should be based upon is of utmost importance. If extensive knowledge is available about

Table 2: Mean quantisation error for all combinations of simulated faults, using (2), $[x_v, p_L, x_{v,ref}]$, as the feature vector.

Offset [%]	Decrease in bandwidth [%]				
	0	5	10	15	20
0.0	2.45e-02	3.00e-02	3.49e-02	4.21e-02	3.08e-02
0.5	1.60e-01	1.68e-01	1.77e-01	1.97e-01	8.54e-02
1.0	1.30e-01	4.59e-01	5.76e-01	3.78e-01	2.79e-01
1.5	1.15e-01	8.64e-01	1.02e+00	8.20e-01	5.40e-01
2.0	1.03e-01	1.66e+00	1.60e+00	1.88e+00	1.83e+00

Table 3: Mean quantisation error for all combinations of simulated faults, using (3), $[x_{v,ref}, p_L]$, as the feature vector.

Offset [%]	Decrease in bandwidth [%]				
	0	5	10	15	20
0.0	7.65e-03	9.74e-03	1.12e-02	1.33e-02	9.17e-03
0.5	4.63e-02	4.33e-02	2.02e-02	8.58e-03	9.66e-03
1.0	3.71e-02	3.41e-02	1.91e-02	9.67e-03	9.35e-03
1.5	3.05e-02	2.95e-02	1.75e-02	1.00e-02	8.83e-03
2.0	2.51e-02	2.84e-02	1.77e-02	9.12e-03	7.82e-03

Table 4: Mean quantisation error for all combinations of simulated faults, using (4), $[x_{v,ref}, x_v]$, as the feature vector.

Offset [%]	Decrease in bandwidth [%]				
	0	5	10	15	20
0.0	6.54e-03	1.08e-02	1.23e-02	1.68e-02	8.13e-03
0.5	2.46e-02	4.31e-02	3.66e-02	5.75e-02	2.85e-02
1.0	2.26e-02	2.21e-01	3.01e-01	1.37e-01	1.59e-01
1.5	2.04e-02	5.04e-01	6.70e-01	4.57e-01	3.80e-01
2.0	1.71e-02	1.03e+00	1.13e+00	1.35e+00	1.51e+00

the complete system, a model based approach capable of identifying the different faults can be chosen. If large amounts of measured/simulated data are available, a data driven approach with the same capabilities is possible. However, in both cases, the question is what will the response be to a unknown fault. Will it be ignored or masked as one or more of the known faults?

Another alternative is to choose a method which does not have the capability to identify faults, only to detect them. One such method, using an SOM, has been described here. Depending of how such a system is built and what sensor signals are used, it will respond to changes in either the component or the complete system.

One possible objection to the comparison between the results in sections 5.1 and 5.2, might be that in the latter case, the ARX parameters are estimated using data from a complete cycle, whereas the monitoring in the first case is performed during each sample. However, in the

Table 5: The quantisation error for the ARX parameters.

Offset [%]	Decrease in bandwidth [%]				
	0	5	10	15	20
0.0	0.0038	0.4799	0.6529	0.5860	0.0355
0.5	0.0522	0.1468	0.1177	0.0446	0.0037
1.0	0.0715	0.1264	0.1193	0.0631	0.0139
1.5	0.0335	0.1138	0.1235	0.0358	0.0108
2.0	0.0310	0.3895	0.1179	0.0375	0.0062

Table 6: The normalised quantisation error for the ARX parameters. Normalised with the q.e. for the normal case.

Offset [%]	Decrease in bandwidth [%]				
	0	5	10	15	20
0.0	1.0	125.3	170.5	153.1	9.3
0.5	13.6	38.3	30.7	11.6	1.0
1.0	18.7	33.0	31.2	16.5	3.6
1.5	8.8	29.7	32.3	9.4	2.8
2.0	8.1	101.7	30.8	9.8	1.6

first case, the result is then averaged over one cycle. The difference is thus made smaller. Secondly, it is a trivial task to move to a recursive implementation of the estimation process in the case of the ARX parameters. In such a case, this approach will definitively be the least demanding, resource-wise, of the two. On the other hand, this approach should be more forgiving for variations in the working cycle, as long as the system still operates somewhat close to the same operating state. This is valid as long as the operational state of the system can still be modelled using the same model and set of parameters. The first approach on the other hand, requires that the input vectors (measured features) can still be described by the same probability distribution.

The choice in the second approach, to use an ARX (2,2) model from $x_{v,ref}$ to p_L is made using domain knowledge of common fluid power systems. It is also valid for a large class of systems, not only an symmetric valve controlled cylinder. At the same time, it is not a good choice for all classes of systems. The system builder would thus need to either disable such a monitoring system for some classes of systems or be given the choice of several models, possibly both classes other than the ARX model, as well as other model orders.

The second approach could be refined in a number of ways. For instance, the addition and use of the delay term, n_k, in the ARX model could improve modelling accuracy and, hence, monitoring performance. This parameter could also quite easily be estimated on-line.

7 CONCLUSION

This work presents a method of combining data driven methods with domain specific knowledge to assemble a condition monitoring system suitable for unsupervised monitoring using the valve as an information gathering device. This may extend the application of hydraulic valves in future systems.

The tools to automatically create a condition monitoring system capable of detecting unknown system states/faults exist. However, it is of crucial importance to carefully consider what faults might conceivably occur and whether it is likely that they will be detected. It is also important to consider whether other changes to the system and its working cycle will show up as faults. Such a system as the one described in this work would have to be reset when the working cycle and/or work load is changed.

The system discussed here is primarily a data driven method using domain knowledge for choosing the feature vector. In the second version discussed, further domain knowledge is used to choose a suitable model type and order.

REFERENCES

[1] A Zachrison and M Sethson. Detection of system changes for a pneumatic cylinder using self-organizing maps. In *Proc. of 2006 IEEE International Symposium on Computer-Aided Control Systems Design*, pages 2647–52, Munich, Germany, October 2006. IEEE. DOI:10.1109/CACSD.2006.285524.

[2] A Zachrison and M Sethson. Self-organising maps for monitoring pneumatic systems. In D N Jonhnston and K A Edge, editors, *Power Transmission and Motion Control 2006*, Power Transmission and Motion Control, pages 181–94. University of Bath, Hadleys Ltd, September 2006.

[3] L Ljung and T Glad. *Modeling of Dynamic Systems*. Prentice Hall, 1994.

[4] T Kohonen. *Self-Organizing Maps*, volume 30 of *Springer Series in Information Sciences*. Springer-Verlag Berlin Heidelberg New York, 3rd edition, 2001.

[5] T Kohonen. The self-organizing map. *Proceedings of the IEEE*, 78(9):1464–80, September 1990. DOI:10.1109/5.58325.

[6] M Kasslin, J Kangas, and O Simula. Process state monitoring using self-organizing maps. In I Aleksander and J Taylor, editors, *Artificial Neural Networks 2: Proceedings of the 1992 International Conference (ICANN-92)*, volume 2, pages 1531–4, Brighton, UK, September 1992. Elsevier, Amsterdam, Netherlands.

[7] T. Hämäläinen, H. Klapuri, J. Saarinen, and K. Kaski. Mapping of SOM and LVQ algorithms on a tree shape parallel computer system. *Parallel Computing*, 23(3):271–89, 1997.

[8] S Rüping, M Porrmann, and U Rückert. SOM hardware-accelerator. In *Workshop on Self-Organizing Maps (WSOM)*, pages 136–141, Espoo, Finland, 4 - 6 June 1997.

[9] S Haykin. *Neural Networks: A Comprehensive Foundation (2nd. ed.)*. Prentice Hall, Upper Saddle River, NJ, 1999.

[10] L Wang, editor. *Support Vector Machines: Theory and Applications*, volume 177 of *Studies in Fuzziness and Soft Computing*. Springer-Verlag Berlin Heidelberg New York, 2005.

[11] JC Principe, L. Wang, and MA Motter. Local dynamic modeling with self-organizing maps and applications to nonlinear system identification and control. *Proceedings of the IEEE*, 86(11):2240–58, 1998.

[12] P Krus and J-O Palmberg. Damping of fluid power systems in machines with high inertia loads. In *JHPS International Symposium on Fluid Power*, Tokyo, Japan, 1989.

[13] F. Zehraoui and Y. Bennani. M-som-art: Growing self organizing map for sequences clustering and classification. *16th European Conference on Artificial Intelligence (ECAI2004), Valancia, Spain, August*, 2004.

Detection of Cylinder and Valve Leakage in Hydraulic Position Servo

Esa Mäkinen and Tapio Virvalo
Institute of Hydraulics and Automation
Tampere University of Technology
P.O.Box 589, 33101 Tampere, Finland
e-mail: esa.makinen@tut.fi, tapio.virvalo@tut.fi

ABSTRACT

Leakage in a cylinder or in a valve increases damping and position error of hydraulic position servo systems, especially under external load. During the operation of servo systems some wear might occur both in servo valves and cylinders causing increasing leakages in control notches of servo valves or in seals of cylinders. Experimental and simulated results show that individual leakage paths can be detected based on their influence on the position error without any extra sensors. If more than one of leakage paths takes places simultaneously, only some of them can be separated. Leakage has only slight influence on the other performance of the system than the steady state position error.

1. INTRODUCTION

Condition Control and Monitoring have a strongly increasing role in the fluid power field. Detecting different malfunctions is the main task in both in Condition Control and Monitoring. In principle, a malfunction can exist in any part of a servo system; i.e. cylinder and load, servo valve, position sensor, controller, and power supply. Problems relate to detection of the correct type of malfunction and what to do after that. Some malfunctions are not so critical, but their influence increases incrementally and deteriorates the performance of the system little by little like a leakage.

There are many kinds of reasons that affect the correct working of both hydraulic and pneumatic cylinder drives. Two main regions where some harm could occur are seals and fasteners. Individual cylinder drives are so cost-critical that in most cases installation of extra sensors is out of the question. This means that incipient malfunction has to be noticed as soon as possible without any extra sensors. From this starting point, the influence and detection of leakage and backlash in a pneumatic cylinder drive [1] and [2], and influence and detection of backlash in a hydraulic cylinder drive [3], have studied in earlier investigations. In this paper the detection of cylinder and valve leakage in a hydraulic cylinder drive position servo is studied.

Power Transmission and Motion Control 2007 Edited by Dr D N Johnston and Professor A R Plummer
© With The Centre for Power Transmission and Motion Control

The earlier investigations indicated that detection of malfunctions without additional sensors is possible, but also that the behaviour and influence of nonlinearities with pneumatic and hydraulic position control systems is somewhat different and must take into account in the detection. Some malfunctions are critical and easy to detect, but typically they are detected too late, while e.g. a leakage is not so critical, but its influence increases little by little and deteriorates the performance of the system little by little. Leakage could be found both in servo valves and cylinders. Leakage has both positive and negative influences on the behaviour of fluid power position servos. Leakage increases damping of cylinder drives independently of which part of system it starts. Some leakage is always present in proportional and servo valves without overlaps. In pneumatics both leakages, in a cylinder or in a valve, influence in the same kind the performance of position servo systems [2]. Servo valve leakage causes always at least low frequency hunting in high performance pneumatic position servo applications, but it may be hard to detect, before it is remarkably high. In pneumatics the best ways to detect piston seal leakage are increased steady state position error while there is a good dynamic behaviour without hunting incipient. According to this study the hunting does not exist in corresponding hydraulic applications.

However, there are other phenomena which influence performance in a similar manner. Such phenomena are leakage in a servo valve, null point drift of a servo valve, changes in a load, changes in friction forces, and changes in supply pressure. Influence of some of those changes can be compensated by retuning the controller. However, it is better in the long term to understand the reason for deterioration of the performance in order to point the right maintenance targets.

The leakage detection strategy used in this paper is straightforward: the output of the servo system is measured, analyzed and then the decision is made. The decision making process is simple. It is based on the knowledge of the influence of different leakage cases on the output of the control system. Some experimental tests of the influence of leakage on the performance of the system are easily realized, but others, especially in servo valves, are tedious and costly. The nonlinear model is used to increase the knowledge of the influence of different leakage modes on the behaviour of the control system. The well-validated nonlinear model can be used as a virtual experimental test setup. The output signal of both simulations and experimental tests is position, which is analyzed in a similar manner in both cases. The main idea is that in real applications no additional sensors would be needed, so only the measured state is the output of the control system.

2. STATE OF THE ART ON LEAKAGE MONITORING OF FLUID POWER SYSTEMS

Monitoring of fluid power systems has increased significantly recently, but there are few papers dealing the influence and detection of backlash in hydraulic or pneumatic cylinder drives as presented in [1] and [3]. Also the influence and monitoring of leakage in pneumatic cylinder drives has not been studied much [2], whereas, there are many papers dealing with the leakage detection and monitoring methods of hydraulic systems. In the following, a short summary of some of these studies is given.

Condition monitoring of fluid power systems can be based on different strategies. Hindman et al /4/ give a good survey dealing with four strategies involving contamination control, parameter/state estimation, artificial neural networks (ANN), and spectral analysis. There are number of studies in which the detection of the leakage is based on additional sensors typically flow meters and/or pressure sensors. Some of these studies also deal with cylinder drives both in open-loop and closed loop cases.

Hindman et al [5] presented a neural network approach applied to an open-loop valve-controlled cylinder drive of a John Deere 410E Backhoe Loader. A nonlinear simulation model was first developed for a direct operated closed-cantered, over-lapped valve controlling a single linear actuator. With the simulation model the influence of different valve leakage paths can be studied. The modelled leakage paths are shown in Figure 1. The same method was utilized in this study.

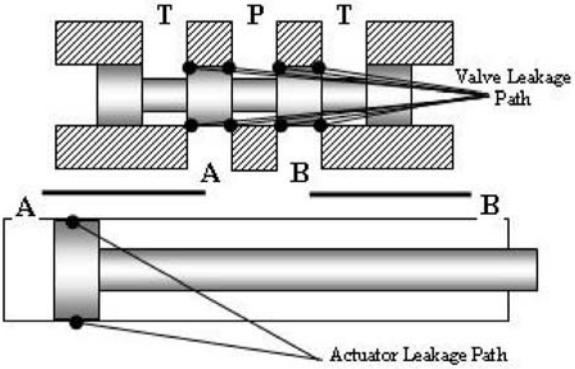

Figure 1 Modelled leakage paths [5]

An artificial neural network (ANN) was applied for the fault detection. The ANN system was first trained with the simulation data and then with the experimental pressure measurements and controller output data. The result indicated that the proposed concept is feasible and applicable for a commercial system also. However, pressure sensors are needed, which complicates and increases the cost of the system.

Watton et al. [6] presented an approach to fault diagnosis of fluid power cylinder drive system, in which number of faults may be determined using rule-based concepts. On-line data and qualitative and quantitative reasoning were used enabling specific faults to be detected. The rule-based expert system was applied to an open-loop flow-controlled cylinder drive. The same leakage cases are studied as in this paper; i.e. piston seal internal leakage, rod seal external leakage, external leakages of lines between the cylinder and the valve. A variety of flow leakages were successfully detected, but with the requirement of flow meters in both cylinder lines.

Watton and Pham [7] presented fault diagnosis and classification using ANN systems applied to a closed loop hydraulic cylinder position control system. Both different leakage types and leakage levels were identified, but fast-acting flow meters were required in this approach. Later Watton and Pham [8] presented a new method utilizing the Linear Predicting Coding (LPC) method to demonstrate that with only pressure transient information, neural networks combined with feature extraction techniques can be utilized to predict both the leakage type and the leakage level.

Watton and Stewart [9] presented in their study different methods that may be used in the context of leakage flow detection for a closed-loop hydraulic cylinder position control system. They also studied possibilities to manage without any additional sensors. The position control cylinder studied was loaded with an external force and the inertia load was negligible, thus the influence of the leakage was not possible with dynamic position responses. The steady state position error data were utilized in leakage detection in single-fault cases, but there were limitations with multiple-fault situations.

3. STUDIED CASE

Both leakage in the cylinder or in the valve, influences the performance of position servo systems. In principle it increases the damping and the position error. In the initial tuning the leakage of the servo valve can most often be compensated by suitable tuning of the servo valve offset. In practice it can be supposed that there are no leakages in newly installed cylinders. During the run of servo systems some wear might occur both in servo valves and cylinders.

The leakage of the piston and rod seals can be represented reasonably well with outside leakage arrangements as depicted in Figure 2. The well-known leakage of the servo valve is impossible to achieve without damaging the valve. A reasonable way to study the influence of servo valve leakage on the performance of the position servo system is through simulation. In order to get reliable results a well-verified model should be used.

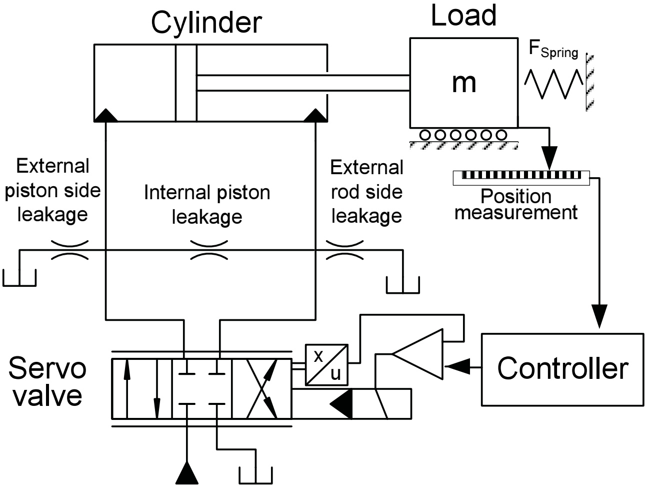

Figure 2 Piston and rod leakages

In this study the positioning of an inertia load with and without a spring-type external force is realized with a hydraulic cylinder drive shown in Figure 2. With experimental tests the basic behaviour under the leakage of cylinder seals can be studied.

The following experimental set-ups were used:

- Cylinder is 63/36-500 (piston/rod-stroke [mm])
  - Inertia load is 2800kg
- Nominal flow of the servo valve is 50l/min
  - Nominal pressure drop/notch is 35bar
  - Critical center
  - Electrical spool position feedback
- Supply pressure is 120bar
- Resolution of position encoder is 0.0016 mm
- Sampling time of controller is 2ms

Required performance specifications:

- Position error less than 0.1 mm
- Overshoot/undershoot less than the allowed position error in step responses
- Settling time in both directions with 80mm strokes less than 1s

The following arrangements were used in experimental tests:

- Inertia load
  - Load is driven (is) step-wise into the same point from both directions
  - Animation of piston seal leakage with orifice diameters 0.4mm and 0.2mm
  - Animation of rod seal leakage with orifice diameter 0.4mm
- Inertia and spring load
  - Load is driven (is) step-wise into the same point from both directions
  - Animation of piston seal leakage with orifice diameter 0.2mm

The testing procedure is as follows. The offset of the servo valve is tuned in the open-loop system and without any external leakage so that there is no drift of the load. The reference responses are tuned without any external leakage according to the performance specifications using the State Controller. Then the external orifices are added and the same responses are taken.

4. EXPERIMENTAL RESULTS

Because the study principle is that no extra sensors are used, the only information that is available for the detection is based on the position signal and the controller signals. The basic assumptions are that the piston leakage influences the position error, load damping and it might also influence the settling time.

As examples, the following experimental step-wise strokes from 200mm to 280mm and from 360mm to 280mm, respectively, are presented. The zoomed position error responses without and with the animated piston leakage are shown in both directions in Figure 3. The leakage orifice diameter is 0.4mm.

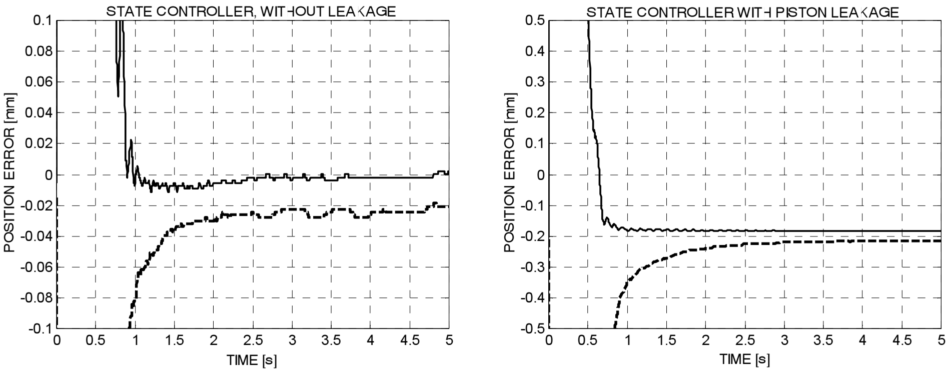

Figure 3. Zoomed measured position error responses in both directions without leakage (left) and with piston seal leakage (right)

The piston seal leakage increases position error in the negative direction as expected. The same influence applies to the rod seal leakage. The performance specifications are fulfilled in both cases.

The velocity responses with and without piston seal leakage are shown in Figure 4. No influence of the piston leakage can be found in the velocity responses mostly because the well-tuned State Controller itself increases the cylinder drive damping.

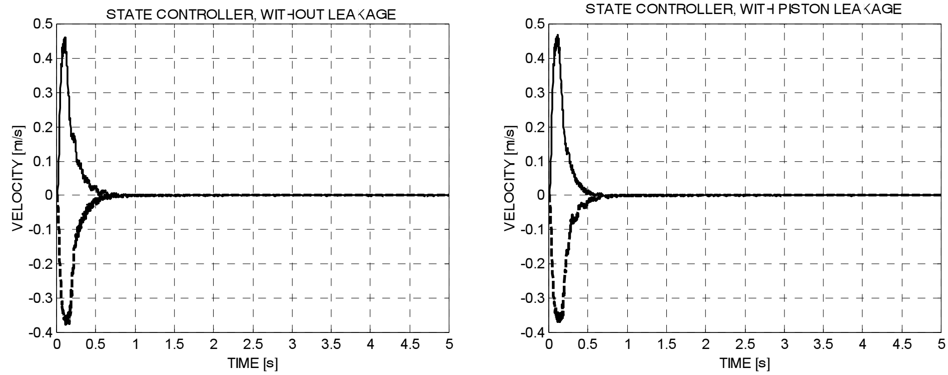

Figure 4. Measured velocity responses without leakage (left) and with piston seal leakage (right) in both directions.

For comparison purpose the position error responses from the point 200mm to the point 280mm with and without animated piston seal leakage are presented in the same figure, Figure 5. In order to test the influence of leakage under external piston force the spring force is applied to the cylinder. The position error responses with and without animated piston seal leakage in both directions are shown in Figure 6. The strokes in both directions are 1mm and the average spring force is 24kN. The piston seal leakage orifice is 0.2mm.

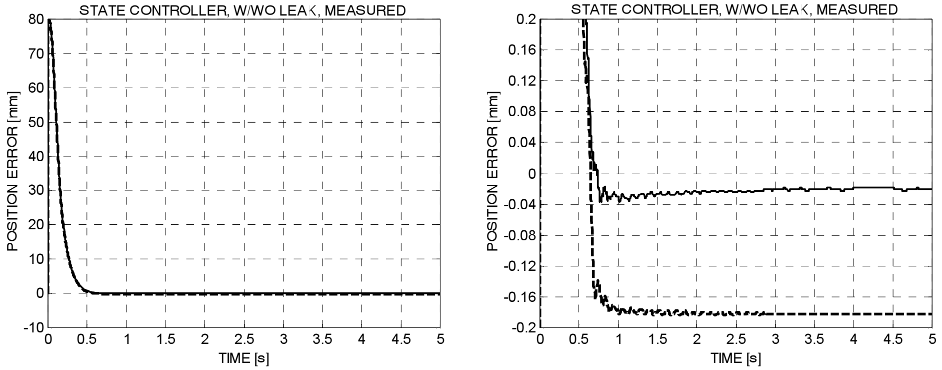

Figure 5. Measured position error responses with (dash) and without (solid) piston seal leakage (left) and zoomed responses (right). From point200mm to point 280mm.

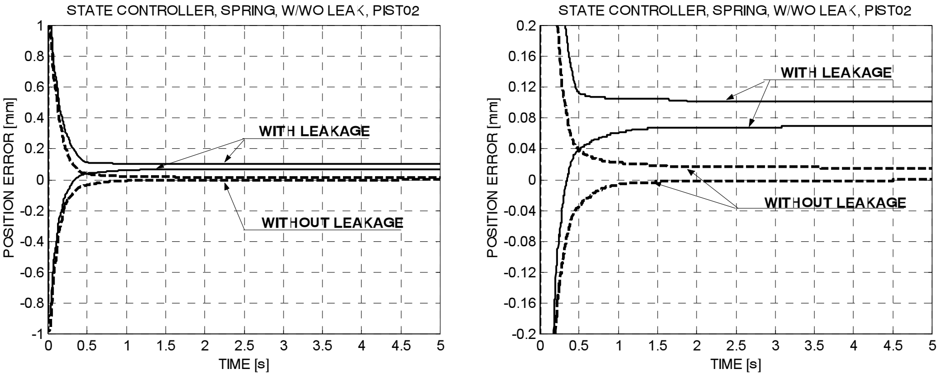

Figure 6. Measured position error responses with (solid) and without (dash) piston seal leakage (left) and zoomed responses (right), spring force 24kN.

According to the experimental study it is very difficult to find differences in dynamic or steady state behaviour between the two cases (with and without cylinder leakage) except in the position error. The leakage of the piston and rod seals generates an increasing position error into the negative direction. The leakage between the piston side of the cylinder and the servo valve increases the position error into the positive direction. The leakage between the rod side of the cylinder and the servo valve increases the position error into the negative direction. The external spring-type force causes the position error with the different sign as without the external force. In all cases the change of the position error is bigger with the bigger leakage. The summary of the influence direction of different leakages on the position error are presented in Table 1.

TABLE 1. Influence direction of different leakages on the position error

	Piston leak.	Rod leak.	Piston ext. leak.	Rod ext. leak.
No ext. force	Negative	Negative	Negative	Negative
With ext. force	Positive	Negative	Positive	Negative

5. SIMULATION MODEL

The hydraulic position servo system is modelled in the usual way. Firstly the cylinder drive model is verified comparing simulated open loop velocity and cylinder chamber pressure responses to experimental responses, when no animated leakage is used. As examples the measured and simulated open loop velocity responses in both directions are shown in Figure 7 and the cylinder chamber pressures in outward direction in Figure 8.

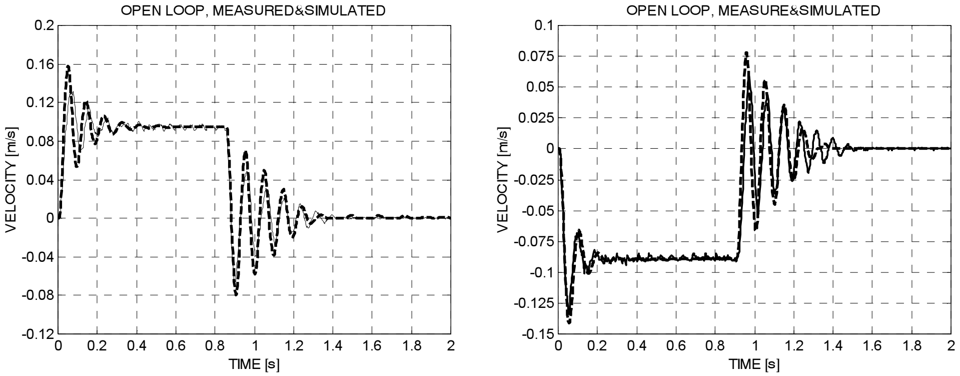

Figure 7. Measured (solid) and simulated (dash) velocity responses in outward movement (left) and inward movement (right)

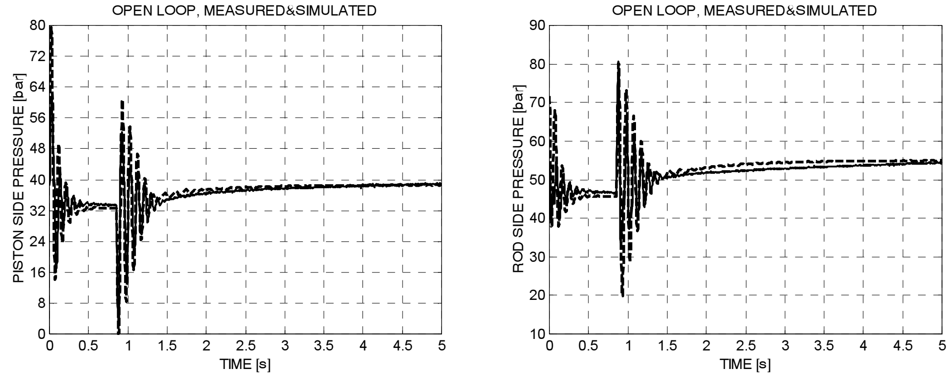

Figure 8. Measured (solid) and simulated (dash) cylinder chamber pressures in inward movement, piston side chamber (left) and rod side (right)

Measured and simulated open loop responses match fairly well. The frequency of oscillations and also damping correspond well to each others. The steady state values of the chamber pressures also match well.

The closed loop model is based on the open loop model. The discrete State Controller is added into the open-loop model and the same feedback gains and sampling time are used in simulations as in experimental tests. The orifices animating the cylinder seal leakages are modelled as turbulence resistances. As examples the position error responses without any animated cylinder seal leakage in outward movements are shown in Figure 9 and with the animated piston seal leakage (orifice diameter 0.4mm) in Figure 10, respectively.

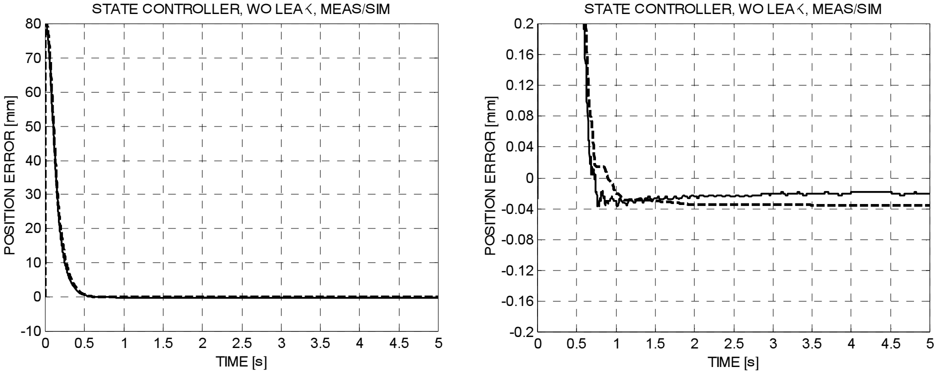

Figure 9. Measured (solid) and simulated (dash) position error responses without leakage (left) and zoomed response (right) in outward movements

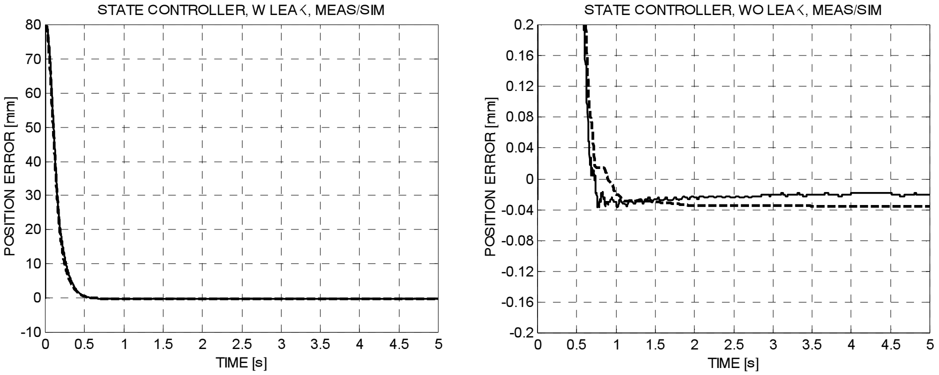

Figure 10. Measured (solid) and simulated (dash) position error responses with piston seal leakage (left) and zoomed response (right) in outward movements

The experimental and simulated position errors match well and with the same valve offset setting the position errors are in the same side of zero.

The measured and simulated velocity responses in outward direction are presented in Figure 11. The measured and simulated velocity responses match well in both cases. No significant difference can be found between cases with and without animated piston seal leakage.

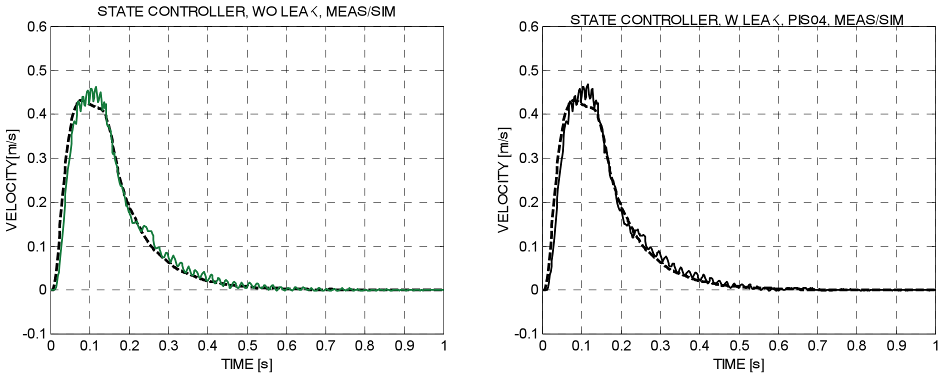

Figure 11. Measured (solid) and simulated (dash) velocity responses without leakage (left) and with piston seal leakage (right) in outward movements

The measured and simulated cylinder chamber pressures in both cases are presented in Figures 12 and 13. The pressure responses match also well in both cases. There are only slight differences between the cases with and without leakage. According to these results it seems that there are slight possibilities to use velocity or chamber pressures as an indicator of cylinder seal leakage.

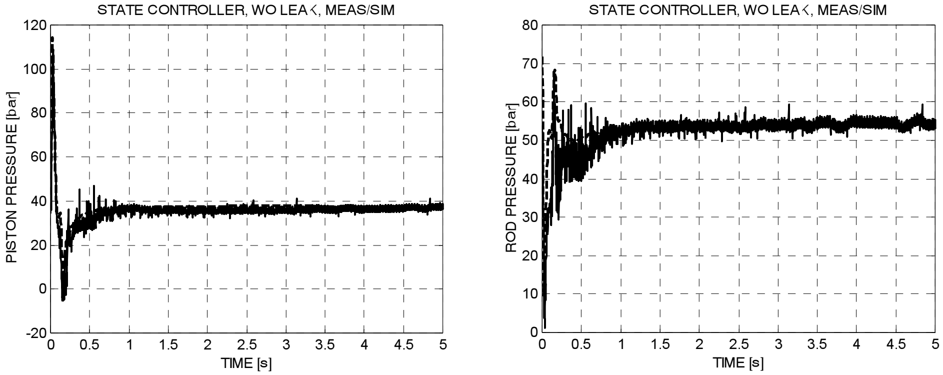

Figure 12. Measured (solid) and simulated (dash) piston side chamber pressure response (left) and rod side pressure response (right) without leakage in outward movements

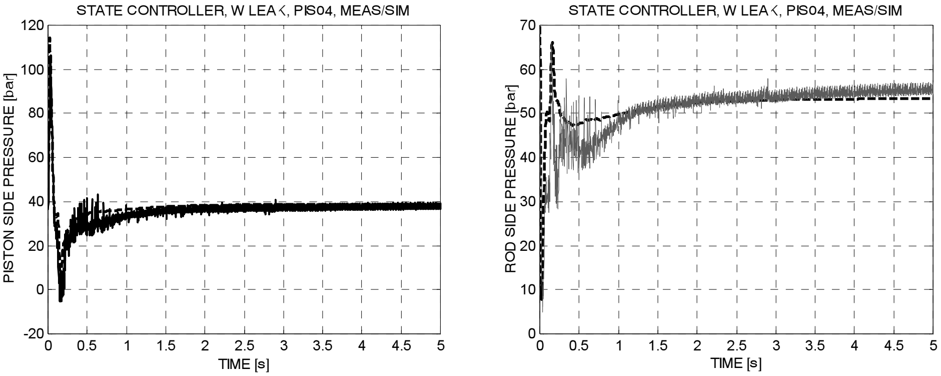

Figure 13. Measured (solid) and simulated (dash) piston side chamber pressure response (left) and rod side pressure response (right) with piston seal leakage, orifice diameter 0.4mm in outward movements

6. INFLUENCE OF DIFFERENT LEAKAGES ON PERFORMANCE

Because it is very time consuming and costly to realize well specified leakages into different parts of the system, especially into the servo valve, the well-validated model and simulation are used. In principle, and in general, the leakage increases the damping in fluid power drives, a property which is utilized in practice. In modern fluid power drives the necessary damping is realized most often by controllers. In all cases the leakage causes some energy loss and reduces the system stiffness. An increased leakage indicates also that some wear has taken place. Leakage could come up in cylinder seals or in a servo valve.

- Leakage in cylinder:
  - Piston seal
  - Rod seal
- Leakage in valve:
  - From piston side work port to tank
  - From supply port to piston side work port
  - From supply port to rod side work port
  - From rod side work port to tank

The leakage of a servo valve depends on its overlaps, null point drift, quality, and condition. It is quite normal that high performance hydraulic servo valves have zero overlaps. In this study it is firstly assumed that the leakage of the servo valve is zero and the study is concentrated to the leakage of the piston and rod seals. Afterwards the leakage of the servo valve is also considered separately and combination with the piston and rod seal leakages. According to the simulation results the following summary can be presented:

- Without external force and asymmetric cylinder
  - Without any leakage the position error is always negative
  - With leakage in piston or rod seal or both the position error is always negative

  - With leakage from piston side work port to tank the position error is always positive
  - With leakage from supply port to piston side work port the position error is always negative
  - With leakage from supply port to rod side work port the position error is always positive
  - With leakage from rod side work port to tank the position error is always negative
- With external restrictive force (outward movement) and asymmetric cylinder
  - Without any leakage the position error is always positive
  - With leakage in piston seal position error is always positive
  - With leakage in rod seal the position error is smaller positive or it is negative
  - With leakage from piston side work port to tank the position error is always positive
  - With leakage from supply port to piston side work port the position error is smaller positive or negative
  - With leakage from supply port to rod side work port the position error is always positive
  - With leakage from rod side work port to tank the position error is smaller positive or negative

The valve zero point drift has a large effect on the position error. The position error is positive or negative depending on the direction of the offset. Modern high performance servo valves have electrical spool position feedback. It is also assumed that the servo valve has electrical spool position feedback which means the zero point drift of the spoon is very small or at least it is possible to detect it.

7. DETECTION OF PISTON SEAL LEAKAGE

According to experimental and simulation results, any reasonable levels of leakage are difficult to detect. It seems that in a high performance position servo system, leakage can be detected by the changes of steady state position errors. In most cases the separation of servo valve and cylinder leakages is impossible without additional tests and measurements. However, it is possible to detect that there is some leakage in the system based on changes in the position error. Already incipient leakage, less that 0.5% of servo valve nominal volume flow, can be detected in a high performance system. This level of leakage has no noticeable effect on the other characteristics expect the position error.

8. DISCUSSION

There are two main fault types in hydraulic drives. There are some catastrophic failures, which take place rapidly and there is no way to predict them and somehow to make preparations against them. Other types of faults take place incrementally such as wear based faults. Leakage is one of the most common faults in fluid power systems. There are two main types of leakage; internal and external. Typically, leakage indicates system wear. It is a good practice to try to detect incipient leakage in hydraulic cylinder position control systems as early as possible in order to schedule maintenance activities effectively.

There are different kinds of leakage in the studied system as listed in Chapter 6. Table 2 summaries the directions of position error changes in different leakage cases.

Table 2. Signs of position error changes with different leakages

	Piston	Rod	Sup.- piston	Piston-tank	Sup.-rod	Rod-tank
No ext. force	Neg.	Neg.	Neg.	Pos.	Pos.	Neg.
Ext. force	Pos.	Neg.	Neg.	Pos.	Pos.	Neg.

The rod seal leakage can be detected visually. Others can be detected case-by-case according to Table 2, if it is possible to realize both load cases. There are other factors, such changes of friction force, load and temperature, which might also cause changes of the position error. The sign of the position error changes of all individual leakages is the same in both direction movements when the sign is different in the case of the friction force changes. The influence of the load changes on the position error can be estimated in the most cases. Some changes of the position error caused by temperature change might be difficult to separate, for instance, from the influences of leakage. The detection of probable leakage based on the position error change is possible in a high performance position servo system. When the change of the position error has the same sign in both direction movements there is good reason to doubt that there are one or more leakage points. The individual leakage paths can be detected, but if there is a combination of two or several leakage paths the detection is impossible based on the position error. The situation is the same if there are in the same time changes of leakage, friction force, and load. An interesting point is that leakage causes hunting in pneumatic position servos, but there is no signal of hunting in hydraulic position servos caused by leakage.

9. CONCLUSIONS

According to this study the following conclusions can be made:

- The change in the steady state position error of a high performance hydraulic cylinder position servo might be a signal that there is leakage in the system
- Already small individual leakage (<0.5% of the nominal flow of the servo valve) can be detected in high performance position servo systems based on the size and sign of the position error change.
- Different leakage paths cannot be separated by the method based on the position error changes.

10. REFERENCES

1. Mäkinen, E. & Virvalo, T. 2005. Detecting and influence of cylinder mounting backlash in pneumatic position servo. 4.IFK, March 25-26, 2004, Dresden pp. 511-522.
2. Virvalo, T. & Mäkinen, E. 2006. Detect of piston seal leakage in pneumatic position servo cylinder drive. In: Konarik, P. (ed.). Proceedings of the 19th International Conference on Hydraulics and Pneumatics, May 30-31, 2006 Prague, Czech Republic pp. 186-194.

3. Mäkinen, E. & Virvalo, T. 2006. Detection and influence of cylinder mounting backlash in a hydraulic position servo. PTMC 2006, University of Bath, UK, 13-15 September 2006 pp. 305-317.
4. Hindman, J., Burton, R., and Schoenau, G. 2002. Condition Monitoring of Fluid Power Systems: A Survey. SAE Journal of Commercial Vehicles, pp. 6975.
5. Hindman, J., Burton, R., and Schoenau, G. 2006. Monitoring the Condition of a Valve and Linear Actuator in Hydraulic Systems. International Journal of Fluid Power, Vol. 7 Number 1 March 2006. ISSN 1439-9776.
6. Watton, J., Lucca-Negro, O. and Stewart, J C. 1994. An on-line approach to fault diagnosos of fluid power cylinder drive systems. Proc Instn Mech Engrs Vol. 208, Part I. pp. 249-262.
7. Le, T., Watton, J. and Pham, D. 1997. An artificial neural network based approach to fault diagnosis and classification of fluid power systems. Proc Instn Mech Engrs Vol. 211, Part I. pp. 307-317.
8. Le, T., Watton, J. and Pham, D. 1998. Fault classification of fluid power systems using a dynamics features axtraction technique and neural networks. Proc Instn Mech Engrs Vol. 211, Part I. pp. 87-97.
9. Watton, J. and Stewart, J C. 1996. Cooperating expert knowledge and artificial neural networks for fault diagnosis of electrohydraulic cylinder position control systems. Proc 3rd JHPS International Symposium on Fluid Power. Yokohama. 217-222.

Pressure Based Fault Detection and Diagnosis of a Digital Valve System

Lauri Siivonen, Matti Linjama, Mikko Huova and Matti Vilenius
Institute of Hydraulics and Automation, Tampere University of Technology

ABSTRACT

Digital valve systems have some unique features concerning fault tolerance. The effect of valve faults can be compensated for if the fault is detected and the controller re-configured accordingly. Fault detection and diagnosis is the key to fault tolerance. If the type, location and magnitude of the fault are known, the system can adapt to it. This paper presents a way to detect faults from the system by using measured pressure signals. A test cycle is developed and tested with certain valve and sensor faults. The results show that it is possible to detect faults from the system using the presented method. Analysis also shows a way to calculate more detailed information of certain valve faults.

1. INTRODUCTION

1.1 Background

Fault detection and diagnosis (FDD) allows a system to accommodate to faults. Without knowing the exact influence of certain fault, the possibility to react is somewhat limited. In a larger view, it might be hard even to detect abnormal behaviour. It is easier to analyze the system if it is divided into smaller parts. In the area of hydraulics this basically means individual components such as pumps, motors, valves, cylinders, sensors etc. Faults are known to appear in almost all components since none of them are perfect. Fault detection of hydraulic components has been researched a lot e.g. with actuators (1), hydraulic fluids (2) and pumps (3). After the fault is detected, it must also be diagnosed. In practice, this means the type, location and magnitude of the fault.

Valves are critical components in hydraulic systems. Without parallel connection, valves may be single point of failure (SPoF) items and therefore might stop the whole system in the case of a failure (4). Probably the most critical systems are in aerospace and nuclear applications where faults may cause extreme consequences (4, 5, 6). In more traditional hydraulic applications, a fault may cause stoppages, down-time and expensive repairs. Sometimes the wasted time is more valuable than the part and in some applications the system itself may be in a difficult location.

Although FDD is vital, it takes more than that to achieve fault tolerance of hydraulic valves. Reacting to fault situation is hard since different kinds of faults cause different

Power Transmission and Motion Control 2007 Edited by Dr D N Johnston and Professor A R Plummer
© With The Centre for Power Transmission and Motion Control

effects and the wrong kind of adaptation may increase it. Reacting into valve faults is difficult in traditional proportional or servo systems. Usually the only possible thing to do is to increase or decrease the control current e.g. in a PWM controlled proportional pilot valve. In critical systems, such as aerospace applications, valves can be doubled or tripled and in case of a failure, the faulty acting valve is isolated from the rest of the hydraulic system and a back-up valve is taken into action. This on the other hand demands at least two valves, which increases price, size and complexity of the hydraulic system and therefore has not become a general solution.

1.2 Digital Hydraulics

Digital hydraulics means a system with certain discrete output values realized with binary components connected in parallel. A digital valve system is in principle a directional flow control valve. It is capable even for accurate trajectory tracking where proportional or servo valves are normally used (7). It usually consists of four digital flow control units (DFCU) that are set into a certain coding scheme. Some possible schemes are binary, Fibonacci and PNM. These all can be modified according to the application and the characteristics of individual on/off valves. An example of a digital valve system is shown in Figure 1.

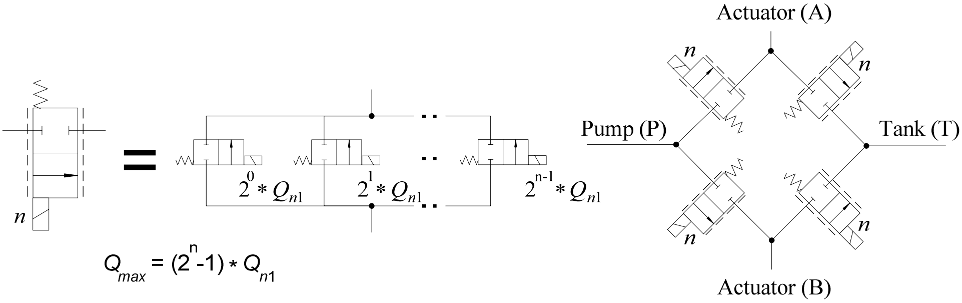

Figure 1 Digital Flow Control Unit (left) and Digital Valve System with four DFCUs (right)

The digital valve system is able to control all four flow paths (P→A, A→T, P→B and B→T) individually with a fully programmable controller. The control code includes all the valve functions. This includes for example anti-cavitation function, counter balance function and energy saving functions (8). In a digital valve system, no extra components are needed.

1.3 Fault Tolerance of Digital Valve System

Parallel connection of hydraulic on/off valves makes fault tolerance possible. No individual on/off valve fault cripples the digital valve system since none of them is vital for operation. If a fault occurs and the system detects it, the controller can be re-configured according to fault diagnosis information. The re-configuration procedure depends on the fault type, location and magnitude.

Table 1 shows five different fault situations. All possible faults that can occur in a valve are not listed in this table since only static faults are studied at this point. For example some dynamic faults such as increasing of opening or closing delay are not included except if the increasing is so long that it seems static to sensors.

Table 1 Some possible fault types of an on/off valve ($0 < x < 1$)

Fault	Opening of valve when control signal is off	Opening of valve when control is on	Case
Normal situation	0	1	-
Valve jammed closed	0	0	I
Valve jammed open	1	1	II
Valve jammed in an intermediate position	x	x	III
Valve does not open fully or valve throughput reduced for another reason	0	x	IV
Valve does not close fully	x	1	V

Fault tolerance of digital hydraulic valve systems has been previously studied by Siivonen et al. and the results have been promising (7, 9, 10). The possibility to adapt into type I fault (See Table 1) has been tested in a real system and the controller re-configuration works well in fault situations (7, 9). The on-line FDD was also tested and the system was capable of switching from normal run to fault mode run before the effect of the fault could be seen in the test system (10). The digital valve system was equipped only with simple and low-cost electronic components that can easily be mounted on normal control electronics. The only problem with this kind of system is that sensors can also break. It is advantageous, if the fault detected can be verified by an independent method.

The analysis of digital hydraulic valve system under fault type II (See Table 1) showed that it is also possible to adapt to this kind of problem (7). The problem with fault types III, IV and V is that the amount of leakage must be known before it can be compensated for. In fault type II, the leakage can be easily calculated from the pressure difference.

1.4 Objectives

The main objective of this paper is extending development to a off-line fault detection method, which can reliably detect all fault types of Table 1. The on-line detection scheme presented in (10) can detect electrical faults only while the method developed in this paper can detect hydraulic faults as well. The methods are independent such that the off-line method can be used to confirm results of on-line diagnostics. The final objective is fully automatic off-line test sequence for fault detection and diagnostics. The fault detection method developed utilizes pressure measurements. These sensors are needed for implementation of control methods of digital valve systems (8) and therefore no extra sensors are needed.

2. PRESSURE BASED FAULT DETECTION

2.1 Assumptions

The system shown in Figure 2 is studied and it consists of an adjustable supply pressure source, digital valve system and actuator. It is assumed that the system has no faults or one valve fault or one sensor fault at a time. Multiple faults make the analysis more complicated and is left as a topic for further studies. It is also assumed that the direction of the load force is known and that load force exceeds friction force. By definition, a positive load force restricts extending movement.

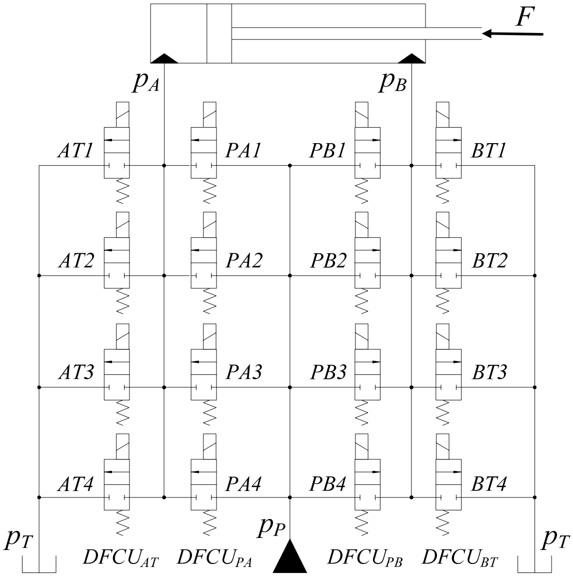

Figure 2 Hydraulic circuit diagram of digital valve system and cylinder

2.2 Detection of Open DFCUs

One problem of pressure based fault detection is that it is difficult to separate valve and sensor faults. The situation becomes easier, if all valves can be closed, i.e. there are no valve faults of type II, III or V. This can be checked by opening one DFCU in turn and detecting if the piston moves or not. If the load force is positive, the test procedure is:

1) Close all valves. If piston moves in retracting direction, $DFCU_{AT}$ is open. If not, $DFCU_{AT}$ is closed.

2) Open two smallest valves of $DFCU_{BT}$. If piston moves in extending direction, $DFCU_{PA}$ is open. If not, $DFCU_{PA}$ is closed.

3) Open two smallest valves of $DFCU_{PA}$. If piston moves in extending direction, $DFCU_{BT}$ is open. If not, $DFCU_{BT}$ is closed.

4) Open two smallest valves of $\mathrm{DFCU_{AT}}$. If piston moves in extending direction, $\mathrm{DFCU_{PB}}$ is open. If not, $\mathrm{DFCU_{PB}}$ is closed.

If the supply pressure can be controlled, open DFCUs from pump side can also be tested without using the position sensor. If $\mathrm{DFCU_{PA}}$ or $\mathrm{DFCU_{PB}}$ leaks, the port pressures should follow the supply pressure. In case of $\mathrm{DFCU_{PB}}$ the supply pressure can be set on certain level and then raised to different level. The $\mathrm{DFCU_{PA}}$ test is similar but the supply pressure should be kept higher than the load pressure.

The test procedure is similar for a negative load force. If open DFCUs are detected, pressure sensors cannot be tested according to the next Section. However, since only one fault is assumed, the pressure sensor test can be skipped if open DFCUs are detected.

2.3 Detection of Sensor Faults

Detection of pressure sensor faults is crucial because sensor signals are the foundation of the fault detection scheme. Normal pressure sensors use a current range of 4-20 mA to transfer the signal. Basically this means that a loose connector or broken cable gives 0 mA. Since 4 mA equals to 0 MPa, 0 mA is a negative pressure. In practice, with 25 MPa sensors this means -6.25 MPa. This of course is impossible and the fault is easy to detect even on-line. If the sensor operates with a voltage signal, the fault is not so easily detected since pressure in e.g. cylinder chamber can be 0 MPa due to cavitation. Another similar problem is that if the offset or gain of the sensor is changed for some reason.

A digital valve system is capable of controlling all flow paths at the same time. This also allows controlling of just one edge to change the pressure at the actuator port. Detection of sensor faults is straightforward if it is assumed that there are no valve faults of type II, III or V. At first, two valves of $\mathrm{DFCU_{PA}}$ are opened. If p_P and p_A show the same value, both sensors are OK. If not, one of them is faulty. Next, two valves of $\mathrm{DFCU_{PB}}$ are opened and p_P and p_B values are compared.

2.4 Detection of Valve Faults

The detection of valve faults is based on a comparison of the steady state chamber pressure to the theoretical pressure. It is assumed that pressure sensors are working and that valves can be modelled with equation

$$Q = K_v u \sqrt{\Delta p}$$

where Q is flow rate, K_v is known flow coefficient, u is the valve opening and Δp is the pressure differential over the valve. Subscripts PAi, ATi, PBi and BTi are used to denote individual valves. Consider, for example, the case of a positive load force and all valves closed. If the piston does not move, it can be concluded that $\mathrm{DFCU_{AT}}$ is closed. If A-pressure differs from p_P, it can be concluded that $\mathrm{DFCU_{PA}}$ is also closed. After that, we can be sure that the piston does not move whatever is opening at the B-side valves. Because the piston does not move, the steady-state pressure at the B-chamber can be solved as follows

$$\sum_{i=1}^{N} K_{v,PBi} u_{PBi} \sqrt{p_P - p_B} = \sum_{i=1}^{N} K_{v,BTi} u_{BTi} \sqrt{p_B - p_T}$$

$$\Rightarrow p_B = \frac{\left(\sum_{i=1}^{N} K_{v,PBi} u_{PBi}\right)^2 p_P + \left(\sum_{i=1}^{N} K_{v,BTi} u_{BTi}\right)^2 p_T}{\left(\sum_{i=1}^{N} K_{v,PBi} u_{PBi}\right)^2 + \left(\sum_{i=1}^{N} K_{v,BTi} u_{BTi}\right)^2}$$

where N is the number of valves of DFCU. Important special cases of Eq. 2 are that if DFCU_{PB} is open and DFCU_{BT} is closed, B-pressure equals to p_P, and if DFCU PB is closed and DFCU BT is open, B-pressure equals to p_T. Let us first seek for fault type I, i.e. closed valve. A possible test procedure is

1) Keep all valves closed and measure B-pressure. If it equals to p_P or p_T , stop testing.

2) Open valve PB1 and check that B-pressure rises. Close valve PB1.

3) Open valve BT1 and check that B-pressure drops. Close valve BT1

4) Repeat 2) and 3) for all valves.

If the pressure does not rise in phase 2, or does not drop in phase 3, the valve has fault type I. If the valve passes this test, it still may have fault IV, which means that it opens only partially. This can be checked by opening valves in pairs (PB1 & BT1, PB2 & BT2 etc.) and comparing the measured B-pressure to the theoretical value. If values are "close enough", it can be concluded that the valve pair in question does not have fault type IV.

More complicated faults are "valve does not close" type faults, i.e. faults II, III and V. Since the faulty acting DFCU is known, the leaking valve can be found by opening a valve so that a cross flow is created from pump to tank port. The leakage can be calculated from the pressure differences with a valve model by comparing it to fully functional system with certain valves open. A type II fault is easier to find since the pressures match directly into some fully functional combination. In fault types III and V the leakage can be calculated and the fault detected by comparing flows with different opening combinations.

3. TEST SETUP

The studied fault detection and diagnosis method is tested in a hydraulic boom equipped with a digital valve system. The tests include pressure sensor test and on/off valve test cycle. The purpose of these tests is to verify the functionality of the pressure sensors and on/off valves with type I and II fault in B-side valves (See table 1).

3.1 Test System

The valve system and sensors are tested with a 4 metre long hydraulic actuated boom. The boom is pivoted at the middle and two hydraulic cylinders are mounted near the centre. The boom can be loaded with iron disks up to -36..36 kN. The cylinders (63/36-200) are connected in parallel and the natural frequency of the system is about 4 Hz. The boom mimics the characteristics of a middle sized mobile machine boom. More detailed information about the boom can be found from references (7, 8, 9, 10).

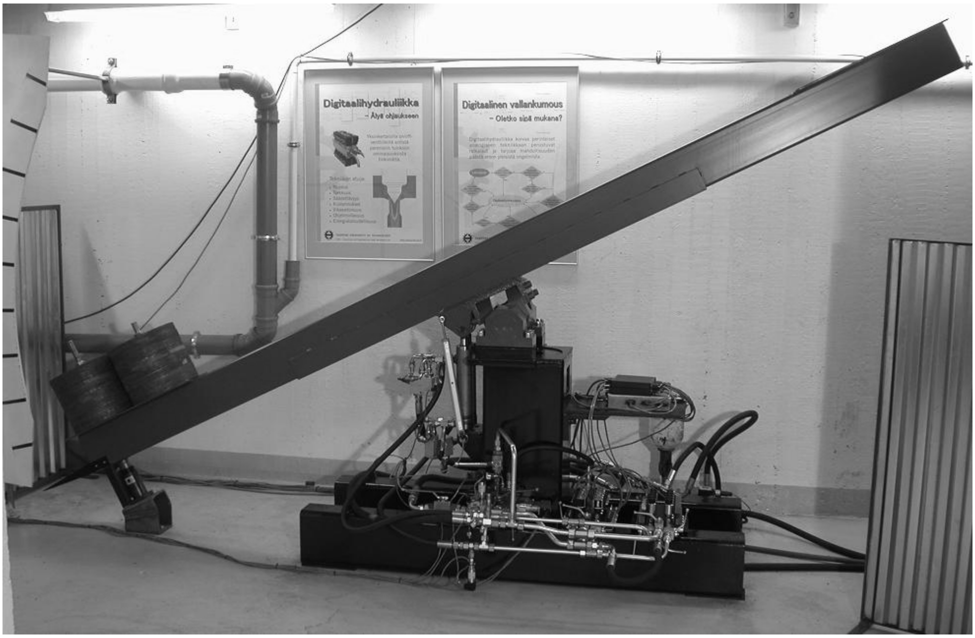

Figure 3 The Test System

The load masses are set to a restrictive load of 400 kg. This creates a load of 36 kN at the cylinder. The supply pressure is controlled by a Bosch Rexroth DBEME 10-5X/200YG24NK31M proportional pressure relief valve using a closed-loop non-linear PI-controller and by utilizing measured characteristic curve and feedforward from flow rate. The supply pressure control mimics a LS-system and the load is measured with pressure sensors. The port pressures are limited with pressure relief valves for safety reasons to 25 MPa.

3.3 The Digital Valve System

The studied digital valve system consists of four DFCUs which are in modified binary series. The binary series is done with orifice disks mounted on the bottom of the cavity between the valve block and the valve. Each DFCU has five Hydac WS08W-01 directly controlled seat type screw-in on/off valves with 12 VDC solenoids. The orifices are set so that the two biggest valves are the same size and smaller ones are set to binary series. This is done in order to increase the maximum flow rate of the DFCU so that it fits to the cylinders installed on the boom. This decreases control performance slightly but is still necessary to achieve reasonable velocity with the boom tip. The exact hydraulic circuit of the valve system, flow rates and performance are better described by Linjama et al. (11). The valves are controlled with a 20 channel control box based on PWM voltage modulation. The control box has internal opening and closing boost in order to improve valve dynamics. The valve system is controlled with an AMD Opteron –based dSPACE DS1006 microcontroller board and the valve control box is controlled via a DS4003 I/O card. The pressures are measured by one Trafaq 8891.74 (p_P) and two Druck PTX 1400 (p_A and p_B) 25 MPa sensors and the current signals (4-20 mA) are converted into voltage signals with 500 Ω precision resistors. The analogue voltage signals are measured with A/D converters.

3.4 Test Cycle

The system is tested off-line with a test cycle based on the methods presented in Section 2. Figure 4 presents a flow chart of the fault detection cycle. It divides into two branches: Type I (OFF faults) and Type II (ON faults) faults. Type I fault tests also include sensor fault tests.

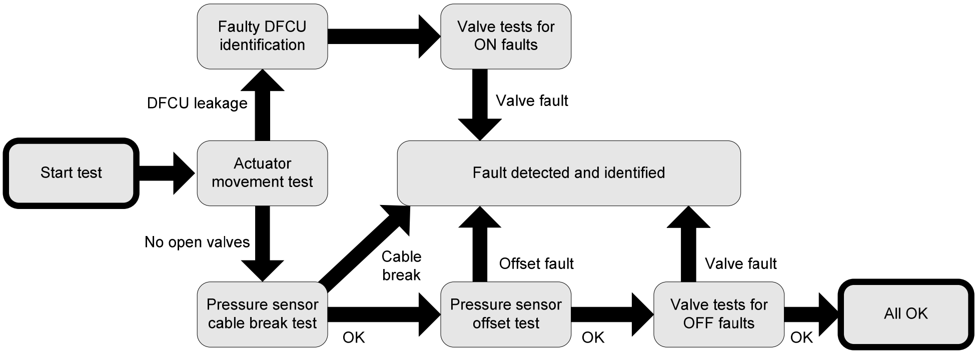
Faulty DFCU identification
Valve tests for ON faults
DFCU leakage
Valve fault
Start test
Actuator movement test
Fault detected and identified
No open valves
Cable break
Offset fault
Valve fault
Pressure sensor cable break test
OK
Pressure sensor offset test
OK
Valve tests for OFF faults
OK
All OK

Figure 4 Flow Chart of the Fault Detection Cycle

The purpose is to detect and analyze valve and sensor faults with pressure sensors. The boom is loaded and no shut-off valves are used so that the piston movement can be seen. The position sensor is used only at the beginning to verify that the boom is not moving because of fault type II in $DFCU_{AT}$. Other tests are performed with pressure sensors only. The system is tested with only one fault at a time. In pressure sensor tests two different kinds of methods are used: if the pressure is negative, a cable break occurs or if the pressures of two sensors in certain circumstances do not match, a fault occurs. If both p_A vs p_P and p_B vs. p_P test fail, the supply pressure sensor is assumed faulty.

4. EXPERIMENTAL RESULTS

The experimental tests included measurements for faults with on/off valves and pressure sensors. The test was not specially optimized for the test system in order to keep the case as general as possible. The acquired data includes all pressure sensor signals, position sensor signal, valve controls and fault signals. Six examples of measurements are plotted into Figures 5, 6 and 7. In all of presented measurements, all fault signals are plotted to the same subplot but they are still different signals. Only one fault is tested at a time so only one fault signal can be seen.

The pressure sensor tests show that if the cable is broken, the pressure signal is negative and the test can be immediately stopped. No valve control or supply pressure change is needed. The supply pressure sensor is tested with another method where the value is compared to a pressure reference value. The test cycle detects that supply pressure signal does not react on the reference. The control signal for the $DFCU_{AT}$ is not plotted in to the presented results since it is zero all of the time.

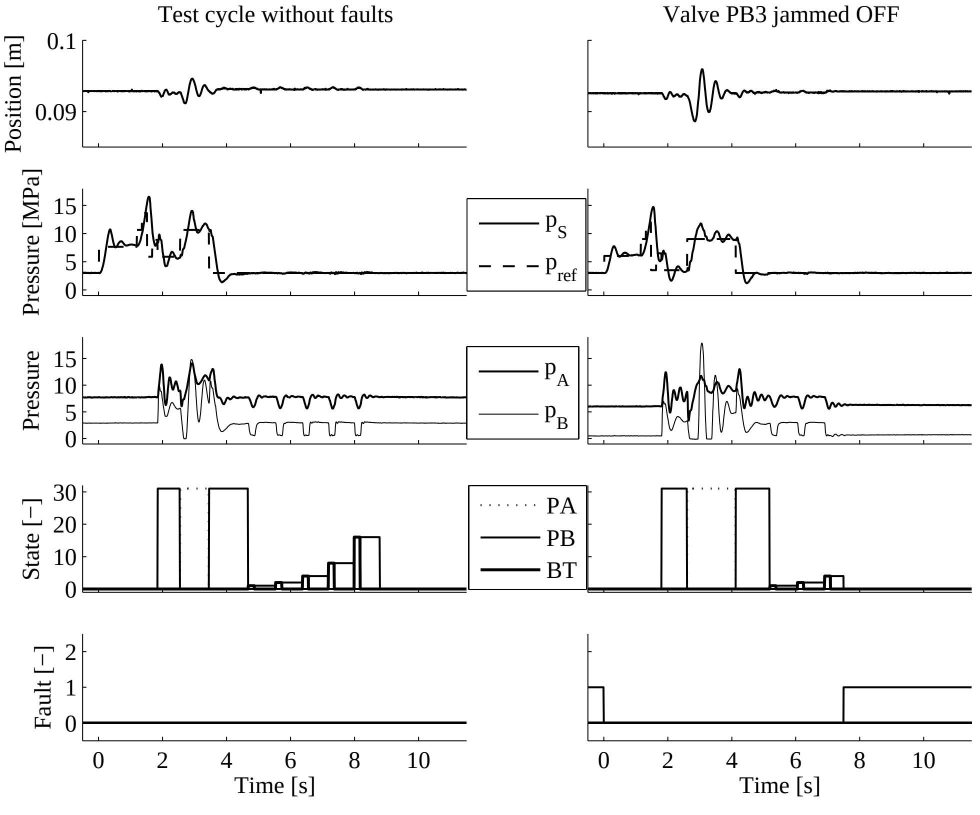

Figure 5 Normal test cycle with no faults and cable break in valve PB3

Figure 5 (left) presents a normal test cycle run without faults. The cycle tests all sensors and valves and no fault signals were raised. The test with valve PB3 shows that during the B-side test at about 6.6 seconds, fault signal $DFCU_{PB}$ of 3 is raised to 1 (type I fault). The faults in other valves create a similar effect.

Figure 6 presents a test where valve BT4 is out of order and the A-side pressure sensor offset is 2 MPa too high. Both faults were detected and located. Results show that the test cycle is capable of detecting faults also in all other measured cases. The pressure sensor cable break is a trivial case and is not presented as a figure since no movement is seen nor valve controls are needed. The cable break fault could also be detected on-line without any problems. The cylinder movement during the valve fault test is relatively small and the pressure transients remain small.

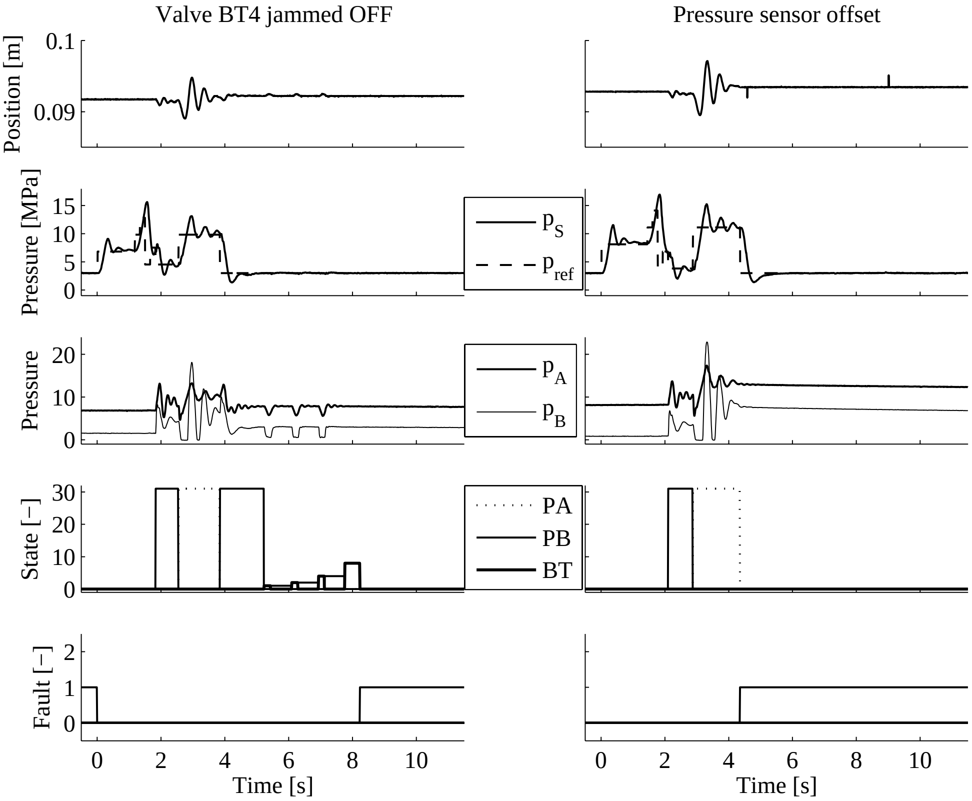

Figure 6 Cable break in valve BT4 and pressure sensor p_A offset fault

Figure 7 presents type II fault in valves PB2 and BT5. In both cases, an open valve is detected and identified by calculating the leakage from the pressure signals. In all measured cases, an error signal 2 is raised as a marker for type II fault. The actuator movement during the test is almost negligible.

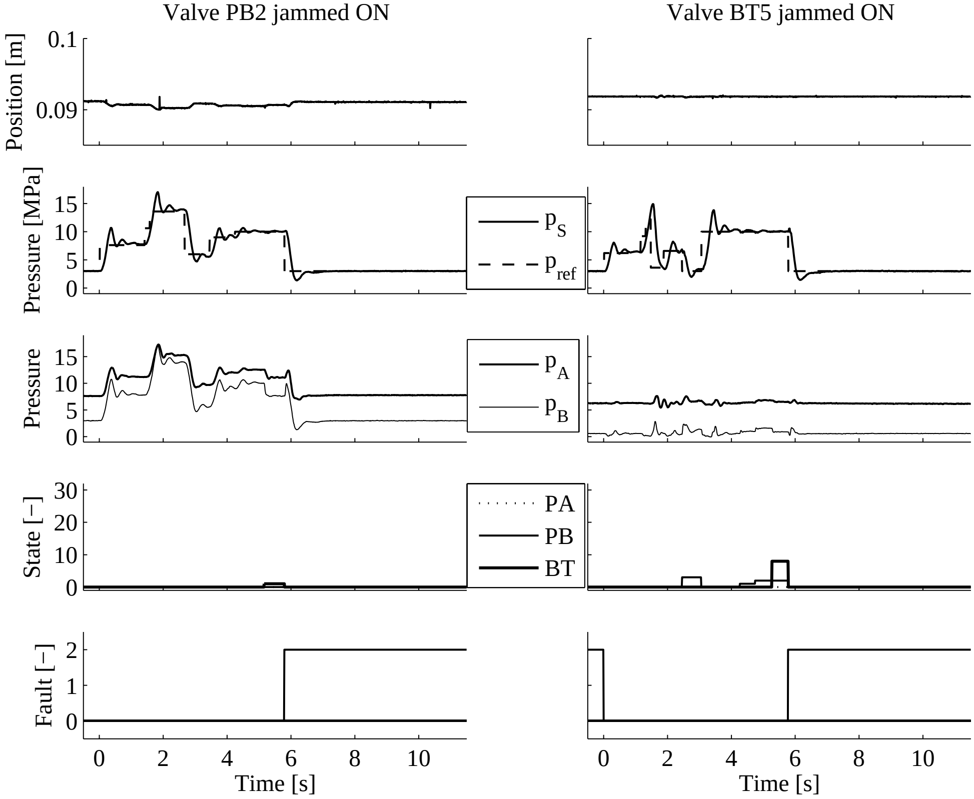

Figure 7 Test cycles with valves PB2 and BT5 jammed open

5. CONCLUSIONS

The digital valve system has unique features concerning fault tolerance. It is capable of operation even if some of the on/off valves are out of order. Fault detection and diagnosis (FDD) tools are needed to find and locate possible faults. Electrical measurement enables possibility for on-line FDD but also creates another problem with possible sensor faults. The digital valve system usually has some pressure sensors to measure and calculate optimal opening combinations and they can also be used for FDD.

This paper presents an off-line pressure based fault detection cycle that is capable of detecting pressure sensor and valve jam faults. Faults are tested using a hydraulic boom and the results show that every single measured fault could be detected and diagnosed. At this point, the tests were performed only for side B valve faults. The results show that all tested faults can be detected and diagnosed. The cylinder movement during the tests is relatively small so the test can also be performed in tight surroundings.

The presented test cycle can be combined with the electrical measurement based FDD in order to improve the test system. After the detected faults are taken care of, the system is ready to continue operation with only a small degradation in valve system performance. The possibilities to operate the system with broken pressure sensor e.g. with an estimate, and jammed valve detection must also be researched. The test system could also be shaped as an automatic valve and orifice calibration system, which allows more flexibility in system design.

ACKNOWLEDGEMENTS

The research was supported by the Academy of Finland (Grant no. 80411)

REFERENCES

1. **Garimella, P. and Yao, B.** 2005. Model based fault detection of an electro-hydraulic cylinder. *Proceedings of American Control Conference.* June 8-10 2005, Portland, OR, USA, pp 484-489.
2. **Park, R.W.** 1997. Contamination control – a hydraulic OEM perspective. *Workshop on Total Contamination Control.* August 1997, Centre for Machine Condition Monitoring, Monash University, Australia.
3. **Johnson, M.A.** 2005. Pump monitoring and diagnosis. World Pumps, January 2005, pp. 34-36.
4. **Jiang, J. and Zhang, Y.** 2006. Accepting performance degradation in fault-tolerant control system design. *IEEE Transactions on Control Systems Technology.* March 2006. Vol 14, No 2, pp. 284-292.
5. **Kopp, C.** 1996. System reliability and metrics of reliability. Slides for lecture series. http://www.csse.monash.edu.au/~carlo/SYSTEMS/Reliability-PHA.pdf (Visited 11.1.2007).
6. **Schreurs, J. and Bednar, F.** 1990. On-line valve monitoring and diagnosis. *Computer Applications in Power*, IEEE, January 1990, Vol 3, Issue 1, pp. 25-29, ISSN 0895-0156.
7. **Siivonen, L.; Linjama, M.; Vilenius, M.** (2005). Analysis of fault tolerance of digital hydraulic valve system. *Proceedings of the Bath Workshop on Fluid Power Transmission & Motion Control* (PTMC'05), September 7-9 2005, Bath, UK, pp. 133-146, ISBN 13 978-0-470-01677-0.

8. **Linjama, M., Huova, M., Boström, P., Laamanen, A., Siivonen, L., Morel, L., Waldén, M. and Vilenius, M.** 2007. Design and implementation of energy saving digital hydraulic control system. *Proceedings of the Tenth Scandinavian International Conference on Fluid Power*. May 21-23 2007, Tampere, Finland, Vol 2, pp. 341-359, ISBN 978-952-15-1759-4.

9. **Siivonen, L., Linjama, M. and Vilenius, M.** 2005. Fault tolerance of digital hydraulic valve system with separately controlled flow paths. *Proceedings of 4th FPNI – PhD Symposium*. Vol 2. June 13-17. Sarasota, FL, USA, pp. 331-343, ISBN 1-4243-0500-4.

10. **Siivonen, L., Linjama, M., Huova, M. and Vilenius, M.** 2007. Fault detection and diagnosis of digital hydraulic valve system. *Proceedings of the Tenth Scandinavian International Conference on Fluid Power*. May 21-23 2007, Tampere, Finland, Vol 1, pp. 211-226, ISBN 978-952-15-1758-7.

Pumps: Modelling, Performance and Noise

A Simulation Study to Reduce Noise of Compact Power-Split-Drive Transmissions

Richard Klop, Kyle Williams, Daniel Dyminski, Monika Ivantysynova
Purdue University Department of Agricultural and Biological Engineering, West Lafayette, IN, USA

ABSTRACT

The aim of this study is to demonstrate a simulation based approach of reducing noise generation in compact power-split-drive transmissions. A compact output-coupled transmission designed for a passenger car is modeled based on a typical drive cycle for inner-city driving. This study identifies noise sources and discusses various methods of noise reduction techniques in a compact power-split transmission. The influence of valve plate design in regards to noise generation over a complete operating range is the primary focus. This study emphasizes the complexity of optimizing for minimum noise generation over a large operating range.

1. INTRODUCTION

The design of power-split-drive transmissions is a fast growing technology seeking applications in new market segments such as passenger cars and commercial vehicles. However, current technology of hydraulic hybrids permits these transmissions to be applied to this market segment based on one primary design drawbacks. Current hydraulic transmissions emit large amounts of noise and need to be more compact. Much research has been conducted to identify noise sources and develop strategies to reduce noise generation in hydrostatic pumps and motors. Previous research suggests that noise generation in axial piston machines is attributed to two primary sources: fluid borne and structure borne noise. The reduction of flow pulsations inherently can reduce pressure pulsations in the hydraulic system. Pressure pulsations in the system are transmitted to hydraulic components causing vibration, thus generating air-borne noise. Likewise, the reduction of oscillating forces produced from a limited number of pistons can reduce vibrations on the swash plate or driving flange. The reduction of both fluid and structure borne noise sources can reduce the overall noise generation in axial piston machines. However, this study applies these discoveries to establish methods to reduce noise generation in a compact power-split output-coupled transmission consisting of two displacement machines. The transmission studied is designed for a passenger car used primarily for inner-city driving. The functions and control strategies are modeled to determine a complete operating map of the transmission. Each displacement machine is modeled using a simulation tool designed for bent-axis type axial piston machines. This simulation tool provides a model to calculate the instantaneous cylinder pressure, the resulting flow pulsation on both ports, oscillating forces exerted on all parts of the rotating group, driving flange moments and internal leakage. This model is used to design a new valve plate for each unit to minimize noise generation. A drive cycle based on low-speed inner-city driving is used to provide a scope to perform valve plate

Power Transmission and Motion Control 2007 Edited by Dr D N Johnston and Professor A R Plummer
© With The Centre for Power Transmission and Motion Control

optimization. This study presents a simulation-based solution to reduce noise generation in compact transmissions. Moreover, this study identifies numerous factors that may be considered and demonstrates the extreme complexity of optimizing for noise reduction in compact transmissions.

2. OPERATIONAL PARAMETER RANGES OF THE OUTPUT COUPLED POWER SPLIT DRIVE

The output coupled PSD shown in Fig. 1 is characterized by the coupling of the hydrostatic transmission (HST) with two displacement machines, unit I and unit II, to the output shaft A of the transmission.

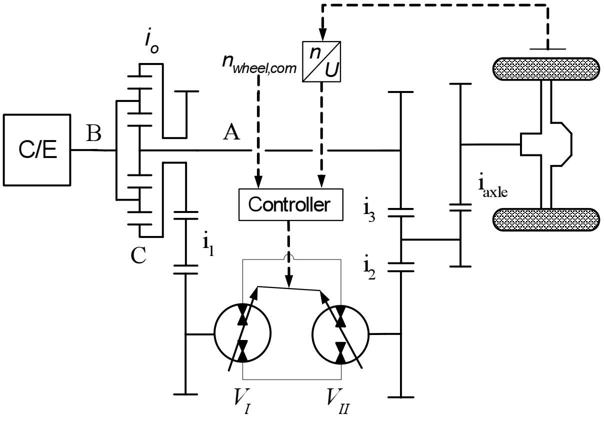

Figure 1 Output coupled power split drive

A strategy for controlling pump and motor displacement assuming a closed loop control of vehicle velocity is shown in Fig. 1. With the proposed closed loop control scheme the volumetric displacement of each unit is adjusted at the same time at any vehicle velocity. This allows the use of a mechanical linkage system for both units and simplifies the pump and motor adjustment system. The operating parameter ranges of both hydraulic displacement machines such as pump speed, n_{I}, motor speed, n_{II}, unit displacement, V, and differential system pressure, Δp, vary greatly under any drive cycle. The task of this section is to present the operating ranges of these parameters under an arbitrary drive cycle for the output coupled power split drive (PSD) shown in Fig. 1 with the intent of providing some operational points in which to optimize the hydraulic units about. To accomplish this task a simulation has been performed in which the operating parameters vary greatly as a result of the chosen drive cycle input. A generic small urban vehicle was simulated under an acceleration cycle as described in Fig. 3. The simulation specifications are shown in Table 1. An engine speed profile shown in Fig. 2 was assumed, with maximum engine speed set to 4000 RPM. The power split drive simulation was accomplished using Power Split Drive Design software PSDD, a software library built in a Matlab/Simulink environment (Mikeska and Ivantysynova, 2002). The software takes into consideration both the mechanical and hydraulic efficiencies of the hydraulic displacement machines and the efficiencies of all other mechanical components such as gears and clutches. The pump speed, n_{I}, and motor speed, n_{II}, are shown in Fig. 4 and Fig. 5, respectively. The resulting differential system pressure is shown in Fig. 6

Table 1 Simulation parameters

Parameter	Symbol	Value	Units
Unit I max displacement	V_I	85 x 10^{-6}	[m^3/rev]
Unit II max displacement	V_{II}	85 x 10^{-6}	[m^3/rev]
Gear ratio 1	i_1	+2.2:1	[-]
Gear ratio 2	i_2	-1.09:1	[-]
Gear ratio 3	i_3	-2.37:1	[-]
Axle ratio	i_{axle}	-4:1	[-]
Standing gear ratio	i_o	-1.6	[-]
Vehicle mass	m_{veh}	1355	[kg]
Dynamic tire roll radius	r_{tire}	.258	[m]
Engine speed max	$n_{eng,max}$	4000	[RPM]

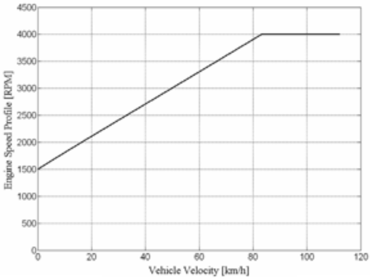

Figure 2 Engine profile

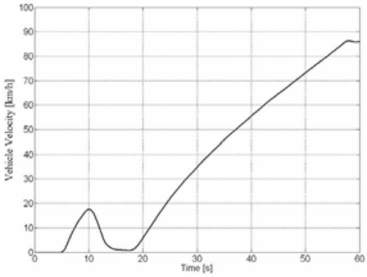

Figure 3 Input velocity signal profile

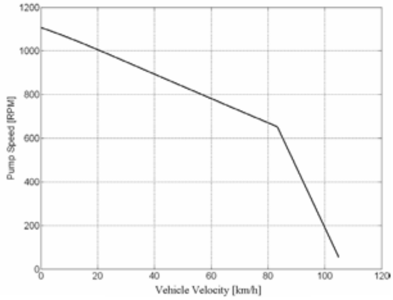

Figure 4 Pump speed

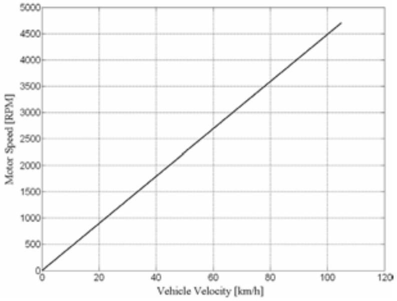

Figure 5 Motor speed

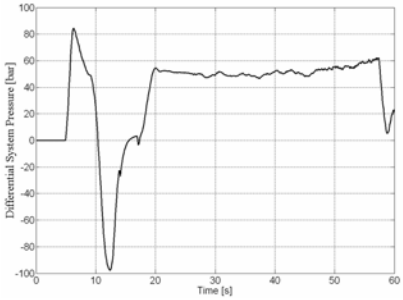

Figure 6 Differential system pressure

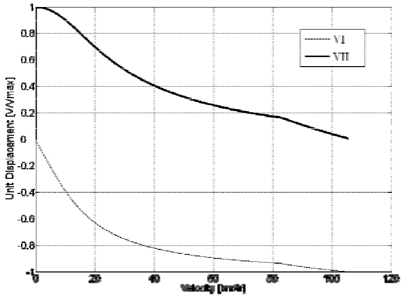

Figure 7 Unit displacements

As can be seen in Figs. 4-7, pump speed, n_{I}, motor speed, n_{II}, differential system pressure, Δp, and unit displacements, V_{I} and V_{II}, vary in a broad range under an arbitrary acceleration cycle.

3. HYDRAULIC NOISE SOURCES IN POWER-SPLIT-DRIVES

One of the main noise sources in compact power-split-drive transmissions are the noise generated by the displacement machines. Noise sources in hydrostatic pumps and motors are attributed to both fluid and structure borne noise.

The use of a finite number of displacement chambers inherently produces flow and force pulsations. The flow pulsations caused by pump kinematics can be calculated by the pump displacement, pump speed and the number of pistons. In practice, the amplitude of flow pulsations is much larger due to the compressibility effects in the oil and reverse flow into the piston chamber. In addition, the real flow pulsation is superimposed by varying gap flows. The resulting flow pulsations on the pump outlet and inlet are the main source of fluid borne noise and are easily transmitted throughout the hydraulic system. Cavitation is another type of fluid borne noise generation that must be considered as a cause of noise in displacement machines.

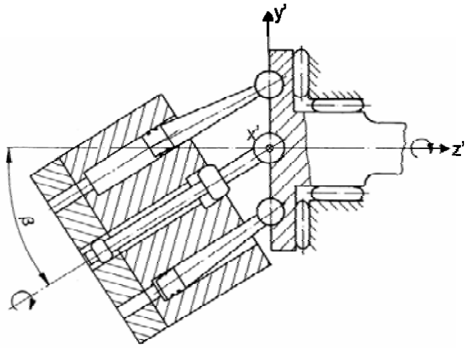

Figure 8 Bent axis general scheme

Induced vibrations transmitted to the pump casing and further to other connecting components represent a source of structure borne noise. Each piston exerts a force on the driving flange depending on the instantaneous cylinder pressure, piston friction and inertia force. These three forces are time dependent and exert a highly oscillating resultant force on the driving flange causing vibration. Consequently, the resultant force acts away from the driving flange center point causing a moment in all three axes. Based on the coordinate system convention shown in Fig. 8, each piston force acts closely to the y'-z' plane. Thus the largest moment amplitude on the driving flange is in the x'-direction. However, moments in all three directions can contribute to structure borne noise and must be considered in designing for noise reduction.

Noise generation in compact power-split-drive transmissions is a unique combination of fluid and structure borne noise sources of each unit. The particular selection of unit sizes, number of pistons, and the length of connecting lines between each unit have a large influence on the resulting pressure pulsations in the system. For example, a system with a considerable amount of line length connecting each unit compared to a compact system with two units placed back-to-back with very little line length will behave very differently. Each unit of the compact system will have a larger influence on one another, creating pressure and force pulsations that are more dependant on the interaction of the units. The selection of number of pistons and unit sizes may vary the required speed of the units, thus changing the frequency and kinematic flow ripple. Fluid flow and force pulsations of different frequencies are superimposed to create resultant forces in the system. Superimposed pressure and force pulsations based on a strong correlation of both units represent the sources of noise in a compact power-split-drive transmission.

A comprehensive method of designing quiet compact power-split-drive transmissions is to consider all noise sources based on the design factors of various unit combinations. That is, an optimization process must encompass all possible combinations of two hydrostatic units including the nature of the assembly and the dependant behavior of both units.

4. PUMP AND MOTOR SIMULATION MODELING

The following model was created for calculating instantaneous cylinder pressure, the resulting flow pulsation on both ports, oscillating forces exerted on all parts of the rotating group, driving flange moments and internal leakage for any bent-axis type axial piston machine. This model provided a foundation to perform valve plate optimization to reduce pressure and force pulsations in the output-coupled transmission studied.

4.1. Instantaneous Pressure in Displacement Chamber

Instantaneous cylinder pressure has a significant impact on both noise sources: oscillating flow pulsations and forces pulsations on the driving flange. The valve plate design determines the profile of the instantaneous cylinder pressure and consequently flow ripple and moments on the driving flange.

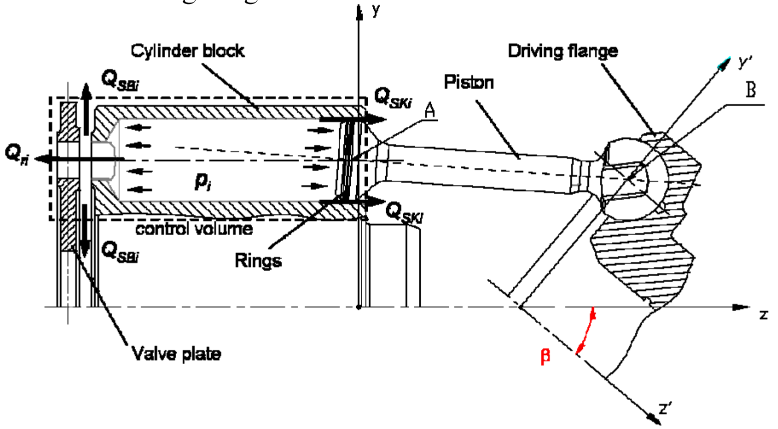

Figure 9 Pressure in displacement chamber

By law of conservation of mass applied to the control volume in Fig. 9, the differential equation for the pressure behavior in displacement chamber is given by

$$\frac{dp_i}{dt} = \frac{K}{V_i}\left(Q_{ri} - Q_{SKi} - Q_{SBi} - \frac{dV_i}{dt}\right) \qquad (1)$$

where K is the fluid bulk modulus and V represents total volume in the displacement chamber. For necessary simplification of this study, leakage flow Q_{SBi} and Q_{SKi} are neglected.

$$V = V_0 - s_k A_k \tag{2}$$

Volume V_0 represents the volume inside the displacement chamber at outer dead point. The change in volume with respect to time is then written as

$$\frac{dV}{dt} = v_k A_k \tag{3}$$

Flow through the valve plate into the high and low pressure ports from cylinder i is denoted by Q_{ri}. Turbulent flow is assumed and calculated based on the valve plate opening area at each angular position. Flow Q_{ri} is calculated separately through each port to capture any cross-flow between the high and low pressure ports.

$$Q_{rHPi} = \alpha_D \cdot A_{rHP} \cdot \sqrt{\frac{2}{\rho}} \cdot \sqrt{|p_i - p_{HP}|} \cdot sign(p_{HP} - p_i) \tag{4}$$

$$Q_{rLPi} = \alpha_D \cdot A_{rLP} \cdot \sqrt{\frac{2}{\rho}} \cdot \sqrt{|p_i - p_{LP}|} \cdot sign(p_{LP} - p_i) \tag{5}$$

The opening area from the displacement chamber to high and low pressure ports is denoted by A_{rHP} and A_{rLP}, respectively. The opening areas are obtained using a simulation tool, AVAS (**A**utomated **V**alve plate **A**rea **S**earch). AVAS is a simulation tool based in Unigraphics developed to analyze the geometry of any given valve plate (Ivantysynova et al, 2004). AVAS requires a valve plate CAD model and cylinder opening geometry of a given pump. AVAS calculates the minimum opening area from the displacement chamber to the output ports at a given angular resolution for one complete revolution of the cylinder block (Fig. 10).

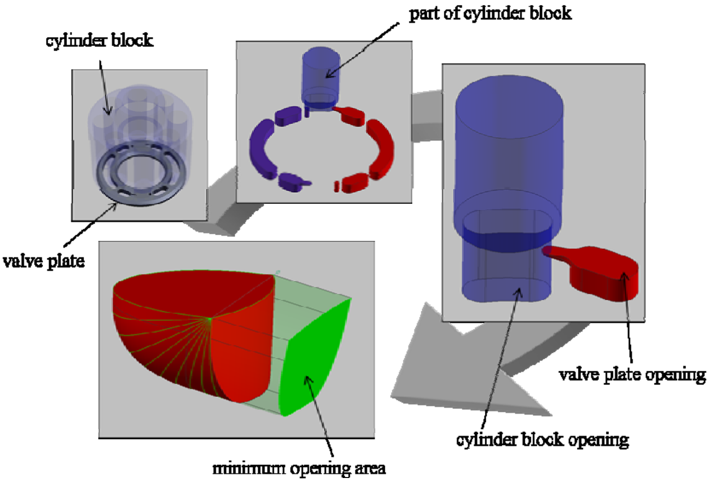

Figure 10 Principle structure of AVAS

Volumetric efficiency is calculated based on the effective and theoretical flow. For the pumping unit and motoring unit, volumetric efficiency is expressed with Eqs. 6 and 7, respectively.

$$\eta_{v\_pump} = \frac{Q_{eff\_pump}}{Q_{theor}} \cdot 100 \tag{6}$$

$$\eta_{v\_motor} = \frac{Q_{theor}}{Q_{eff\_motor}} \cdot 100 \tag{7}$$

The effective flow for the pumping unit is characterized by the discharge flow. The effective flow for the motoring unit is dependant on the summation of input flow and internal leakage flow, *Q*s. Theoretical flow is calculated based on the derived displacement volume and unit speed.

$$Q_{eff\_pump} = Q_{rHPi} \tag{8}$$

$$Q_{eff\_motor} = Q_{rHPi} + Q_s \tag{9}$$

$$Q_{theor} = V_i \cdot n \tag{10}$$

4.2. Driving Flange Moments

Oscillating forces exerted on the driving flange have a significant impact on structure borne noise. Oscillating forces exerted on the piston are transmitted to the driving flange, consequently creating a moment about three axes. These moments are iteratively minimized in the valve plate optimization process.

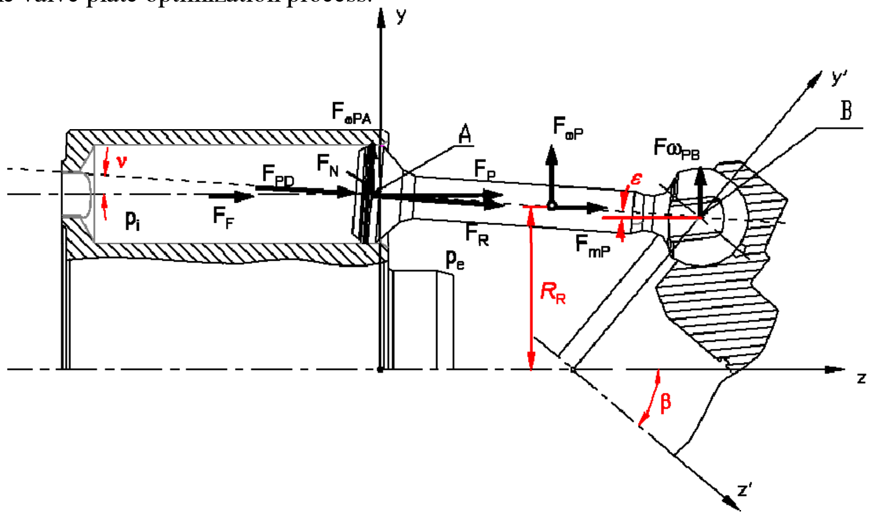

Figure 11 Forces exerted on piston

The largest magnitude of force exerted on the piston is due to pressure in the displacement chamber. The pressure force F_{PD}, is given by

$$F_{PD} = A_P \cdot (p_i - p_e) = \frac{\pi \cdot d_P^2}{4} \cdot (p_i - p_e) \tag{11}$$

where A_P is the area of the piston surface and *d*p is the outermost piston diameter. The inertia force, F_{mP}, is described by the piston mass, m_p, piston angular velocity, ω, radius to the piston center of mass, R_R, piston angular position, φ, and the driving flange angle relative to the cylinder block, β.

$$F_{mP} = -m_P \cdot a_R = m_P \cdot \omega^2 \cdot R_R \cdot \sin\beta \cdot \cos\varphi \tag{12}$$

The centrifugal force acting on the piston center of the mass is calculated as follows.

$$F_{\omega P} = m_P \cdot R_R \cdot \omega^2 \tag{13}$$

The resultant force, F_P acting along the cylinder axis at point A consists of the pressure force, centrifugal force, and friction force. However, for simplification in this particular study, friction force is not considered.

$$F_P = F_{PD} + F_{mP} + F_F \tag{14}$$

Calculating force components acting at point B requires the distance from the piston center of mass to point A, l_{lp}, as well as the total distance from point A to point B, l_p at each angular position. These lengths may be calculated based on the geometrical parameters shown in Fig. 12 . The centrifugal force component in the ball-joint on driving flange at point B is described as well as each corresponding component in the x-y-z coordinate system.

$$F_{\omega PB} = \frac{F_{\omega P} \cdot l_{PA}}{l_P} \tag{15}$$

$$F_{\omega PBx} = F_{\omega PB} \cdot \sin\varphi \tag{16}$$

$$F_{\omega PBy} = F_{\omega PB} \cdot \cos\varphi \tag{17}$$

$$F_{\omega PBz} = 0 \tag{18}$$

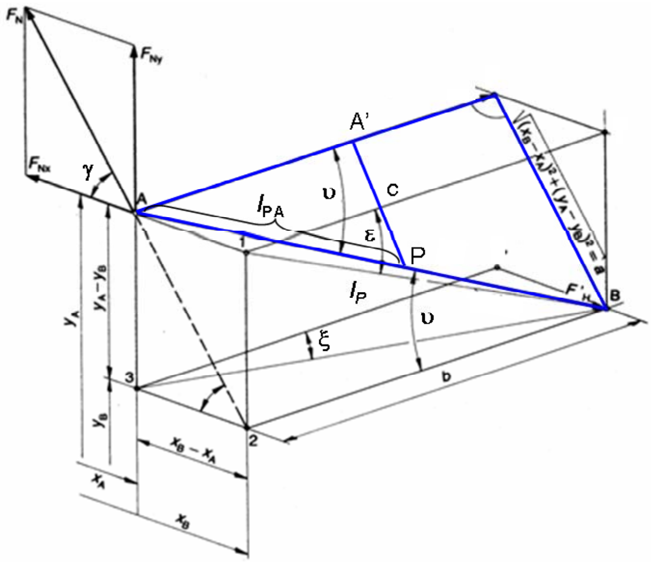

F_N
F_{Ny}
F_{Nx}
γ
A
A'
l_{PA}
υ
c
ε
P
l_P
F'_H
B
ξ
υ
b
1
2
3
y_A
$y_A - y_B$
y_B
$x_B - x_A$
x_A
x_B
$\sqrt{(x_B - x_A)^2 + (y_A - y_B)^2} = a$

Figure 12 Diagram to determine force components at driving flange point B

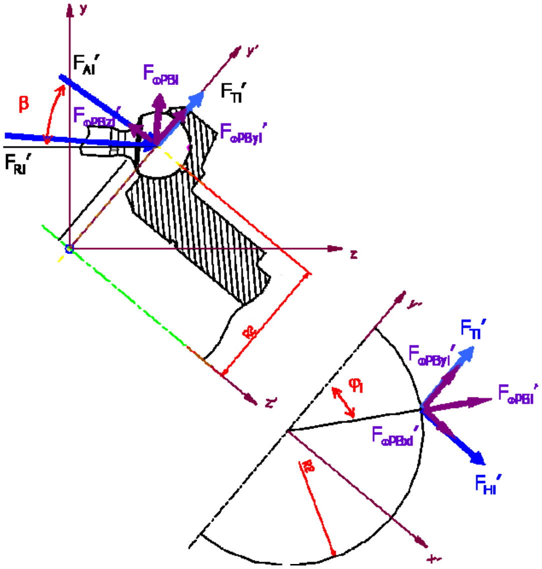

y
y'
F_{AI}'
$F_{\omega PBI}$
F_{TI}'
β
$F_{\omega PBzI}'$
$F_{\omega PByI}'$
F_{RI}'
z
z'
y'
F_{TI}'
$F_{\omega PByI}'$
φ_I
$F_{\omega PBI}'$
$F_{\omega PBxI}'$
F_{HI}'

Figure 13 Forces acting at driving flange

The piston rod force F_R is resolved at point B as well as calculating force components F_R' and F_H' as shown in Fig. 13.

$$F_R' = \frac{F_P}{\cos\varepsilon} \tag{19}$$

$$F_H' = F_P \cdot \tan\xi \tag{20}$$

The resultant force coaxial to the piston, F_R', is calculated with an axial component, F_A', and a radial component, F_T', as shown in Fig. 13 .

$$F_A' = F_R' \cdot \cos(\beta - \varepsilon) \tag{21}$$

$$F_T' = F_R' \cdot \sin(\beta - \varepsilon) \tag{22}$$

The components of the centrifugal force in the *x', y'* and *z'* directions at point B are given by

$$F_{\omega PBxi}' = F_{\omega PBi} \cdot \cos\beta \cdot \sin\varphi \tag{23}$$

$$F'_{\omega\mathrm{PByi}} = F_{\omega\mathrm{PBi}} \cdot \cos\beta \cdot \cos\varphi \tag{24}$$

$$F'_{\omega\mathrm{PBzi}} = -F_{\omega\mathrm{PBi}} \cdot \sin\beta \cdot \cos\varphi \tag{25}$$

Therefore, the components of the resultant force acting on driving flange and the total force may be described.

$$F'_{\mathrm{x}} = \sum_{i=1}^{z} F'_{\mathrm{Hxi}} + \sum_{i=1}^{z} F'_{\omega\mathrm{PBxi}} \tag{26}$$

$$F'_{\mathrm{y}} = \sum_{i=1}^{z} F'_{\mathrm{Tyi}} + \sum_{i=1}^{z} F'_{\omega\mathrm{PByi}} \tag{27}$$

$$F'_{\mathrm{z}} = \sum_{i=1}^{z} F'_{\mathrm{Azi}} + \sum_{i=1}^{z} F'_{\omega\mathrm{PBzi}} \tag{28}$$

$$F' = \sqrt{F'^{2}_{\mathrm{x}} + F'^{2}_{\mathrm{y}} + F'^{2}_{\mathrm{z}}} \tag{29}$$

Based on the forces acting on the driving flange, the moments about *x'*, *y'* and *z'* axes are obtained.

$$M'_{\mathrm{x}} = \sum_{i=1}^{z} y'_{\mathrm{Ai}} \cdot F'_{\mathrm{Azi}} + \sum_{i=1}^{z} y'_{\omega\mathrm{PBi}} \cdot F'_{\omega\mathrm{PBzi}} \tag{30}$$

$$M'_{\mathrm{y}} = -\sum_{i=1}^{z} x'_{\mathrm{Ai}} \cdot F'_{\mathrm{Azi}} - \sum_{i=1}^{z} x'_{\omega\mathrm{PBi}} \cdot F'_{\omega\mathrm{PBzi}} \tag{31}$$

$$M'_{\mathrm{z}} = -\sum_{i=1}^{z} x'_{\mathrm{Ti}} \cdot F'_{\mathrm{Tyi}} + \sum_{i=1}^{z} y'_{\mathrm{Hi}} \cdot F'_{\mathrm{Hxi}} \tag{32}$$

5. VALVE PLATE OPTIMIZATION STRATEGY

A comprehensive method of redesigning both valve plates of two bent-axis type axial piston machines used in a compact power-split-drive transmission to reduce noise generation must consider the following factors: flow pulsations in both high and low pressure ports, oscillating forces and moments exerted on the driving flange, and localized insufficient pressure causing cavitation. Furthermore, each factor must be minimized throughout a complete operating range of the transmission with high emphasis around the typical drive cycle. Moreover, investigating superimposed pressure and force pulsations generated by the interaction of both units allows for a more complete simulation of the entire system. For simplification purposes, this study focuses on strategies to minimize noise sources over a complete operating range by simulating each unit independently.

Much research in developing methods to reduce fluid and structure borne noise sources in axial piston machines has been conducted. One of the most common noise reduction techniques is to modify the opening and closing areas of the valve plate with the use of pre-compression grooves. Other techniques include providing cross port, cross-angle, air-release grooves, a check valve timing device, valve plate indexing and pre-compression volume. The method chosen for this study is to design pre-compression grooves using cross-port. The addition of cross-flow between high and low pressure ports reduces efficiency and is carefully monitored during the optimization process.

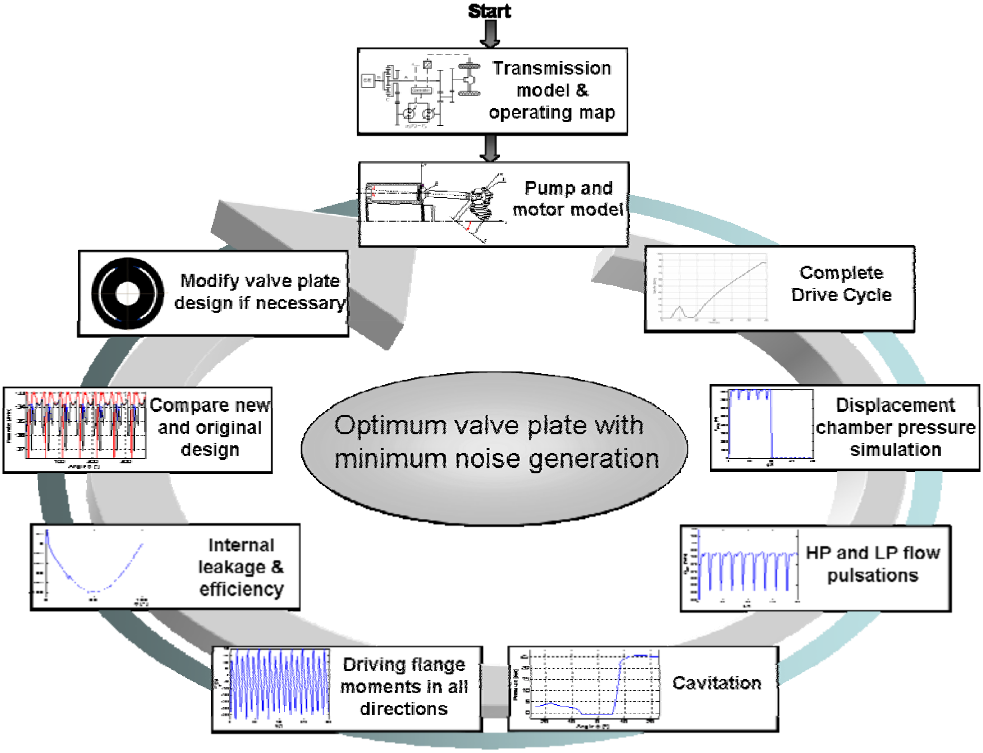
Start
Transmission model & operating map
Pump and motor model
Complete Drive Cycle
Displacement chamber pressure simulation
HP and LP flow pulsations
Cavitation
Driving flange moments in all directions
Internal leakage & efficiency
Compare new and original design
Modify valve plate design if necessary
Optimum valve plate with minimum noise generation

Figure 14 Optimization strategy

The optimization process considering relevant noise source factors is illustrated in Fig. 14. Firstly, a model of the output-coupled transmission is created and used to determine a complete operating map over a given speed range. Secondly, each unit is modeled to allow the calculation of instantaneous cylinder pressure, high and low pressure port flow pulsations, driving flange moments in all directions, and internal leakage and efficiency. The original design is simulated over a complete operating range of the transmission based on a desired drive cycle; this is used a reference throughout the optimization process. Next, a new valve plate is designed and simulated over select operating points in the drive cycle. The new valve plate design is modified and the simulation process is repeated until all noise sources, i.e flow ripple on both ports and amplitudes of moments applied on the driving flange, are minimized throughout the operating range while maintaining system efficiency. This optimization strategy requires a keen understanding of how the displacement chamber pressure dictates flow and force pulsation. Groove designs may vary in size and shape; however, the opening area between the displacement chamber to the outlet/inlet port for the fluid is the primary factor to consider.

6. SIMULATION RESULTS

The studied output-coupled transmission is comprised of two identical 85cc bent-axis type axial piston machines. Each unit was simulated throughout a complete operating map specified in Section 2; both units were optimized with high emphasis on the chosen drive cycle. Table 2 describes all operating parameter combinations chosen for simulation. Many valve plates were created and simulated during several iterations of the optimization cycle; however, a total of 324 simulations were carried out once the optimized valve plate was determined. Each unit with both the standard design as well as the optimized design is simulated at each operating point for comparison.

Table 2 Operating parameter combinations used in simulation

Δp [bar]	Vehicle Speed [km/hr]	Pump Speed [rpm]	Motor Speed [rpm]	Pump Disp. angle [%max]	Motor Displ. angle [%max]
20,30,40,50,60,70,80,90,100	5	1080	225	20.0	97.0
20,30,40,50,60,70,80,90,100	10	1060	450	38.5	90.5
20,30,40,50,60,70,80,90,100	20	1005	890	63.0	70.0
20,30,40,50,60,70,80,90,100	30	950	1345	75.0	53.0
20,30,40,50,60,70,80,90,100	40	895	1795	82.0	40.5
20,30,40,50,60,70,80,90,100	50	835	2240	86.5	32.0
20,30,40,50,60,70,80,90,100	60	780	2690	89.5	25.5
20,30,40,50,60,70,80,90,100	70	725	3140	92.0	21.0
20,30,40,50,60,70,80,90,100	80	670	3585	93.0	17.0

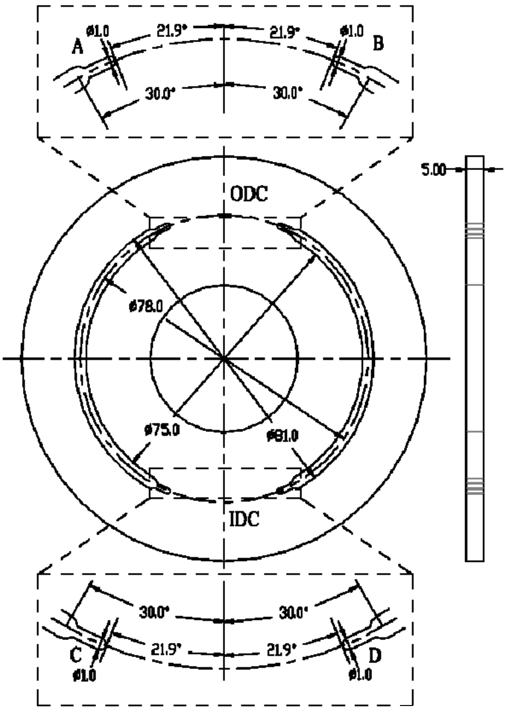

Figure 15 Original valve plate design used for both pump and motor

Figure 15 illustrates the original valve plate design used for both pumping and motoring units. Pre-compression grooves drilled through the complete thickness of the valve plate are used; however no cross-flow was present. This valve plate is symmetric with identical groove designs at the ODC (outer dead center) and IDC (inner dead center) of both high and low pressure ports.

Figures 16 and 17 illustrate new valve plate designs for the pumping unit (left) and the motoring unit (right). The direction of rotation for both units is in the counter-clockwise direction. Both valve plates are asymmetrical; they are designed with distinct groove lengths at both the ODC and IDC.

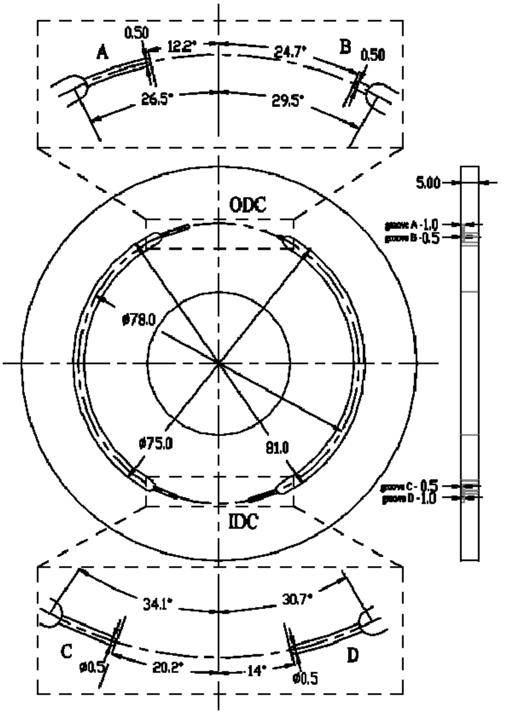
A
0.50
12.2°
24.7°
B
0.50
26.5°
29.5°
ODC
5.00
groove A-1.0
groove B-0.5
ϕ78.0
ϕ75.0
81.0
groove C-0.5
groove D-1.0
IDC
34.1°
30.7°
C
ϕ0.5
20.2°
14°
ϕ0.5
D

Figure 16 Optimized valve plate design for pumping unit

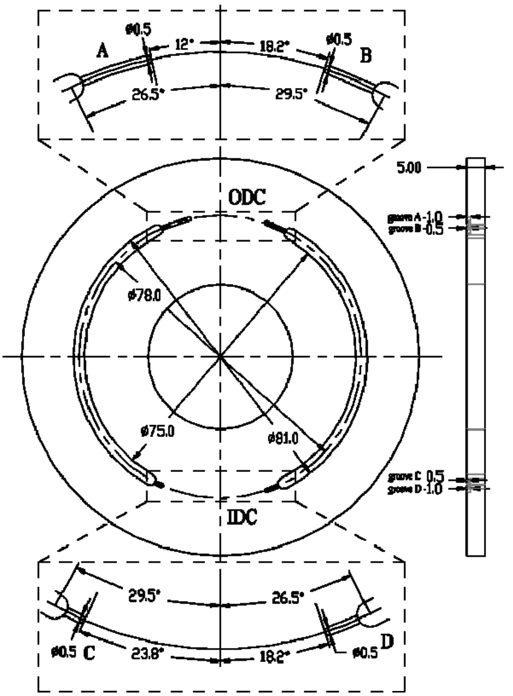
ϕ0.5
A
12°
18.2°
ϕ0.5
B
26.5°
29.5°
5.00
ODC
groove A-1.0
groove B-0.5
ϕ78.0
ϕ75.0
ϕ81.0
groove C 0.5
groove D-1.0
IDC
29.5°
26.5°
ϕ0.5 C
23.8°
18.2°
ϕ0.5
D

Figure 17 Optimized valve plate design for motoring unit

Each design utilizes cross-porting as well as pre-compression grooves machined to a specified depth. This groove design improves control of the opening area during severe pressure increases and decreases, thus, influencing oscillating flows and forces. Furthermore, sufficient control of de-pressurization can avoid localized pressure drops below atmospheric pressure causing potential for cavitation.

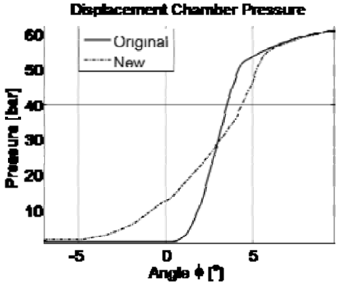

Figure 18 Pressure rise

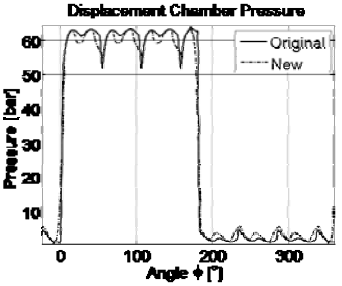

Figure 19 Instantaneous chamber pressure

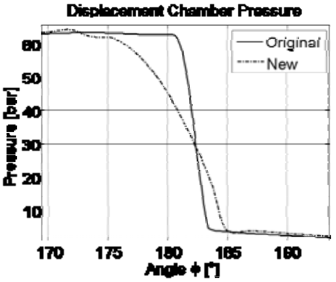

Figure 20 Pressure drop

Figure 19 illustrates the predicted displacement chamber pressure profile over one shaft revolution; Figs. 18 and 20 illustrate a closer image of pressure rise and fall. Figure 19 compares the pressure profile of the pumping unit with the original and new valve plate design simulated at a vehicle speed of 80 km\hr and a pressure difference of 60 bar.

Instantaneous displacement chamber pressure dictates both the oscillating flows in both ports as well as oscillating forces on the driving flange. Figure 21 illustrates a comparison between the original and new design of flow pulsations and oscillating moments for 60 degrees of one shaft revolution.

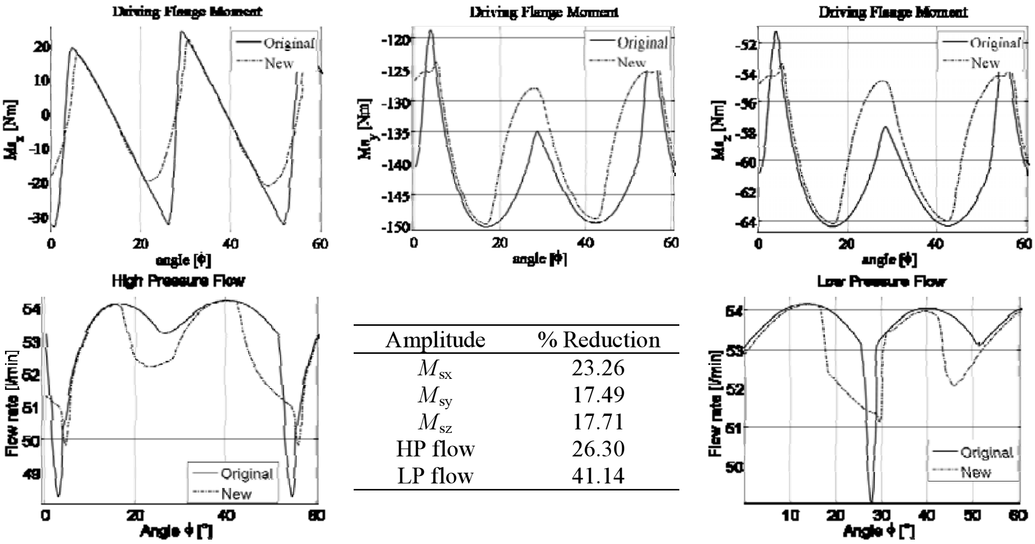

Amplitude	% Reduction
M_{sx}	23.26
M_{sy}	17.49
M_{sz}	17.71
HP flow	26.30
LP flow	41.14

Figure 21 Pump simulation comparison at vehicle speed = 80 km/hr and Δp = 60 bar

Such data illustrated in Figs. 18 through 21 were obtained in simulations of both displacement machines at all operating points over an entire operating map; however, noise source reductions only along the specified drive cycle were considered during optimization. Figure 22 illustrates the drive cycle in which the optimization process was based. The pressure profile on the left represents the pressure difference throughout the drive cycle used in simulation, which is based on the model described in section 2. This plot illustrates the same pressure difference shown in Fig. 6; however, this is plotted over vehicle speed in [km/hr]. Negative pressures are achieved in simulation to represent vehicle braking; the mode of each unit is switched. The center plot displays the absolute value of the pressure difference. Consideration of changing modes of each displacement unit is beyond the scope of this study. Therefore, the profile on the right represents the adjusted pressure difference profile throughout the drive cycle for which optimization is based.

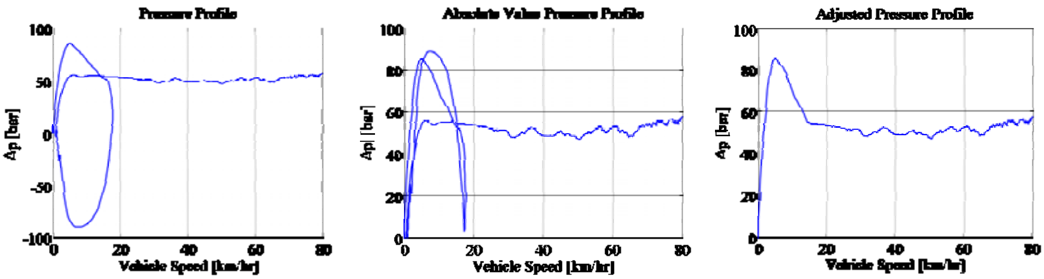

Figure 22 Drive cycle

All data is presented as contour plots illustrating flow pulsation amplitudes, driving flange moments, and volumetric efficiency over the entire operating range of the transmission. Figure 23 shows plots of high (top) and low (bottom) pressure port flow ripples in [L/min] of the original (left) and new (center) designed pumping unit; additionally, contour plots of HP and LP flow ripple reductions in percentage is shown in the far right column. Figure 23 displays varying contours of flow pulsation amplitudes (left and center) and percent reductions (right) throughout varying system pressure differences and vehicle speeds. The adjusted pressure profile from Fig. 22 is also plotted to illustrate the optimized drive cycle. Flow ripples in both ports were reduced over the entire operating map from 10-40%.

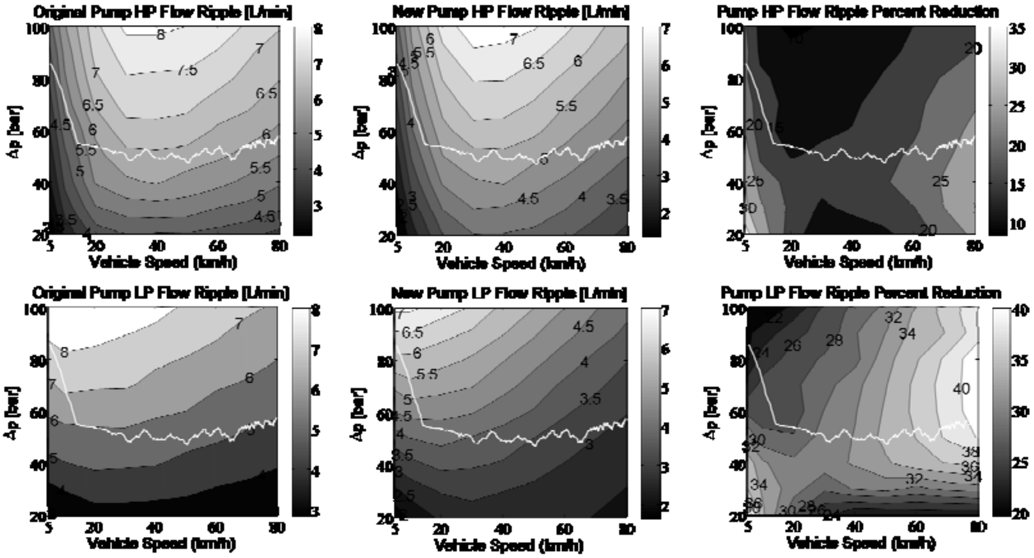

Figure 23 Pump flow ripples and percent reductions over operating range

Figure 24 illustrates driving flange moment amplitudes about the x (top), y (middle) and z (bottom) axes for the pumping unit. Contour plots showing the original (left), new design (center), and percent reductions (right) of moment amplitudes are displayed. Reductions of moment amplitudes in the x-direction were almost always positive reaching up to 40%.

Note that reductions throughout the specified drive cycle fall in the range of 20-40%. Reductions of moment amplitudes in the y-direction range from 6-16% where the maximum reductions occur throughout the specified drive cycle. Moment amplitude reductions in the z-direction were reduced up to 15% where positive reductions occurred throughout the entire drive cycle and nearly the entire operating map.

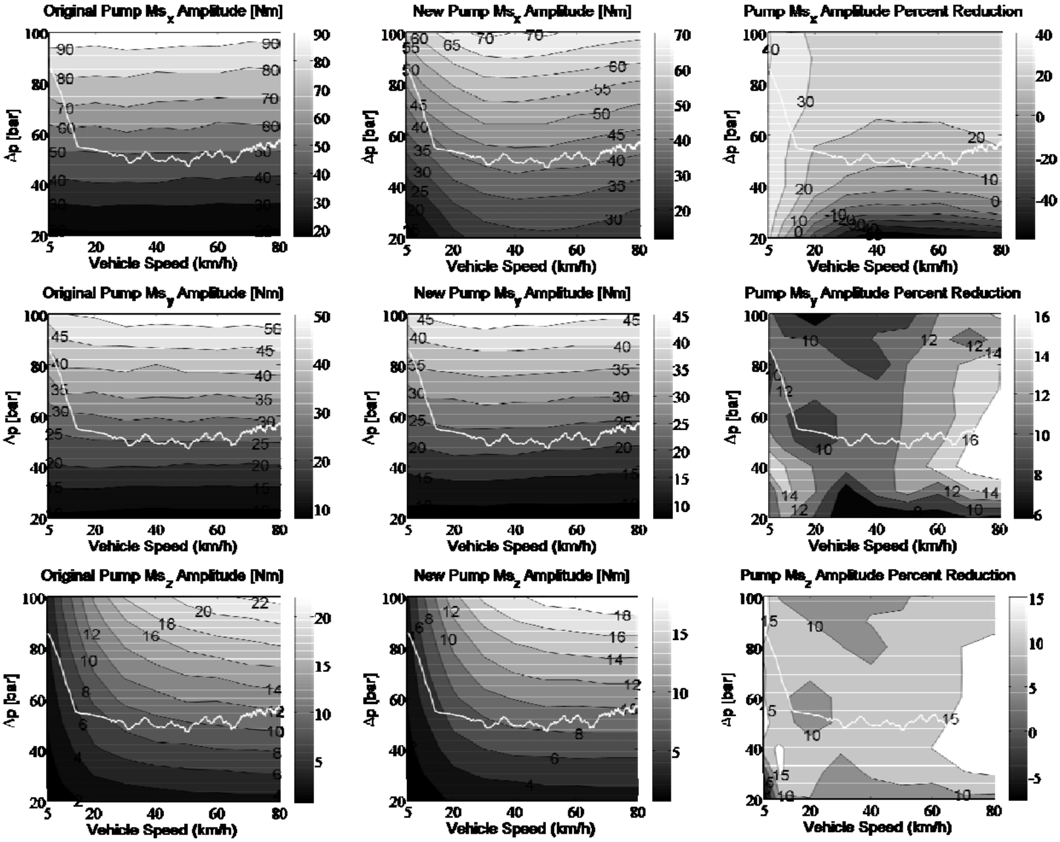

Figure 24 Pump moment amplitudes and percent reductions over operating range

Figure 25 displays contour plots representing volumetric efficiency as a percentage of the original design (left), new design (center), and the difference (right). The use of cross-ports in the new design produces more internal leakage; this is a compromise in the optimization process. Volumetric efficiencies were calculated based on compressibility losses and internal leakage only; no gap flows were considered. It is assumed that the majority of volumetric efficiency reduction is incurred by internal leakage. Reductions of volumetric efficiency throughout a majority of the specified drive cycle are less than 1%.

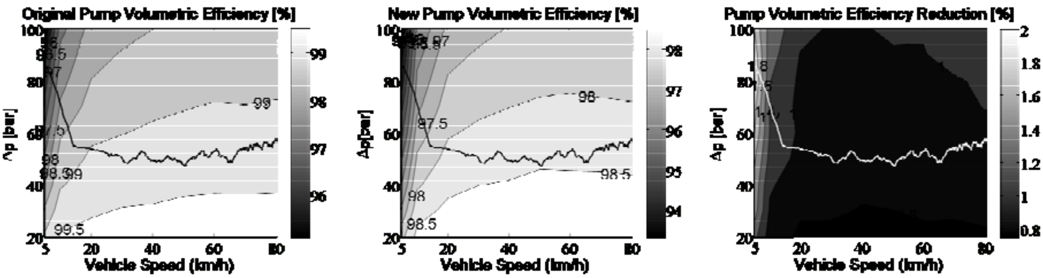

Figure 25 Pump volumetric efficiencies and percent reductions over operating range

Results of flow ripple in both ports and driving flange moment amplitudes about all three axes for the pumping unit indicate significant reductions over the optimized drive cycle as well as reductions over the entire operating map. Such noise source reductions were achieved with a minimum expense of volumetric efficiency.

Similar plots illustrating results of fluid and structure borne noise predictions were also created for the motoring unit; however, due to a constraint on the paper length, only high pressure port flow, driving flange moment in the x-direction, and volumetric efficiency plots are shown. Figure 26 illustrates flow ripple [L/min] in high pressure ports of the old (left) and new (center) designs for the motoring unit as well as the reduction expressed in percentage (right). High pressure flow ripple reductions range from 20-40% over the optimized drive cycle and remain positive for nearly the entire operating map. Low pressure flow ripple reductions range from 0-40% over the optimized drive cycle and also remain positive for nearly the entire operating map; however, these contour plots are not shown.

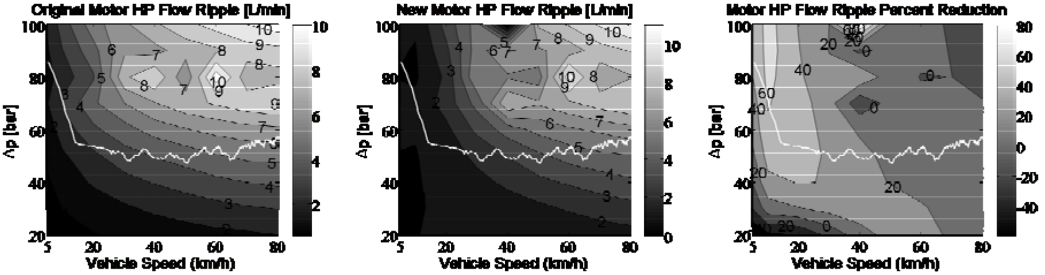

Figure 26 Motor flow ripples and percent reductions over operating range

Figure 27 illustrates driving flange moments about the x axes of the motoring unit. Moment amplitudes in [Nm] of the old (left) and new (center) design as well as the reduction expressed in percentage (right) is illustrated. Moment amplitude reductions in the x-direction range from 20-40% throughout the optimized drive cycle and remain positive for nearly the entire operating map. Amplitude reductions in the y and z-directions range from 20-60% throughout the optimized drive cycle and also remain positive for nearly the entire operating map; however, these contour plots are not shown.

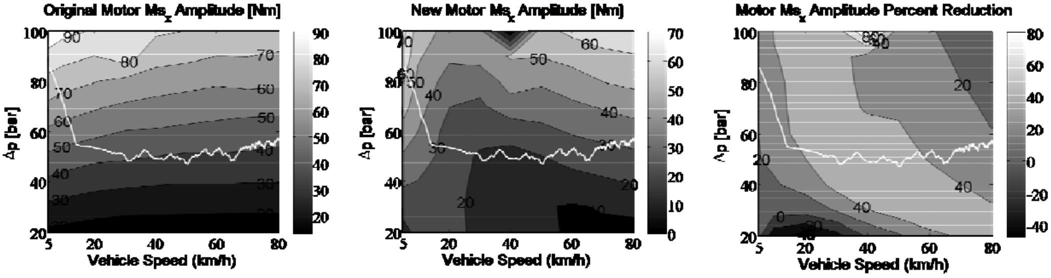

Figure 27 Motor moment amplitudes and percent reductions over operating range

Figure 28 illustrates motor volumetric efficiency of the old (left) and new (center) designs as well as the percent reduction (right). Reductions of volumetric efficiency occurred due to the compromise between adding internal leakage and minimizing flow and pressure pulsations. Reductions over a majority of the cycle were less than 1%.

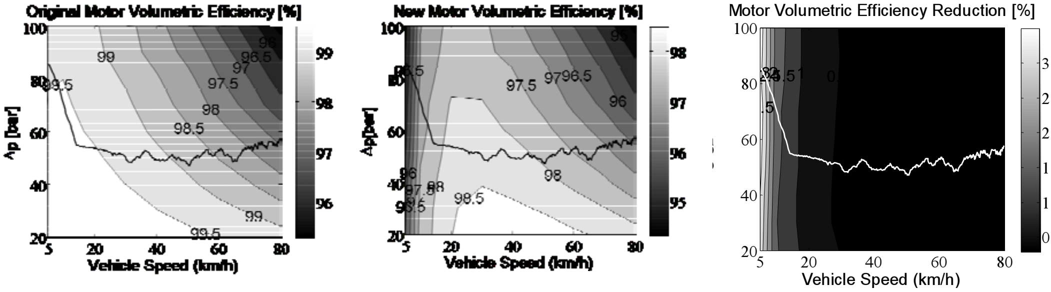

Figure 28 Motor volumetric efficiencies and percent reductions over operating range

7. CONCLUSION

This study demonstrates a simulation based approach of reducing noise generation in compact power-split-drive transmissions. A standard output-coupled transmission consisting of two identical bent-axis type axial piston machines was modeled. A complete operating map of the transmission was determined, and a typical drive cycle based on inner-city driving was simulated. Each displacement machine was modeled to calculate instantaneous displacement chamber pressure, flow pulsations in both ports, oscillating driving flange moments and volumetric efficiency. Strategies for noise reduction in compact power-split-drive transmissions were introduced; numerous factors influencing noise generation were described composing an extremely complex process necessary to achieve noise reduction. Valve plate optimization was carried out to propose possible solutions; this study presented reductions in flow ripples at both ports and oscillating driving flange moment amplitudes over a large operating map while maintaining volumetric efficiency at a reasonable level. This study emphasizes the extremely complex nature of noise reduction in power-split-drive transmissions.

8. NOMENCLATURE

A	Center of piston end in displacement chamber	[-]
A_{k}	Piston area	[m^2]
a_R	Piston acceleration	[m/s^3]
A_{rHP}	Opening area on the HP side	[m^2]
A_{rLP}	Opening area on the LP side	[m^2]
B	Center of piston ball	[-]
C/E	Combustion Engine	[-]
d_{P}	Piston diameter	[m]
$F_{\omega P}$	Centrifugal force in the piston center of the mass	[N]
$F_{\omega PA}$	Centrifugal force in the piston end	[N]
$F_{\omega PB}$	Centrifugal force in the piston head	[N]
$F_{\omega PBx}\ F_{\omega PBy}\ F_{\omega Pyz}$	Centrifugal force in the piston head x, y, z components	[N]
F'	Resultant force acting on the driving flange	[N]
F'_A	Axial component of the force F'_R	[N]
F'_{Ai}	Axial component of F'_{R}	[N]
F'_H	Normal component of the force F_R in the piston head	[N]
F'_R	Tangential component of F_R	[N]
F'_T	Component of F'_R perpendicular to F'_A	[N]
$F'_x F'_y\ F'_z$	Resultant driving flange force along x', y', z' axes	[N]
F_{F}	Friction force acting on piston rings	[N]
F_{mP}	Inertia force of the piston	[N]
F_{N}	Normal component of F_{R}	[N]
F_{Nx}	x-component of normal force F_{R}	[N]
F_{Ny}	y-component of normal force F_{R}	[N]
F_P	Resultant axial force	[N]
F_{PD}	Pressure force exerted on the piston	[N]
F_R	Force acting along piston axis	[N]
i	Number of the pistons	[-]
$i_1\ i_2\ i_3$	Gear ratio 1, 2, 3	[-]
i_{axle}	Gear ratio of axle	[-]
i_o	Standing gear ratio	[-]
K	Bulk modulus	[Pa]
l_P	Piston length (from point A to B)	[m]
l_{PA}	Distance between center of the mass and the end of the piston	[kg]
l_{PB}	Distance between center of the mass and the head of the piston	[kg]
M'_{r}	Resultant driving flange moment	[Nm]
$M'_{\mathrm{x}}\ M'_{\mathrm{y}}\ M'_{\mathrm{z}}$	Driving flange moment about x', y', z' axis	[Nm]
M_{eng}	Engine torque	[Nm]
M_{I}	Unit I torque	[Nm]
M_{II}	Unit II torque	[Nm]
m_P	Piston mass	[kg]
m_{veh}	Vehicle mass	[kg]
M_{wheel}	Wheel torque	[Nm]
n	Pump speed	[rpm]
n_D	Driving flange speed in x-y-z coordinates	[rpm]
n_{eng}	Combustion engine speed	[rad/s]

n_{I}	Unit I speed	[rad/s]
n_{II}	Unit II speed	[rad/s]
$n_{\mathrm{wheel,com}}$	Commanded wheel speed	[rad/s]
P	Center of mass of piston	[-]
p_e	Pressure in case	[Pa]
P_{eng}	Engine power	[W]
p_{HP}	High pressure	[Pa]
p_i	Pressure in displacement chamber	[Pa]
p_{LP}	Low pressure	[Pa]
P_{wheel}	Wheel power	[W]
Q	Volumetric flow rate	[m^3/s]
$Q_{\mathrm{eff\_motor}}$	Effective flow rate for motoring unit	[m^3 /s]
$Q_{\mathrm{eff\_pump}}$	Effective flow rate for pumping unit	[m^3 /s]
Q_{rHPi}	Flow through the HP side	[m^3 /s]
Q_{ri}	Flow through the valve plate	[m^3 /s]
Q_{rLPi}	Flow through the LP side	[m^3 /s]
Q_{s}	Internal leakage	[m^3 /s]
Q_{SBi}	Gap flow between cylinder block and valve plate	[m^3 /s]
Q_{SKi}	Gap flow between piston and cylinder	[m^3 /s]
Q_{theor}	Theoretical flow rate	[m^3 /s]
R_1	Cylinder block pitch radius	[m]
R_2	Driving flange pitch radius	[m]
R_{R}	Distance between piston center of mass and z axis	[m]
r_{tire}	Dynamic roll radius	[m]
S_{k}	Piston displacement	[m]
t	Time	[s]
V_{I}	Unit I displacement volume	[m^3/rev]
V_i	Volume	[m^3]
V_{II}	Unit II displacement volume	[m^3/rev]
v_P	Piston velocity	[m/s]
v_{veh}	Vehicle velocity	[m/s]
x, y, z	Cylinder block coordinates	[m]
x', y', z'	Driving flange coordinates	[m]
$x_{\mathrm{A}}, y_{\mathrm{A}}$	Position of point A, x and y-components	[-]
$x_{\mathrm{B}}, y_{\mathrm{B}}$	Position of point B, x and y-components	[-]
α_D	Flow coefficient	[-]
β	Swivel angle	[°]
Δp	Differential system pressure	[Pa]
γ_D	Angular position of point *C*	[°]
γ, γ_R	Angles	[°]
$\varepsilon, \varepsilon_R$	Angle	[°]
$\eta_{\mathrm{v\_motor}}$	Volumetric efficiency of motoring unit	[%]
$\eta_{\mathrm{v\_pump}}$	Volumetric efficiency of pumping unit	[%]
ν, ν_R	Angle	[°]
ξ, ξ_R	Angle	[°]
ρ	Fluid density	[Kg/m^3]
φ	Angular shaft position	[°]
ω	Piston angular velocity	[rad/s]

REFERENCES

1 **Carl, B., Ivantysynova, M. and Williams, K.** 2006. Comparison of Operational Characteristics in Power Split Continuously Variable Transmissions. *SAE Commercial Vehicle Engineering Congress & Exhibition.* Rosemont, IL, USA *SAE Technical Paper 2006-01-3468*

2 **Grabbel, J. and Ivantysynova, M.** 2005. An investigation of swash plate control concepts for displacement controlled actuators. *International Journal of Fluid Power, Vol. 6 (2005), No.2 August 2005. pp.19- 36.*

3 **Harrison, A.M. and Edge, K. A.,** 2000. Reduction of axial piston pump pressure ripple. *Proceedings of The Institution of Mechanical Engineers, Vol 214 Part I, p53-63.*

4 **Huang, C. and Ivantysynova, M.** 2003. A new approach to predict the load carrying ability of the gap between valve plate and cylinder block. *Bath Workshop on Power transmission and Motion Control PTMC 2003*, Bath, UK, pp. 225 – 239.

5 **Ivantysyn J.** and **Ivantysynova M.** 2001. *Hydrostatic Pumps and Motor, Principles, Designs, Performance, Modeling, Analysis, Control and Testing.* New Delhi. Academic Books International. ISBN-81-85522-16-2.

6 **Ivantysynova M., Seeniraj G., Huang C.,** 2005. Comparison of different valve plate designs focusing on oscillating forces and flow pulsation. *The Ninth Scandinavian International Conference on Fluid Power, SICFP '05, Linköping, Sweden.*

7 **Ivantysynova, M.** 2003. Prediction of pump and motor performance by computer simulation. *1st International Conference on Computational Methods in Fluid Power Technology.* Melbourne November 2003, Australia, pp. 505 – 522.

9 **Ivantysynova, M. and S.K. Christiansen** 2005. Automatic Valve Plate Design based on optimized Pressure Profile. Las Vegas, USA. *Technical Paper NCFP I05-14.1.*

10 **Ivantysynova, M. et al** 2002. Prediction of swash plate moment using the simulation tool CASPAR. *ASME International Mechanical Engineering Congress*, New Orleans, USA, *IMECE 2002-39322.*

11 **Ivantysynova, M. et al** 2004. Computer Aided Valve Plate Design - An Effective Way to Reduce Noise. *2004 SAE International Commercial Vehicle Engineering Congress* , Chicago, IL, USA, *SAE Technical Paper 2004-01-2621.*

12 **Ivantysynova, M. et al** 2004. Computer Aided Valve Plate Design - An Effective Way to Reduce Noise. *2004 SAE International Commercial Vehicle Engineering Congress* , Chicago, IL, USA, *SAE Technical Paper 2004-01-2621.*

14 **Mikeska, D. and Ivantysynova, M.** 2002. Virtual prototyping of power split drives. *Proc. Bath Workshop on Power Transmission and Motion Control PTMC 2002*, Bath, UK, pp. 95 – 111.

15 **Ossyra, J.C. and Ivantysynova, M.** 2004. Application for a Direct Optimization Procedure for Drive Line Control. *Bath Workshop on Power Transmission and Motion Control PTMC 2004*, Bath, UK, pp. 53 – 69.

18 **Seeniraj, G.K. and Ivantysynova, M.** 2006. Impact of valve plate design on noise, volumetric efficiency and control effort in an axial piston pump. *ASME International Mechanical Engineering Congress, Chicago, USA, IMECE2006-15001.*

19 **Wieczorek, U. and Ivantysynova, M.** 2002. Computer Aided Optimization of Bearing and Sealing Gaps in Hydrostatic Machines - The Simulation Tool CASPAR. *International Journal of Fluid Power,* Vol. 3 (2002), No.1, pp. 7-20.

Flow Pulsation Reduction for Variable Displacement Motors using Cross-angle

L. Ericson, J. Ölvander, and J-O. Palmberg
Department of Management and Engineering, Linköpings universitet, Sweden

ABSTRACT

This paper considers using the cross-angle in variable displacement hydraulic machines. The cross-angle is a fixed displacement angle around the axis perpendicular to the normal displacement direction. The cross-angle changes the angles to the pistons top and bottom dead centres as a function of the fraction of displacement in such a way that the valve plate timing is varied and different pre-compression and decompression angles are obtained.

A non-gradient optimisation technique, the Complex method, is used together with a comprehensive simulation model in order to find the optimal cross-angle for a variable displacement hydraulic motor. The paper shows that the cross-angle can be used to reduce noise in variable displacement motors. One issue that makes the motor application more difficult is the increased dependence between outlet and inlet flow ripple which is not found in pump applications. Furthermore, the paper discusses how to use the cross-angle for machines which can work both as a motor and a pump.

1 INTRODUCTION

One main drawback with hydraulic systems is noise, mainly created in hydrostatic pumps and motors. The noise arises from flow ripple, forces and bending moments due to the rapid increase and decrease of the pressure in the machines. The flow ripple can be divided into two parts: kinematic and compressible flow ripple. Kinematic flow ripple is created due to the limited number of pumping elements and is difficult to change, whereas compressible flow ripple is created due to compressibility effects in the pumping chambers. One simple and well known modification is to add a pre-compression angle and a decompression angle to the valve plate to obtain a pre-compression of the fluid before the cylinder reaches the high pressure kidney, and a decompression of the fluid before the low pressure kidney. This design is very sensitive to different operation conditions, [1]. The pre- and decompression angles can be optimised for a specific displacement angle, pressure level and rotation speed but if the conditions are changed the angles are no longer optimal any more and the design can even increase the noise level for certain conditions. One way to tune the valve plate timing, i.e. the opening angles to the valve plate's kidneys, is to revolve the valve plate, [2].

Power Transmission and Motion Control 2007 Edited by Dr D N Johnston and Professor A R Plummer
© With The Centre for Power Transmission and Motion Control

Other methods to improve the design of the valve plate in order to reduce flow ripple include pressure relief groove [3] and pre-compression filter volume [4], which are less sensitive to changing operation conditions. However, there are many other more or less complicated methods to reduce noise in hydraulic systems, see for instance [5]. All existing features are more or less dependent on operation conditions or include movable parts to reduce noise at different conditions.

Hydraulic systems tend to be developed for more and more varied operation conditions and this involves the machines as well. If the power losses are to remain small the machines have to be adapted to the different working conditions and this implies that the noise reduction features need to be insensitive to changing working conditions, if the machine is to work quietly under all operating conditions.

One feature with no movable parts which changes the machine's port timing depending on the operating condition is the cross-angle. The cross-angle is a fixed displacement angle perpendicular to the normal displacement angle. The effect of the cross-angle is that the top and bottom dead centres move with the displacement of the machine. Thus, it could in some ways be compared to a revolving valve plate, but with less flexibility as the cross-angle is fixed. However, with the cross-angle it is possible to make the pulsations less sensitive to variations in the displacement of the machine.

The cross-angle was first patented by Citroen [6] and appeared in literature eleven years later in 1974, [7] and [8]. The cross-angle has been exhaustively investigated in [9] and [10], and in [11] the cross-angle is experimentally tested with good results. In these references the investigations have been made for variable displacement pumps, but there is evidence that the same feature can improve fluid pulsations in motors as well.

In the literature concerning noise reduction in hydraulic systems, the focus is on pumps, which are usually taken to be the biggest source of fluid borne noise. However, hydraulic motors are also major fluid-borne noise creators. The features which are used in pumps to reduce noise are believed to be useful in motors too, but there is not much literature on this issue. In [12] a bent-axis motor is investigated and from the results the pressure ripple generated in motors can be compared to the levels in pumps.

The remainder of the paper has the following structure. First, the cross-angle is described in more detail and studied using a simplified mathematical model. In the next section the optimal cross-angle for a variable displacement motor is investigated using a non-gradient optimisation technique together with a comprehensive simulation model. This is followed by a study of the possibility of using the same cross-angle and valve plate for both motor and pump operation. The paper concludes with a discussion and a presentation of the conclusion drawn.

The machine studied in this paper is a 195 cm^3/rev variable nine-piston bent-axis machine with a displacement angle of $\pm$ 40° with both clockwise and anti-clockwise rotation. The dead volume in the cylinders is relatively small. One important limitation of the investigated machine is that the high and low pressure kidneys are not swapped.

2 THE CROSS-ANGLE AND ITS EFFECTS

The cross-angle is a fixed displacement angle, γ, perpendicular to the normal displacement angle, α. This results in an adjustment of the dead centre angle η, as a combination of the displacement angle and the cross-angle, see figure 1. A pump's resulting inclination is shown in figure 1(b). A machine which can have negative displacement angles with the same high pressure kidney will work as a motor, and the obtained inclination is shown in figure 1(c). As long as the high and low pressure kidney do not swap, the same direction of the cross-angle can be used for both motor and pump operation.

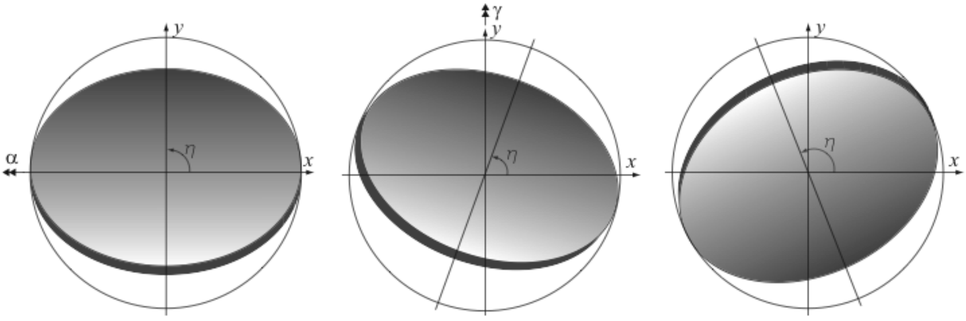

(a) Pump - ε = [0,1], $\gamma = 0$ (b) Pump - ε = [0,1], $\gamma > 0$ (c) Motor - ε = [-1,0], $\gamma > 0$

Figure 1: Swash plate orientation for pump and motor cases. (a) With a positive displacement angle α, i.e. the inclination around the x-axis, the dead centre angle η is 90°. (b) By displacing the pump also in the cross-angle direction, i.e. around the y-axis, the new inclination direction is obtained as a combination of α and γ. (c) The machine has a negative displacement angle and works as a motor with an increased angle to the dead centre axis.

For a pump with a cross-angle, the dead centre angle is decreased when the displacement angle varies from $\varepsilon = 1$ to $\varepsilon = 0$, see figure 2(a). In the motor case, when the displacement varies from $\varepsilon = -1$ to $\varepsilon = 0$, η is increased, see figure 2(b).

The cross-angle results in additional pre- and decompression due to the change of the location of the top and bottom dead centres respectively. The pre-compression increases when the displacement angle decreases, which is needed for optimal pressure equalisation. The top dead centre location, η, is calculated according to equation (1) when the cross-angle is introduced.

$$\eta = arctan\frac{-tan\alpha}{tan\gamma} \tag{1}$$

There is also a small change in the total displacement angle of the machine, equation (2), and the piston movement x_p, equation (3).

$$\beta = arccos\left(\frac{1}{\sqrt{tan^2\alpha + tan^2\gamma + 1}}\right) \tag{2}$$

$$x_p = R_d sin\beta cos(\omega t) \tag{3}$$

where $\omega t = 0$ at top dead centre and R_d is the radius of the driving flange. A more detailed explanation of equations (1) - (3) can be found in [9].

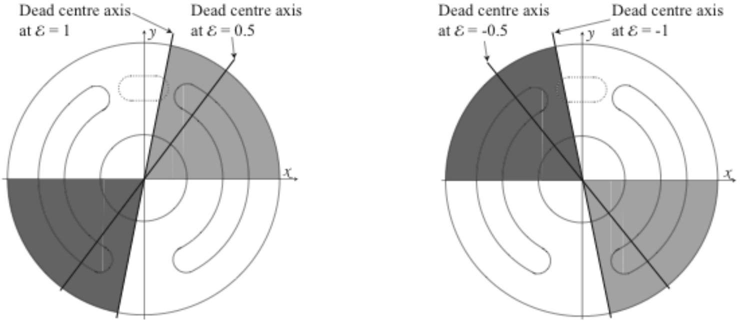
Dead centre axis at ε = 1
Dead centre axis at ε = 0.5
y
x
Dead centre axis at ε = -0.5
Dead centre axis at ε = -1
y
x

(a) Pump - ε = [0,1]

(b) Motor - ε = [-1,0]

Figure 2: The movements of the dead centre for a machine with a positive cross-angle during displacement changes. The dark grey part shows the area where the top dead centre moves and the light grey part is the area where the bottom dead centre moves when the displacement varies.

The cross-angle affects only sensitivity to changes in displacement angle and rotational speed, but not in pressure variations. The cross-angle can be used as a complement to other design features such as pre-compression filter volume and pressure relief grooves, but in this study only pre- and decompression angles are investigated.

2.1 Simplified mathematical model

To obtain a good view of the cross-angle needed to determine the correct top and bottom dead centre locations (TDC and BDC respectively), a simple model of the machine can be derived from the geometry of the machine and the continuity equation. With this model an approximate cross-angle for optimal design can be obtained. For a complete investigation of the optimal design, a comprehensive simulation model is needed, as will be presented in section 3.

In [9], Johansson lays the foundation of the derivation of the mathematical model shown below, but instead of the BDC, the TDC is calculated to achieve optimal decompression, i.e. correct pressure equalisation before the cylinder reaches the high pressure kidney. In this simplified model no consideration is taken to gradual opening to the kidneys, nor is leakage considered.

The cylinder volume at TDC, V_2, is compressed from V_1 during the time period t_1 to t_2 which results in an increase in pressure from low pressure p_l to high pressure p_h. This can be calculated using the continuity equation (4).

$$\begin{aligned} \int_{t_1}^{t_2} \sum q_{in} dt &= \int_{V_1}^{V_2} dV + \frac{V_1}{\beta_e} \int_{p_l}^{p_h} dp \\ \Rightarrow \Delta V &= \tfrac{V_1}{\beta_e}(p_h - p_l) + V_{loss} \end{aligned} \tag{4}$$

where $\Delta V = V_1 - V_2$ is the volume that needs to be compressed to achieve correct cylinder pressure when the cylinder connects to the high pressure kidney. β_e is the effective bulk modulus. The term V_{loss} refers to the flow that may leave the cylinder if the TDC is still not reached after the cylinder has been connected to the high pressure kidney. This happens if $\eta \geq \frac{\pi}{2} + \psi_2$, according to figure 3. The term V_{loss} can be calculated as

$$V_{loss} = \pi R_p^2 R_d sin\beta (1 - cos(\frac{-\pi}{2} - \psi_2 + \eta)) \tag{5}$$

where R_p is the piston radius.

The volume compression ΔV is achieved by a piston movement according to equation (6).

$$\Delta V = \pi R_p^2 (x_2 - x_1) \tag{6}$$

where x_2 is the piston position at TDC and x_1 refers to the cylinder volume V_1, which is when the low pressure kidney closes to the cylinder. The piston movement according to equations (3) and (6) gives

$$\begin{aligned} \Delta V &= \pi R_p^2 R_d sin\beta (1 - cos(\omega t^*)) \\ \Rightarrow \omega t^* &= arccos\left(1 - \frac{\Delta V}{\pi R_p^2 R_d sin\beta}\right) \end{aligned} \tag{7}$$

where ωt^* is the angle from the position where the cylinder closes to the low pressure kidney to the TDC, i.e. the angle where pre-compression occurs, illustrated in figure 3. The largest obtainable pre-compression angle is when $\omega t^* = \pi/2$; if this happens ΔV is too big to compress. The final dead centre can be calculated as

$$\eta = \frac{\pi}{2} + \omega t^* - \psi_1 \tag{8}$$

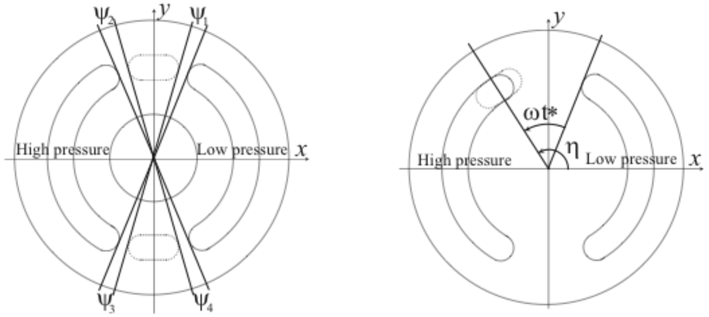

Figure 3: The valve plate definitions in the equations above. $\psi_1 - \psi_4$ are the overlap angles, η is the angle to the dead centre, and ωt^* is the angle where the pre-compression occurs.

The difference between the desired dead centre, equation (8) and the obtained dead centre, equation (1), can be minimised by optimising the overlap angles, ψ_1 - ψ_4, and the cross-angle, γ. Figure 4(a) shows the optimised results for both pre-compression at top dead centre and decompression at bottom dead centre. The figures show both the desired location of the dead centre and the obtained dead centre with the cross-angle implemented. If no cross-angle is used, the obtained dead centre angle can be compared to a constant value at all the displacements. The optimal cross-angle for pre-compression according to the simple model and with the parameter specified in section 1 is 6.6° and 1.4° for decompression.

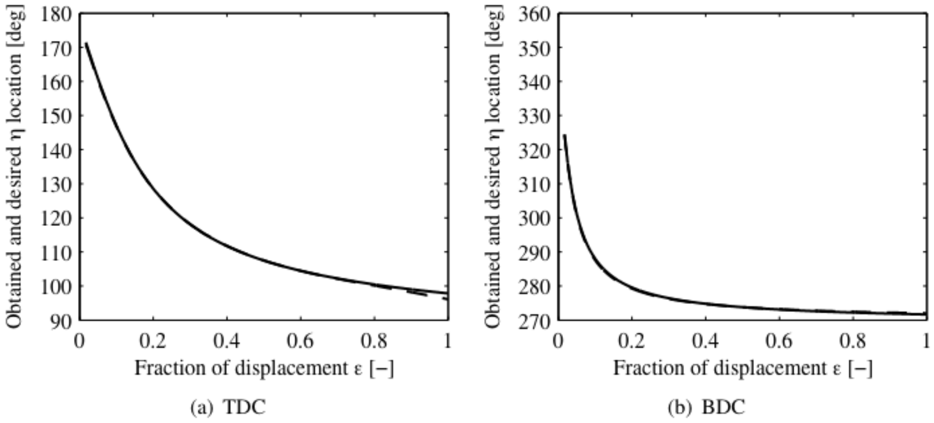

(a) TDC

(b) BDC

Figure 4: Desired (solid) TDC respective BDC angles compared to obtained (dashed) angle at different displacement angles. The two curves almost are identical. The best cross-angle is 6.6° for the TDC and 1.4° for the BDC with a simple mathematical model.

3 OPTIMISATION OF A COMPREHENSIVE SIMULATION MODEL

A comprehensive simulation model for a complete positive displacement hydraulic machine was created in the simulation program HOPSAN, [13], which is used mainly for hydraulic simulations. The model includes different states, such as cylinder pressure, piston forces, moments, and flow from each cylinder. Furthermore, the model makes it possible to investigate influences from pressure relief grooves, pre-compression filter volumes, a cross-angle etc.

3.1 Optimisation

In [10], optimisation of the cross angle for a variable displacement pump is performed both in frequency and time domains with multi-objective functions which include swash-plate moment, resulting piston force, and inlet and outlet flow ripple. The results for the different objectives give approximately the same design.

In this paper, flow ripple peak to peak value in the time domain is considered to be the main objective. The multi-objective problem formulation includes two individual objectives, high and low pressure flow ripple respectively, measured at three different displacements $\varepsilon = -1$, $\varepsilon = -0.5$ and $\varepsilon = -0.05$. Pressures and rotation speed are kept constant throughout the paper. High pressure is 25 MPa, low pressure is 0.5 MPa, and rotation speed 2000 rev/min. The optimisation problem includes some constraints, viz. the maximum cylinder pressure is limited to 3 MPa over the high pressure level, the minimum pressure is 0.05 MPa in order to avoid cavitation, and no leakage between the kidneys is allowed in order to avoid power losses. The design variables, $\mathbf{x}$, include the four kidney opening and closing angles, $\psi_1 - \psi_4$, and the cross-angle, γ. Pressure relief grooves and pre-compression filter volume can also be used, but to simplify the optimisation and to show the effect of the cross-angle alone, only pre- and decompression angles are used as flow ripple minimisers. Thus, the optimisation problem could be formalised according to equation (9).

$$\begin{aligned} \min\ F(\mathbf{x}) &= (f_{high}(\mathbf{x}), f_{low}(\mathbf{x}))^T \\ g_j(\mathbf{x}) &\leq 0, \quad j = 1,2,3 \\ x_i^l \leq x_i &\leq x_i^h, \quad i = 1,\ldots 5 \end{aligned} \tag{9}$$

$g_j(\mathbf{x})$ represents the pressure and leakage constraints and x^l and x^h represents the lower and upper limits for the kidney angles and the cross angle. The multi-objective optimisation problem stated in equation (9) is solved using the complex method [14], [15]. The complex method is a non-gradient based optimisation method that has been successfully used to optimise hydraulic systems in for example [9], [16]. The Complex method is a single objective optimisation method so the problem stated in equation (9) has been reformulated using a weighted sum with the weighting factor λ. The constraints are added to the objective function using penalty functions, see equation (10).

$$\begin{gathered} \min\ F(\mathbf{x}) = \lambda f_{high}(\mathbf{x}) + (1-\lambda) f_{low}(\mathbf{x}) + \sum_{j=1}^{3} p_j(\mathbf{x}) \\ x_i^l \leq x_i \leq x_i^h \\ \lambda \in \{0,1\} \end{gathered} \tag{10}$$

The individual objectives, f_{high} and f_{low}, are calculated based on the peak-to-peak value of the flow ripple in the high (q_{high}) and low (q_{low}) pressure kidneys for three different displacements, see equation (11).

$$\begin{aligned} f_{high}(\mathbf{x}) &= \sum_{\varepsilon} \max(q_{high}) - \min(q_{high}) \\ f_{low}(\mathbf{x}) &= \sum_{\varepsilon} \max(q_{low}) - \min(q_{low}) \end{aligned} \qquad \text{where} \qquad \varepsilon = -1, -0.5, -0.05 \tag{11}$$

3.2 Optimisation results

A resulting Pareto optimal front is obtained by solving equation (10) for different values of the weighting factor λ. The Pareto front illustrates the trade-off between the two competing objectives, see figure 5. For the cross-angle optimisation, optimal pre-compression and decompression require different values of the cross-angle. The best results for the high pressure flow ripple are obtained with a cross-angle of around 6°, whereas optimal low pressure flow ripple is obtained with a cross-angle of 3°. The best cross-angle for the total flow ripple (the sum of the high and low pressure flow ripple) is around 4°, which will be used as a fair compromise between the two objectives. Please observe that each point on the Pareto front is a different design with different values for the opening and closing of the valve plate kidneys, i.e. a different valve plate is required for each cross-angle.

3.3 Flow ripple analysis

In the analysis below the flow ripple in both time and frequency domains for a machine with a 4° cross-angle is studied and compared to a machine with ordinary pre- and decompression without a cross-angle. Both designs have a valve plate which is optimised to give as low flow

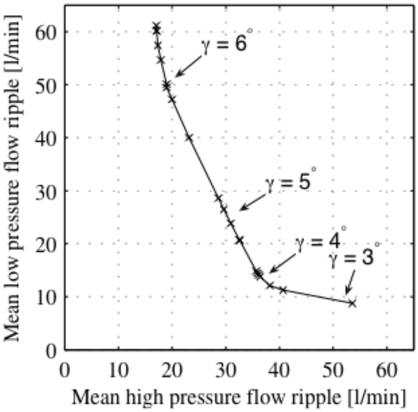

Figure 5: Pareto optimal front illustrating the trade-off between the flow ripple in the high and low pressure kidneys. The x-axis shows the average peak to peak value of the high pressure flow ripple at three different displacement angles, whereas the y-axis shows the mean peak to peak value of the low pressure flow ripple. The arrows indicate values of the optimised cross-angle at different locations on the Pareto front.

ripple as possible. Figure 6 shows the flow ripple results for the high pressure kidney for three different displacement angles, ε = -1, -0.5, -0.05. For full displacement angle, there is no significant difference between the two designs in frequency domain. In time domain the flow ripple appears later when a cross-angle is used because of the greater angle to the dead centre position. For smaller displacement angles the cross angle design shows improvements in both time and frequency domain, except for the fundamental frequency. This is caused by the increase in the available pre-compression angle and the kinematic flow ripple is increased therefore.

The flow ripple for the low pressure kidney is shown in figure 7. The results are improved for all displacement angles in both time and frequency domain, except for full displacement angle where the results are comparable.

In the analysis above a cross-angle which minimises the total flow ripple is used, but it may not be the best choice for all applications. If a bigger cross-angle is chosen, the high pressure flow ripple is decreased at the expense of the low pressure flow ripple. This can be justified if the high pressure flow ripple tends to spread in the system more than low pressure flow ripple. However, with a smaller cross-angle and a change of valve plate design the low pressure flow ripple can be decreased at the expense of the high pressure flow ripple.

4 DIFFERENT OPERATIONAL CONDITIONS

There is evidence that the cross-angle can be beneficial for machines operating both as motor and pump. As long as the low and high pressure kidneys are not swapped, the same direction of inclination of the cross-angle can be used. In figure 8(a), the obtained Pareto optimal front for pump operation is shown in circles. The pump operation is implemented by changing the displacement angle from negative to positive values. The procedure for creating the Pareto front for the pump case is the same as for the motor case.

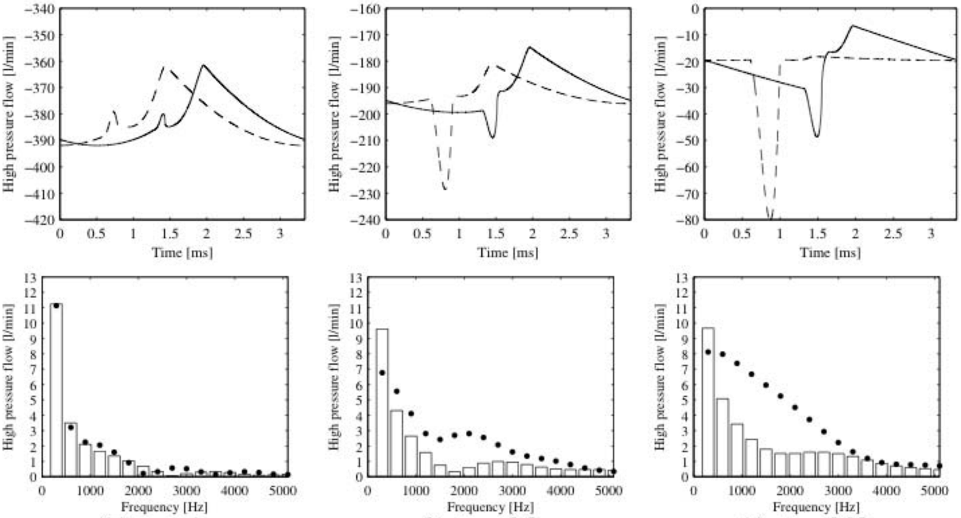

(a) $\varepsilon = -1$ (b) $\varepsilon = -0.5$ (c) $\varepsilon = -0.05$

Figure 6: Time and frequency domain flow ripple in the high pressure kidney with a cross-angle of 4°, solid lines and bars, compared to an optimised pre- and decompression valve plate with no cross-angle, dashed lines and points.

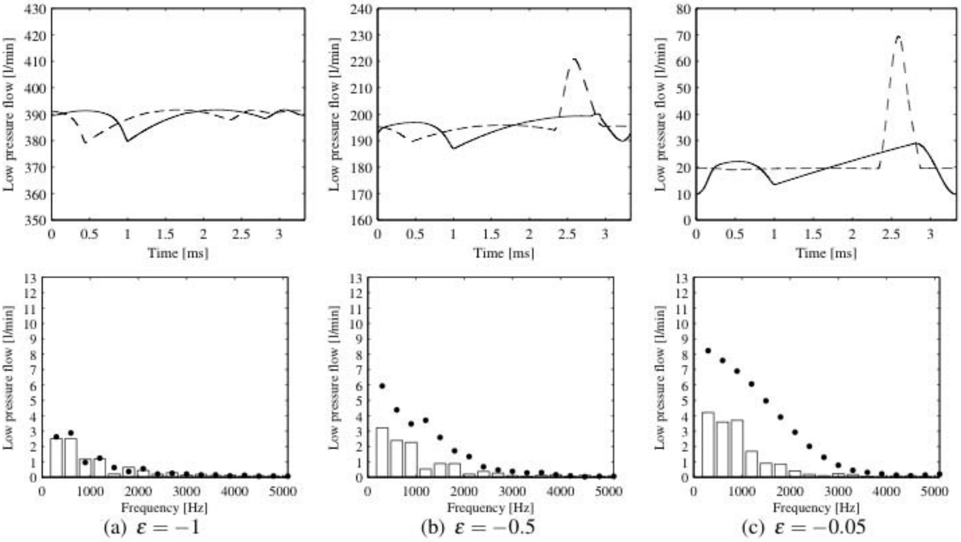

(a) $\varepsilon = -1$ (b) $\varepsilon = -0.5$ (c) $\varepsilon = -0.05$

Figure 7: Time and frequency domain flow ripple in the low pressure kidney with a cross-angle of 4°, solid lines and bars, compared to an optimised pre- and decompression valve plate with no cross-angle, dashed lines and points.

The best results for high and low pressure flow ripple are obtained with a cross-angle between 3° and 6°. This is the opposite to the motor case, which is shown in figure 8(a). However, the best cross-angle for the total flow ripple for the pump is between 3° and 4°. A comparison of the total flow ripple for motor and pump operation is shown in figure 8(b). The best cross-angle to minimise the total flow ripple is the same in both cases, $\gamma = [3°,4°]$.

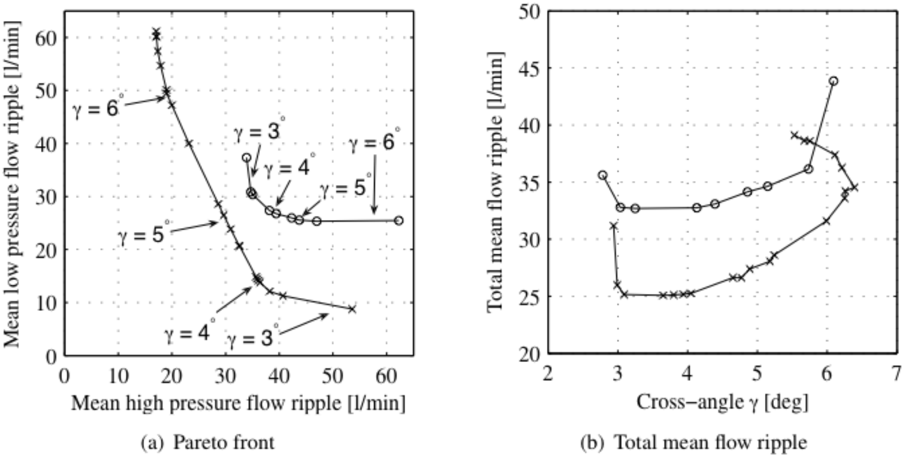

(a) Pareto front

(b) Total mean flow ripple

Figure 8: Left: Pareto front for motor case, crosses, compared with pump case, circles. Right: The mean total flow ripple for motor and pump respectively.

4.1 Compromise valve plate design

The same cross-angle size can be used to minimise the total flow ripple for both motor and pump operation. It should, however, be noted that pump and motor operation need different pre- and decompression angles of the valve plate. Hence, a valve plate optimised for motor operation is different to an optimal valve plate for pump operation. This is illustrated in figure 12 for a machine with no cross-angle. Figure 9 illustrates the kidneys' opening and closing angles for different cross-angles and operation conditions. The kidneys' opening and closing angles rotate anti-clockwise when the cross-angle is increased for the motor case and clockwise for the pump case. This is the same direction as the TDC and BDC are moved when the cross-angle value varies.

In order to design a valve plate for both motor and pump operation, a compromise between the kidney angles needs to be found. Studying the curves for the closing angle of the high pressure kidney it can be seen that they cross each other at $\gamma \approx 4°$. Also, the curves for the opening angle at the high pressure kidney are similar in both motor and pump case at $\approx 4°$, so for these angles no compromise is needed. The closing and opening angles of the low pressure kidney diverge more distinctly. The low pressure kidney's closing angle needs to be determined by the motor angle in order to prevent excessive pressure peaks. The low pressure kidney's opening angle is determined by the pump angle in order to avoid cavitation.

The comparison in this case is made with a zero-lapped valve plate. If an optimisation of the pre- and decompression angles is performed for both the pump and motor case simul-

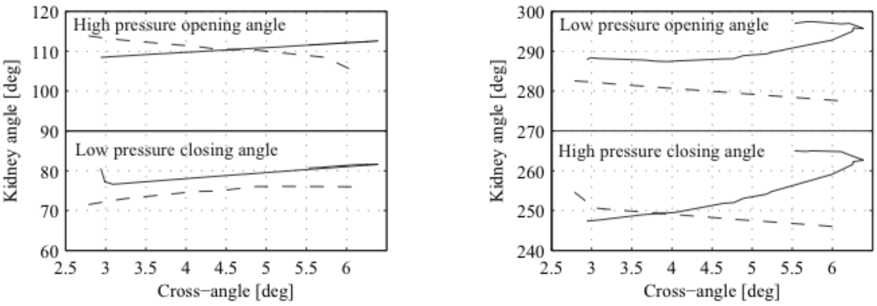

Figure 9: Left: Angles between low and high pressure kidney. Right: Angles between high and low pressure kidney. Solid lines are for motor and dashed lines are for pump.

taneously, the results become very similar to a zero-lapped valve plate and are caused by preventing cavitation and pressure peaks. This is illustrated in a certain sense in figure 12. Figure 10 shows the flow ripple in frequency domain for high and low pressure kidney respectively when the machine works as a motor and figure 11 shows the flow ripple for the pump case.

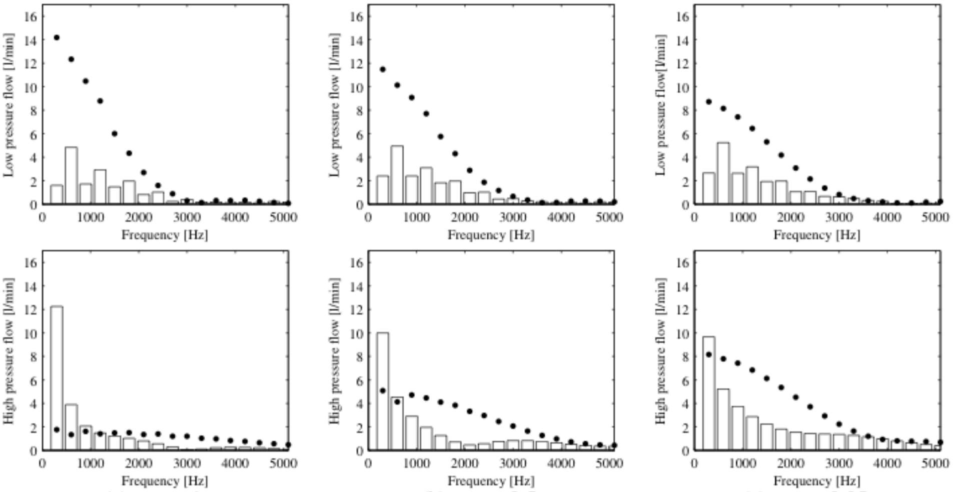

(a) $\varepsilon = -1$ (b) $\varepsilon = -0.5$ (c) $\varepsilon = -0.05$

Figure 10: Flow ripple in low pressure kidney, upper graphs, and high pressure kidney, lower graphs, with $\gamma = 4^\circ$, bars, compared to a zero-lapped valve plate, points, when the machine works as a motor.

The results are improved for all displacement angles in both the time and frequency domain except for low frequencies in the high pressure kidney at $\varepsilon < 0$. This problem is not caused by the cross-angle but the nature of the pre- and decompression for the motor case. The decompression angle is obtained through closing the high pressure kidney earlier, i.e. improvement of the low pressure flow ripple is obtained by changing the high pressure kidney. When the closing angle is altered, the kinematic part of the flow ripple is changed. In the motor case this results in an increase in the kinematic flow ripple. In the pump case the kinematic flow ripple is also increased but at the same time the compression contribution in the fundamental

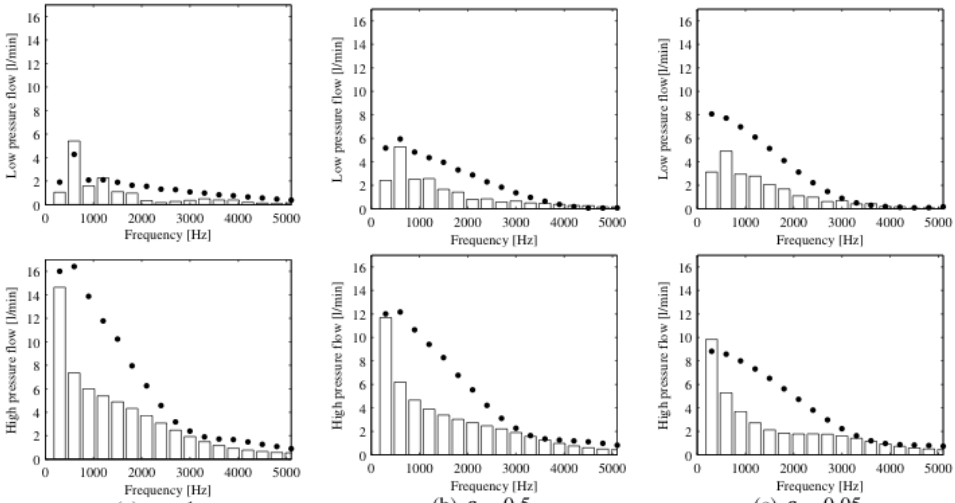

(a) $\varepsilon = 1$ (b) $\varepsilon = 0.5$ (c) $\varepsilon = 0.05$

Figure 11: Flow ripple in low pressure kidney, upper graphs, and high pressure kidney, lower graphs, with $\gamma = 4^\circ$, bars, compared to a zero-lapped valve plate, points, when the machine works as a pump.

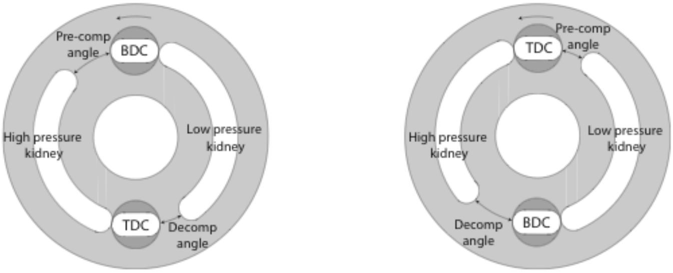
Pre-comp angle
BDC
High pressure kidney
Low pressure kidney
TDC
Decomp angle
Pre-comp angle
TDC
High pressure kidney
Low pressure kidney
Decomp angle
BDC

(a) Pump (b) Motor

Figure 12: The difference between pre- and decompression angle for motor and pump case respectively. The rotation direction is shown with the single pointed arrow in the figures.

frequency is decreased.

In order to obtain a single figure of merit, the results in figures 10 and 11 can be reformulated based upon the Root Mean Square (RMS) of the harmonic content for all graphs, equation (12). With this method a scalar value is obtained that can be used to compare the total flow ripple from the machine with and without the cross-angle.

$$Q_{RMS} = \sqrt{\sum_{i}\sum_{j}\sum_{\varepsilon}(q_{ij\varepsilon})^2} \qquad \text{where} \qquad \begin{aligned} i &= \text{harmonic frequencies} \\ j &= \text{high, low} \\ \varepsilon &= |0.05, 0.5, 1| \end{aligned} \tag{12}$$

The RMS value without a cross-angle implemented is 68 l/min and with a cross-angle it is 41 l/min. This means that the total flow ripple for all displacement angles has been reduced by 40 %.

5 DISCUSSION AND CONCLUSIONS

This paper considers the effect of using a cross-angle concept in order to reduce flow ripple in hydraulic piston motors and in machines operating both as pumps and motors. It is a simulation study. Earlier simulation studies of pumps presented by the authors have been experimentally verified, proving that the simulation models and the optimisation strategy are reliable.

Optimisation is used to find the proper cross-angle value as well as the corresponding four port plate angles. The cross-angle concept relies on pre-compression and decompression. This means that the method is most useful for machines operating at constant pressure but varying speed and displacement setting. The pressure build up for pre-compression is insensitive to speed variations, however pressure equalisation between cylinder and port kidney has a small speed dependence, which is a topic for ongoing research. One restriction in this study is that the high pressure port of the machine is defined.

The use of pre-compression and decompression effectively reduce the compressibility part of the flow ripple but the ripple caused by kinematic effects is increased. The result is that the higher harmonics are reduced compared to other means of influencing the flow ripple.

In the motor case, it is shown that the total flow ripple can be reduced by this concept compared to ordinary pre- and decompression valve plate. It is shown that the optimal cross-angle reduces the flow ripple over the whole range of displacement settings.

For machines operating both as pumps and motors the concept is shown to be useful as well. In this case a compromise must be made between the two operating conditions. In some operating points the fundamental frequency is increased. However, the overall flow ripple is reduced considerably. The increase in noise level at some frequencies may be justified in order to obtain a lower noise level under other operation conditions and at other frequencies. Furthermore, the cylinder pressure rate in the machine decreases when pre- and decompression angles are used and this results in less structural vibrations.

If the high pressure flow ripple is important when the machine works as a motor, another choice of cross-angle value can be considerated in order to reduce the increase of flow ripple in the high pressure kidney. The objective function in the optimisation problem can also be reformulated in order to restrain the fundamental frequency in the high pressure kidney. In these ways, the low pressure flow ripple is increased while the high pressure flow ripple is decreased in the motor case.

Another operating condition is when the machine changes direction of rotation. If the displacement direction is positive (pump case) and the rotation direction is changed with retained high pressure kidney, the machine works as a motor. In this case, the dead centre angle lies as shown in the pump case in figures 1(b) and 2(a). When no cross-angle is used the pre- and decompression angles can be illustrated as in figure 12(a) with opposite rotation direction and slightly different size of the angles. The compromised valve plate design works adequately for this case.

As long as the high and low pressure side are not swapped, the same size and inclination direction of the cross-angle can be used with a compromise valve plate. The cross-angle can also be used in combination with pre-compression filter volume and pressure relief grooves to improve sensitivity to pressure variations.

REFERENCES

[1] A Johansson. Noise reduction of hydraulic systems - design considerations and methods. Licentiate thesis no. 953, Division of Fluid and Mechanical Engineering Systems, Linköpings universitet, Linköping, Sweden, 2002.

[2] T Grahl. Geräuschminderung an axialkolbenpumpen durch variable umsteuersysteme. *O+P, Ölhydraulik und Pneumatik*, pages (5):437–443, November, 1989.

[3] J-O Palmberg. Modelling of flow ripple from fluid power piston pumps. In *Proceedings of 2nd Bath International Power Workshop*, Bath, UK, September, 1989.

[4] M Pettersson, K Weddfelt, and J-O Palmberg. Reduction of flow ripple from fluid power piston machines by means of a precompression filter volume. In *Tenth Aachen Colloquium on Fluid Power Technology*, Aachen, Germany, March 17-19, 1992.

[5] K.A Edge. Designing quieter hydraulic systems - some recent developments and contributions. In *Proceedings of the Fourth JHPS International Symposium*, Tokyo, Japan, November, 1999.

[6] Citroen. *Improvements in or relating to swash plate pumps*. Published at The Patent Office, 25 Southampton Buildings, London W C 2. Index at acceptance: -Class 102(1),AI B(8 B:9), A(3 G 4 A:455 A). International classification: - F 05 b, January 16, 1963.

[7] B O Helgestad, K Foster, and F K Bannister. Pressure transients in an axial piston hydraulic pump. In *Proc of the Institution of Mechanical Engineers*, pages (188)(17/74):189–199, 1974.

[8] L.V Balkind. Calculating the moments of the swash plate of a rotary axial piston pump. *Vestnik Mastinostroeniya*, 4:(54):17–24, 1974.

[9] A Johansson, J Andersson, and J-O Palmberg. Optimal design of the cross-angle for pulsation reduction in variable displacement pumps. In *Proceedings of The Bath Workshop on Power Transmission and Motion Control, PTMC*, Bath, UK, September, 2002.

[10] A Johansson, J Andersson, and J-O Palmberg. Influence from the cross-angle on piston forces and bending moments in variable hydraulic piston pumps. In *the 7th International on Fluid Control, Measurement and Visualization, FLUCOME'03*, Sorrento, Italy, August, 2003.

[11] A Johansson, J Ölvander, and J-O Palmberg. Experimental verification of cross-angle for noise reduction in hydraulic piston pumps. *Proc. IMechE, Part I: J. Systems and Control Engineering*, 221(I3), pp. 321-330, 2007.

[12] T Ichiyanagi, E Kojima, and Edge K A. The fluid-borne noise characteristics of a bent axis motor established using the 'secondary source' method. In *Proceedings of the Fifth Scandinavian International Conference on Fluid Power*, Linköping, Sweden, May 28-30, 1997.

[13] HOPSAN. Hopsan, a simulation package, user's guide. Lith-ikp-r1704, Division of Fluid and Mechanical Engineering Systems, Linköpings universitet, Linköping, Sweden, April, 1998.

[14] M J Box. A new method of constraint optimization and a comparision with other methods. *Computer Journal*, (8):42–52, 1965.

[15] P Krus and J Andersson. Optimizing optimization for design optimization. In *ASME Design Automation Conference*, Chicago, USA, September 2-6, 2003.

[16] J Andersson. *Multi-objective Optimization in Engineering Design - Application to Fluid Power Systems*. PhD thesis, Division of Fluid and Mechanical Engineering Systems, Linköpings universitet, Linköping, Sweden, September 2001. Dissertation No. 657.

HIGH-FREQUENCY AXIAL VIBRATION IN A COMBINED PUMP UNIT WITH GEAR STAGE

M.S. Gasparov, A.N. Kruchkov, L.V. Rodionov, E.V. Shakhmatov
Faculty of Flying Engines, Samara State Aerospace University, Russian Federation

ABSTRACT

In the paper reasons of high axial vibrations of the pump unit including gear and screw-centrifugal stages are investigated. It is shown that the gear stage is a main source of axial vibrations. The essential increase in the axial forces is due to the asymmetrical (in the axial direction) hydraulic unloading of the closed volumes. The axial displacements of the mobile axial bearing under pressure oscillations cause high-frequency axial vibration. From mobile and motionless axial bearings it is transferred to the manifold and further the screw-centrifugal rotor vibration is excited. Calculation of the axial forces acting in the gear stage is presented in the paper. The model of high-frequency vibrations of the pump is developed. The results of simulation have been verified through comparison with experimental data.

1. INTRODUCTION

Reliability and working capacity of the aircraft engine in many respects is defined by functioning of its systems and, first of all, fuel and control systems. The pumps are the most loaded elements of such systems. They are, on the one hand, basic sources of pressure oscillations and vibrations. On the other hand, fuel pumps are themselves subjected to significant dynamic overloads. The combined pump units including screw-centrifugal and gear stages (SCS and GS) have a wide range of application (Fig. 1)

In such pump unit the thrust bearing of SCS is the most loaded part. In the paper the reasons of increased axial vibration of the combined pump causing the increased SCS bearing wear are investigated.

Power Transmission and Motion Control 2007 Edited by Dr D N Johnston and Professor A R Plummer
© With The Centre for Power Transmission and Motion Control

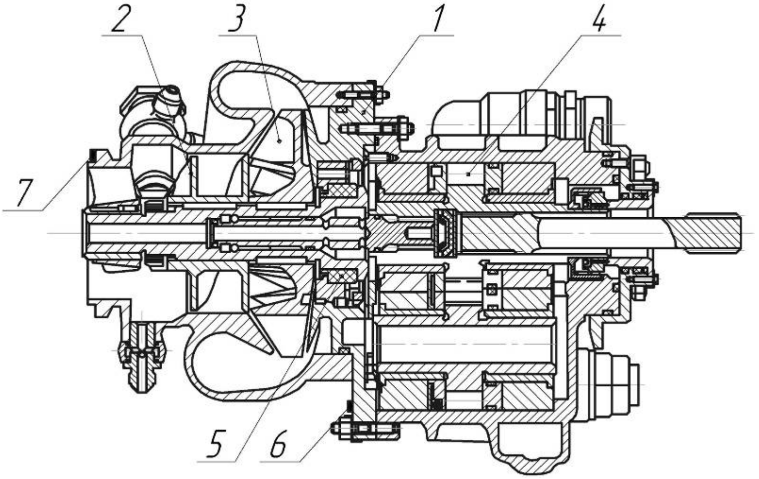

Figure 1. The design concept of the combined pump unit.
1 - case; 2 screw; 3 centrifugal impeller; 4 gear stage; 5 - drive; 6,7- sensor.

During measurements it is established that the main contribution to an axial vibration spectrum at the fuel input flange and at the flange of SCS and GS joint is introduced by high-frequency components (Fig. 2).

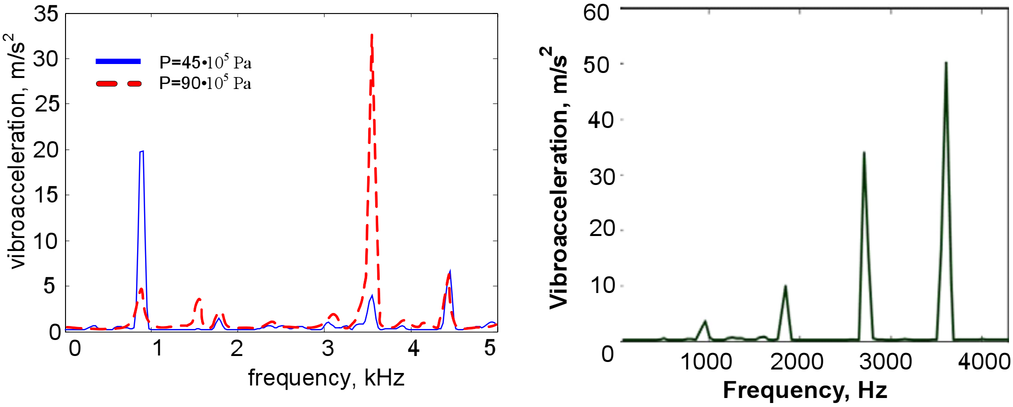

a) b)

Figure 2. Spectra of an axial vibration (n=4800 rpm): a) at the fuel input flange at two pressures (the sensor 7); b) at the flange of SCS and GS joint (the sensor 6).

2. BASIS OF THE THEORY

Let's observe the sources of vibrations in the stages. The analysis of the gear stage and the processes in a meshing zone has shown that a principal cause of high-frequency axial vibration is non-uniformity of the axial forces acting from working fluid on mobile and fixed axial bearings.

Presence of a damping cavity of a mobile bearing leads to the force uncompensated $F_L(t) \neq F_R(t)$ (Fig. 3) which is considered in the developed mathematical model.

High-frequency vibration from mobile and fixed axial bearing is transmitted to a case, and further the SCS rotor vibration is excited.

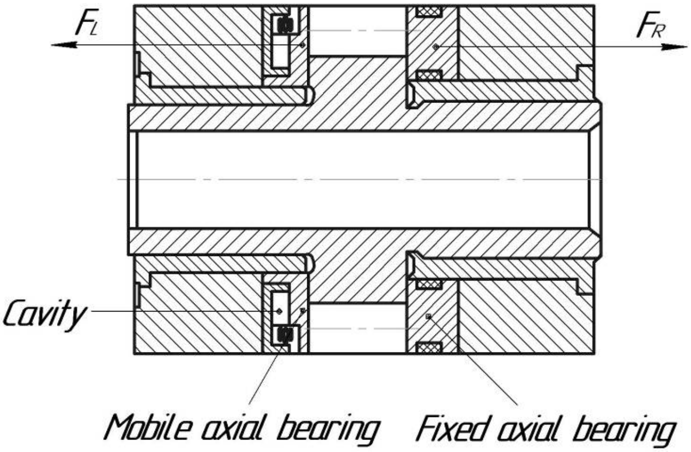

Figure 3. Scheme of axial forces acting on bearings.

The most significant axial excitation source for rotor SCS is the tip vortex [1, 2, 6]. These disturbances interacting with vibroacoustic influences from GS produce the screw blades oscillations that increase at the natural frequencies (Fig.4).

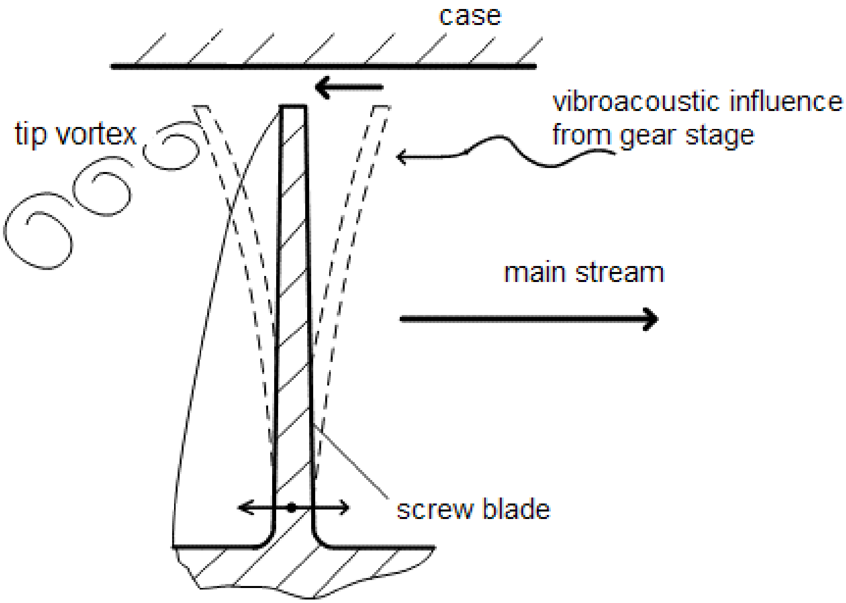
case
vibroacoustic influence from gear stage
tip vortex
main stream
screw blade

Figure 4. Screw blade oscillations due to separation of a tip vortex and a vibroacoustic influence of GS.

3. MODEL OF AN ACOUSTIC – VORTICAL RESONANCE OF SCREW

In connection to complexity of direct measurements of the bearings vibrations the pressure oscillations at the screw input are modeled as the most reflecting the rotor vibration. Because of operating process complexity there is not its adequate analytical description. Therefore the model in the form of set of three models is offered: a hydrodynamic model of SCS, a solid-state model of a feed screw and vibroacoustic models of GS (Fig.5).

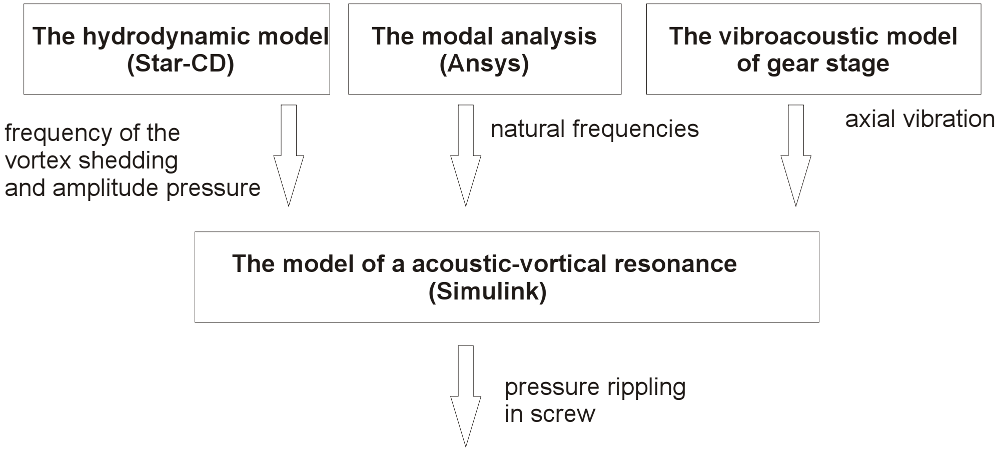
The hydrodynamic model
(Star-CD)
The modal analysis
(Ansys)
The vibroacoustic model
of gear stage
frequency of the
vortex shedding
and amplitude pressure
natural frequencies
axial vibration
The model of a acoustic-vortical resonance
(Simulink)
pressure rippling
in screw

Figure 5. Structure of model of an acoustic – vortical resonance of screw with influence from gear stage.

3.1. The hydrodynamic model

The hydrodynamic model of a flow structure in SCS is realized in the Star-CD package by means of a method of monitoring volumes.

Construction of a computational grid of the SC pump in standard programs of computing fluid dynamics is difficult enough because of the minimal tooling for geometrical modeling. Therefore three-dimensional geometrical model of SCS is previously built. Boundary conditions at the pump input and at the drain branch pipes (inlet1, inlet2) are the flow velocities (Fig. 6). The SCS rotor operates at the corresponding rate of 4800 rev/min. Effect of turbulence is described by $k-\varepsilon$ model for high Reynolds numbers.

As a result of calculation the structure of a tip vortex is obtained (Fig.7) which parameters permit to determine frequency of the vortex shedding:

$$f=\frac{v\cdot Sh}{l_k}=\frac{Sh\sqrt{2g\cdot\Delta H}}{l_k},$$

where *Sh* - a Strouhal number (0,2 - 0,3), l_k - an end face thickness of the feed screw blade, ΔH - a pressure drop at a circumferential part of the blade, v - characteristic flow rate.

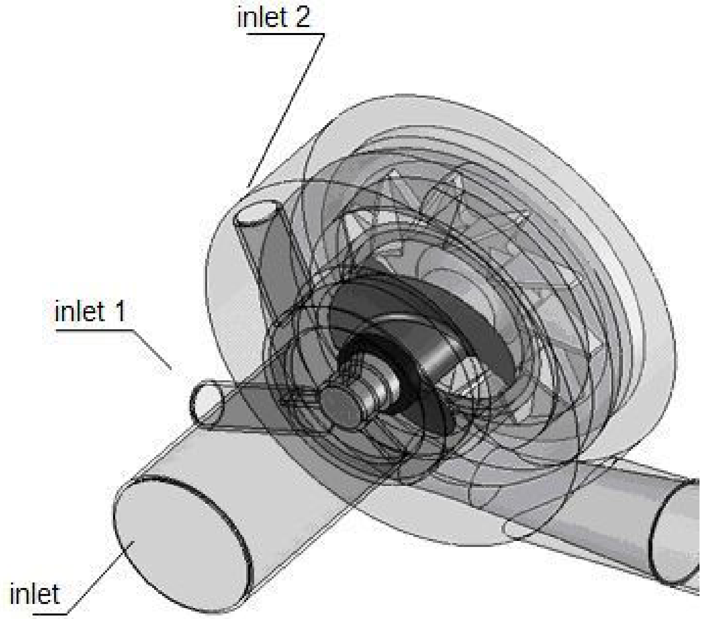

Figure 6. 3D model of the screw-centrifugal stage.

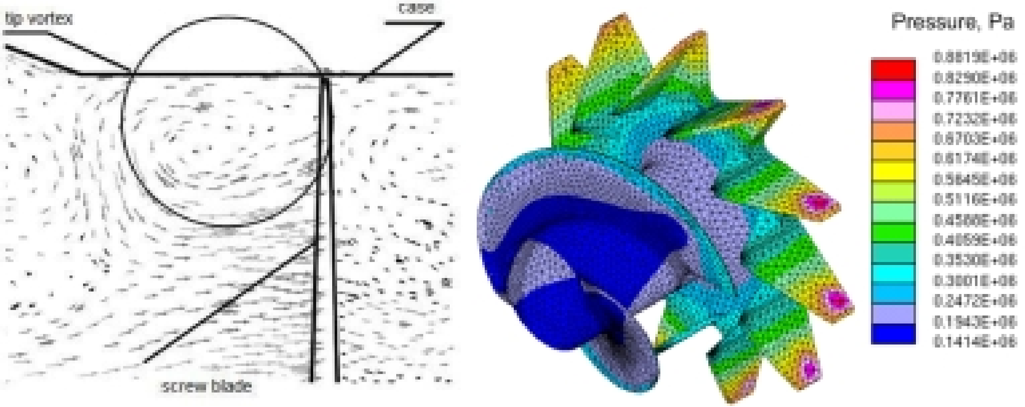

Figure 7. A tip vortex and pressure distribution at n=4800 rev/min, Q=1200 kg/h.

3.2. The modal analysis

The modal analysis of screw wheels natural vibration modes is realized by means of finite elements method in Ansys program. As a result of the modal analysis 10 forms of natural oscillations over the range from 0 up to 10 kHz (Fig.8) are discovered. Natural frequencies of a feed screw are presented in tab. 1.

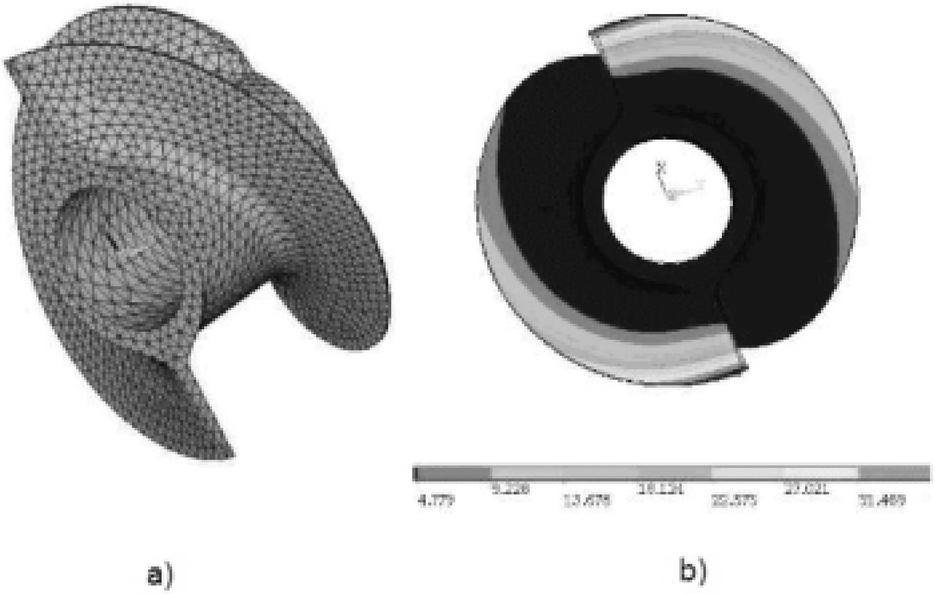

Figure 8. The finite element grid (a) and the form of natural oscillations of the screw at 3562 Hz (b).

Table 1. Paired natural frequency of the screw

№	1	2	3	4	5	6	7	8	9	10
Frequency, Hz	3562	3563	3967	3971	4456	4457	4925	4928	5436	5438

At definition of natural frequencies of the screw, due to of an irregularity of a grid and presence of two blades have gained paired natural frequency of the screw. Thus we shall lead results of table 1 to a following view.

Table 2. Natural frequency of the screw

№	1	2	3	4	5
Frequency, Hz	3562	3967	4456	4925	5436

For check of adequacy natural frequencies have been determined experimentally by tapping. The screw was suspended on a thread and excited by a wood hammer. A change of a sound pressure was recorded by means of a microphone on distance 30 cm. The spectrum of natural frequencies (Fig.9) corresponds to the calculated values.

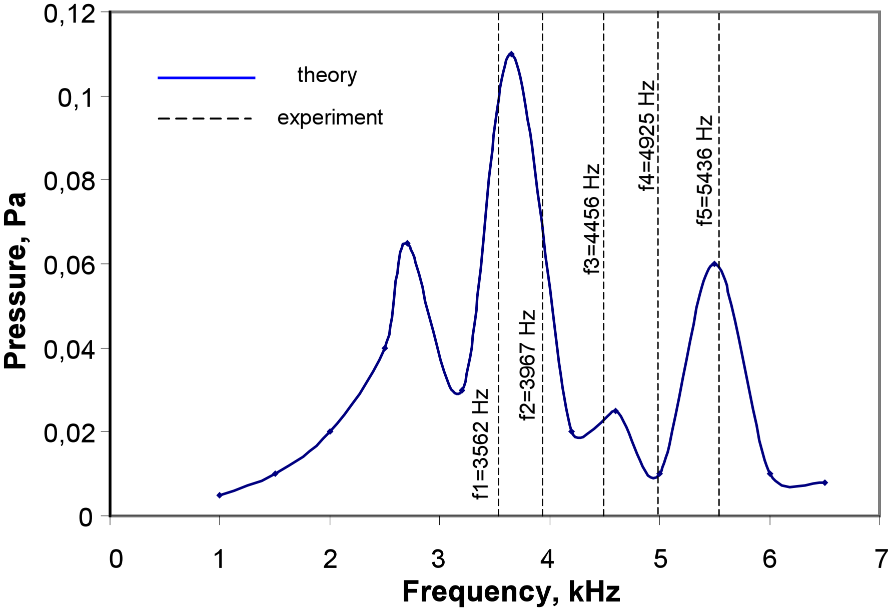

Figure 9. A spectrum of natural frequencies of the screw.

3.3. Vibroacoustic model

Vibroacoustic model of GS considers uncompensated forces. The calculation of the axial forces acting in the GS is conducted. Because of complexity of the account of all parameters influencing on gear stage following assumptions are accepted:

- The end gap is constant on all surface while actually there are beating of adjoining end surfaces of gear wheels and sealing parts and manufacturing inaccuracy of these planes.
- Delivery pressure is large enough and effect of one of end planes rotation at angular velocity Ӟɤ ǝ̈n the pressure value in the gap is negligible that is confirmed by experimental data at the delivery pressure aboutӞ100 bar.
- Pressure variation in a tooth space volume in a radial direction is negligible. Actually such variation occurs due to centrifugal forces of rotating liquid particles and also due to a fluid leakage in a radial direction through an end clearance.
- Assuming laminar flow in narrow slots it is supposed that the pressure in a direction from periphery to the center drops from ß̈$_{\mathrm{OUT}}$ up to ʈ $_{\mathrm{IN}}$ following to the logarithmic law.

The specified model axial vibroacoustic loadings considers efforts $F_R(t)$ and $F_L(t)$ as sets of forces of pressure $F_1(t)$ and $F_2(t)$, acting on bearing from a liquid which are being in tooth space of driving and driven gears:

$$F_i(t)=\begin{cases} \dfrac{(P_{DEL}-P_{SUC})\cdot S}{\varphi}\cdot\beta_i(t)+P_{SUC}\cdot S & if \quad 0\le\beta_i(t)\le\varphi, \\ P_{DEL}\cdot S & if \quad \varphi<\beta_i(t)\le\varphi+\psi, \\ \dfrac{(P_{SUC}\cdot S-F_\beta)\cdot 2}{\beta_{MESH}}\cdot\beta_i(t)+\dots & if \quad \varphi+\psi<\beta_i(t)\le\varphi+\psi+\beta_{MESH}/2, \\ \dots+F_\beta-\dfrac{(P_{SUC}\cdot S-F_\beta)\cdot 2}{\beta_{ZAP}}\cdot(\varphi+\psi) & if \quad \varphi+\psi+\beta_{MESH}/2<\beta_i(t)\le\varphi+\psi+\chi \\ P_{SUC}\cdot S & \end{cases}$$

where $i=1{,}2$; $F_\beta=k\cdot P_{DEL}\cdot S$ - increase in an axial thrust during the moment of formation of the meshing volume; P_{DEL} - a delivery pressure; P_{SUC} - a suction pressure; S - the square of a tooth space; ű - an angle of a conversion zone from delivery pressure to a suction pressure; ɣ - an angle of a zone of a total delivery pressure; ɢ - an angle of a zone of suction pressure; β_{MESH} - an angle of the meshing volume; k - the coefficient considering growth of pressure at formation of meshing volume.

Calculation of $F_2(t)$ is spent at $\beta_2(t)=\beta_1(t)+180/z$; where $\beta_1(t)$, $\beta_2(t)$ - current angular positions of driving and driven gear.

For a mobile bearing the account of a time delay due to acts of a damping cavity of a bearing is inducted. Resultant axial thrust acting in gear stage of the pump unit is equal to a difference of loadings on fixed and mobile bearings (Fig. 10a) in which spectrum high-frequency components dominate (Fig. 10b).

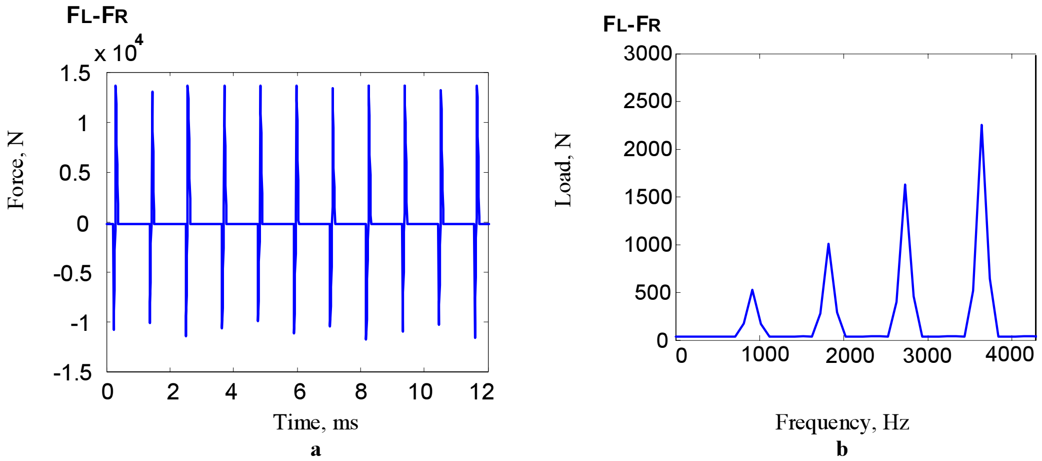

Figure 10. The resultant axial force (a) and its spectrum (b).

The acoustic-vortical resonance model of a screw is realized in Simulink (Matlab) package. Output information from the previous three models is represented in the form of signals:

1. Parameters of pulsations of pressure of vortex cavitations are modeled as noise process. The amplitude and frequency range of it is defined from hydrodynamic model;
2. Vibration of the screw from affecting of GS is modeled by means of the calculated axial vibration which amplitude defined in view of experimental factors;
3. Natural frequencies of the screw are modeled in the form of a set of narrow-band filters according to the gained design values.

On an exit from acoustic -vortical model spectral characteristics of pulsations of pressure in SCS are presented.

4. CONCLUSIONS

Adequacy of model of vortical disturbances interaction in SCS with oscillating blades of a screw in view of GS effect proves true by comparison of experimental and design spectra of pressure oscillations (Fig.11).

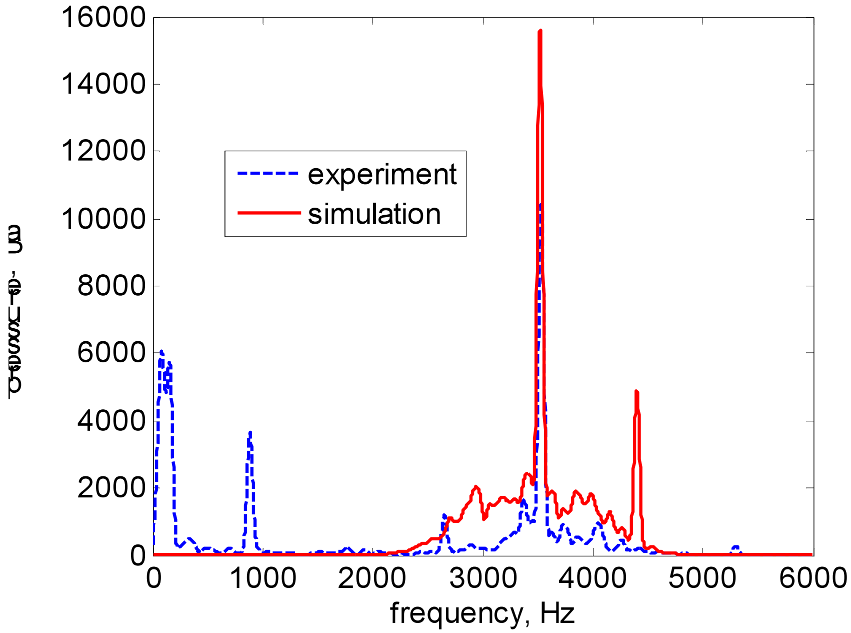

Figure 11. Experimental and design spectra of pressure oscillations at the SCS input at Pout GS = 95·10^5 Pa, Q= 6000 kg/h.

Thus the mechanism of high-frequency loading of SCS rotor is proved, caused by a coincidence of natural frequencies of screw blades with the oscillation frequency excited by a gear stage and tip vortexes tearing off the screw blade.

5. REFERENCES

1. Karelin V.JA. Cavitation in centrifugal and axial-flow pumps. Moscow, "Engineering industry", 1975. (Russian)
2. Kinelev V.G., Vasilev J.N., Kurochkin S.N. Physical model of a cavitating screw-centrifugal pump operating at a wide range of consumption. Self-excited oscillatory and cavitation in pump systems. / Kiev: Sciences. Dumka, 1976. pp. 100- 107. (Russian)
3. Pressure oscillations in jet and fly-off flows /A.N.Antonov, V.M. Kuptsov, V.V. Komarov. - ʃ .: Engineering industry. 1990.272 pp. (Russian)
5. The Physical fundamentals of a sound formation in air blowers / A.V.Roman, D.V.Bazhenov, L.A.Bazhenov. - ʃ .: Science, 1988. - 173 pp.
6. Shapiro A.S. Structure of real flow in centrifugal and axial-flow pumps. ʃ GIU, Moscow, 2004.

Tribological Simulation of a Hydrostatic Swash Plate Bearing in an Axial Piston Pump

A. Wohlers ***and*** **H. Murrenhoff**
Institute for Fluid Power Drives and Controls, RWTH Aachen University, Germany

ABSTRACT

This paper will present the realization of a transient hydrostatic simulation for the tribological contact swash plate bearing. To simulate the kinetic motion of the swash plate as well as the forces acting at the bearings the relevant components of the pump are built up in the multi-body simulation software MSC.ADAMS. The transient calculation of the tribological reacting forces, without partial contacts as well as for mixed lubrication is based on the Average Flow Model (AFM) in combination with the contact model of Greenwood and Williamson. The hydraulic system of the pump including the hydrostatic compensation is modelled with the hydraulic simulation program DSH*plus*. The integration of the three simulation parts in one simulation environment renders possible the description of the complex interaction between hydraulics, mechanics and tribology in an axial piston pump. In addition to a compendium of the implemented theory and a description of the different simulation parts this paper shows simulation results.

NOMENCLATURE

E	Youngs modulus
F	tribocontact-force
$K_{damping}$	damping coefficient
T	tribocontact-torque
h	local gap height
U	relative velocity in rotation-direction
p	local pressure
Ŭ	deflection angle of the swash plate
ů	roughness of surface
ɖ	viscosity of oil
v	Poisson's ratio
ɕ$_1$,ɕ$_2$	global coordinate system variables
ū	AFM flow factor
g	local oil temperature
Ű	fluid shear stress

Power Transmission and Motion Control 2007 Edited by Dr D N Johnston and Professor A R Plummer
© With The Centre for Power Transmission and Motion Control

1. INTRODUCTION

For setting up a variable volume flow in axial piston pumps the swash plate has to be swivel-mounted. This can be realized either by using roller bearings or hydrostatic bearings. In modern mobile hydraulics hydrostatic bearings are preferred because of their small size. A good mechanical efficiency and a fast adjustment of the swivel angle can be achieved by improving the propagation of the lubrication film, which correlates to an increasing local gap height. As a result the leakage flow rises and therefore the volumetric efficiency rate decreases. This effect has to be considered in the design process of the swash plate bearing and the hydraulic system. Including all relevant parameters the simulation tool introduced in this paper helps to understand the characteristics of the tribological system. This contribution is a step forward to the realization of virtual prototyping of hydraulic systems (4,6).

2. SIMULATION STRUCTURE

The simulation of the hydrostatic swash plate bearing is based on three parts: a multi-body simulation, a hydraulic circuit simulation and a tribological simulation. While the multi-body simulation gives an output of the kinematics of the moving parts of the axial piston pump and the resulting forces at the two bearings of the swash plate, the pressure forces at the pistons that have to be applied are calculated in the hydraulic circuit simulation. Furthermore the pressure in the hydrostatic compensation cavity is calculated in this circuit. The simulation is completed by a tribological model that provides an insight into the lubricated gap of the hydrostatic bearings. An integrative simulation of all parts makes detailed information regarding the dynamic behaviour of the whole tribological system available.

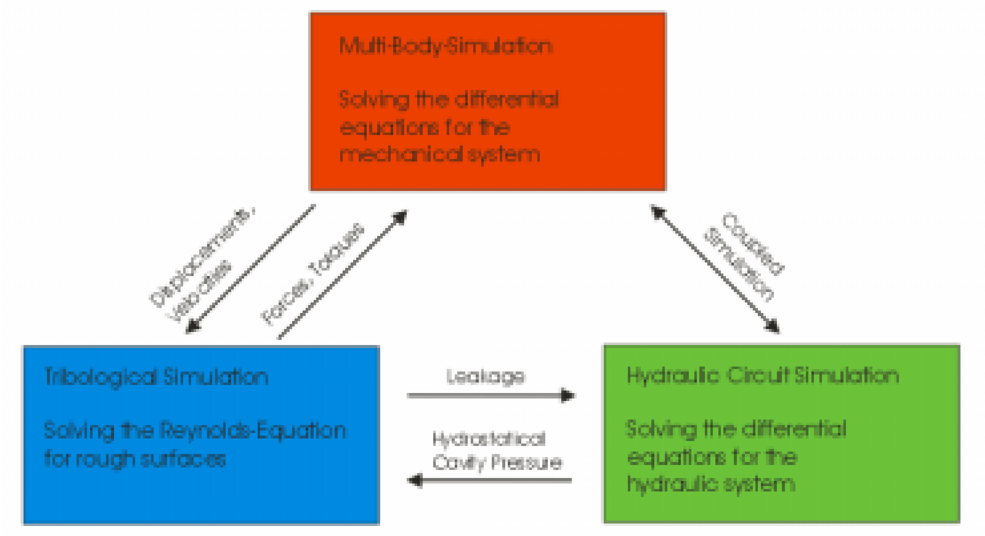
Multi-Body-Simulation
Solving the differential equations for the mechanical system
Displacements, Velocities
Forces, Torques
Coupled Simulation
Tribological Simulation
Solving the Reynolds-Equation for rough surfaces
Leakage
Hydrostatical Cavity Pressure
Hydraulic Circuit Simulation
Solving the differential equations for the hydraulic system

Figure 1 Overview of the simulation structure

3. MODELING THE TRIBOLOGICAL CONTACT

The relation between the gap geometry and the pressure profile that will result in the gap of the hydrostatic bearings is given by the transient Reynolds-equation (3):

$$\frac{\partial}{\partial \xi_1}\left(\frac{h^3}{\eta}\cdot\frac{\partial p}{\partial \xi_1}\right)+\frac{\partial}{\partial \xi_2}\left(\frac{h^3}{\eta}\cdot\frac{\partial p}{\partial \xi_2}\right)=6\cdot\frac{\partial(h\cdot U)}{\partial \xi_1}+12\frac{dh}{dt}$$

with $\frac{dh}{dt}=\frac{\partial h}{\partial t}+U\cdot\frac{\partial h}{\partial \xi_1}$ and $\eta = f(p,\vartheta)$.

This form of the equation cannot be used for our application. If there is any asperitiy contact, which is assumed for some operating conditions, the equation will not be valid anymore. In this case the Average Flow Model (AFM) can be applied. The transient Reynolds equation is extended by phenomenological flow factors that have to be calculated anew for every change in boundary conditions.

$$\frac{\partial}{\partial \xi_1}\left(\Phi_{\xi_1}\frac{h^3}{\eta}\cdot\frac{\partial p}{\partial \xi_1}\right)+\frac{\partial}{\partial y}\left(\Phi_{\xi_2}\frac{h^3}{\eta}\cdot\frac{\partial p}{\partial \xi_2}\right)=6\cdot U\cdot\left(\frac{\partial \hat{h}_t}{\partial \xi_1}+\sigma\frac{\partial \dot{\Phi}_{\xi_1}}{\partial \xi_1}\right)+12\frac{d\hat{h}_t}{dt}$$

In case of very low gap heights, the average height, which is defined as the distance between two surfaces, cannot be used any longer. If h^* Ò3 the roughness of the surfaces is of the same order of magnitude as the gap height itself. Alternatively the gap height can be approximated by the following polynomial (1):

$$\hat{h}_t=\frac{3\cdot\sigma}{256}\left(35+\frac{h^*}{3}\left(128+\frac{h^*}{3}\left(140+\left(\frac{h^*}{3}\right)^2\left(-70+\left(\frac{h^*}{3}\right)^2\left(28-5\left(\frac{h^*}{3}\right)^2\right)\right)\right)\right)\right)$$

with $h^*=\frac{h}{\sqrt{\sigma_1^2+\sigma_2^2}}$.

The resulting multi-dimensional differential equation cannot be solved analytically. Therefore the calculation has to be based on numerical methods. By usage of the Finite-Difference-Method the contact zone has to be divided into several elements as shown in **figure 2**.

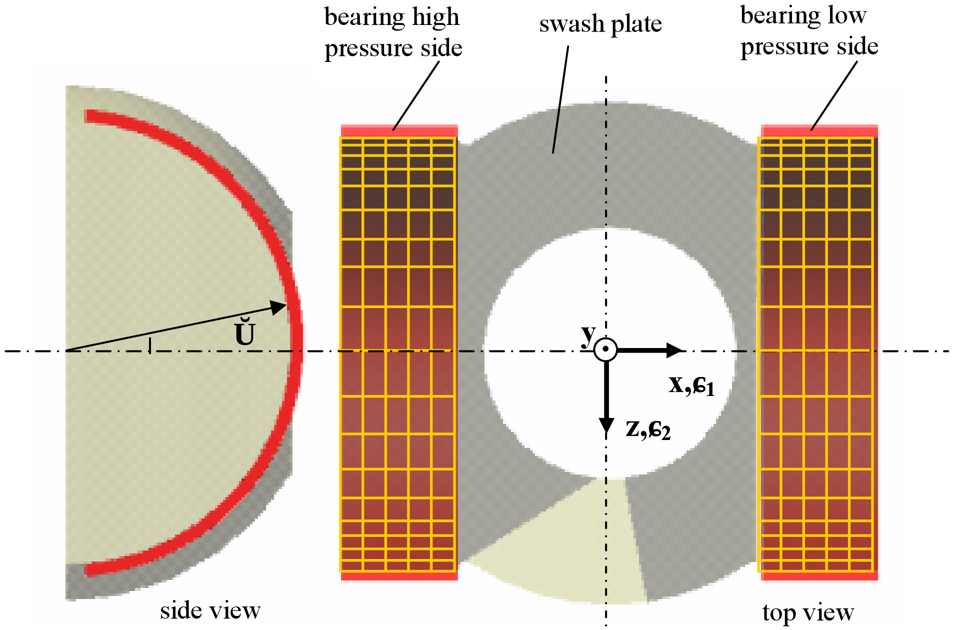

Figure 2 Finite Difference Model of the hydrostatic bearings

The accelerated Gauss-Seidel algorithm allows computing the fluid pressure distribution. In the case of h^* Ò4 there are asperity contacts between the swash plate and the bearings. The resulting contact pressure in these elements can be calculated using:

$$p_{contact}(h^*) = \pi \cdot \frac{16}{15} \cdot \sqrt{2} \cdot \left(\frac{1-v_1^2}{E_1} + \frac{1-v_2^2}{E_2} \right)^{-1} \cdot \sqrt{\frac{\sigma}{\beta}} \cdot 3{,}48 \cdot 10^{-5} \cdot (4-h^*)^{7{,}05} \cdot (n_R \cdot \beta \cdot \sigma)^2$$

with $n_R \cdot \beta \cdot \sigma \approx 0.05$

Together with the resulting normal forces on the swash plate surface there are tangential forces which can be derived from the inner fluid shear stress and the contact shear stress. The fluid shear stresses will be calculated by:

$$\tau_{\xi_1} = \eta \cdot \frac{U}{h} \cdot \left(\dot{\Phi}_f + \dot{\Phi}_{f\xi_1} \right) + \Phi_{f\xi_1} \cdot \frac{h}{2} \cdot \frac{\partial p}{\partial \xi_1}$$

$$\tau_{\xi 2} = \Phi_{f\xi_2} \cdot \frac{h}{2} \cdot \frac{\partial p}{\partial \xi_2}$$

The contact shear stresses can be calculated upon the contact pressure using a constant friction coefficient that can be experimentally determined by tribometer tests:

$$\tau_{x,contact} = \mu_0 \cdot p_{contact}$$

The resulting forces can be calculated by integrating the pressures and the shear stresses over the length L and the width B of the contact zone:

$$F_x = \int_{\xi_1=0}^{L} \int_{\xi_2=0}^{B} \begin{pmatrix} \left(p(\xi_1 \cdot \xi_2) + p_{contact}(\xi_1 \cdot \xi_2)\right) \cdot \cos\alpha \\ + \left(\tau_{\xi_1}(\xi_1,\xi_2) + \tau_{x,contact}(\xi_1,\xi_2)\right) \cdot -\sin\alpha \end{pmatrix} d\xi_2 d\xi_1$$

$$F_y = \int_{\xi_1=0}^{L} \int_{\xi_2=0}^{B} \begin{pmatrix} \left(p(\xi_1,\xi_2) + p_{contact}(\xi_1,\xi_2)\right) \cdot \sin\alpha + \\ + \left(\tau_{\xi 2}(\xi_1,\xi_2) + \tau_{x,contact}(\xi_1,\xi_2)\right) \cdot -\cos\alpha \end{pmatrix} d\xi_2 d\xi_1$$

$$F_z = \int_{\xi_1=0}^{L} \int_{\xi_2=0}^{B} \left(\tau_{x,contact}(\xi_1,\xi_2) + \tau_{\xi 2}(\xi_1,\xi_2)\right) d\xi_2 d\xi_1$$

By considering the distance of each element to the point of load incidence the torques, especially the damping torque in rotating direction, can be calculated analogically. On the one hand the damping should not be too high, to avoid losses and a long adjustment time. On the other hand the damping reduces rotation vibrations. Therefore a compromise has to be found. By defining a damping coefficient simulation results of parameter variations can be compared to each other (6).

$$K_{damping} = \frac{T_{damping}}{\omega}$$

Figure 3 gives an overview of the process chart in the tribological simulation.

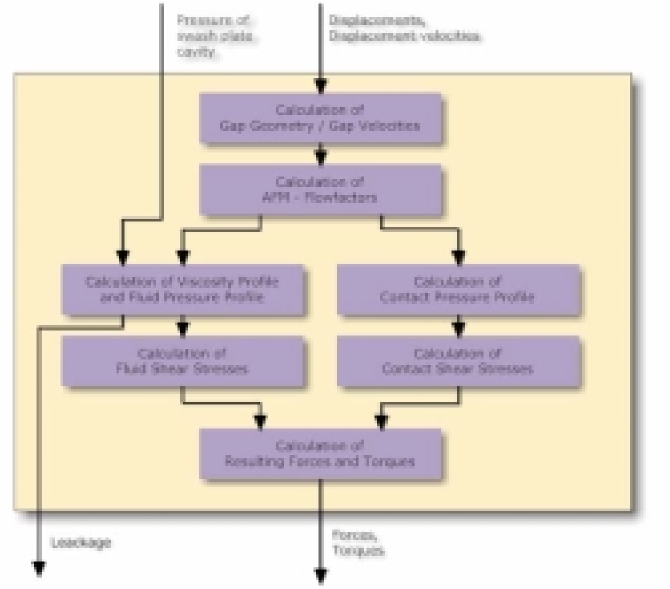
Pressure of
swash plate
cavity
Displacements,
Displacement velocities
Calculation of
Gap Geometry / Gap Velocities
Calculation of
APM - Flowfactors
Calculation of Viscosity Profile
and Fluid Pressure Profile
Calculation of
Contact Pressure Profile
Calculation of
Fluid Shear Stresses
Calculation of
Contact Shear Stresses
Calculation of
Resulting Forces and Torques
Leackage
Forces,
Torques

Figure 3 Overview of the tribological simulation

4. MODELLING THE MULTI-BODY-SYSTEM

A model of an axial piston pump was built up in the multi-body-simulation software MSC.ADAMS. Instead of using a cylindrical joint to mount the swash plate a six component force was applied. The values of this general force are calculated by the tribological gap-flow simulation introduced previously.

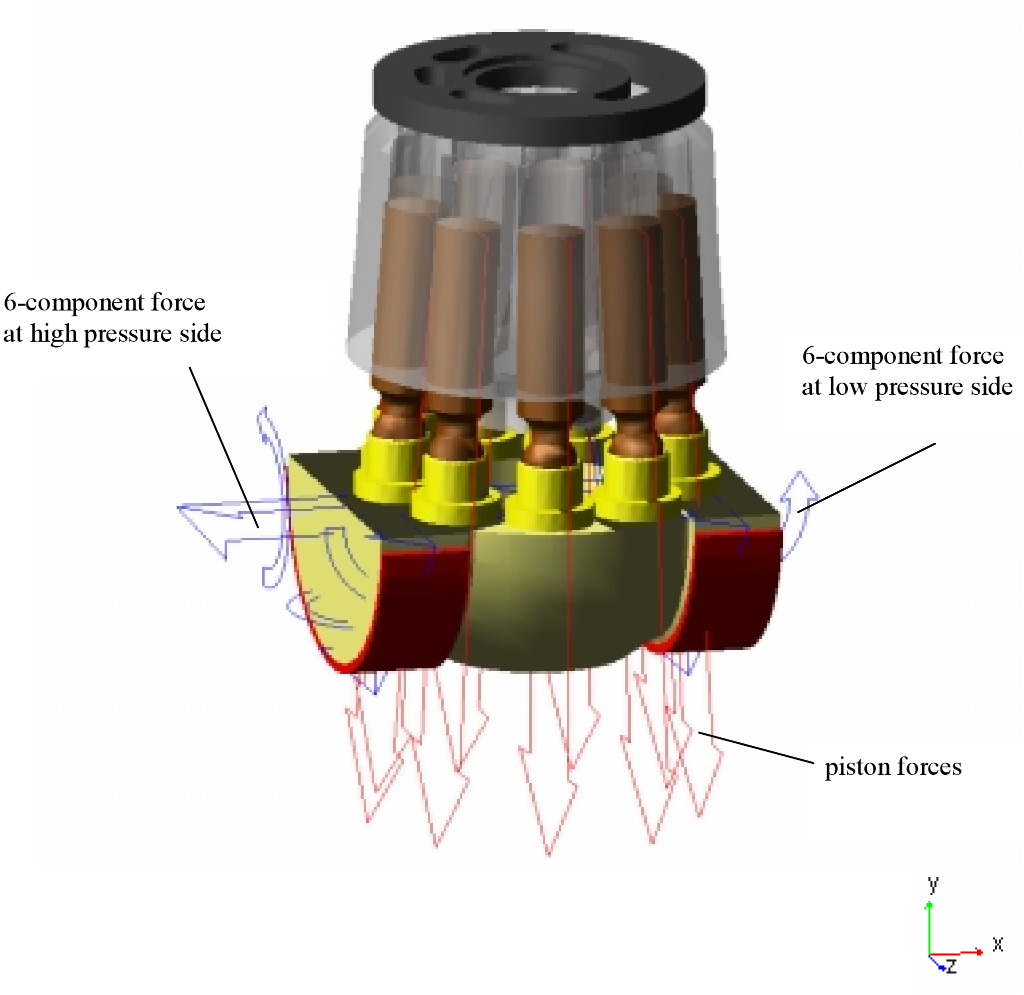
6-component force at high pressure side
6-component force at low pressure side
piston forces
y
x
z

Figure 4 Multi-body simulation model of an axial piston pump

Each piston is applied with a single component force normal to its front face. These pressure forces are calculated by the co-simulation with the STC module (Simulation Tool Chain) of DSH*plus*.

5. MODELLING THE HYDRAULIC CIRCUIT

To determine the current pressure of each piston in each position, a hydraulic model of the piston pump was programmed in DSH*plus*.

The displacements and the velocities of the pistons are measured in MSC.ADAMS. Moreover, the information about the time dependent relative position to the swash plate is transferred to the hydraulic simulation. Because of this architecture the simulation is very flexible. The simulated pressures at the pistons are sent back to the kinematic simulation sequentially.

With an implemented model of the control plate the overlapping areas of the pistons to the high and the low pressure sides can be determined. Upon that information the oil flow over the control plate is calculated. The control plate can be fully parameterized. There is also the possibility of applying pressure grooves and bores.

To compute the pressure inside the swash plate cavity the leakage flow of the bearing has to be taken into account. The leakage volume flow can be derived from the pressure profile. The specific volume flows can be determined as follows:

$$\hat{q}_{\xi_1} = -\Phi_{\xi_1} \cdot \frac{h^3}{12 \cdot \eta} \cdot \frac{\partial p}{\partial \xi_1} + U \cdot \left(\hat{h}_t + \sigma \cdot \dot{\Phi}_{\xi_1} \right)$$

$$\hat{q}_{\xi_2} = -\Phi_{\xi_2} \cdot \frac{h^3}{12 \cdot \eta} \cdot \frac{\partial p}{\partial \xi_2}$$

An integration of these values over the control area border lines that are slightly exceeding the cavity describes the leakage flow (2):

$$Q_{Leakage} = \oint \hat{q}_{\xi_{1,2}} \, dl$$

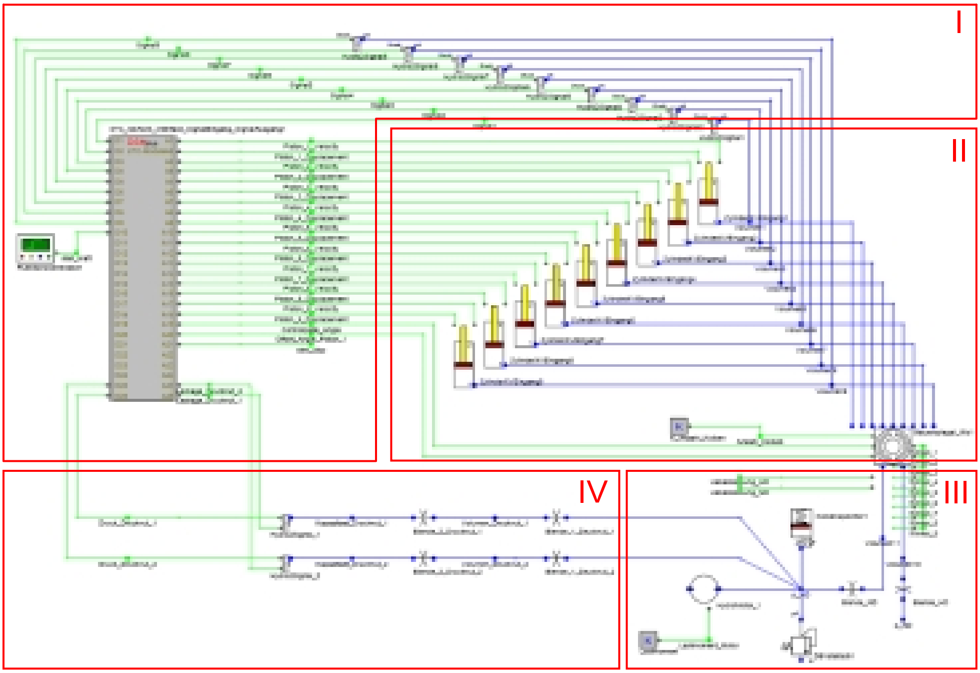

Figure 5 Model of the hydraulic circuit

Figure 5 shows the four blocks of the hydraulic circuit model. The interface to the multi-body simulation is realized in block I. Block II contains the calculation of the motor part of the pump, block III the conductive part with the hydraulic consumers. The calculation of the cavity pressure is realized in block IV.

6. SIMULATION RESULTS

A co-simulation of the hydraulic and the mechanical model was conducted for a swivel out process from 0° to 12.5° degrees. **Figure 6** shows the results of the hydraulic simulation. The diagrams at the left side of the figure show the displacement and the velocity of one piston and the overlapping area at the control plate to the high and the low pressure side. The graphs at the right side show the simulated pressure at one piston and a combination of all pressures.

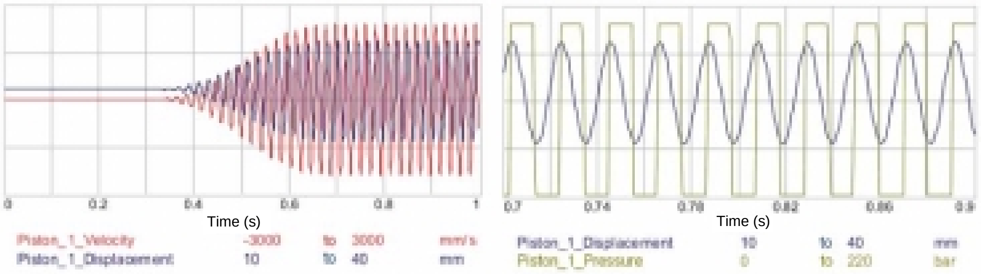

Figure 6 Results of the hydraulic simulation

The pressure forces at the pistons that are used in the mechanical simulation correlate directly to the pressures that are calculated in the hydraulic circuit model. **Figure 7** shows the time shifted strokes of the pistons.

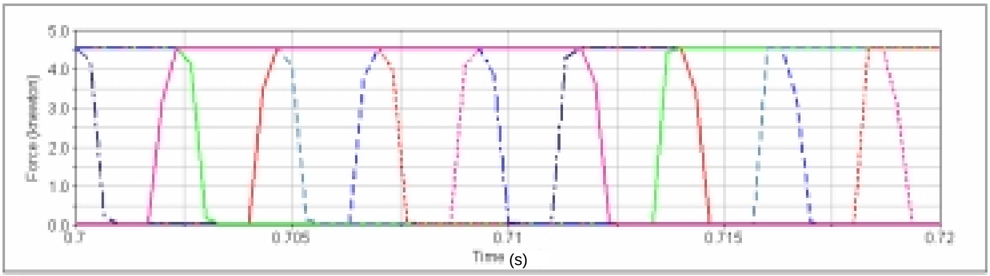

Figure 7 Pressure forces at the pistons

Figure 8 shows the resulting bearing forces at the high and the low pressure side. Both the y- and the z-components of the bearing force are oscillating. This is due to the varying number of pistons that are connected to the high pressure side. While the averaged y-component of the resulting force is almost constant the z-component increases with the angle of the swash plate adjustment.

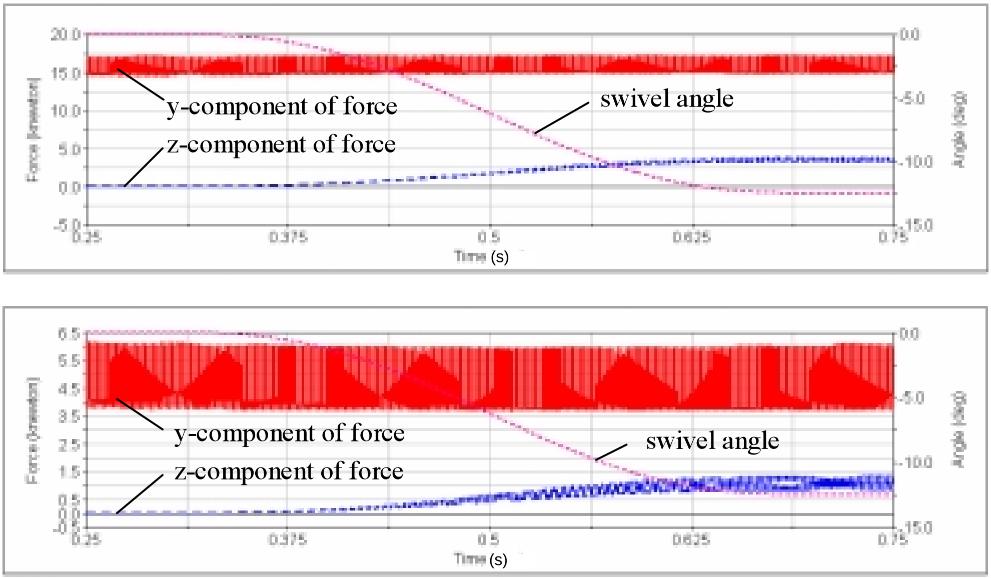

Figure 8 Resulting bearing forces at high and low pressure side during swivelling

A full simulation of all three simulation parts was done for a swivel angle of 12.5°. **Figure 9** shows a snap-shot of the gap geometry and the relative local velocities of the surfaces of the tribological contact.

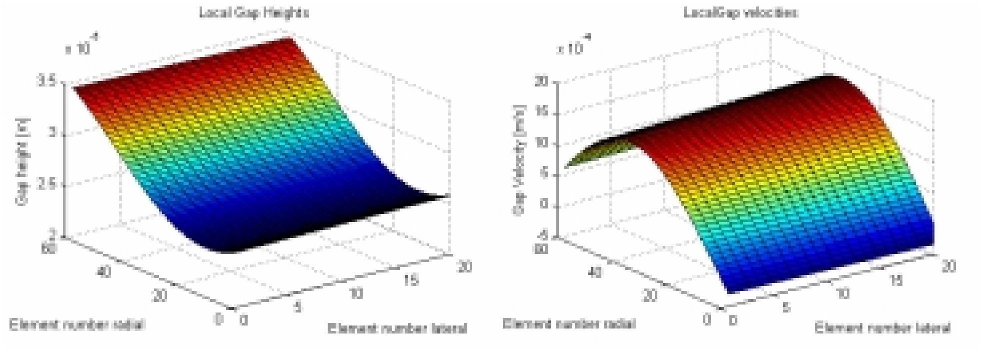

Figure 9 Local gap height and local relative gap velocity

Figure 10 shows the pressure profile and the shear stresses which are both needed for the force calculation at this moment.

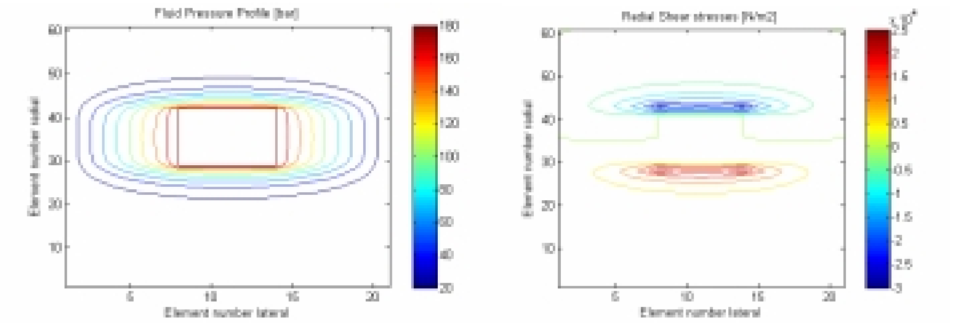

Figure 10 Fluid pressure and radial shear stress profile

Figure 11 illustrates the calculated tribological forces. They show the typical characteristics of the resulting forces.

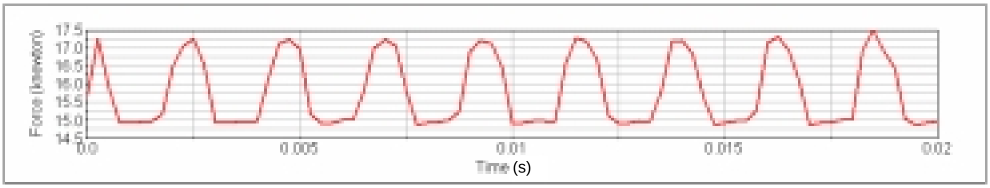

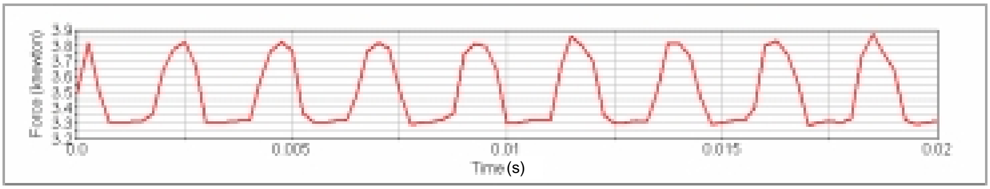

Figure 11 Resulting Forces at the high bearing at pressure side (y- and z-component)

Because of the oscillating forces acting on the swash plate there is a displacement of the swash plate which is shown in **figure 12**.

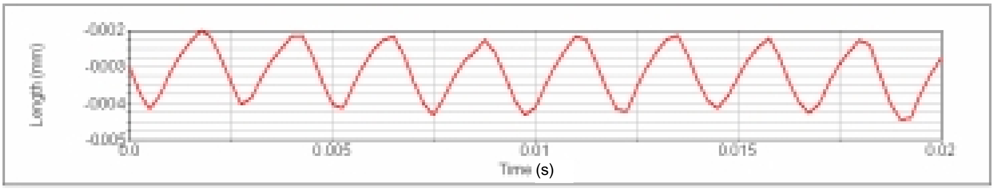

Figure 12 Transient results of the displacement in y-direction

This displacement results in changing gap geometry and therefore the quantity of leakage flow changes. **Figure 13** illustrates this effect.

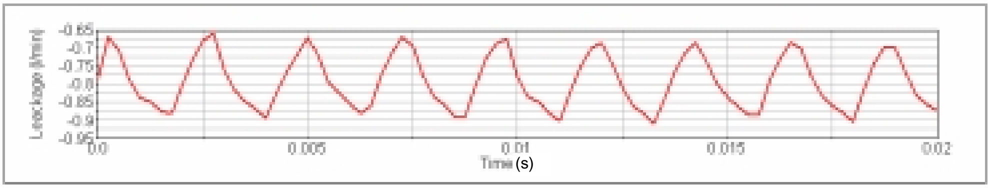

Figure 13 Transient results of the leackage

The change of leakage results in a pressure pulsation in the cavity, which is depicted in **figure 14**.

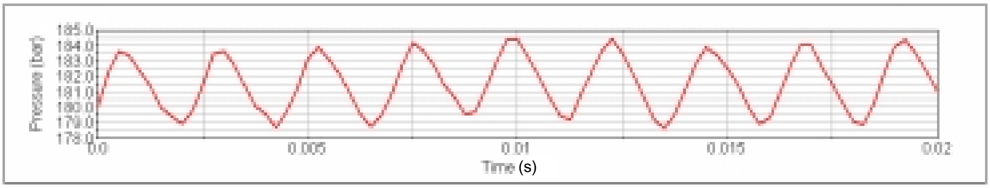

Figure 14 Transient results of the pressure

To show the performance of the simulation tool an exemplary parameter variation was conducted for the capacity of the hydrostatic bearing cavity. **Figure 15** shows a comparison of the pressure for an original capacity (solid line), a doubled capacity (interrupted line) and a halved capacity (dotted line). The results demonstrate that the amplitude of pressure pulsation increases for small cavities.

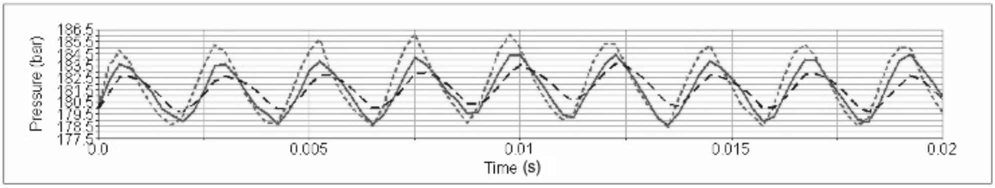

Figure 15 Pressure for Variation of Cavity Capacity

5. CONCLUSIONS

The simulation tool presented here can be used to simulate a hydrostatic swash plate bearing. The way of implementation of the tribological simulation allows to use existent multi-body simulation models. Alternatively new models can easily be generated by importing geometries from CAD-programs. The hydraulic model can be parameterized so that impacts on the systems resulting from parameter variations can be analyzed during the design process. The tribological model is compiled and linked to a dynamic link library. Therefore it can easily be implemented.

Exemplary simulation results show the functional capabilities. The simulation tool enables a better understanding of the tribological system and the impact of all relevant parameters. Sensitivity analysis can be done. In addition to that the results could be used to improve or to parameterize existing analytical models. For this purpose it is necessary to verify the simulation with experimental results.

REFERENCES

(1) A. Kleist Berechnung von Dicht- und Lagerfugen in hydrostatischen Maschinen [Calculation of sealing and bearing joints in hydrostatic machines], Dissertation RWTH Aachen 2002

(2) M. Deeken Using modern CAE tools to simulate hydrostatic displacement units, O&P, October 2005

(3) H. Murrenhoff Grundlagen der Fluidtechnik Teil1: Hydraulik [Fundamental principle of fluid technology, Part 1: Hydraulics], Script for lecture, RWTH Aachen 2005

(4) M. Liu Dynamisches Verhalten hydrostatischer Axialkolbengetriebe Schriftenreihe des Instituts für Konstruktionstechnik Ruhr [Dynamic performance of hydrostatic axial piston transmissions
series of publications issued by the Ruhr Institute for Design

Engineering] Bochum University Volume 01.1 2001

(5) G. Sanchen Simulationswerkzeug zur Auslegung der tribologischen Kontakte in hydrostatischen Kolbenverdrängern [Simulation tool for the dimensioning of tribological contacts in hydrostatic piston displacement units], GfT Tagung, Göttingen 1999

(6) X.Zang, J.Cho Damping on the Swash Plate of an Axial-Piston Pump, Proceedings of the American Control Conference, Chicago, Illinois, June 2000

Modelling

Modelling and measurement of the compliance and friction losses of screwjack electromechanical actuators

Wissam KARAM, Jean-Charles MARE
Laboratoire de Génie Mécanique INSA/UPS
Département de Génie Mécanique INSA
135 Avenue de Rangueil, 31077 Toulouse Cedex 4, France
wissam.karam@insa-toulouse.fr Jean-charles.mare@insa-toulouse.fr

ABSTRACT

In this communication, the behaviour of a roller screw electromechanical actuator (EMA) is studied around the null velocity in order to provide accurate models for force control applications, typically dynamic load generators for aerospace test benches. The first part is dedicated to the power needs and the test bench design with special consideration to architecture and stiffness. In the second part, an upgraded nut-screw model is proposed in accordance with experimental results. Measurement processes are discussed in detail, covering parameters identification and data filtering, while applied to mechanical losses and compliance variation due to preload. This work is performed in a non intrusive way (external view) so that it can be applied by systems integrators without disassembling the EMA.

1. INTRODUCTION

Thanks to the development of high performance power electronics, motors and mechanical transmission; electromechanical actuation is now well established in low power position control applications. In the field of linear motion, numerous on-the-shelf screwjacks can today cover wider and wider domains, including high speed or/and high accuracy applications. Opposite to that, it appears that there is a lack of experience feedback concerning the use of electromechanical actuators as dynamic force generators driving moving loads. The present work has been initiated by flight control actuators suppliers. Up till now, qualification, certification and endurance tests of such actuators are performed using valve controlled electro-hydraulic dynamic force generators. In order to provide order of magnitudes, Table 1 summarizes the common load generator requirements for low speed (aileron of single aisle commercial aircraft) and high speed (heavy helicopter main rotor actuator) applications.

Power Transmission and Motion Control 2007 Edited by Dr D N Johnston and Professor A R Plummer
© With The Centre for Power Transmission and Motion Control

	Low speed application *Representative of single aisle commercial aircraft*	High speed application *Representative of heavy helicopter*
Stall force	50 kN	60 kN
No load speed	30 mm/s	200 mm/s
Nominal force Nominal speed	25 kN 26 mm/s	
Stroke	50 mm	100 mm
Cycles	2000 at 12 kN full stroke, low frequency 6,5 Mcycles at 4 mm/s, 0.5 to 5 mm magnitude, 20 kN static + 2 kN/mm 2 Mcycles 10 mm/s, 2 mm to 8 mm, 9 kN static + 0.5 kN/mm 3 Mcycles 0.6 mm/s, 9 kN static + 0.5 kN/mm	2 mm, 0.1 to 15 Hz, 20 kN static 15 mm, 0.5 Hz, 30 kN static +25 kN dynamic at 20 Hz 50 mm, 1 Hz, 10 kN static + 12 kN dynamic at 20 Hz

Table 1. Typical flight control dynamic test requirements

For low power applications (typically less than 5 kW), it is thought best to switch to electromechanical actuation that is more attractive when price, easiness of control and environment are considered. Unfortunately, there are no real experience feedbacks in performing such tests with force controlled EMAs. This situation generates a real need to develop engineering methodologies enabling power sizing, natural dynamics evaluation, performance prediction and control synthesis. Some proposals of EMA architectures, power sizing, global modelling and natural dynamics analysis have already been presented in [1]. Most of the time, the roller-screw is studied considering geometry, stiffness and machining [7] & [8]. On its side, this communication deals with the methodology to analyse and model the EMA actuator around the null velocity, focusing on friction losses. Experimental data are taken from an EMA prototype supplied by SKF, in response to the low speed specification of Table 1. In addition, the test bench is supposed to reproduce the effective operation of the flight control actuator to be tested, according to:

- the equivalent load inertia effect m_e , with a mean value of 600 Kg,
- the equivalent anchorage and transmission stiffness k_e of 1.4 10^7 N/m.

2. TEST BENCH

The test bench, that has been designed to assess the EMA prototype, is representative of development or production ones that are used by flight control actuator (FCA) suppliers and aircrafts makers. Additional sensors have been installed to provide more data on the force generator performance.

2.1 Mechanical architecture

In order to minimize weight and size, the inertia effect I is reproduced using a transformer TF thanks to the Huygens law. It is implemented combining an in-line geometry and a rotating crank shaft. As seen on Figure 1-a, the two actuators are both connected at the same eccentred point on the crankshaft while a rotating inertia is fixed centred on the rotation axis. In such a way, only two masses of 8 kg are required to reproduced the 600 kg equivalent mass, taking benefit of the transformer ratio $(a/b)^2$.

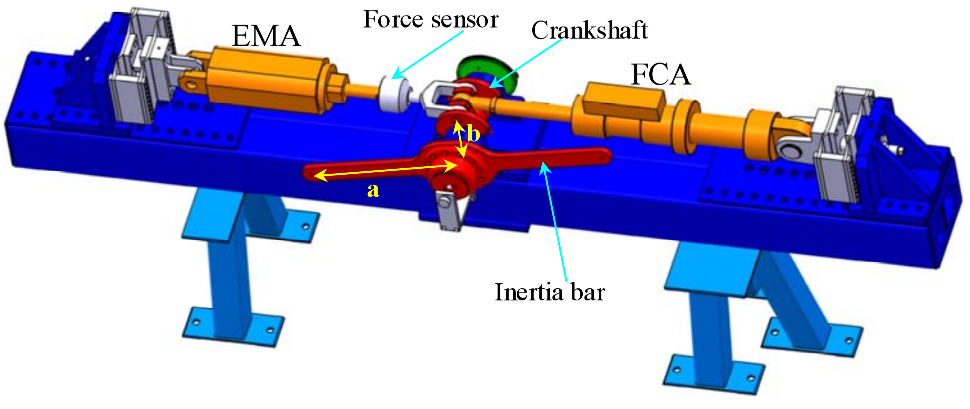
EMA
Force sensor
Crankshaft
FCA
b
a
Inertia bar

a) General 3D view

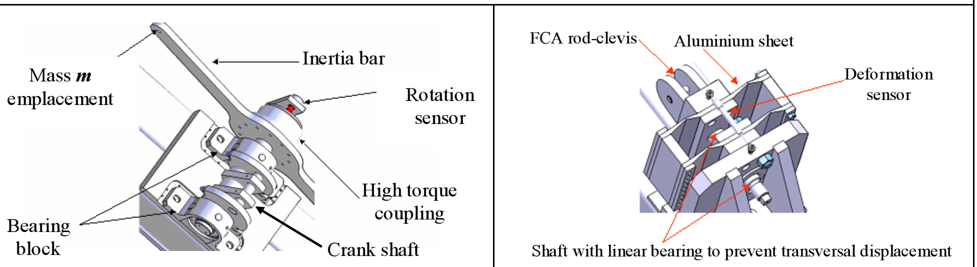
Mass *m* emplacement
Inertia bar
Rotation sensor
High torque coupling
Bearing block
Crank shaft
FCA rod-clevis
Aluminium sheet
Deformation sensor
Shaft with linear bearing to prevent transversal displacement

b) Design to reproduce inertia effect

c) Design to reproduce compliance effect

Figure 1. Test bench design

Such a test bench design allows multiple applications apart the testing of force controlled EMAs. If both actuators are position controlled, static and dynamic force equalisation methods can be assessed. This subject is of particular importance when different kinds of actuators drive the same load in an active-active mode.

2.2 Stiffness

As said earlier in the introduction, the test bench must allow reproducing the equivalent anchorage stiffness k_e of the airframe. This is performed using two size-optimised aluminium sheets that are fixed between the FCA connector and the test bench structure, Figure 1-c. On its side, the test bench stiffness is designed to be at least ten times higher.

The EMA prototype has been used to load and measure the effective compliance of the bench and of the reproduced anchorage stiffness. Figure 2 shows that the deformation is quite linear, the effective stiffness values being consistent with the upper requirements.

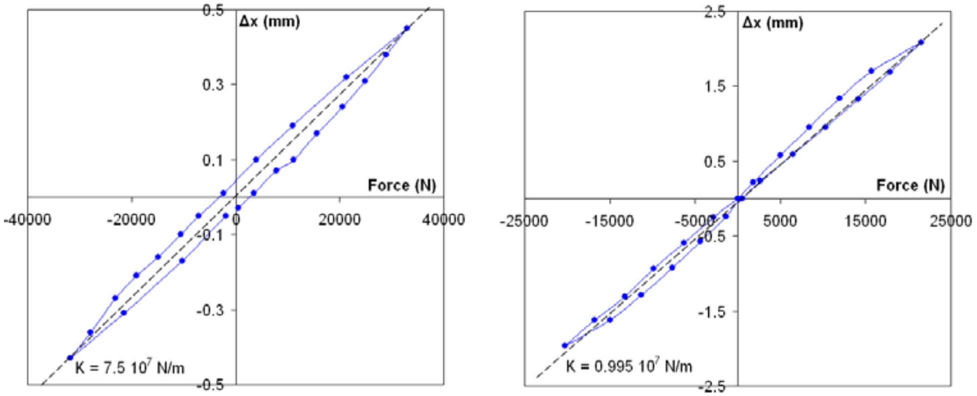

Test bench compliance Anchorage compliance

Figure 2. Measured compliances

3. EMA PROTOTYPE

The EMA prototype, Figure 3, is made of a 58/80 amps Parvex Digivex Power Motion (DPM) and a 6 kW Parvex ND860 EAF brushless motor that directly drives an inverted roller-screw (3 mm pitch, 30 mm diameter). With a 170 mm stroke, it is able to develop a 50 kN permanent stall force and a 0.21 m/s no-load velocity. The permanent maximum output power is 5.1 kW (35 kN @ 0.146 m/s). A parking brake is included for safety reasons to hold external loads in position when de-energised.

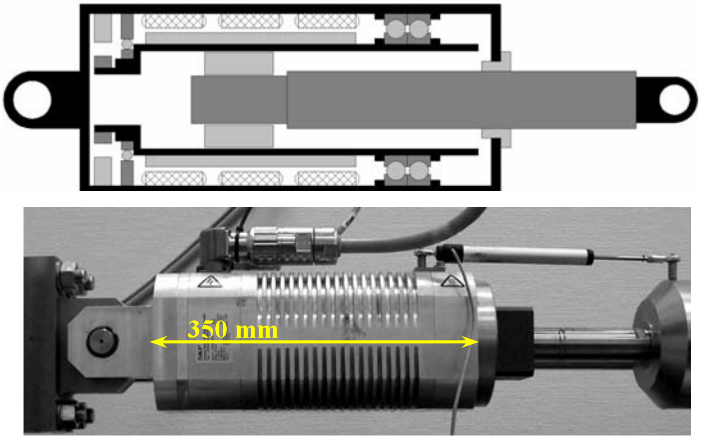

Figure 3. EMA prototype under study

3.1 Modelling approach

In position control applications, the outer control loop applies to a low dynamic state variable (position, the second time integral of acceleration). For common position control design, the simulated and experimental positions can be quite similar, even if the upper state variables are badly predicted by the model (thanks to the filtering effect of a double integration). Opposite to that, the force control applies to high dynamics state variables. For this reason, the performance prediction accuracy is much more sensitive to modelling errors.

When the hydraulic technology is used for dynamic loading, the modelling effort has to be put on seals friction and servovalve behaviour around the null opening. However, thanks to the high pressure gain of critical closed centre valves, the performance prediction is quite robust against friction modelling. Oppositely, electromechanical actuators involve high ratio mechanical reducers that generate complex friction and poor (or null) reversibility. This situation requires the designer to develop advanced transmission models that are able to accurately reproduce force losses and reversibility.

Friction modelling is well documented in [2], [3] &[4] but parameters identification and irreversibility are generally not considered, as most of the applications deal with position control. This particularly applies to roller-screws were the only available information is often provided by the supplier as a mechanical efficiency coefficient, without any distinction of the mode of operation (aiding load or opposite load). In an earlier author's communication [1], a roller-screw friction model has been proposed in order to link this data to the friction coefficient of an equivalent ACME screw, as given below.

Motor torque vs. output force
$$T = \left[\frac{\tan\alpha + \mu\,\mathrm{sgn}(\mathcal{P})}{1 - \mu\,\mathrm{sgn}(\mathcal{P})\tan\alpha}\right]\frac{d}{2}F \qquad (1)$$

Velocity dependant friction
$$\mu = \mu_C + (\mu_S - \mu_C)\exp\left[-(V_s / V_r)^2\right] + f_\mu |V_s| \qquad (2)$$

Sliding velocity vs. motor speed
$$V_s = \frac{d\cos\beta}{2}\,\omega_{sn} \qquad (3)$$

with	- F	[N]	force from screw to load
	- $\mathcal{P}$	[kW]	transmitted power
	- d	[m]	nut-screw nominal diameter
	- f_μ	[s/m]	viscous coefficient
	- T	[Nm]	torque from rotor to nut
	- V_r	[m/s]	reference velocity for Stribeck effect
	- V_s	[m/s]	equivalent sliding velocity
	- α	[rd]	lead angle
	- β	[-]	lead angle tangent
	- μ	[-]	equivalent overall friction coefficient
	- μ_C	[-]	equivalent Coulomb friction coefficient
	- μ_S	[-]	equivalent Stribeck friction coefficient
	- ω_{sn}	[rd/s]	relative angular velocity between the screw and the nut

This model does not consider the nut-screw axial preload that is used to reduce/cancel the transmission backlash [5]. The usual recommended axial preload is F_p = 35% of the maximum axial load. In that manner, under an external force of F_p, the contact on the loaded side of the thread has achieved its maximum stiffness and the other side is fully unloaded. The torque required to compensate for the axial preload is calculated from the transmission ratio and the practical direct efficiency as follows:

$$T_P = \frac{p}{\pi}\left(\frac{1}{\eta_P}-1\right)F_p \tag{4}$$

$$\eta_{dP} = 0.9\eta_d = \frac{1}{1+\mu\pi d/p} \tag{5}$$

with	- F_P	[N]	preload force
	- p	[m]	screw lead
	- T_P	[Nm]	preload torque
	- η_d	[-]	direct efficiency
	- η_{dP}	[-]	practical direct efficiency

During motion, the preload force is balanced by the driving torque and acts as an opposite load F_p, whatever the direction of motion and output force. In order to upgrade the effort losses model of the EMA, it is preferred to include the preload effort loss in the model at the driving torque level as shown in Figure 4. In that manner, it is possible to merge it with axial and thrust bearings losses that act on the rotor/nut shaft assembly, as there is no mean for the EMA user to distinguish each loss source.

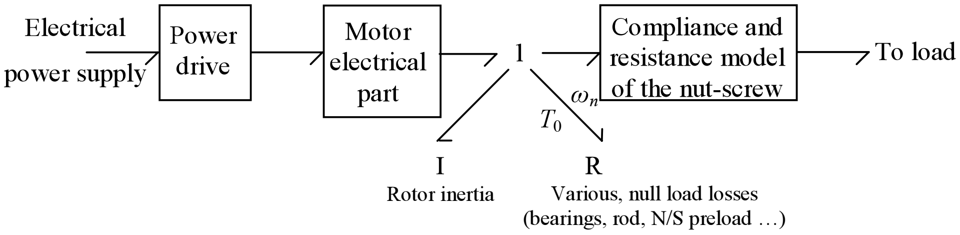
Electrical
power supply
Power drive
Motor electrical part
1
Compliance and resistance model of the nut-screw
To load
ω_n
T_0
I
Rotor inertia
R
Various, null load losses
(bearings, rod, N/S preload …)

Figure 4. Word Bond-graph of the EMA

Accordingly, the overall driving torque T_0 [Nm] under null external force, including the preload torque, is modelled by eq. (6), as a function of the rotor speed ω_n [rd/s] involving 5 parameters relative to the Coulomb, viscous, quadratic and Stribeck effects:

$$T_0 = \left[T_{0C} + f_v|\omega_n| + f_q\omega_n^2 + T_{0S}e^{-|\omega_n|/\omega_r}\right] sgn(\omega_n) \tag{6}$$

with	- T_{0C}	[Nm]	Coulomb torque
	- f_v	[Nm/(rd/s)]	viscous friction coefficient
	- f_q	[Nm/(rd/s)^2]	quadratic friction coefficient
	- T_{0S}	[Nm]	Stribeck torque
	- ω_r	[rd/s]	reference velocity

Under stuck conditions, the torque T_0 can be calculated using the common Lugre, Karnopp or Reset integrator approaches that are now available in many simulation software.

3.2 Parameters identification process

The model proposed in equation (6) involves five parameters. Such dissipative parameters cannot be predicted by calculus from physical knowledge and must be identified from experiments. For that, it is of particular importance to define an adequate process that must be consistent with the testing constraints.

In the present case, the aim of the work is to develop identification procedures with a customer view rather than an EMA designer approach. This forbids any possibility to insert sensors within the EMA to ensure non intrusive measurements. In the same manner, no modification of the industrial electronic power drive is allowed. The proposed methodology is based on these views in order to be applicable by system designers that integrate industrial components.

The rotor angular position and velocity are available from the EMA resolver that is used for commutation control. The power drive also delivers an estimate of the electromagnetic torque calculated from the equivalent direct current supplied to the motor. Test bench sensors provide additional information like force to load, EMA extension, structure deformation and load position.

The experiments purpose is to acquire sufficient data that would enable the identification of the different torque losses coefficients. To discern the additional friction model from the roller-screw model, all experiments were made with zero external load and with the minimum amount of external inertia. The no-load losses were identified using two different approaches, both of them running the EMA under velocity control. The velocity setpoint is fixed in accordance with the physical limitations imposed by the screw stroke and the supply voltage or current. Magnitude and frequency setting are combined to get the wider identification range.

a) Constant velocity

In this case, thanks to the STIMULI generator present in the Parvex software, the EMA is forced to follow a trapezoidal velocity profile. The driving torque is measured in the constant velocity domain, once the response has become steady.

b) Sine velocity

In the second approach, the EMA is forced to follow a sine velocity profile, producing cosine position and acceleration. This experiment also allows identifying the equivalent rotating inertia I_m [kgm^2] which driving torque is proportional to its angular acceleration.

The data flow of the EMA test bench is displayed on Figure 5.

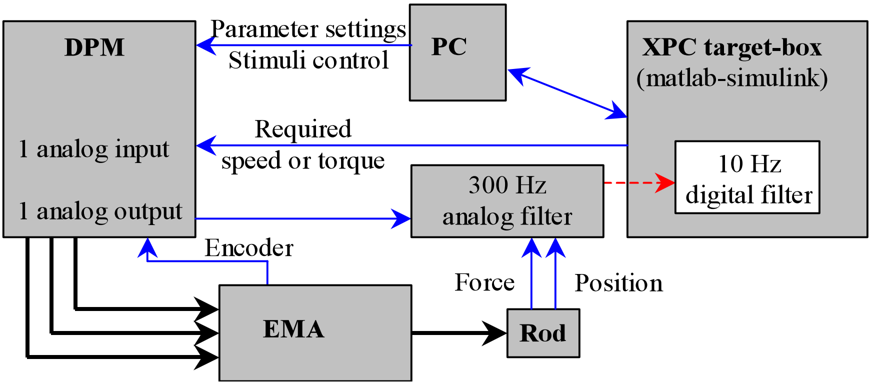

Figure 5. Data flow on EMA test bench

Two main problems have to be overcomed to run the experiments.

The first one deals with the power drive that generates useful signals for rotor position and speed and that estimates the electromagnetic torque. Even if these data can be monitored within the EMA power drive software, only one signal is available from outside through a single channel embedded digital-to-analog converter. For this reason, it has been decided to not separate the power controller from the electrical motor for modelling purposes as the user has no mean to identify separately the individual models. According to the supplier's data, the electromagnetic torque responds to the current setpoint with a 600 Hz second order dynamics. Thus, the electromagnetic torque can be considered as proportional to the current setpoint.

The second difficulty is related to the electromagnetic interferences (EMI) that are generated by the high current, high frequency commutation. A very efficient solution can be found in synchronizing the acquisitions with the clock driving the power electronics. Unfortunately this signal is not a standard output on industrial power drives. Full symmetrical wiring of all sensor signals also offers an interesting solution. Once again, many sensors conditioners do not offer this capability. For the present measurements, a low-pass filtering has been applied to all measurements (300 Hz analog anti-aliasing filter plus 10 Hz digital filter after acquisition).

As far as measurements are performed at low frequency, the magnitude effect of the data filtering keeps negligible. Oppositely, even at low frequency, the phase lag significantly alters the measurements, especially at the speed reversion where the friction torque is discontinuous due to the Coulomb effect. The constant speed measurements are neither affected by such signal alterations nor by inertia effects. On the other side, special attention must be paid for sine speed experiments for which the following procedure has been designed:

Step 1. Acceleration calculus

Even filtered, the velocity measurement is very noisy and does not allow any derivation to get useful acceleration data (see Figure 6, top right). For this reason, a pure velocity signal is identified from the effective one, using a least-squares method. Position and acceleration are then obtained by analytical integration or derivation of the ideal sine velocity.

Step 2. Compensation of filters phase lag

The driving torque, equation (6), must be calculated using the effective velocity. This is achieved by adding a lead phase on the measured velocity that compensates the measurement phase lag. Then, the calculated torque loss is filtered to be compared with the measured one.

3.3 Torque losses experimental results

The most interesting experimental results for no-load torque losses are summarised on Figure 6. The upper left plot is dedicated to the constant speed measurements while other plots concern the sine speed measurements. Experimental results are plotted in grey and the original, not submitted to measurement phase lag loss characteristic, is displayed for indication (note the discontinuity around the null velocity). The five friction parameters have been identified using a least-squares approach applied to the simulated and measured torque losses.

T_{0C} = 2.374 Nm f_v = 0.0161 Nm/(rd/s) f_q = 0 Nm/(rd/s)^2

T_{0S} = -1.2 Nm ω_r= 19.78 rd/s I_m = 0. 00846 kgm^2

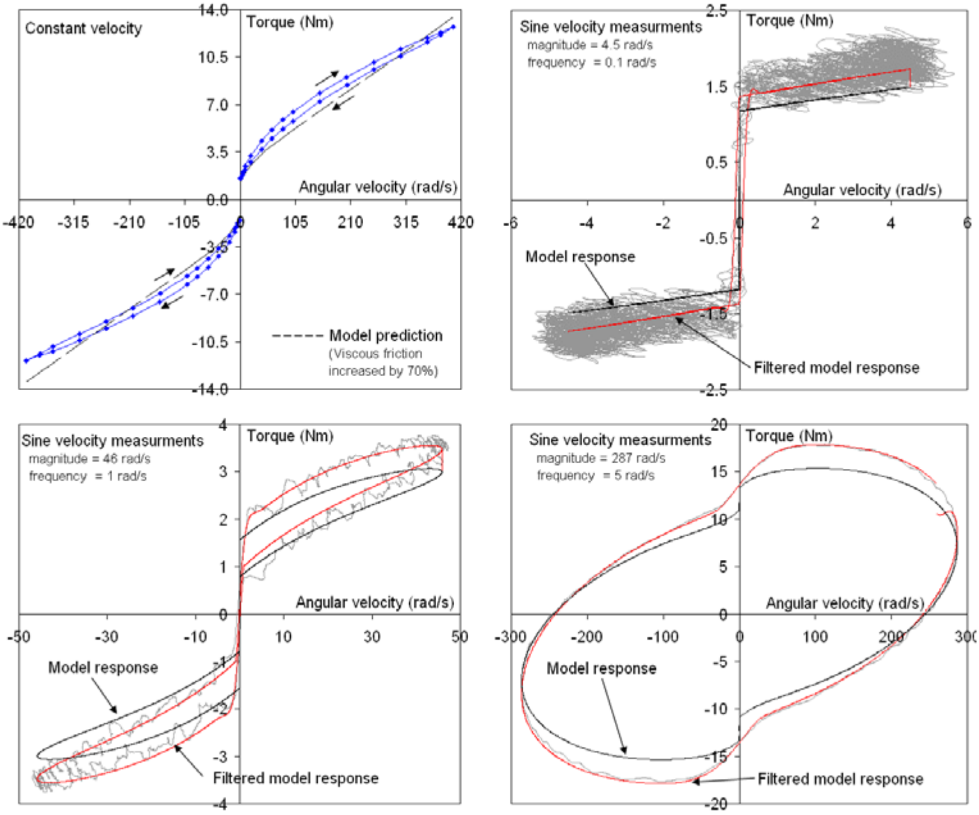

Figure 6. Overall no-load torque losses

The sine speed plots show that this unique set of parameters gives a very accurate prediction for all magnitudes and frequencies. However, it can be seen on the top left plot that this set of parameters underestimates the torque losses measured at constant speed. Increasing the viscous effect by 70 % for this experiment gives satisfactory prediction when other parameters are conserved. It is also interesting to notice on this plot that the Stribeck effect is negative, as confirmed by the value of T_{0S} , that is quite an uncommon situation.

When related to equations (1) to (3), the breakaway friction torque $T_{0C} + T_{0S}$ can be used to estimate the axial preload. Considering an equivalent nut/screw friction coefficient of 0.01 (common value leading to a direct efficiency of 0.76, an indirect efficiency of 0.68), it gives $F_p = 3$ kN that is only 6% the max external load.

3.5 EMA stiffness

The EMA compliance can alter significantly the closed loop performance. By preloading the nut-screw assembly, the manufacturer can remove backlash. But unfortunately, this reduces the service life and the mechanical efficiency.

The actuator stiffness can be roughly estimated given the nut-screw supplier's data [5] and the bearings types and location. Experiments cannot be avoided when more realistic information is expected. In this attempt, two experimental procedures are hereby suggested:

a) Passive

In absence of specific mean to hold the rotor angle, the parking brake can be used to perform blocked rotor experiment. This allows to switch off the power electronics and to avoid any measurement disturbance due to EMI. In this approach, the EMA is loaded by an external force while its extension is measured through low range, high sensitivity position sensors. This way is limited by the parking brake capability (9 Nm in the present case). If not negligible, the brake torsional compliance may lead to underestimated stiffness.

b) Active

The EMA is controlled in position in such a way to maintain the same output extension, whatever the external load. The rotor angle is plotted as a function of the external load after low-frequency filtering to remove EMI noise. This solution is however sensitive to the stick-slip phenomena that generates a stepped motion.

Figure 7 displays the EMA stiffness measured using the first approach. It can be noticed that the overall stiffness is lowered by 3 around the null external load.

The measured overall stiffness, Figure 7, displays a "lost motion" area around the null transmitted force that is representative of a partial preloading of the screw/nut transmission. Even if there is no visible backlash, the EMA stiffness is reduced by 2.8 in the "lost motion" area. This can significantly influence the low magnitude response that will suffer from such a reduced stiffness.

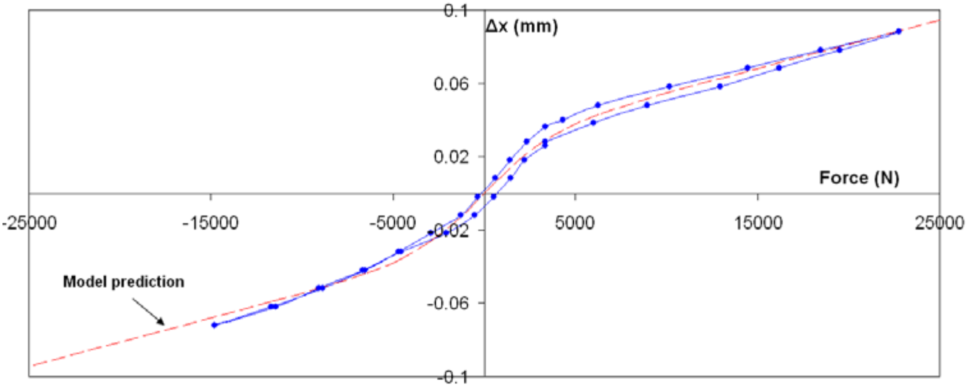

Figure 7. EMA stiffness measured by passive mean

For this reason, it may be important to include this non linear stiffness in the screw model. It is suggested to represent this effect by the following equation:

$$\Delta x = \frac{1}{k_0} F_s + \frac{F_r}{k_l} \tanh(F_s / F_r) \tag{7}$$

with	F_r	[N]	reference force
	F_s	[N]	axial force applied to the screw
	k_0	[N/m]	high load stiffness
	k_l	[N/m]	low load stiffness
	Δx	[m]	overall jackscrew deformation under axial force

The best fitting model is found with $k_0 = 3.79\ 10^8$ N/m, $k_l = 1.34\ 10^8$ N/m, $F_r = 3829$ N and produces a lost motion of $k_l/F_r = 28$ µm. It is here interesting to notice that the reference force F_r, that is representative of the width of the "lost motion" area, is of same magnitude as the estimated preload force F_p.

3.6 Reversibility

In order to predict accurately the force response, the screwjack model must be able to reproduce the influence of operating conditions on the mechanical efficiencies. A typical experiment pointing out this effect is presented in Figure 8. An open loop motor torque control (20 Nm static + 10 Nm sinusoidal @ 50 rd/s) is applied to the EMA that is directly connected to the FCA anchorage stiffness. The ideal EMA output force (lossless model with rotor inertia effect) is simulated and plotted as a reference. The effective output force is compared with two dissipative models outputs:

Model a) Unique friction coefficient
The transmission loss model is taken from equations (1) and (6) using the parameters identified in 3.3. The only parameter still to be identified is the overall friction coefficient µ of the nut-screw.

Model b) Friction coefficient depending on operating mode
In this case, the µ coefficient takes two different values according to the load type (aiding or opposite).

The direct efficiency allows us to identify the friction coefficient from area 1 so that the simulated response fits the effective one (η_d =0.81, μ=0.0075). For model a, the friction coefficient also fixes the indirect efficiency (η_i =0.76) that gives inaccurate result in area 2. The mean EMA force corresponds to the mean value of the lossless model force but is not representative of the evolution of the experimental force. A satisfactory agreement is finally found by adjusting the friction coefficient for opposite loads (η_i =0.59, μ=0.013), leading to model b.

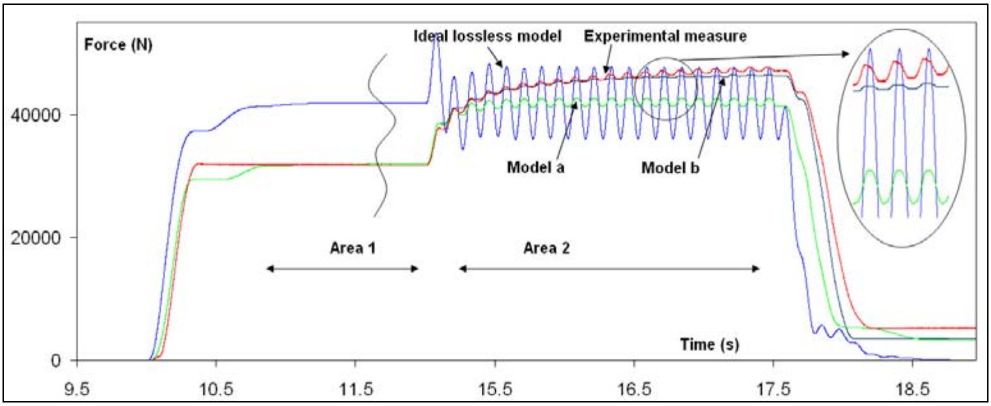

Figure 8. Efficiencies experiment

Figure 9 presents the model built in the AMESim environment [6] to perform the above models implementation.

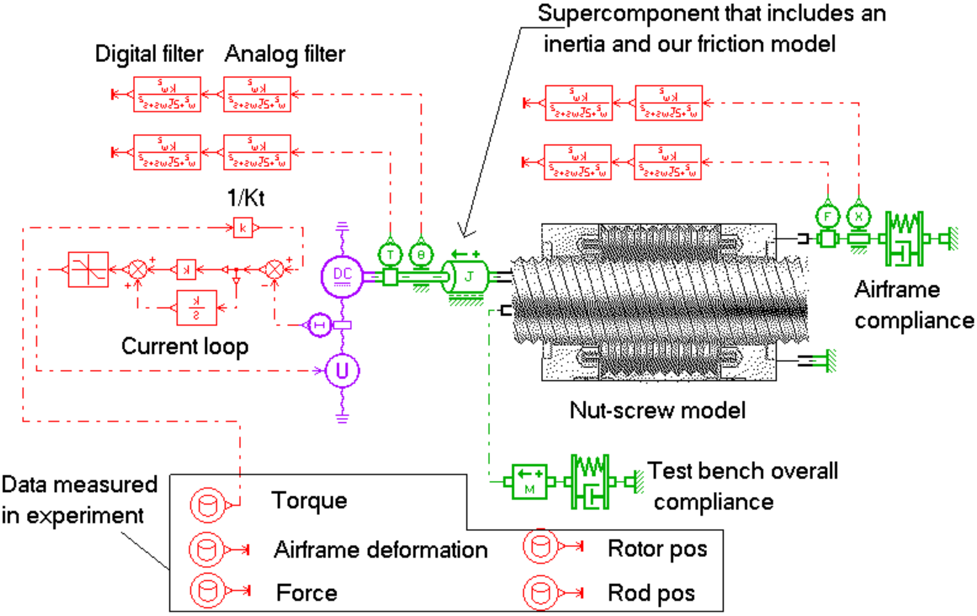
Digital filter
Analog filter
Supercomponent that includes an inertia and our friction model
1/Kt
k
DC
J
T
θ
F
X
M
U
Current loop
Airframe compliance
Nut-screw model
Test bench overall compliance
Data measured in experiment
Torque
Airframe deformation
Force
Rotor pos
Rod pos

Figure 9. AMESim model

4. CONCLUSION

The roller-screw EMA has been studied with the aim to develop accurate models for force control applications. The influence of the nut-screw preload that is used to reduce backlash has been studied starting from the suppliers calculation sheets. An experimental procedure has been proposed and implemented to allow model structure and parameters identification. Mechanical losses due to the preload have been modelled considering Coulomb, viscous, quadratic and Stribeck effects. Experimental results showed an increasing Stribeck effect and a negligible quadratic friction. On its side, the measurement of the EMA compliance revealed partial backlash compensation leading to lost motion effect for which a model has been proposed. A work is now in progress to merge together all the partial models presented in this communication in order to get efficient predictions of the EMA functioning.

REFERENCES

[1] **Karam W, Maré J-C.**, Comparison of EMA and HA performance for dynamic load simulators, *Power Transmission and Motion Control (PTMC 2006)*, pp 211-224, Hadleys Ltd, 2006
[2] **Armstrong-Lehouvry B.**, Control of machines with friction, *Kluwer Academic Publishers*, Dordrecht, 1991, ISBN 0-7923-9133-060
[3] **Olson H., Astrom K.J., Canudas de Wit C.,** Friction Models and Friction Compensation, November 28, 1997, www.control.lth.se/~kja/friction.pdf
[4] **Dupont P, Armstrong B.**, Elasto-Plastic friction model: contact compliance and stiction, *American control conference (Chicago-Illinois, June 2000)*, pp 1072-1077.
[5] SKF roller screws technical data 4351EN, pp 1-80, *SKF linear motion*, Montigny le Bretonneux, France, 2005-06
[6] AMESim, *Advanced Modelling Environment for Simulation*, Imagine SA, Roanne, France
[7] **Otsuka J, Fukada S.**, Fundamental study planetary screw structure coefficient friction, *Bull. Japan Soc. Of Prec. ENGG.*, Vol. 21, No. 1 (Mar. 1987), pp 43-48
[8] **Otsuka J, Osawa T.**, Study planetary roller screw comparison static stiffness vibration characteristics those ball screw, *Bull. Japan Soc. Of Prec. ENGG.*, Vol. 23, No. 3 (Sept. 1989), pp 217-223

Numerical Analysis of the Hydraulic Circuit of a Commercial Common Rail Diesel Fuel Injection System

Philipp Beierer, Kalevi Huhtala, and Matti Vilenius
Tampere University of Technology, Institute of Hydraulics and Automation, Finland

ABSTRACT

The trend in modern diesel combustion engine technology aims for fast acting injection systems that operate at pressures of 1500 bar and more. The Common Rail (CR) system is one typical representative of this development. It offers maximum flexibility in respect to injection pressure and timing. Due to these characteristics new challenges arise which need to be tackled if the full potential of this technology is to be used.

This paper introduces a numerical model of a commercial CR diesel fuel injection system. The analysis is made mainly in 1D and partly in 3D. The simulation results are compared to measurements. Finally, the model is used to perform a parameter study of the hydraulic circuit.

1. INTRODUCTION

High pressure common rail (CR) systems represent the state of the art in diesel fuel injection systems. A high pressure pump, a pressure reservoir or accumulator, connection lines, injectors, and an electronic control unit define in principle the core of the system. Due to the modular layout the fuel injection process is decoupled from the pressure generation. The main advantages are evident—CR systems allow a flexible selection of the injection parameters; injection pressure, duration, timing, and fuel delivery rate can be adjusted for optimized combustion. As a result, modern diesel engines with CR technology promote lower fuel consumption and fewer emissions while increasing at the same time the engine performance [1, 2].

Presently, commercial CR systems are operated at injection pressures of 1500 bar and more. For an efficient combustion of the fuel the injection process itself is split into several time separated events. By employing for example pilot, main, and post injection, a single injection event is in the range of some hundred microseconds [3].

It is apparent that the CR technology introduces also new challenges. Firstly, the high pressure level in the system requires that the individual components are adapted to the

Power Transmission and Motion Control 2007 Edited by Dr D N Johnston and Professor A R Plummer
© With The Centre for Power Transmission and Motion Control

increased pressure load. Secondly, the interconnection of several pressurized volumes represents a dynamic system. Information is not passed instantly through the pressurized domain but in form of longitudinal pressure waves that travel at finite speed [4]. Considering the aforementioned characteristic times, it is probable that the injection process is affected by the system dynamics. Generally, the delivery rate of an injector is defined by the hydraulic head. Hence, pressure oscillations at the needle seat of the injector have a direct impact on the actual mass flow through the nozzle holes and the combustion behaviour, respectively. The problem becomes particularly important for the case of multiple injections at the same injector. Generally, the pressure oscillation that is triggered by the early injections affects the flow rate of subsequent injections [5]. On the other hand, pressure oscillations may also travel through the system where they might have an impact on neighbouring injectors [6].

The analysis of modern diesel fuel injection systems is complicated by the high pressure level and the short time characteristics and length scales, respectively. Besides the very time consuming nature of experimental investigations, direct measurements are also limited to selected observation points. Simulation models are therefore a necessity not only to enlarge the number of studied variables but also to obtain a better understanding of localized phenomena that affect the overall behaviour of the system. Latter aspect assumes that the model is based on physical grounds and not on stochastic methods. As for example van Bebber [7] demonstrates, it is possible to use a stochastic approach for evaluating roughly a large number of parameters at relatively short time. However, by its definition the method is not suitable to provide qualitative statements about individual components.

The present paper addresses the need for a better understanding of pressure oscillations inside of a CR diesel fuel injection system. For this purpose, the authors utilise a numerical model that is based on physical laws. The first part of the article focuses on the modelling approach itself, i.e. the underlying theory and other aspects that become important when simulating high pressure hydraulic systems. Subsequently follows a comparison of some modelled findings to measured results. A thorough discussion of latter work can be found in [8]. Finally, the analysis of the simulation results focuses on the impact of the connection line between rail and injector (geometrical study) and injection time (only single injections) and pressure on the oscillation behaviour at the injector inlet. The main output parameters include maximum pressure amplitudes, frequency and damping of the pressure oscillation, and the amount of injected volume.

2. SIMULATION MODEL

2.1 Simulation Environment

The core of the numerical simulations is conducted in the GT-Fuel environment, version 6.2[1]. The commercial code consists of the three modules pre processor (GT-ISE), solver, and post processor (GT-Post). For modelling fluid flow through ducts and passages, the code solves simultaneously the complete Navier-Stokes equations in 1D [9]. Depending on the boundary definitions it is also possible to include fluid structure interaction (FSI) and rigid body dynamics. Latter aspect becomes important in case significant boundary displacement has to be included in the model.

---

[1] Gamma Technologies Inc.

The basic set of equations for solving the fluid field is defined by:

Continuity: $$\frac{dm}{dt} = \sum_{boundaries} mflx$$

Momentum: $$\frac{d(mflx)}{dt} = \frac{dp \cdot A + \sum_{boundaries} (mflx \cdot u) - \frac{\rho \cdot u^2}{2} \cdot A \cdot \left(4 \cdot C_f \frac{dx}{D} + C_p\right)}{dx}$$

Energy: $$\frac{d(m \cdot e)}{dt} = p \frac{dV}{dt} + \sum_{boundaries} (mflx \cdot H) - h \cdot A_S \cdot \left(T_f - T_w\right)$$

where:

$mflx$	boundary mass flux into the volume
m	mass of volume
V	volume
p	pressure
ρ	density
A	cross-sectional flow area
A_S	heat transfer surface area
e	total internal energy per unit mass
H	total enthalpy
h	heat transfer coefficient
T_f	fluid temperature
T_w	wall temperature
u	velocity at the boundary
C_f	skin friction coefficient
C_p	pressure loss coefficient
D	equivalent diameter
dx	length of mass element in flow direction
dp	pressure differential acting across dx

The system of equations is discretized over control volumes which are based on a staggered grid approach. For time accuracy the code employs an adaptive explicit scheme that ensures the fulfilment of the Courant condition at all times [9, 10]. One of the biggest differences to concepts that are traditionally used in the field of fluid transients is the way the code computes the speed of sound in the fluid. The method of characteristics for example requires as an input parameter the definition of the bulk modulus, which implies the sonic speed itself [11]. GT-Fuel on the other hand utilises a state equation of the fluid and the above listed equations to compute this parameter during the solution process [10].

In order to represent vector quantities adequately at flow splits, GT-Fuel uses locally a three dimensional representation of the momentum equation. Thus, actual geometrical details are preserved to a great extend in the simulation model. Finally, the effect of frequency dependent friction is considered through extending the skin friction coefficient C_f by an additional empirical, transient term.

2.2 Numerical Modelling of the CR System

Figure 1 depicts a photograph of the CR test bench that defines the basis of the numerical simulation [8]. Note that for this analysis only one injector is mounted to the rail (port 5).

Figure 3 shows the corresponding model in the GT-Fuel environment. The upper part shows the main components of the hydraulic circuit: pressure supply, rail, connection pipes between rail and injector and the injector itself. Latter item is represented in the main model by a single block which points to the underlying sub-model of the injector (see lower part of Figure 3). For easier orientation, Figure 2 shows schematically the main elements of the solenoid controlled CR injector.

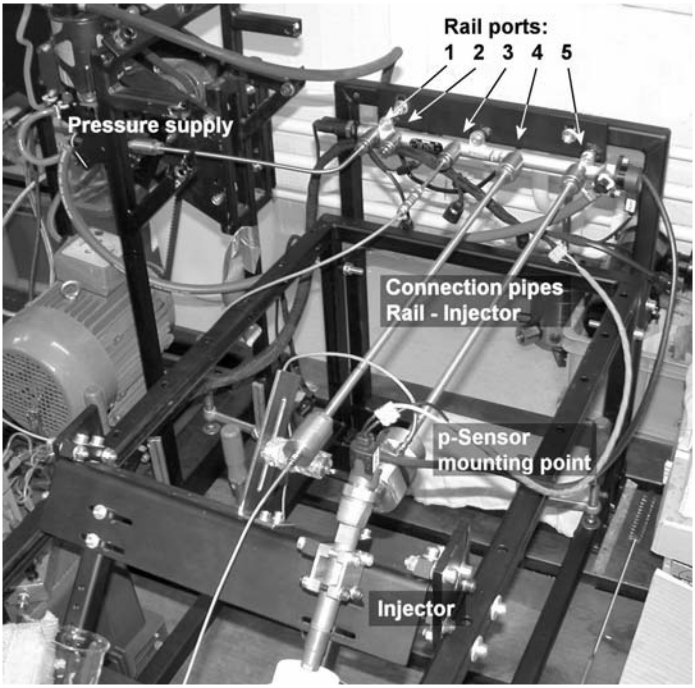
Rail ports:
1 2 3 4 5
Pressure supply
Connection pipes
Rail - Injector
p-Sensor
mounting point
Injector

Figure 1. CR test bench

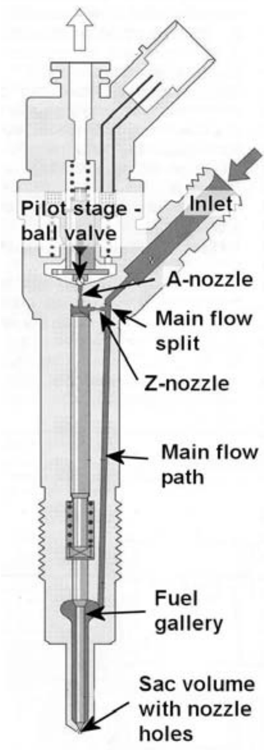
Pilot stage -
ball valve
Inlet
A-nozzle
Main flow
split
Z-nozzle
Main flow
path
Fuel
gallery
Sac volume
with nozzle
holes

Figure 2. CR injector (schematic) [12]

The working principle of this type of injector falls into the category of needle lift steered injectors [13]. This means that the injection pressure is constantly present inside of the injector. The injection event is initiated by opening the pilot stage ball valve. Fuel that is present above the plunger exits via the A-nozzle. As the Z-nozzle diameter is smaller than the A-nozzle, the pressure on the top side of the plunger decreases. Conversely, the full injection pressure still acts on the needle ring area inside the fuel gallery and the wetted needle shoulders upstream of the needle seat. Because of the resulting force imbalance the injector needle lifts together with the plunger and fuel is injected via sac volume and nozzle holes into the surrounding atmosphere. The injection process is terminated again by releasing the solenoid current. The pilot ball valve closes and the fluid pressure above the plunger recovers to the initial state. Due to the larger area ratio of top to bottom the combined mass of plunger and needle moves downwards where it seals off the sac volume from the pressure supply.

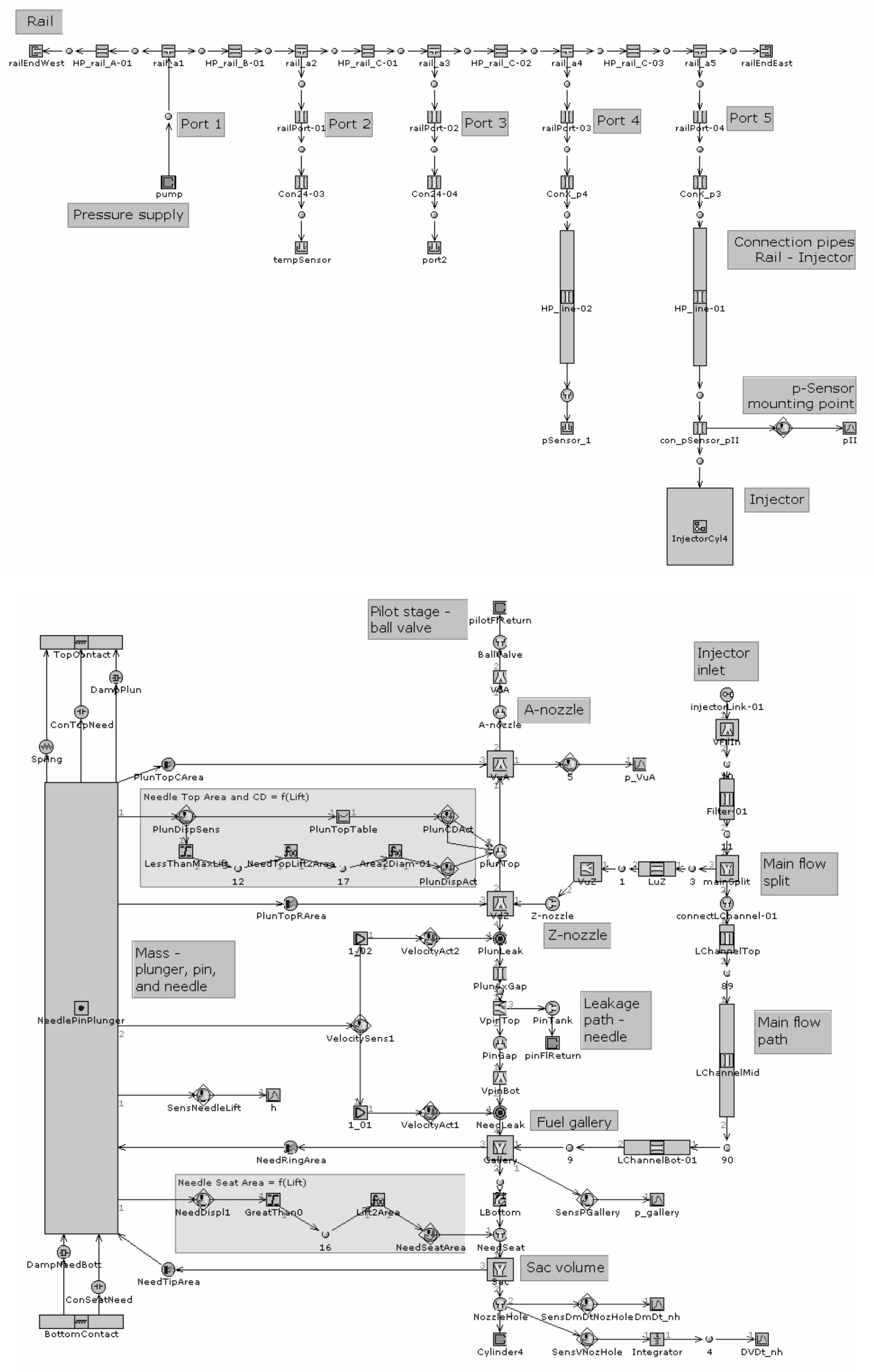
Rail
railEndWest
HP_rail_A-01
rail_a1
HP_rail_B-01
rail_a2
HP_rail_C-01
rail_a3
HP_rail_C-02
rail_a4
HP_rail_C-03
rail_a5
railEndEast
Port 1
Port 2
Port 3
Port 4
Port 5
railPort-01
railPort-02
railPort-03
railPort-04
pump
Pressure supply
Con24-03
Con24-04
ConK_p4
ConK_p3
tempSensor
port2
Connection pipes Rail - Injector
HP_line-02
HP_line-01
p-Sensor mounting point
pSensor_1
con_pSensor_pII
pII
Injector
InjectorCyl4
Pilot stage - ball valve
pilotFlReturn
BallValve
VbA
A-nozzle
Injector inlet
injectorLink-01
VFilIn
TopContact
DampPlun
ConTopNeed
Spring
PlunTopCArea
VuA
5
p_VuA
Needle Top Area and CD = f(Lift)
PlunDispSens
PlunTopTable
PlunCDAct
LessThanMaxLift
NeedTopLift2Area
Area2Diam-01
PlunDispAct
12
17
plunTop
Filter-01
VuZ
1
LuZ
3
mainSplit
Main flow split
PlunTopRArea
VdZ
Z-nozzle
connectLChannel-01
LChannelTop
Mass - plunger, pin, and needle
1_02
VelocityAct2
PlunLeak
PlunAxGap
VpinTop
PinTank
pinFlReturn
Leakage path - needle
NeedlePinPlunger
VelocitySens1
PinGap
VpinBot
Main flow path
LChannelMid
SensNeedleLift
h
1_01
VelocityAct1
NeedLeak
Fuel gallery
NeedRingArea
Gallery
9
LChannelBot-01
90
Needle Seat Area = f(Lift)
NeedDispl1
GreatThan0
Lift2Area
16
NeedSeatArea
LBottom
SensPGallery
p_gallery
NeedSeat
DampNeedBott
NeedTipArea
Sac
Sac volume
ConSeatNeed
BottomContact
NozzleHole
SensDmDtNozHole
DmDt_nh
Cylinder4
SensVNozHole
Integrator
4
DVDt_nh

Figure 3. GT-Fuel CR model – top: main circuit, bottom: CR injector sub-model

The main model parts of the hydraulic circuit are based on pipe, flow split and orifice objects as it is presented in Figure 3. The pipe block is generally utilised for cylindrical segments that transmit longitudinal waves. In order to predict accurately wave propagation, pipe blocks are different than the other objects further sub-divided by a user defined discretization length. For the present model this parameter has been chosen in the range of 3 mm, which is found to be a good compromise between solution accuracy and required CPU time.

It is apparent that the previously presented working principle of the injector is strongly affected by the internal flow condition and force balance. The interaction between the solid body (single mass for plunger, pin, and needle) and the flow field is indicated in the lower part of Figure 3 through connection lines and blocks in the centre and left. For example, we discuss at this place the modelling of the plunger top area in GT-Fuel. Generally, a combination of volumes and orifices defines the pilot stage of the injector model. Directly above the plunger, i.e. downstream of the Z-nozzle, the volume varies as a function of plunger lift *dz*. For *dz* close to its maximum value an additional orifice between the A- and Z-nozzle becomes effective. The latter one is responsible that the plunger does not hit the upper wall but stops just slightly before it. Indeed, the physics of the interaction are a main characteristic of the injector. In order to get a better understanding of the system we therefore enhanced the GT-Fuel model by the results of a transient three dimensional fluid-rigid body simulation in ANSYS-CFX 10.0[2]. While neglecting at this place further details concerning the model setup, the authors present in Figure 4 the utilised grid (left) and a snapshot of streamlines (only half domain) and pressure contours at the plunger top wall (right). Based on these results it is evident that for example not only the plunger top orifice diameter but also its discharge coefficient is a function of plunger lift. The corresponding implementation in the GT-Fuel model is indicated by the upper grayed out box, left hand side of the injector sub-model (Figure 3).

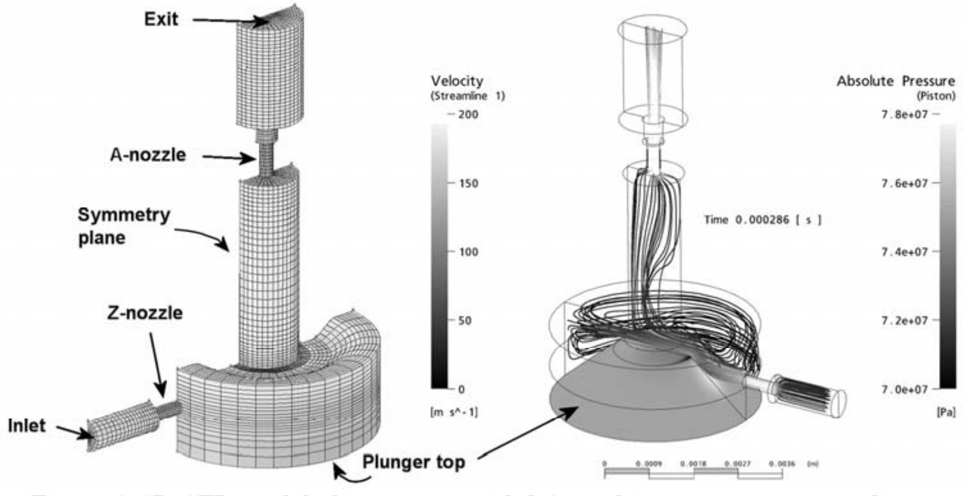

Figure 4. 3D CFD model plunger top; grid (left) and instantaneous streamlines, pressure contour (right)

---

[2] ANSYS Inc.

Although a lot of detail is included in the model of the injector, the authors want to emphasise that this component is not the main subject of this study. In fact, the injector model is made only as detailed as necessary but as simple as possible. The latter aspect explains why we utilise for example a look-up table to define the opening profile of the pilot stage ball valve instead of modelling explicitly the solenoid and its mechanical parts. Secondly, it is assumed that the high pressure pump can be modelled by a partial constant pressure source that is attached directly to the rail. The measurements show that the mean system pressure drops slightly during the injection process due to the finite delivery rate of the high pressure pump [8]. Accordingly, the level of the constant pressure source in the model is adapted during the simulation to the measured mean pressure level. The rail and connection pipes of the GT-Fuel model are defined to be perfectly rigid. One numerical study with flexible walls, not presented here, has shown that the differences are only marginal when compared to the rigid boundary setup. Indeed, the solution of the additional equations for the pipe structure increases considerably the required CPU time. The measurement and the simulation model utilise a fluid that corresponds to the ISO-4113 standard. It is therefore assumed that the fluid of the experiment and the fluid of the GT-Fuel simulation behave same at the studied pressure and temperature levels. Finally, the numerical analysis in this paper considers same as for the measurement only single injection events.

3. RESULTS

3.1 Comparison of Simulation Results to Measurement Data

In Figure 5, the authors present for various setups a comparison of the simulated and measured pressure history at the injector inlet. Overall, the simulation matches well with the measured signal. For a connection pipe with d_p = 2.4 mm and l_p = 400 mm (Figure 5, upper plot left side), it appears that for the highest injection pressure the simulated amplitudes are slightly too large between t = 11 ms and 17 ms. On the other hand, in case the valve activation time is set to t_{inj} =800 µs and a smaller connection line between rail and injector (d_p = 1.6 mm, l_p = 200 mm), the simulation predicts a somewhat higher oscillation frequency than the measurement (Figure 5, lower plot right side).

Figure 6 depicts for a setup with a connection pipe diameter of d_p = 2.4 mm a comparison of the oscillation frequency as a function of injection pressure and pipe length. Note that all frequency values are normalised to the measured data at p_{set} = 1000 bar and l_p = 400 mm. As the graph shows, the simulated pressure oscillation falls slightly behind the measured signal in case the model employs a short connection pipe.

Finally, Figure 7 presents for example, for a pipe setup of l_p = 600 mm and d_p = 3.2 mm, the measured and computed volume per injection as a function of injection time and pressure, respectively. Most apparent in this graph is the large discrepancy between the data sets in case an injection duration of 400 µs is combined with injection pressures higher than 500 bar. Then again, by considering the total amount of injected mass for each setup, the discrepancy appears in a different perspective. According to the measurements, the injected mass increases for this configuration as a function of injection pressure from 1.2 mg to 13.45 mg per injection. As it is reported in more detail in [8], the method for determining the injected mass is based on the measurement with a high precision scale. Instrument accuracy, arbitrary measurement errors, and the potential discrepancy of the actual fluid properties to the state that is assumed in the simulation model may easily sum up to a recognisable difference. Certainly, the model of the injector itself may have a weakness at this injection time although the fault is not detectable for example from the pressure history at the injector inlet (see Figure 5, upper plot right side).

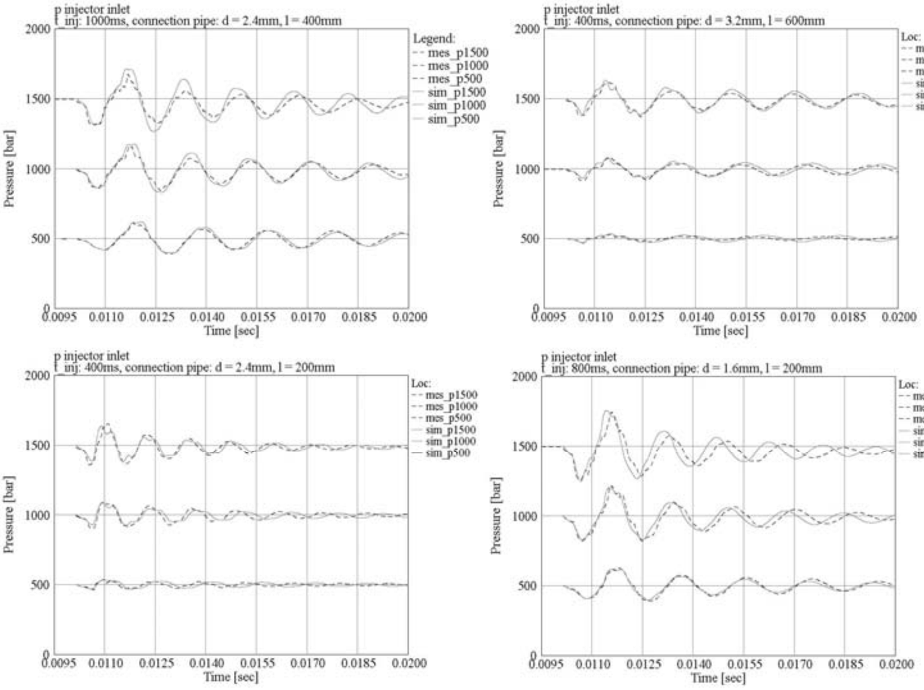

Figure 5. Pressure at injector inlet; measured ((mes_) dashed) vs. simulated ((sim_) solid)

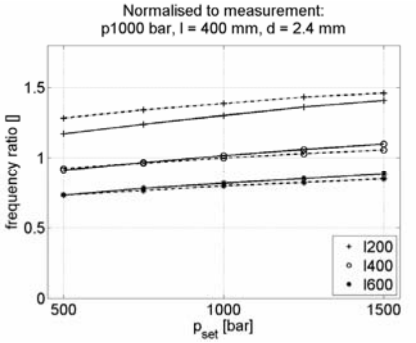

Figure 6. Frequency - normalised; measurement (dashed), simulation (solid)

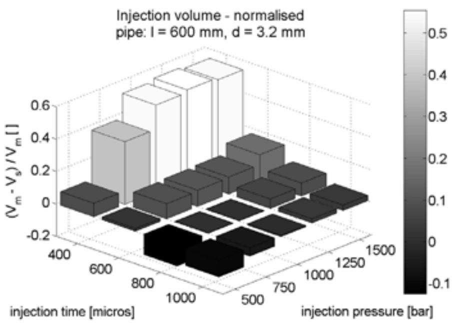

Figure 7. Injected volume, normalised to measurement

3.2 Discussion of Simulation Results

Altogether, we have studied 180 different configurations. This analysis sets emphasis as it is indicated in the introduction on the geometry of the connection pipe between rail and injector (pipe length l_p and diameter d_p) and injection characteristics (injection pressure p_{set} and duration for a single injection t_{inj}). Following Table 1 gives a summary of the setup details. Note that some of the following plots use the actual distance l between rail chamber and injector inlet and not the explicit pipe length l_p. Due to the limited space the authors present in this paper only a short summary of the analysis methods and findings, respectively.

Table 1 Summary of case definitions

injection pressure p_{set} [bar]	500, 750, 1000, 1250, 1500
injection duration t_{inj} [μs]	400, 600, 800, 1000
fluid temperature [K]	310.5
fluid	GT-Fuel ISO 4113 oil

type No. connection line rail to injector / dead end		**length l_p [mm]**		
		200	400	600
diameter d_p [mm]	1.6	*7301353*	*7301354*	*7301359600*
	2.4	*7301343*	*7301344*	*7301349600*
	3.2	*7301233*	*7301234*	*7301239600*

In the first part of the analysis we set our attention to the amplitude characteristics of the pressure oscillation at the injector inlet. The main parameters are the maximum positive amplitude *p_max* and the first two negative peaks *p_min,1* and *p_min,2* (see Figure 8). As it is shown in Figure 9 the maximum positive pressure amplitude increases for smaller pipe diameters. The variation thereby is not linear but indicates a large gradient for small d_p. In case a long connection pipe setup is compared to the equivalent with small l_p, the lower part of Figure 9 states that longer pipes generally lead also to larger

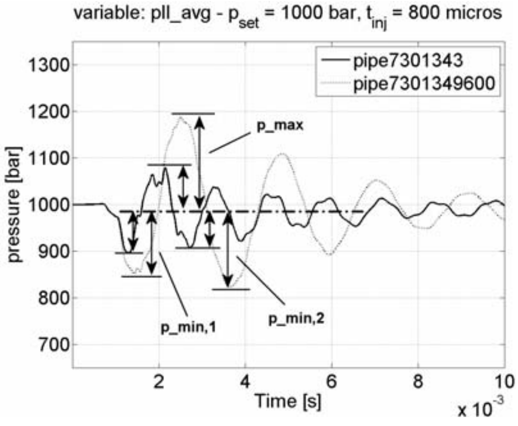

Figure 8 Definition of pressure amplitudes

amplitudes. Although not shown at this place, the simulation results predict that this phenomenon appears particularly strong for cases with low injection pressures, long injection times, and small pipe diameters. In respect to injection pressure, the upper plots of Figure 9 confirm the general expectation: a large injection pressure leads to a large positive pressure amplitude. However, this trend is not same for all setups but varies in intensity as a function of for example the pipe diameter d_p.

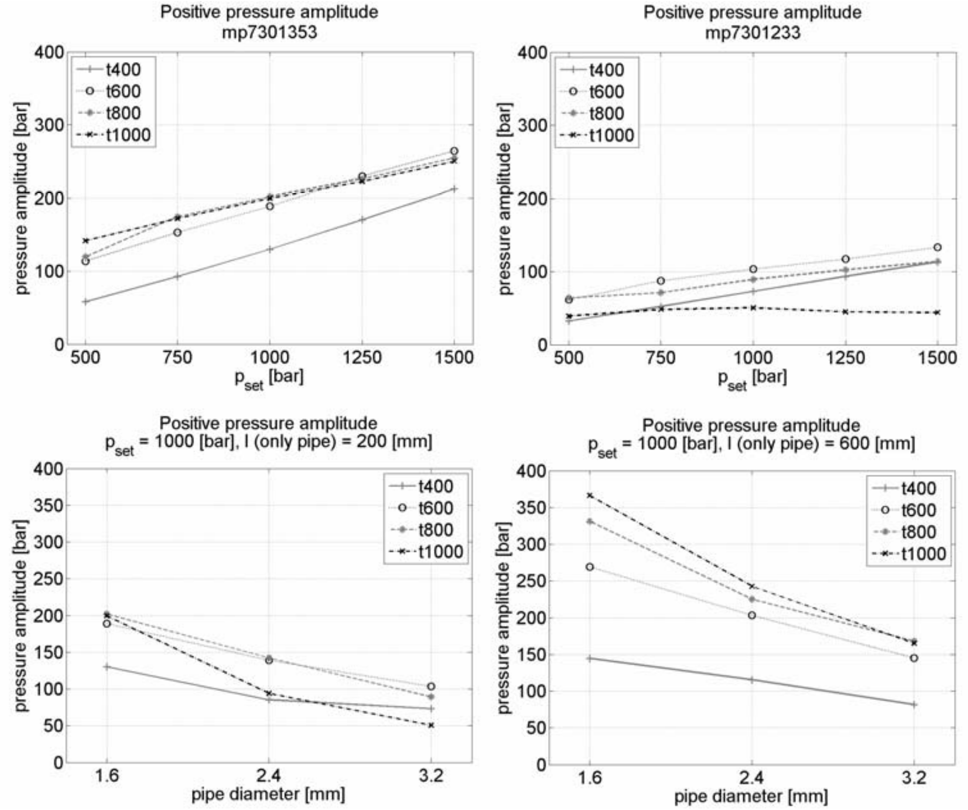

Figure 9. *p_max* for various configurations

Figure 10 depicts for various configurations the development of the first and second negative pressure peak. Generally, the same trends appear as for *p_max*—a small pipe diameter causes larger absolute amplitudes and the gradient of amplitude change increases at the lower end of the d_p range. The upper part of Figure 10 aligns with the measurement by predicting some configurations that show a larger *p_min,2* than *p_min,1*. Latter parameter shows also a special connection to l_p. Without presenting other plots of this category the simulation confirms the existence of a finite length for which *p_min,1* becomes independent of the pipe length.

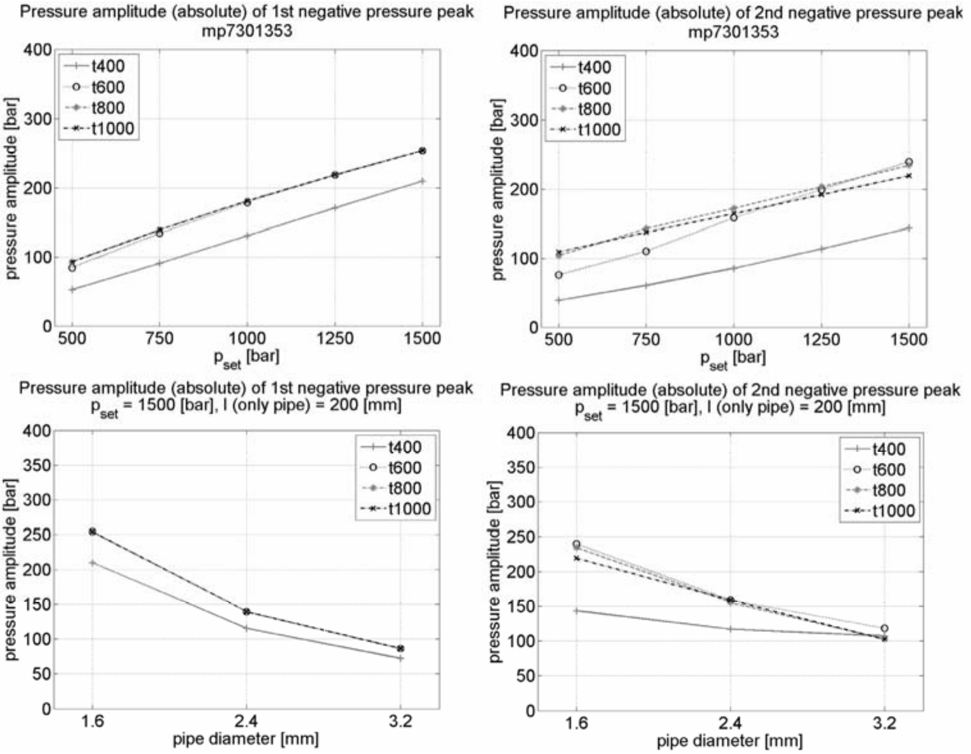

Figure 10. ***p_min,1*** **(left) and** ***p_min,2*** **(right) for various configurations**

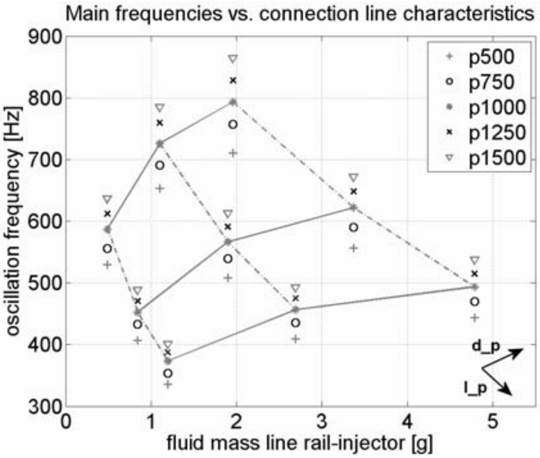

Figure 11. Oscillation frequency vs. fluid mass

By analysing the oscillation frequency of the pressure oscillations it appears that the explicit time period is not a function of the injection time. Consequently, Figure 11 presents frequencies that are averaged over the utilised needle opening times. We want to emphasise that in this plot the abscissa is defined by the fluid volume between the rail chamber and the injector inlet. Firstly, the plot reveals the validity of the expected trend, i.e. the oscillation frequency increases for increasing injection pressure. It comes also not as a surprise that the frequency drops for increasing pipe lengths (Figure 11, compare solid lines). Indeed, most outstanding in this plot is the fact that a larger pipe diameter d_p leads to a faster pressure oscillation (Figure 11, compare dashed lines). As it is shown, the impact of d_p varies as a function of pipe length.

For analysing the damping of the oscillation, the authors employ two methods. The first method assumes that the pressure oscillation can be described by a dynamic system of second order. For such a system the step response can be described by the following equation:

$$y = K \cdot e^{-\frac{\omega_e \cdot D}{\sqrt{1-D^2}} \cdot t} \cdot \left(\cos(\omega_e \cdot t) + \frac{D}{\sqrt{1-D^2}} \cdot \sin(\omega_e \cdot t) \right)$$

This equation is subsequently fitted to the simulated signal by using the Matlab[3] optimization toolbox. The procedure results in values for the static transmission coefficient K, the damped natural frequency ω_e, and the damping coefficient D.

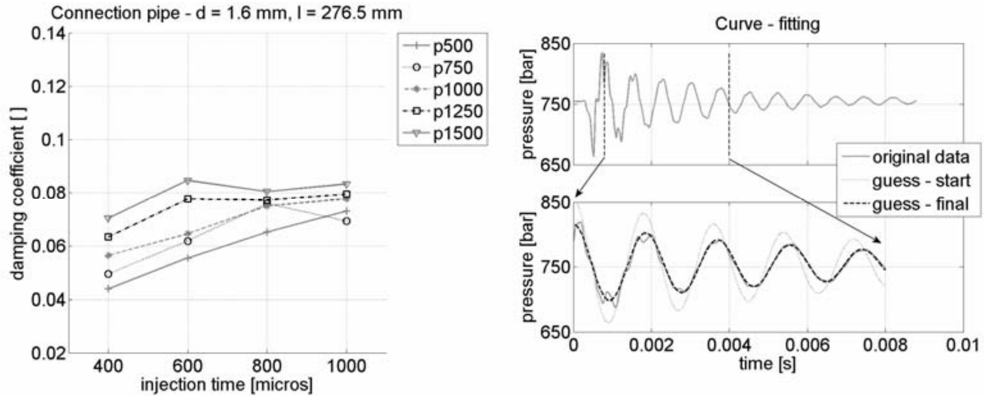

Figure 12. Damping of pressure oscillation – method: curve fitting

Figure 12 shows the procedure (right) and some example results for various setups (left). Alternatively to the curve fitting procedure we evaluate in the second method the explicit decay of the amplitudes from peak to peak. It has to be mentioned that this approach leads not to an explicit solution parameter but to a method that is suitable to qualitatively compare different setups with each other (see [8] for further details). If the damping is expressed by a single parameter, it can be said that generally the equivalent damping coefficient is smaller than 0.15. Secondly, the injection time appears to have only a mild impact on the amplitude decay. On the other hand the simulation confirms the measurement through indicating higher damping at higher pressure levels. Comments concerning the pipe geometry are omitted in this paper as the corresponding results are too diverse to present them at this limited space.

---

[3] The MathWorks, Inc.

Finally, Figure 13 shows for example for two configurations some plots of the simulated injection volume per injection over injection time. Despite the discrepancy between measurement and simulation at the injection time of 400 μs (see previous section), the overall fit of the data is very good. This includes also the kink of the p_{set} = 750 bar curve at 800 μs. The source of this phenomenon has not been revealed yet. However, we believe that this feature is caused by some injector dynamics. The parameter injection pressure and injection time alter in an expectable way the amount of the injected fuel. A higher pressure or longer needle opening results in an increase of the injected volume. On the other hand, the shape of the curves suggest also that somewhere between 400 and 600 μs injection time some system state is changing—from times longer than 600 μs, the slopes tend to be parallel. Finally, the pipe geometry seems to have only a marginal impact on the volume. For example the amount of fuel increases slightly for increasing pipe diameters as Figure 13 indicates.

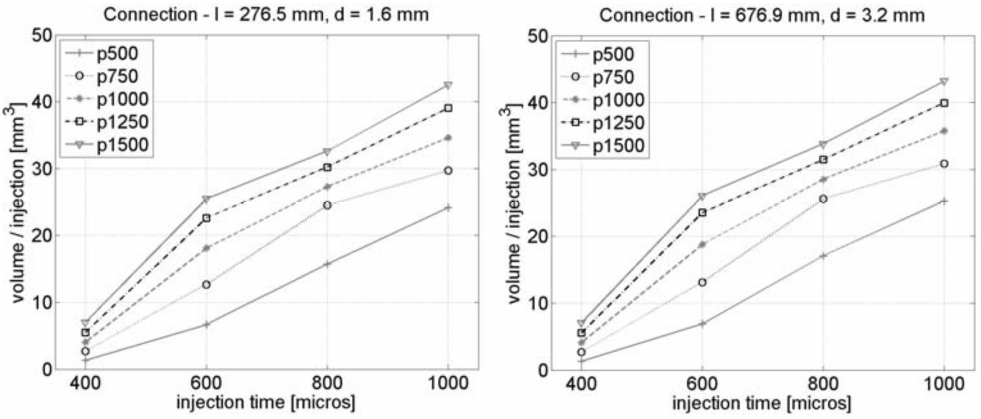

Figure 13. Injected volume for various configurations

4. CONCLUSIONS

In this paper, the authors present a numerical model for modelling the hydraulic circuit of a commercial CR diesel fuel injection system. In this work emphasis is set on the accurate modelling of characteristic system features. As is shown in the discussion of the numerical model the authors combine the advantage of a detailed but local three dimensional simulation with the benefit of a time efficient one dimensional simulation.

Overall, the model shows good agreement with the measurement. Slight discrepancies can be found for some setups for the predicted amplitudes and oscillation frequency. In respect to the injected mass per injection the relative error seems to be largest for the setups with the shortest injection time. Nevertheless, the absolute difference is small when considering the measurement accuracy and other uncertainties.

The analysis of the studied parameters shows that all parameters affect the analysed variables. Following, we list a summary of the most important findings:

- pressure amplitudes are non-linearly related to the pipe geometry
- oscillation frequency is a function of the connection pipe diameter (besides the injection pressure and the connection pipe length)
- amplitude decay is primarily dependent on the injection pressure (impact of pipe geometry is not presented)
- impact of pipe geometry on injected volume is negligible

5. OUTLOOK

One of the main targets of the near future is to extend the amount of studied variables. On the one hand, we are interested to refine the range of existing parameters in order to obtain a better picture of the correlation between the individual variables. On the other hand, the model can also be extended to include further parameters. The simulation model will certainly be used to study more detailed the internal flow of the injector. By doing this, we expect to find some answers on how some phenomena are related to the injector characteristics and circuit dynamics, respectively.

6. REFERENCES

1. Accumulator fuel-injection from Bosch. Innovative perspectives for low-emission, quiet-running diesel engines. Stuttgart, Germany: Robert Bosch GmbH, Diesel Systems
2. Diesel fuel-injection system Common-Rail. Plochingen, Germany: Robert Bosch GmbH, Diesel Systems, Edition 2005
3. van Basshuysen, Richard and Fred Schaefer, eds. Handbuch Verbrennungsmotoren. 2nd edition. Braunschweig, Germany: Vieweg & Sohn Verlagsgesellschaft mbH, 2002
4. Ingard, K. U. Fundamentals of waves and oscillations. Cambridge, England: Cambridge University Press, 1988
5. Bianchi, G.M. et al. "Numerical Investigation of Critical Issues in Multiple-Injection Strategy Operated by a New C.R. Fast-Actuation Solenoid injector." SAE Paper 2005-01-1236 2005
6. Pontoppidan, M., F. Ausiello, G. Bella, and S. Ubertini. "Study of the Impact on the Spray Shape Stability and the Combustion Process of Supply Pressure Fluctuations in CR-Diesel Injectors." SAE Paper 2004-01-0023 2004
7. van Bebber, D. "Reduction of Pressure Waves in Common Rail Systems by Improving System Design Parameters." Conference Proceedings, 5. International Fluid Power Conference – IFK. Aachen, Germany, 2006

8. Beierer, P., K. Huhtala, M. Vilenius. “Experimental Study of the Hydraulic Circuit of a Commercial Common Rail Diesel Fuel Injection System.” SAE Paper 2007-01-0487 2007
9. Anderson, John D. Computational Fluid Dynamics. International edition. New York, USA: McGraw-Hill, 1995
10. Gamma Technologies, Inc. GT-FUEL User’s Manual and Tutorial. Version 6.2. Gamma Technologies, Inc., September 2006
11. Wylie, E. B. et al. Fluid Transients in Systems. London, England: Prentice-Hall International Limited, 1993
12. Robert Bosch GmbH, Diesel-engine management. 2nd edition. Stuttgart, Germany: Robert Bosch GmbH, 1999
13. Bargende, M., U. Essers, eds. Dieselmotorentechnik 2000. Renningen, Germany: Expert Verlag, 2000

Experimental Study on the use of a Dynamic Neural Network for Modeling a Variable Displacement Load Sensing Pump

LESLIE LI, DOUG BITNER, RICHARD BURTON and GREG SCHOENAU
Department of Mechanical Engineering, University of Saskatchewan
Saskatoon, Saskatchewan, Canada
Contact: richard.burton@usask.ca

ABSTRACT

Conventional approaches to modeling use physical knowledge of the system behavior to develop describing equations which can be analytically or numerically solved. The use of input and output data for model identification is also a very powerful modeling technique. The approach used in this study also uses input and output information but makes no attempt to relate the information to any analytical form or physical phenomena. It is a "black box" approach which employs dynamic artificial neural networks as its basis. Such models are particularly useful when the physical relationships, nonlinearities and parameter values of the system are very difficult to measure or quantify.

This study involves a variable displacement pump which does display complex properties and relationships. The intent was to obtain a black box model of the pump which would capture both the steady state and dynamic characteristics of the pump and which then would be integrated into a system model for a load sensing unit. The paper presents a particular modeling form that defines what the input and outputs of the model should be. The paper also introduces dynamic neural units and dynamic neural networks which constitute the "innards" of the black box.

In the first phase of the study, a nonlinear model of a variable displacement pump (verified experimentally in other studies) was used as the "plant" to be modeled. The dynamic neural network could be trained to capture the dynamic properties of the pump but the steady state performance was unsatisfactory. The approach then was to manually develop a modification equation or postprocessor to compensate for the steady state error. This approach was very successful in that the model output could follow the actual plant output in a satisfactory manner for many different input shapes.

In the second phase of the study, the compensation equation was not deemed to be an acceptable or practical way to reduce the steady state error. A static neural network

Power Transmission and Motion Control 2007 Edited by Dr D N Johnston and Professor A R Plummer
© With The Centre for Power Transmission and Motion Control

replaced the compensation equation and trained to "learn" the compensation equation. This approach was also very successful with both the static and dynamic characteristics being captured by the neural based black box.

The third phase of the study involved setting up an experimental pump and test facility to obtain input – output data under typical operating conditions. The experimental data was used to first train the dynamic neural network and subsequently the static compensating neural network. The results were considered to be acceptable for modeling purposes and it was concluded that the combination of a Dynamic Neural Network and a Static Neural Network could be used to capture the steady state and dynamic characteristics of a load sensing pump over a wide range of operating conditions.

1 INTRODUCTION

Simulating hydraulic components and systems always remains a challenge due to the presence of many nonlinearities that dictate the performance of these devices (1). A load sensing pump is one such device which is a system made up of a series of smaller components each of which display nonlinear behavior under certain conditions. Identifying these nonlinearities mathematically and capturing the actual performance characteristics are extremely difficult and as such many approximations (linearization) have to be made to create a reasonable model. Under well defined operating conditions, many models have been developed which yield very acceptable performance when compared to their physical counterparts [(2), (3), (4) and (5)]. However, if the operating conditions deviate substantially from those upon which parameter values have been estimated or nonlinearities linearized, substantial errors can be encountered.

A somewhat different approach is based on the "black box" concept, in which only input and output information is used to model the system performance (often labeled as system identification). Thus a model involving dynamic equations is not created; only the input output physical relationships are captured. The advantage of this approach is that if the actual component is modified structurally, without having the input or output variables change, a retraining of the black box is all that is required using new input/output information. This approach has been successfully applied to the simulation of hydraulic components [(6), (7) and (8)].

The black box used in this study was a Dynamic Neural Network (DNN) which utilized Dynamic Neural Units (DNUs). In this approach, the DNN is subjected to a wide range of typical operating input/output operating measurements from a component or system and then is "trained" to mimic the component behavior. If the DNN is able to accurately reproduce the output of its physical counterpart with input measurements that it was not trained for, the DNN is said to be generalized and thus represents the physical component in a satisfactory fashion.

In a series of earlier studies, a variety of dynamic neural network morphologies were used to assess the feasibility of the approach when applied to a load sensing pump [(8), (9) and (10)]. In the study by Li et al (10), the feasibility of using a particular morphology of DNN introduced by Gupta et al [(11) and (12)] was established using an experimentally verified nonlinear model of a load sensing pump. The objective of this research and indeed, of this paper was to expand upon the work of Li (13) and to establish the feasibility of the approach when applied to a physical load sensing pump subjected to typical operating conditions.

The paper will first introduce the concept of a DNU and DNN and then summarize the earlier work by Li et al (10). The experimental test system to generate the experimental data will be considered and the results of the training and testing of the DNN/load sensing pump presented. The paper will conclude with a discussion of the results and of the applicability of the approach to other systems in a broader sense.

2 LOAD SENSING PUMP MODEL INPUTS AND OUTPUTS

Consider the load sensing pump (LSP) shown in Figure 1. The objective of a load sensing pump is to maintain the pressure drop ($P_s - P_L$) across the controlling orifice constant in the presence of varying loads (P_L). By keeping the pressure drop low (typically 1MPa), flow control (Q_p) in an energy efficient fashion is possible. The LSP is composed of the pump, controlling orifice, compensator spool and pump controlling spool. The pump, compensator spool and pump controlling spool are generally integral to the LSP with the controlling orifice a distinct external unit. However, it was shown in Li that to avoid problems associated with "unique input/output relationships", the inputs into the DNN load sensing model must be the control pressure P_c, and the pump pressure P_s with Q_p, the pump flow, being the output.

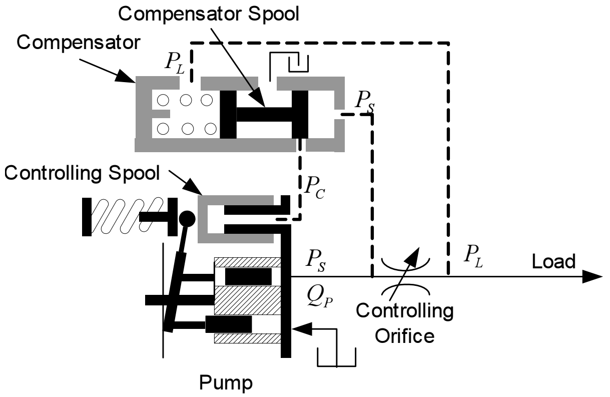

Figure 1 Schematic of the load sensing pump

3 THE DYNAMIC NEURAL UNIT (DNU) AND THE DYNAMIC NEURAL NETWORK (DNN)

A Neural Network is a simple combination of basic units called neurons. These neurons are combined in series or parallel forming layers and are subject to input output information in the training mode. The training of the network consists of adjusting neuron gains until the output of the network mimics, within a specified tolerance, the output of the actual device.

The network is then "tested" using input and output data for which it has not been trained. Details of neural networks and their training algorithms are referred to in the many excellent references on the topic (14). If the input/output relationship is not dynamic, then the standard feed-forward neural network (often called a Static Neural Network, SNN) can be used. If the input/output relationship contains dynamic information, such as occurs in the load sensing pump, then a DNN must be used. The DNN is comprised of Dynamic Neural Units (DNUs) which contain time delayed feed-forward and time delayed feedback paths. One such DNU is shown in Figure 2(a). Training consists of adjusting the coefficients a_i and b_i in a prescribed fashion (11).

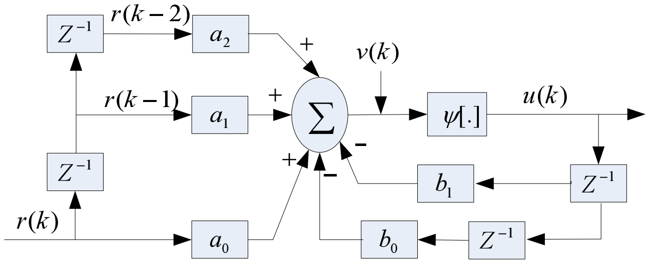

(a) Basic Dynamic Neural Unit (DNU) based on Gupta et al (11)

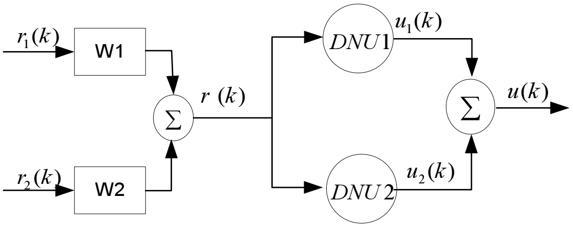

(b) DNN form

Figure 2 Basic Dynamic Neural Unit (DNU) and DNN adopted in this study

Two DNU's were combined in parallel to form the DNN that was used in this study (Figure 2(b)). Other combinations were tried but this one was found to provide the best performance whilst minimizing the computer executions. Training consisted of adjusting the weights (coefficients) of the two DNN's as well as W1 and W2. Details can be found in [(10) and (13)].

4 INITIAL FEASIBILITY STUDIES

In (10), the feasibility of using a DNN to capture the dynamics of the pump was established; however, the steady state results were not acceptable. Li (13) then developed a set of compensating equations which were based on observing the error at many operating conditions. These equations acted as a postprocessor to the DNN and the steady state error was substantially reduced. Despite this success, it was concluded that developing a "human" based post processor was not an acceptable method for reducing the error. It was recommended that an alternate approach be used.

In this study, it was decided that a postprocessor could in fact be another static neural network which could be trained using steady state information that was output from the DNN. This is shown schematically in Figure 3. P_s and P_c and the output from the trained DNN became inputs to the SNN (Figure 4). The same data used to train the DNN was again used to train the SNN. Typical test results of the load sensing pump model are shown in Figures 5 and 6. For comparison, the trained output of the DNN alone is shown to illustrate the ability of the DNN to capture the dynamics of the pump, but not to mimic the steady state performance.

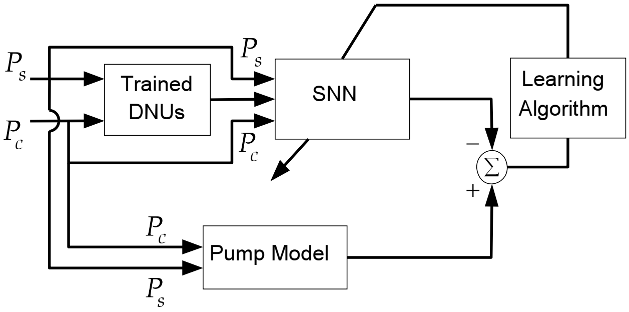

Figure 3 Modified DNN using a SNN as a postprocessor

It is evident from Figures 5 and 6 that the SNN could be used as a postprocessor to the DNN to successfully reproduce the response of the pump model when subjected to common inputs. Small errors are noticeable but it was believed that these would fall within acceptable simulation limits. It was concluded then that the DNN and SNN combination was acceptable in mimicking the steady state and dynamic performance of a load sensing pump for the data for which it was trained.

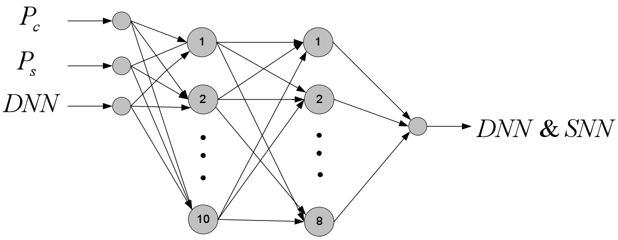

Figure 4 SNN structure used in this study

5 EXPERIMENTAL RESULTS

The real test for the DNN, SNN combination was to train the model to experimental data. To create data which would expose the pump to a wide range of expected operating conditions, a special experimental system was established and is shown in Figure 7. P_c was controlled independently using an external pressure control servo system and P_s was controlled using a proportional relief valve, as shown. The pump flow Q_p was measured as the output variable. A summary of the instrumentation and components used in the study is given in Table 1.

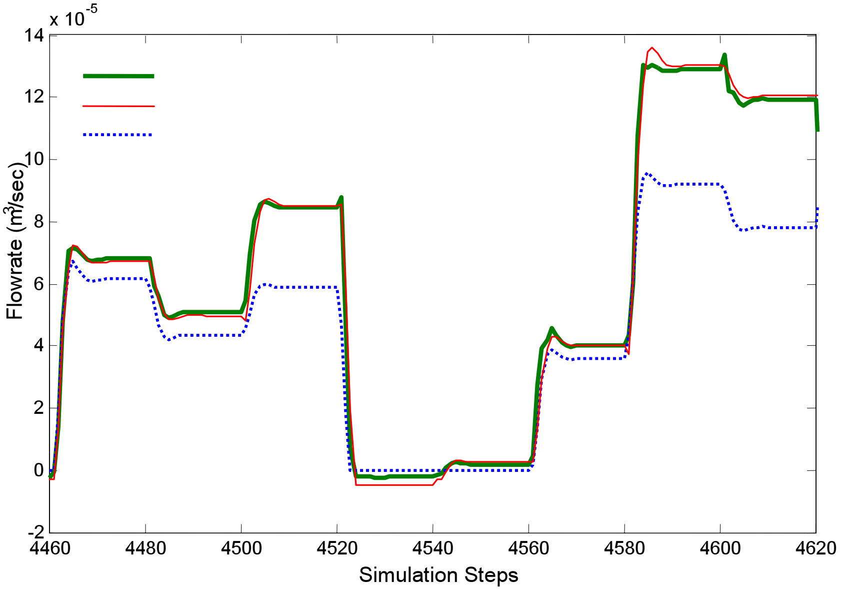

Figure 5 First sample test results from a DNN and SNN combination

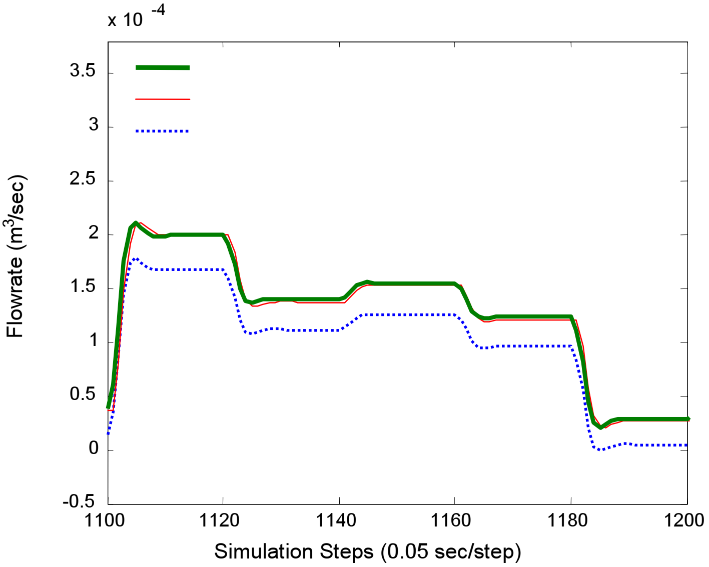

Figure 6 Second sample test results from a DNN and SNN combination

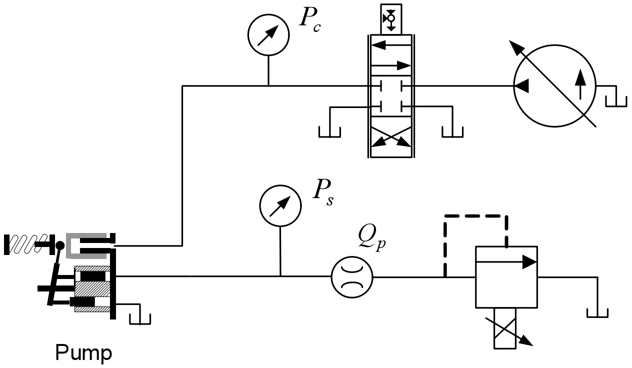

Figure 7 Experimental test rig to independently produce training data

P_c and P_s were then input into the DNN/SNN model and training initialized as was done with the simulated load sensing pump model. When the training error reached a steady minimum value, training was stopped and the model was tested with data not used in training. Three typical test results (labeled study #1, #2 and #3) showing the input P_c and P_s as well as the output flow rates are given in Figures 8, 9 and 10. In the flow figures, the predicted flow rates from the DNN alone are also presented for comparison purposes.

Table 1 Summary of instrumentation and hydraulic components used in the study

Variable	**Instrumentation & Hydraulic Components**
P_c	Schaevitz P723-0025 sensor and Measurement Group 2120A amp.
P_s	Schaevitz P723-0025 sensor and Measurement Group 2120A amp.
Q_p	Hersey-Ramapo flow meter and Measurement Group 2120A amp.
	Krohn-Hite low pass RC filters (75Hz) for P_c, P_s, and Q_p signals
	National Instruments Lab-PC-1200 A/D - D/A board
	Deere AL75305 load sensing pump
	Brand Hydraulics EFC12-20-12 proportional flow control valve
	Waterman 21C40SRP-11 proportional relief valve
	Moog 15-010 pressure control servo valve
	Vickers PVB10 pressure compensated hydraulic power supply

To test the trained DNN/SNN model in a 'real world' system, the load sensing pump was connected to a flow control valve and load as shown in Figure 11. The flow rate was varied with a proportional flow control valve and the load pressure P_L was varied with a proportional relief valve to simulate a typical load sensing pump application. The resulting P_s, P_c and Q_p were measured; P_s and P_c were input into the trained DNN/SNN model (trained using data from the previous studies) and the resulting predicted and actual pump flow compared.

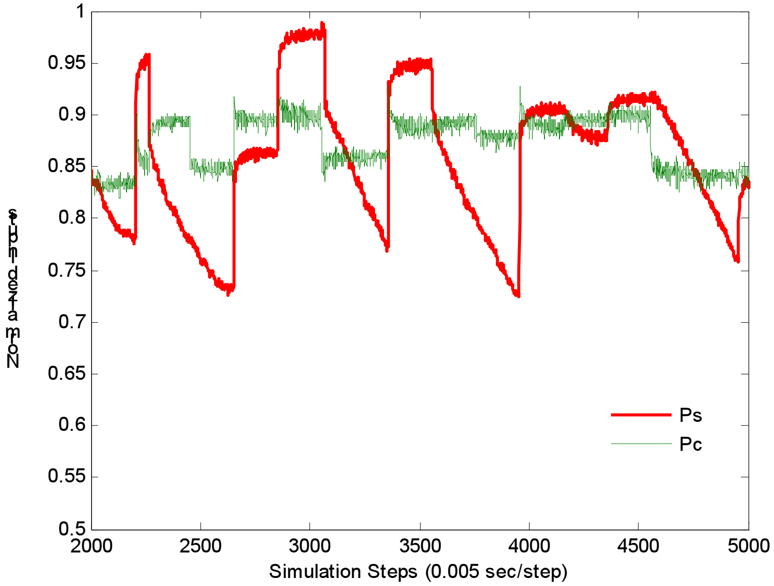

Figure 8(a) Typical test inputs Ps and Pc for study #1

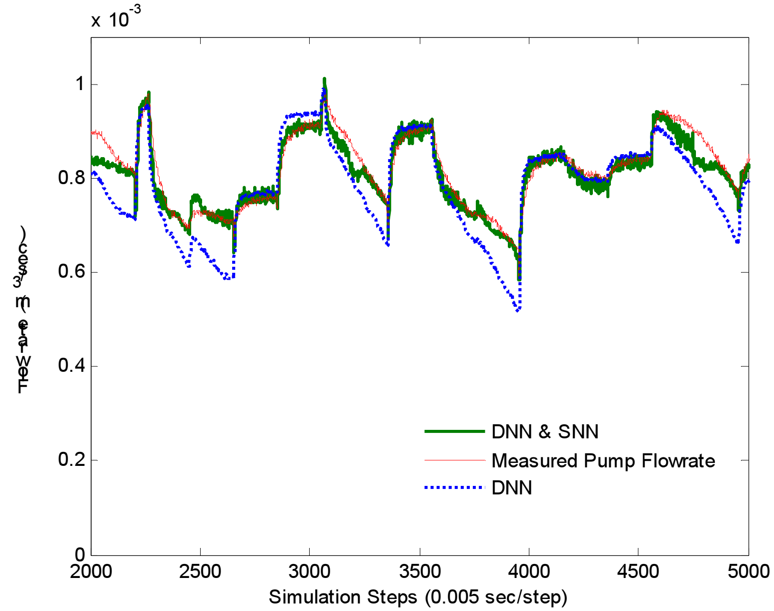

Figure 8(b) Typical test output flow rates for study #1(predicted and actual)

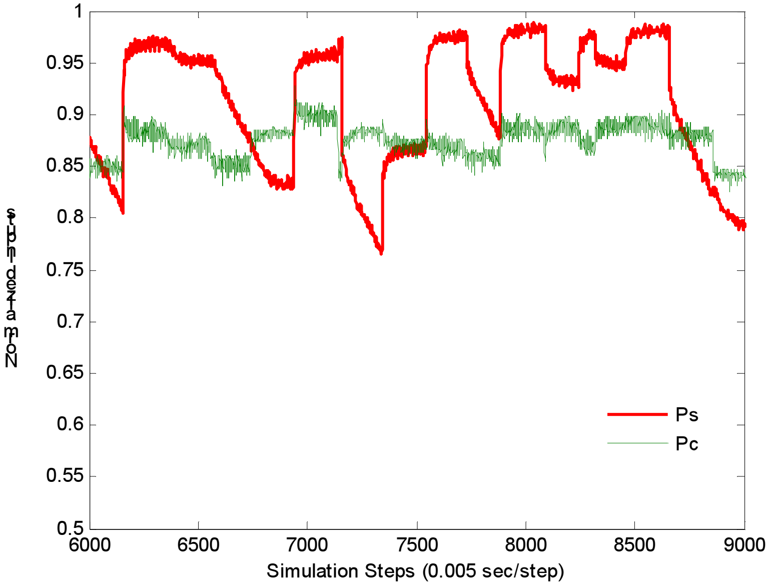

Figure 9(a) Typical test inputs Ps and Pc for study #2

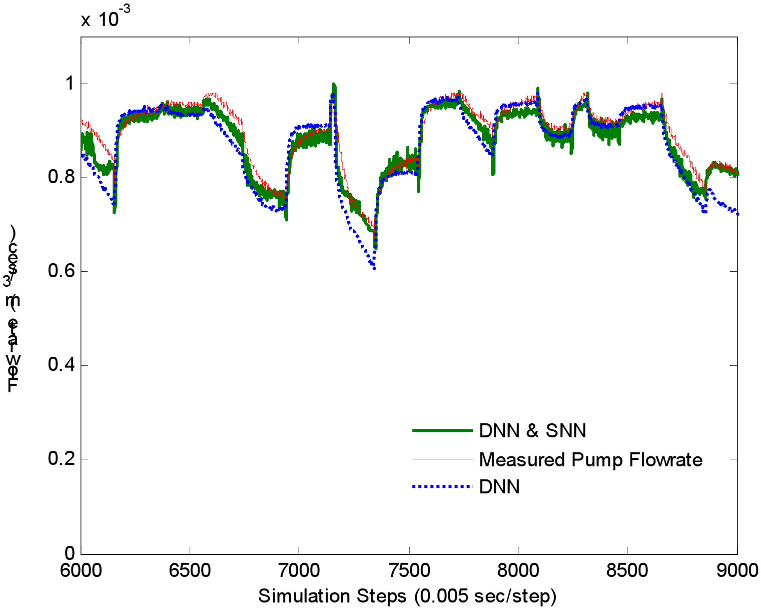

Figure 9(b) Typical test output flow rates for study #2 (predicted and actual)

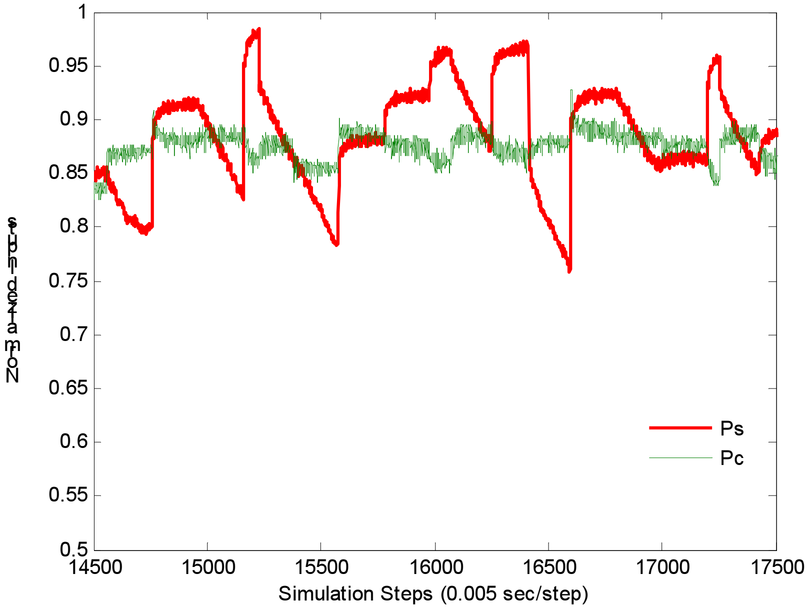

Figure 10(a) Typical test inputs Ps and Pc for study #3

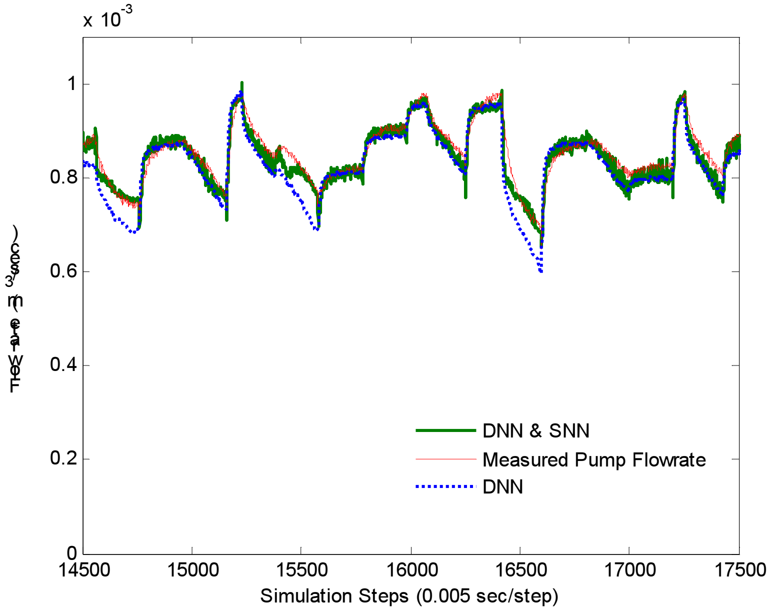

Figure 10(b) Typical test output flow rates for study #3 (predicted and actual)

Typical results are shown in Figure 12. From the results, it is evident that there is a slight shift between the measured pump flow and the trained DNN/SNN flow. It was discovered that a very small change in the pressure P_c had a large influence on the level of the DNN/SNN flow. A shift in P_c over an extended period of time (days) can occur quite readily in experimental systems as a result of amplifier drift. This test was indeed, completed several days after the original experimental training data was obtained. When a change of -20 psi or (-5%) was made in P_c, very close agreement between the results occurred. This change is shown in Figure 12 as the Adjusted DNN/SNN flow.

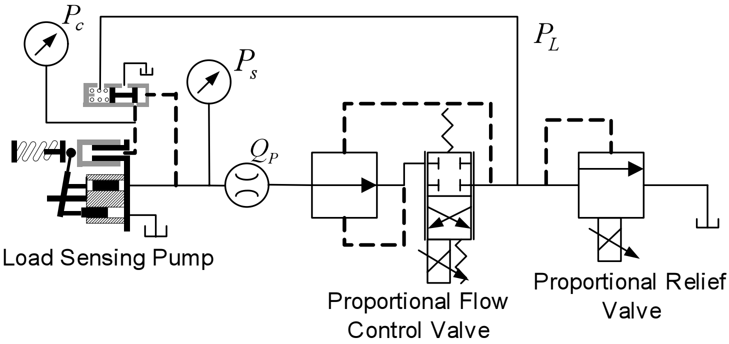

Figure 11 Experimental test rig to produce the training data and testing data

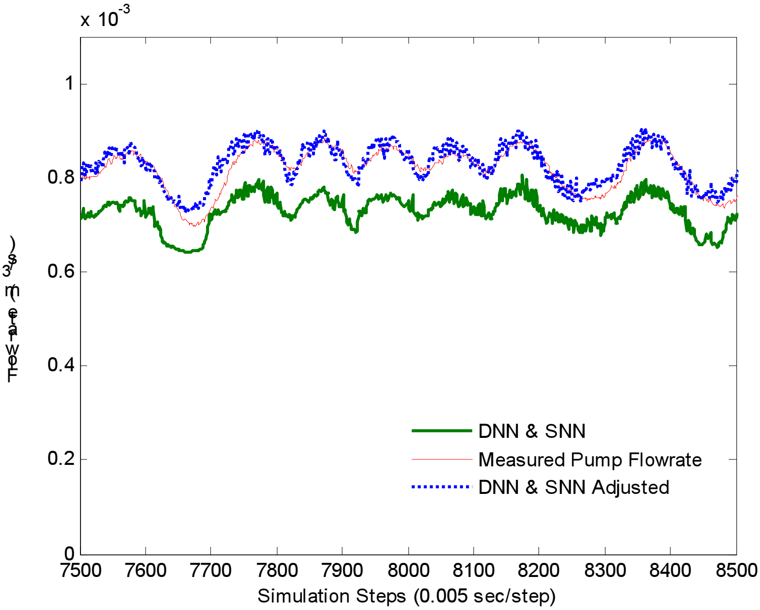

Figure 12 Typical results when data is trained on an independent system and tested on an actual load sensing system

As a last test, the DNN/SNN was both trained and tested on the load sensing pump system shown in Figure 11. Training data and testing data were obtained at the same time. Typical results are shown in Figure 13. It is quite apparent that the combined model predictions follow the experimental results closely, but are not as good as the results shown in all of the other figures. Upon reflection, it was observed that the original training epoch, in which the test correlations were very good, contained fairly "rich" training data in that P_s and P_c were controlled independently. In the last test, P_s essentially followed P_c and hence the richness of the testing signals was not as good.

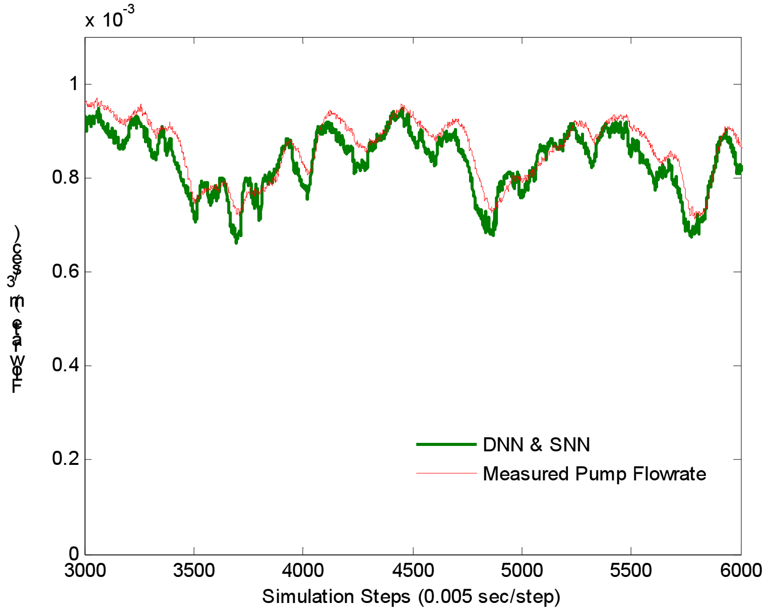

Figure 13 Typical results when data is trained and tested on an actual load sensing system

6 DISCUSSION AND CONCLUSIONS

In this study, the use of a DNN to mimic or simulate the performance of an experimental load sensing pump was examined. As was the case for earlier feasibility models on an equation based load sensing pump, the DNN by itself was able to capture the dynamics of the load sensing pump, but the steady state prediction was poor. Introducing a SNN as a postprocessor was shown to improve the steady state results significantly without affecting the dynamic prediction to any great extent (for both the equation based pump and the actual load sensing pump). It was concluded that the DNN/SNN combination could be considered for simulation purposes, a very good model of the experimental load sensing pump. Observation of the traces in the figures does show occasionally, points where the predicted flow output deviates slightly from the actual output. In most cases, the specific combination of the two input pressures did not appear as part of the training data or appeared very seldom over the complete epoch of training data (a "richness" consideration). This stresses the importance of a carefully designed experiment to ensure a fairly uniform spectrum of data and of collecting the data for both the training and testing at the same time.

The fact that the DNN was not able to capture both the steady state and the dynamic characteristics of the pump was surprising. During the training process, the "weights" or coefficients of the DNN should start to converge to a steady value as the error approaches a minimum value. An observation of the DNN weights over the last steps of training showed that the feedback (b_i, Figure 2 (a)) and feed forward (a_i Figure 2(a)) weights did converge to a constant value but the "proportional" weights W1 and W2, Figure 2(b), did not. This has opened up a future area of research that the authors do intend to explore further.

It was concluded that the DNN/SNN combination could be used to simulate the dynamic and steady performance of a load sensing pump. It remains a future research effort to compare this model to an equation based model and to integrate the model into a system simulation of a load sensing system.

REFERENCES

(1) Manring, N.D., 2005. Hydraulic Control Systems, John Wiley & Sons, NY.

(2) Krus, P. 1988. On Load Sensing Fluid Power Systems with Special Reference to Dynamic Properties and Control Aspects, PhD thesis, No 198, Department of Mechanical Engineering, Linkoping, Sweden, (ISBN 91-7870-402-2).

(3) Book, R. and Goering, C., 1997. Load Sensing Hydraulic System Simulation, Applied Engineering in Agriculture, ASAE, Vol. 13 (1), pp 17 – 25.

(4) Wu, D., Burton, R. Schoenau, G. amd Bitner, D., 2002. Establishing Operating Points of a Linearized Model of a Load Sensing System, International Journal of Fluid Power, Vol. 3, No. 2. pp 47 – 54.

(5) Erkkila, M. 1999. Practical Modelling of Load Sensing Systems, Proceedings of the Sixth Scandinavian International Conference on Fluid Power, SICFP'99, Tampere, Finland, pp 445.

(6) McNamara, J., Edge, K., and Vaughan, N., 1997. Hybrid Analytical/Neural Network Model of Variable Displacement Pump Dynamics, American Society of Mechanical Engineers, The Fluid Power and Systems Technology Division (Publication) FPST, v4, Fluid Power Systems and Technology, p 71-76.

(7) Watton, J. and Xue, Y., 1997. Simulation of Fluid Power Circuits Using Artificial Network Models (Part 1 and 2), Proc, Instn. Mech. Engrs.- Part I, Vol. 211, pp.417-438.

(8) Xu, X. P., Burton, R. and Sargent, C., 1997. Experimental Implementation of a Neural Simulator, Fluid Power Systems and Technology, Vol. 4, November, pp.21- 26.

(9) Lamontagne, D, Burton, R. Ukrainetz P., and Ruan, J. 2003. Investigations in Modeling a Load Sensing Pump using Neural Networks, Proceedings of the Fourth International Symposium on Fluid Power Transmission and Control (ISFP'2003), Wuhan, PRC, pp 151-158.

(10) Li, Leslie, Burton, R and Schoenau, G. 2006, Feasibility Study on the use of dynamic Neural networks (DNN's) for modeling a variable displacement load sensing pump, Proceeding of the MINEC 2006 ASME International Mechanical Congress and Exposition, Nov., Chicago, paper number 15588.

(11) Gupta M. and Rao, D.,1993. Dynamic neural Units and Function Approximation, IEEE Conf. On Neural Networks, San Francisco, pp. 743-748, March 18- April 1.

(12) Song, Y. and Gupta M., 1999. Dynamic Neural Controller for Complex Nonlinear Systems, IEEE North Saskatchewan Symposium, Saskatoon, pp. 25-40, November 16.

(13) Li, Leslie, 2007, Investigation in modeling a Load-Sensing Pump using Dynamic Neural Unit Based Dynamic Neural Networks, M.Sc thesis, University of Saskatchewan.

(14) Narendra, K.S, and K.Parthasarthy K. 1990. Identification and Control of Dynamical Systems Using Neural Networks, IEEE Trans. Neural Networks, Vol. 1, pp. 4-27.

ACKNOWLEDGMENTS

The authors would like to acknowledge the financial support from the National Science and Engineering Research Council (NSERC) of Canada during this project and the University of Saskatchewan, Department of Mechanical Engineering for it financial contribution in the form a scholarship.

Modeling, Simulation and Identification of the Electrohydraulic Speed Governors for Kaplan Turbines by AMESim

Nicolae VASILIU, Constantin CALINOIU, Daniela VASILIU
University POLITEHNICA of Bucharest

ABSTRACT

The paper contains a report on using AMESim to design and tune a patented type of electrohydraulic digital speed governor for KAPLAN hydraulic turbines. Modeling, simulation and experimental identification are shortly presented. The governor contains two connected position loops included in a speed loop or a power loop. The fine-tuning of the electro hydraulic servo systems by AMESim saved time and gets the possibility of a deeper investigation of the main design parameters influence. The actual performance of the prototype (time response, accuracy, static drop, dynamic drop etc.) was found in good agreement with the theoretical prediction, and CEI demands.

1 DEFINING A NEW GENERATION OF SPEED GOVERNORS

A large synchronous power zone raises many technical problems, leading to the refurbishing of many power units in order to satisfy the severe demands concerning the energy quality.

The balance between generation and consumption within a large synchronous area is achieved using speed and power governors. By the joint action of all interconnected power generators, this “primary control” ensures the operational reliability for the power system of the synchronous area and establishes the system frequency at a stationary value after a disturbance or an incident in the time frame of seconds, but without restoring the reference values of system frequency and power exchanges. In an interconnected network, quasi-steady-state frequency deviations and power interchange deviations will exist between the various control areas, as a result of corrective action by primary control in response to a sudden variation in consumption or generation.

The “secondary control” is a centralized automatic function to regulate the power generation in a control area based on power reserves in order to maintain the interchange power flow at the exchange program with other control areas. This kind of control also has the task to correct the lost capacity in a control area by restoring the primary control

Power Transmission and Motion Control 2007 Edited by Dr D N Johnston and Professor A R Plummer
© With The Centre for Power Transmission and Motion Control

reserves. The secondary control operates for periods of several minutes on a set of power plants included in this control loop. The overall reliability of the electric power supply grid essentially depends on the power distribution instead of the generation and transmission. Both the above tasks need high quality speed and power governors for all power units, but the most important role is played by the hydropower units, which must react very quick to a sudden local or overall load change. Taking into account the "weight" of the power unit in the overall power balances, one can establish the proper settings of each power unit speed governor. The main performance parameter from this point of view is the "frequency dead band" within the power set point is not changed. A large dead band means a "quiet" steady-state operation of the power unit, protecting all the joints and sealing components against the premature wear, which increases the control forces, the insensitivity and the leakages of control oil and water. The second operating parameter defining the steady-state power unit behavior is the speed static drop, defining the power set point change as a function of the system frequency change. A small power unit is not suitable for system frequency control, and usually has a big speed static drop to avoid "continuous power slide".

The classical speed and power governors of the hydropower units are built in two versions: hydro mechanical and electro hydraulic ones. Usually, the speed error amplification by two or three hydro mechanical servomechanisms is a reliable one, but without a very carefully manufacture and a very clean oil it leads to a big backlash, which generates random oscillations, and uncertain dynamic behavior.

The main features of the classical hybrid electro hydraulic governors are: the use of the moving coil electro hydraulic converters, and the keeping of a hydro mechanical servomechanism in the power stage. The lack of the converter spool position feedback generates a lot of troubles in the whole control system in a dirty hydraulic circuit. The mechanical feedback from the wicket gates servomotor needs a precise position correlation between the hydraulic turbine and the governor. The permanent vibration of the feedback connection generates undesired noise in the whole control system. A cam and a short stroke position transducer, which requires a very precise mechanical tuning, achieve the correlation between wicket gates position and the runner blades positions.

The rapid development of the industrial digital computers, and the great progress achieved in the field of the proportional servo valves, created the practical conditions to design a new generation of speed and power governors, solving the above problems.

2 PRELIMINARY RESEARCHES

The authors developed a new hardware and software solution in order to completely replace the old generation of hydro mechanical and electrohydraulic speed and power governors of the KAPLAN and FRANCIS turbines used in the hydropower plants managed by the hydropower Romanian authority (1).

From an industrial point of view, the main idea of the new concept described in this paper is the use of high-quality industrial electro hydraulic and electronic components only, in order to avoid manufacturing problems, high prices, and the manufacturer permanent technical assistance need. Starting from this objective defined by the industrial practice, during a few years, the high quality commercially available electrohydraulic flow amplifiers, and their servo controllers were fully tested in the Fluid Power Systems Laboratory of the Power Department from University POLITEHNICA of Bucharest. The classical flapper-nozzle electro hydraulic servo valves contain an internal feedback but need very clean oil (permissible contamination class of pressure fluid – 6, as per NAS 1638). So, they are not suitable for controlling the speed and the power of the large hydraulic turbines without a permanent and very expensive effort of cleaning the control oil. The first generation of proportional valves was much more tolerant to contaminants, but had a poor dynamics. The second generation of high speed proportional servo valves (DDV) offers all the qualities required for controlling the speed of the hydraulic turbines, keeping the filtering conditions at an economic level (permissible contamination class of pressure fluid is between 7 and 9, as per NAS 1638. In the frame of a permanent agreement with the Automatic Division of BOSCH COMPANY, a servo controller and a four-way DDV were tuned in order to be used instead a moving coil converter (2), (3).

Three series of static and dynamic test have been performed: in the Fluid Power Systems Laboratory of the above university, in the Speed Governor Laboratory of the RESITA MACHINES MANUFACTURER CO., and in the IRON GATES II HYDROPOWER STATION, by replacing one converter a time for a turbine. The entire laboratory test performed in the frame of an electro hydraulic servomechanism showed the same dynamics as a classical two-stage force feedback servo valve. The test performed in the factory speed governor bench pointed out a very good static and dynamic behavior. The final test, performed on an axial turbine of 24 MW, showed the full ability of the BOSCH DDV to control the speed and the power, with a very small null oil consumption.

The last generation of proportional single stage servo valves produced by MOOG, PARKER and BOSCH includes the servo controller (On Board Electronics – OBE). Such a way, the valve becomes a linear component, which converts a voltage into a flow with a very small time constant (about 5 ms). This type of valve was found as the best choice for replacing the moving coil converter in the old electro hydraulic speed governors. The experiments carried out on a ful size flow speed governor control valve (figure 1 and 2) have shown a very good steady-state and dynamic behavior: the step input response reveals a small time constant (about 50 ms). The use of a single stage BOSCH DDV in combination with an adequate spool position transducer may be regarded as a cheap solution for turning a mechanical speed governor into an electro hydraulic one. This option is a normal one for high quality control valves, using a very clean control oil.

3 MAIN FEATURES OF THE NEW TYPE OF SPEED GOVERNORS

For flows higher than 40 l/min, BOSCH Company developed a new series of two-stages DDV, including the entire electronic interface in a single unit. The response time of such a valve is 50% less than for the combination between a three-way moving coil converter and a big size four-way control valve used in a classical speed governor. After a full laboratory test, these high-speed proportional control valves, and the corresponding analogue servo controllers supplied by BOSCH COMPANY were chosen as basic components for the new speed governor. For stability reasons, the steady-state characteristics of the power stage have a smaller slope in the null point region than the average slope. This feature is very important when the hydropower unit has the task to contribute to the frequency control of the national power system. In that case, the sensibility of the governor is about 10 mHz. A small flow gain for small inputs generates small oil flows; so, the valve is acting as a physical low-pass filter, which is protecting the joints and the sealing of the guide vane system against premature wear. At the same time, the oil consumption is kept at a low level. Using very reliable position transducers, and heavy-duty hydraulic cylinders, two electro hydraulic servomechanisms were designed and tested in order to be used for the control of the wicket gates and turbine runner openings. At this level, the parameters optimization was performed by AMESim and SIMULINK from MATLAB.

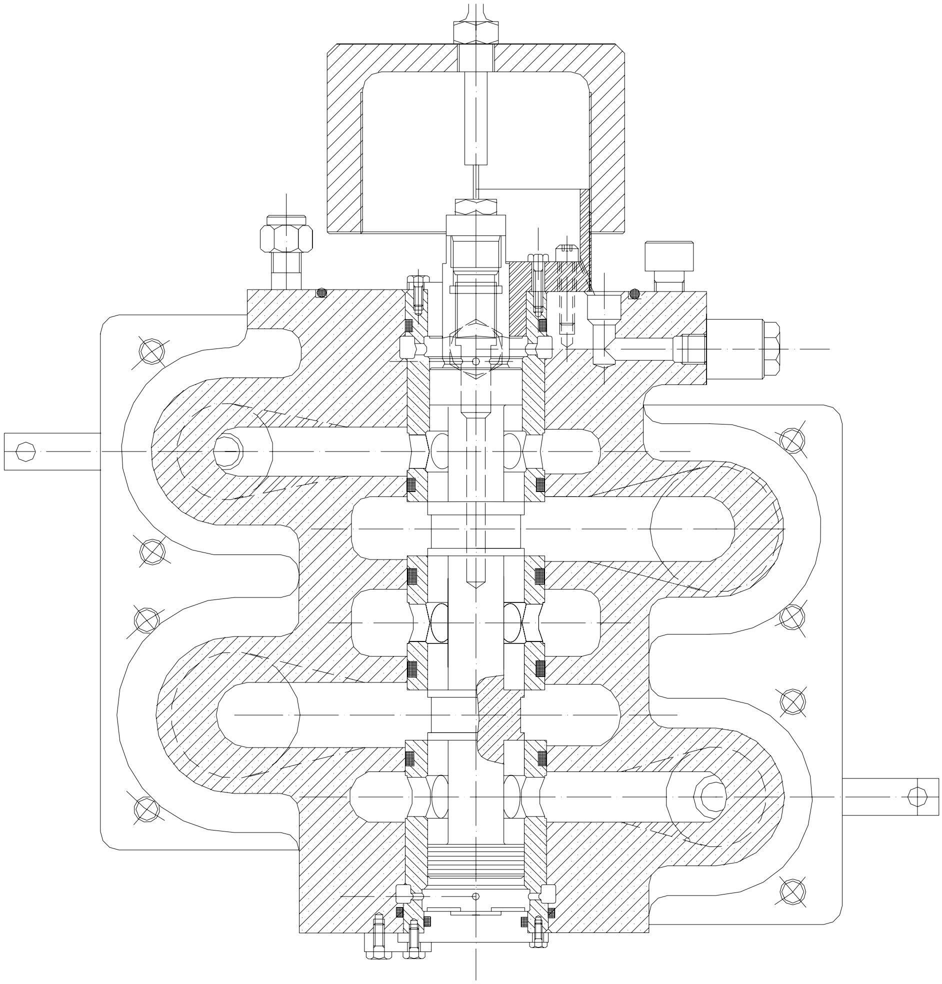

Figure 1 Main control valve of a speed governor with spool position transducer replacing a mechanical feedback

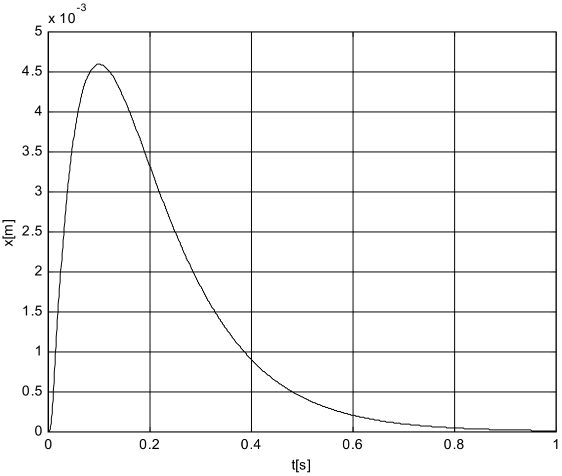

Figure 2 Main valve spool response for a 1 V step input

All the computations were performed in order to replace the hydromechanical speed and power governor of the hydropower unit from the RAMNICU VALCEA Hydropower Station, located on the Olt river (2 units of 23.5 MW). A realistic mathematical model was built by the aid of a practical identification of the operating parameters, taking into account the real technical state of the hydropower unit.

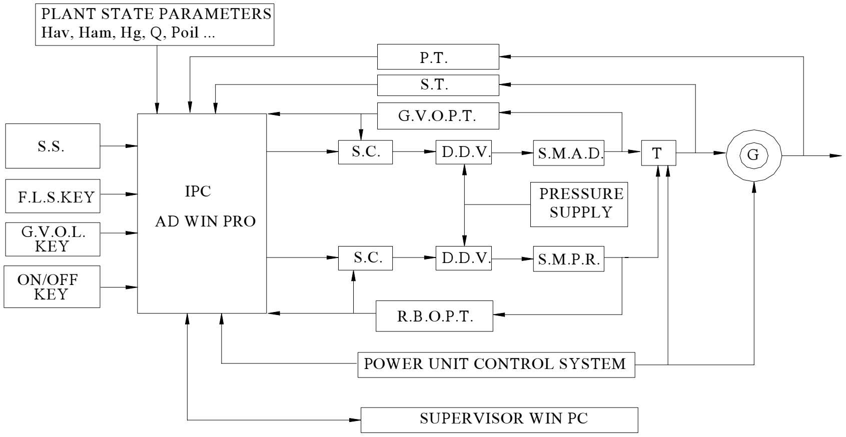
PLANT STATE PARAMETERS
Hav, Ham, Hg, Q, Poil ...
P.T.
S.T.
G.V.O.P.T.
S.S.
F.L.S.KEY
G.V.O.L. KEY
ON/OFF KEY
IPC
AD WIN PRO
S.C.
D.D.V.
S.M.A.D.
T
G
PRESSURE SUPPLY
S.C.
D.D.V.
S.M.P.R.
R.B.O.P.T.
POWER UNIT CONTROL SYSTEM
SUPERVISOR WIN PC

Figure 3 The structure of the new speed and power governor for KAPLAN turbines: S.S. – synchronizing system; F.L.S. KEY - frequency/load setter key; G.V.O.L. KEY - guide vanes opening limiter key; P.T. - power transducer; S.T. - speed transducer; G.V.O.P.T. - guide vanes opening position transducer; S.C. - servo controller; D.D.V. - direct drive valve; S.M.A.D. - guide vanes servomotor; S.M.P.R. - runner blades servomotor; R.B.O.P.T. - runner blades opening position transducer; T - turbine

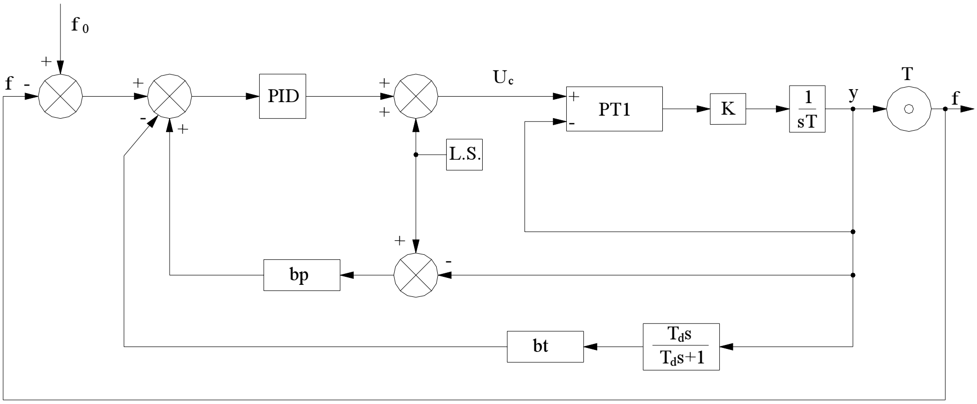
f0
+
f
-
+
-
+
PID
+
+
Uc
+
-
PT1
K
1/sT
y
T
f
L.S.
+
-
bp
bt
TdS/(TdS+1)

Figure 4 Bloc diagram of the speed governor: f – frequency; fo – frequency setting; bp – static speed droop; bt – transient speed droop; L.S. – load setting

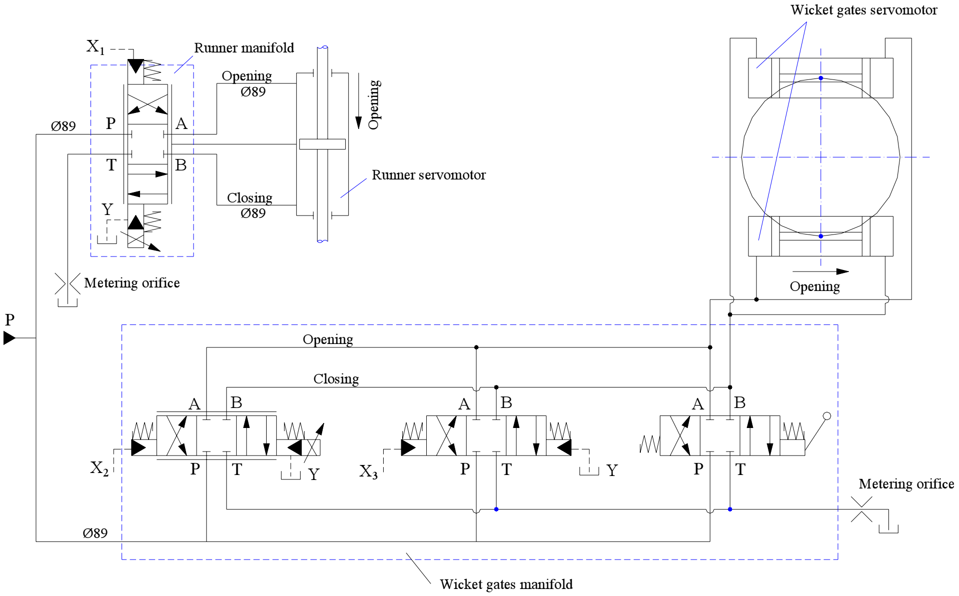
Wicket gates servomotor
X1
Runner manifold
Opening
Ø89
Opening
Ø89
P
A
T
B
Runner servomotor
Closing
Ø89
Y
Metering orifice
Opening
P
Opening
Closing
A
B
A
B
A
B
X2
P
T
Y
X3
P
T
Y
P
T
Metering orifice
Ø89
Wicket gates manifold

Figure 5 Hydraulic diagram of the new speed governor

The fast and precise control of the two blades systems positions, by two reference voltages, creates the possibility of a major simplicity for the governor structure (figs. 3,4,5,6). The main task of the industrial process computer remains the generation of the reference voltage for the guide vanes servomechanism, and then the reference voltage for the runner blades servomechanism, in order to obtain maximum overall efficiency.

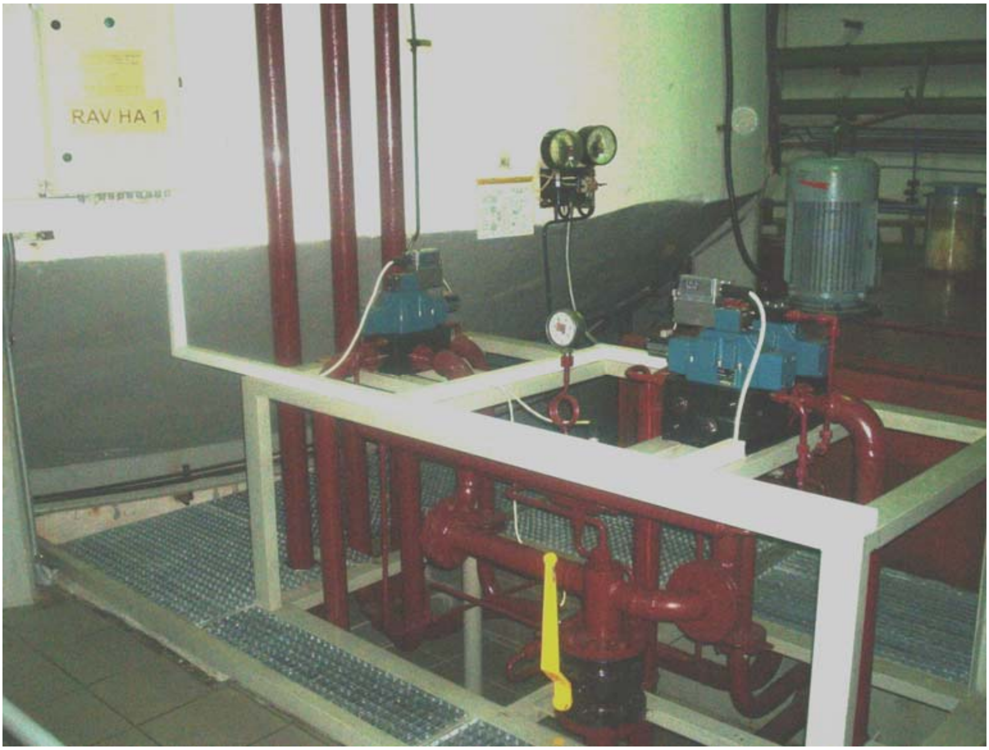

Figure 6 New speed governor hydraulic assembly front view

The emergency hydropower unit shutdown task is usually performed by the guide vane servo valve, but a four-way directional flow valve is also available to prevent any speed overshot, which may occur due to governor failure. The control of this valve is always done by the overall protection system of the hydropower unit. The choice of the industrial process computer (IPC) and the graphical user interface (GUI) was the second main problem in the design of the new governor.

The control market is very rich in this field, but the programming languages and the supervising manner can create major difficulties when the controlled process is uncertain and dangerous in the failure situations, as in the case of hydraulic turbines speed control loss. Even the overall time constant of a medium size hydraulic turbine is about 7 seconds, the angular acceleration can reach high values if the servomotor is not reacting in due time, or the connection between the two blade systems is affected by a position transducer failure.

Taking into account the possibility of using a high level programming language, and the MS WINDOWS operating system full compatibility, the industrial process computer ADWIN PRO created by KEITHLEY Company from U.S.A. was chosen as governor core. This computer basically contains a powerful SHARK DSP, running at 40 MHz. The control software was written in ADBASIC, which is a simple and direct programming environment. As an interface computer for programming and supervising the control process, another industrial computer was chosen: a Pentium III heavy-duty panel computer running under WINDOWS XP, produced by ICP Company from TAIWAN. As data acquisition and dialog software, TEST POINT 4 from CAPITAL EQUIPMENT CORPORATION (S.U.A.) was chosen.

A common access memory partition on ADWIN PRO is available for full data exchange between the two computers. This arrangement allows a direct experimental fine governor tuning on site, all operating parameters recording for "event viewer", and a very useful graphical interface designed as a direct aid for plant operators. The speed governor can operate in the following working sequences: start/stop of the power unit, following the selected setting, normal shut down, and emergency shut down.

The governor can be configured for controlling the following parameters: power unit speed (for insulated operation), turbine water flow (for cascade operation), output unit power, and upstream water level. Every 5 milliseconds the IPC executes the statements of the program stored in a reliable flash memory. The interface computer stores all the process information with the same sample rate on a static HDD.

Among different problems raised by the new governor design, the power unit rotation speed measurement was a special one due to the very low nominal rotation speed (100 rot/min). For security reasons, two measurement systems were designed. A set of magnetic pick-ups and a toothed wheel supply the input information for a four channels high-speed counter included in the IPC. A sliding average up-graded at every computation cycle is good enough for control purposes.

Another tacho-generator was designed for protection reasons only, by a set of pick-ups, an ABB four-channel high-speed counter and a reliable PLC from the same company. The main problem of these measurement systems is the strong electromagnetic perturbation introduced by the power unit itself.

4 EXPERIMENTAL RESULTS

The above ideas were applied to produce the prototype of the speed governor suited for a medium size KAPLAN turbine. A long series of numerical simulations was performed by AMESim in order to find out the best control algorithm and the optimal values for the free parameters (4), (5). Figure 7 shows the simplest simulation network for the transient generated by a small system frequency deviation. A typical simulation result is presented in figure 8, containing the unit start and load. Another tuning stage was performed by a dedicated HIL test bench (6). The actual performance was found in good agreement with the theoretical prediction. The figure 9 shows the variation of the main operating parameters during the start and the load of the hydropower unit. To avoid a long unit "launch", the first step of this process is the full opening of the runner. The opening of the guide vanes, which follows, have to be a little greater than that needed for the free of charge turbine running at the synchronizing speed. When the frequency arrives at 45 Hz, the governor starts the action of bringing the frequency at the nominal value of 50 Hz.

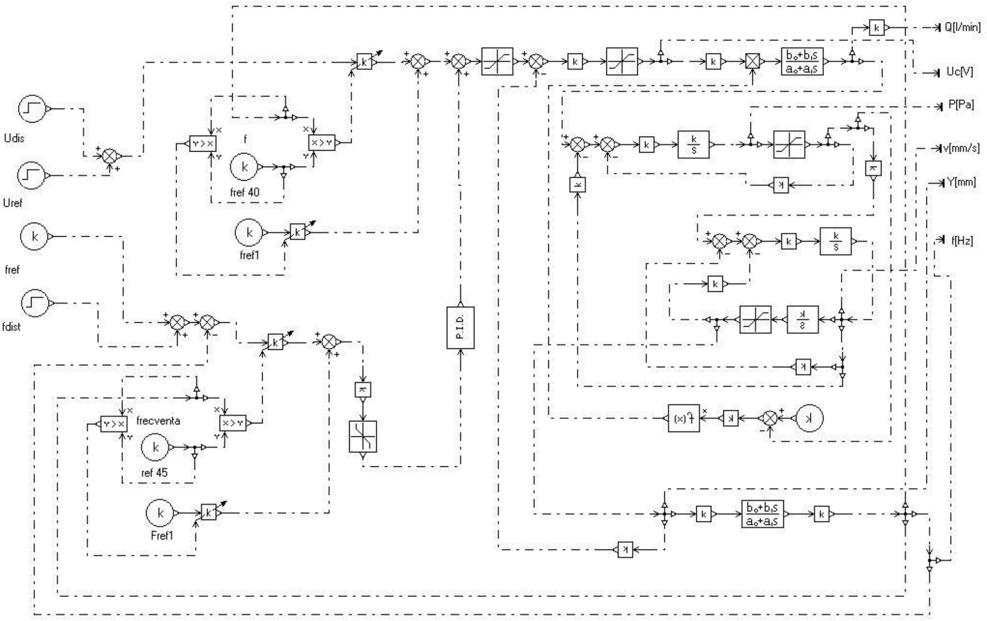
Udis
Uref
fref
fdist
f
fref 40
fref1
frecventa
ref 45
Fref1
P.I.D.
Q[l/min]
Uc[V]
P[Pa]
v[mm/s]
Y[mm]
f[Hz]

Figure 7 AMESim simulation network of the hydropower unit start and load

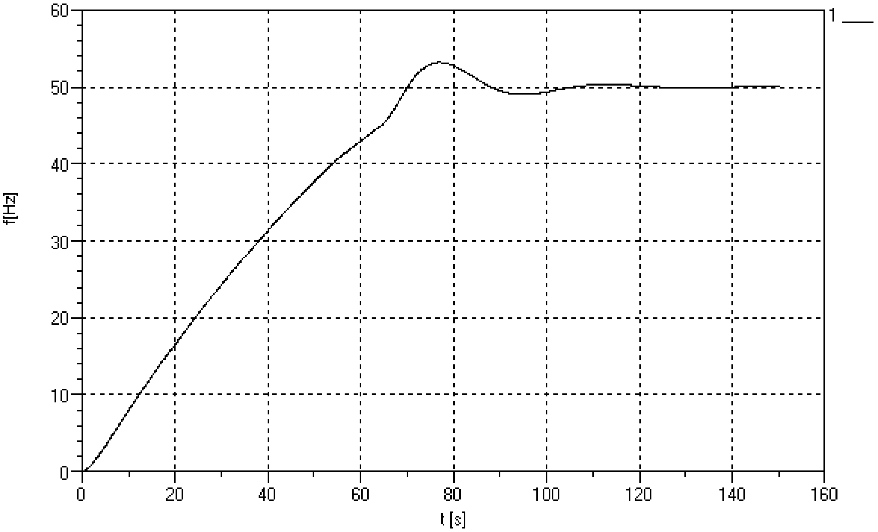

Figure 8 Typical hydropower unit start (simulation by AMESim)

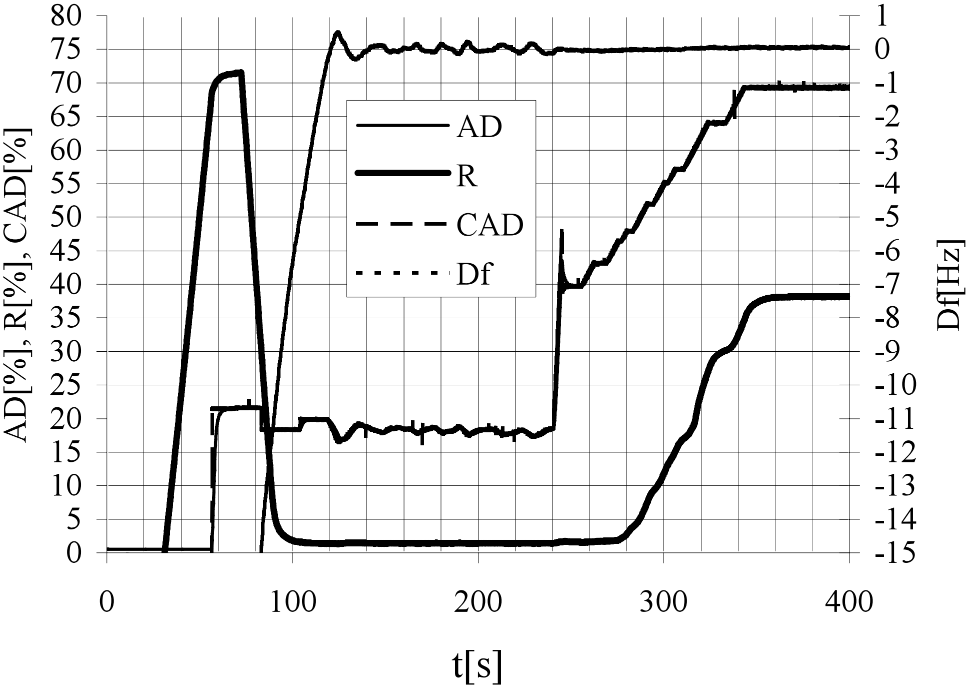

Figure 9 Parameters variations during the start and the load of the hydropower unit: AD – guide vanes servomotor stroke [%]; R – runner blades servomotor stroke [%]; CAD - guide vanes servomotor stroke order [%]; Df – frequency error [%]

After a few oscillations, the operator is ordering the beginning of the automatic synchronization by the aid of a dedicate process computer included in the protection system of the power unit. After a few small oscillations, all the conditions needed to connect the generator at the national power system are fulfilled, and the generator is switched ON. At this moment, the governor is setting the power at the minimum operational value to avoid the output instability. Finally, the operator is loading the power unit by acting the load-setting key at the value demanded by the power schedule. All the above process is a normal one, and the operator task is the same as before, when the governor was a hydro mechanical one.

The figure 10 is presenting the operating parameters variation during a load rejection without shut down. The generator is loosing the load by a protection device, which is turning off the electric line switch. The over speed is not overcoming 11 Hz, and the minimum frequency value is not lower than 46 Hz. In less than 33 seconds, the frequency error becomes less than 1 Hz, the whole transient not overcoming 50 seconds. The final load (internal power stations services) is very low. Therefore, the guiding vanes servomotor is keeping the nominal value for free running turbine, and the runner opening is kept at a very small value. All the described process had a normal evolution. The governor time constant for small frequency input step (200 mHz) is very low: about 2 s (figure 11). This quality allows the use of the hydropower unit for secondary control.

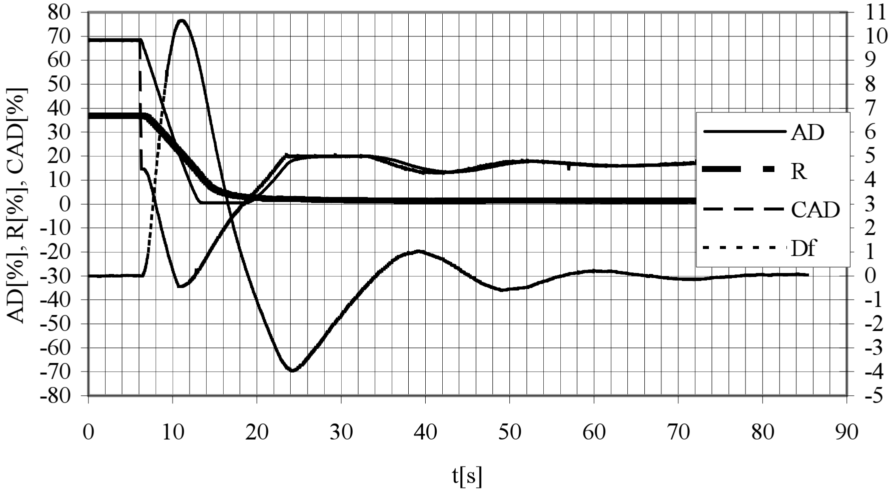

Figure 10 Parameters variation during a load rejection without shut down

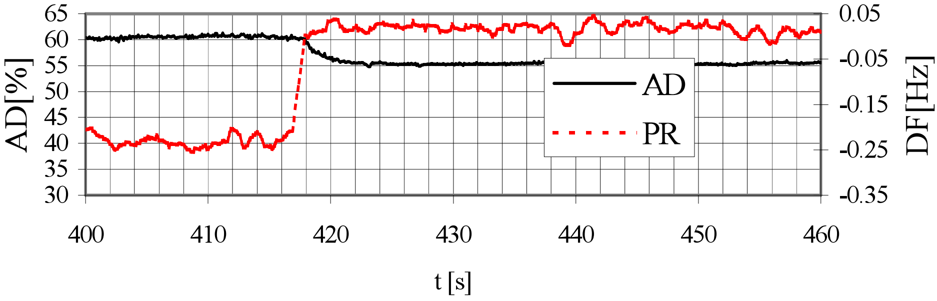

Figure 11 Governor response for 200 mHz frequency step input (P=10 MW, b_p=10%)

5 CONCLUSIONS

The governor was fully tested a long period according to the international standard [7]. All the official quality indices were accomplished in normal conditions. After a few month of normal operation, the main conclusion is a positive one: the new type of electro hydraulic speed has to be promoted for new and refurbished hydropower stations.

ACKNOWLEDGMENTS

The authors are grateful for all the technical support received from HIDROELECTRICA S.A. and HIDROSERVICE S.A. during the whole implementation period. Also, the co-operation with EAST ELECTRIC – BOSCH REXROTH S.R.L., V.T.C. - ABB S.R.L., and CAD - CAM Technology S.R.L. was very fruitful.

REFERENCES

1. Vasiliu, N., Calinoiu, C., Digital Electro Hydraulic Speed Governor for KAPLAN Turbines. Romanian Patent No. 120101/2003.
2. Vasiliu, D., Calinoiu, C. and Vasiliu, N., Governing Hydraulic Turbines By Servo Solenoid Valves – Numerical Simulation And Test, 2000 ESS CONFERENCE, The Society for Computer Simulation, Hamburg, 2000.
3. *** Servo Solenoid Valves Technical Specification 13/2, BOSCH - Automation Technology, Stuttgart, 1999.
4. Vasiliu, N., Vasiliu, D., Fluid Control Systems, Vol.I, Technical Press House, Bucharest, 2005.
5. *** AMESim R 4.3. User Manual. Imagine, Roanne, 2006.
6. Vasiliu, N., Vasiliu, D., Călinoiu, C., Ofrim, D. - Digital Control Systems for Synchronizing Hydraulic Servo Cylinders. Scientific Bulletin of the Politehnica University of Timisoara, Transactions on Mechanics Special Issue. The 6th International Conference on Hydraulic Machinery and Hydrodynamics Timisoara, Romania, October 21 - 22, 2004.
7. IEC, Guide to specification of hydraulic turbine control systems, International Electrotechnical Commission, Geneva, 1998.

THE FULL VEHICLE SIMULATION – A VIRTUAL TEST ENVIRONMENT FOR MOBILE HYDRAULIC SYSTEMS

A SCHUMACHER and **H-H HARMS**
Institute of Agricultural Machinery and Fluid Power, Technical University of Braunschweig, Germany

ABSTRACT

A full vehicle simulation of an agricultural tractor has been built up at the Institute of Agricultural Machinery and Fluid Power (ILF) to examine the potential and the quality of a driving dynamics simulation.

This model will be used for simulation of the hydraulic system as well as the driving dynamics in order to test hydraulic features for the vehicle (e.g. a traction control system or a vibration reduction). Key point of the simulation is the driving dynamics of the vehicle. First results of the verification show a very good quality of the simulation. Therefore it can be assumed, that the model will be a powerful tool for the developing process of hydraulic systems and electronic control units.

1 INTRODUCTION

The usage of computers for the engineering design has increased incredibly. But computer based simulation is not only used for the development of components, it is used for simulating the behaviour of the whole system, too. It enables calculation of the response of the system due to the new component. The system may be a hydraulic system used in a tractor – or the whole tractor.

Analysing the vehicle-producing industries, it becomes evident, that driving dynamics simulations are used and approved in the automotive sector long-time. In the agricultural or construction machinery sector these simulations are not as common as in the automotive – even though an increasing usage is recordable.

Power Transmission and Motion Control 2007 Edited by Dr D N Johnston and Professor A R Plummer
© With The Centre for Power Transmission and Motion Control

The creation of a tractor model for a simulation, based on the tractor Fendt Xylon available at the institute (Figure 1) will be shown in this report.

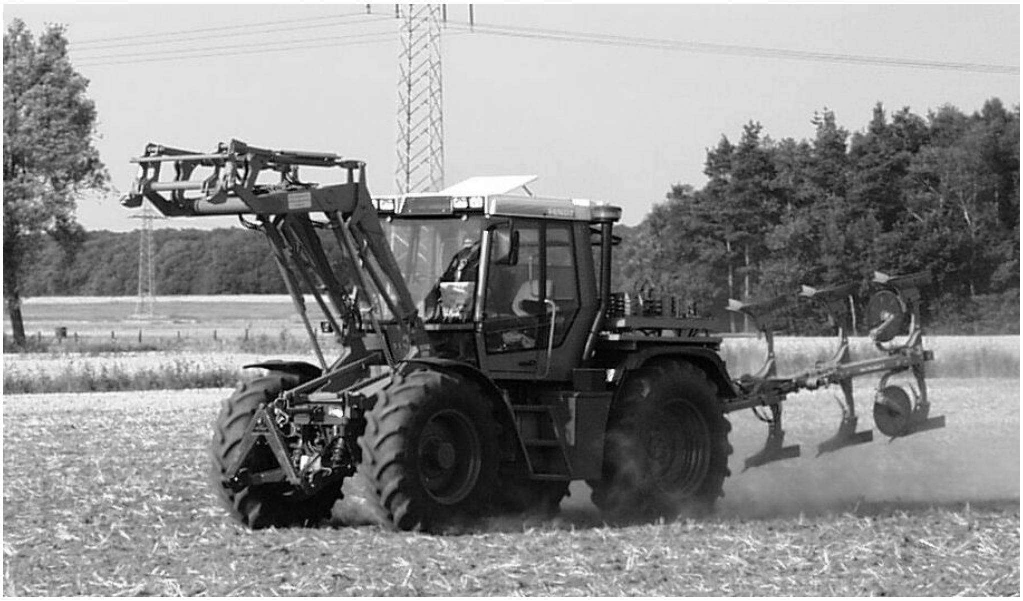

Figure 1: Fendt Xylon with front end loader and attachment

The Requirements of the simulation are:

1. The vehicle model should calculate the driving behaviour of the tractor. Offering the possibility to optimise parameters of a control system and/or the complete control system, the response of the vehicle model should be as realistic as possible. This requires a model build up highly detailed in reference to the mechanical properties like the inertia and the driving dynamics determining factors (e.g. tyre parameters or suspension stiffness).
2. Supposing that the hydraulic simulation can not be realised with the vehicle simulation programme with the required complexity, an interface between two programmes is necessary. According to that, for every part of the model an ideal simulation will be deployed.
3. For a better illustration the results of the simulation have to be animated. Therefore an animation, that can be used for a public presentation should be included. This reduces the potential simulation platforms, which can be applied for this purpose.

Regarding a coupled analysis of the hydraulic and mechanic states occurring during movements of the tractor, the most important stimulations from the vehicle to the hydraulic system are the oscillating moves of the vehicle, especially the pitch and yaw oscillation. These oscillations cause movements at an attachment (e.g. front end loader or plough as shown in figure 1) which induct pressure variations and other effects to the hydraulic system. The analysis of these effects and simulation of a potential anti-oscillation module is one of the key points of this model.

2 BUILDING UP THE MODEL

To get better results a simulation programme for the mechanical system and one for the hydraulic system will be used as mentioned in the introduction. Based on these three key points, the **m**ulti-**b**ody-**s**ystem (MBS) programme ADAMS will be the platform for simulating the driving behaviour of a vehicle and for the hydraulic system MatLab was appointed.

The building-up of the model in ADAMS is a geometrical construction like it is in a CAD programme: The parts of the model are composed of a Boolean addition/subtraction of simple bodies like a box or a cylinder. Therefore the model can be built up in great detail depending on the grade of detail of the composed parts. After defining the driving forces, torques, and motions of special parts like steering parts, the results of the simulation are the driving behaviour of the vehicle. These results can be animated and evaluated in a post-processor. Thus a film of the results (e.g. the motion of the model) can be made.

Due to the reduced complexity of the hydraulic toolbox which is offered by ADAMS the hydraulic system will be mapped in MatLab/Simulink, a block-diagram based programme. The equations describing the technical correlation of the simulation model are displayed in a block diagram. MatLab is often used to simulate hydraulic systems because of the absence of affordable and flexible hydraulic simulation programmes in the past. But simulating the driving dynamic of a vehicle the equations become too complex for a block diagram. A further deficiency of MatLab (regarding this model) is the illustration of the results: The results can only be viewed in a plot. A video-animation of the model is not possible without a special toolbox.

The comparison of both programmes shows: ADAMS is very useful for simulating the mechanical part of the model as a MBS-programme. The building up is very easy and may lead to a highly detailed model. With build-in postprocessors, ADAMS offers high quality rendering possibilities for an animation of the results so that pictures and films are the output result as well as diagrams.

MatLab/Simulink is well known for hydraulic simulation but without proper animation of the results (only diagrams). Nevertheless, a video-like animation is not required: For example the pressure variation during a motion of a cylinder can hardly be visualised in a film, it can only be plotted in a graph.

Both programmes have to be coupled for a combined simulation, which means a combination of the mechanic and hydraulic system. Fortunately, ADAMS and MatLab offer an interface to connect themselves together. The interacting mode is a co-simulation in this case. Co-simulation determines a master-slave configuration: One programme acts as master which controls the slave. In the ADAMS-MatLab co-simulation ADAMS works as the master and MatLab as the slave. This requires ADAMS to calculate the output variables first and passing the data to MatLab; then MatLab calculates the results and returns again them to ADAMS as input.

This method will become evident with a hydrostatic drivetrain for example [14]: The wheel is the interfacing part between both programmes: ADAMS calculates the vehicle's reactions depending on a driving torque and thus the wheel speed. The driving torque is calculated in the Simulink model. The wheel speed is necessary for the hydraulic simulation to evaluate the flow rate, the pivoting angle of the motors and the pump and the driving torque. Thus the combination of both programmes is a circulation. The Figure 2 shows the Simulink model with the interface-block (dark grey) to the ADAMS model. [10], [11], [13]

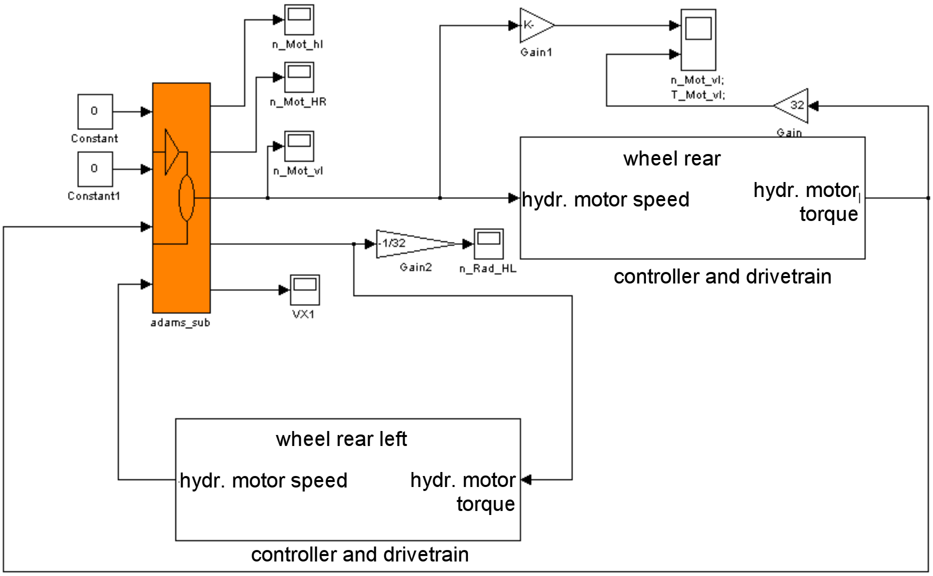
n_Mot_hl
n_Mot_HR
n_Mot_vl
K-
Gain1
n_Mot_vl;
T_Mot_vl;
32
Gain
0
Constant
0
Constant1
adams_sub
wheel rear
hydr. motor speed
hydr. motor torque
controller and drivetrain
-1/32
Gain2
n_Rad_HL
VX1
wheel rear left
hydr. motor speed
hydr. motor torque
controller and drivetrain

Figure 2: Co-simulation of ADAMS and Simulink: The Simulink model

2.1 Vehicle model

A realistic behaviour of the vehicle should be provided with this simulation for high simulation quality. This demands either a high detailed model or a good knowledge about the driving dynamics determining parameters e.g. inertia. Unfortunately these parameters are difficult to evaluate: The effort to get them is disproportional high (swinging the complete vehicle) so that the better way is to create a high detailed model.

A special – but in this manuscript not specified – demand on this simulation is, that the model should deliver adequate results without the possibility of verifying the assumed values separately by measurements or experiments – only a full vehicle verification was possible. This means that the inertia or tyre parameters could not be evaluated exactly. Methods had to be found which allow the estimation of necessary parameters with an acceptable tolerance.

An advantage of ADAMS regarding this problem is the geometric model construction: With a given geometry and material ADAMS calculates the inertia and mass of every part. Therefore, the complete geometry should exactly measured and modelled in the simulation –as shown in Fig 3.

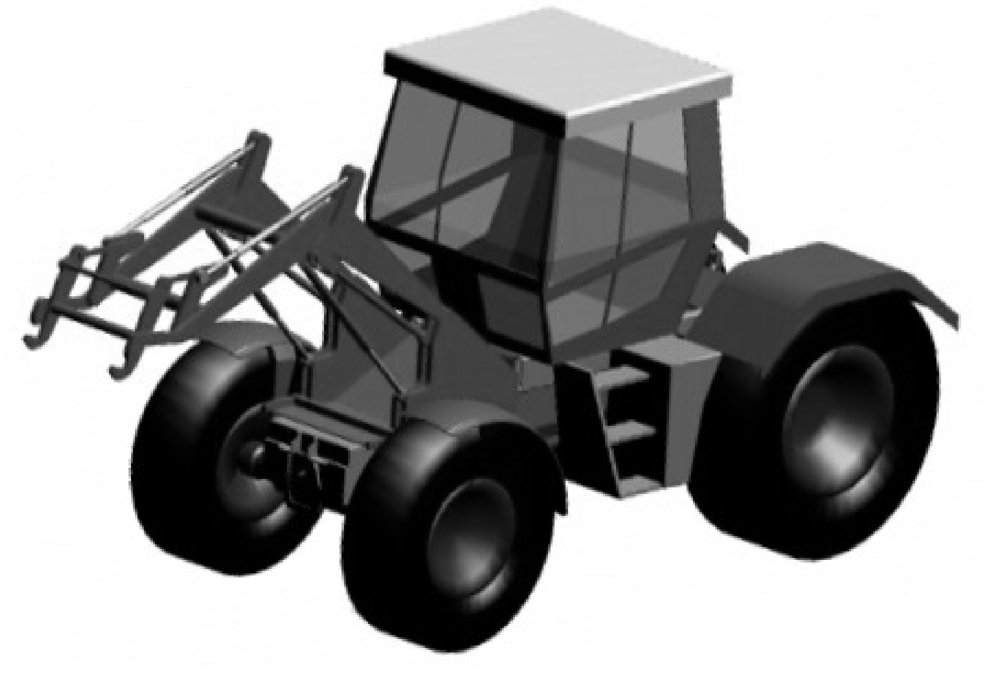

Figure 3: Model of the Fendt Xylon – without rear attachment

The disadvantage of ADAMS regarding this problem is that any part of the tractor must be modelled very detailed, even the engine with every part must be build up in the model. It becomes evident, that the method is improper.

A more appropriate method for the appraisal of the inertia is the calculation. Formulas exists for agricultural tractors which allow the approximation of the inertia. Consequently, the principal axes' moments of inertia will be calculated using these formulas. Datasets of different tractor types are findable in the literature [4],[13],[17],[18] so that a rough approximation of the error tolerance using the formulas can be obtained. For instance, the formula for the roll inertia [4]:

$$I_{xx} = 215.857 \cdot EXP(0.4494M) \text{, with } M\text{: tractor mass in tons} \quad (1)$$

Comparisons with the datasets of different tractors shows the error tolerance using this formula is up to 15%.

An other important part of the vehicle simulation is the tyre model. The tyre model calculates the forces and torques acting at the vehicle due to the motion of the vehicle. It is evident that these forces should be as realistic as possible to obtain an accurate motion of the vehicle. Because of the special tyres that agricultural machines use – compared with on-road-vehicles – a standard ADAMS tyre model can not be applied to the tyre: the vehicle behaviour would not be correct. So a special tyre model had to be generated which considers the properties of agricultural tyres.

Completed tests with the ADAMS standard tyre models (based on the "magic formula" to calculate the tyre forces [8]) have shown that the lateral and longitudinal forces generated are to small for gaining a realistic vehicle behaviour. This causes the above mentioned new creation of the tyre model and gave the possibility of including different surfaces and grounds – something ADAMS can hardly handle.

The longitudinal forces are of somewhat less importance, because the traction and slip behaviour of the tyre is not inspected yet. The influence of longitudinal forces onto yaw and pitch oscillation is marginal – compared with the influence of the vertical and lateral forces.

In the future, the model will be expanded with the ground mechanics. Key point of the expanded model will be the balance of the tyre forces and the ground forces: The tyre forces are depending on the contact between the ground and the tyre. Using the procedure of Ammon [1], Pacejka [10], or other common tyre models, the ground condition depending effects (e.g. adhesion coefficient) are represented by static graphs. Implementing the ground reaction forces, the behaviour of the ground will be shown more exactly. Calculating the vertical tyre forces with the ground reaction as [12] mentioned, not only the ground mechanics but also different elevation profiles will be considered without multiple spring-damper or other complicated tyre models. Longitudinal and lateral forces will be evaluated with the shear of the ground due to the slip and skew of the tyre.

These methods for calculating the tyre forces are not implemented yet, so the longitudinal force will be calculated using the damper-like method of Ammon, presented in [1]. Varying road surfaces will be considered with varying "damper"-coefficients. Key point is, that the tyre generated forces are like damper forces, depending on the velocity difference between tyre and ground.

The more important forces, the vertical and lateral force, are calculated using the tyre data which are determined on a test bench [2], [3], [6], [7],[12].

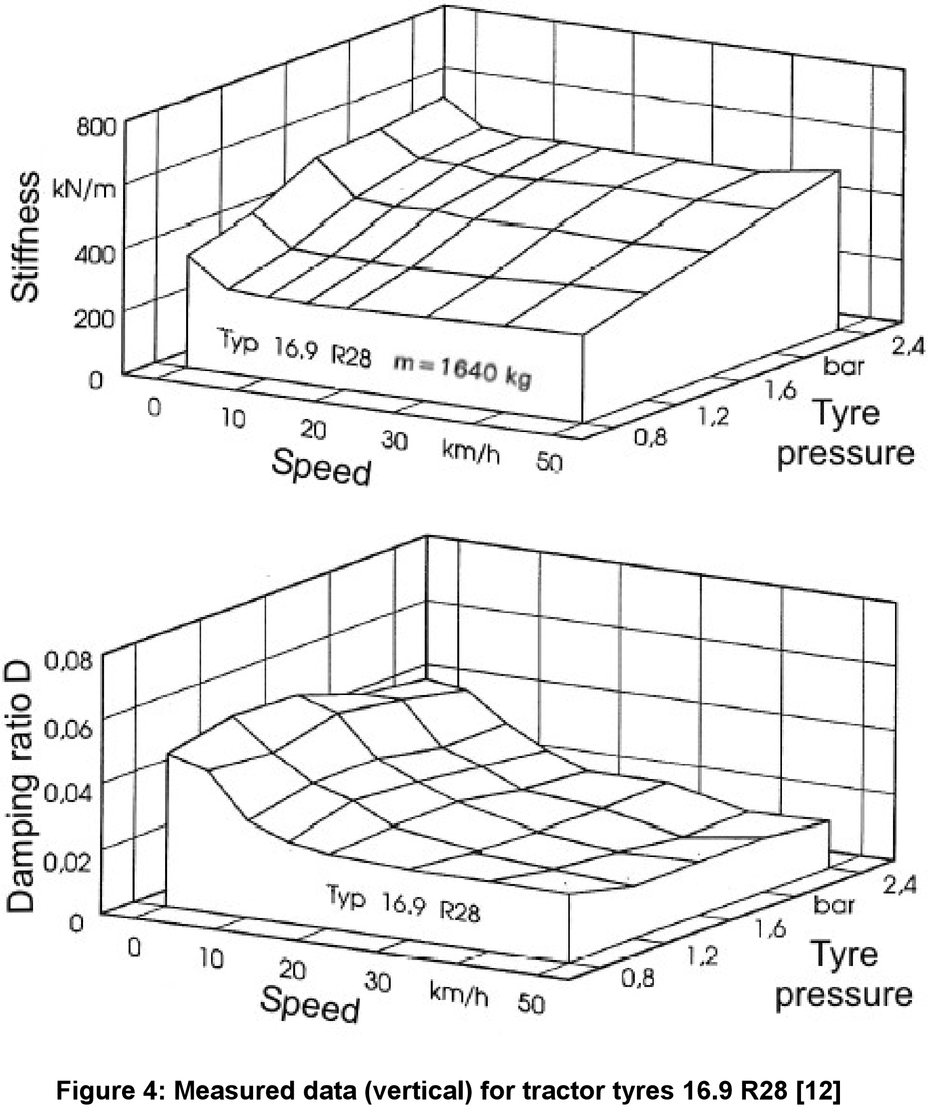

Figure 4: Measured data (vertical) for tractor tyres 16.9 R28 [12]

Using these tyre maps, the effects of parameters like speed and tyre pressure will be respected. While the tyre pressure is an parameter which will be defined at simulation start (although an variation of the pressure during simulation is not only interesting for simulating tyre pressure regulation systems but also possible with this model), the vehicle speed is a continuously varying parameter during simulation – with a high influence onto the tyre stiffness and damping ratio. These effects are important for a proper yaw and pitch behaviour and normally not implemented in standard tyre models.

The aligning and camber torques are not important for this model because the steering torque is not used yet. The steering will be done by a defined movement of the steering cylinder, not by a force applied onto the cylinder. However, the tyre model could be enhanced with these torques in the future.

2.2 Hydraulic model

One of the focal points in this project is to get a realistic behaviour of the vehicle. With the validated vehicle model, it's possible to add the hydraulic parts. The interfering of the vehicle and the hydraulic system can be obtained then. The advantage of the coupling of a mechanical and a hydraulic simulation consists of including this interfering between the two parts. Normally, simulating hydraulic components or systems, the external loads are assumed and impressed on the system. A dynamic change due to the perturbation every part causes to each other can not be analysed. Should this model be used for designing components and controller, especially this perturbation is necessary to be reproduced by the model.

3 VERIFICATION OF THE MODEL

If a model is used to calculate any parameter based on the model behaviour, it is necessary to validate the model. The results are not reliable enough for creating controllers or anything else depending on the model unless one has validated. The problem is, that a special demand at this project was the building up of a vehicle model without the possibility to verify the mechanical properties like inertia. Unfortunately, taking a look at a typical driving manoeuvre, the yaw rate is mainly determined by the yaw inertia of the vehicle (I_{zz}) and the tyre forces. Both can hardly be calculated and are to be defined/approximated thus.

This causes a certain unsureness: If both parameter sets are estimated and a verification shows a good match with measured data from real vehicles, both approximations can be good or that way that the discrepancies correct themselves to a good match. To avoid these unsureness, deeper knowledge about one of these parameter sets must be gained. Fortunately, the standard tyres for agricultural tractors are often measured, so the tyre parameters which are necessary for a vehicle dynamics simulation could be obtained more easily than inertia values. The principal correctness of the tyre forces can be tested with steady state manoeuvres.

Lateral forces will be reviewed with the steady-state skidpad testing. If the vehicle is in steady-state conditions, the inertia has no influence on the forces: the lateral forces F_Y are balanced with the centrifugal force F_C:

$$m\frac{v^2}{r} = F_C = F_y = f(\alpha, F_Z) \tag{2}$$

This verification could be done with different speeds and/or radii. The force F_C is calculated with the given speed and radius of the simulation. The lateral force is calculated via a literature based map, depending on the vertical force F_Z and the skew of the tyre. The skew is the parameter to be compared (simulation vs. literature) and indicates the error tolerance of the force calculation. The variety of F_Y due to imprecise vertical forces (neglecting the effects of dynamic vertical force changing due to the roll movement) is small enough. This means, that calculating the vertical force with a literature based map too will not cause too big errors in the lateral force.

The balance between F_C and F_Y will adjust itself in every steady-state manoeuvre, but with inaccurate tyre force calculations the skew will differ from reality – by a constant radius and speed. So the skew of different steady-state manoeuvres was compared with the measured data found in the literature and it has shown a good match.

The vertical force will be verified in steady-state too. The force will be calculated via maps too. The tyre deflexion at different speeds and loads can be compared with the measured data (literature) to verify the model. The tyre damping behaviour is verified with the transient response. Important for this test is, that the transient pulse will not revolve the vehicle so that the moments of inertia will not have influence on the movement.

Even though this test will not verify the dynamic behaviour of the tyre it must be assumed that the tyre model will be good enough for vehicle dynamics simulations, because continuative tests of the tyre forces (without the influence of the inertia of the vehicle) could not be done at the institute.

The tests which could be done at the institute are full vehicle tests. The tractor is equipped with sensors to measure speed, acceleration (longitudinal, lateral and vertical) and turning rates (yaw, pitch and roll). Also an bigger location for steady-state manoeuvres exists with a surface of concrete. To test the yaw and pitch behaviour of the tractor and verify the model, the following two test will be done: step steer and vertical impulse.

3.1 Step steer test

The graph in Figure 5 shows the vehicle's response on the step steer manoeuvre. The tractor was accelerated up to *5 – 5.5* $^{m}/_{s}$, but the acceleration phase is not shown in the graph. To realise the step steer, a high steering gradient was applied, about 30$^{\circ}/_{s}$ (at the wheel).

Obviously, there is an offset in the yaw rate during acceleration phase until the steering gradient was applied. This offset is caused by local circumstances, the step steer location could not be reached without steering.

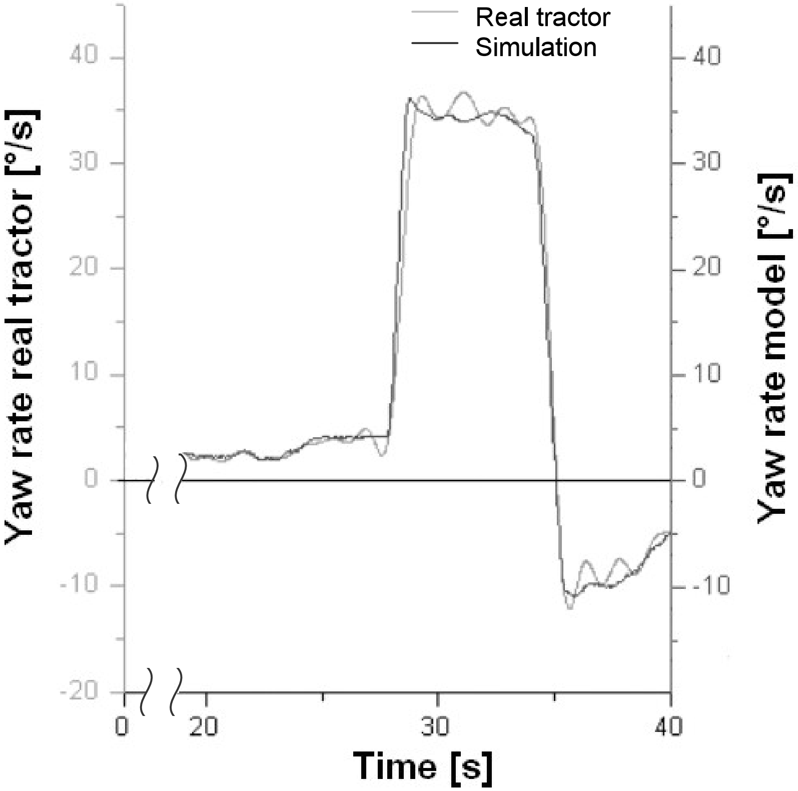

Figure 5: Measured and calculated yaw rate – step steer

The yaw rate was measured at the real vehicle on the front axle and beneath the vehicle's centre of gravity (CG). Carrying out measurements in the centre of gravity was not possible because it was not accessible. Nevertheless – neglecting the effect of the displacement of the yaw axis through rolling – it does not matter where the yaw rate is measured, because a vehicle yaws at any position nearly identical. The effect of displacing the yaw axis is very small and will be left unconsidered.

The results, which can be obtained from that test:

1.) The lateral damping in the model is higher than at the real tractor. This causes the tractor to produce yaw-oscillations due to a steering stimulation the model does not show. The reason is located in the tyre model – lateral parameters are very difficult to gain and so these parameters are approximated.

    An additional fact causing this effect: These vibrations are caused by the front end loader. The bearings of the loader do have tolerances (bearing play), which causes the loader (during this test in an upper position as shown in figure 7) to oscillate. This bearing plays are not realised in the model. Additional, the roughness of the ground has an influence on these vibrations: At the end of the steering ramp manoeuvre the ground surface changed. In the model an even ground without any roughness is used.

2.) The comparison of characteristic data shows:

    Peak response time: Model 1 *s*; Tractor 1.48 *s*. Deviation: 31%
    Amplification factor: Model: 35.1; Tractor: 34.3. Deviation: 3%

Normally, a deviation of 31% will not cause satisfaction, but the test is an extreme manoeuvre. The assumption made is, that if the behaviour of the simulation during extreme manoeuvres is close enough to reality, the match during normal cruises is even better. Figure 6 substantiates this assumption.

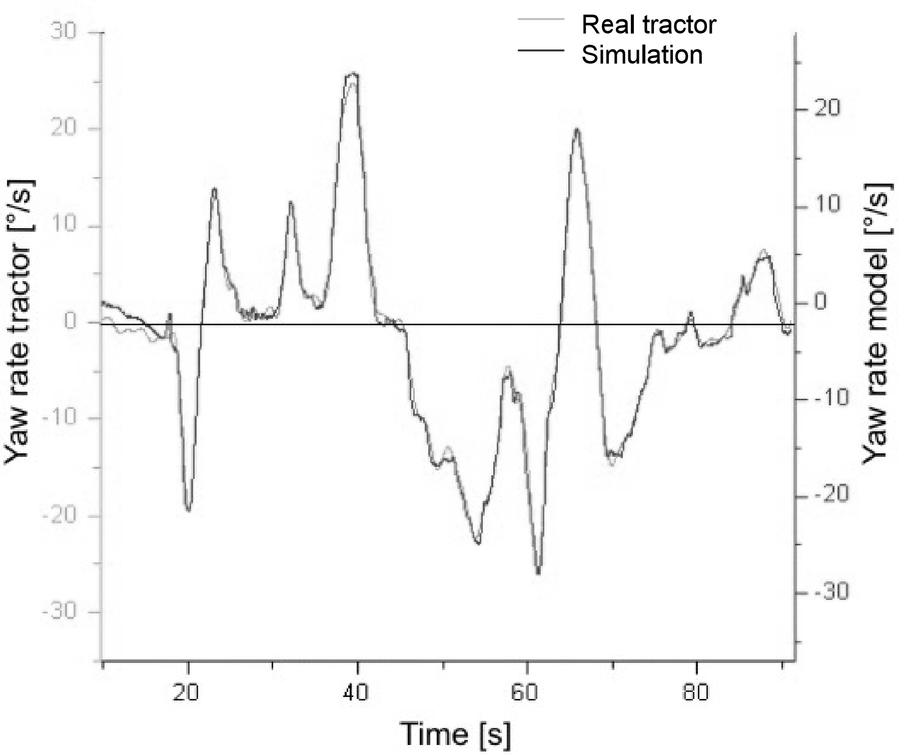

Figure 6: Measured and calculated yaw rate – normal cruise

The yaw rates during the normal cruise are matching very good. This is an indication for a good approximated yaw-inertia I_{ZZ} .

The overall correlation between model and reality is very good. Including the fact, that the step steer with a high gradient is an extreme manoeuvre, it can be stated, that these differences can be neglected. Even with the mentioned uncertainness regarding the parameter estimation, the simulation delivers a very good steering behaviour of the vehicle especially by the simulation of normal manoeuvres.

3.2 Vertical impulse test

For the vertical impulse test a constant velocity of approximately 2.4 $^{m}/_{s}$ was adjusted. The vehicle hit two timber with both axles consecutively. The timber dimensions are 80 *mm* of height and 80 *mm* of width.

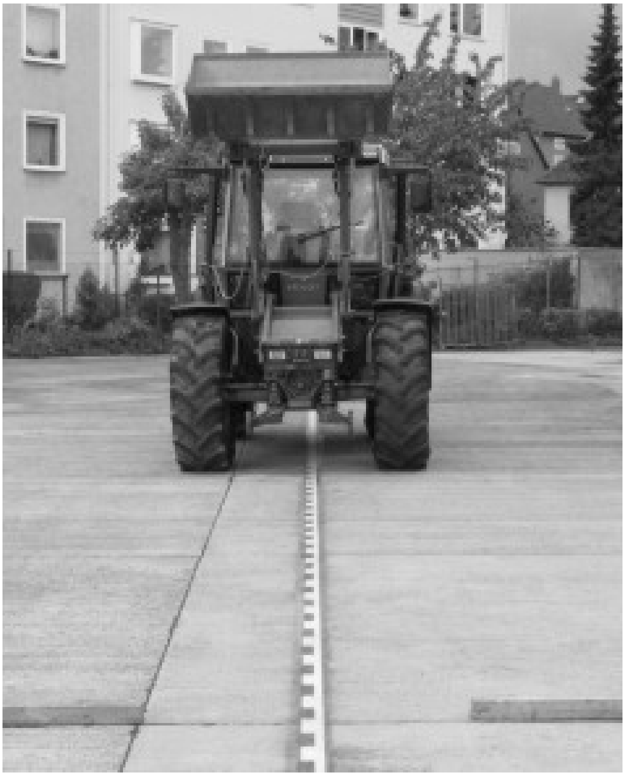

Figure 7: Vertical impulse via two timber

In Figure 8 the measured pitch rate of the real tractor and the model are shown. The graph begins with the front axles' hit of the timber. The acceleration of the tractor to reach the speed of 2.4 $^{m}/_{s}$ is not shown in the figure.

The front axle hit the timbers at 24 *s*, the rear axle at 26.5 *s*. Between 24 and 26.5 *s* the vehicle oscillates with a frequency. The rear axle is the centre of rotation, because only the front axle was stimulated. After passing the timbers with the rear axle, the vehicle changes the oscillation and reacts with oscillating in the vertical eigenfrequency.

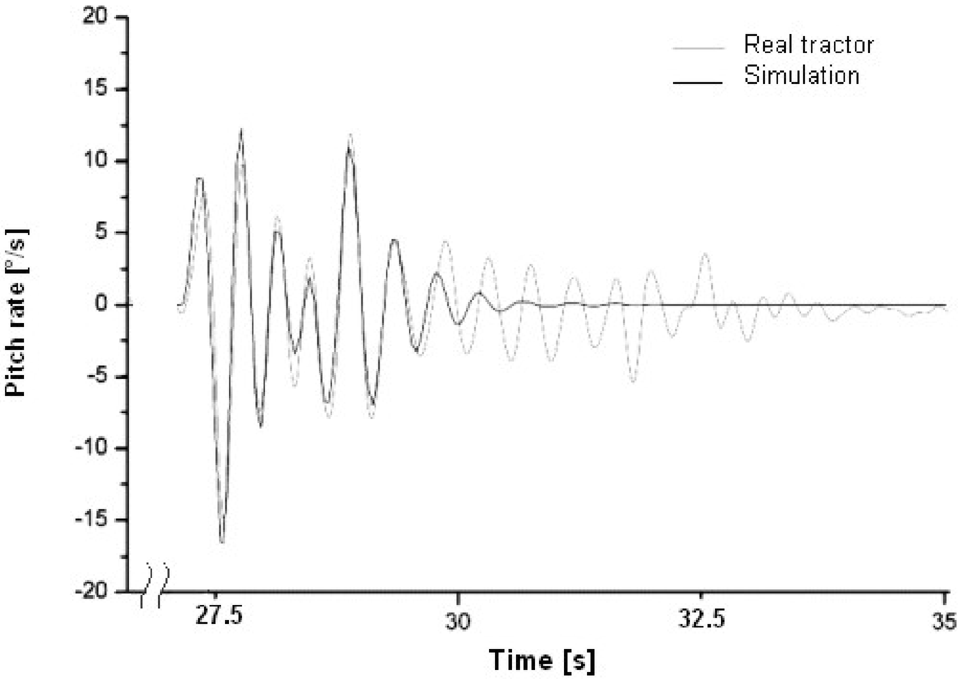

Figure 8: Measured and calculated pitch rate

The comparison of the results:

1.) The pitch frequency for the model stimulated at the front axle matches the frequency of the real tractor with a value of 2.6 *Hz*. This indicates a good pitch inertia *Iyy*.

2.) The pitch-eigenfrequencies of the model and the tractor are 2.29 *Hz*. Interesting is the discrepancy starting at 29.5 *s*: The tractor remains in a light damped oscillation mode while the model is completely damped. This indicates an overdamped tyre model behaviour at low pitch rates. But increasing the damping coefficient would result in higher amplitudes at higher pitch rates too. Thus, the used coefficient is a compromise showing a satisfying vehicle behaviour in vertical dynamics.

3.3 Review of the Verification

Looking at the variations between the simulation and the real tractor it becomes evident, that the simulation quality is high. Simulating a good lateral behaviour of a vehicle is difficult because a good tyre model and tyre parameters as exact as possible are required therefore. The results shown in Figure 5 and 6 demonstrate, that this goal had been fulfilled – the simulation shows a adequate match especially during normal cruises.

Also the vertical motion shows a good match between simulation and reality, but it depends more on the tyre model. This bares a basic problem for a complete vehicle simulation: The complex tyre mechanics. The vertical damping of the tyre could be improved by using a non-linear relation between tyre damping and deflexion speed.

Furthermore it had to be considered that the presented manoeuvres are extreme manoeuvres. The differences become lower at less extreme manoeuvres. Comparing “normal cruise”-measurements the differences are negligible. Hence, including the reasons for these differences, it can be stated that these differences do not reduce the high simulation quality.

4 CONCLUSION

The developing process of new components or systems requires even in the off-road machinery area complete vehicle simulations including the vehicle model and models for subsystems like the hydraulic systems. This causes the problem that a simulation platform, which is useful for vehicle simulation, is not useful for other simulation often.

The first key point of this project was the development of a driving dynamics model of a tractor which will be a platform for other subsystem models. The tractor model was build in ADAMS, a custom made tyre model was implemented. For subsystems which needs special simulation requirements (e.g. hydraulic systems) the co-simulation could be used.

The verification of the model indicates a good quality. The model displays the motion of the Fendt Xylon tractor close to the reality – especially during normal manoeuvres. Some simulation results will be better with further verifications, because needed parameters can be enhanced therewith. Thus, a powerful simulation and development tool has been created which will act as a virtual test environment for tractor hydraulic components and control systems.

5 REFERENCES

[1] Ammon, D. (1997) Modellbildung und Systementwicklung in der Fahrzeugdynamik, Teubner Verlag, Stuttgart

[2] Barrelmeyer, T. (1995) Längs- und Seitenkräfte an Traktorreifen, Landtechnik 5

[3] Barrelmeyer, T. (1997) Längs- und Seitenkräfte an Ackerschlepperrädern, Agrartechnische Forschung 3 H.2

[4] Böhler, H. (2001) Traktormodell zur Simulation der dynamischen Belastungen bei Transportfahrten, Fortschritt-Bereicht VDI

[5] Harms, H.-H. (2002) Landmaschinen und Traktoren II, Lecture, TU Braunschweig

[6] Langenbeck, B. (1992) Untersuchung zum Fahrverhalten von Ackerschleppern unter besonderer Berücksichtigung der Reifeneigenschaften, Fortschritt-Bericht VDI

[7] Maulick, T. (2000). Ein neues Verfahren zur Berechnung von Reifenparametern, Expert Verlag, Stuttgart

[8] Mitschke, M. (1972) Dynamik der Kraftfahrzeuge, Springer-Verlag, Berlin

[9] Mitschke, M. (1990) Dynamik der Kraftfahrzeuge, Band C, Springer-Verlag, Berlin

[10] n.n. (2003) Documentation of ADAMS 12.0, MSC Software

[11] n.n. (2003) Documentation of Matlab/Simulink R13 (2004)

[12] Osetinsky, A. (2004) Traction performace simulation of a pushed/pulled driven wheel, Transactions of the ASAE, Vol. 47(4), p. 981-994

[13] Pickel, P (1993) Simulation fahrdynamischer Eigenschaften von Traktoren, Fortschritt-Bereichte VDI

[14] Schumacher, A. (2005). Kombinierte Simulation am Beispiel eines hydrostatischen Fahrantriebs, Landtechnik

[15] Schumacher, A. (2006). A driving dynamics model for off-road vehicles with hydrostatic drivetrain, FPNI Symposium Sarasota

[16] Sharon, I. (1975) Untersuchungen über die Schwingungseigenschaften großvolumiger Niederdruckreifen, Forschungsbericht Agrartechnik VDI, Berlin

[17] Spät, R. (2003) Dynamische Kräfte an Standardtraktoren und ihre Wirkung auf den Rumpf, Fortschritt-Bereichte VDI

[18] Thomas, B. (2001) Konzeption und Simulation eines passiven Kabinenfederungssystems für Traktoren, Shaker Verlag

A Fourier-Galerkin-Newton method for periodic nonlinear transmission line problems

Helmut Kogler[1], Bernhard Manhartsgruber[2], Rainer Haas[2]
1)Linz Center of Mechatronics GmbH
Altenbergerstr. 69, 4040 Linz, Austria
2)Institute of Machine Design and Hydraulic Drives
Johannes Kepler University, Altenbergerstr. 69, 4040 Linz, Austria

ABSTRACT

The problem of pressure and flow-rate oscillations in periodically excited transmission line systems arises in a number of fluid power applications. The fluid-borne noise problem in the suction and delivery lines of pumps has been studied by a large number of authors in the past. More recent applications can be found in the simulation of common-rail diesel injection and hydraulic valve actuation systems in the automotive industry. In the case of laminar flow with small pressure oscillations around a stationary operating point, a linear model can be used and the system answer to periodic excitations can be computed efficiently in the frequency domain. Even in the case of nonlinear boundary conditions, e.g. a valve with a quadratic pressure drop, combined time and frequency domain methods have been used by a number of authors in order to maintain the benefits of frequency domain modelling of transmission lines. A much harder problem arises if the nonlinearity is distributed along the transmission line. In this paper, a Fourier-Galerkin-Newton method is applied to laminar transmission line flow with a nonlinear compressibility law. The viscous effects are modelled by the linear, frequency dependent friction model in the form due to Kagawa et al. For the spatial discretisation a Galerkin approach with a staggered grid is taken from literature. In order to treat periodic problems efficiently, the solution is parameterised by Fourier series. The approach results in a large scale, nonlinear system of equations to be solved for the periodic system response to periodic excitations.

1 INTRODUCTION

In many applications of hydraulic drives it is sufficient to characterise the wave propagation in the fluid through the well known linear theory, e.g. [1, 2], which claims a linear material law. Obviously this theory only holds at a sufficient mean pressure and relatively small pressure amplitudes. Especially in systems working at low pressure, e.g. tank lines, one is not able to assume that the fluid density is independent of the pressure, because of the amount

Power Transmission and Motion Control 2007 Edited by Dr D N Johnston and Professor A R Plummer
© With The Centre for Power Transmission and Motion Control

of separated gas in the fluid - see Figure 1. So the compressibility of the fluid ends up in a nonlinear relationship between density and pressure. Furthermore, this nonlinearity is distributed along the transmission line. So the advanced reader immediately comprehends that this circumstance leads to a system of nonlinear partial differential equations, which generally requires quite a large effort to be solved. In the case of cyclically operating hydraulic applications, one is able to constrain the nonlinear partial differential equations exclusively to periodic solutions and thus the problem becomes manageable. On the other hand it is important to mention, that the assumption of periodic solutions implicates the neglection of possibly occurring subharmonic phenomena.

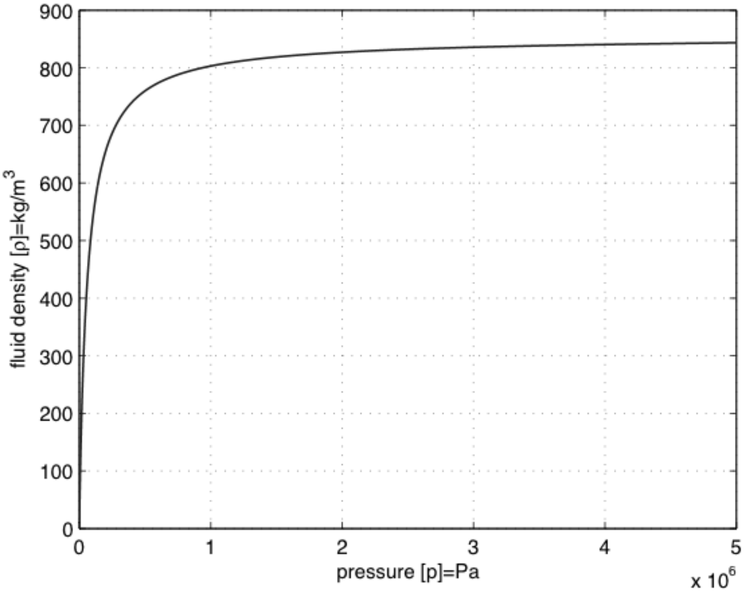

Figure 1: Effective density of the gas-oil mixture dependent on the pressure.

In this paper the modelling of a straight pipe line with a constant circular cross section at laminar flow and with a nonlinear law of material is treated. The pipe flow problem can be treated as a one-dimensional wave propagation problem with a dynamic friction model covering the effect of the radial velocity distribution. The further intention is to show how the obtained partial nonlinear differential equations can be solved for the case of periodic solutions using Fourier's transformation between the time and the frequency domain. The spatial discretisation will be realised by a Galerkin approach with a staggered grid which is taken from established literature [3].

2 A NONLINEAR TRANSMISSION LINE MODEL

A mathematical model for the behaviour of fluid transmission lines can be derived from the basic conservation laws for mass, momentum and energy as well as a constitutive equation describing the material behaviour of the fluid. Due to the assumptions given in the previous section, the only sources of nonlinearity can be found in nonlinear convective terms in the Navier-Stokes equations and in a nonlinear constitutive relationship between pressure and fluid density.

2.1 A nonlinear material model

The influence of entrained air on the low-pressure behaviour of fluid power systems is well known. A simple model for a gas-liquid mixture can be derived by assuming small bubbles of gas in a carrier liquid, for instance mineral oil.

In the absence of gas bubbles and for constant temperature, the relationship between the hydrostatic pressure p and the oil density ρ_{oil} is given by

$$\frac{\partial \rho_{oil}}{\rho_{oil}} = \frac{\partial p}{E_{oil}\left(p\right)} \quad \text{with} \quad \rho_{oil}\left(p_0\right) = \rho_0$$

For moderate values of p, the bulk modulus of compressibility E_{oil} can be assumed as a constant and the resulting exponential solution for $\rho_{oil}\left(p\right)$ is usually approximated by

$$\rho_{oil} = \rho_0 \left(1 + \frac{p - p_0}{E_{oil}}\right). \tag{1}$$

For the gas bubbles, an isothermal compression and expansion is assumed resulting in

$$p_0 V_{0,gas} = p V_{gas}. \tag{2}$$

At the reference pressure level p_0, the volumetric ratio of gas vs. liquid is parameterised as

$$\alpha = \frac{V_{0,gas}}{V_{0,oil}}. \tag{3}$$

The average density of the mixture can be stated as

$$\rho = \frac{m_{oil} + m_{gas}}{V_{oil} + V_{gas}}.$$

The mass m_{oil} is obviously known by $\rho_0 V_{0,oil}$. The mass of the gas fraction can be computed from the state equation of an ideal gas

$$m_{gas} R_s T = p_0 V_{0,gas}.$$

The volume of the oil fraction at a certain pressure is given by its initial volume and the density change due to eq. (1) whereas the volume of the gas fraction is given by eq. (2). Substitution of these results in the definition of the average density yields

$$\rho = \frac{\rho_0 V_{0,oil} + \frac{p_0 V_{0,gas}}{R_s T}}{\frac{V_{0,oil}}{1 + \frac{p - p_0}{E_{oil}}} + V_{0,gas} \frac{p_0}{p}}.$$

This can be further simplified by use of the volumetric ratio α according to eq. (3):

$$\rho = \frac{\rho_0 + \frac{\alpha p_0}{R_s T}}{\frac{1}{1+\frac{p-p_0}{E_{oil}}} + \alpha \frac{p_0}{p}} \tag{4}$$

2.2 Conservation of mass and momentum

As outlined in the introduction, the pipe flow problem can be treated as a one-dimensional wave propagation problem with a dynamic friction model covering the effect of the radial velocity distribution. Thus the flow rate $Q(x,t)$ is used instead of the axial velocity in the following equations.

The conservation of mass along the transmission line simply reads

$$R^2 \pi \frac{\partial}{\partial t} \rho(x,t) = -\frac{\partial}{\partial x}\left(\rho(x,t)\, Q(x,t)\right).$$

The momentum balance in the axial direction requires

$$\frac{D}{Dt}\left(\rho(x,t)\frac{Q(x,t)}{R^2\pi}\right) = -\frac{\partial}{\partial x} p(x,t) - \rho(x,t)\, f(Q(x,t))$$

where $\rho(x,t)\, f(Q(x,t))$ denotes the pressure loss per unit length due to viscous friction. In the stationary case, the pressure drop is given by the Hagen-Poiseuille law as

$$f(Q(x,t)) = \frac{8\nu}{R^4\pi} Q(x,t).$$

For the instationary case, a frequency domain description is available in the form [1]

$$f\left(\widehat{Q}(x,s)\right) = \frac{s}{R^2\pi}\left(\frac{J_0\left(\sqrt{-\frac{s}{\nu}}R\right)}{J_2\left(\sqrt{-\frac{s}{\nu}}R\right)} + 1\right)\hat{Q}(x,s) \tag{5}$$

with the kinematic viscosity ν, the internal pipe radius R, the Laplace variable s, as soon as J_0 and J_2 denoting the Bessel functions of the first kind with order 0 and 2 respectively. Thus eq. (5) can be approximated by a model due to Kagawa et al [4] by

$$\begin{aligned} f(x,t) &= \frac{8\nu}{R^4\pi} Q(x,t) + \frac{4\nu}{R^4\pi}\sum_{i=1}^{k} y_i(x,t) & (6) \\ \frac{dy_i}{dt} &= m_i \frac{dQ(x,t)}{dt} - \frac{\nu n_i}{R^2} y_i(x,t), \quad i = 1, 2, \ldots, k & (7) \end{aligned}$$

in the time domain. For m_i and n_i up to $k = 10$, see [4].

2.3 A scaled model

A proper scaling of the mathematical model is desirable for two reasons. Firstly, a dimensionless model usually contains a reduced set of parameters giving better insight into the parameter influence. Secondly, the scaling can be used to improve the numerical properties of the model.

In a first step, the independent variables x and t are replaced by dimensionless coordinates ξ and τ. The axial coordinate is re-scaled by the line length L, i. e.

$$\xi = \frac{x}{L}.$$

For the time scaling, the time-periodic nature of the problem suggests a scaling with the excitation frequency

$$\tau = \omega_{exc} t.$$

The time period of the periodic wave propagation problem is thus mapped onto the interval $0 \leq \tau \leq 2\pi$. The pressure is scaled by a characteristic pressure p_s, for instance a supply pressure value or a typical pressure excitation amplitude:

$$\psi\left(\xi,\tau\right) = \frac{p\left(x,t\right)}{p_s} = \psi$$

The flow rate scaling

$$q\left(\xi,\tau\right) = \frac{\sqrt{E\rho_0}}{p_s R^2 \pi} Q\left(x,t\right) = q$$

is motivated by the Joukowsky relation. A unit step in the scaled pressure ψ will result in a unit step in the scaled flow rate q and vice versa. The material law (4) is scaled using the mass density ρ_0 of the fluid at the reference pressure p_0. This can be written as

$$\tilde{\rho} = \frac{\rho}{\rho_0} = \left(1 + \alpha \frac{p_0}{\rho_0 R_s T}\right) \frac{1}{\frac{1}{1+\frac{\psi p_s - p_0}{E}} + \alpha \frac{p_0}{\psi p_s}}.$$

By defining the dimensionless parameters

$$\varepsilon = \frac{p_s}{E}, \quad \psi_0 = \frac{p_0}{E}, \quad \tilde{\rho}_\alpha = \frac{p_0}{\rho_0 R_s T}$$

the material law reads

$$\tilde{\rho} = \left(1 + \alpha\tilde{\rho}_\alpha\right) \frac{\varepsilon\left(1 + \psi\varepsilon - \psi_0\right)\psi}{\left(\psi_0 + \psi_0\psi\varepsilon - \psi_0^2\right)\alpha + \psi\varepsilon}.$$

With the scaling of the Kagawa-terms

$$\tilde{y_i}\left(\xi,\tau\right) = \frac{\sqrt{E\rho_0}}{p_s R^2 \pi} y_i\left(x,t\right) = \tilde{y_i}$$

and the definitions above one can reduce the number of independent parameters. Following the equation of continuity takes the dimensionless form

$$L_1 = \tilde{\omega}\frac{\partial \tilde{\rho}}{\partial \tau} + \varepsilon \left(\frac{\partial \tilde{\rho}}{\partial \xi} q + \tilde{\rho} \frac{\partial q}{\partial \xi} \right) = 0, \tag{8}$$

the mass balance reads

$$L_2 = \left(\tilde{\omega}\frac{\partial \tilde{\rho}}{\partial \tau} + \varepsilon q \frac{\partial \tilde{\rho}}{\partial \xi} \right) q + \tilde{\rho} \left(\tilde{\omega}\frac{\partial q}{\partial \tau} + \varepsilon q \frac{\partial q}{\partial \xi} \right) + \frac{\partial \psi}{\partial \xi} + 8 D_n \tilde{\rho} \left(q + \frac{1}{2} \sum_{i=1}^{k} \tilde{y}_i \right) = 0 \tag{9}$$

and the equations representing the friction due to Kagawa

$$L_{3,i} = \omega_{exc} \left(\frac{d\widetilde{y}_i}{d\tau} - m_i \frac{dq}{d\tau} \right) + \frac{\nu n_i}{R^2} \widetilde{y}_i = 0, \quad i = 1, 2, \ldots, k \tag{10}$$

using

$$\tilde{\omega} = \omega_{exc} \frac{L}{\sqrt{\frac{E}{\rho_0}}} \qquad D_n = \frac{\nu L}{\sqrt{\frac{E}{\rho_0}} R^2}$$

as dimensionless parameters of the system of differential equations.

3 GALERKIN METHOD

The nonlinear partial differential equations (8) and (9) have to be discretised along the scaled length ξ and the scaled time τ. The spatial discretisation along ξ can be achieved by using a Galerkin approach with a staggered grid as depicted in Figure 2. The pressure, flow rate and friction state distribution is approximated by the set of equations

$$\begin{aligned}
\widehat{p}(\xi, \tau) &= \psi_0(\tau)\, wp_0(\xi) + \sum_{j=0}^{N} \psi_{2j+1}(\tau)\, wp_{2j+1}(\xi), \\
\widehat{q}(\xi, \tau) &= \sum_{j=0}^{N} q_{2j}(\tau)\, wu_{2j}(\xi) + q_{2N+1}(\tau)\, wu_{2N+1}(\xi) \quad \text{and} \\
\widehat{\widetilde{y}}_i(\xi, \tau) &= \sum_{j=0}^{N} \widetilde{y}_{i,2j}(\tau)\, wu_{2j}(\xi) + \widetilde{y}_{i,2N+1}(\tau)\, wu_{2N+1}(\xi), \; i = 1, \ldots, k
\end{aligned}$$

using the weighting functions wp and wu defined in Figure 2.

With these definitions one can eliminate the only spatial coordinate via integrating the equations (8) up to (10) within the corresponding intervals of the spatial discretisation. This

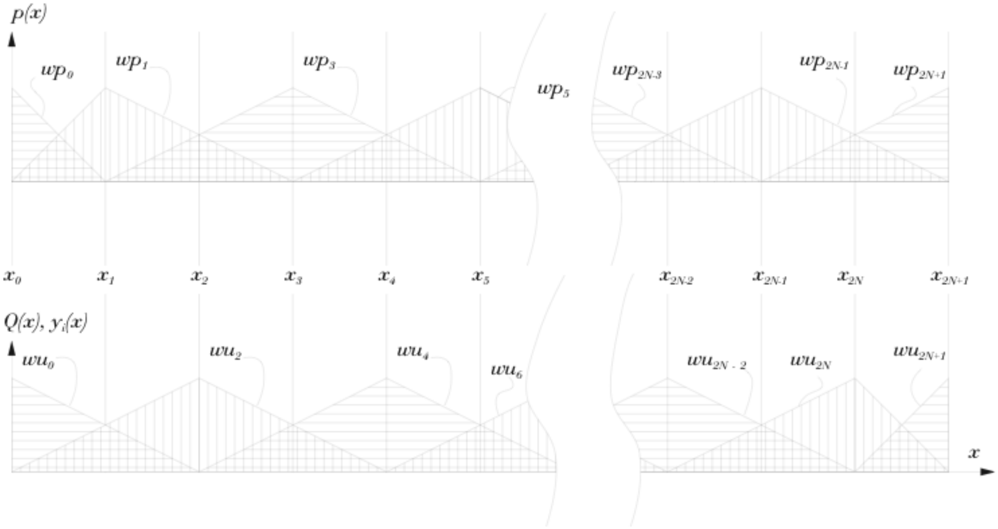

Figure 2: Staggered grid spatial discretisation.

method is called subdomain collocation [5] and its integrals read

$$\begin{aligned}
\int_0^{\frac{1}{2N+1}} L_1\left(\widehat{p},\widehat{q},\xi,\tau\right)d\xi &= 0\\
\int_{\frac{2j+1}{2N+1}}^{\frac{2j+3}{2N+1}} L_1\left(\widehat{p},\widehat{q},\xi,\tau\right)d\xi &= 0,\ j=0,\ldots,N-1\\
\int_{\frac{2j}{2N+1}}^{\frac{2j+2}{2N+1}} L_2\left(\widehat{p},\widehat{q},\widehat{\widetilde{y}}_i,\xi,\tau\right)d\xi &= 0,\ j=0,\ldots,N-1\\
\int_{\frac{2N}{2N+1}}^{1} L_2\left(\widehat{p},\widehat{q},\widehat{\widetilde{y}}_i,\xi,\tau\right)d\xi &= 0\\
\int_{\frac{2j}{2N+1}}^{\frac{2j+2}{2N+1}} L_{3,i}\left(\widehat{q},\widehat{\widetilde{y}}_i,\xi,\tau\right)d\xi &= 0,\ j=0,\ldots,N-1,\ i=1,\ldots,k\\
\int_{\frac{2N}{2N+1}}^{1} L_{3,i}\left(\widehat{q},\widehat{\widetilde{y}}_i,\xi,\tau\right)d\xi &= 0,\ i=1,\ldots,k,
\end{aligned}$$

which can be written as a system of equations

$$\mathbf{e}\left(\mathbf{z},\dot{\mathbf{z}},\theta\right)=\mathbf{0} \tag{11}$$

with

$$\begin{aligned}
\mathbf{z} &= \left[z_1,\ldots,z_{(N+2)(2+k)}\right]^\top\\
&= \left[\psi_0,\ldots,\psi_{2N+1},q_0,\ldots,q_{2N+1},\widetilde{y}_{1,0},\ldots,\widetilde{y}_{1,2N+1},\ldots,\widetilde{y}_{k,0},\ldots,\widetilde{y}_{k,2N+1}\right]^\top
\end{aligned}$$

the state vector and the parameter vector $\theta=[L,R,E,\nu,\rho_0,\widetilde{\rho}_\alpha,\alpha,p_0,p_s,\varepsilon,\omega_{exc}]$ in the time domain. At this point it is important to mention, that one is only interested in periodic solutions of the dynamical behaviour of the pipe. So it is easy to understand that the time functions of the entries in $\mathbf{z}$ can be transformed into the frequency domain via a Fourier transformation to

$$z_i\left(\tau_m\right) = a_{0,i} + \sum_{j=1}^{N_\omega} \left(a_{j,i} \cos\left(j\tau_m\right) + b_{j,i} \sin\left(j\tau_m\right)\right)$$

and further it is simple to calculate the derivatives of the state vector, which can be written as

$$\dot{z}_i\left(\tau_m\right) = \sum_{j=1}^{N_\omega} \left(-a_{j,i} j \sin\left(j\tau_m\right) + b_{j,i} j \cos\left(j\tau_m\right)\right)$$

with $\tau_m = \frac{m}{N_{fft}} 2\pi$, $m = 0 \ldots N_{fft} - 1$, N_{fft} as the number of samples per period and N_ω as the number of accounted frequencies. Considering the spectral components $a_{j,i}$ and $b_{j,i}$ it is possible to transform equation (11) into the frequency domain. Following, one obtains a nonlinear system of equations with the unknown variables $a_{j,i}$ and $b_{j,i}$. This system of equations can be solved via established algorithms. The obtained solution can be easily transformed back into the time domain and thus the problem is concluded.

4 RESULTS

The considered pipe line, which is depicted in Figure 3, is basically characterised by the physical parameters specified in Table 1. The pressure excitation on the left end ($\xi = 0$) of the pipe has the form of a cosine at constant frequency. The dynamic excitation is superimposed on a certain mean pressure such that pressure values of the excitation are located in the approximately linear domain of the material law. The interesting output is the pressure signal at the opposite end of the pipe ($\xi = 1$), assuming that the pipe is closed at this position ($q(1, \tau) = 0$). Further the discretisation of the pipe is listed in Table 2, which is very important to get the expected results.

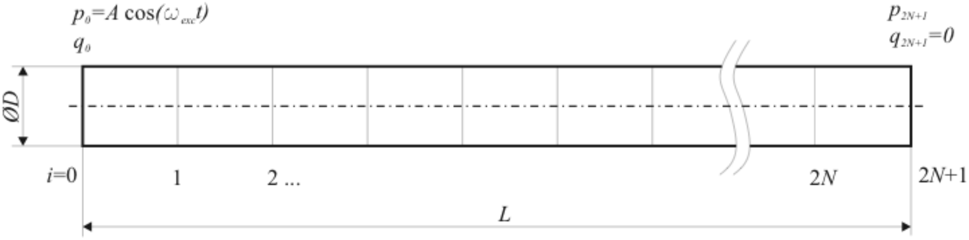

Figure 3: Discretised pipe line.

The first result represents the system output at the excitation frequency $\widetilde{\omega} = 0.06$ (see Figure 4), which is far below the first eigenfrequency of the pipe. So the output pressure is nearly the input pressure.

Table 1: Example parameter set.

L	5	m	pipe length
R	$5e^{-3}$	m	pipe (internal) radius
ρ_0	860	$\frac{kg}{m^3}$	density of the gas free fluid at reference pressure
p_s	$100e^5$	Pa	scale pressure
ν	$40e^{-6}$	$\frac{m^2}{s}$	kinematic viscosity
E	$1.6e^9$	Pa	bulk modulus of compressibility of the liquid phase
α	5	$\%$	volume ratio of gas vs. liquid at reference pressure
T	300	K	absolute temperature
R_s	287	$\frac{J}{kgK}$	specific gas constant
p_0	$1.0e^5$	Pa	reference pressure

Table 2: Parameters of discretisation.

N	10	characteristic number of elements
k	0	number of Kagawa friction terms
N_{fft}	128	number of samples per period
N_ω	10	number of accounted spectral components

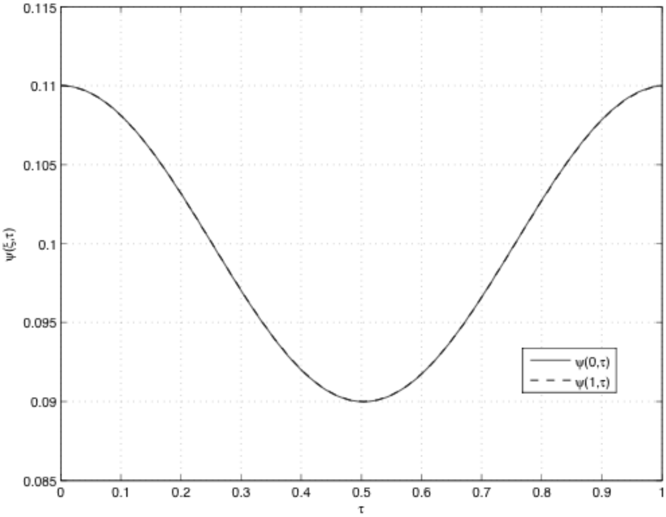

Figure 4: Excitation pressure vs. output pressure at $\widetilde{\omega} = 0.06$.

It is a more interesting case, when the excitation frequency increases. With an increase of the excitation frequency towards the first natural frequency (λ - quarter resonance at $\widetilde{\omega} = \frac{\pi}{2}$), the amplitude of the output pressure gets consequently higher. A closer look at Figure 5 shows, that the output pressure does no longer represent a response of a linear system. Looking at the mean value ($\overline{\psi} = 0.1$) one can see, that the attribute of a constant phase shift over one period at linear systems is already violated.

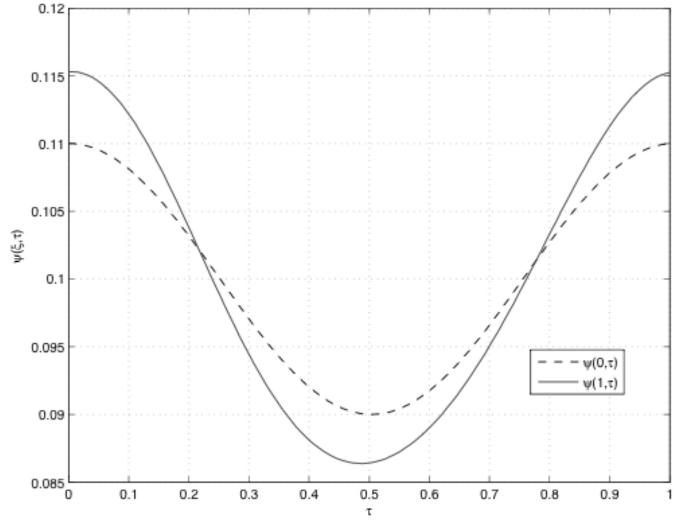

Figure 5: Excitation pressure vs. output pressure at $\widetilde{\omega} = 0.785$.

The most interesting case is shown in Figure 6, where the excitation frequency is quite near the first eigenfrequency of the pipe. One can immediately see, that the curve of the output pressure is flattened at the lower values. This can be explained by the nonlinear material law, because at very low pressures the effective bulk modulus of the fluid tends to zero and thus the alteration of the pressure tends to zero too.

5 CONCLUSIONS AND OUTLOOK

In the previous sections the modelling of nonlinear wave propagation at laminar flow in a transmission line at very low pressure rates could be described efficiently and the results for periodic solutions were presented. The considerations assume a constant bulk modulus of the fluid, a linearised material law of the liquid phase and an isothermal change of state of the gas in the fluid. So the further field of research in future will concentrate on using the nonlinear material law of the liquid phase and using a polytropic change of state of the entrained gas in the fluid. Moreover the decrease of the calculation time will be part of the work in future.

Considering an expansion of this theory to entire networks of pipes, which are situated at applications working cyclically down to very low pressure values, this method delivers interesting insight to the dynamical behaviour and gives hope to eliminate well known problems on real applications.

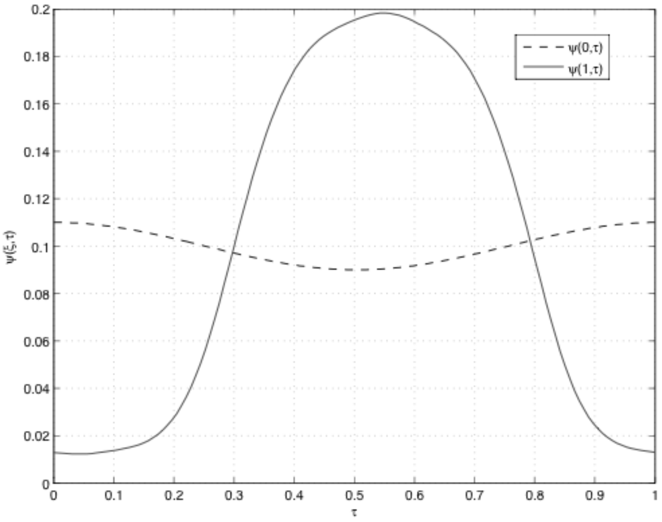

Figure 6: Excitation pressure vs. output pressure at $\widetilde{\omega} = 1.57$.

6 Acknowledgment

The authors gratefully acknowledge the sponsoring of this work by the 'Linz Center of Mechatronics' in the framework of the Kplus program of the Austrian government. This program is funded by the Austrian government, the province of Upper Austria and the Johannes Kepler University Linz.

References

[1] A.F. D'Souza and R. Oldenburger. Dynamic response of fluid lines. *Trans. ASME, J. Basic Engng*, 86:589–598, 1964.

[2] H. Theissen. *Die Berücksichtigung instationärer Rohrströmung bei der Simulation hydraulischer Anlagen*. Dissertation, Rheinisch-Westfälische Techn. Hochschule Aachen, 1983.

[3] J.-J. Shu, C.R. Burrows, and K.A. Edge. Pressure pulsations in reciprocating pump piping systems, part 1: modelling. *Proc. Instn. Mech. Engrs.*, 211(I):229–237, 1997.

[4] T. Kagawa, I.-Y. Lee, A. Kitagawa, and T. Takenaka. High speed and accurate computing method of frequency-dependent friction in laminar pipe flow for characteristics method. *Trans Jap Soc Mech Engrs B*, 49:2638–2644, 1993.

[5] K.J. Bathe. *Finite element procedures*. Prentice Hall, 2nd edition, 1995.

Applications

Optimised Pace Drive Concept for Glass Panel Conveyors

David Prust
Hubertus Murrenhoff
Institute for Fluid Power Drives and Controls, RWTH Aachen University, Germany

ABSTRACT

In the production of flat screens, semi conducting material is deposited onto large glass panels. This requires a considerable number of different processes similar to those used in the fabrication of computer chips. As the production cannot be carried out on a single device, the panels have to be transported between different working stations, avoiding contamination or damage. For this purpose, conveyors comprising of a number of wheels, part of which are electrically driven, are state of the art. However, these wheel conveyors are prone to impair the glass substrates due to skid marks on the glass surface. The general workaround for this problem is the use of wheels whose skid marks can be easily removed. Yet, in order to reduce the production cost of the displays, cleaning processes should be kept to a minimum, as they do not contribute to the desired function of the display, but only cover up for imperfect manufacture.

A significant amelioration could be achieved by replacing the wheel conveyor with a pneumatic pace drive comprising of an array of suction pads mounted to rodless cylinders. Their suction pads are capable of establishing a reliable connection with the glass surface, reducing the risk of slipping, and thus the extent and the amount of marks. In order to achieve a steady movement, the panel is passed on from one suction pad to the next. The combination of an optimised control strategy with an integrated design provides better functionality as well as low running costs.

This paper presents methods to optimise the design of pneumatic pace drives concerning running costs as well as accuracy.

Power Transmission and Motion Control 2007 Edited by Dr D N Johnston and Professor A R Plummer
© With The Centre for Power Transmission and Motion Control

1 INTRODUCTION

Within the scope of a project funded by the Deutsche Forschungsgemeinschaft (German Research Foundation, DFG), the Institute for Fluid Power Drives and Controls (IFAS) of RWTH Aachen University and the company FESTO AG & Co. KG are developing a concept for a conveyor based on a pneumatic pace drive. The goal is to present an alternative to established electrically driven devices, which complies with the high demands of display manufacture.

During the manufacture of flat liquid crystal displays, semi-conductive structures are deposited on an appropriate substrate carrier. State of the art is the use of large glass panels as substrate carriers which are coated with integrated circuits. After a series of assembly steps the completed displays are cut out of the substrate. Currently glass panels of up to 2.2 m by 2.4 m, with a thickness of 0.5 to 0.8 mm and a weight of up to 15 kg, are used, while there is an intention to use even larger panels, with a thickness below 0.5 mm. Due to the coating of the substrate carrier with semi-conductive material, any contamination of the glass surface has to be prevented. However, as several special working stations are necessary to process the substrate during the process, it is inevitable to transport the panels from one working station to another. A typical transport system consists, for example, of one or more loading docks, several transport modules with inspection devices and an end stocker, where the panels are stored until further processing. While being transported, the glass panels typically move at speeds of 0.3 metres per second with a gap of 100 to 200 millimetres between them.

The transport of the panels bears the risk of contamination of the substrate due to dust, which settles onto the surface, or due to abrasion, which is caused by the contact of handling devices with the substrate. Contamination due to particles is counteracted by keeping the production line within a cleanroom environment.

Impairment of the panels by a handling device however, has to be avoided by providing a handling technology that treats the substrates as gently as possible. The very sensitive semi-conductive surface on the upper side of the panels may not be touched in any way. The corresponding restrictions are comparable to those in the handling of wafers. Unfortunately, due to the dimensions and the weight of the panel compared to a wafer, contact-free handling technologies like devices using Bernoulli- or ultrasound-effects do not apply or come at high costs due to high energy consumption. Therefore, contact on the top surface is not permitted.

The large scale and the small thickness of the panels impose further restrictions upon the transport system. For example, the substrates can be flexed easily without provoking any damage. Fissures however, which can easily be induced by small impacts around the edge of the panel, expand quickly and cause the substrate's destruction. Zones which are close to the substrate's edges are therefore inappropriate for handling purposes such as alignment. Another requirement is to adequately support the panel in order to prevent excessive bending.

In order to meet these requirements, the panels are often transported on wheel conveyors as shown in **Figure 1**. Usually, only a fraction of the wheels are actively driven, while the others support the substrate. The driven wheels are operated by synchronized electric motors in order to achieve equal speeds on all driven wheels. The axial alignment of the panels is achieved by cylindrically shaped wheels along the substrate's sides.

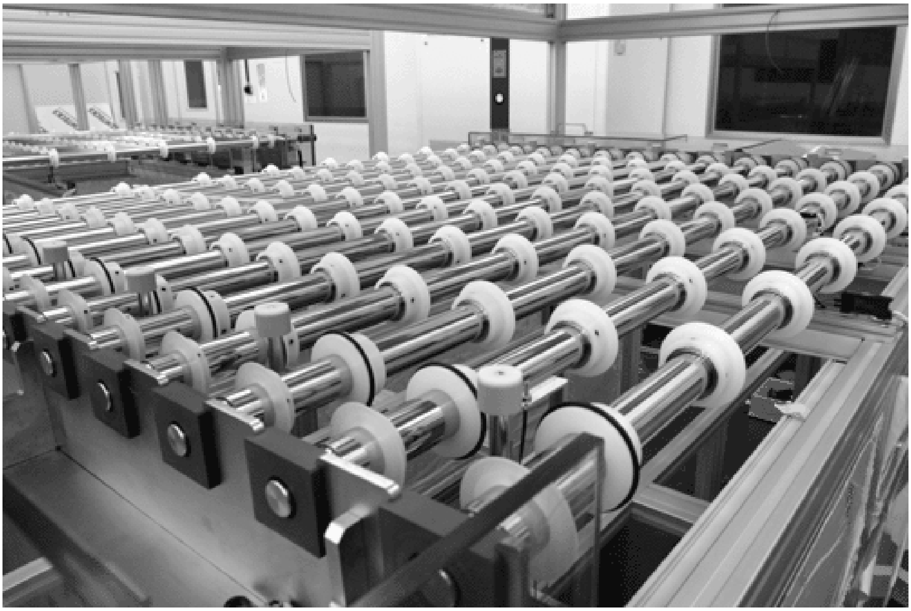

Figure 1: Electrically driven wheel conveyor, Inatech Co., Ltd, Korea

Although the wheel conveyor provides a quite simple and obvious solution to the problem of transporting flat panels, its main downside is the low traction between the driven wheels and the glass surface. Since the transmission is based on force-locking, the friction between wheel and surface must be large enough to transfer the drive's acceleration to the substrate and to compensate for the forces imposed on the panel by the friction of the passive wheels which support and align the substrate.

Provided that dry friction is present, the maximum force which can be used to propel the panel yields

$$F_{a,\max} = \mu F_G = \mu g m_{Substrate} \tag{1}$$

where μ is the friction coefficient, F_G is the gravity force of the panel and $m_{\mathrm{Substrate}}$ is the mass of the panel.

The friction coefficient between wheel and glass surface typically yields values among 0.1 and 0.3. This is worsened if only some of the wheels are driven, as then only a fraction of the panel's weight contributes to the friction force. That way, the remaining force that can be transferred in order to accelerate the substrate is rather small. The passive support wheels have to be accelerated by the moving panels, and therefore hinder their acceleration as well.

If the resistance imposed by the passive wheels and the inertia of the panel exceeds the maximum force that can be transferred by the contact surface, the driven wheels start to skid on the glass surface. The skidding causes marks on the surface, which have to be removed before further processing. In order to facilitate the cleaning process, wheels made of materials, the residue of which can be easily removed, are preferred. Therefore, the wheels are often made of Polyetheretherketone (PEEK) which unfortunately features a very small friction coefficient, and thus, raises the risk of skidding.

2 PNEUMATIC DRIVE CONCEPT

The main goal of the pace drive project, funded by the Deutsche Forschungsgemeinschaft, is to demonstrate that the disadvantages of the established wheel conveyors can be eliminated by an alternative drive concept. A prototype of the pace drive, developed in collaboration of FESTO and the Institute of Fluid Power Drives and Controls, will demonstrate the new concept's ability to meet the requirements mentioned before, as well as to reduce the downsides of established devices. As the main disadvantage of wheel conveyors is the risk of skidding, the first step in order to improve the drive concept is to find a way to establish a secure and skid-free contact between the drive and the glass panel. The contact device must therefore provide a high holding force, but may not overstress the substrate.

This can be achieved by securing the glass substrate with suction pads from underneath. Evacuating the suction pad enables it to generate a high normal force towards the surface of the glass panel. Moreover, the normal force generated is independent of the panel's weight. That way, it can provide high holding forces even in case of low friction coefficients, creating a reliable, skid-free connection. By optimizing the suction pads geometry, the stress imposed on the substrate can be minimized. If the suction pad is torsion-proof, it is possible to inhibit angular deviations of the panel as well, so that the constant alignment of the substrate by additional alignment devices can be kept to a minimum. Exact alignment would only be necessary before loading the substrate into a working station. This contributes to the protection of the panel's edges, which are prone to destruction due to small impacts, and avoids the necessity of a symmetric design in order to reduce angular moments.

The transport movement can be realized using a pneumatic drive. Rodless cylinders provide compactness and are therefore well suited for the task. In order to realize a continuous forward movement, at least two pneumatic drives, with one suction pad each, are required. The continuous movement is created by an alternating movement of the drives, during which one of the drives moves forwards while being in contact with the panel. The other drive moves backwards at the same time in order to reach its starting position and takes over the panel after having accelerated until transport speed is reached. This way, the glass panel is always attached to either one of the drives. A key precondition to achieve handing over the panel from one drive to the next is that both drives move at equal speed at the time of handoff.

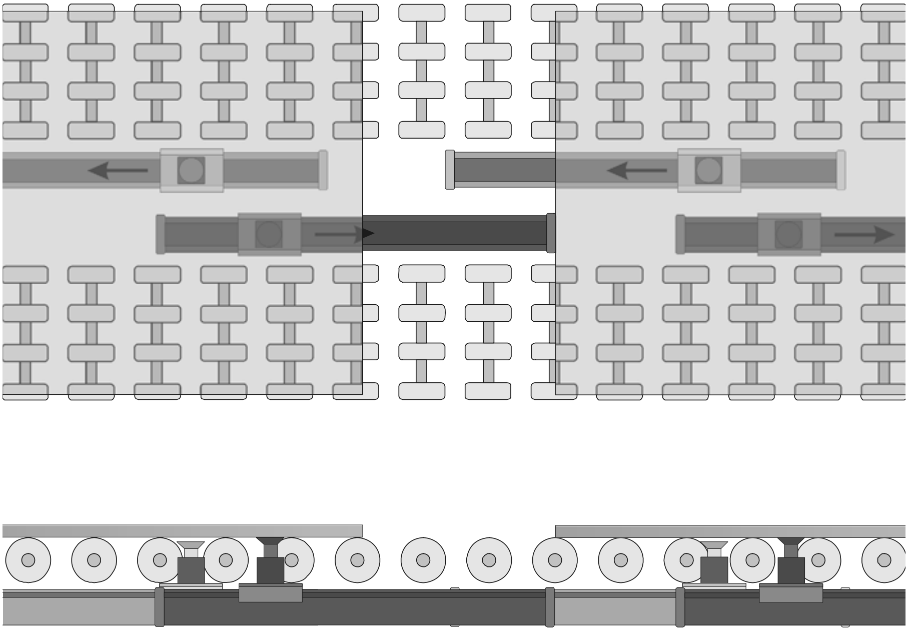

Figure 2: Functional principle of a pneumatic pace drive

The pace drive concept has to meet new requirements considering the operation and control of pneumatic drives. The properties of the pneumatic drives are defined by constraints which are significantly different from those of a regular handling device. For a regular handling device the necessary drive stroke is defined exclusively by the distance the drive has to bridge, unlike the pace drive, the stroke of which is influenced by its velocity along with a variety of factors, which will be exemplified as follows.

3 DIMENSIONING THE PACE DRIVE

In order to create a continuous movement of the panel with discontinuously working pneumatic drives, it is required that at least two drives alternately take over the transport of the work piece. The motion sequence of each drive consists initially of an acceleration phase, during which the drive reaches the desired conveyor speed. The acceleration phase is followed by the handover of the panel from the suction pad which was in contact before. During this phase it is required that both drives move at exactly the same speed, as a difference would lead to skidding of one of the suction pads, which would leave an unwanted mark. The length of this handover period is defined by the time necessary to bring the suction pad into contact with the substrate’s surface and evacuate it. After the handover is completed, the actual transport phase begins, during which the panel is being transported by the drive. After another handover, the drive whose suction pad is no longer attached to the panel will return to its starting position and restart the cycle, in order to reach the desired speed again.

If two pneumatic cylinders are being used to create the conveying movement, their movement sequences are shifted by half a cycle. If a continuous conveyor movement is desired, it has to be ensured that the transport phase is long enough to allow the drive whose suction pad is disconnected to return to the starting position and reaccelerate until the conveyer speed is reached. The required cylinder stroke is consequently deduced from the time required for each phase of the motion sequence and the travel within this period.

The required stroke can be calculated from an acceleration profile, which can be chosen according to process requirements e.g. a jerk-minimised motion. Jerk-minimised motion can be achieved for example by a trapezoidal or sinusoidal gradient of the acceleration profile, so that the acceleration reaches its maximum value smoothly rather than jumping to the desired value. By defining a sequence of time steps, the acceleration can be represented by a piecewise function, as in **equation (2)**.

$$a_{\text{target}}(t) = \begin{cases} a_{\max}\dfrac{t-t_0}{t_1-t_0} & \forall\, t \in [t_0, t_1[\\ a_{\max} & \forall\, t \in [t_1, t_2[\\ a_{\max} - a_{\max}\dfrac{t-t_2}{t_3-t_2} & \forall\, t \in [t_2, t_3[\\ 0 & \forall\, t \in [t_3, t_6[\\ -a_{\max}\dfrac{t-t_6}{t_7-t_6} & \forall\, t \in [t_6, t_7[\\ -a_{\max} & \forall\, t \in [t_7, t_8[\\ -a_{\max}\dfrac{t-t_8}{t_9-t_8} & \forall\, t \in [t_8, t_9[\\ 0 & \forall\, t \in [t_9, t_{10}[\end{cases} \qquad (2)$$

The function defines a trapezoidal shape of the acceleration plot as shown in **Figure 3**. Events during one movement cycle are indicated by points named t_0 through t_{10}. The acceleration and deceleration phases take place between the time steps t_0 through t_3 and t_6 through t_9 respectively. At t_3, the previously inactive suction cup starts closing onto the glass surface and is being evacuated, in order to establish a secure connection between panel and drive. The suction gripper on the second drive, which had been active throughout the first drive's acceleration period, is then retracted and therefore hands the panel over. At t_4, the handover of the substrate from one drive to the next has just finished. From this moment on, the panel is moved on by one of the drives only. Meanwhile, the second drive returns to its starting position, accelerates to the conveyor speed and prepares for the next handover procedure. The transport phase ends at t_5 when another handover begins. After that, the drive decelerates and returns to its starting point in order to repeat the sequence.

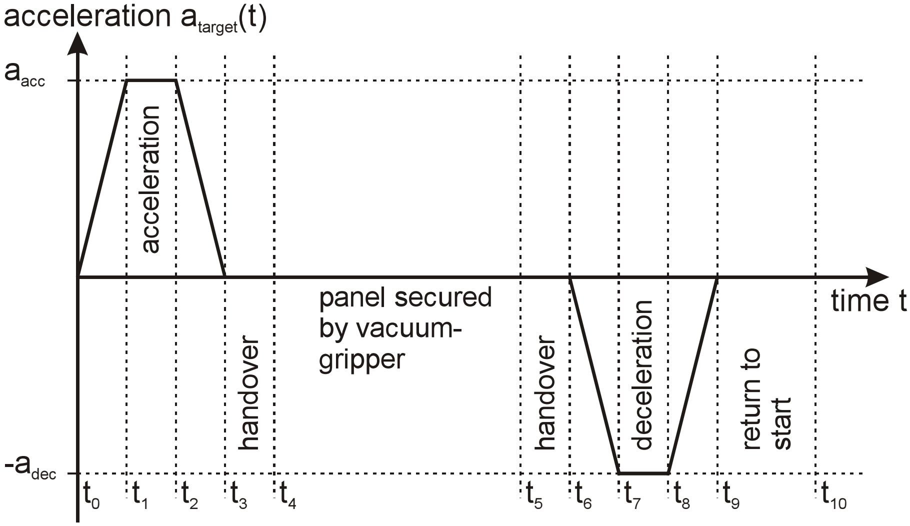

Figure 3: Acceleration plot

By integrating the function with respect to t, the functions for velocity and stroke can be obtained. Together with appropriate constraints the functions form a system of equations which allows for the identification of the required drive stroke. Some of these constraints correspond to the drive properties, while others can be chosen in order to maximise the transport phase. This is of importance for an economic operation of the conveyor, as a maximised transport phase assures a high efficiency of the drive.

While dimensioning the pace drive, various requirements, which might counteract each other, can be taken into account. For example, one goal of the dimensioning can be to determine the minimal drive stroke necessary to allow for a certain conveyor speed, i.e. the constant speed at which the glass panels are transported. Thus, a minimum requirement can be defined, i.e. the pneumatic drive to be chosen must feature at least the calculated stroke. Otherwise, the desired conveyer speed cannot be achieved.

The graph in **Figure 4** shows the required minimal drive stroke in order to assure a conveyor velocity of 0.3 m/s against the maximum acceleration and the required time t_{h_off} to perform the handover. That is, in order to achieve a continuous panel movement of 0.3 m/s, the necessary cylinder stroke corresponds to the maximum acceleration of the drive and the time needed for handing the panel over from one drive to another.

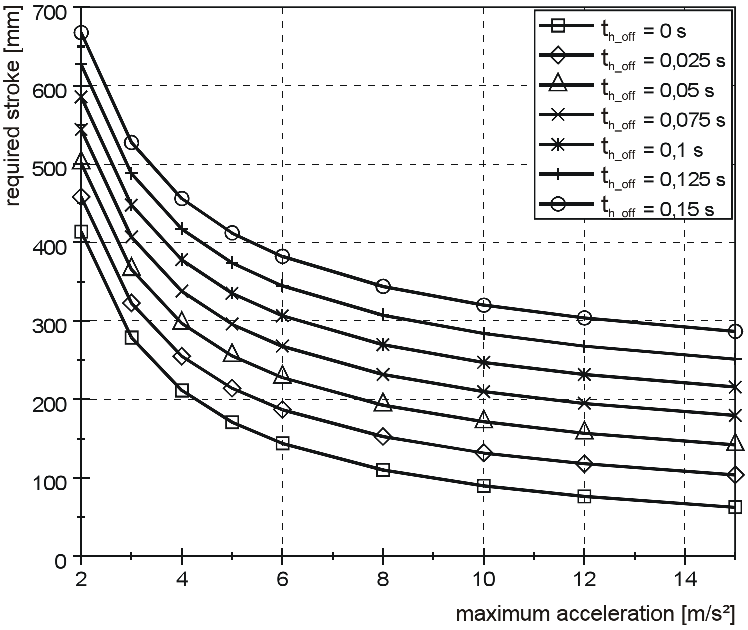

Figure 4: Required drive stroke for a conveyor speed of 0.3 m/s against max. acceleration and handoff time

The time spent during the handover process is basically defined by the period in which the suction pads can be evacuated. At present, periods between 0.1 s to 0.15 s are achievable, given an appropriate size of the vacuum cup in order to secure the panel. If a handover period of 0.125 s and a maximum acceleration of 10 m/s^2 are assumed, the required minimal drive stroke to achieve the desired movement yields 285 millimetres. Therefore, the pace movement can be obtained with relatively compact pneumatic cylinders.

In order to allow for an economic operation of the pace drive, it is essential that the demanded transporting task can be realised at the least expense possible. Pneumatic drives feature the advantage of being relatively inexpensive as well as being easily operated using a centralised pressure supply. A disadvantage is the low efficiency of the generation of compressed air. To counteract this downside, it is necessary to ensure that the drive itself works as economically as possible. The required amount of pressurised air is firstly affected by the geometry of the pneumatic cylinder of the pace drive, but can also be influenced significantly by an effective control strategy [1]. The latter can be utilised to reduce the consumption of compressed air noticeably.

The part of the air consumption which is affected by the cylinder's geometry, can already be reduced during the concept phase of the pace drive. Therefore it is of interest, whether an optimized geometry can be found, that assures an economic operation.

Taking costs of purchase and operation of a pneumatic cylinder, related to the amount of substrate which can be transported during its lifetime, into account, the costs can be estimated against the cylinder stroke. The estimate incorporates the capital expenditure to purchase necessary components like valves, lines and position transducers. When plotting the operational cost against the drive stroke, the graph in **Figure 5** is obtained.

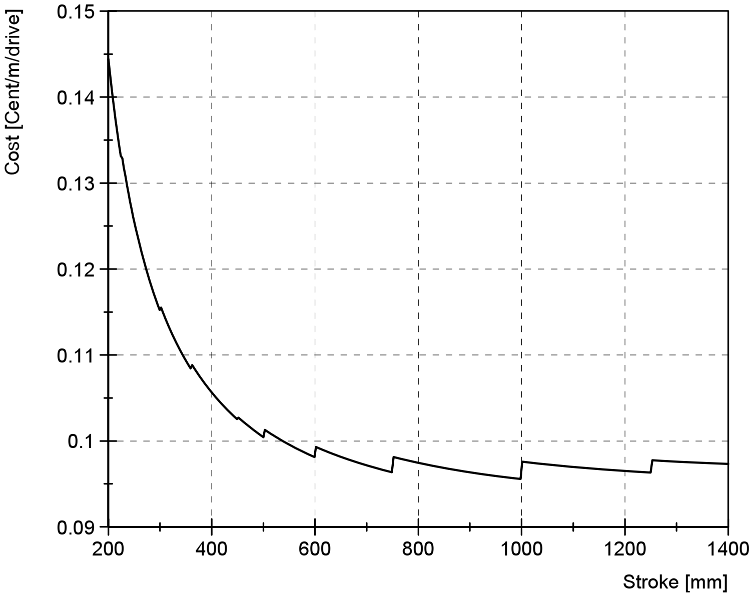

Figure 5: Running cost against drive stroke

The calculation is based on catalogue prices for the required components. The cost of one cubic meter of compressed air at a pressure of 6 bar is approximated by 0.054 Euro. This value is based on data obtained from the Federal Ministry of Economics and Technology [5] which specifies the energy costs for the Asian-Pacific region as 0.093 Euro/kWh in 2003. Taking the properties of an appropriate compressor into account, a raw estimate of the expenses can be calculated. Naturally the actual operational cost can vary depending on the individual case. Therefore the graph serves as a means of clarification in order to show the influence of the cylinder stroke upon the costs. The discontinuous characteristics of the graph are due to the position sensor, which is only available at certain lengths and therefore raises the costs abruptly, when a larger range is required.

For the required minimal stroke of 285 millimetres, the calculation yields a cost of 0.118 Cents per meter of conveyed substrate per cylinder. Thus, if for example 50 pairs of cylinders are necessary for the entire conveyor assembly, the cost would amount 0.118 Euro per meter of transported substrate, whereas the transport device would be capable of conveying an estimated 2500 kilometres of glass panels during its lifetime of approximately 3.7 million cycles.

The graph in **Figure 5** shows a minimum at a drive stroke of 1000 millimetres. The larger stroke enables the drive to convey more substrate per cycle, which results in a cost benefit although the initial costs for components are higher. 2500 kilometres of glass panels would be conveyed at a price of 0.096 Cents/m/cylinder, which would amount to a total benefit of

552.4 € per drive over the lifetime. Given that the entire conveyor system requires a large amount of drives, the benefit is significant. Thus, a pneumatic drive featuring a stroke of 1000 millimetres can be regarded as being the optimal choice for the task from an economic point of view.

4 SERVO-PNEUMATIC CONTROL

In order to meet the requirements for an optimised conveyor device, the drive speed has to be precisely controlled. This is of special importance during the handover procedure, as differing speeds of the suction pads in contact with the panel could cause the substrate to lose its proper angular alignment. Furthermore, the pace drive must feature a possibility to change the transport speed during operation. That way, the pneumatic drive would be capable of controlling the gap between the substrates.

In the scope of servo-pneumatic controls, many innovative concepts have been developed over the past years. Amongst those are nonlinear controls, for example the first exact linearization of a pneumatic servo-drive by [3], or controls employing inverse dynamics, as presented in [2]. Göttert describes in [4] a concept for the position control of servo-pneumatic drives, involving both linear controllers combined with a nonlinear feed forward control as well as nonlinear controls based on exact linearisation.

The above mentioned publications focus on exact position control, as the controls proposed derive from drives used in handling tasks, such as the picking and placing of objects, or the tracking of a desired trajectory. Those tasks require very high precision in positioning. Consequently, the concepts presented are of high complexity in order to assure the desired functionality. The pace drive however, requires much less accuracy, as its main feature is to convey substrates at a constant speed. As high accuracy is only essential while the panel is coupled to the suction device, a lower preciseness during other phases of drive motion can be tolerated. From an economical point of view, a precise control during these phases is not desirable. It only raises the complexity of the control, but doesn't contribute to the objective, which is merely to ensure that the correct speed is reached and maintained during the transport period of each drive. Therefore, the pace drive basically has just one operational point around which exact control is required. Thus, the control of the pace drive can be designed quite simply, which will be exemplified shortly as follows.

In order to be inexpensive, the control should require only few sensors. For example, only the actual position and speed signals are available. Still, the drive should be capable of reaching the desired conveyor speed quickly and maintaining it within an acceptable tolerance.

Pneumatic drives have the feature of being easily adjustable to maintain a constant speed by restricting the air flow on the exhaust side of the drive. Taking advantage of this and using the desired velocity as input, the input signal for the exhaust valve can be calculated from the valve's conductance compared to the conductance needed in order to reach the desired speed. The outlet flow restricted by the valve is usually a supercritical flow. Therefore the mass flow through the valve yields

$$\dot{m}^{*} = C_{\mathrm{Valve}} p_1 \rho_0 \sqrt{\frac{T_0}{T_1}} \qquad (3)$$

With $\dot{m}^{*}$ as the mass flow, C_{Valve} as the valve's Conductance, p_1 as the pressure in the cylinders exhaust side, i.e. before the valve, ρ_0 as the reference density of air under technical conditions, i.e. at $T_0 = 293.15$ K and 1 bar. T_1 is the temperature of the air inside the cylinder, as corresponding to p_1.

At the operational point, the drive moves at a constant speed. Assuming that friction and other forces imposed upon the drive are constant, the pressure in the outlet side of the cylinder can be considered to be constant as well. Therefore, the mass flow can be expressed as the product of the piston's cross section A_{Cyl}, the drive's velocity v_{Cyl} and the density ρ_1, as in **equation (4)**.

$$\dot{m}^{*} = A_{\mathrm{Cyl}} v_{\mathrm{Cyl}} \rho_1 \qquad (4)$$

Combining **equations (3)** and **(4)** yields

$$A_{\mathrm{Cyl}} v_{\mathrm{Cyl}} \rho_1 = C_{\mathrm{Valve}} p_1 \rho_0 \sqrt{\frac{T_0}{T_1}}$$

$$\Leftrightarrow C_{\mathrm{Valve}} = \frac{A_{\mathrm{Cyl}}}{R_0 \rho_0 T_0} v_{\mathrm{Cyl}} \qquad (5)$$

with $p_1 = R_0 \rho_1 T_1$

and assuming $T_0 = T_1$

The calculated conductance can then be transformed into the valve's input signal in order to adjust the valve to the desired conductance. Combined with a closed loop control of the velocity, the drive would already feature sufficient accuracy if the goal was to achieve a continuous movement. However the cyclic movement of the pace drive requires a perpetual change of direction, and in order to preserve as much of the drive stroke for conveying the substrate, the time in which the drive changes direction and reaches the desired speed must be kept as short as possible. If only the valve input necessary for a constant velocity is forwarded, the drive reaches the commanded speed too slowly to assure an acceptable functionality. This is due to the fact that the exhaust side of the moving cylinder first has to be depressurized in order to allow for the piston to be accelerated in the opposing direction. Thus, it is beneficial to speed up the valves reaction whenever a direction change is to be conducted. This can be achieved by generating a signal for the acceleration necessary to perform the velocity change, and forwarding it as valve input, where the signal can either be forwarded after being multiplied with a proportional factor or rather being processed by a response algorithm which boosts the valve input when high acceleration is needed, and lessens its influence when only small changes occur. For example the acceleration gain can be defined as follows:

$$U_{\text{Input}}\left(a_{\text{target}}(t)\right) = \begin{cases} U_{\max} & \forall a_{\text{target}}(t) \;\middle|\; a_{\text{target}}(t) \geq a_{\text{threshold}} \\ 0 & \forall a_{\text{target}}(t) \;\middle|\; -a_{\text{threshold}} > a_{\text{target}}(t) < a_{\text{threshold}} \\ -U_{\max} & \forall a_{\text{target}}(t) \;\middle|\; a_{\text{target}}(t) \leq -a_{\text{threshold}} \end{cases} \tag{7}$$

Where U_{Input} is the input signal, $a_{target}(t)$ is the target acceleration as in equation (2) and $a_{threshold}$ is a chosen threshold beyond which the valve is forced to open despite of the signals generated by the controller or the feed forward signal for the velocity.

The present design incorporates a mono-flop element which holds the acceleration gain input for a certain period of time, in order to boost the drive's acceleration. This results in the pneumatic cylinder reaching the desired speed within a short amount of time, without any influence from the controller. It is therefore capable of reacting quickly. **Figure 6** shows a sketch of the control design.

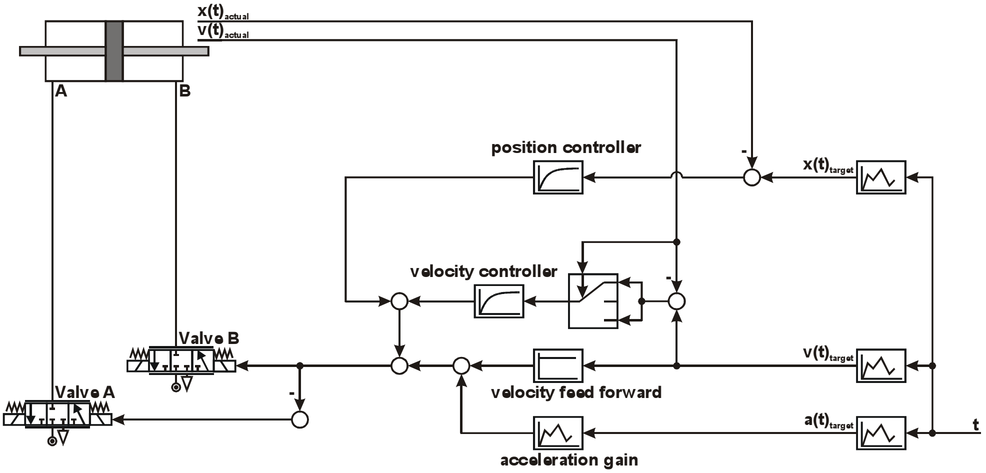

Figure 6: Control design of the pneumatic pace drive

Combined with a closed loop control for the drive's velocity and position, the drive provides an acceptable accuracy. Both are controlled by first order lag elements, whereas the velocity controller is inactive unless the drive's actual speed has already closely approached the desired value. Once this occurs, the controller switches on and can therefore operate at a higher gain without causing oscillations. The position control is included to prevent the drive from hitting the end position, as this would lead to the drives destruction. **Figures** 7 and **8** show plots of simulation results comparing desired trajectory and velocity against their actual values. The simulation has been carried out using DSH*plus*.

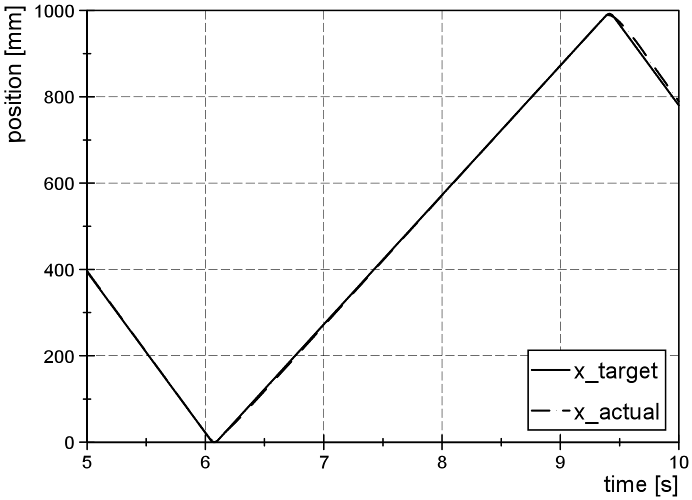

Figure 7: Comparison of target trajectory with actual trajectory

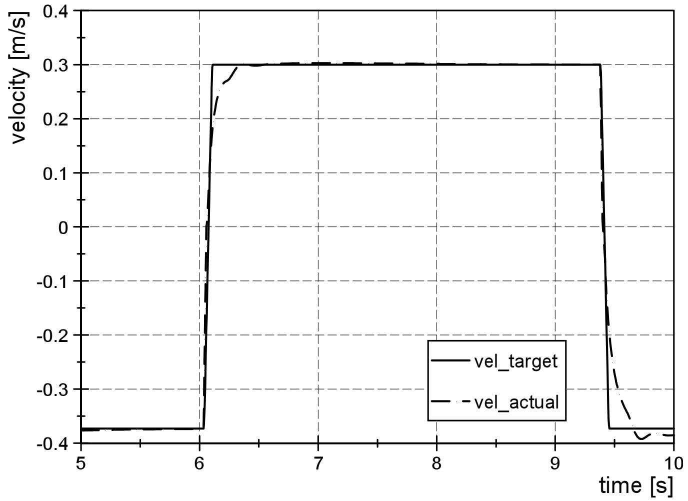

Figure 8: Comparison of target velocity with actual velocity

Admittedly, the control design cannot rival controls based on complex models, but it shows acceptable accuracy and features some advantages over more complex designs, which include simple implementation and low cost. Considering the large amount of drives necessary in order to provide a complete conveyor assembly, simplicity and therefore low cost must be emphasized, as the pace drive can only compete with established devices by providing at least the same functionality at lower overall cost.

5 CONCLUSION

The pneumatic pace drive offers a promising alternative over established electrically driven conveyors. If economic aspects are considered within the design, the overall costs can be significantly reduced, raising the acceptance of this new drive concept. Adding to this is a superior performance, reducing unwanted impairment of the glass panels during transport. A method to choose an appropriate pneumatic cylinder considering its economic efficiency as well as a simple but well adapted controller design was presented, which allows for good accuracy while being easy to implement and therefore economically efficient.

6 REFERENCES

[1] Gauchel, W.: Entwicklung und Regelung eines integrierten und flexiblen servopneumatischen 2-Backengreifers (Design and control of an integrated, flexible, servo-pneumatic 2-Jaw Gripper), Dissertation, RWTH Aachen University, 2006

[2] Sesmat, S., Scavarda, S., Lin-Shi, X.: Verification of electropneumatic servovalve size using non-linear control theory applied to cylinder position tracking, 4th Scandinavian International Fluid Power Conference, Tampere, Finland, Sept. 1995, S. 504-513.

[3] Richard, E., Scavarda, S.: Nonlinear Control of Pneumatic Servodrive, Proc. 2nd Bath Int. Fluid Power Workshop, Bath, Great Britain, 1989, S. 59-75.

[4] Göttert, M.: Bahnregelung servopneumatischer Antriebe (Position Control of servo-pneumatic drives), Dissertation, Siegen University 2003.

[5] Bundesministerium für Wirtschaft und Energie: Energiedaten: Zahlen und Fakten, nationale und internationale Entwicklung (Federal Ministry of Economics and Technology: Data on Energy prices, facts and figures, national and international development), Germany, dated from June 2006, http://www.bmwi.de/Navigation/Technologie-und-Energie/Energiepolitik/energiedaten.html

Electric hydrostatic drive – a concept for the clamping unit of a high-speed injection moulding machine

S Räcklebe and S Helduser
Institute of Fluid Power (IFD), Technische Universität Dresden, Germany

ABSTRACT

The paper deals with modelling, simulation and performance improvements of an electric hydrostatic driven clamping unit of a high-speed injection moulding machine. Main objective is to demonstrate the use of coupled simulation in the development of drive systems. Special attention is given to the modelling of components and subsystems of the hydrostatic drive concept but also on energy efficiency. Simulation results are validated by measurements.

NOMENCLATURE

A	cm²	area
d	mm	viscous friction
D	mm	damping ratio
f	Hz	frequency
F	N	force
h	mm	stroke
J	kg m²	inertia
K'	bar	bulk modulus of oil
n	1/min	speed
m	kg	mass
M	Nm	torque
p	bar	pressure
P	W	power
Q	dm³/min	volume flow rate
T	s	time constant
V	cm³	volume
x	mm	position
η	-	efficiency

Power Transmission and Motion Control 2007 Edited by Dr D N Johnston and Professor A R Plummer
© With The Centre for Power Transmission and Motion Control

1 INTRODUCTION

High-speed injection moulding machines are discontinuous periodic working machines that are made to produce as many as possible good quality plastic parts per time period. These facts set very high requirements on the whole drive system because of the complex plastic production process and the very short machine cycle time. That is why injection moulding machines have always given an essential stimulus to the development of new or improved hydraulic components and systems. Over the last years they have given impetus to advancements of hydraulic drive technology with regard to control features, energy efficiency and noise reduction /1/. **Fig. 1** gives an overview about available drive concepts in injection moulding machines. They can be divided in hydraulic, hybrid and electro-mechanical systems.

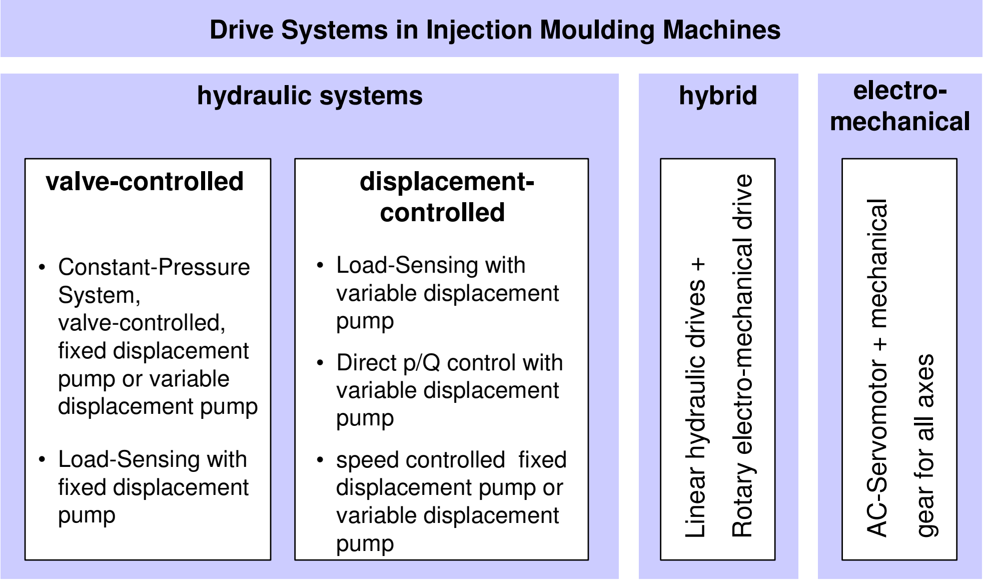
Drive Systems in Injection Moulding Machines
hydraulic systems
hybrid
electro-mechanical
valve-controlled
• Constant-Pressure System, valve-controlled, fixed displacement pump or variable displacement pump
• Load-Sensing with fixed displacement pump
displacement-controlled
• Load-Sensing with variable displacement pump
• Direct p/Q control with variable displacement pump
• speed controlled fixed displacement pump or variable displacement pump
Linear hydraulic drives + Rotary electro-mechanical drive
AC-Servomotor + mechanical gear for all axes

Fig. 1 Drive systems in injection moulding machines

The availability of modern power electronics for speed variable motors with an acceptable price has pushed the development, investigation and test of electric hydrostatic drive concepts. The main advantage is the direct volume flow control. Therewith, the efficiency is increased because immanent throttling losses of valves are avoided. Energetic investigations of different concepts lead to the fact that the speed variable, variable displacement pump is the most efficient /6/; however, the command response of this concept is not as good as necessary for high-speed injection moulding because of the superposition of motor and pump adjustment. The dynamic results point out the speed variable constant displacement pump as the best solution /1, 6/. **Fig. 2** shows the energetic behaviour of different duty points of pump controlled and speed controlled hydrostatic drive. The speed variable constant displacement pump is more efficient without load and in medium load duty point, but also approximately comparable with pump controlled drive in full load.

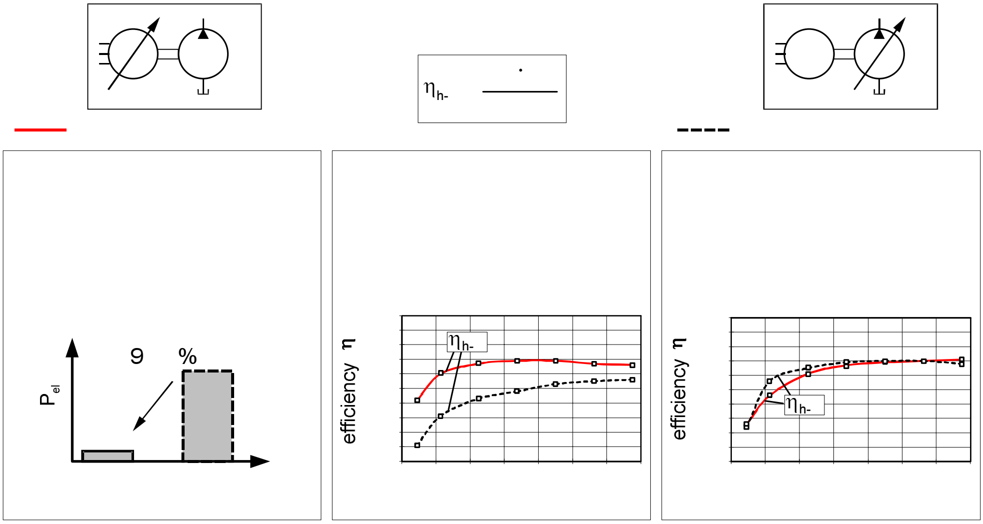

Fig. 2 Comparison of power consumption and efficiency /2/

2 CLAMPING UNIT

The clamping unit of an injection moulding machine has to realise two functions. The first is to open and close the mould in a defined position range and specific time period. The second is to lock/ unlock the mould parts with a process dependent clamping force. To realise these functions the drive concepts for clamping units mentioned in Fig. 1 are available. However, because of the needed high dynamics in high-speed injection moulding there are three relevant drive concepts for the clamping unit: the valve controlled system with constant pressure, the speed controlled constant displacement pump and the electro-mechanic drive, **Fig. 3**.

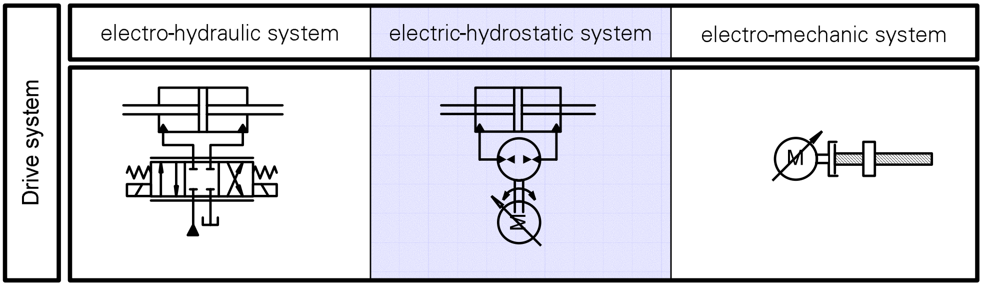

Fig. 3 Drive systems for high-speed injection moulding machines

All of these concepts can be found in small size machines (up to 1.000 kN clamping force). Medium size machines (from 1.000 kN up to 7.000 kN) are often equipped with valve controlled systems with constant pressure or speed controlled constant displacement pumps. The range of big size machines (about 7.000 kN) is in many cases equipped with valve controlled system with constant pressure. These drives realise the fast movement with low force. However, a further device is necessary to built up the clamping force. There are typical options used e.g. a toggle gear or a separate cylinder with a connector system and sometimes to reduce cylinder size a pressure amplifier, **Fig. 4**. One option that is often used is the mechanical toggle. It unifies the two functions of fast mould movement and the clamping force built up in one element. The advantage is to have only one active element.

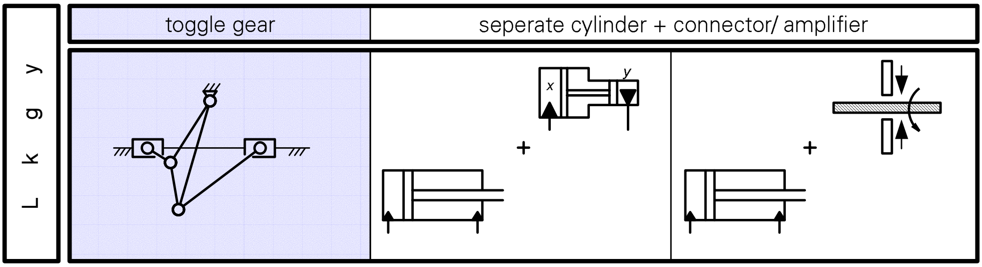
L k g y
toggle gear
seperate cylinder + connector/ amplifier
x
y
+
+

Fig. 4 **Locking systems for the clamping unit of an injection moulding**

3 MODELLING OF THE CLAMPING UNIT

The clamping unit of a prototype at the IFD consists of the following subsystems: the controller, the servo motors, the displacement machines, the cylinder and the multi-body toggle system, **Fig. 5**.

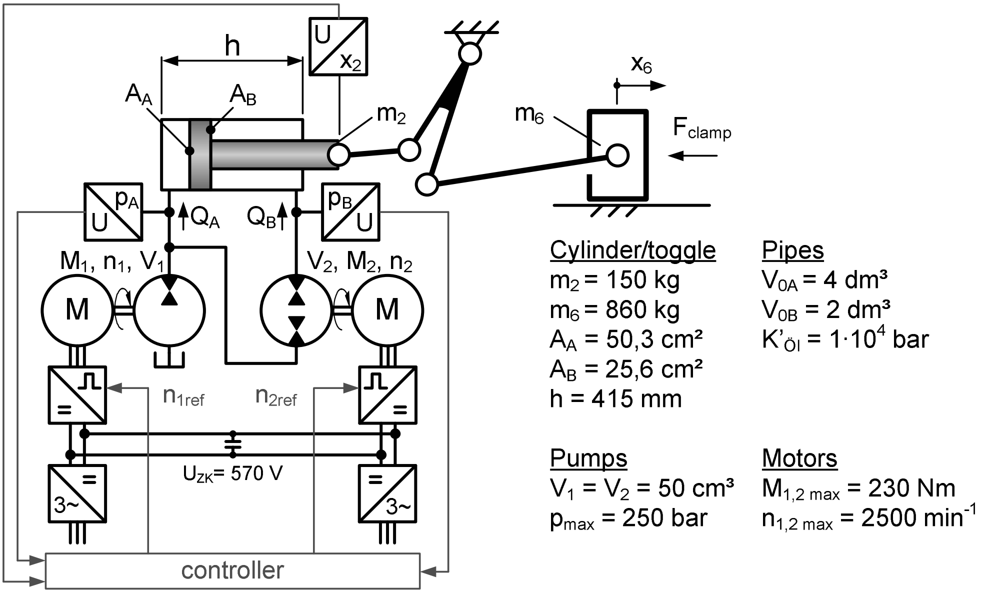
h
U
x2
AA
AB
m2
m6
x6
Fclamp
pA
U
QA
QB
pB
U
M1, n1, V1
V2, M2, n2
M
M
n1ref
n2ref
UZK= 570 V
3~
3~
controller
Cylinder/toggle
m2 = 150 kg
m6 = 860 kg
AA = 50,3 cm²
AB = 25,6 cm²
h = 415 mm
Pipes
V0A = 4 dm³
V0B = 2 dm³
K'Öl = 1·10^4 bar
Pumps
V1 = V2 = 50 cm³
pmax = 250 bar
Motors
M1,2 max = 230 Nm
n1,2 max = 2500 min^-1

Fig. 5 **System and parameters of the electric-hydrostatic clamping unit**

3.1 Hydraulic subsystem

The hydraulic mechanic subsystem consists of the displacement unit supplying oil flow to the hydraulic cylinder via the connected pipes. The description of the displacement unit and the hydraulic cylinder is shown in the equivalent circuits in **Fig. 6**. Main equations are the flow continuity, pressure build up, force and torque equilibrium given in equations (1) to (8).

External leakage of the internal gear pump is implemented in the model with pressure and speed dependent volumetric efficiency. The unknown internal leakage is set to zero. Cylinder leakage is neglected because of very good volumetric efficiency.

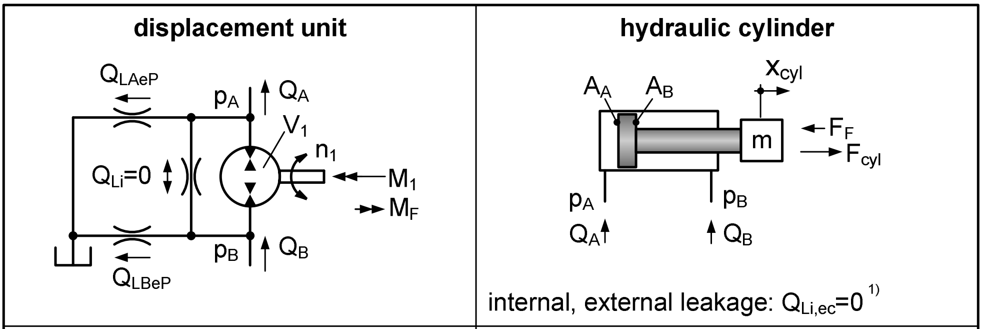

$$Q_{A,B} = V_1 \cdot n_1 - Q_{Le} \qquad (1)$$

$$Q_{Le} = Q_1 \cdot \left(1 - \eta_{vol}\right) \qquad (2)$$

$$M_1 = V_1 \cdot \frac{\left(p_A - p_B\right)}{2\pi} + M_F \qquad (3)$$

$$M_F = \varphi \cdot d_\varphi + sign(\varphi) \cdot M_C{}^{2)} \qquad (4)$$

$$F_L = \left(p_A - p_B\right) \cdot A_A = m \cdot x_2 + F_F \qquad (5)$$

$$F_F = x_2 \cdot d_x + sign\left(x_2\right) \cdot F_C{}^{2)} \qquad (6)$$

$$p_A = \frac{K'}{V_A} \cdot \quad Q_{(A)}\, dt \qquad (7)$$

$$p_B = \frac{K'}{V_B} \cdot \quad Q_{(B)}\, dt \qquad (8)$$

1) according to /2/ good cylinders are approximately without leakage
2) friction force/torque description is used according to /3/

Fig. 6 Description of hydraulic displacement and cylinder subsystem

3.2 Mechanic subsystem

The mechanic subsystem consists of a multi-body toggle mechanism that is driven by the differential area hydraulic cylinder. The cylinder is applying a force to the cross clamp of the toggle gear, Fig. 5. Out of this force and the toggle levers masses the movement of the system starts. Because of the non-linear characteristics of the toggle system there is a ratio dependent reduced mass applying on the cylinder that influences also the cylinder eigenfrequency. This characteristic is shown in **Fig. 7** and is an important value of its dynamic behaviour.

To obtain this characteristic not only attention has to be paid to the toggle gear ratio but also to the cylinder volume. This feeds to an eigenfrequency that result out of the superposition of changing oil volume and the changing reduced mass (equation 9).

$$f_0(x_2) = \frac{1}{2 \cdot \pi} \cdot \sqrt{\frac{K'_{Oil}}{m_{red}(x_2)} \cdot \left(\frac{{A_A}^2}{V_{0A} + V_A(x_2)} + \frac{{A_B}^2}{V_{0B} + V_B(x_2)} \right)} \qquad (9)$$

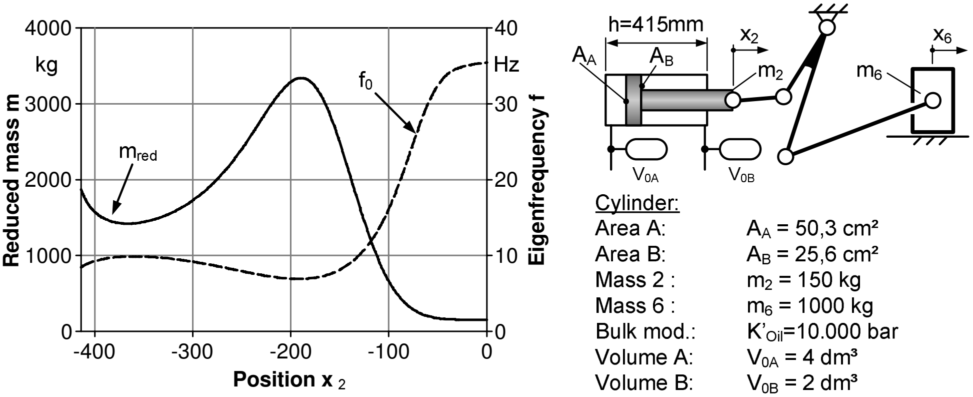

Cylinder:	
Area A:	A_A = 50,3 cm²
Area B:	A_B = 25,6 cm²
Mass 2 :	m_2 = 150 kg
Mass 6 :	m_6 = 1000 kg
Bulk mod.:	K'_{Oil}=10.000 bar
Volume A:	V_{0A} = 4 dm³
Volume B:	V_{0B} = 2 dm³

Fig. 7 Eigenfrequency of the cylinder with reduced mass

3.3 Electric subsystem

In system simulation simplified models of components and subsystems often fulfil the needed requirements. They should have an equivalent static and dynamic characteristic. The description of the AC servomotor is realised with use of simplified block diagram as derived in /8/. This model has been extended by some non-linearity (e.g. torque, power limit), **Fig. 8**.

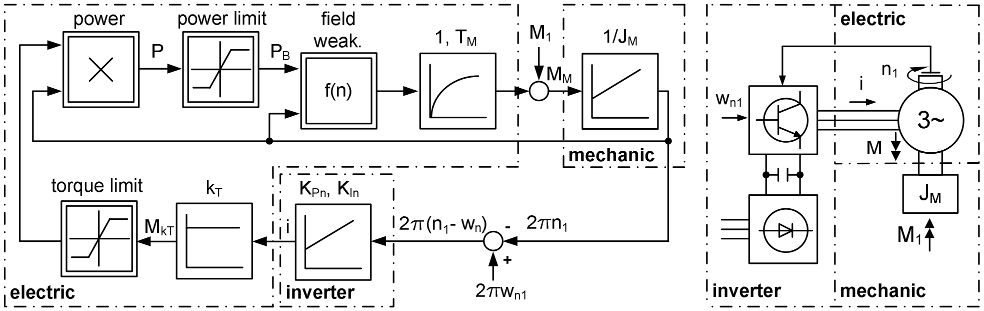
power
power limit
field weak.
P
P_B
f(n)
1, T_M
M_1
M_M
1/J_M
mechanic
torque limit
k_T
M_kT
K_Pn, K_In
i
2π(n_1- w_n)
-
2πn_1
+
2πw_n1
electric
inverter
electric
w_n1
n_1
i
3~
M
J_M
M_1
inverter
mechanic

Fig. 8 Simplified block diagram of AC servomotor

Fig. 9 (left) shows the step response characteristics of the AC-servomotor simulation model and measurements. It can be found a good accordance in speed response. In Fig. 9 (right) a comparison of simulated and measured torque characteristics are shown and good accordance for the simplified model can be obtained. The eigenfrequency of the simplified motor is approximately $f_{0M} = 32{,}8$ Hz and the damping ratio of $D_M = 0{,}8$. The non-linear second order model of the AC-servomotor shows good results compared with the measurements on a motor test rig.

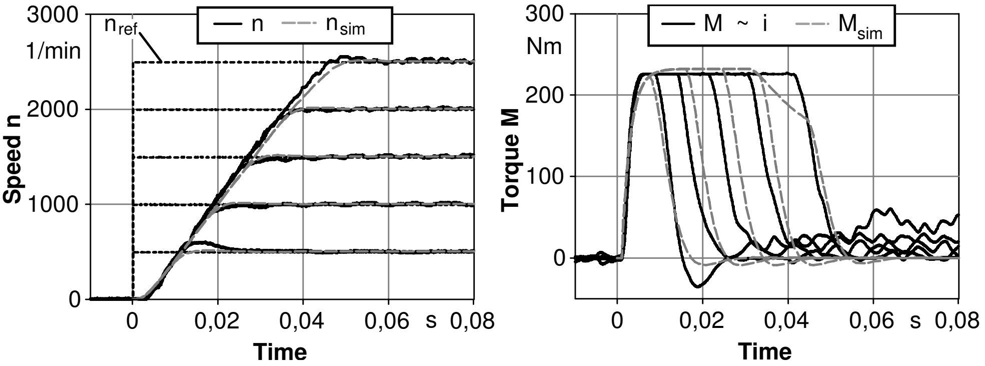

Fig. 9 Comparison of step response and torque characteristic of AC-servomotor

4 CONTROLLER

According to the plant dynamic characteristics as shown in Fig. 7 the system controller is chosen as a proportional controller with velocity feed forward and load pressure feed backward. Load pressure feed backward is inactive depending on a certain position range where the plants eigenfrequency is increasing.

AC-servomotors are also used to control the pressure of the displacement chambers A and B of the cylinder. The aim is to realise shifting pressure values in chamber A and B according to the necessary load pressure for cylinder movement. The influence between position and pressure controller has been decoupled by use of the cylinder area ratio, **Fig. 10**.

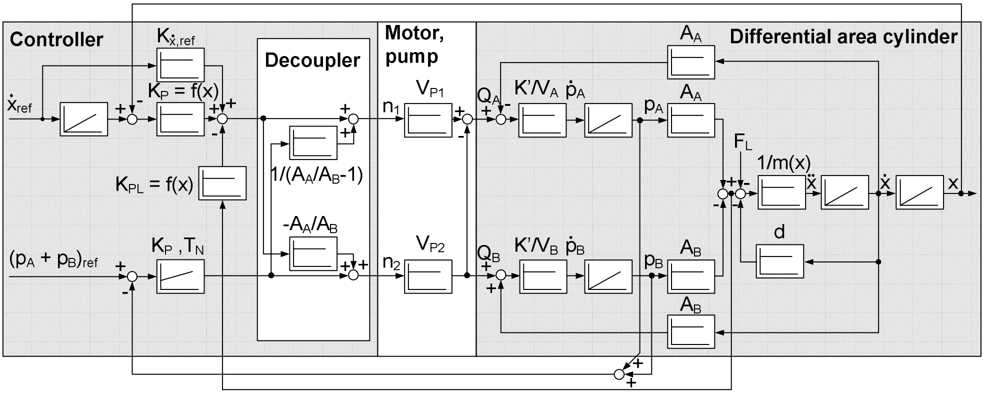
Controller
K_ẋ,ref
K_P = f(x)
ẋ_ref
K_PL = f(x)
(p_A + p_B)_ref
K_P , T_N
Decoupler
1/(A_A/A_B-1)
-A_A/A_B
Motor, pump
V_P1
n_1
V_P2
n_2
Q_A
Q_B
K'/V_A
ṗ_A
p_A
K'/V_B
ṗ_B
p_B
A_A
A_B
Differential area cylinder
F_L
1/m(x)
ẍ
ẋ
x
d

Fig. 10 Simplified block diagram of the clamping unit prototype

5 RESULTS

Fig. 11 shows the simulation results of position, velocity and pressure of the non-linear simulation model compared with prototype measurements. It can be obtained that the dynamic behaviour shows good response characteristics. A dry-cycle time (according to EUROMAP 6 standard) of $T = 1{,}4$ s could be realized where stroke is 70 % of tie bar distance and clamping force is 70 % of maximum clamping force (1.600 kN). This is a good value in comparison to available industrial high-speed injection moulding machines (up to $T = 1{,}45$ s for 1.500 kN machine).

Simulation and measurement results of pressure values show that during movement there is an overall good accordance. In the case of clamping force build-up and release and in some position range there is an explicit difference. This results from the toggle joint friction that increases during the clamping force build-up and in the real machine because of the increased transmitting force. The simulation model considers no description of joint friction, so some differences have to occur.

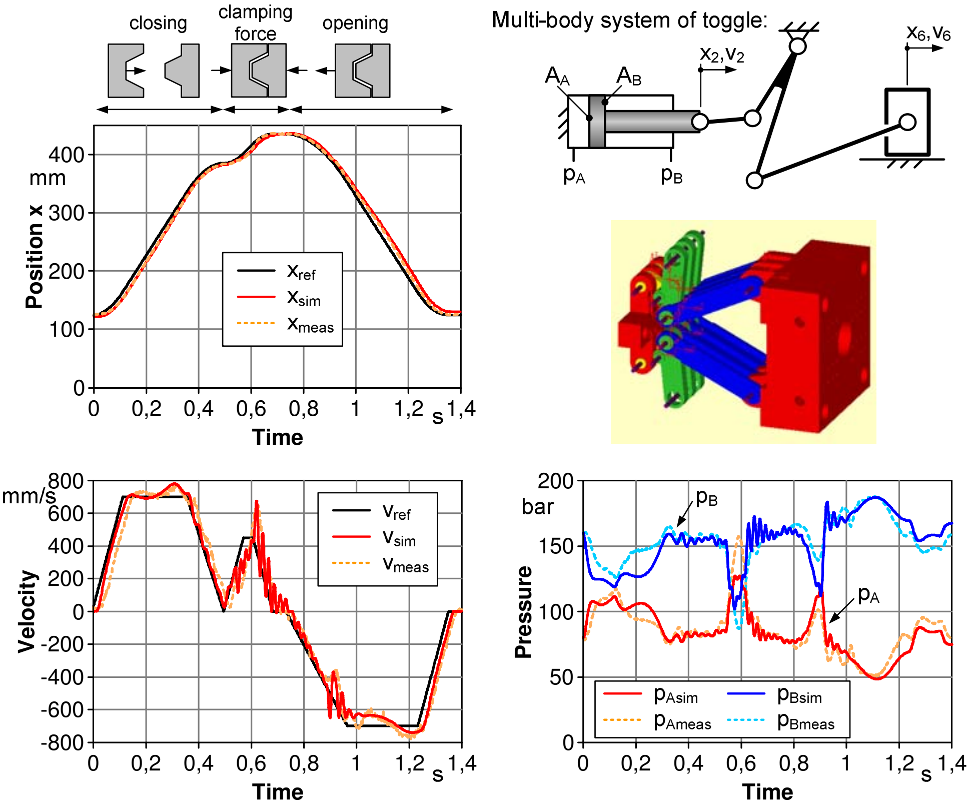

Fig. 11 Position, velocity and pressure result curves of the clamping unit prototype

6 CONCLUSIONS AND OUTLOOK

There are a lot of drive concepts and locking devices for clamping units of high-speed injection moulding machines available. The modelling and simulation of a high-speed clamping unit with electric hydrostatic drives and a toggle mechanism has been demonstrated. During the development period the use of simulation can give important advice for component choice and the feasibility of available concepts. The reachable dynamic of a real machine can be obtained with simulation investigations. Also the requirements of electric motors (e.g. maximum necessary speed and torque), the hydraulic system requirements of pump (displacement volume and pressure level) can be determined.

One difficulty is to develop reliable sub-models that represent the real components in a good way. Therefore a good experience but also experimental investigations may help to find reliable parameters that are necessary for subsystem development in simulation.

Prototype investigations provide information about feasibility of structure and components as well as the obtainable dynamic performance of the developed system. The velocity and position response show good accordance compared with the measurements on the prototype. Investigations of the prototype show that the simulated dry-cycle time of $T = 1{,}4$ s (stroke: 70 % of tie bar distance, clamping force: 70 % of max. clamping force) is reachable. Also the simulated pressure characteristic show good results compared with measurements. One uncertain point that leads to differences is the joint friction that has to be covered in the simulation model for further investigations.

The next step in the use of simulation for a high-speed injection moulding machine is the investigation of a new concept with increased compactness of the clamping unit by use of hydraulic multi-actuator drive system. Therewith, the eigenfrequency of the system will be increased despite of the increased toggle ratio. Also in real application the actuation load is changing depending on the manufactured part. That feeds to suboptimal controller parameters that are only adjusted for one constant load. To avoid manual corrections in case of load changes an adaptation, estimation or identification system has to be implemented, that changes controller parameters for optimal performance.

/1/ Helbig, A. Injection Moulding Machine with Electric-Hydrostatic Drives
3rd International Fluid Power Conference Aachen, Germany 2002

/2/ Helduser, S. Fluidtechnische Antriebe und Steuerungen
Arbeitsblätter zur Vorlesung, TU Dresden 2006

/3/ Helduser, S. Antriebstechnik/ Aktorik
Arbeitsblätter zur Vorlesung, TU Dresden 2006

/4/ N.N. SimulationX Handbook
ITI GmbH, Dresden 2006

/5/ Neubert, Th. Untersuchung von drehzahlveränderbaren Pumpen
Dissertation, TU Dresden 2002

/6/ Neubert, Th. Kunststoffmesse K'2001 in Düsseldorf
Helbig, A. Ölhydraulik und Pneumatik (O+P) 46, 2002 Nr. 3

/7/ Neubert, Th. Neuigkeiten von der K 2004
Räcklebe, S. Ölhydraulik und Pneumatik (O+P), 2005 Nr. 1
Wehner, D.

/8/ Rühlicke, I. Elektrohydraulische Antriebssysteme mit drehzahlveränderbarer
Pumpe, Dissertation, TU Dresden 1997

/9/ Schönfeld, R. Elektrische Antriebe
Springer-Verlag, Berlin Heidelberg 1995

/10/ Weingart, J. Calculation of the Energy Efficiency of a modern Hydraulic
Injection Moulding Machine, PTMC, Bath 2006

Energy storing and recovering in loading and un-loading cycles of forward loader

Tapio Virvalo [*], Wei Sun [**]
[*] IHA/TUT, P.O.Box 589, 33101 Tampere, Finland
[**] IMCE, Zhejiang University, Hangzhou, China

ABSTRACT

An important topic in R&D of mobile machines, for instance forest machines, is the improving of energy utilization. Important machines in timber harvesting chains are forward loaders. Booms of these kinds of machines are quite heavy and their reach range is large. The efficiency or energy utilization of these machines is quite poor. Loads under gravitational force are typical in loading and un-loading work cycles of forward loaders. Possibilities to utilize the gravitational force influencing one or two degree of freedom in some other degree of freedom are studied in a forward loader case. The basic idea studied is to use the outflow of the lift and jib cylinders to drive the telescope-cylinder. The outflows of the lift and jib cylinders are used directly or via the accumulator in the telescope-cylinder. Control valve assembly and accumulator are in very important roles in proposed method. The set-up and control strategy of valves are studied. The size of the accumulator is optimized taking care of environment and working condition. The energy consumptions of traditional and proposed systems are compared in different work cycles.

1. INTRODUCTION

Forward loaders have important role in forest industry. Most effective method in forest harvesting is to use the machine pair: a harvester and forward loader. The harvester cuts down trees, cuts off branches, and cut the log into certain lengths (the method is called cut-to-length). The forward loader collects logs into its load space and carries them typically to roadside and piles them there. The forward loader raises logs from ground to the load space and then un-loads the load space lowering logs into piles or ground again [1], [2], and [3]. The forward loader is an interesting one of these two machines from the energy consumption's point of view [4].

As an example a forward loader is shown in Figure 1. There are three cylinder driven degree-of-freedoms (DoF) in forward loaders; lift, jib, and telescope-cylinders, Figure 1. During the load and un-load work cycles, different cylinders may have counteracting loads or overrunning loads in the same time. For instance, during the un-loading cycle in a certain

Power Transmission and Motion Control 2007 Edited by Dr D N Johnston and Professor A R Plummer
© With The Centre for Power Transmission and Motion Control

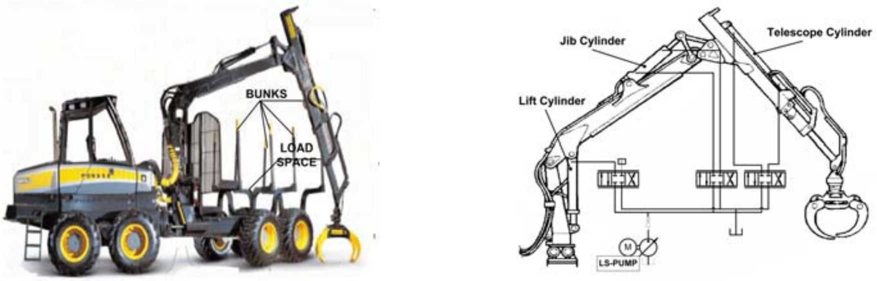

Figure 1. Forward loader (Ponsse Oyj) left, cylinders of degree of freedoms, right

stage, both the lift cylinder and the telescope-cylinder has an overrunning load. Previous study has shown that in this case the outflow of the lift cylinder can be utilized in the telescope-cylinder instead of the flow from the pump [4]. The extra outflow of the lift cylinder can be stored into the accumulator. During the return movements, the accumulator can offer the required flow for the telescope-cylinder (no load). This means significant energy saving since the telescope-cylinder may not need the flow from the pump at all in both back and forth movements. The basic idea of the energy storing and recovering system is shown in Figure 2 when the combination of the lift and telescope-cylinder is used in the un-loading cycle.

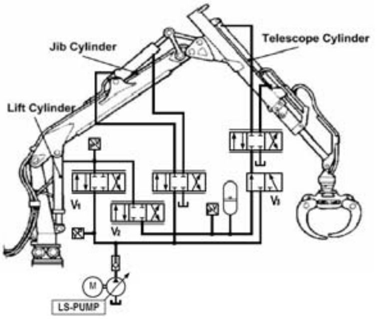

Figure 2. Modified hydraulics for lift and telescope-cylinders (un-loading cycle)

This idea is extended in this study to deal with the combination of the jib and telescope-cylinder in the loading cycle. During the loading cycle the jib cylinder has an overrunning load and the telescope-cylinder has a counteracting load. In this case the outflow of the jib cylinder can be utilized in the telescope-cylinder during the lifting of the load. The extra outflow of the jib cylinder can be stored into the accumulator. During the return movements the required flow of the telescope-cylinder (no load) is taken from the accumulator. There might be situations in both loading and un-loading cycles that other couple of DoFs can be active in the way described above.

2. MOTIVATION OF STUDY

According to the previous simulation it seems that reasonable results in the reducing of energy consumption can be achieved in the un-loading cycle [4]. It has also found out that proposed system functions properly. According to this study the energy reduction is around 20% in the whole un-loading cycle in the studied example work cycle. It seems that it is possible to find suitable switching logic between the control valves and that the performance of normal commercial mobile valves is good enough for this purpose.

The jib cylinder has an overrunning load during the loading cycle. The jib cylinder is bigger than the telescope-cylinder. The extended idea is to use the combination of the jib and telescope-cylinders during the loading cycle in the same way as the combination of the lift and telescope-cylinders in the un-loading cycle. This means some modifications of the control valves of the jib cylinder, but other wise the hydraulic system is the same as in previous case. The principle is shown in Figure 3. The question is can this combination be used the same efficient way as the lift and telescope-cylinders.

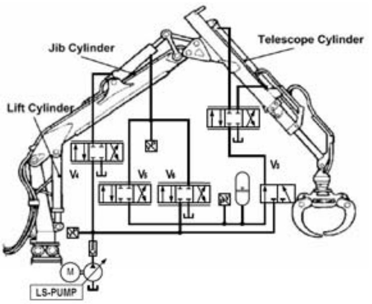

Figure 3. Modified hydraulics for jib and telescope-cylinders (loading cycle)

After the previous study [4] there are still questions waiting for more studies and answers. Quite many assumptions have done during that study. For instance the load is assumed to be 400kg. In practice loads vary in large range. It is possible that the pressure of the lift cylinder is not high enough to drive the telescope-cylinder and fulfil the accumulator in all work cycles. That is why the valve V3 (Figure 2) is required. The same situation might occur also when the combination of the jib and telescope-cylinder is considered (Figure 3). The optimum size of the accumulator is also a little bit difficult question, especially, if the proposed idea is extended also between the jib cylinder and the telescope-cylinder. The behaviours of booms and accumulators in these kinds of applications are not very clear [5], [6], [7], and [8]. Environment temperature and dynamic loading influence sometimes quite strongly to the performance of accumulators. These factors are not taken into account in the previous study. That is why the performance of the accumulator should be study more carefully, especially when also loading cycle and the combination of jib and telescope-cylinder is included.

3. MODELLING OF SYSTEM

The mechanical parts of the boom are modelled as a rigid body. These rigid body models are used in order to find out more easily the following issues.

- Validity of working principle of the idea.
- Suitable control algorithms of valves.
- Suitable size of valves and accumulator.

- Suitable control strategy when pressure of accumulator is not high enough for the telescope-cylinder.

Comparison of energy consumptions of different systems is also more clear when the dynamics of the boom flexibility is avoid. The modelling is made in a normal way by using free bodies and basic equations.

The basic hydraulics is modelled according to principles presented in [9]. This modelling includes the following parts.

- Lift, jib and telescope-cylinders
  - Friction forces modelled based on [10]
- Valves
  - Static characteristics including dead band and hysteresis [11]
  - Dynamics with saturations
- Electrically controlled Load Sensing pump [12]
- Pipes and hoses
  - Bulk module and reduced mass

In order to estimate the validity of the model some comparisons between measured and simulated responses have been made. The best way to evaluate the validity of the model is to compare measured and simulated open loop velocity and pressure responses. The validation of the basic model (mechanisms and basic hydraulics) is made DoF by DoF giving step-wise control signals to one control valve at a time. Some examples are shown in Figures 4 and 5. The constant pressure pump is used in these responses. Figures show that the measured and simulated responses match fairly well meaning that the basic model is

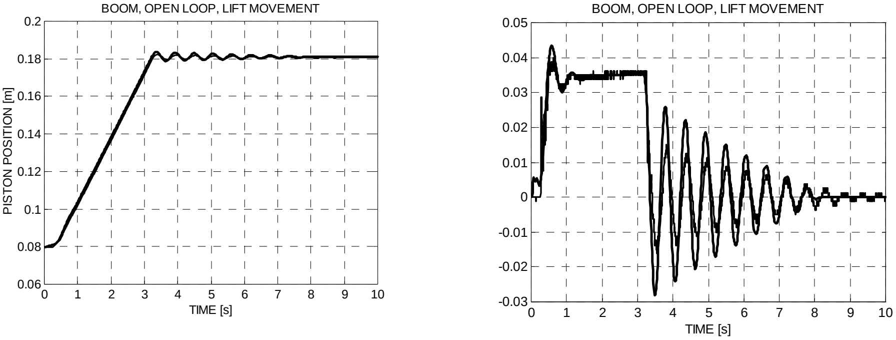

Figure 4. Measured and simulated position (left) and velocity open loop responses of lift cylinder

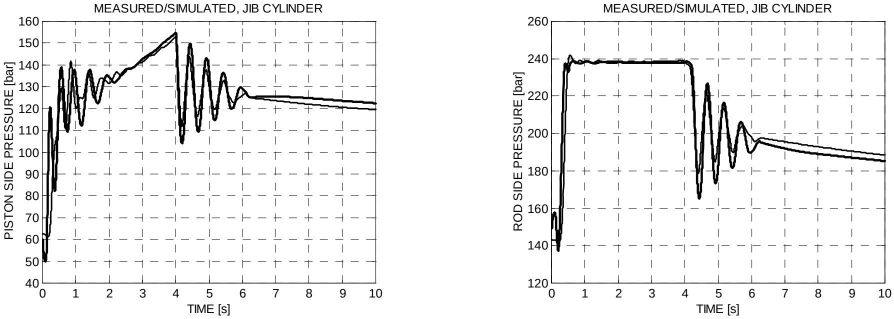

Figure 5. Measured and simulated piston side (left) and rod side chamber pressure open loop responses of jib cylinder

good enough to be used in this kind of study. The telescope-cylinder is fully out in these examples and the load is 500 kg. The control signals in both cases are so long pulses that the velocities reach the steady state value. The low natural frequency of 2 Hz can be seen in the responses of the lift and jib cylinders.

3.1 Model of accumulator

The important new component in the proposed method is an accumulator. In previous study [4] the accumulator has been modelled according to the ideal gas and adiabatic process without considering possible energy losses. According to [13] a common way is to assume that the efficiency of accumulators is 0.95. In order to achieve more realistic results in possible energy saving the accumulator should be modelled more carefully. The most common accumulators used in mobile applications are bladder accumulators. To model an accumulator, the most important thing is to find a group of equations describing the relations between the state variables (p, T, V) of the nitrogen, which must be considered as a real gas. The modelling of the accumulator is based on Figure 6 and references [6], [14], [15], and [16]. Considering that the nitrogen in the hydraulic accumulator will work under about 30 MPa and –10 ~ +60°C, it is no longer an ideal gas. The change in its internal energy dE can be described as

$$dE = m \cdot \left\{ c_V(p,T) \cdot dT + \left[T \cdot \left(\frac{\partial p}{\partial T} \right)_V - p \right] \cdot dv \right\} \tag{1}$$

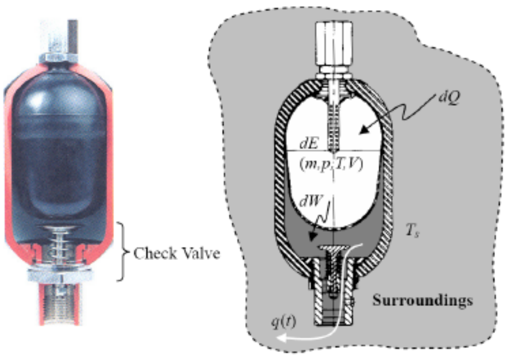

Figure 6. Bladder accumulator (left) and definitions for modelling

The derivative of gas temperature T can be obtained as

$$\frac{dT}{dt} = \frac{\alpha \cdot A}{m \cdot c_V(p,T)} (T_s - T) - \frac{T}{c_V(p,T)} \cdot \left(\frac{\partial p}{\partial T} \right)_V \cdot \frac{q(t)}{m} \tag{2}$$

In order to have a better accuracy of $(\partial p / \partial T)_V$, the Beattie-Bridgman equation (BB-equation) is introduced:

$$p = \frac{RT}{v^2} \left(1 - \frac{c}{vT^3} \right) \left[v + B_0 \left(1 - \frac{b}{v} \right) \right] - \frac{A_0}{v^2} \cdot \left(1 - \frac{a}{v} \right) \tag{3}$$

Where R, A_0, B_0, a, b, and c are constants which have the following values for nitrogen [14]:

$R = 296.77$ J/kg/K
$A_0 = 174.12$ m^5/kg/s^2
$B_0 = 1.8007\times10^{-3}$ m^3/kg

$a = 9.3375\times10^{-4}$ m^3/kg
$b = -2.4736\times10^{-4}$ m^3/kg
$c = 5.0948\times10^{-8}$ K^{3}m^3/kg

From the derivation of the BB-equation, $(\partial p/\partial T)_V$ can be written as

$$\left(\frac{\partial p}{\partial T}\right)_V = \frac{R}{v^2}\left(1+\frac{2c}{vT^3}\right)\left[v + B_0\left(1-\frac{b}{v}\right)\right] \tag{4}$$

The basic accumulator model can be set up based on the equations (1)-(4). The parameters in equation 2 including heat transfer coefficient "α" and the area of the external surface of the closed system "A", are difficult to measure or calculate. However, using the method introduced by Korkmaz [17], considering that the typical work condition of the accumulator will be at a pressure of 25 MPa and a temperature of 50°C, a variable so-called "thermal time constant" τ is defined as the following equation:

$$\tau = \left[\frac{m\cdot c_V(p,T)}{\alpha\cdot A}\right]_{\substack{p=25\times10^6\,\mathrm{Pa}\\ T=323.15\mathrm{K}}} = \frac{m\cdot \bar{c}_V}{\alpha\cdot A} \tag{5}$$

Then, the equation can be rewritten as

$$\frac{dT}{dt} = \frac{1}{\tau}\cdot\frac{\bar{c}_V}{c_V(p,T)}\cdot(T_s - T) - \frac{T}{c_V(p,T)}\cdot\left(\frac{\partial p}{\partial T}\right)_V\cdot\frac{q(t)}{m} \tag{6}$$

Based on the above equations 2-6 the simulation model can be established.

As examples two simulation results are shown in Figure 7, when isothermal, adiabatic and real gas processes are used.

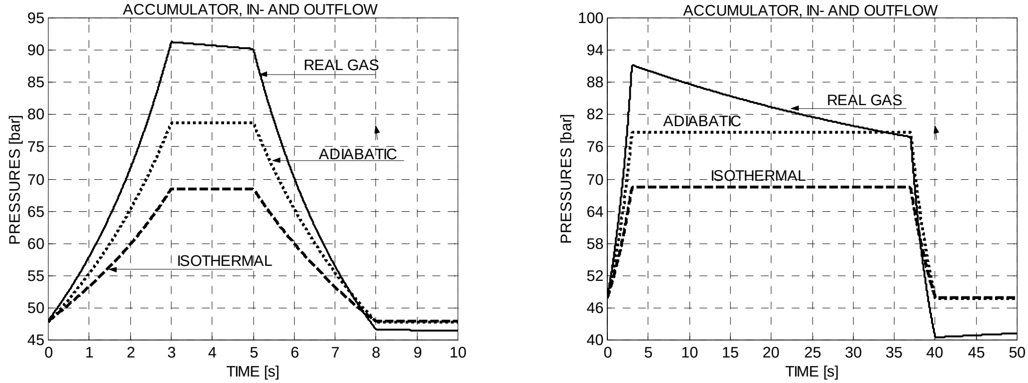

Figure 7. Simulation results fast response (left) and slow response (right)

The following parameters are used.

- Accumulator total volume 0.008 m^3
- Initial gas volume 0.003 m^3
- Pre-charge pressure of gas 3 MPa
- Initial gas temperature 40°C
- Surrounding temperature 20°C

The used thermal time constant in these simulations is 50 s. The volume flow to and from the accumulator is 30 l/min in both cases. The volume change is 0.0015 m^3 during in- and outflow.

According to these simulations it seems that it is reasonable to model the accumulator as a real gas process. However, the work cycles are relatively short in the forward loader applications. The thermal effect seen in Figure 7 is not remarkable, but the difference between the behaviours of accumulator pressures of the different modes is significant.

4. COMPONENTS OF PROPOSED SYSTEM

The main changes to the traditional hydraulic system are that the accumulator is added, the pressure sensors are added, and the valve set-up is different. The specifications of the steady state and dynamics performance of the control valve are the same, but the connections of the valves are different and there are also some additional valves, see Figures 2 and 3.

4.1 Size of accumulator

In order to estimate the size of the accumulator the amount of oil required to drive the telescope-cylinder back-and-forth as well and the needed pressure level during these movements are estimated. This estimation is based on typical work path and working range shown in Figure 8.

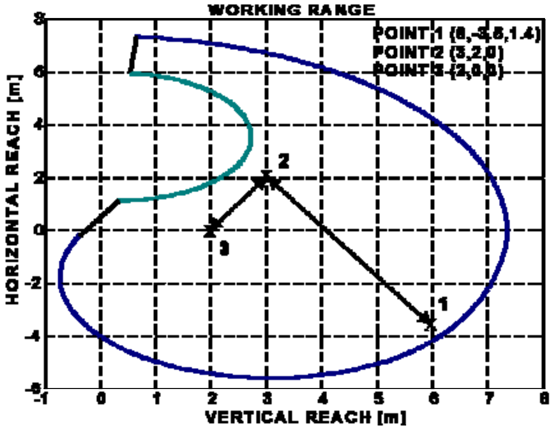

Figure 8. Work range of boom and corner points of movements of studied work cycle

The telescope-cylinder is used during the movement between points 1 and 2 and it makes it full stroke, Figure 8. The responses of the piston force of the telescope-cylinder in loading and un-loading movements are shown in Figure 9. The size of the telescope-cylinder is 50/32-1400 (piston diameter/rod diameter-stroke [mm]). The amount of oil required to full stroke is 0.00274 m^3 into the piston side and 0.00162 m^3 into rod side.

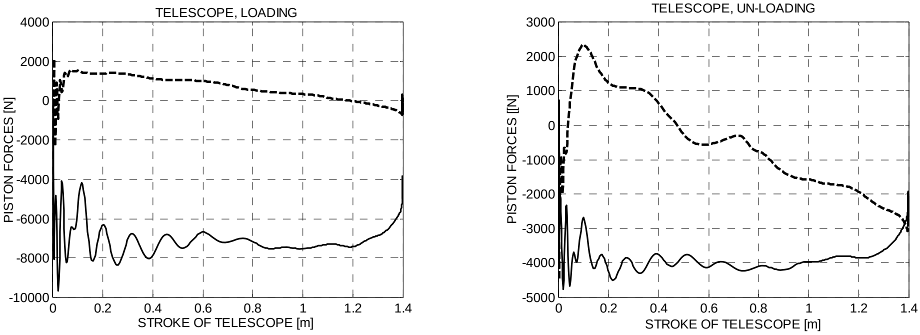

Figure 9. Piston forces of telescope-cylinder as a function of piston position, loading (left) and un-loading stages (right), load=500kg

The relations between the cylinders in movements between points 1 and 2 (back and forth, Figure 8) are as follows

* Loading cycle, from point 1 to point 2
    * The jib cylinder is moving outward (overrunning load) and the telescope-cylinder inward (counteracting load).
    * The volume change of the jib cylinder is 2.75 l (outflow)
    * The volume change of the telescope-cylinder is 1.6 l (inflow)
        * Some extra oil is going to the accumulator, 1.15 l
* Return movement in loading cycle, from point 2 to point1
    * The telescope-cylinder in moving outward and it takes oil from the accumulator
        * The volume change of the telescope-cylinder is 2.7 l
* Un-loading cycle, from point 2 to point 1
    * The lift cylinder is moving inward (overrunning load) and the telescope-cylinder outward (overrunning load)
    * The volume change of the lift cylinder is 6.1 l (outflow)
    * The volume change of the telescope-cylinder is 2.7 l (inflow)
        * Some extra oil is going to the accumulator, 3.4 l
* Return movement in un-loading cycle, from point 1 to point2
    * The telescope-cylinder in moving inward and it takes oil from the accumulator
    * The volume change of the telescope-cylinder is 1.6 l

According to these figures there is no problem with oil amount balance between the lift and telescope-cylinders in the un-loading work cycle, but in the loading work cycle the amount of oil is not enough for driving the telescope-cylinder back from the point 2 to the point 1. Because in the loading cycle during movement from the point 2 to the point 1 the lift cylinder is moving inward (overrunning load) the needed additional oil to drive the telescope-cylinder outward can be taken from the lift cylinder.

From the accumulator size point of view the inward movement of the telescope-cylinder in the un-loading cycle from the point 1 to the point 2 is most critical. At the end of this movement the pressure in the accumulator should be at least $F/A2=4500N/0.0012\ m^2 = 3.8$ MPa. This means that the pre-charge pressure of the accumulator should be higher than 3.8 MPa. Based on simulations the outflow pressures of the lift and jib cylinders are higher than 10 MPa at overrunning load when the load is 400 kg or higher. According to above figures the initial specifications of the accumulator are: the pre-charge pressure 4 MPa, the maximum pressure more than 10 MPa, the minimum pressure 4.5 MPa, and the required out-coming amount of oil 2.7 l. According to eq.(1)-(6) and with these figures the estimated size of the accumulator is 7 l.

5. STUDIED SYSTEM

The basic studied hydraulics is depicted in Figure 1 and the whole proposed hydraulic system is when the system depicted in Figures 2 and 3 are put together. The whole working range of the boom is shown in Figure 8 as well as the corner point of the movement path of the studied work cycles (points 1, 2, and 3).

The studied loading and un-loading work cycles can be divided into four movements. In the loading the load is first gripped on the ground, point 1. Then it is raised to the point 2 over the bunk ends of the load space (see Figure 1). After that the load is lowered into the load space and there the load is released, point 3. Then the gripper (tip of the boom) is driven back to the point 1 via the point 2. In the un-loading work cycle the load is first gripped at the point 3 in the load space. Then it is raised to the point 2 over the bunk ends and lowered into the point 3 on the ground, where the load is released. Then the gripper is driven back to the point 3 via the point 2. In practice the boom has to be also rotated in these kinds of work cycles, but the rotational movements are not included into this study.

Two systems are compared: A) the traditional system with LS-pump and un-symmetric valves of the jib and telescope-cylinders and B) the proposed system according to hydraulics shown in Figures 2 and 3. The proposed system has also a LS-pump and un-symmetric valves of the jib and telescope-cylinders. In addition the valves V2, V3, V5, and V6, the accumulator, and three pressure sensors are included. In both cases the energy consumption of the whole loading and un-loading work cycles are calculated. The best way to compare the energy consumptions of two different systems is to compute the energy taken from the pump. There are different ways to compute the efficiency [6], but they do not give clear picture in the cases where the energy storing and recovering are used.

6. RESULTS

For simplicity all four movements in both work cycle cases are calculated separately and the energy consumptions of each movement are summed in order to get the total energy consumption during one whole work cycle. Some relatively small errors are done in this kind of calculation, but they do not influence comparison result. The gripper weights 100 kg and it is assumed that the nominal load is 400 kg. The whole cycle time of both work cycles is 14 s. From the point 3 to the point 2 and back it takes 3 s in both directions and in both work cycle cases. From point 2 to the point 1 and back it takes 4 s in both directions and in both work cycle cases. It is assumed that each movement profile is reasonable smooth. The velocity profile of each movement is the trapezoid. During both work cycles the following movements of different cylinders take place.

Table 1	Mov. 1↔2	Mov. 2↔3
Lift cylinder	Yes	Yes
Jib cylinder	Yes	Yes
Telesc. cylinder	Yes	No

The following computed hydraulic energy (pump output) is used in different parts of the loading work cycle of the traditional and proposed systems, Table 2.

Table 2	Mov. 1 - 2	Mov. 2 - 3	Mov. 3 - 2	Mov. 2 -1	Whole cycle	Change
Trad. [kNm]	147	8	21	43	219	-
Prop. [kNm]	130	6	20	27	173	-21%

The following computed hydraulic energy (pump output) is used in different parts of the un-loading work cycle of the traditional and proposed systems, Table 3

Table 3	Mov. 3 - 2	Mov. 2 - 1	Mov. 1 - 2	Mov. 2 -3	Whole cycle	Change
Trad. [kNm]	33	78	88	4	203	-
Prop. [kNm]	33	44	78	4	159	-21%

The results show that in the studied case the energy consumption of the proposed system is significantly lower in both work cycles than the energy consumption of the traditional system. Further simulations show that the relation of the energy consumptions of two systems remains at the same level with all loads. The relationship between forces (pressures) of different DoFs is approximately independent on the size of loads. Because the pressure of the accumulator depends on the amount of the oil and the pre-charge pressure, the pre-charge pressure should be matched to loads. The lift and jib cylinders should be able to deliver oil into the accumulator and the pressure of the accumulator should be high enough to be able to drive the telescope-cylinder. In this case some kind of average load (400 kg) is used. Higher loads do not cause any extra problems, but with loads less than 200 kg the pre-charge pressure of the accumulator should be lower in order to work properly.

8. DISCUSSION

In this stage of the study it can be said that the proposed system functions properly in both the loading and un-loading work cycles. The energy reduction is around 20% in the studied cases. It is possible to find suitable switching logic between valve V1, V2, V3, V4, V5, and

V6, Figures 2 and 3. This makes it possible to drive the boom in the normal way without noticing the energy save and recovery. The proposed method realizes the switching between valves so smoothly that no oscillations of the boom are generated. From the dynamics point of view interesting work phase is during the return movements of the loading cycle. The oil amount loaded into the accumulator from the jib cylinder during movement from the point 1 to the point 2 (Figure 8) is not enough for the return movement of the telescope-cylinder from the point 2 to the point 1. Then the needed extra oil is taken from the lift cylinder. This is shown as an example in Figure 10. The velocity responses of the lift and telescope-cylinders are shown in Figure 10, when switching between valves V1 and V2 takes place due to pressure relation between the accumulator and lift cylinder.

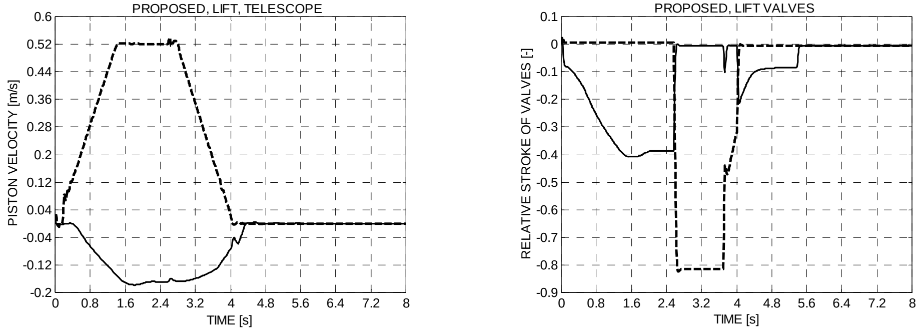

Figure 10. Velocity response of lift (solid line) and telescope-cylinder (dashed line), left. Response of lift cylinder valves, solid line from cylinder to tank and dashed line from cylinder to accumulator, right

The accumulator pressure has dropped under the lift cylinder pressure at time 2.6 s and the lift cylinder is driving the telescope-cylinder since that. As can be seen the velocity responses of both lift and telescope-cylinders are smooth (Figure 10 left) and the switching between lift cylinder valves (Figure 10 right) can not be noticed. The outflow of the lift cylinder goes to the accumulator line when the valve V2 is switched on (dashed line between 2.6 s and 3.7 s)

The biggest energy losses take place in the control valve partly due to pressure compensators [18]. Traditional mobile valves with pressure compensators do not allow any active damping of oscillations which are one of the main problems in these kinds of boom applications. The proposed system use so called electrical pressure compensation which makes it possible to achieve lower energy losses in the control valves and improve possibilities to damp oscillations. The basic idea is based on estimated velocity of the cylinders and the use of suitable controllers. Experimental studies show that velocities of cylinders can be estimated accurately enough at least from energy consumption reducing point of view [4] and [19]. According to simulations the steady state and dynamic characteristics of mobile valves are good enough and make the proposed control method possible.

Still there are questions waiting for more studies and answers. Quite many assumptions have to be done during this study. In practice the cylinder pressures vary in large range due to the load and the orientation of the boom. It is possible that the pressure of the lift and jib cylinder is not high enough to drive the telescope-cylinder and fulfil the accumulator in all work cycles. That is why the valve V3 (Figures 2 and 3) is required. The switching between the valves V1, V2, V5, V6 and the valve V3 and it influence to energy consumption has to be studied.

Nowadays the control valves of these kinds of booms are in the same compact package with common supply and tank lines. The allowed pressure in tank lines of these packages is quite low. This means that the proposed system can not be directly used with existing valve packages. This means some extra costs and maybe some problems in size and location of valves. The size of the accumulator (7 l) is reasonable and does not cause any significant location problems. Because of the cross-utilization of the DoFs the possible power losses in the accumulator are not important, especially with higher loads.

The average power during both work cycles is 14 kW. It can be estimated that during normal working one loading or un-loading cycle is done in one minute. The reduced average power is 0.66 kW in one hour. If it is assumed that the fuel consumption of the diesel engine is 250 g/kWh, the fuel saving in one hour is 0.2 l. In typical two shifts the fuel saving in one year is around 700 l.

Simulation is used in this study. Of course it causes some uncertainties for instance due to simplifying assumptions and numerous non-linearities. On the other hand the simulation model bases on well-known models of hydraulics and mechanical structure of the boom. Anyway it can be considered that simulation results so far give promising basement for further studies.

9. CONCLUSIONS

According to this study mostly based on simulations the following conclusion can be made:

- Proposed method is working and it gives promising results for reducing energy consumption in forward loaders both in loading and un-loading work cycles.
- Performance of traditional proportional mobile valves seems to be good enough, but some re-design is desirable in order to achieve more compact valve package.
- Robustness of proposed control method requires experimental tests.

10. REFERENCES

1. https://www.ponsse.com/
2. www.deere.com/en_US/cfd/forestry/deere_forestry/
3. http://www.komatsuforest.fi/english/index.html
4. Liang, X. & Virvalo, T. 2002. Accumulator-Charged Drive for a Hydraulic Boom to Save Energy. 2002 ASME, IMECE2002, November 17-22, 2002, New Orleans, Louisiana, USA 2 6 p
5. Liang, X. 2002. On Improving Energy Utilization in Hydraulic Booms, Acta Polytechnica Scandinavica, Mechanical Engineering Series No. 160, Tampere, Finland 2002
6. Sun, W. 2004. On Study of Energy Saving System for Hydraulic Manipulators. No.

519 Tampere University of Technology, Tampere, Finland, 2004. 207 p

7. Virvalo, T. & Sun, W. 2005. Improving energy utilization in hydraulic booms - what it is all about. 6th ICFP'2005, April 5-8, Hangzhou, China pp. 55-65.
8. Virvalo, T. & Seppälä, J. 2006. Cross utilizing degree of freedoms of boom in energy saving concept. PTMC 2006, University of Bath, UK, 13-15 September 2006 pp. 31-43.
9. Virvalo, T. 1993. Modelling hydraulic position servo realized with commercial components. 3rd International Conference on Fluid Power Transmission and Control, Zhejiang University, Hangzhou China, 13-16 September 1993. 6 p.
10. Olsson, H, 1996, Control Systems with Friction. PhD thesis, Lund Institute of Technology, University of Lund, 1996.
11. Virvalo, T. 2005. Compensation of dead band and hysteresis of proportional valve. Proceedings of the 50th National Conference on Fluid Power, March 16-18, 2005, Las Vegas, Nevada USA pp. 233-241.
12. Mare, J. C, 2001. Simplified model of pressure regulated, variable displacement pumps for the sizing of complex hydraulic. 5th ICFP2001, Hangzhou, China 1-3 April, 2001, 5 p.
13. http://www.engineersedge.com/hydraulic/accumulator_equations.htm
14. K-E. Rydberg, Hydraulic Accumulators as Key Components in Energy Efficient Mobile Systems, 6th International Conference on Fluid Power Transmission and Control, Hangzhou, China, 2005, pp.124-129.
15. J. Nyman, J. Bärnström and K-E. Rydberg, Use of Accumulators to Reduce the Need of Electric Power in Hydraulic Lifting Systems, 8th Scandinavian International Conference on Fluid Power, Tampere, Finland, May 2003, vol.1 pp.311-326.
16. Sun, W. & Virvalo, T. 2005. Simulation study on a hydraulic-accumulator-balancing energy-saving system in hydraulic boom. Proceedings of the 50th National Conference on Fluid Power, March 16-18, 2005, Las Vegas, Nevada USA pp. 371-381.
17. Korkmaz Feridun, Hydrospeicher als Energiespeicher, Springer-Verlag, Berlin, 1982
18. Liang, X, Virvalo, T., Linjama, M. 1999. The Influence of Control Valves on the Efficiency of a Hydraulic Crane, 6th SICFP1999, Tampere, Finland, 1999, 12 p
19. Kannisto S. and Virvalo T. 2002: Valve Manufacturer Specification Based Hydraulic Velocity Servo. ASME, Mechanical Engineering Congress and Exposition, New Orleans, USA, CD-vol. 2: Fluid Power, 17.-22.11.2002, 6 p.
20. Vickers/Eaton: http://hydraulics.eaton.com/products/valves_mobile_erc.htm

An electropneumatic control and actuation system for the vanes of the variable geometry turbine of a turbocharged diesel engine

Andrea Almondo
GM Powertrain Europe S.r.l - Torino (Italy) – andrea.almondo@it.gm.com
Giovanni Jacazio
Department of Mechanics - Politecnico di Torino (Italy) – giovanni.jacazio@polito.it

ABSTRACT

The study of an electropneumatic control and actuation system is herein presented, that performs a closed loop control of the boost pressure of a turbocharged diesel engine using electrical signalling and pneumatic actuation. The pneumatic actuator force is controlled by modulating the vacuum pressure generated by a camshaft driven pump. A proportional solenoid valve accepts the control signals from an electronic controller, thereby varying the pressure on one side of a spring loaded pneumatic actuator; the resulting force balance determines the actuator piston position, which in turn drives the turbine vanes. The modulation of the turbine vanes permits to control the turbocharger power, thus varying the engine boost pressure. This is measured by a sensor, and a pressure control loop is closed with a law using a combination of PID and feed-forward control.

The development of both linear and non linear models describing the interaction between engine, turbocharger and control strategy can be instrumental in assessing the system performance both in steady-state and transient conditions, determining the optimal control, establishing the maximum acceptable tolerances of the system components to meet the pressure control accuracy, and in evaluating the merits of adding an internal position control loop for the actuator position. Interesting applications of this model based approach have been proposed in literature by Rask and Sellnau [1], Moskwa and Hedrick [2] and Filipi et al. [3].

The paper first outlines the boost pressure control system architecture and characteristics, then it describes the system model and presents the most significant results and lessons learned during the control system study by means of linear and non linear models.

1 FUNCTION OF A BOOST PRESSURE CONTROL SYSTEM IN A DIESEL ENGINE

The optimum performance of turbocharged diesel engines is obtained when the boost pressure in the intake manifold is appropriately tuned to the engine operating conditions; a con-

Power Transmission and Motion Control 2007 Edited by Dr D N Johnston and Professor A R Plummer
© With The Centre for Power Transmission and Motion Control

tinuous control of the boost pressure is beneficial for reducing emissions and fuel consumption, and for improving performance and driveability of the vehicle. An optimal value of the overcharging pressure exists for each engine working condition that ensures the best combination of engine performance, emissions and fuel consumption. In an engine equipped with Variable Geometry Turbine (VGT), the control of the boost pressure is performed by varying the orientation of the vanes of the turbine nozzle; a change of the vanes angle brings about a variation of the turbine output torque driving the compressor and thus a change of the amount of gas energy converted into compressor energy, thereby permitting the control of the boost pressure. In a similar way, in an engine with Waste Gate (WG), the control of boost pressure is performed by-passing a certain amount of exhaust gas flow from the turbine, thus controlling the power input to the compressor.

The analytical study here presented has been applied to a 1.9 litres, 4 cylinder, VGT turbocharged diesel engine. A pictorial view of the boost pressure control system is shown in figure 1.

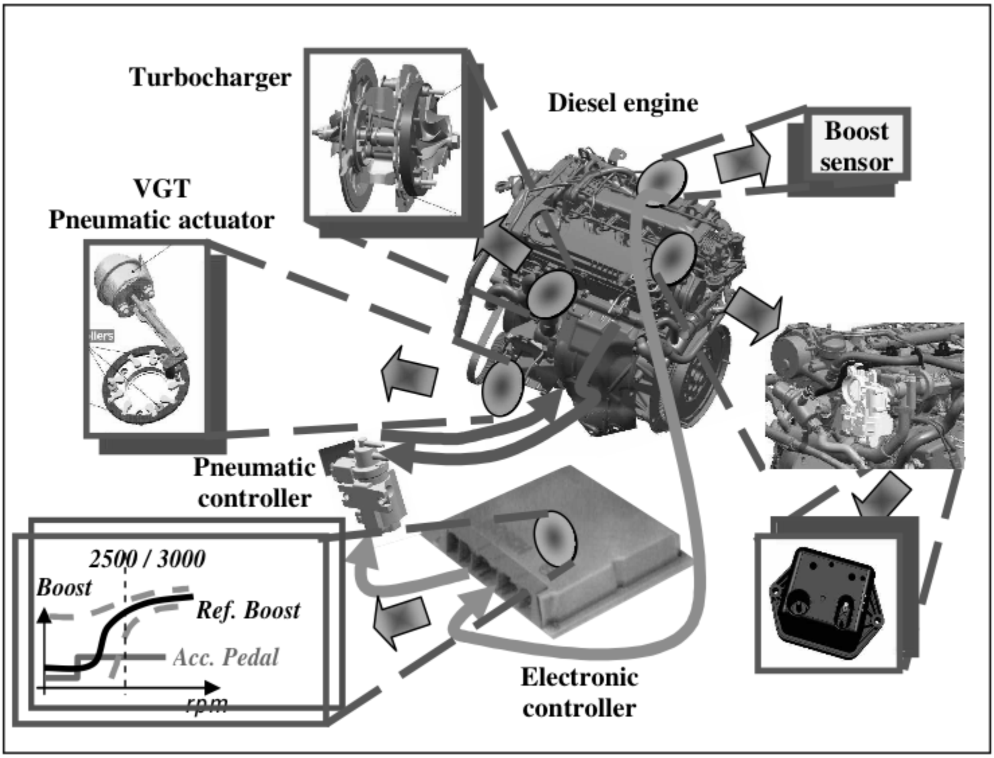

Figure 1 View of the boost pressure control system components

2 SYSTEM ARCHITECTURE

The boost pressure control system is a closed loop system using electrical signalling, pneumatic actuation and turbocharger physical characteristics to continuously adapt the boost pressure to the engine demand. The boost pressure command is determined by the engine electronic controller as a function of the engine working point and of the pedal position, according to an engine control strategy aimed at optimizing the overall engine performance. The boost pressure command is then compared by the electronic controller with the actual boost pressure measured by a boost sensor, thereby closing the boost pressure feedback loop. An error signal is thus generated that is processed by a dedicated control law to eventually provide the control signal to a proportional solenoid valve that modulates the vacuum pressure inside a single acting spring-loaded pneumatic actuator. The actuator output is connected via a suitable linkage to the unison ring of the vanes of the compressor stator. The balance between the pressure force and the spring force acting upon the piston jack determines the piston position and thus the angular position of the vanes, which in turn brings about the change of the boost pressure. A schematic of the pneumatic actuation system is shown in figure 2.

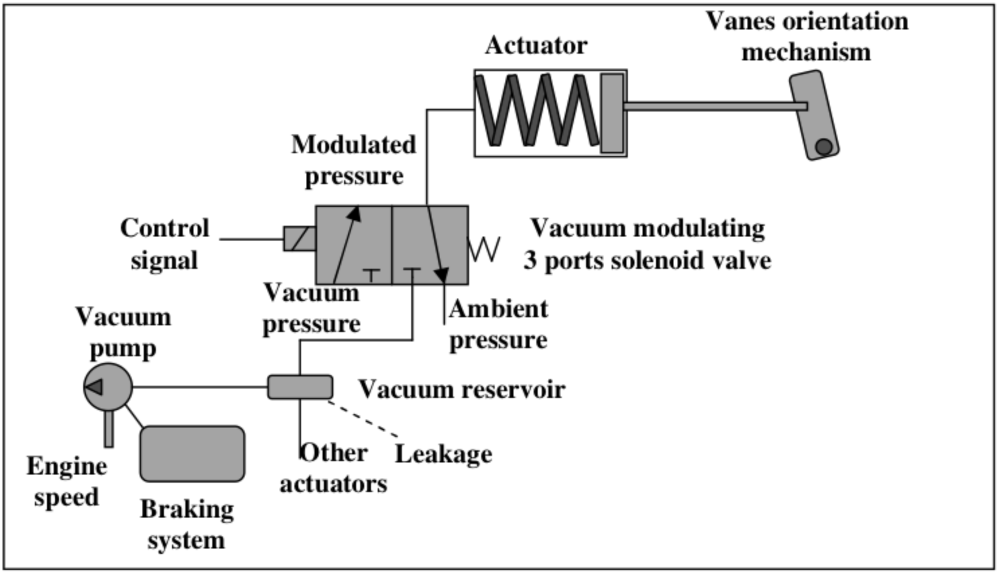

Figure 2 Schematic of the pneumatic actuation system

The vacuum pressure necessary for the system operation is created by a vacuum pump, whose primary function is to generate the vacuum necessary to operate the vehicle power braking system. The boost pressure control system takes advantage of the available vacuum, however, the vacuum generation system is configured in a way to ensure priority of usage to the power braking system; in no way the operation of the boost pressure control system can impair the performance of the power braking system. This characteristic is obtained by a suitable configuration of the pump ports and does not rely on external signals. In some applications, an additional reservoir located in the pump suction line provides a reserve of air at low pressure to ensure an unabated performance also under severe duty cycle conditions. Leakages from the ambient into the pneumatic system limit the minimum vacuum pressure also in case of no flow required by the actuators; such minimum pressure value depends upon the vacuum pump characteristics and for the system herein described was slightly above 0.1 bar.

The proportional solenoid valve accepts the control signal from the electronic controller and modulates the pressure level inside the actuator volume at a suitable value in the range between the vacuum pressure established by the vacuum pump and the ambient pressure. The rod end side of the actuator is connected to the ambient, therefore, when a certain degree of vacuum is created on the head end side of the actuator, a pressure force is generated acting in the direction of retracting the actuator. The actuator piston is also subjected to the force of a spring acting in the direction of keeping the actuator extended; as the pressure on the head end side of the actuator decreases, the retracting pressure force increases until it overcomes the spring force eventually causing the actuator to retract, thus compressing the spring up to the point in which a new force balance is reached. The movement of the actuator piston is converted by the linkage mechanism into a rotation of the compressor vanes which brings about a variation of the boost pressure.

3 MAIN COMPONENTS DESCRIPTION AND MODELLING

The vacuum pump is a vane type pump directly connected to one of the cam shafts. The pump has two suction ports (a main port connected to the power brake system and an auxilary port, provided with an orifice and connected to the other utilities) and a discharge port connected to the ambient. The rotor carries two vanes 180° apart and rotates in the direction such to first suck air from the main port and then from the auxilary port; this configuration automatically provides a priority to the power brake system connected to the main port, since the vacuum level in the auxilary line can never be lower than that of the main line. The mathematical model has been developed using the pump suction capability as a function of the rotational speed, describing the diminished suction on the auxiliary port as a function of the pressure increase internally to the pump due to flow rate from brake circuit and taking into account internal leakages from ambient pressure port to vacuum ports.

The vacuum pressure modulating valve is a 3-way, proportional solenoid valve operating on a flow-on-demand concept; one port is connected to the vacuum line, another (control port) to the actuator, and the third one to the ambient. The control signal generated by the electronic controller determines the input voltage applied to the solenoid valve coil and eventually the force acting upon the valve plunger. The plunger is also subjected to the force of a spring and to a pressure force dependent on the values of ambient, vacuum and controlled pressure. If no flow is required by the actuator, an equilibrium condition is reached in which the vacuum port is kept closed by the plunger while the pressure in the controlled line is at the value necessary to keep the actuator in the position that will eventually determine the required boost pressure. A change of the control signal leads to a change of the force on the plunger and to a resulting force unbalance that causes a movement of the plunger such to connect the control port either to vacuum or to ambient depending on the variation of the control signal; a flow to/from the actuator will thus take place that will continue as long as a new equilibrium of the forces acting on the plunger is reached. Since the control signal has changed, this new equilibrium condition is obtained for a new value of the controlled pressure, and in this new steady state condition no more flow is drawn from the vacuum line, which minimizes the power consumption. In the model this behaviour is described through the mathematical model of two orifices connecting the controlled pressure port respectively with vacuum port and ambient port. The discharge coefficient of each of these two orifices is proportional to the error between controlled pressure and target pressure, proportional to control voltage. Moreover the dynamics of the vacuum pressure modulating valve (and so the dynamics of discharge coefficient change over time) is represented by a single-order lag with a time constant τ_P. The voltage control is performed by the electronic controller with a PWM technique with a cycling frequency of 300 Hz.

The actuator is a single acting, spring loaded linear actuator whose head side is connected to the controlled vacuum pressure line and the other side is connected to the ambient. When the controlled pressure is equal to the ambient pressure, the spring force keeps the actuator fully extended; as the controlled absolute pressure decreases below 0.9 bar, the resulting pressure force overcomes the spring preload causing the actuator retraction. Since the spring has a constant stiffness, there is a linear relationship between the actuator position and the controlled pressure; the fully retracted position for the actuator is obtained for a controlled absolute pressure of 0.5 bar. The dynamics of the actuator is that of a second-order system with a transfer function, modelling the inertia, stiffness and friction damping effects:

$$\frac{\bar{y}}{\bar{p}_A} = \frac{G_A}{\frac{s^2}{\sigma_A^2} + 2\zeta_A \frac{s}{\sigma_A} + 1} \tag{1}$$

where y is the actuator piston position, p_A the pressure inside the cylinder, σ_A the resonant frequency, ζ_A the damping factor, G_A the actuator gain, s the Laplace transform variable.

The turbine vanes are driven by the actuator through the linkage mechanism and their angular position eventually determines the value of the boost pressure. The dynamic relationship between boost pressure variation and vanes position is given by a first-order lag (turbo-lag), mainly determined by the turbocharger rotational inertia and the intake manifold plenum capacitance effect, and, since the vane angular position is proportional to the actuator piston position, the transfer function between boost pressure p_B and actuator position y can be written as:

$$\bar{p}_B = \frac{G_M}{\tau_M s + 1} \bar{y} \tag{2}$$

where G_M is the combined turbocharger and linkage gain, and τ_M is the relevant time constant.

The boost pressure sensor is of resistive type and its dynamic response is order of magnitudes faster than that of the other system components, such that its transfer function can be viewed as a pure gain.

4 CONTROL STRATEGY

The closed loop control of the boost pressure is performed with a modified PID control algorithm associated with a feed-forward compensation as shown in the block diagram of figure 3. The electronic controller uses the available information on fuel demand and engine speed to determine the value of the boost pressure command by using a predetermined look-up table based on the engine performance map. The boost pressure command is compared to the boost pressure feedback to generate the servoloop error which is processed by a proportional + integral control algorithm; the controller also performs the time derivative of the feedback signal which is added to the output of the PI control law; the resulting signal is limited by a saturation block and is then summed up to the feed-forward compensation signal to obtain the control signal driving the vacuum pressure modulating valve. As for the boost pressure command, the feed-forward compensation signal is computed by using another look-up table which is built according to the engine performance map.

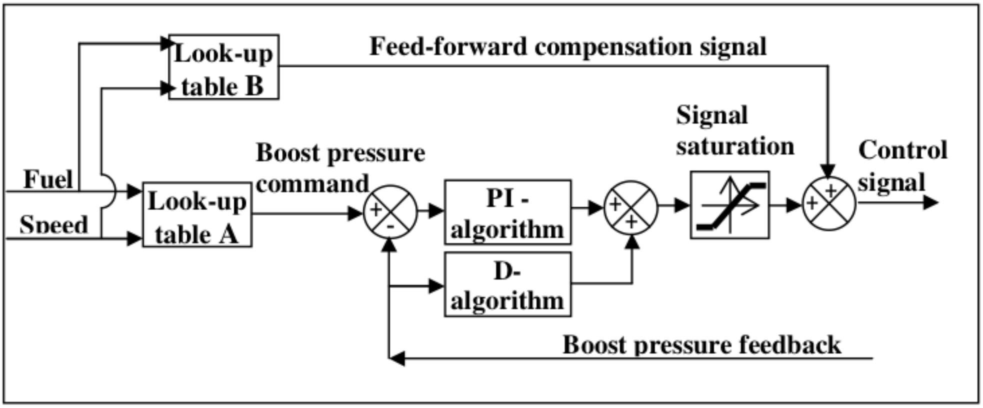

Figure 3 Block diagram of the control law

The rationale of this modified PID control law, in which the PI portion is applied to the servoloop error and the D portion to the feedback signal, is to make the system less sensitive to the noise of the boost pressure command resulting from fluctuations of the fuel demand, yet introduce some artificial damping into the servoloop to improve its dynamic characteristics. This solution, though effective to minimize the system noise, could make the system slow in responding to actual rapid changes of fuel demand and engine speed, since the derivative algorithm only acts on the feedback signal. To make up for that, a feed-forward compensation signal is generated by a second lookup table and added to the summed output of the PI and D algorithms to create the valve control signal; the effect of the feed-forward compensation is in fact to inject downstream in the control loop the information of the changes of the input variables, thereby enabling the control system to react faster.

5 SYSTEM MODEL AND SIMULATIONS

Two mathematical models of the boost pressure control system were prepared implementing the models of the system components, organized as shown in figure 4.

A linear system model was first prepared to assess the system stability and set the values of the control law parameters. This model was built starting from the linearization of the PID controller model, from the linearization of the solenoid valve flow characteristics as a function of controlled vacuum pressure error and introducing the second order and first order models describing the mechanical equilibrium of the actuator and the relationship between turbine vanes position and boost pressure response (figure 5).

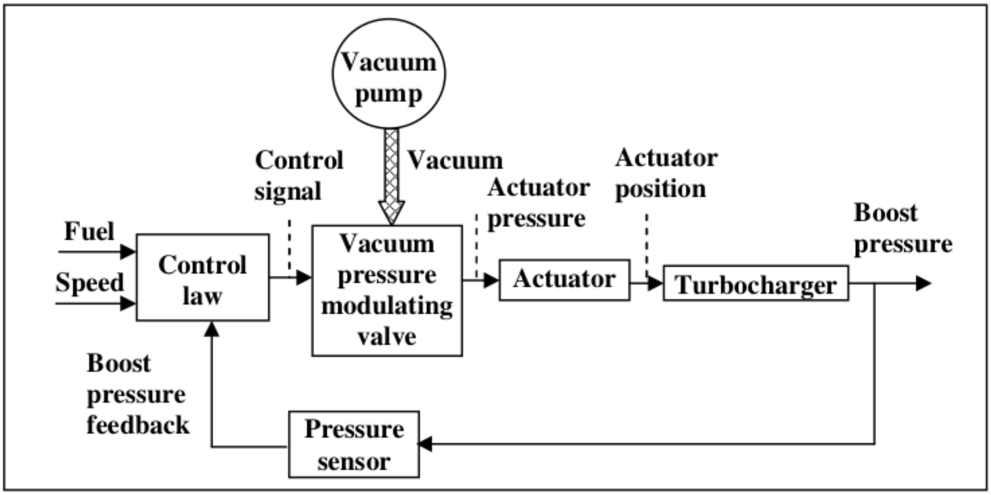
Vacuum pump
Control signal
Vacuum
Actuator pressure
Actuator position
Boost pressure
Fuel
Speed
Control law
Vacuum pressure modulating valve
Actuator
Turbocharger
Boost pressure feedback
Pressure sensor

Figure 4 Concept block diagram of the boost pressure control system

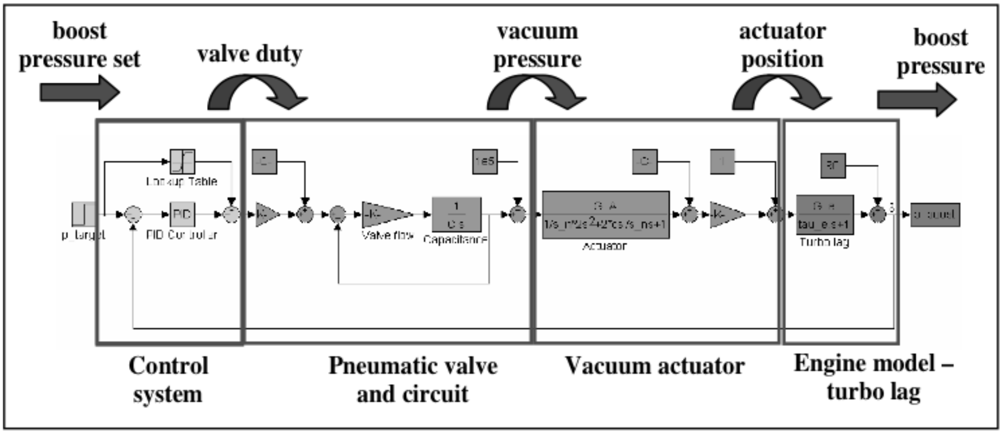
boost pressure set
valve duty
vacuum pressure
actuator position
boost pressure
Lookup Table
p_target
PID Controller
Valve flow
Capacitance
Actuator
Turbo lag
Control system
Pneumatic valve and circuit
Vacuum actuator
Engine model – turbo lag

Figure 5 Block schematic of the boost control system linearized model

Once the suitable values of these parameters were established, the system frequency response was determined (figure 6). Starting from the open loop Bode diagram, obtained with the linear model, the weight of each subsystem on the overall system performance can be highlighted, showing that the turbocharger time constant is the main parameter in determining the boost pressure control dynamics.

A non-linear model of the system was then prepared that integrated a Matlab/Simulink model of the pneumatic actuation system with a unidimensional fluid dynamic code simulating the engine behaviour (GT-POWER [4]), in analogy with the works of He et al. [5, 6]. This simulation code enables to perform a precise computation of the boost pressure for the entire engine working point, both in transient and steady state conditions. A model validation was performed by comparing the simulation results with experimental measures, both in steady state and transient conditions. As an example, the boost pressure variation as a consequence of a sudden load increase (injected quantity passing from 30 to 40 mm^3/st) at a constant engine speed of 3500 rpm is shown in figure 7, highlighting a good accordance between experimental results and simulated behaviour.

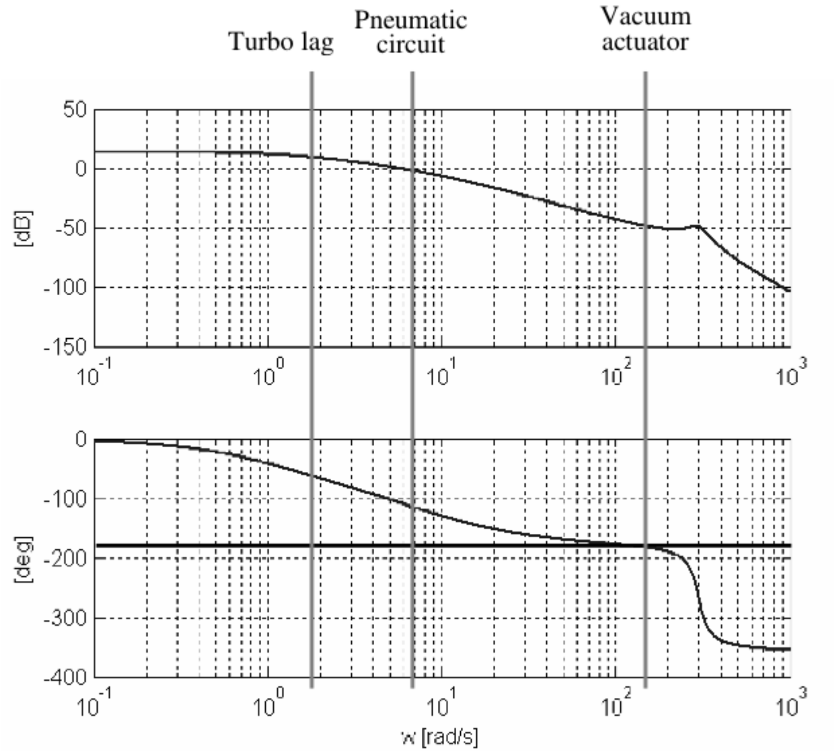

Figure 6 **Open loop Bode diagram of the boost control system linear model with indication of the transfer function poles position**

The association of this engine model with the dedicated Matlab/Simulink model for the pneumatic servoactuation system provided a powerful tool for assessing the system behaviour over the whole range of operating conditions, which included the evaluation of the effects of components tolerances and degradations, such as:

- tolerance of the characteristic of the vacuum modulating valve (duty cycle vs. pressure)
- tolerance of the characteristic of the vacuum actuator (position vs. pressure) due to spring variations, rod length variations and manual calibration
- backlash in the vane positioning mechanism
- effect of hysteresis
- friction increase originating from soot deposition and mechanism aging and wear

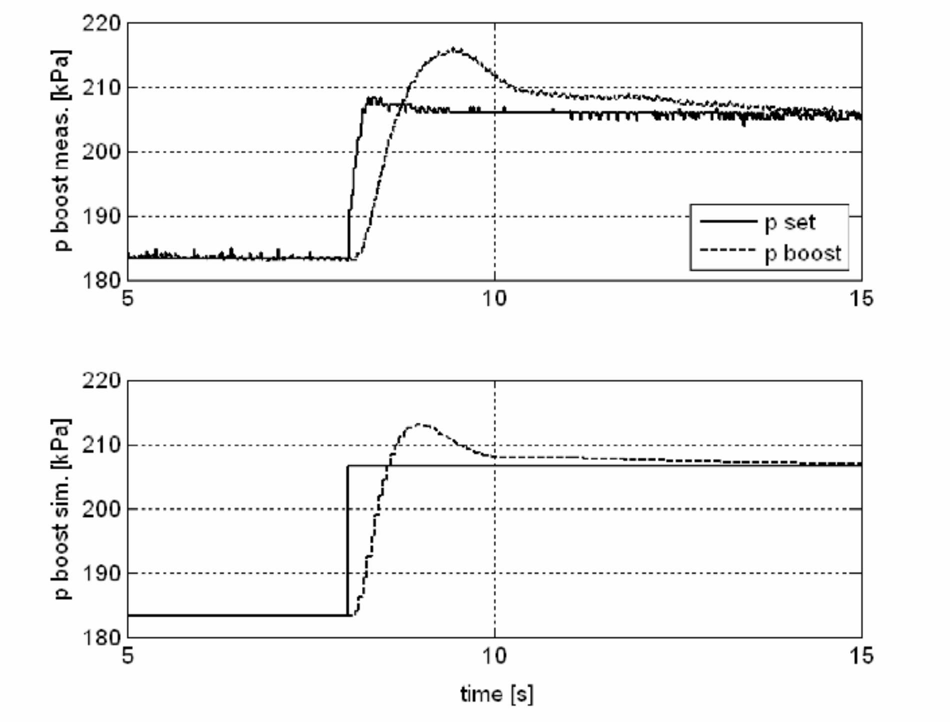

Figure 7 Comparison between experimental (upper diagram) and simulated (lower diagram) behaviour of the boost pressure during a load step at 3500 rpm engine speed

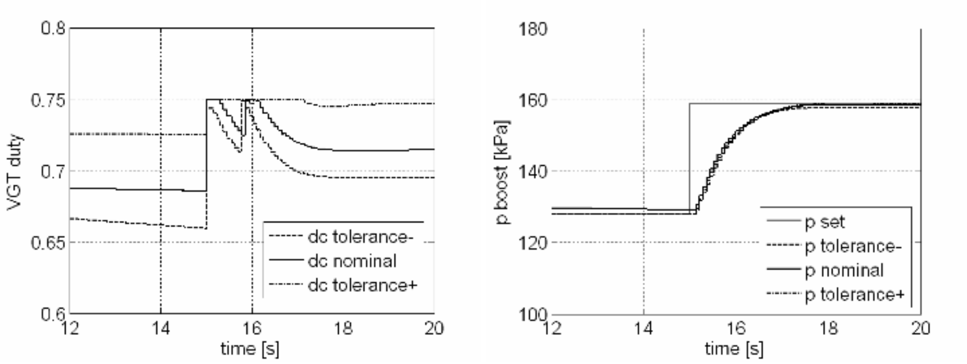

Figure 8 Simulation results; duty cycle and boost pressure diagram for an injected quantity step (from 31 to 46 mm3/st) at 1500 rpm (+/- 1 mm rod length deviation)

The robustness of the boost pressure control system could thus be ascertained. As an example, in figure 8, the effect of an actuator rod length variation in production is analysed by means of the non linear model, showing that the closed loop control is capable to adapt the command to solenoid valve (diagram on the left) in order to minimize the errors in boost pressure (diagram on the right).

6 LESSONS LEARNED AND SYSTEM IMPROVEMENTS

The proposed simulation approach has proved to be effective in analysing the effect of component tolerances and deviations on the accuracy of the boost pressure control system, both in steady state and dynamic conditions. The capability of the control strategy to reduce the system sensitivity to these deviations has thus been studied for different kind of variations and for different specifications of accuracy for the boost control.

In a second part of the study the effect on the system performance of the introduction of a position sensor on the vacuum actuator, building an internal position control loop, has been investigated. The control law was then modified as shown in figure 9: the control signal resulting from the outer boost pressure servoloop now becomes the actuator position command, which is compared to the actuator position feedback to generate the actuator position error.
This signal is processed by a second PI control law and it is added to the feed-forward compensation signal to create the control signal to the vacuum pressure modulating valve.

New simulations were run for a system with this new architecture and significant improvements were observed. Figure 10 shows the results obtained from the simple linear model of the complete system, with and without actuator position feedback loop. It can be seen from this diagram that the introduction of the internal loop slightly reduces the response time, which is anyhow limited by the turbo-lag. The main effect of the internal position loop is to reduce the overshooting of the pressure value for a step response and to improve the accuracy during transients.

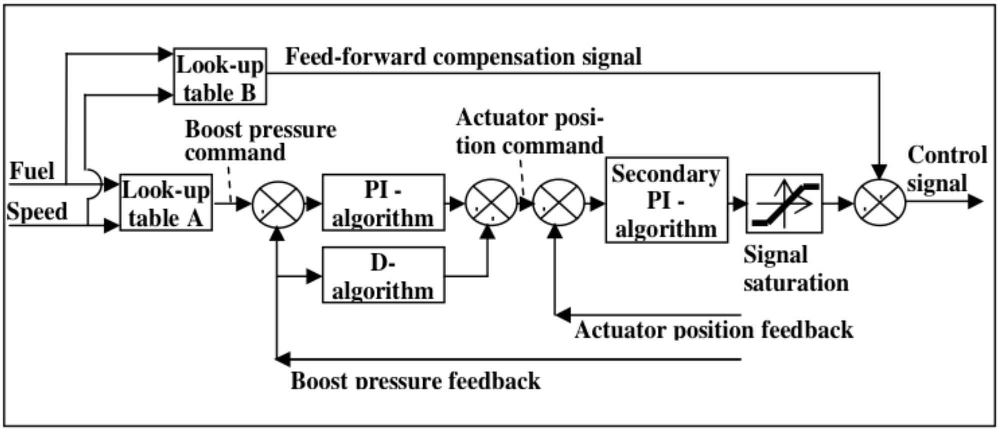
Look-up table B
Feed-forward compensation signal
Boost pressure command
Actuator position command
Control signal
Fuel
Speed
Look-up table A
PI - algorithm
Secondary PI - algorithm
D- algorithm
Signal saturation
Actuator position feedback
Boost pressure feedback

Figure 9 New control law with an actuator feedback loop

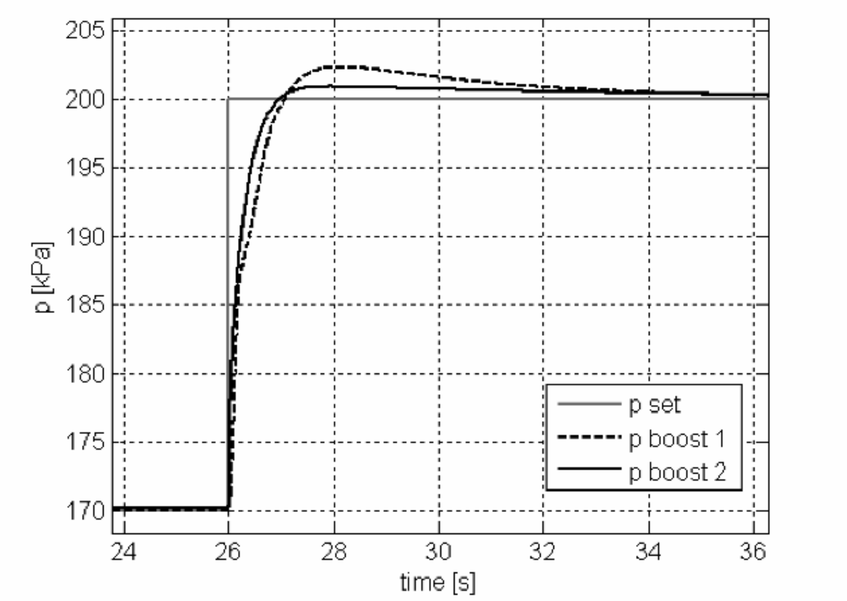

Figure 10 Application of the linear model to the evaluation of boost control: improvements with the introduction of actuator position feedback (continuous line)compared with the simple boost feedback (dashed line)

7 CONCLUSIONS

The work herein presented is the result of an R&D activity performed by GM Powertrain Europe, together with the Department of Mechanics of the Politecnico di Torino aimed at improving the performance of the boost pressure control system of a turbocharged diesel engine. The research activity was primarily focused to analyze the interactions among control strategy, actuation system performance and engine characteristics in controlling the boost pressure, and to assess the effects of components tolerances and malfunctionings on the whole system behaviour. The system performance assessment was then followed by an investigation on possible improvements, and a solution implementing the position feedback sensor on the actuator was analysed, that proved to be effective in enhancing the system dynamic response, accuracy and robustness.

REFERENCES

[1] RASK, E.; SELLNAU M.
Simulation-Based Engine Calibration: Tools, Techniques, and Applications
SAE International, 2004-01-1264
2004 SAE World Congress, Detroit, Michigan, March 8-11, 2004

[2] MOSKWA, J.J.; HEDRICK, J.K.
Modelling and Validation of Automotive Engines for Control Algorithm Development
ASME Journal of Dynamic Systems, Measurement and Control
Vol. 114, No. 2, pp. 278-285, June 1992

[3] FILIPI, Z.; WANG Y.; ASSANIS, D.
Effect of Variable Geometry Turbine (VGT) on Diesel Engine and Vehicle System Transient Response
SAE International, 2001-01-1247
2001 SAE World Congress, Detroit, Michigan, March 5-8, 2001

[4] Gamma Technologies
GT-POWER User Manual
Version 6.1, 2004

[5] HE, Y.; LIN, C.; GANGOPADDHYAY A.
Integrated Simulation of the Engine and Control System of a Turbocharged Diesel Engine
SAE International, 2006-01-0439
2006 SAE World Congress, Detroit, Michigan, April 3-6, 2006

[6] HE, Y.
Development and Validation of a 1D Model of a Turbocharged V6 Diesel Engine Operating Under Steady-State and Transient Conditions
SAE International, 2005-01-3857
Powertrain & Fluid Systems Conference and Exhibition, San Antonio, Texas USA, October 24-27, 2005

Systems and Control

Metering Poppet Valve System Control

C. Harvey O. Cline and Roger C. Fales
Mechanical & Aerospace Engineering, University of Missouri-Columbia

ABSTRACT

Metering poppet valves are being developed to regulate flow in place of more common spool valves. This is due to certain advantages offered by metering poppet valves. However, these advantages cannot be fully realized until control design challenges involving stability and performance are solved. A design for a two-stage metering poppet valve is presented. For control, several researchers have used feedback linearization to cancel part of a hydraulic system's nonlinearities in spool valves. In this work, nonlinearities are cancelled in the input-output relationship of the metering poppet valve. Reference tracking of the flow is analyzed.

1. INTRODUCTION

Poppet valves have been available for many years but limited in use to provide pressure-relief in high-powered hydraulic circuits. Recently, there has been an interest in developing poppet valves for flow metering applications (1), (2), (3), (4), (5). The poppet valve offers certain advantages over the spool valve. Mainly, poppet valves have extremely low leakeage when closed, they require less precise machining, they are capable of adjusting themselves with wear, and they are self-flushing and therefore less sensitive to contamination (6). Key disadvantages to using the poppet valve for flow metering are centered around dynamic instability issues (7), (8). The literature suggests that nonlinearities, such as flow forces and damping on the metering element, are responsible for these instabilities (8), (9), (10). However, they have yet to be clearly understood.

Few metering poppet valves are available to the hydraulic industry due to these poorly understood instabilities. The valves which are made available compromise performance for stability. For one such valve, simulation and experimental results (1), (11) were used to design a metering poppet valve which, in simulation, is relatively stable and able to meet certain open loop performance criteria (12), (13). Despite these design goals, this valve is still susceptible to the instabilities.

Feedback linearization is one nonlinear control method developed to handle system nonlinearities and draw from linear systems control theory to ensure stability and performance (14). Open literature contains studies where both feedback linearization is applied to metering spool valves (15) and control is used with metering poppet valves (16). However, no studies of feedback linearization with metering poppet valves have been found. The present research uses simulation methods to explore the possibility of using an input-

---

Power Transmission and Motion Control 2007 Edited by Dr D N Johnston and Professor A R Plummer
© With The Centre for Power Transmission and Motion Control

output, feedback linearization controller to control the flow across a metering poppet valve designed for both stability and performance. The results include an analysis of the robustness of the controller.

The valve model used in the study was developed by Muller & Fales (11), (12) to simulate a two-stage, electro-hydraulic, forced-feedback poppet valve (Fig. 1). Referring now to Fig. 1, the valve is in the closed position with high pressure connected to the inlet port and low pressure connected to the outlet port. In order to raise the main poppet off its seat, current is supplied to the solenoid actuator which forces the pilot poppet off the seat. Fluid is then allowed to flow from the control volume through this orifice to the outlet port (Q_2). With the pilot poppet initial opening, the flow through the control volume inlet orifice (Q_1) is smaller than the flow through the pilot poppet orifice producing a net outflow from the control volume and decreasing the pressure. The pressure in the control volume decreases to a level where the net force on the main poppet is in an upward direction, effectively lifting it off its seat. This opens an orifice between the high pressure inlet port and low pressure outlet port which passes a metered flow (Q_3). The upward movement of the main poppet pushes on the pilot poppet through the feedback spring.

2. NOMENCLATURE

A_c	Area of the main poppet exposed to the control pressure	K_1	Flow gain for the control volume inlet orifice
A_L	Area of the main poppet exposed to the load pressure	K_2	Flow gain for the pilot poppet orifice
A_s	Area of the main poppet exposed to the supply pressure	K_3	Flow gain for the main poppet orifice
a_1	Area of the inlet orifice to the control volume	K_4	Flow gain for the load orifice
a_4	Area of the orifice from the load volume to the tank	X_{sid}	Initial displacement of the feedback spring
B_p	Pilot poppet damping coefficient	P_L	Fixed load pressure (at the outlet port)
b_m	Main poppet linear damping coefficient	P_s	Supply pressure (at the inlet port)
C_d	Orifice discharge coefficient	P_t	Tank pressure
h_2	Slope for the pilot poppet orifice	V_c	Fluid volume in the control volume
h_3	Slope for the main poppet orifice	V_L	Fluid volume in the load volume
k	Feedback spring coefficient	β	Fluid bulk modulus
M	Mass of the main poppet	ρ	Fluid density
m	Mass of the pilot poppet		

3. MATHEMATICAL MODEL

The model used to simulate the forced-feedback metering poppet valve is a 6th order model composed of four governing equations: two mass-spring-damper equations of motion for the main and pilot poppets, a pressure rise rate equation for the control volume, and a pressure rise rate equation for the load volume. Positive displacements for the poppets were defined as displacements into the control volume. Both poppets are prohibited from negative displacements by their poppet seats ($x_m \geq 0$, $x_p \geq 0$).

For the main poppet, Newton's second law of motion was applied with terms accounting for linear damping forces, the feedback spring force, pressure forces above and below the poppet and flow forces (Eq. 1).

$$\begin{aligned} M\ddot{x}_m &= -b_m\dot{x}_m - k\left(x_m + x_p + X_{sid}\right) - P_cA_c \\ &\quad + P_sA_s + P_LA_L - 0.72C_d^2h_3x_m\left(P_s - P_L\right) \end{aligned} \tag{1}$$

The pilot poppet was modeled similarly with terms accounting for damping forces, the feedback spring force, flow forces, and the solenoid actuator force (Eq. 2).

$$m\ddot{x}_p = -B_p\dot{x}_p - k\left(x_m + x_p + X_{sid}\right) - 0.72C_d^2h_2x_p\left(P_c - P_L\right) + F \tag{2}$$

The solenoid force was confined to a range between 0 and 60 Newtons. In addition, the simplifying assumption was made that the pilot poppet is instantly pressure balanced and damping is not "physically" modeled. This damping is lumped with the linear damping and represented as B_p in the model.

The dynamics of the control volume pressure were simulated by Eq. 3:

$$\dot{P}_c = \frac{\beta}{V_c - A_cx_m}\left(Q_1 - Q_2 + A_c\dot{x}_m\right), \tag{3}$$

where $Q_1 = K_1\sqrt{P_s - P_c}$ & $Q_2 = K_2x_p\sqrt{P_c - P_L}$. (4), (5)

The assumption has been made that the volume change of the control volume resulting from pilot poppet movement is small compared to its nominal volume and therefore the volume change here is due solely to main poppet movement. The further simplification was made to neglect the flow contribution from the pilot poppet's movement due to its comparatively small area and displacement relative to the main poppet. For the load volume, its dynamics were simulated by a fixed volume connected to a tank through an orifice. The dynamics of the load volume were simulated using Eq. 6:

$$\dot{P}_L = \frac{\beta}{V_L}\left(Q_2 + Q_3 - Q_4\right) \tag{6}$$

where $Q_3 = K_3x_m\sqrt{P_s - P_L}$ & $Q_4 = K_4\sqrt{P_L - P_t}$. (7), (8)

All flows (Eqs. 4, 5, 7, and 8) were simulated with the classic orifice equation with the flow gains calculated as follows:

$$K_1 = a_1C_d\sqrt{\frac{2}{\rho}}\,,\quad K_2 = h_2C_d\sqrt{\frac{2}{\rho}}\,, \qquad (9), (10),$$

$$K_3 = h_3 C_d \sqrt{\frac{2}{\rho}}, \quad K_4 = a_4 C_d \sqrt{\frac{2}{\rho}}.$$

(11), (12)

Although it is possible to simulate bidirectional flow through the valve, flow was restricted as shown in Fig. 1 and pressures restricted as follows ($P_t \le P_L \le P_c \le P_s$). The total flow out of the valve is the sum of the flows across the pilot and main poppets (Eq. 13).

$$Q_{out} = Q_2 + Q_3 \tag{13}$$

For controller design, the model was represented in the state space form. In addition, the load dynamics were dropped and represented by a fixed load pressure parameter, P_L:

$$\dot{\vec{x}} = \vec{f}(\vec{x}) + \vec{g}(\vec{x})u \tag{14}$$

$$y = h(\vec{x}) \tag{15}$$

$$\vec{x} = \begin{bmatrix} x_1 & x_2 & x_3 & x_4 & x_5 \end{bmatrix}^T = \begin{bmatrix} x_m & \dot{x}_m & P_c & x_p & \dot{x}_p \end{bmatrix}^T \tag{16}$$

$$\vec{f}(\vec{x}) = \begin{bmatrix} x_2 \\ \frac{1}{M}[-b_m x_2 - k(x_1 + x_2 + preload) - x_3 A_c + P_s A_s + P_L A_L \\ -0.72 C_d^2 h_3 x_1 (P_s - P_L)] \\ \frac{\beta}{V_c - A_c x_1}\left(K_1 \sqrt{P_s - x_3} - K_2 x_4 \sqrt{x_3 - P_L} + A_c x_2\right) \\ x_5 \\ \frac{1}{m}\left[-B_p - k(x_1 + x_2 + preload) - 0.72 C_d^2 h_2 x_4 (x_3 - P_L)\right] \end{bmatrix} \tag{17}$$

$$\vec{g}(\vec{x}) = \begin{bmatrix} 0 & 0 & 0 & 0 & \frac{1}{m} \end{bmatrix}^T \tag{18}$$

$$u = F \tag{19}$$

$$h(\vec{x}) = K_2 x_4 \sqrt{x_3 - P_L} + K_3 x_1 \sqrt{P_s - P_L} \tag{20}$$

4. INPUT-OUTPUT FEEBACK LINEARIZATION CONTROLLER

Eqs. 14-20 represent the system in a form which is suitable for input-output, feedback linearization. The elements which need to be developed to complete this linearization are a change of variables and a state feedback control law. The development of the transformation map (Eq. 21) for the change of variables will be discussed next. The state feedback control law used to linearize the input-output map will be clear from the transformed system.

$$\vec{z} = \vec{T}\left(\vec{x}\right) = \begin{bmatrix} \vec{\phi}\left(\vec{x}\right) \\ \vec{\psi}\left(\vec{x}\right) \end{bmatrix} = \begin{bmatrix} \vec{\eta} \\ \vec{\xi} \end{bmatrix} \tag{21}$$

The transformed system takes the form of Eqs. 22 - 24 below, also known as the normal form:

$$\dot{\vec{\eta}} = \vec{f}_0\left(\vec{\eta},\vec{\xi}\right), \tag{22}$$

$$\dot{\vec{\xi}} = A_c\vec{\xi} + B_c\gamma\left(\vec{x}\right)\left[u - \alpha\left(\vec{x}\right)\right], \tag{23}$$

$$y = C_c\vec{\xi}\ , \tag{24}$$

$$\text{where } A_c = \begin{bmatrix} 0 & 1 & 0 & \dots & 0 \\ 0 & 0 & 1 & \dots & 0 \\ \vdots & & \ddots & & \vdots \\ \vdots & & & 0 & 1 \\ 0 & \dots & \dots & 0 & 0 \end{bmatrix}, B_c = \begin{bmatrix} 0 \\ 0 \\ \vdots \\ 0 \\ 1 \end{bmatrix}, C_c = \begin{bmatrix} 1 \\ 0 \\ \vdots \\ 0 \\ 0 \end{bmatrix}^T \tag{25}$$

Its development started with the derivation of the system's input-output map. This was obtained by taking successive time derivatives of the output equation (Eq. 20) ($\dot{y}\ \ddot{y}\ \dots\ y^{(\rho)}$) until u appeared with a nonzero coefficient.

$$y^{(\rho)} = -\gamma\left(\vec{x}\right)\alpha\left(\vec{x}\right) + \gamma\left(\vec{x}\right)u \tag{26}$$

Here, ρ is referred to as the relative degree. For the metering poppet valve system defining output as in Eq. 20, the relative degree is 2 and thus Eq. 20 was differentiated a second time to obtain:

$$\ddot{y} = -\gamma\left(\vec{x}\right)\alpha\left(\vec{x}\right) + \gamma\left(\vec{x}\right)u\ , \tag{27}$$

$$\gamma\left(\vec{x}\right) = \frac{K_2\sqrt{x_3 - P_L}}{m}\ , \tag{28}$$

$$\begin{aligned} \alpha\left(\vec{x}\right) = -\frac{m}{K_2\sqrt{x_3 - P_L}}\{\left(\dot{x}_1\right)dh_{x_1} + \left(\dot{x}_2\right)dh_{x_2} + \left(\dot{x}_3\right)dh_{x_3} + \left(\dot{x}_4\right)dh_{x_4} + \\ \frac{1}{m}(-B_p - k\left(x_1 + x_4 + preload\right) - 0.72C_d^2h_2x_4\left(x_3 - P_L\right))dh_{x_5}\} \end{aligned}\ , \tag{29}$$

$$\begin{aligned} dh_{x_1} = \frac{A_c\beta K_2x_4}{2\left(V_c - A_cx_1\right)^2\sqrt{x_3 - P_L}}(K_1\sqrt{P_s - x_3} \\ - K_2x_4\sqrt{x_3 - P_L} + A_Cx_2) \end{aligned}\ , \tag{30}$$

$$dh_{x_2} = K_3\sqrt{P_s - P_L} + \left(\frac{A_c\beta}{V_c - A_cx_1}\right)\frac{K_2x_4}{2\sqrt{x_3 - P_L}}\ , \tag{31}$$

$$\begin{aligned} dh_{x_3} &= -\frac{\beta K_2 x_4}{4\left(V_c - A_c x_1\right)\sqrt{x_3 - P_L}}\left(\frac{K_1}{\sqrt{P_s - x_3}} + \frac{K_2 x_4}{\sqrt{x_3 - P_L}}\right) \\ &\quad -\left(\dot{x}_3\right)\frac{K_2 x_4}{4\left(x_3 - P_L\right)^{3/2}} + \left(\dot{x}_4\right)\frac{K_2}{2\sqrt{x_3 - P_L}} \end{aligned}, \tag{32}$$

$$dh_{x_4} = -\frac{\beta K_2^2 x_4}{2\left(V_c - A_c x_1\right)} + \left(\dot{x}_3\right)\frac{K_2}{2\sqrt{x_3 - P_L}}, \tag{33}$$

$$dh_{x_5} = K_2\sqrt{x_3 - P_L}\,. \tag{34}$$

At this point, it is important to note that examination of Eq. 28 indicates that $\rho = 2$ for $x_3 \neq P_L$. This defines a necessary set ($D_0 = \left\{x \in \Re^5 \mid P_L < x_3 \leq P_s\right\}$) for the valid operation of this input-output, feedback linearization controller.

The normal form decomposed the system into an external part Eqs. 23 & 24 and an internal part eq. 22. This decomposition was determined by the relative degree and thus the external state variable was a 2 x 1 transformed state vector. The transformation that maps to the external part consisted of the time derivatives of the output equation:

$$\vec{\xi} = \vec{\psi}\left(\vec{x}\right) = \begin{bmatrix} \xi_1 \\ \xi_2 \end{bmatrix} = \begin{bmatrix} \psi_1\left(\vec{x}\right) \\ \psi_2\left(\vec{x}\right) \end{bmatrix} = \begin{bmatrix} y\left(\vec{x}\right) \\ \dot{y}\left(\vec{x}\right) \end{bmatrix}. \tag{35}$$

Since the system is a 5th order system, the internal state variable was a 3 x 1 transformed state vector:

$$\vec{\eta} = \vec{\phi}\left(\vec{x}\right) = \begin{bmatrix} \eta_1 \\ \eta_2 \\ \eta_3 \end{bmatrix} = \begin{bmatrix} \phi_1\left(\vec{x}\right) \\ \phi_2\left(\vec{x}\right) \\ \phi_3\left(\vec{x}\right) \end{bmatrix}. \tag{36}$$

The transformation for the internal part should be chosen to exclude the input *u* from these dynamics and thus the criterion for choosing $\vec{\phi}\left(\vec{x}\right)$ is:

$$\frac{\partial\vec{\phi}\left(\vec{x}\right)}{\partial\vec{x}}g\left(\vec{x}\right) = 0\,. \tag{37}$$

In the present research, the control objective was to design a state feedback control law such that the output asymptotically tracks a reference signal *r(t)*. For output tracking of a reference signal, a further change of variables was defined:

$$\vec{e} = \vec{\xi} - \vec{R}\,,\ \text{where}\ \vec{R} = \begin{bmatrix} R_1 \\ R_2 \end{bmatrix} = \begin{bmatrix} r \\ \dot{r} \end{bmatrix}. \tag{38}$$

$$\Rightarrow \dot{\vec{\eta}} = \vec{f}_0\left(\vec{\eta}, \vec{e} + \vec{R}\right) \tag{39}$$

$$\dot{\vec{e}} = A_c\vec{e} + B_c\left\{\gamma(\vec{x})\left[u-\alpha(\vec{x})\right]-\ddot{r}\right\} \text{ where } A_c = \begin{bmatrix} 0 & 1 \\ 0 & 0 \end{bmatrix}, B_c = \begin{bmatrix} 0 \\ 1 \end{bmatrix} \qquad (40), \quad (41)$$

The input-output map was then linearized by the following control law:

$$u = \alpha(\vec{x}) + \beta(\vec{x})(v + \ddot{r}) \qquad (42)$$

where $\beta(x) = \gamma^{-1}(x)$ (43)

producing the results:

$$\dot{\vec{\eta}} = \vec{f}_0\left(\vec{\eta}, \vec{e} + \vec{R}\right) \qquad (44)$$

$$\dot{\vec{e}} = A_c\vec{e} + B_c v \qquad (45)$$

Substitution of $\vec{e}$, $\dot{\vec{e}}$, A_c, and B_c produces the controlled form of the input-output map:

$$\ddot{y} = v + \ddot{r}. \qquad (46)$$

Controller design was completed by choosing v to be a PD controller ($v = -\vec{K}\vec{e}$) such that $A_c - B_c\vec{K}$ was Hurwitz and the internal state variable $\vec{\eta}(t)$ was bounded for all $t \geq 0$. Determining $\vec{K}$ to satisfy the criterion was straightforward. However, to insure that $\vec{\eta}(t)$ was bounded, the system must be minimum phase. This is addressed next.

5. ANALYSIS OF ZERO DYNAMICS

The system is minimum phase if its zero dynamics have an asymptotically stable equilibrium point in D_0. The zero dynamics are determined by setting $\xi = 0$ in Eq. 44 to obtain:

$$\dot{\vec{\eta}} = \vec{f}_0(\vec{\eta}, 0). \qquad (47)$$

In the present research, the zero dynamics were determined using the system prior to the transformation by restricting $\vec{x}$ to the set: $Z^* = \left\{\vec{x} \in D_0 \mid y = \dot{y} = 0\right\}$ and setting $u = \alpha(\vec{x})|_{\vec{x} \in Z^*}$ in eqs. 14 & 15. Using eq. 20 and its first time derivative with the necessary set of validity D_0, it was determined that $Z^* = \left\{\vec{x} \in D_0 \mid x_1 = x_2 = x_4 = x_5 = 0\right\}$. In order for x_2 and x_5 to be maintained at zero, $\dot{x}_2$ and $\dot{x}_5$ must also be zero. The zero dynamics are thus:

$$kX_{sid} + x_3 A_c = P_s A_s + P_L A_L + F_{stm}, \qquad (48)$$

$$\dot{x}_3 = \frac{\beta}{V_c}\left(K_1\sqrt{P_s - x_3}\right). \tag{49}$$

This result can be inferred. If the flow is restricted to zero, both poppets must be closed and not moving. If this happens at a time just after the main poppet has closed, but prior to the supply line and control volume reaching equilibrium, high pressure fluid will flow into the control volume (Q_1) until equilibrium is reached at $x_3 = P_s$. The increased pressure force from the control volume on the head of the already closed main poppet will be balanced by the force of the seat, represented in Eq. 48 as F_{stm}. It is thus clear that in the set D_0 the zero dynamics have an asymptotically stable equilibrium point at $x_3 = P_s$ and the system is minimum phase. To complete the discussion, $\vec{\eta}(t)$ is only bounded for sufficiently small $\vec{e}(0)$, $\vec{\eta}(0)$, and $\vec{R}(t)$. The set in which $\vec{e}(0)$, $\vec{\eta}(0)$, and $\vec{R}(t)$ are sufficiently small must be a subset of D_0 and the necessary and sufficient set of operation for this input-output, feedback linearization controller. In the present research $\vec{x}(0) = 0$ and $\vec{R}(0) = 0$ thus, $\vec{e}(0) = 0$ and $\vec{\eta}(0) = 0$. *r(t)* was restricted to the range between 0 and 90 L/min and was sufficiently small.

6. RESULTS & DISCUSSION

The control strategy developed above has been tested in a series of simulations. The attention focused on the response of controller tracking to different operating conditions, parameter perturbations, and disturbances. In the results that follow, the reference trajectory was the step response of a linear, second order system with a damping ratio of 0.5 and natural frequency of 50 hz. The step occurred at 0.2 s. Nominal operating conditions were chosen to be: supply pressure (P_s) = 21 MPa and pressure drop across the valve (ΔP) = 2.1 MPa. These conditions were chosen as nominal due to the fact that valve geometry produces a flow of 120 LPM with the main poppet fully open at a pressure drop of 2.1 MPa. To serve as a benchmark, a PID controller was tuned.

For nominal conditions, the responses of both controllers are plotted in Fig. 2. The input-output controller performed well, with close tracking of the reference trajectory. This result indicates that for these conditions, the system nonlinearities were canceled by the controller causing the closed loop system to behave like the second order linear system it was tracking. Shortly after the step to the reference system at 0.2 s, a small deviation of the flow from the reference trajectory occurred. Pictured more closely in Fig. 3, this deviation was the result of controller saturation.

As discussed above, the solenoid force was confined to a range between 0 N and 60 N. This range served to limit the controller's output and thus the expression for the controller in Eqs. 42 and 43 is incomplete. To complete this expression, Eq. 42 is redefined:

$$u_T = \alpha(\vec{x}) + \beta(\vec{x})(v + \ddot{r}). \tag{50}$$

The effective controller output is then defined as follows:

$$u = u_T + F_s \tag{51}$$

$$\text{where } F_s = \begin{Bmatrix} 0, \; if \;\; 0 \le u_T \le 60 \\ -u_T + 60, \; if \;\; u_T > 60 \\ -u_T, \; if \;\; u_T < 0 \end{Bmatrix} \tag{52}$$

With this completed controller expression, Eq. 46 must be corrected:

$$\ddot{y} = v + \ddot{r} + \gamma(\vec{x})F_s = \begin{Bmatrix} v + \ddot{r}, \; if \;\; 0 \le u_T \le 60 \\ -\gamma(\vec{x})\alpha(\vec{x}) + \gamma(\vec{x})60, \; if \;\; u_T > 60 \\ -\gamma(\vec{x})\alpha(\vec{x}), \; if \;\; u_T < 0 \end{Bmatrix}. \tag{53}$$

Eq. 53 is the final equation needed for an analytical understanding of the effects of controller saturation on the model. Eqs. 29 and 31 indicate that when the main poppet opens, its acceleration ($\dot{x}_2$) causes a dramatic decrease in $\alpha(\vec{x})$ and thus u driving both variables to negative values. Since the flow also increases dramatically with the opening of the main poppet, this response from the controller is meant to attenuate the flow increase and maintain reference signal tracking. However, the effective input signal saturates at zero. Eq. 53 indicates that $\ddot{y} = -\gamma(\vec{x})\alpha(\vec{x})$ when $u = 0$. With $\alpha(\vec{x})$ becoming increasingly more negative, $\ddot{y}$ becomes increasingly more positive and thus y increases when the effective input saturates at zero due to $\alpha(\vec{x})$. As the main poppet slows, its decreased acceleration allows the effective input u to rise above zero and resume reference tracking. As the results show, this effect was present in all simulations to varying degrees.

Displayed in Fig. 4 are the results of controller tracking at four different conditions: (1) P_s = 21 MPa, ΔP = 2.1 MPa; (2) P_s = 28.9 MPa, ΔP = 10 MPa; (3) P_s = 30 MPa, ΔP = 20 MPa; (4) P_s = 35 MPa, ΔP = 35 MPa. In all conditions, tracking was close until the main poppet opened and the controller saturated at its lower limit. Upon controller saturation, the flow spiked with the magnitude of the spike dependent on the ΔP. Following the flow deviation, the controller reestablished tracking of the dynamic time behavior of the reference signal. The flows at all four conditions exhibited the same rise time and settling time as the reference signal.

Despite the dynamic time behavior being reestablished, full recovery was not achieved due to tracking error in all conditions. The magnitude of the tracking error was also dependent on the ΔP as was the magnitude of the flow deviation. This suggests that the tracking error was dependent on controller saturation as was the flow deviation. As further support of this, in conditions 2, 3 and 4, where tracking error is increasingly noticeable, the valve flow oscillates with high frequency and low amplitude. Examination of the controller in these conditions revealed that the controller continuously saturated at its lower limit. The controller was trying to eliminate the errors in reference tracking, but was prohibited by the system's limitations.

To test the response of the controller to disturbances, two simulations were run during which the supply pressure was increased at 1 s to 23 MPa and 28.9 MPa from the nominal condition. The results of the simulations are shown in Fig. 5. The response to the disturbance in each simulation was a transient spike which lasted no longer than 50 ms. For the increase to 28.9 MPa, the spike was twice as large with a slightly longer duration. In both simulations controller saturation accounted for the magnitude of the height of the spikes. Close steady state tracking was restored in both cases. It should be noted that the pressure disturbance occurred after reaching steady state conditions. This, along with the nominal operating conditions, likely explains the ability of the controller to reestablish reference tracking. This is in contrast to cases following initial pressure deviations of lower magnitude at more extreme operating conditions, Fig. 4.

To test the robustness of the model, certain parameters in the model were separately increased by as much as 50 % and decreased by as much as 40 %. Simulations were then run in the nominal conditions. The parameters chosen were those which might have the most variation in time and from valve to valve based on real world considerations: the area of the inlet orifice to the control volume (a_1), the slope for the pilot poppet orifice (h_2), and the slope for the main poppet orifice (h_3). The results of these simulations are displayed in Figs. 6 & 7. Not displayed are robustness results to variations in h_3 because the controller proved to be very robust to changes in this parameter. The results can be explained as follows: for those parameters which are changed in the model, the terms which they are associated with in the input-output map will not be eliminated. Instead, there will be residual nonlinear terms multiplied by the parameter perturbations remaining in the input-output map. These residuals affect the response of the closed loop system and, if large enough, will destabilize it.

7. CONCLUSIONS

Although the results are promising, there are some causes for concern. The occurrence of relatively large flow spikes at sufficiently large pressure drops is troubling. These spikes occurred when the main poppet opened and in those simulations which saw upstream pressure disturbances at 1.0 s. Even though both spikes occurred at different times in the simulations, both were the result of controller saturation. The initial deviation of the flow in response to the opening of the main poppet or upstream pressure disturbances was intense enough to cause the controller to saturate in attempts to maintain tracking. In higher pressure conditions, simulations show that tracking of the reference signal is not reestablished following the initial flow deviation. It is believed that this is also a result of controller saturation. Controller saturation is a highly undesirable situation due to the fact that when the controller reaches its lower bound, the flow increases opposite the intended action of the controller causing further flow deviations.

Thus, it is possible that the central cause for the troubling behavior of the closed loop system is controller saturation. Future research should further explore linear techniques to determine the inner controller (v) such that this is avoided. Also, nonlinear techniques such as gain scheduling could be applied to attenuate or even eliminate some unwanted, time dependent behavior. It is necessary that future work address the controller saturation issue and sensor measurements before lab testing can proceed.

8. REFERENCES

[1] Zhang, R., Alleyne, A. G., Prasetiawan, E. A., "Performance Limitations of a Class of Two-Stage Electro-Hydraulic Flow Valves." International Journal of Fluid Power, Vol. 3, 2002, No. (1).
[2] Schexnayder, L. F., "Poppet Valve with Force Feedback Control." U.S. Patent 5 421 545, Jun. 6, 1995.
[3] Aardema, J. A., "Pilot Valve for a Flow Amplifying Poppet Valve." U.S. Patent 5 645 263, Jul. 8, 1997.
[4] Yang, X., Paik, M. J., Pfaff, J. L., "Pilot Operated Control Valve Having a Poppet With Integral Pressure Compensating Mechanism." U.S. Patent 6 745 992, Jun. 8, 2004.
[5] Yang, X., Stephenson, D. B., Paik, M. J., "Hydraulic Poppet Valve with Force Feedback." U.S. Patent 6 869 060, Mar. 22 2005.
[6] Manring, N.D., *Hydraulic Control Systems*. Hoboken, NJ: John Wiley & Sons, 2005, pp. 224-228.
[7] Hayashi, S., 1995, "Instability of Poppet Valve Circuit." JSME International Journal Series C, Vol. 38, No. (3), pp. 357-366.
[8] Funk, J.E., "Poppet Valve Stability. Journal of Basic Engineering, June 1964, pp. 207-212.
[9] McCloy, D., "Compensation of Steady State Flow Forces in Valves." Hydraulic Pneumatic Power, March 1969, pp. 150-158.
[10] Johnston, D., Edge, K., Vaughan, N. 1991. Experimental Investigation of Flow and Force Characteristics of Hydraulic Poppet and Disc Valves." Proceedings of the Institution of Mechanical Engineers Part A, Vol. 205, No. (A3), pp. 161-171.
[11] Fales, R. 2005. "Stability and Performance Analysis of a Metering Poppet Valve." ASME International Mechanical Engineering Congress and Exposition, Orlando, FL.
[12] Muller, M., Fales, R., 2006. "Design and analysis of a Two-Stage Poppet Valve for Flow Control." American Control Conference, Minneapolis, MN.
[13] Muller, M.T., 2005. *Modeling, Design, and Control of Forced-Feedback Metering Poppet Valve System*. M.S. thesis, University of Missouri-Columbia.
[14] Khalil, K., *Nonlinear Systems*, Upper Saddle River, NJ: Prentice Hall,2002, pp 505-550.
[15] Jelali, M., Kroll, A., *Hydraulic Sevo-systems: Modeling, Identification and Control*, London: Springer-Verlag London Limited, 2003, p.217.
[16] Opdenbosch, P., Sadegh, N., Book, W., 2004. "Modeling and Control of an Electro-hydraulic Poppet Valve." ASME International Mechanical Engineering Congress and Exposition, Anaheim, CA.

9. FIGURES

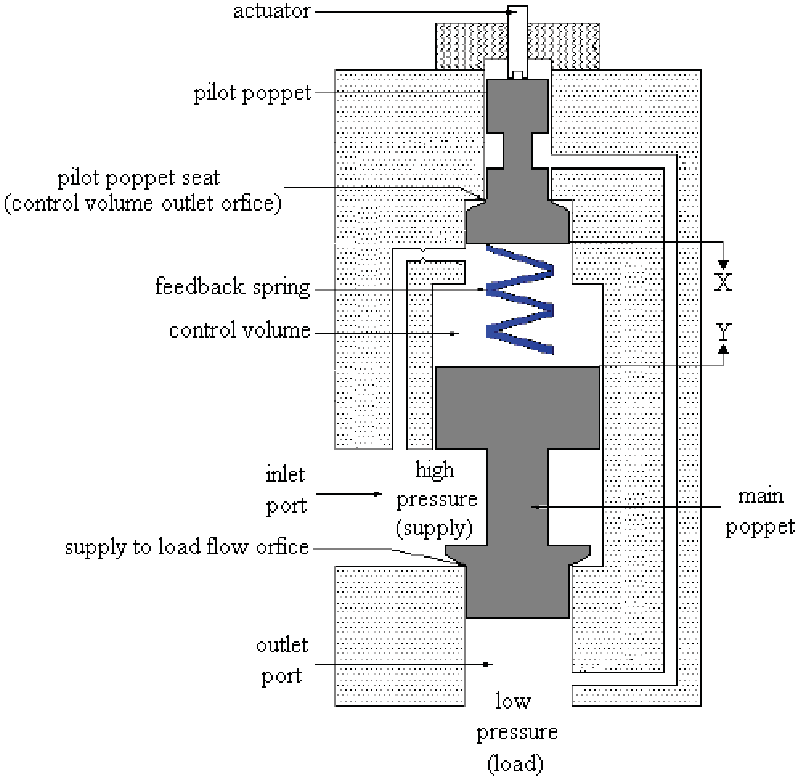
actuator
pilot poppet
pilot poppet seat
(control volume outlet office)
feedback spring
control volume
X
Y
inlet
port
high
pressure
(supply)
main
poppet
supply to load flow office
outlet
port
low
pressure
(load)

Figure 1: Forced-feedback metering poppet valve configuration

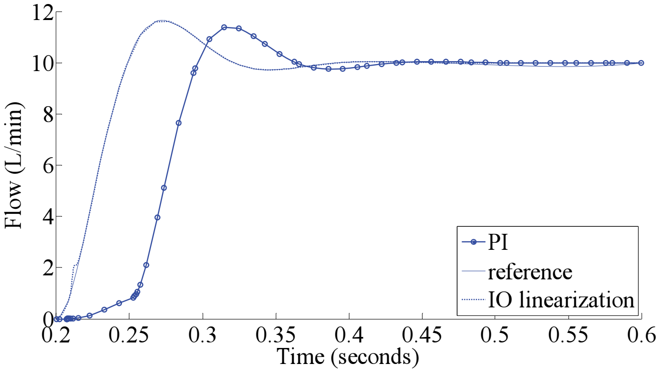

Figure 2: Controller comparison at a supply pressure of 21 MPa and a pressure drop of 2.1 MPa

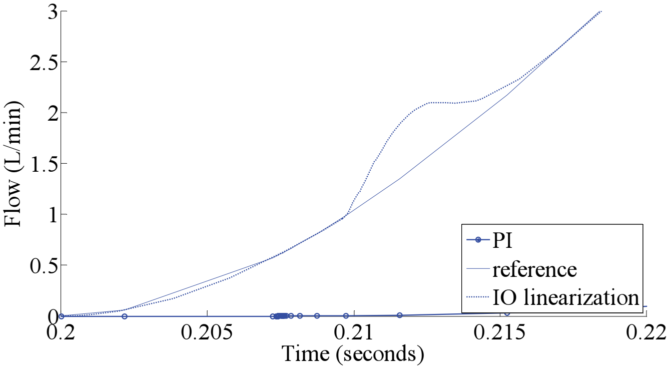

Figure 3: Controller comparison at a supply pressure of 21 MPa and a pressure drop of 2.1 MPa, effect of controller saturation

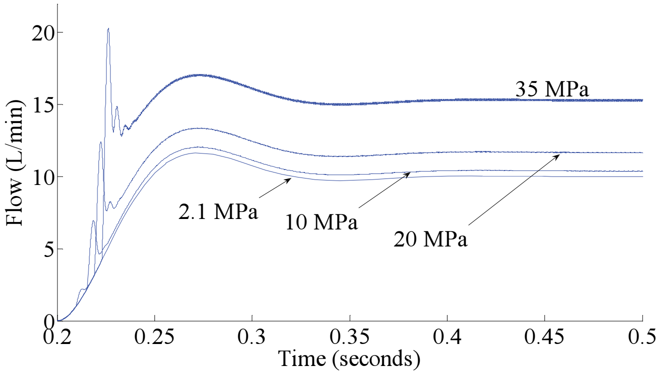

Figure 4: Response in different operating conditions

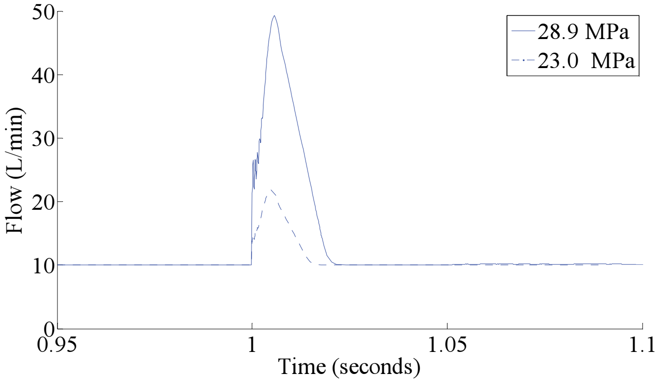

Figure 5: Response to supply pressure disturbances

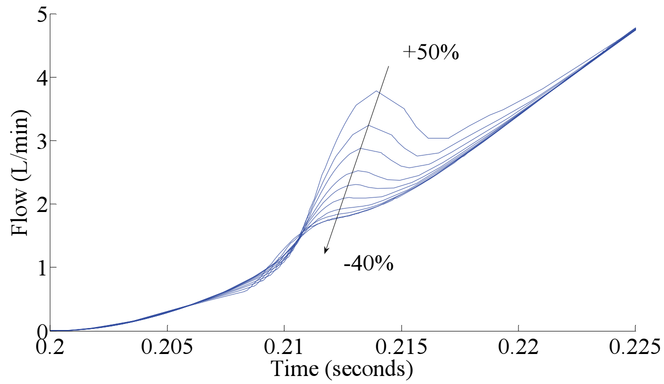

Figure 6: Robustness to changes in the area of the inlet orifice to the control volume

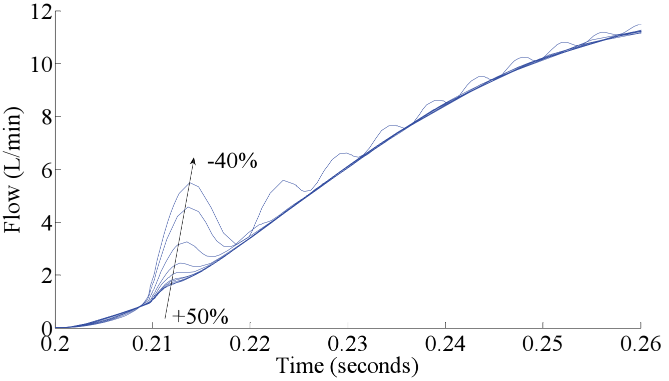

Figure 7: Robustness to changes in the slope for the pilot poppet orifice

On Stability and Dynamic Characteristics of Hydraulic Drives with Distributed Valves

Matti Linjama, Mikko Huova and Matti Vilenius
Tampere University of Technology, Institute of Hydraulics and Automation

ABSTRACT

The basic principle of distributed valves is to replace single-spool valve with several independent valves. Systems with distributed valves can save energy and have potential for better controllability but they are more difficult to control because of increased degrees of freedom. This paper presents different distributed valve configurations and develops general non-linear and linearised state-space models for them. The models developed cover all different valve configurations and control strategies as well as different feedbacks. Characteristics of some P-type position control strategies are analysed and it is shown that controllability of differential connection is equal or even better than controllability of traditional inflow-outflow control.

1 INTRODUCTION

It is well known that traditional valve controlled hydraulic systems cannot be optimized simultaneously for small power losses, good controllability and cavitation avoidance. This is true especially, if load force varies significantly. The reason for this is that single spool can be optimized for one operation point only. One way to overcome these problems is to use so called distributed valves. The basic idea is to separate inflow and outflow functions by using two or more control valves instead of one. The approach allows simultaneous control of velocity and pressure, which can be utilized e.g. in energy saving. Figure 1 presents some alternatives found in literature. The first version, Fig. 1 (a), consists of two three way valves and it has been studied in (1–4). This type of valve is commercially available (5). The second type, Fig. 1 (b), has four two-way valves and it has been studied in (6, 7). This version is also commercially available (8). The "Digital Hydraulics" approach (9, 10) belongs to this class even if the implementation is based on on/off valves instead of proportional valves. The third version, Fig. 1 (c) has an extra valve between A- and B-ports and it has been studied e.g. in (11). The fourth version, Fig. 1 (d), has valve from supply to tank and this version has been studied in (12, 13). A natural extension of these valve systems is full six-valve version shown in Fig. 1 (e). One feature, which is not seen in Fig. 1, is that valves can be bidirectional or reverse flow can be implemented by check valves.

Power Transmission and Motion Control 2007 Edited by Dr D N Johnston and Professor A R Plummer
© With The Centre for Power Transmission and Motion Control

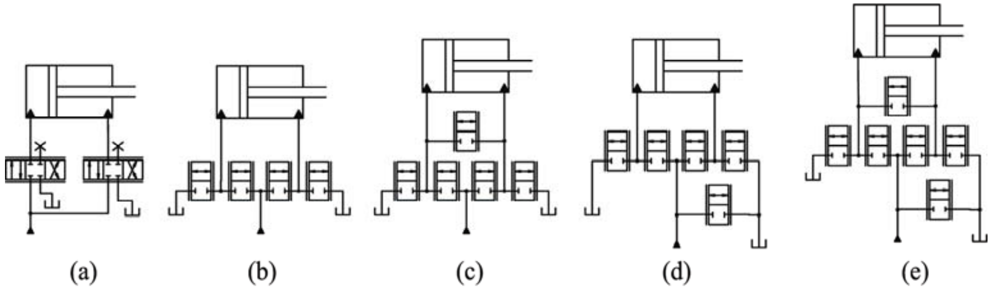

Figure 1. Different distributed valve systems.

The most popular control method for distributed valves is model-based control. Mattila (1) uses feedback linearization in order to implement independent pressure control of chamber pressures. The outer-loop controller consists of position and velocity feedbacks. Yuan and Lew (3) use linearization and sliding mode control while Liu and Yao (11) utilise adaptive robust control based on non-linear model. A simpler model based approach has been used by Linjama et al. (9, 10), in which a steady-state model of the system is utilized. Another control approach is the use of linearization and transfer function models, which has been used by Elfving and Palmberg (2), Eriksson et al. (4) and Yao et al. (13). A common feature of all above mentioned control approaches is complexity, which makes them difficult to apply. Traditional control methods, such as P-controller or P-controller plus dynamic pressure feedback, have not been studied with distributed valves.

One special feature of distributed valves is capability for different driving modes, e.g. normal inflow-outflow control and differential connection. Proper selection of driving mode is essential in implementation of energy saving and this topic has been studied in (7, 8, 10, 11). Different driving modes have different dynamics, which must be considered in the control design.

Fundamental difference between traditional and distributed valve systems is that the system with distributed valve is multi-input multi-output (MIMO) system. Control theory of MIMO systems is more complicated and the traditional transfer function approach is not well suited for MIMO systems. Fortunately, state-space approach is more general and can be used to develop linearised model needed in analysis and control design. The main objective of this paper is to develop a general purpose state-space model, which includes all different distributed valve configurations, control modes and feedbacks. The second objective is to study stability of different control modes under simple P-type control and to develop rules for selection of driving mode and opening ratio of valves.

2 GENERAL MODEL OF HYDRAULIC DRIVE WITH DISTRIBUTED VALVE

2.1 System Studied and Assumptions

The most general distributed valve system is shown in Fig. 1 (e). However, the valve from supply to return is normally not used to control actuator but only to implement supply pressure control and tandem center function. Thus, this valve can be neglected and system of Fig. 1 (c) is studied. Following assumptions are used:

- 2/2 proportional valves are ideal (fast, linear, etc.)
- Pipeline dynamics can be neglected
- Friction force is function of velocity only
- Tank pressure p_T is constant
- Mechanism behaves like constant inertia plus arbitrary external force F

The assumptions are used mainly to simplify equations. Valve dynamics can be included in the well-known way and general mechanism model can be included as described in (14). A detailed drawing of the system together with notation used is shown in Figure 2. The inputs of the system are control signals of valves (u_{PA}, u_{AT}, u_{PB}, u_{BT}, u_{AB}), external force F and supply pressure p_P. Outputs of the system are piston position x, piston velocity v and chamber pressures p_A and p_B.

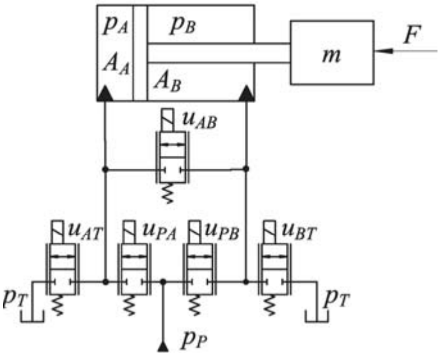

Figure 2. The system studied and notation used.

2.2 Non-Linear Model

Non-linear model can be achieved from the basic equations (15). Flow rate of valves is described by the standard equation of turbulent flow

$$Q(p_{in}, p_{out}, u, K) = Ku\sqrt[*]{p_{in} - p_{out}} \tag{1}$$

where p_{in} and p_{out} are inlet and outlet pressures, K is constant flow coefficient, and $\sqrt[*]{\bullet}$ is a shortcut for signed square root $\operatorname{sgn}(\bullet)\sqrt{|\bullet|}$. System dynamics can be described with following non-linear differential equations

$$\begin{aligned} m\ddot{x} &= A_A p_A - A_B p_B - F - F_\mu(\dot{x}) \\ \dot{p}_A &= \frac{1}{C_A(x)}\left(Q(p_P, p_A, u_{PA}, K_{PA}) - Q(p_A, p_T, u_{AT}, K_{AT}) - Q(p_A, p_B, u_{AB}, K_{AB}) - A_A\dot{x}\right) \\ \dot{p}_B &= \frac{1}{C_B(x)}\left(Q(p_P, p_B, u_{PB}, K_{PB}) - Q(p_B, p_T, u_{BT}, K_{BT}) + Q(p_A, p_B, u_{AB}, K_{AB}) + A_B\dot{x}\right) \end{aligned} \tag{2}$$

where hydraulic capacitances C_A and C_B are

$$C_A(x)=\frac{A_A x+V_{0A}+V_{hA}}{B_o}+\frac{V_{hA}}{B_h}\ ,\ C_B(x)=\frac{A_B(x_{\max}-x)+V_{0B}+V_{hB}}{B_o}+\frac{V_{hB}}{B_h} \tag{3}$$

and B_o and B_h are bulk moduli of oil and hose, V_{0A} and V_{0B} dead volumes including pipes and V_{hA} and V_{hB} are volumes of hoses between valves and cylinder. State vector $\boldsymbol{z}$ and input vector $\boldsymbol{u}$ are defined as follows

$$\boldsymbol{z}=\begin{bmatrix} x & \dot{x} & p_A & p_B \end{bmatrix}^{\mathrm{T}}\ ,\ \boldsymbol{u}=\begin{bmatrix} u_{PA} & u_{AT} & u_{PB} & u_{BT} & u_{AB} & F & p_P \end{bmatrix}^{\mathrm{T}} \tag{4}$$

After that, Eq. 2 can be expressed in the standard form

$$\dot{\boldsymbol{z}}=\boldsymbol{f}(\boldsymbol{z},\boldsymbol{u})=\begin{bmatrix} z_2 \\ \left(A_A z_3-A_B z_4-u_6-F_\mu(z_2)\right)/m \\ \left(Q(u_7,z_3,u_1,K_{PA})-Q(z_3,p_T,u_2,K_{AT})-Q(z_3,z_4,u_5,K_{AB})-A_A z_2\right)/C_A(z_1) \\ \left(Q(u_7,z_4,u_3,K_{PB})-Q(z_4,p_T,u_4,K_{BT})+Q(z_3,z_4,u_5,K_{AB})+A_B z_2\right)/C_B(z_1) \end{bmatrix} \tag{5}$$

2.3 Linearized Model

The model of Eq. 5 can be linearised at point $\boldsymbol{z}=\boldsymbol{z}_0$, $\boldsymbol{u}=\boldsymbol{u}_0$ as follows

$$\dot{\tilde{\boldsymbol{z}}}=\mathbf{A}\tilde{\boldsymbol{z}}+\mathbf{B}\tilde{\boldsymbol{u}}\quad ,\quad \mathbf{A}=\left.\frac{\partial \boldsymbol{f}}{\partial \boldsymbol{z}}\right|_{\boldsymbol{z}=\boldsymbol{z}_0,\boldsymbol{u}=\boldsymbol{u}_0}\quad ,\quad \mathbf{B}=\left.\frac{\partial \boldsymbol{f}}{\partial \boldsymbol{u}}\right|_{\boldsymbol{z}=\boldsymbol{z}_0,\boldsymbol{u}=\boldsymbol{u}_0} \tag{6}$$

where $\tilde{\boldsymbol{z}}=\boldsymbol{z}\text{-}\boldsymbol{z}_0$ and $\tilde{\boldsymbol{u}}=\boldsymbol{u}\text{-}\boldsymbol{u}_0$. Assuming viscous friction only, $F_\mu(\dot{x})=b\dot{x}$, and applying Eq. 6 to Eq. 5, following state matrix **A** and input matrix **B** are achieved

$$\mathbf{A}=\begin{bmatrix} 0 & 1 & 0 & 0 \\ 0 & -b/m & A_A/m & -A_B/m \\ -\dfrac{A_A}{B_{eff}C_A}f_3 & -\dfrac{A_A}{C_A} & \mathbf{A}(3,3) & \dfrac{K_{AB}u_{50}}{2C_A\sqrt{|z_{30}-z_{40}|}} \\ \dfrac{A_B}{B_{eff}C_B}f_4 & \dfrac{A_B}{C_B} & \dfrac{K_{AB}u_{50}}{2C_B\sqrt{|z_{30}-z_{40}|}} & \mathbf{A}(4,4) \end{bmatrix}$$

$$\mathbf{A}(3,3)=-\frac{1}{2C_A}\left(\frac{K_{PA}u_{10}}{\sqrt{|u_{70}-z_{30}|}}+\frac{K_{AT}u_{20}}{\sqrt{|z_{30}-p_T|}}+\frac{K_{AB}u_{50}}{\sqrt{|z_{30}-z_{40}|}}\right) \tag{7a}$$

$$\mathbf{A}(4,4)=-\frac{1}{2C_B}\left(\frac{K_{PB}u_{30}}{\sqrt{|u_{70}-z_{40}|}}+\frac{K_{BT}u_{40}}{\sqrt{|z_{40}-p_T|}}+\frac{K_{AB}u_{50}}{\sqrt{|z_{30}-z_{40}|}}\right)$$

$$\mathbf{B}=\begin{bmatrix} 0 & 0 & \dfrac{K_{PA}\sqrt[*]{u_{70}-z_{30}}}{C_A} & 0 \\ 0 & 0 & -\dfrac{K_{AT}\sqrt[*]{z_{30}-p_T}}{C_A} & 0 \\ 0 & 0 & 0 & \dfrac{K_{PB}\sqrt[*]{u_{70}-z_{40}}}{C_B} \\ 0 & 0 & 0 & -\dfrac{K_{BT}\sqrt[*]{z_{40}-p_T}}{C_B} \\ 0 & 0 & -\dfrac{K_{AB}\sqrt[*]{z_{30}-z_{40}}}{C_A} & \dfrac{K_{AB}\sqrt[*]{z_{30}-z_{40}}}{C_B} \\ 0 & -1/m & 0 & 0 \\ 0 & 0 & \dfrac{K_{PA}u_{10}}{2C_A\sqrt{|u_{70}-z_{30}|}} & \dfrac{K_{PB}u_{30}}{2C_B\sqrt{|u_{70}-z_{40}|}} \end{bmatrix}^{\mathrm{T}} \tag{7b}$$

where f_3 and f_4 are the third and fourth elements of $\boldsymbol{f}$ and all elements are calculated at the linearization point. Output matrix **C** depends on outputs wanted. For example, position output is obtained as follows

$$x-x_0=\begin{bmatrix}1 & 0 & 0 & 0\end{bmatrix}\tilde{z}\triangleq\mathbf{C}\tilde{z} \tag{8}$$

Equation 7 shows that system dynamics depend on design, such as load mass, piston areas, friction and hydraulic capacitances, as well as valve control signals and pressure differentials over valves. Hydraulic capacitances depend on piston position and valve control signals on required piston velocity.

2.4 Position-Controlled System

The linearised model of Eq. 7 is general and suitable for analysis of hydraulic actuator with traditional or distributed valves, with constant or variable supply pressure, and with different feedbacks (position, velocity, pressure). The model can also be used to analyse the effect of force or supply pressure disturbances, or system with controlled supply pressure. This paper concentrates on position feedback systems with constant supply pressure p_{P0} and load force F_0.

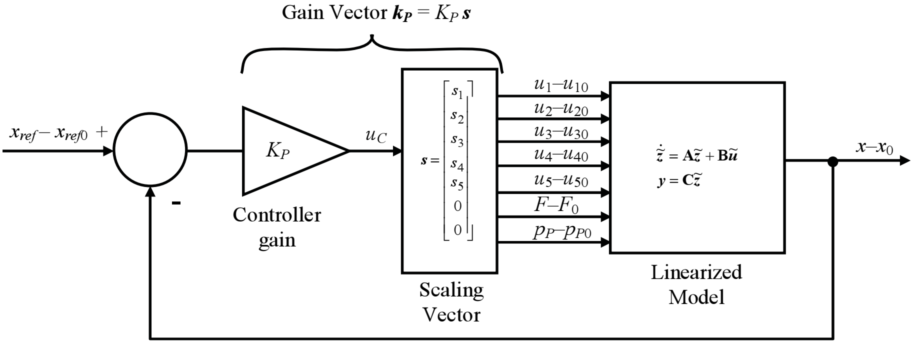
Gain Vector $\boldsymbol{k_P} = K_P\,\boldsymbol{s}$
$x_{ref} - x_{ref0}$
+
-
K_P
Controller gain
u_C
$s = [s_1\ s_2\ s_3\ s_4\ s_5\ 0\ 0]^T$
Scaling Vector
u_1-u_{10}
u_2-u_{20}
u_3-u_{30}
u_4-u_{40}
u_5-u_{50}
$F-F_0$
p_P-p_{P0}
$\dot{\tilde{z}} = \mathbf{A}\tilde{z} + \mathbf{B}\tilde{u}$
$y = \mathbf{C}\tilde{z}$
Linearized Model
$x-x_0$

Figure 3. Block diagram of the closed-loop position control system.

In order to simplify analysis, it is assumed that all valves have the same flow capacity, i.e. $K_{PA} = K_{AT} = K_{PB} = K_{BT} = K_{AB} \mathrel{\hat{=}} K$. P-type control is assumed and controller can be expressed as a constant gain vector $\boldsymbol{k}_P$, which is divided into two parts; controller gain K_P and scaling vector $\boldsymbol{s}$. Scaling vector distributes control signal to correct valves and scales control signal such that gain from u_C to piston velocity is one, see Fig. 3. Note that the complete system is single-input single-output system even if it has five internal control signals. Elements of scaling vector determine control strategy and pressure differentials over valves. Some possible control laws (CL) are

$$\begin{aligned}
\boldsymbol{s} &= \begin{bmatrix} s_1 & 0 & 0 & s_4 & 0 & 0 & 0 \end{bmatrix}^{\mathrm{T}} && \text{(CL1 : Inflow - outflow mode, extending)}\\
\boldsymbol{s} &= \begin{bmatrix} 0 & s_2 & s_3 & 0 & 0 & 0 & 0 \end{bmatrix}^{\mathrm{T}} && \text{(CL2 : Inflow - outflow mode, retracting)}\\
\boldsymbol{s} &= \begin{bmatrix} s_1 & 0 & s_3 & 0 & 0 & 0 & 0 \end{bmatrix}^{\mathrm{T}} && \text{(CL3 : P - side differential mode, extending or retracting)}\\
\boldsymbol{s} &= \begin{bmatrix} s_1 & 0 & 0 & 0 & s_5 & 0 & 0 \end{bmatrix}^{\mathrm{T}} && \text{(CL4 : Differential mode via AB - valve, extending or retracting)}
\end{aligned} \tag{9}$$

Control strategies CL1 and CL2 are similar to traditional four-way proportional valve and ratios s_1/s_4 and s_2/s_3 determines symmetry/asymmetry of spool. More control strategies can be developed by controlling three, four or five valves simultaneously, and/or including e.g. pressure feedback.

2.5 Determination of Linearization Point

Proper selection of linearization point is important in order to achieve correct model. The most difficult task is to find correct values for pressures and valve control signals as they depend on control strategy and target velocity. It is also well known that linearised model gives all too small damping near zero velocity. This is many times compensated by using artificially high value for viscous friction and by using non-zero valve openings in linearization. In this paper, the linearization is made at small non-zero velocity such that the valve openings are small but not zero. This means that problems at zero velocity are avoided but the system still has low damping. Linearization point is determined by first selecting x_0, v_0, p_{P0} and F_0, and then solving steady-state pressures and control signals. For CL1, steady-state values can be solved from equations

$$\begin{gathered}
u_{20} = 0,\ u_{30} = 0,\ u_{50} = 0,\ u_{40} = u_{10} s_4 / s_1,\ F_0 = p_{A0} A_A - p_{B0} A_B \\
v_0 = \frac{K u_{10} \sqrt{p_{P0} - p_{A0}}}{A_A},\ v_0 = \frac{K u_{40} \sqrt{p_{B0} - p_T}}{A_B}
\end{gathered} \tag{10}$$

These seven equations are solved for $\{u_{10}, u_{20}, u_{30}, u_{40}, u_{50}, p_{A0}, p_{B0}\}$, which results in

$$\text{CL1:}\quad \begin{gathered}
u_{10} = \frac{A_B v_0}{K} \sqrt{\frac{s_1^2 / s_4^2 + \gamma^3}{\gamma p_{P0} - p_T - F/A_B}},\ u_{40} = u_{10} s_4 / s_1,\ u_{20} = 0,\ u_{30} = 0,\ u_{50} = 0 \\
p_{A0} = \frac{p_{P0}\, s_1^2 / s_4^2 + \gamma^2 p_T + \gamma^2\, F_0 / A_B}{\gamma^3 + s_1^2 / s_4^2},\ p_{B0} = \left(p_{A0} A_A - F_0\right) / A_B
\end{gathered} \tag{11}$$

where $\gamma = A_A/A_B$. Steady-state values can be derived similarly for other control laws:

$$\text{CL2:}\quad \begin{aligned} &u_{20} = -\frac{A_B v_0}{K}\sqrt{\frac{s_2^2/s_3^2+\gamma^3}{p_{P0}-\gamma p_T+F/A_B}}\ ,\ u_{30} = u_{20}s_3/s_2\ ,u_{10}=0,\ u_{40}=0,\ u_{50}=0 \\ &p_{A0} = \frac{\gamma^2 p_{P0}+p_T\, s_2^2/s_3^2+\gamma^2\, F_0/A_B}{\gamma^3+s_2^2/s_3^2}\ ,\ p_{B0} = (p_{A0}A_A - F_0)/A_B \end{aligned} \tag{12}$$

$$\text{CL3:}\quad \begin{aligned} &u_{10} = \frac{A_B v_0}{K}\sqrt{\frac{s_1^2/s_3^2+\gamma^3}{(\gamma-1)p_{P0}-F/A_B}}\ ,\ u_{30} = u_{10}s_3/s_1\ ,u_{20}=0,\ u_{40}=0,\ u_{50}=0 \\ &p_{A0} = \frac{\left(s_1^2/s_3^2+\gamma^2\right)p_{P0}+\gamma^2\, F_0/A_B}{s_1^2/s_3^2+\gamma^3}\ ,\ p_{B0} = (p_{A0}A_A - F_0)/A_B \end{aligned} \tag{13}$$

$$\text{CL4:}\quad \begin{aligned} &u_{10} = \frac{A_B v_0}{K}\sqrt{\frac{s_1^2/s_5^2+(\gamma-1)^3}{(\gamma-1)p_{P0}-F/A_B}}\ ,\ u_{50} = u_{10}s_5/s_1\ ,u_{20}=0,\ u_{30}=0,\ u_{40}=0 \\ &p_{A0} = \frac{p_{P0}\, s_1^2/s_5^2+(\gamma-1)^2\, F_0/A_B}{s_1^2/s_5^2+(\gamma-1)^3}\ ,\ p_{B0} = (p_{A0}A_A - F_0)/A_B \end{aligned} \tag{14}$$

where it is assumed that supply pressure and load force are such that piston moves in extending direction with CL3 and CL4. These control laws can be used in retracting direction also, but they are not studied in this paper. Also, CL2 is not studied any more but the effort is in extending direction of movement. The linearization points satisfy steady-state equations of the system, which means that terms f_3 and f_4 are zero in Eq. 7.

3 DYNAMIC CHARACTERISTICS OF A HYDRAULIC DRIVE WITH DISTRIBUTED VALVE

3.1 Hydraulic Drive Studied

A simplified model of the joint actuator of (16) is used as an example system. The system is shown in Figure 4 and the seesaw mechanism is modelled as a constant inertia. Parameter values of the system are given in Table 1. Natural frequencies of the original model and simplified model are shown in Figure 5. The figure shows that the simplified model cannot fully capture the effect of piston position on natural frequency because it neglects kinematics of the boom.

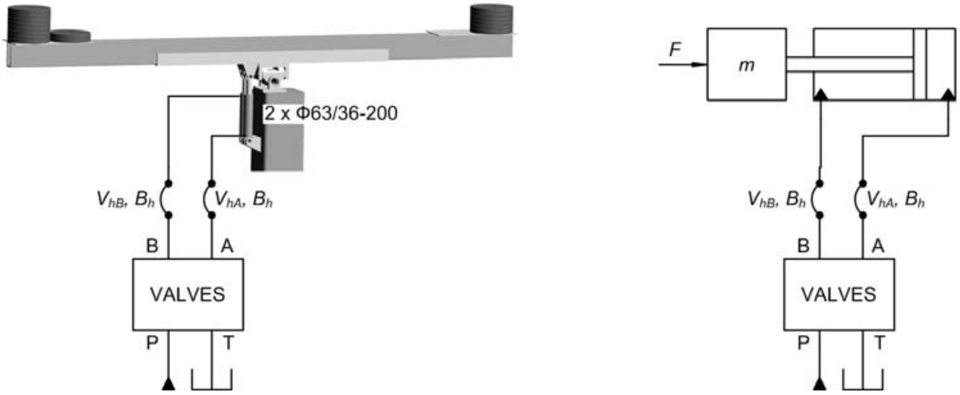

Figure 4. The original system (5) (left) and its simplified model (right).

Table 1. Parameters of the simplified model.

Parameter	Description	Unit	Value
A_A	Piston area, piston side	m^2	$2\times\left(0.063^2\,\pi/4\right)$
A_B	Piston area, piston rod side	m^2	$A_A-2\times\left(0.036^2\,\pi/4\right)$
m	Effective load mass	kg	53 000
F	Load force	kN	-36 … 36
p_P	Supply pressure	MPa	3 … 25
b	Viscous friction coefficient	Ns/m	2 000
V_{0A}	Dead volume, A-side	m^3	0.00012
V_{0B}	Dead volume, B-side	m^3	0.00012
B_o	Effective bulk modulus of oil	MPa	1100
V_{hA}	Volume of hose between valve and cylinder, A-side	m^3	0.000226
V_{hB}	Volume of hose between valve and cylinder, B-side	m^3	0.000226
B_h	Bulk modulus of hose	MPa	400
x_{max}	Piston stroke	m	0.2
K	Flow coefficient of valves	$m^3s^{-1}Pa^{-0.5}$	6×10^{-7}

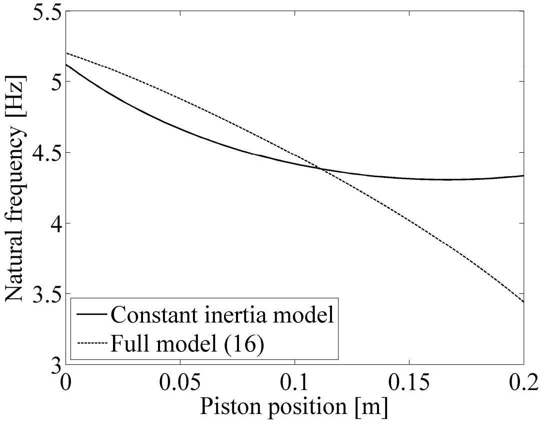

Figure 5. Calculated natural frequency of the original system (16) and the simplified constant inertia model. Load mass is 400 kg.

3.2 Methods Used to Determine Stability and Performance

Following procedure is used to determine degree of stability and performance:

1) Select x_0, v_0 and F_0
2) Select p_{P0} such that pressure differential Δp over both active valves is at a certain target value when they are equal.
3) Select control law and elements of scaling vector $\boldsymbol{s}$ such that their ratio is at target value.
4) Calculate linearization point, create linearised model and calculate DC-gain of the system from u_C to velocity with selected $\boldsymbol{s}$. Divide $\boldsymbol{s}$ with DC-gain, which causes that velocity gain of the system (from u_C to piston velocity) is one.
5) Calculate gain margin at different piston positions.
6) Select controller gain K_P such that gain margin is at least 10 dB.
7) Plot step response using non-linear model and determine rise time, settling time and overshoot

Gain margin of phase 5 tells directly the degree of stability. Phase margin is not used as a measure because it is always close to 90° in lightly damped position servo.

3.3 The Effect of Opening Ratio, Control Strategy, Piston Position and Supply Pressure on Stability

An important question with distributed valves is how to distribute control action for different valves. The same loop gain can be achieved with infinitely many different gain combinations. However, the ratio between openings of valves determines pressure differentials over valves, which have an effect on stability. The effect of opening ratio is studied with two velocities, $v_0 = \{0.01, 0.05\}$ m/s and two Δp values, $\Delta p = \{1, 3\}$ MPa. Load force is selected 20 kN, which allows the use of differential connections without too high supply pressure. Desired Δp values are achieved with following supply pressures: 4.9/8.3 MPa for CL1, 15/25 MPa for CL3 and 12.9/19 MPa for CL4. Figures 6–8 present gain margins as a function of gain ratio at some piston positions and linearization points studied. The gain ratio is scaled such that the pressure differential over both control valves is achieved at ratio of one.

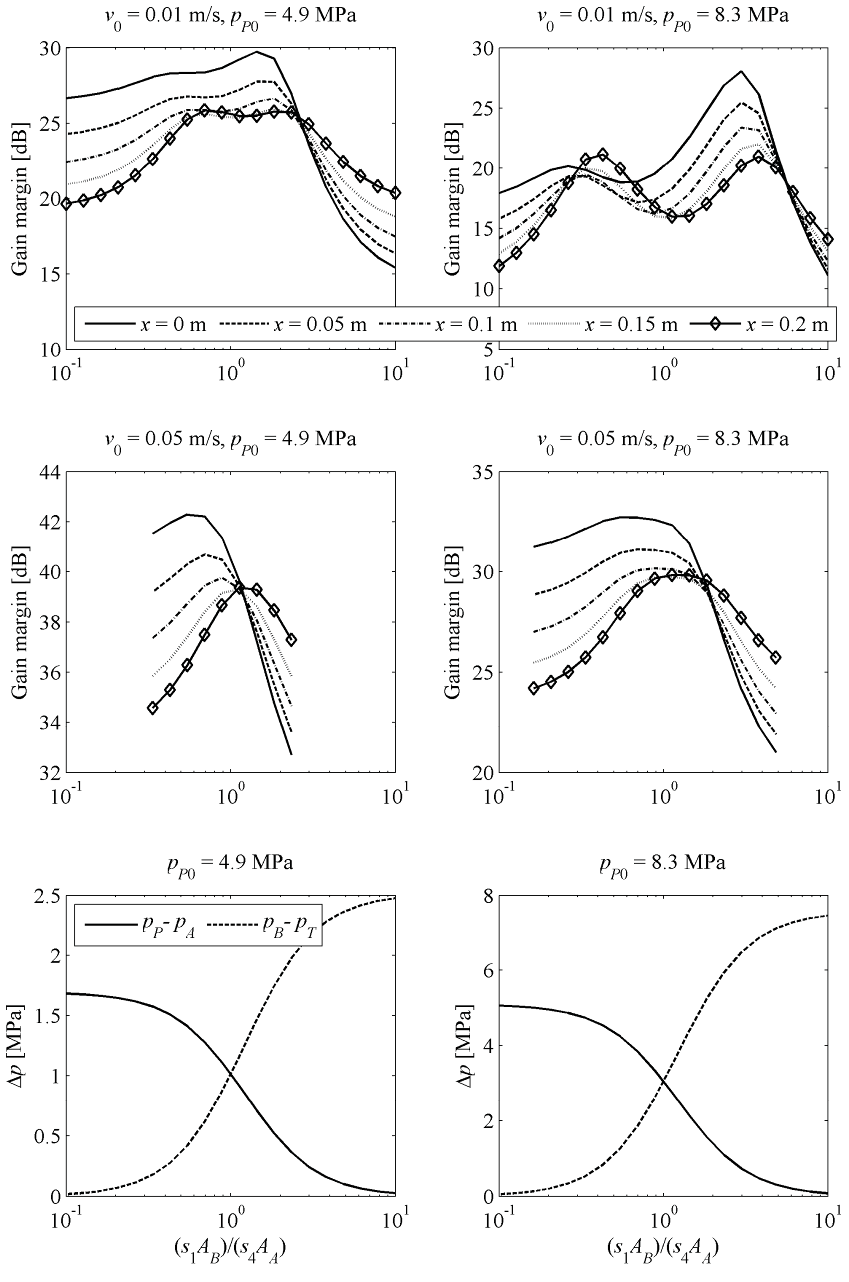

Figure 6. Gain margin of the linearised system with control law CL1. Load force F_0 is 20 kN.

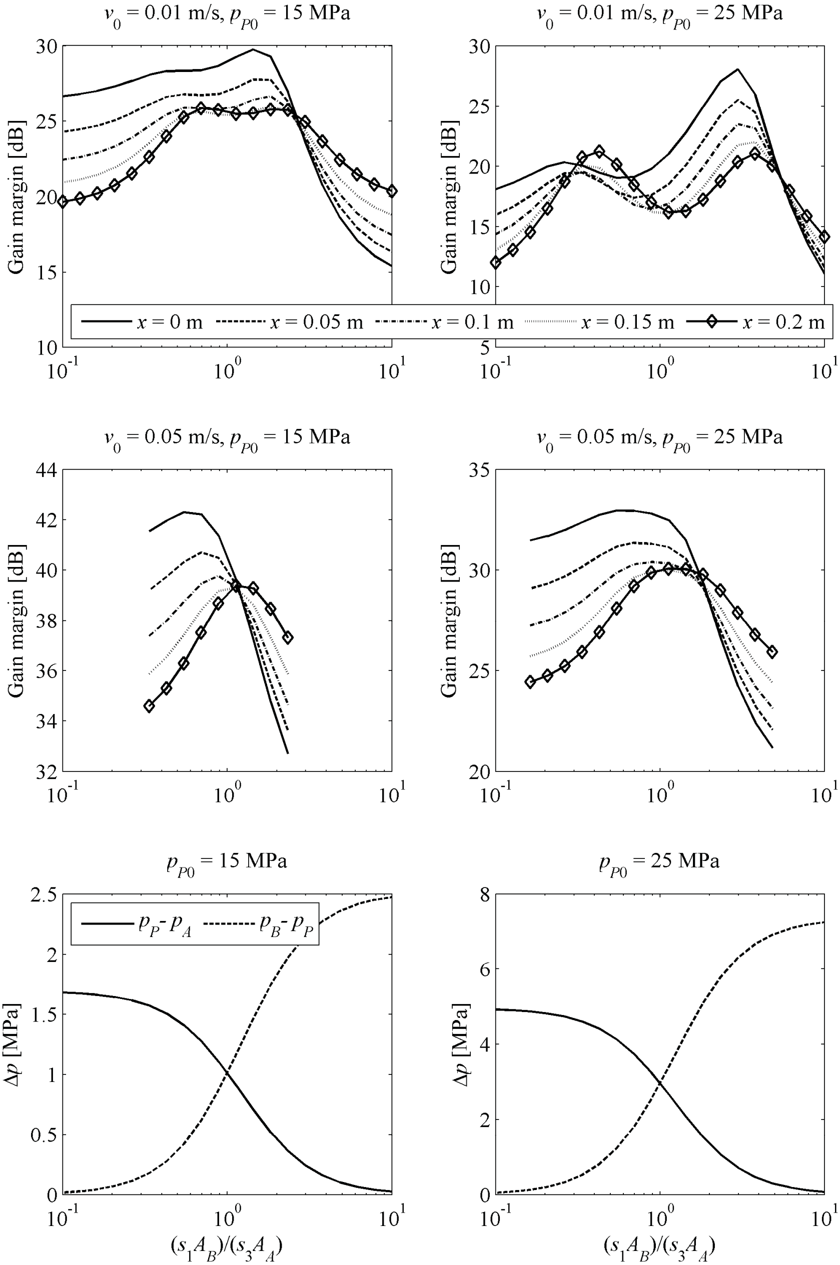

Figure 7. Gain margin of the linearised system with control law CL3. Load force F_0 is 20 kN.

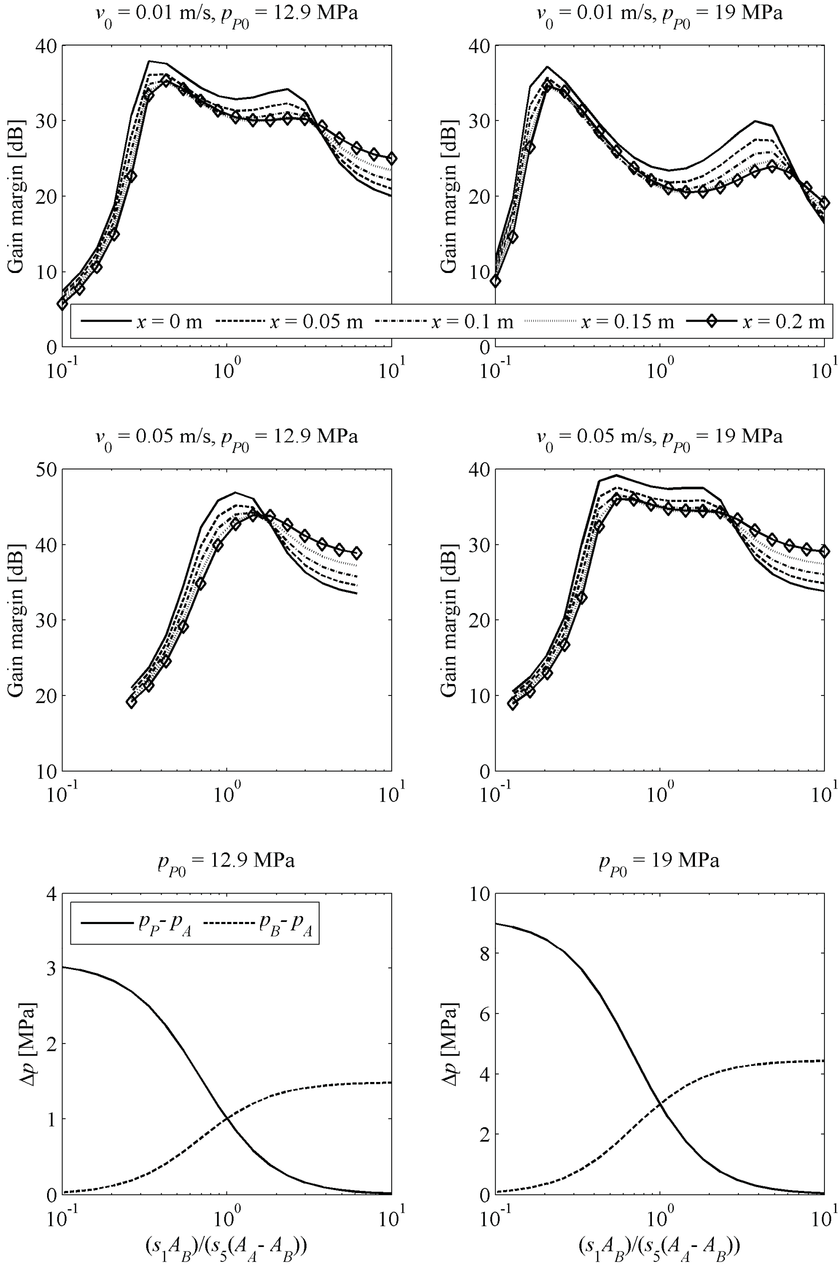

Figure 8. Gain margin of the linearised system with control law CL4. Load force F_0 is 20 kN.

Following conclusions can be drawn from figures 6–8:

P1) CL1 and CL3 have identical gain margin
P2) CL4 has the highest gain margin
P3) The smallest gain margin is usually achieved with maximum piston position
P4) Low velocity decreases gain margin
P5) High pressure differential decreases gain margin
P6) Gain margin decreases rapidly if gain ratio is too big or too small.
P7) At higher velocities, good selection for gain ratio is A_A/A_B for CL1 and CL3, and $(A_A–A_B)/A_B$ for CL4. This equals to "matched spool" i.e. same pressure differential over both active valves. At low velocities, it seems to be better to select bigger gain ratio for CL1 and CL3, and smaller gain ratio for CL4.

Property P1 can be understood from the structure of **A** and **B** matrices of the system (Eq. 7). The effect of inputs u_3 and u_4 on elements of **A** and **B** is exactly the same if pressure differentials are the same. Property P2 can also be understood by analysing the structure of **A** matrix. Hydraulic damping is introduced by elements **A**(3,3), **A**(3,4), **A**(4,3) and **A**(4,4), and control signal u_5 has positive effect on all these elements while the other control signals have an effect on one element only. This is seen also in Figure 8, in which the highest gain margin is achieved when u_5 is much bigger than u_1. Property P3 is related to asymmetry of cylinder and relatively big dead volumes, which causes that the natural frequency of the system at minimum near the maximum stroke. Property P4 confirms well known fact that damping is smallest at small velocities. Property P5 is counterintuitive and can be explained by analysing elements of **A** matrix. Higher pressure differential means smaller valve opening and both have negative effect on "damping elements" of **A** (i.e. **A**(3,3), **A**(3,4), **A**(4,3) and **A**(4,4)). Properties P6 and P7 states that it is important to have significant pressure drop over both active valves.

Properties P1 and P2 means that stability of differential connection is as good as or even better than stability of traditional inflow-outflow control. This is contradictory result because the differential connection is normally considered as difficult to control. The reason for this misunderstanding is that differential connection is normally implemented by connecting B-side directly to A-side or to pump via a check valve, which is identical to very small gain ratio. All curves of figures 6–8 show that gain margin reduces rapidly when gain ratio approaches zero.

3.4 Simulation Results

The non-linear model of Eqs 1–3 is used to verify previous results. The first set of simulations compares closed-loop ramp responses of the non-linear system near $x = 0.15$ m. The slope of the reference is selected to be 0.01 m/s and Δp-value of 1 MPa is used together with matched flow conditions. Figures 6–8 show that the gain margin is about 25 dB for CL1 and CL3, and about 30 dB for CL4. Simulated critical gain of the non-linear model is 20 m^{-1} (26 dB) for CL1 and CL3, and 32 m^{-1} (30 dB) for CL4, which are consistent with predictions of the linearised model. Controller gain is selected to be one third of the critical gain, which results in K_P= 6.7 m^{-1} for CL1 & CL3, and K_P = 10.7 m^{-1} for CL4. Corresponding ***s*** vectors are $[10.34\ \ 0\ \ 0\ \ 6.96\ \ 0]^T$ for CL1 & CL3 and $[3.39\ \ 0\ \ 0\ \ 6.98\ \ 0]^T$ for CL4. Figure 9 shows simulated responses and results confirm the facts that CL1 and CL3 behave identically, and that CL4 allows much higher gain than CL1 or CL3.

Figure 10 presents some simulations with CL4. The pump pressure is raised to 19 MPa while the loop-gain is kept at $K_P = 10.7\ s^{-1}$ in CASE I. This simulation verifies the fact that increasing pressure differential over valve decreases stability. Note that the effect of pump pressure on system gain is considered in the calculation of *s*. The pump pressure is kept at 19 MPa but opening ratio is decreased to one fourth in CASE II and stability improves significantly. Thus, the predictions of the linearised model about gain margin are correct.

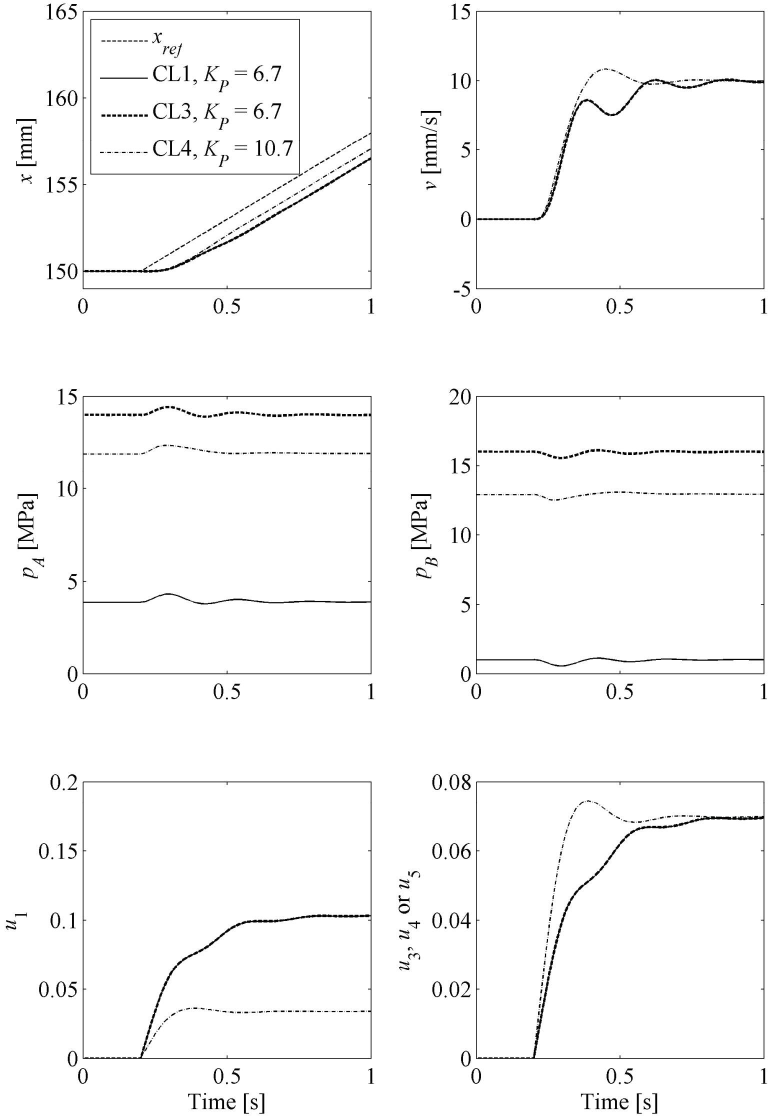

Figure 9. Closed-loop ramp responses of the non-linear model near *x* = 0.15 m. Controller gains are selected to be one third of critical gain.

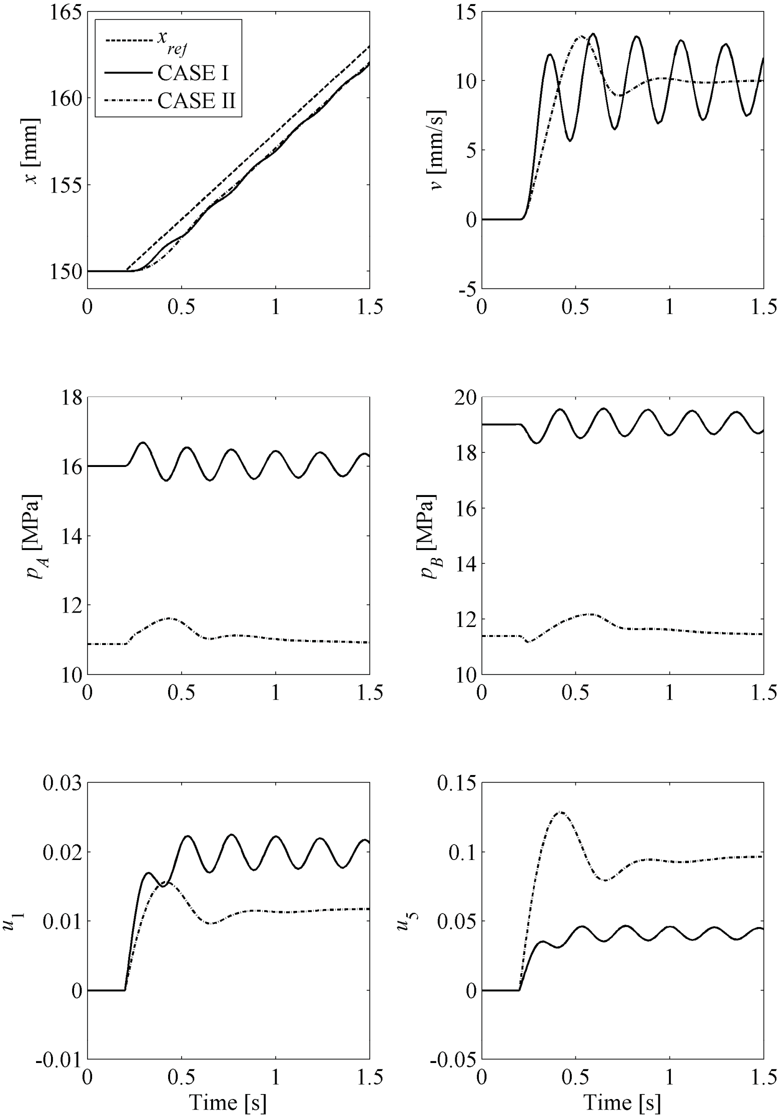

Figure 10. Closed-loop ramp responses of the non-linear model with CL4 and p_P = 19 MPa. CASE I: K_P = 10.7 m^{-1}, $s = [1.96\ 0\ 0\ 0\ 4.04]^T$. CASE II: K_P = 10.7 m^{-1}, $s = [1.19\ 0\ 0\ 0\ 9.82]^T$.

4 CONCLUSIONS

General non-linear and linearised state-space models of hydraulic drives with distributed valves have been developed. These models can be utilized in development of control methods for systems with distributed valves. The simulation results show that linearised model can accurately predict stability of the system near the linearization point. Results also show that systems with distributed valves have complex characteristics and their tuning differs from traditional systems. One important result of this paper is that differential connection does not decrease stability of the system, if both sides of actuator are under active control. Especially, the differential connection via separate cross valve improves stability and controllability of the system. On the other hand, traditional differential connection via check valve decreases stability significantly. Probably a new result is that small pressure differential over valve improves stability. Small pressure differential increases also sensitivity and this topic needs further research.

ACKNOWLECGEMENT

The research was supported by the Academy of Finland (Grant no. 80411).

REFERENCES

1 Mattila, J. 2000. On Energy Efficient Motion Control of Hydraulic Manipulators. Dissertation, Tampere University of Technology, Publications 312, Tampere, Finland.

2 Elfving, M. & Palmberg, J.-O. 1997. Distributed Control of Fluid Power Actuator – A Load Sensing Application of a Cylinder with Decoupled Chamber Pressure Control. Proceedings of the Fifth Scandinavian International Conference on Fluid Power, May 28–30, 1997, Linköping, Sweden, pp. 159–170.

3 Yuan, Q. & Lew, J. 2005. Modeling and Control of Two Stage Twin Spool Servo-Valve for Energy-Saving. 2005 American Control Conference, June 8–10, 2005, Portland, OR, USA, pp. 4363–4368.

4 Eriksson, B., Larsson, J. & Palmberg, J.-O. 2006. Study on Individual Pressure Control in Energy Efficient Cylinder Drives. Proceedings of 4th FPNI–PhD Symposium, June 13–16, 2006, Sarasota, Florida, USA, pp. 77–99.

5 Anon. 2005. Eaton Ultronics Management System. Brochure No. E-VLDI-MR003-E2, May 2005 (Eaton Corporation).

6 Jansson, A. & Palmberg, J.-O. 1990. Separate Controls of Meter-in and Meter-out Orifices in Mobile Hydraulic Systems. International Off-Highway & Power Plant Congress and Exposition, Milwaukee, WI, USA.

7 Shenouda, A. & Book, W. J. 2005. Selection of Operating Modes of a Multi-Functional Hydraulic Device. 2005 ASME International Mechanical Engineering Congress and Exposition, Nov. 5–11, Orlando, Florida, USA, 11 p.

8 Pfaff, J. 2005. Distributed Electro-Hydraulic Systems for Telehandlers. The 50th National Conference on Fluid Power, March 16-18, 2005, Las Vegas, USA. pp. 779–784.

9 Linjama, M. & Vilenius, M. 2005. Improved Digital Hydraulic Tracking Control of Water Hydraulic Cylinder Drive. International Journal of Fluid Power, Vol. 6, No 1, pp. 29–39.

10 Linjama, M., Huova, M., Boström, P., Laamanen, A., Siivonen, L., Morel, L., Waldén, M., & Vilenius, M. 2007. Design and Implementation of Energy Saving Digital Hydraulic Control System. Accepted for publication in The Tenth Scandinavian International Conference on Fluid Power, May 21–23, 2007, Tampere, Finland.

11 Liu, S. & Yao, B. 2002. Energy-Saving Control of Single-Rod Hydraulic Cylinders with Programmable Valves and Improved Working Mode Selection. The 49th National Conference on Fluid Power, Las Vegas, Nevada, USA, pp. 81–91.

12 Hu, H. & Zhang, Q. 2002. Realization of Programmable Control Using a Set of Individually Controlled Electrohydraulic Valves. International Journal of Fluid Power, Vol. 3, No 2. pp. 29–34.

13 Yao, J., Kong, X.-D., Shan, D.-S., Gao, Y.-J., Han, D. & Zhang, Q. 2005. Study on Using a Multifunctional Integrated Valve in Controlling an Asymmetric Hydraulic System. The 50th National Conference on Fluid Power, March 16–18, 2005, Las Vegas, NV, USA, pp. 585–593.

14 Linjama, M. & Virvalo, T. 1999. State-Space Model for Control Design of Multi-Link Flexible Hydraulic Cranes. Proceedings of the Sixth Scandinavian International Conference on Fluid Power, May 26-28, 1999, Tampere, Finland, pp. 981–998.

15 Watton, J. Fluid Power Systems: Modeling, Simulation, Analog and Microcomputer control, 1989 (Prentice Hall International, Hemel Hempstead).

16 Linjama, M. & Vilenius, M. 2004. Digital Hydraulic Control of a Mobile Machine Joint Actuator Mockup. Bath Workshop on Power Transmission and Motion Control, Sept. 1–3, 2004, Bath, UK, pp. 145-158.

Symposium on Power Transmission & Motion Control, PTMC'07, Sept 12-14, 2007, Bath, England

Pressure tracking control for a self-energizing hydraulic brake

Matthias Liermann, Christian Stammen, Hubertus Murrenhoff
RWTH Aachen University, Germany
Institute for Fluid Power Drives and Controls
Steinbachstr. 53, 52074 Aachen, Germany
Matthias.Liermann@ifas.rwth-aachen.de

Abstract

A new hydraulic brake utilizing a self-energizing effect is developed at the Institute for Fluid Power Drives and Controls (IFAS). Contrary to a conventional hydraulic braking actuator it has no pneumatic or hydraulic power supply. It features a supporting cylinder, which conducts the braking force into the bogie. The braking force pressurizes the fluid in the supporting cylinder and is the power source for pressure control of the actuator. The only interface connection is the electrical braking force reference signal from a superior control unit.

The dynamics of the self-energizing electro-hydraulic brake is open-loop unstable. The ratio of piston areas between supporting cylinder and actuator is such, that an existing braking force causes a higher supporting pressure than is needed to produce the actual normal force. In this paper the hydraulic mechanic brake design is derived from given requirement specifications. A mathematical description of the brake dynamics is presented in combination with a friction coefficient model for more realistic simulations. The closed loop control is developed on the basis of the analytical description of the open loop dynamics .

Keywords: hydraulic, self-reinforcement, self-energizing, brake, pressure control, trains, controller development, friction coefficient model, stability criterion, SEHB

1 Introduction

The new brake concept of Self-energising Electro-Hydraulic Brake (SEHB) combines high force-to-weight ratio of hydraulic actuation with flexibility of digital control and efficiency by using the principle of self-energisation. It is being developed at the Institute for Fluid Power and Controls (IFAS, RWTH Aachen University) within a research project funded by the DFG (German Research Foundation). The SEHB concept was introduced in [1],[2]. It offers the

Power Transmission and Motion Control 2007 Edited by Dr D N Johnston and Professor A R Plummer
© With The Centre for Power Transmission and Motion Control

advantages of hydraulic brake actuation without disadvantages of a centralized bogie power supply, which are explained in [3]. This is possible by the principle of self-energisation. The wheelset's inertia momentum is used by each calliper as the source of power to supply hydraulic pressure for braking. Only low electric power for the operation of hydraulic valve(s), pressure sensors and controller electronics is required to operate the brake. One of the major advantages of this concept is the possibility to control the actual braking torque, as explained in section 2 "Working principle of SEHB". Conventional friction brakes can only control the perpendicular force. Due to uncertainty of friction coefficient, the actual friction force is unknown. Section 3 "Dynamics of self-energisation" compares the SEHB to other self-reinforcing brake principles and provides a mathematical analysis of the dynamic process. In section 4 "Design parameters of the non-linear simulation model" mechanical and hydraulic design parameters of the brake are explained, which are the basis for the non-linear simulation model for verification of the SEHB concept. Since the friction coefficient has strong influence on the brake dynamics, a state dependent model is presented, which has been derived from manufacturer test data. With the simulation model it is possible to study the systems closed loop dynamic behaviour. In section 5 "Controller development for SEHB" it is shown analytically and in non-linear simulation how a proportional acting controller stabilises the open loop dynamics presented in section 3. Different control devices can be used for closed loop stabilization. Proportional valves for pressure control often feature negative overlap which leads to leakage in the closed position. In opposition switching valves are leakage free in the closed position but have limited performance for small signal amplitudes. The substitution of one 4/3-way control valve by four 2/2-way fast-switching valves also yields more degrees of freedom for control.

2 Working principle of SEHB

The idea of SEHB is, that the pressure needed for actuation of a hydraulic disc brake is gained from hydraulic support of the friction force. Unlike conventional brakes, where the brake calliper is fixed, in the SEHB concept it is movable tangential to the friction contact. A hydraulic supporting cylinder connects the calliper to the bogie structure, thus fixing it between two columns of oil, see **Fig. 1**.

In the case of braking, the friction force acts on the supporting cylinder causing a pressure difference. Independent of which chamber is pressurised and which is released, the configuration of four check valves assures that the lower line has the higher pressure and the upper line is low pressure. A control valve connects high- and low-pressure side with the chambers of the brake actuator. If the right flow-scheme of the control valve is active, high-pressure is applied on the piston face, while the ring side of the brake actuator is connected to low-pressure, thus opening the positive feedback of supporting pressure on braking pressure. As will be shown in Section 3 it depends on ratio between piston areas whether self-energisation takes place. If the left flow-scheme of the control valve is active, the piston face chamber is relieved, while the piston ring side is charged, reducing the actuator force yielding a negative feedback of the supporting pressure on the braking pressure.

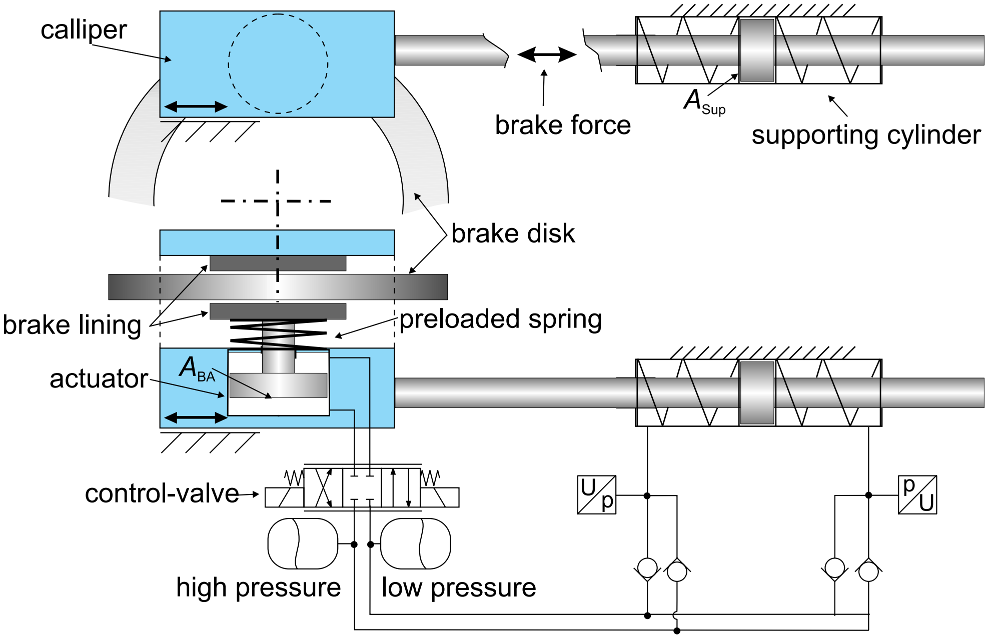

Figure 1: Principle of Self-energising Electro-Hydraulic Brake, (SEHB)

It is easy to imagine, that in the case of positive feedback the braking pressure would constantly rise without a closed loop control, which acts to close the control valve when the desired friction force is achieved (negative feedback). Therefore the SEHB needs an additional feedback loop to be stable. This feedback is not shown in Fig. 1, but it can easily be provided by measuring the load pressure in the supporting cylinder with pressure transducers and magnetic actuation of the valve by a controller device. An alternative could be a hydro-mechanic feedback, where the pressure in the supporting cylinder is used to actuate the spool of the control valve. The set value would be a hydraulic or mechanic actuation. In that case no electric components would be needed.

While the necessity of a closed loop control might look like a drawback of SEHB at first, it is also one of its major advantages: it allows the direct control of the actual braking force, independently of friction coefficient changes. The load pressure in the supporting cylinder can be used as control variable for closed loop control. Since the load pressure is in direct relation to the friction force, SEHB offers the possibility to control the actual retardation torque on the brake disk. Conventional friction brakes only control the perpendicular actuator force. Since the friction coefficient μ is influenced by parameters like speed, brake pressure and temperature, conventional brakes can only estimate the actual friction force F_{brake} and the retardation torque respectively. The retardation torque, however, is the control variable for vehicle dynamics control systems like the Electronic Stability Program (ESP). This is obvious, since the vehicle dynamics is influenced by the retardation of a wheel and not by the actuator force of the brake calliper.

3 Dynamics of self-energisation

In this section the dynamics of the self-energising effect of SEHB is described analytically using a linearised model. The static precondition for self-energisation as presented in [2] is:

$$\frac{A_{\mathrm{Sup}}}{A_{\mathrm{BA}}} \overset{!}{\leq} \mu \cdot \frac{2}{i_{\mathrm{L}}} \tag{1}$$

It limits the maximum ratio between the piston area A_{Sup} of the supporting cylinder and A_{BA} of the brake actuator, which must (!) be smaller than the friction coefficient μ times 2 divided by the ratio i_{L} between friction and supporting force.

$$i_{\mathrm{L}} = \frac{F_{\mathrm{brake}}}{F_{\mathrm{Sup}}} \tag{2}$$

The ratio $\frac{A_{\mathrm{Sup}}}{A_{\mathrm{BA}}}$ must be designed such, that for the lowest possible friction coefficient μ the condition is still fulfilled and self-energisation can happen. For the controller development of SEHB not only the precondition but also the dynamics of self-energisation is very important. It will be examined in the following paragraphs.

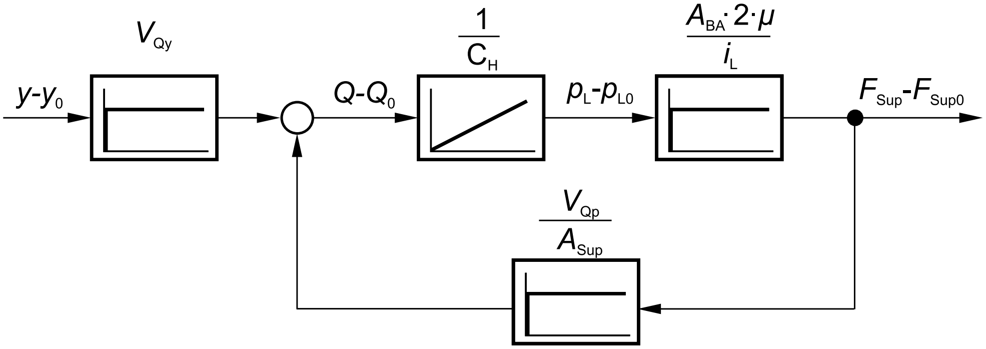

Figure 2: Linear system model of open loop SEHB

By some simplifications and linearisation of the non-linear system, a reduced order linear model shown in **Fig. 2** is obtained. The supporting force F_{Sup}, which is the control variable for the closed loop control, is directly proportional to the load pressure p_{L} of the actuator via the piston area A_{BA} divided by the transmission ratio i_{L} . The factor $2 \cdot \mu$ is due to the fact that a calliper has two friction contacts. The rise of load pressure is determined by the capacity C_{H} of and the flow Q into the actuator , which is controlled by the valve. The valve flow rate depends both on the valve opening y and the pressure difference Δp over the valve. Eq. 3 is the discharge equation for a sharp edged valve opening y with a discharge coefficient B.

$$Q = B \cdot y\sqrt{\Delta p} \tag{3}$$

The linearisation of Eq. 3 yields two factors V_{Q_y} and $V_{\mathrm{Q}_{\Delta p}}$, which describe the independent influence of change of valve opening y or pressure difference Δp on the change of valve discharge flow Q.

$$Q = Q_0 + V_{\mathrm{Q}_y} \cdot (y - y_0) + V_{\mathrm{Q}_{\Delta p}} \cdot (\Delta p - \Delta p_0) \tag{4}$$

The pressure difference over the valve is proportional to the supporting force F_{Sup} by $\frac{1}{A_{\mathrm{Sup}}}$. When the precondition of self-energisation Eq. 1 is fulfilled, the pressure difference over the valve is positive, meaning that the pressure in the supporting cylinder is always higher than the pressure in the actuator. Therefore, when the right flow scheme of the control valve in Fig. 1 is applied, V_{Q_y} and $V_{\mathrm{Q}_{\Delta p}}$ are positive and the closed loop brake dynamics is unstable, as evident from the positive feedback loop depicted in Fig. 2. The transfer function G_s of the open loop characteristic is

$$G_s = \frac{V_{\mathrm{Q}_y} \frac{A_{\mathrm{BA}}}{C_{\mathrm{H}}} \frac{2\mu}{i_{\mathrm{L}}}}{s - \frac{V_{\mathrm{Q}_{\Delta p}} A_{\mathrm{BA}}}{C_{\mathrm{H}} A_{\mathrm{Sup}}} \frac{2\mu}{i_{\mathrm{L}}}} \tag{5}$$

Fig. 3 shows the location of the pole of the transfer function in the right semi-plane at $s = \frac{V_{\mathrm{Q}_{\Delta p}} A_{\mathrm{BA}}}{C_{\mathrm{H}} A_{\mathrm{Sup}}} \frac{2\mu}{i_{\mathrm{L}}}$. The factor $\frac{A_{\mathrm{BA}}}{A_{\mathrm{Sup}}} \frac{2\mu}{i_{\mathrm{L}}}$ is between 1 (lowest friction coefficient μ_{min} where precondition of self-energisation is fulfilled) and ratio $\frac{\mu_{\mathrm{max}}}{\mu_{\mathrm{min}}}$, which can be > 5. The factor V_{Q_y} and especially $V_{\mathrm{Q}_{\Delta p}}$ are dependent on the operating point of linearisation. The system's step response in time domain is described by Eq. 6

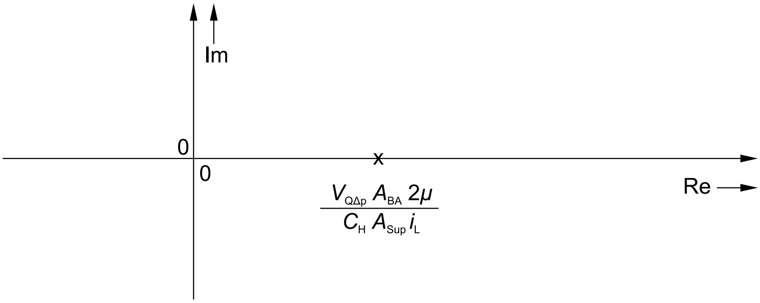
Im
0
0
Re
x
$\frac{V_{\mathrm{Q\Delta p}} A_{\mathrm{BA}}\, 2\mu}{C_{\mathrm{H}} A_{\mathrm{Sup}} i_{\mathrm{L}}}$

Figure 3: Location of (unstable) open loop pole of the simplified linear Model of SEHB

$$F_{\mathrm{Sup}} = \frac{V_{\mathrm{Q}_y} \cdot A_{\mathrm{Sup}}}{V_{\mathrm{Q}_{\Delta p}}} (e^{\frac{V_{\mathrm{Q}_{\Delta p}}}{C_{\mathrm{H}}} \frac{A_{\mathrm{BA}}}{A_{\mathrm{Sup}}} \frac{2\mu}{i_{\mathrm{L}}} \cdot t} - 1) \tag{6}$$

The supporting force increases or decreases exponentially depending on the sign of $V_{\mathrm{Q}_{\Delta p}}$. As already stated above, $V_{\mathrm{Q}_{\Delta p}}$ is positive when the right flow scheme of the control valve is applied. It becomes negative when valve opens in the opposite direction.

The analysis of the open loop characteristic is the basis for a subsequent controller design in section 5. Before focussing on the controller, Section 4 presents parameters of the first prototype design and how they are derived from requirement specifications. The same parameters are also used for non-linear numerical simulation of the system, which serves the verification of the simplified linear model.

4 Design parameters of SEHB

This section describes the design parameters of the first SEHB prototype, which are a result of iterative steps of design and simulation analysis.

Performance specification The performance specification is derived from the target application of the brake, defined by the research project “EABM”, funded by the German Research Foundation (DFG). The basic specification is based on the presumption that a passengers railway car does not necessarily need to be heavier than a comparable road vehicle, a bus.

- Maximum speed: $v_0 = 120\ \frac{\mathrm{km}}{\mathrm{h}}$
- Maximum waggon load: $m = 13.6\ \mathrm{t}$
- Two pairs of individual wheels, four disc brakes
- Diameter of wheel (new / old): $d_{\mathrm{wheel}} = 920\ \mathrm{mm}/840\ \mathrm{mm}$

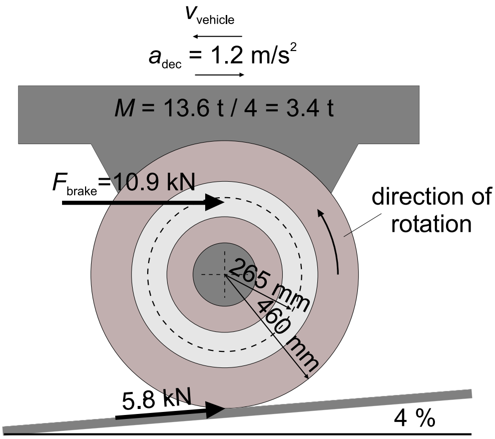

Figure 4: Requirement specifications for design of SEHB

General performance requirements for railway brakes are normed for specific railway types, [4]. For a maximum stopping distance of $500\ \mathrm{m}$ at maximum velocity and an estimated response time of $0.8\ \mathrm{s}$, the brake must provide a maximum deceleration of a little less than $d = 1.2\ \frac{m}{s^2}$. The maximum retardation force F_d is calculated by multiplying the mass inertia per disc brake times deceleration plus a constant force resulting from slope of $s = 4\ \%$ and gravity g, **Fig. 4**. The rotary inertia of wheels and drives is included with a factor $k_r = 1.1$ in the translatory inertia.

$$F_d = \frac{m}{4}(k_r d + sg) = 5822\ \mathrm{N} \tag{7}$$

The maximum friction force F_{brake} acting on a friction radius of $r_\mathrm{f} = 245\ \mathrm{mm}$ then yields:

$$F_\mathrm{brake} = F_d \frac{d_{\mathrm{wheel}_\mathrm{new}}}{2 \cdot r_\mathrm{f}} = 10931\mathrm{N} \tag{8}$$

4.1 Hydraulic and mechanic design

Fig. 5 shows the proposed design of the prototype featuring a pivot-mounted pin-slide calliper with a double action cylinder. The supporting cylinder in this concept is mounted on the calliper. The spherical joint at the end of the supporting piston is connected to a fixed frame.

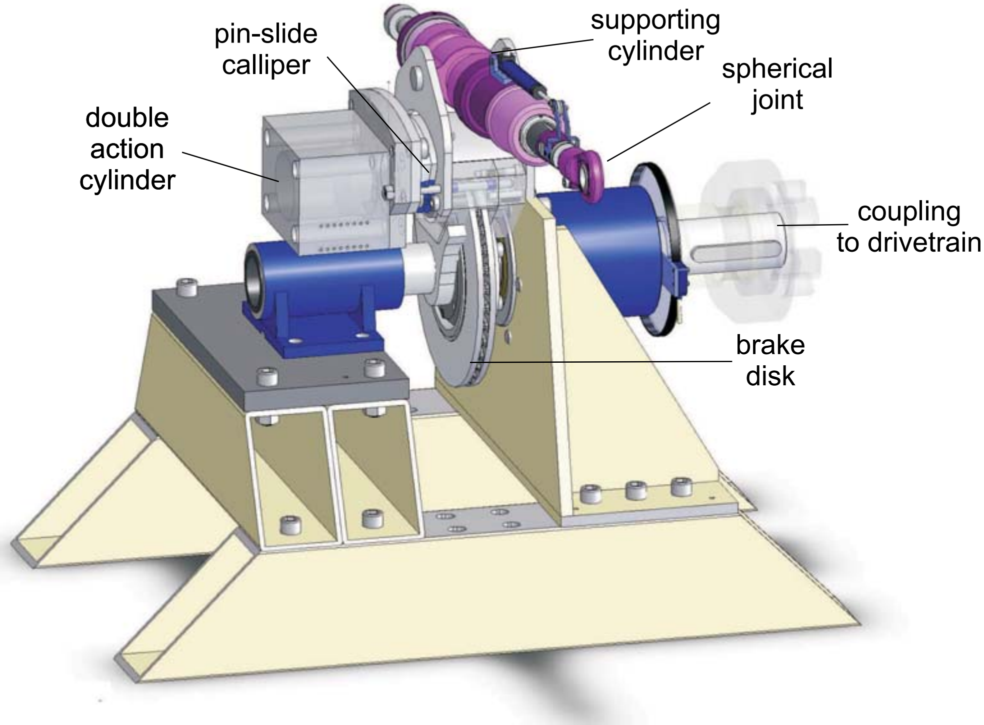

Figure 5: Design of the SEHB prototype

A DSH*plus* simulation model served the verification of the general SEHB concept and this prototype design in particular. **Fig. 6** illustrates the layout of the model. It is comprised of a hydraulic section with cylinders, accumulators and valves, and a signal section including the state dependent friction coefficient and the closed loop control. The following paragraphs describe the geometric and hydraulic configuration added by some information about performance characteristics of the hydraulic components needed for the simulation.

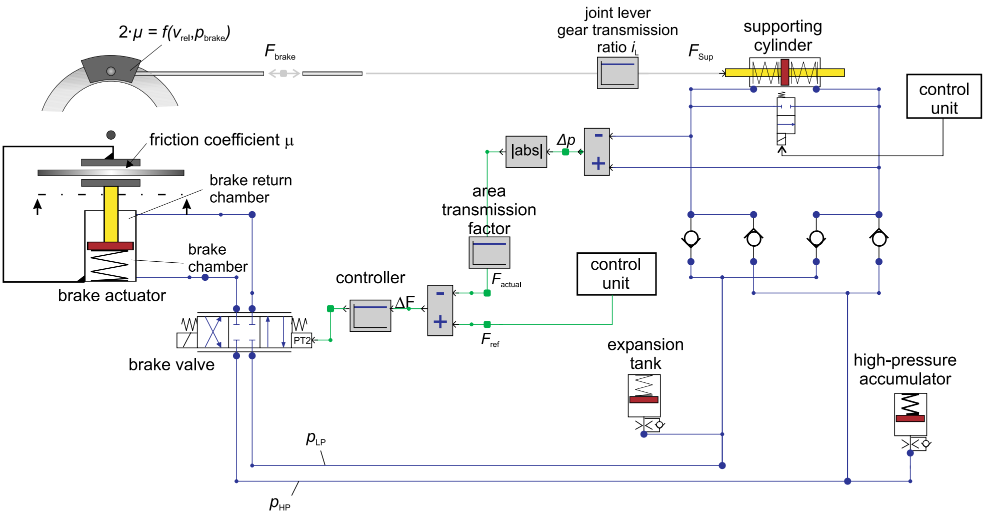
2·μ = f(v_rel,p_brake)
F_brake
joint lever gear transmission ratio i_L
F_Sup
supporting cylinder
control unit
friction coefficient μ
|abs|
Δp
-
+
brake return chamber
area transmission factor
brake chamber
controller
ΔF
F_actual
control unit
brake actuator
PT2
F_ref
brake valve
expansion tank
high-pressure accumulator
p_LP
p_HP

Figure 6: Layout of the brake simulation model

Gear ratio The attachment of the supporting cylinder above the calliper leads to a reduced supporting force compared to the braking force. The gear transmission ratio is

$$i_{\mathrm{L}} = \frac{F_{\mathrm{brake}}}{F_{\mathrm{Sup}}} = \frac{r_{\mathrm{sup}}}{r_{\mathrm{fric}}} = 1.8 \tag{9}$$

Cylinders The supporting cylinder has a piston diameter of $d_{1\mathrm{Sup}} = 40$ mm and a piston rod diameter of $d_{2\mathrm{Sup}} = 25$ mm. At maximum brake force (Eq. 8) according to Eq. 9 the supporting force is $F_{\mathrm{Sup}} = 6072.8$ N resulting in a maximum pressure of $p_{max} = 79.3$ bar. Friction of the supporting cylinder is parametrised with 50 N breakaway force.

The size of the actuator follows from the precondition of self-energisation, Eq. 1. According to Eq. 1 for a minimum friction coefficient of $\mu > 0.14$ a differential cylinder with piston diameter of $d_{1\mathrm{BA}} = 80$ mm is sufficient. It has a piston rod diameter of $d_{2\mathrm{BA}} = 50$ mm with 70 mm stroke. Friction is parametrised with 200 N breakaway force.

Springs Braking of SEHB results in movement of the supporting cylinder. Therefore after every braking the supporting cylinder should retract to the middle position. The retraction springs in the supporting cylinder are pre-stressed with 130 N to overcome friction and pull the cylinder into middle position when the switching valve, connecting the chambers of the supporting cylinder, is opened. The cumulative stiffness of the springs is 2 $\frac{\mathrm{N}}{\mathrm{mm}}$.

The spring in the actuator serves to initiate the self energised braking. When the control valve opens, the brake piston moves forward to override clearance, due to the spring force, establishing the friction contact. Therefore the spring force $F_{\mathrm{Spring}_{\mathrm{BA}}}$ must exceed the actuator friction force $F_{f\mathrm{BA}}$ and pressure force $F_{\Delta p}$ in the brake actuator. The pressure force is calculated by Eq. 10

$$F_{\Delta p} = \Delta p_{\mathrm{BA}} \cdot d_{2\mathrm{BA}}^2 \frac{\pi}{4} \tag{10}$$

When the high pressure accumulator is discharged, $F_{\Delta p}$ is acting against the spring, when the right flow scheme of the valve is activated and the self energisation has not yet initiated. In this case the brake control unit should open the valve in the opposite direction. Once a friction contact is established, to initiate the self energisation, the initial friction force $\mu \cdot F_{\mathrm{Spring}_{\mathrm{BA}}}$ achieved by the actuator must exceed the resistance of the supporting cylinder to pressurize the fluid. The resistance of the supporting cylinder consists of friction force $F_{f\mathrm{Sup}}$ and the spring force $F_{\mathrm{Spring}_{\mathrm{Sup}}}$ for retracting the supporting cylinder. The total spring force of the actuator $F_{\mathrm{Spring}_{\mathrm{BA}}}$ thus yields, Eq. 11:

$$F_{\mathrm{Spring}_{\mathrm{BA}}} = F_{\Delta p} + F_{f\mathrm{BA}} + \frac{F_{f\mathrm{Sup}} + F_{\mathrm{Spring}_{\mathrm{Sup}}}}{2\mu^2} \tag{11}$$

In the present design the spring in the actuator applies 1612 N in middle position and has a stiffness of $16\ \frac{\mathrm{N}}{\mathrm{mm}}$.

Accumulators The high-pressure accumulator has a storage capacity of $8\ \mathrm{ml}$, enough for retracting the actuator for more than $3.5\ \mathrm{mm}$. The expansion tank has a storage capacity of $141\ \mathrm{ml}$. Fully charged it generates a system pressure of around 5 bar on the low-pressure side. The accumulator is fully charged when the brake piston is completely retracted.

Control valve(s) The brake valve depicted in the simulation model shown in Fig. 6 is a zero-overlapped 4/3-way control valve with $2\ \frac{\mathrm{l}}{\mathrm{min}}$ nominal flow at $35\ \mathrm{bar}$ and 30 Hz natural frequency. The low value is intended to accentuate the fact that robust, reasonably priced components can be used. A drawback of conventional control valves is their leakage in the closed position. Since each side of the supporting cylinder brake contains just $38\ \mathrm{ml}$, leakage of the control valve in the closed position cannot be tolerated. Therefore alternatively four 2/2-way fast-switching valves will be used for brake control.

Fluid The parameters of the fluid simulate the behaviour of HLP 46 hydraulic fluid. Pressure dependency of the bulk modulus and the influence of contained air is accounted for [6]. The bulk modulus has a significant influence on the initiation performance of the brake, as proved by simulation. To account for this effect, an undissolved air content of 0.1% has been parameterised.

Calliper, lining, disc The mechanical stiffness of the brake calliper c_{cal} and brake disk c_{disk} is estimated to be $175\ \frac{\mathrm{N}}{\mathrm{mm}}$. The stiffness of a brake pad c_{pad} can be calculated from the bulk modulus of the lining E_{lin}, the surface area A_{pad} and thickness h_{pad}. According to data sheet information of a typical organic brake lining for trains the bulk modulus is $E_{\text{lin}} = 300\,\frac{\text{N}}{\text{mm}}$. The surface area A_{pad} of normed UIC brake pads is either 350 or $400\ \text{mm}^2$, [5]. The smaller size is chosen because the aim of the corporate research project "EABM" is, that the brake will be integrated into one unit together with an electric motor which will be primarily used for braking. Each brake pad has a thickness of $30\ \text{mm}$. The stiffness c_{pad} calculates to

$$c_{\text{pad}} = E_{\text{lining}} \frac{A_{\text{pad}}}{h_{\text{pad}}} = 350\,\frac{\text{kN}}{\text{mm}} \tag{12}$$

The stiffnesses of calliper c_{cal}, brake disk c_{dis} and the two brake pads are acting in series. Their total stiffness c_{tot} calculates to

$$c_{\text{tot}} = \left(\frac{2}{c_{\text{pad}}} + \frac{1}{c_{\text{disk}}} + \frac{1}{c_{\text{cal}}}\right)^{-1} = 87.5\,\frac{\text{kN}}{\text{mm}} \tag{13}$$

A low total mechanical stiffness results in a long stroke of the supporting cylinder for each braking. At the beginning of a simulation a clearance of $0.5\ \text{mm}$ is parametrised between brake pads and disc.

4.2 Friction coefficient model

With the SEHB concept it is possible to control the actual friction force independently of friction coefficient changes. This advantage can be demonstrated in simulation using a state dependent friction coefficient model. For this purpose, a friction model has been derived in the context of this research project. The friction test data, that was used to fit the model, was supplied by a brake lining manufacturer. Test protocols were used according to standardised brake tests [5], which are required before the approval of railway brake pads. **Fig. 7** shows a selection of friction curves used to verify the model which is described in the following.

The formation and degradation of the friction layer between two friction partners is a dynamic process influenced by friction layer condition itself, normal force, surface pressure, friction velocity and temperature. The interaction of these parameters and qualitative influence on the friction coefficient is described in [7], [8] and [9] on the basis of phenomenological observation from numerous friction tests. Based on similar presumptions about the formation and degradation of the friction layer, [10] proposes a quantitative dynamic friction model in form of differential equations. A difficulty concerning this model is, that it requires knowledge about specific parameters of the tribological system, which can only be obtained by certain measurements.

For the purpose of this research a more pragmatic approach was chosen, motivated by [11], who propose a relationship between friction on the one side and pressure and velocity on the other in form of a simple algebraic equation. Many physical phenomena have exponential character and can be approximated by equations of the form

$$Y = a \cdot X^b \tag{14}$$

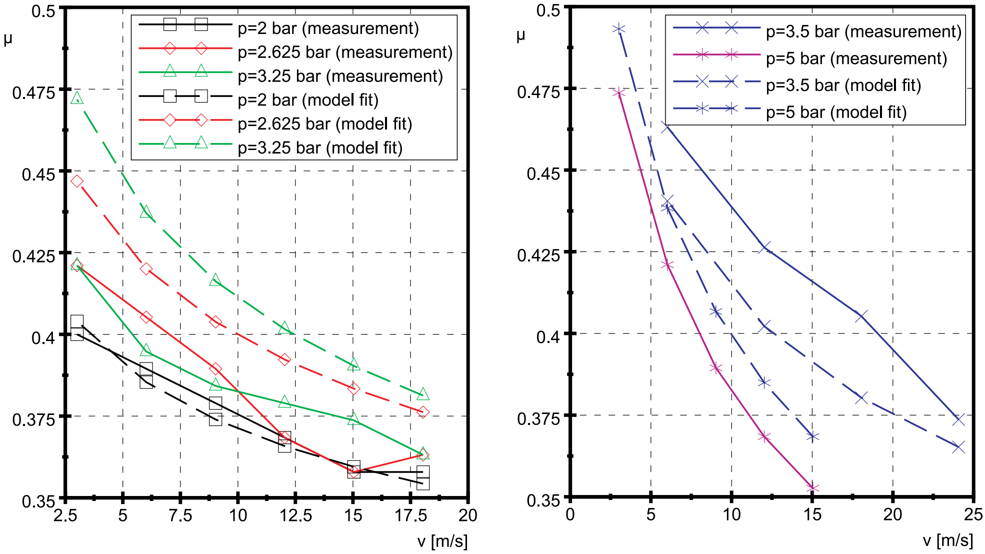

Figure 7: Comparision between friction test data and model fit

With a and b as constants. The logarithm of Eq. 14 yields

$$\log(Y) = b \cdot \log(X) + \log(a) \tag{15}$$

which is a line in $\mathbb{R}^2$. It was found, that especially the relationship between friction coefficient and velocity can be well described by Eq. 15 with $Y = \mu$ and $X = (1 + \frac{v}{v_0})$. After a curve fitting between measured friction coefficient and Eq. 15, for a surface pressure of 2.6 bar the deviation between measured and calculated friction coefficient was below $2\ \%$. The influence of surface pressure on friction coefficient is evident in Fig. 7, but it is not as monotonous as the influence of velocity. It could be shown that the influence of surface pressure can be approximated through adaption of factors a and b in Eq. 15:

$$a = -0.428 \frac{p}{p_0} \qquad b = -0.1106 (\frac{p}{p_0})^{-0.703} \tag{16}$$

The surface pressure p and the velocity v are related to arbitrarily chosen references $p_0 = 10$ bar and $v_0 = 1\ \frac{\mathrm{m}}{\mathrm{s}}$. As can be seen in Fig. 7, the biggest deviation of $12.1\ \%$ between model fit and measurements is found for a surface pressure of 3.25 bar. The average deviation is $4.6\ \%$.

Of course, the model in Eq. 15 is only valid for values of surface pressures, for which data was available $(2 - 5$ bar). Values for smaller pressures were extrapolated using a 3rd-order polynomial with a continuous transition into a minimum friction value of $\mu = 0.3$. The complete friction coefficient map is shown in **Fig. 8**.

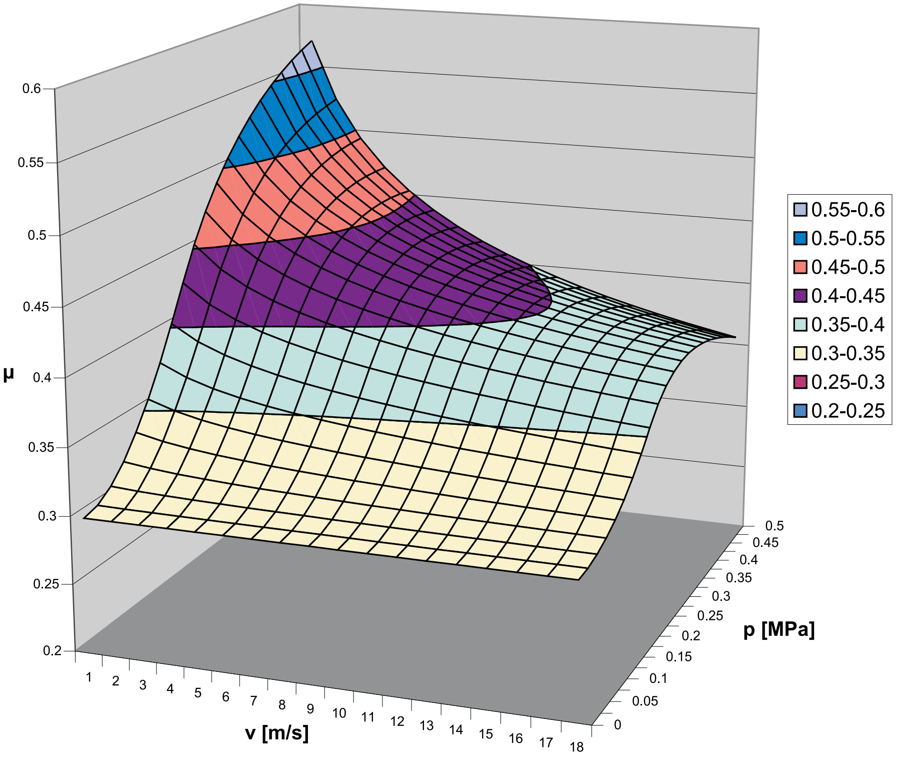

Figure 8: Friction coefficient map in dependency of friction velocity v and surface pressure p

5 Controller development for SEHB

The open loop characteristic derived in section 3 (Eq. 5) gives an analytical explanation of the open loop instability of SEHB. In the following paragraphs it is used to show how a proportional acting controller is able to stabilise the system.

Fig. 9 shows the closed loop system of SEHB. For reasons of simplicity the valve dynamics are neglected, supposing that the valve dynamics is higher than the pressure dynamics of the brake.

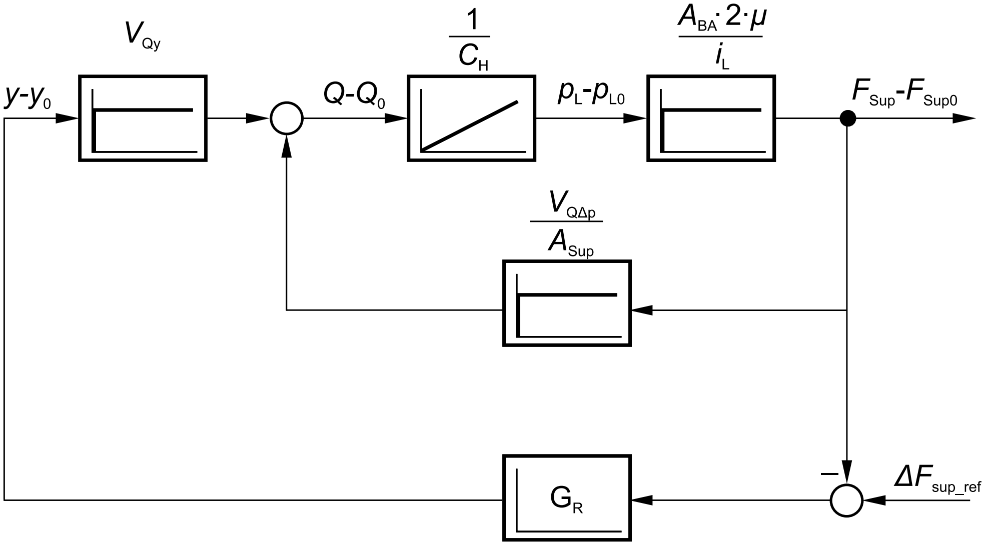

Figure 9: Linear system model of closed loop SEHB

The transfer function $G(s)$ of the closed loop system is

$$G(s) = \frac{G_{\mathrm{R}} V_{\mathrm{Q}_y} \cdot \frac{A_{\mathrm{BA}} 2\mu}{C_{\mathrm{H}} i_{\mathrm{L}}}}{s + \frac{A_{\mathrm{BA}} 2\mu}{C_{\mathrm{H}} i_{\mathrm{L}}} (G_{\mathrm{R}}(s) V_{\mathrm{Q}_y} - \frac{V_{\mathrm{Q}_{\Delta p}}}{A_{\mathrm{Sup}}})} \tag{17}$$

The location of pole of the closed loop system is determined by the transfer function $G_{\mathrm{R}}(s)$ of the controller. For stability the pole must be in the negative s semi-plane. Therefore the criterion for stability using a proportional acting controller ($G_{\mathrm{R}}(s) = K_{\mathrm{R}}$ is:

$$K_{\mathrm{R}} V_{\mathrm{Q}_y} > \frac{V_{\mathrm{Q}_{\Delta p}}}{A_{\mathrm{Sup}}} \tag{18}$$

V_{Q_y} and $V_{\mathrm{Q}_{\Delta p}}$ depend very much on the operating point chosen for linearisation. For a robust controller, the scope of possible values for V_{Q_y} and $V_{\mathrm{Q}_{\Delta p}}$ is yet to be determined in future work.

Fig. 10 shows the result of a step response of the closed loop system according to Eq. 6. The proportional controller gain is $0.9 \cdot 10^{-3}\ \frac{y_{\mathrm{max}}}{N}$. At $t = 6$ s, the step response leads to an opening of the control valve. The brake actuator is pressed onto the brake disk due to its integrated spring within approximately 60 ms. The friction coefficient rises from its minimum value of 0.3. The resulting friction force must yet rise to a certain value before at $t = 6.075$ s until the brake-away force of the supporting cylinder is reached and the supporting piston starts to move to build up pressure for the self-energisation process. At $t = 6.145$ s the high pressure piston-accumulator moves against block leading to a small step in the supporting force. The control valve closes continuously while the supporting force rises. At $t = 6.3$ ms it reaches the reference value and the valve is completely closed.

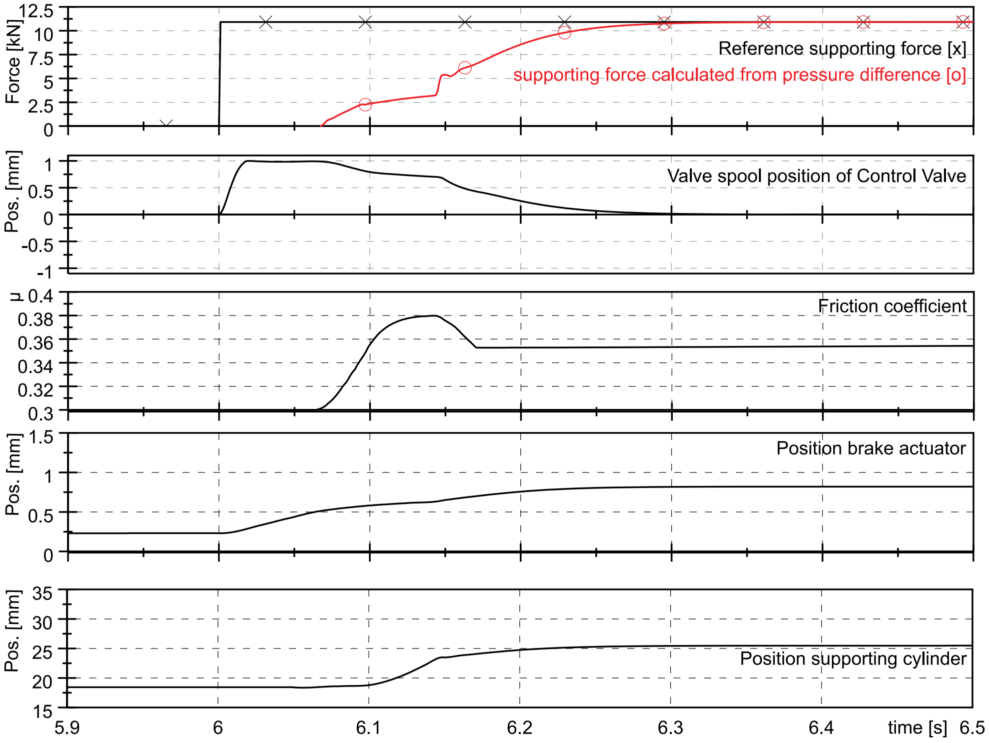

Figure 10: Simulation of non-linear SEHB system model for a step response

The dead time after the reference step is bigger, when the high pressure accumulator is not charged at the beginning of braking. This effect has been studied in [1],[2].

6 Conclusion

This article presented an analytical description of the dynamics of the self-energizing effect of SEHB by linearisation of the open loop system. It is shown, that without control the open loop system is unstable.

The interdependency of the design parameters and their calculation on the basis of requirement specifications, which were given through the framework of the research project “EABM”, funded by the German Research Foundation (DFG), were explained. The resultant set of parameters were used for the non-linear system simulation and for the first prototype design.

For demonstration of the independency of a varying friction coefficient on the effective retardation of SEHB, a friction coefficient model was implemented in the simulation, derived from measurement data, kindly provided by a manufacturer of railway brake linings.

The controller development was described on the basis of the linearized model, yielding an analytic criterion of closed loop stability when using a proportional acting controller.

Future work is concerned with a global stability criterion for SEHB on the basis of estimation of value ranges of V_{Q_y} and $V_{\mathrm{Q}_{\Delta p}}$. Also the use of fast-switching valves will be discussed. Results of theoretical analysis and simulation studies have to be compared with the prototype test data for verification purpose.

The authors thank the German Research Foundation (DGF) for funding this project.

References

[1] Matthias Liermann, Christian Stammen *Self-Energising Hydraulik Brake for Rail Vehicles [Selbstverstärkende hydraulische Bremse für Schienenfahrzeuge - Intelligentes, Integriertes Einzelrad-Antriebs-Brems-Modul]*, Ölhydraulik und Pneumatik O+P 10/2006, 500-507

[2] Matthias Liermann, Christian Stammen, Hubertus Murrenhoff *Development of A Self-energising Electro-Hydraulic Brake (SEHB) for Rail Vehicles*, The Tenth Scandinavian International Conference on Fluid Power, SICFP'07, May 21-23, 2007, Tampere, Finland

[3] Johannes Carsten Kipp *Elektrohydraulische Bremssysteme für schienengebundene Nahverkehrsfahrzeuge*, ZEV+DET Glasers Annalen, Vol 119 , 518–524, 1995.

[4] DIN EN 13452-1 *Railway applications – Braking – Mass transit brake systems - Part 1: Performance requirements*, 2005

[5] UIC 541-3 *Brakes - Disc brakes and their application - General conditions for the approval of brake pads, 5th Edition*, International Union of Railways, Railway Technical Publications, July 2004

[6] Hubertus Murrenhoff *Grundlagen der Fluidtechnik, Band 1: Hydraulik (Fundamentals of Fluid Power Technology)*, 4th Edition, Shaker Aachen, 2005

[7] F. Musiol *Erklärung der Vorgänge in der Kontaktzone von trockenlaufenden Reibpaarungen über gesetzmäßig auftretende Phänomene im Reibprozess [Explanations on the processes in the friction layer between dry friction partners based on friction phenomena]*, Dissertation TU Berlin, 1994

[8] D. Gauger *Wirkmechanismen und Belastungsgrenzen von Reibpaarungen trockenlaufender Kupplungen [Physical mechanisms and load limits of friction partners of dry couplings]*, Dissertation TU Berlin, 1998

[9] S. Dörsch *Periodische Veränderungen lokaler Kontaktgrößen in Reibpaarungen trockener Bremsen [Periodical fluctuations of local contact parameters of dry brakes]*, Dissertation TU Berlin, 2004

[10] G.-P. Ostermeyer *Friction and wear of brake systems*, Forschung im Ingenieurwesen, Volume 66, Number 6 / October 2001, Springer Verlag

[11] H. Uetz; J. Wiedemeyer *Tribologie der Polymere [Tribology of Polymers]*, Hanser-Verlag, München, 1985

Independent force control of pneumatic McKibben actuators using the multiplexing technique

Ville Jouppila
Institute of Machine Design/Laboratory of Virtual Technology
Tampere University of Technology
PL 589, FIN-33101 Tampere, Finland
ville.jouppila@tut.fi

Asko Ellman
Institute of Machine Design/Laboratory of Virtual Technology
Tampere University of Technology
PL 589, FIN-33101 Tampere, Finland
asko.ellman@tut.fi

ABSTRACT

Traditionally in fluid power systems, each actuator is provided with an individual control valve that is often quite an expensive and weighty component. In multiplexed control, a single control valve is shared among a number of actuators providing cost and weight savings. In this study, the multiplexing is carried out with one pressure regulator and several high-speed on/off valves. It has been proven that multiplexed force control of pneumatic muscles is a good option for applications where multiple actuators have similar tasks with low dynamics [9].

In this paper, the possibility of controlling the forces of the pneumatic McKibben actuators individually with a multiplexing control method is studied. The characteristics of the actuator with low friction and hermetical structure enable its use especially in force control applications. The actuator can maintain its pressure and thus the generated force for a relatively long time after it is disconnected from the pressure line. This provides a possibility to increase the time between the muscle actuations in the multiplexed control cycle. During this gap period, the pressure regulator can be adjusted to the pressure level demanded by the next muscle, providing an independent force control of the muscles. The multiplexed force control concept is studied by simulations and verified with actual measurements.

Power Transmission and Motion Control 2007 Edited by Dr D N Johnston and Professor A R Plummer
© With The Centre for Power Transmission and Motion Control

1. INTRODUCTION

Recent advances in pneumatic valve technology include low cost high-speed valves and accurate pressure regulators. Combined with digital technology, they can be used to develop new control systems. Pneumatic technology has traditionally been used in processes where a simple, high-speed, low cost and reliable action is needed. Mainly due to the compressibility of air, accurate control has been difficult, which has limited the use of pneumatics in advanced applications. However, pneumatic actuators have properties such as compactness, low cost, high power-to-weight ratio and simplicity that are desirable factors in many applications. To overcome the shortcomings, a number of advanced pneumatic components have been developed, of which the most promising is the Pneumatic Artificial Muscle (PAM). Together with the developments in the valve technology, this technology provides an interesting and potentially very successful alternative actuation source for many advanced applications as well. [2]

Compared to a cylinder, a pneumatic muscle not only has higher power-to-weight and power-to-volume ratios, but it is also almost frictionless and has zero leakage. As a result, the behavior of the muscle is less non-linear than that of a cylinder. The characteristics of the actuator enable it to be used in simple positioning systems and as a gas spring. Despite the actuator's nonlinear force-to-contraction characteristics, many motion and force control methods have been applied to it with a sufficient level of accuracy [1,2,7,11]. Additionally, the actuator is extremely well-suited for force-controlled gripping and pressing applications due to the proportional pressure-to-force relation.

Traditionally in fluid power systems, each actuator is provided with its own controlling device such as a proportional or servo valve, which is a fairly expensive and weighty component. In many applications where high power-to-weight and power-to-volume ratios are needed (e.g. aircrafts, mobile machines), it would be an advantage if multiple actuators could be controlled using a single controlling device (Fig. 1). It is obvious that the flow rate for the actuators is substantially reduced by using this multiplexing technique. So the method will not work in applications with high demand for dynamics. [14.]

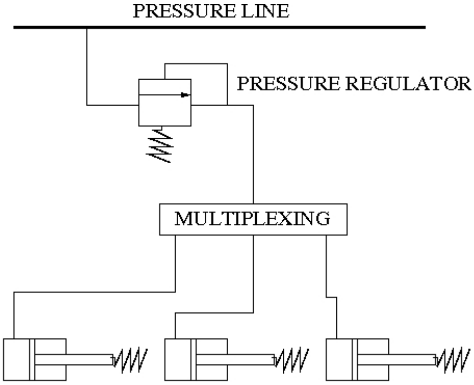

Figure 1. Principle of multiplexing.

Instead, the pressure/force applications with no need of substantial fluid flow could be configured to share a single control valve among multiple channels. A pneumatic muscle has promise for use in multiplexed control systems due to its interesting properties. For example, in gripping applications with a solid object, the muscle length and volume do not change much and the force output of the actuator can be controlled by pressure alone.

In our previous study [10], the force control of multiple McKibben actuators using the multiplexing technique was examined experimentally. The results indicated that the concept is a good low cost option for low dynamic force control applications. However, it was assumed that the actuators have similar tasks and the controlling pressure remains the same for all actuators. It was noted that due to the negligible leakage the muscle can maintain its pressure for a relatively long time. As a conclusion, the gap time between the muscle actuations could be increased, giving an opportunity to adjust the pressure regulator between the muscle actuations. In that case, the muscle pressures and further the forces could be controlled independently. In this study, the system is first modeled and then investigated by simulations. Finally, the concept is verified experimentally.

2 SYSTEM MODELING

A schematic diagram of our test rig is shown in Figure 2. A service unit is connected to a pressure network providing a supply pressure (7 bar) for the pressure regulator (Festo MPPES-3-1/8-6-010) which controls the system pressure. The multiplexer unit consists of four high-speed directional on/off valves providing a connection between the pressure regulator and the muscle actuators (Festo MAS-10). The return ports of the multiplexer valves are plugged. The pressure regulator is controlled by the DSpace hardware and the high-speed valves by the logic unit. The sensor data is recorded with a National Instruments DAQ card.

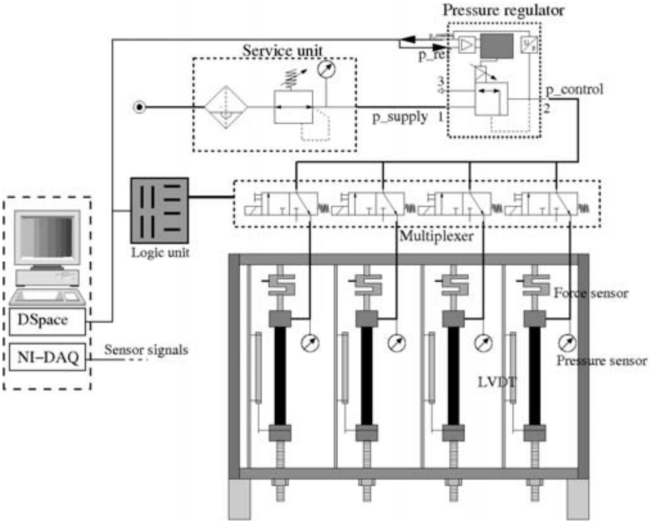

Figure 2. System setup.

2.1 McKibben actuator model

The McKibben muscle is an actuator that consists of a rubber tube and non-extensible fiber surrounding [6]. The Festo fluidic muscle (Fig. 3) used in this research differs slightly from the general McKibben type muscle. The fiber of the Fluidic Muscle is knit in the tube itself offering easy assembling and improved hysteresis and non-linearity compared to a conventional one.[8]

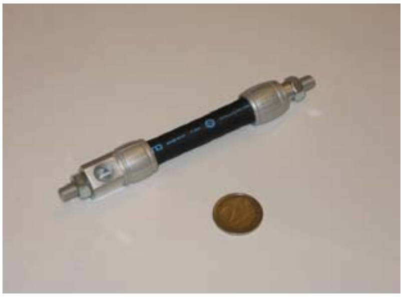

Figure 3. Festo fluidic muscle.

When the muscle is inflated with compressed air, it widens. A tensile unidirectional force thereby arises as well as a contraction movement in the longitudinal axis. The force is at its maximum at the beginning of the contraction and it decreases with increasing contraction (Fig. 4) [6]. The nominal force contraction curve shows an interesting point. When the muscle length is kept constant the force is an almost linear function of the muscle pressure.

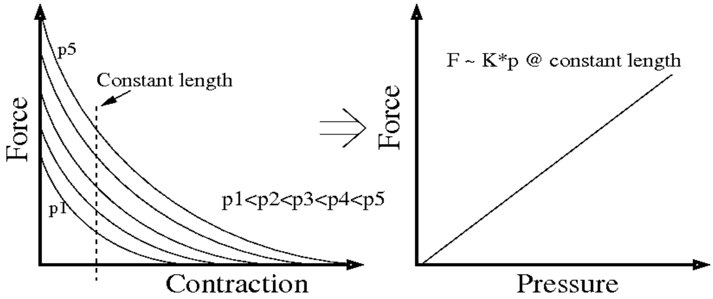

Figure 4. Nominal force-contraction curves at different pressure levels for a typical pneumatic muscle actuator.

2.1.1 Static characteristic modeling

The nominal force-to-contraction diagram shows the non-linear characteristics of the muscle. Modeling of the muscle force has typically based on the consideration of virtual work and conservation of energy providing a relationship between the actuator tension, pressure and length. In many studies, the muscle force is described as a function of pressure, relaxed actuator length and weave geometries [2,4,12,13]. Using the principle of virtual work and energy conservation the muscle force can be expressed with an equation

$$F = -p\frac{dV}{dL},$$

where p is the internal muscle pressure, V is the muscle volume and L is the muscle length. The use of the previous equation supposes knowledge of the material geometries. In the Festo fluidic muscle, the weave geometries are difficult to determine and so an alternative approach is needed. The actuator can be assumed to have a variable-stiffness characteristics acting as a variable gas-spring [4,5]. The stiffness per unit pressure *K(p,L)* is a function of pressure and muscle length. The force equation can then be written as

$$F_{static}(p,L) = K(p,L)p(L - L_{\min}(p))$$

where $L_{min}(p)$ is the theoretically possible minimum length for the respective pressure. The stiffness for a constant pressure remains close to a constant for the large contractions (>5%). When the muscle length is near to its nominal length the stiffness changes considerably. An exponential fit can be approximated to describe this stiffness behavior

$$K(p,L) = a * e^{\lambda_1 * L} + b * e^{\lambda_2 * L * f(p)}$$
$$f(p) = c_1 p^2 + c_2 p + c_3$$

The coefficients a, b, c_1, c_2, c_3, $_1$ and $_2$ were found by using manual iteration.

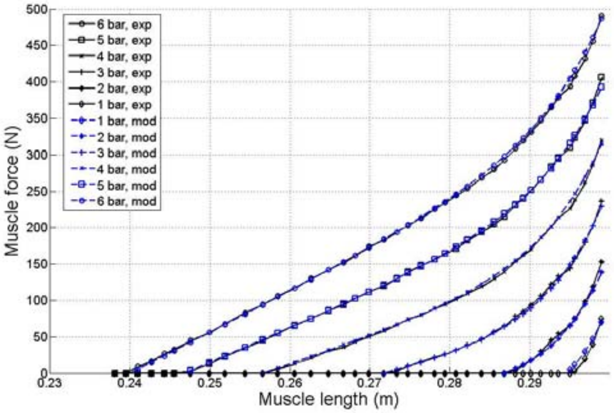

Figure 5. Estimated vs. measured static muscle force.

In figure 5, the force predicted by the static model is compared with actual measurements. In the measurements, the muscle force data was collected for 6 different pressure levels over the whole contraction range. The model estimates the force quite accurately for almost every pressure and length. Only for low pressures with muscle length near the nominal length the model slightly differs from the experimental data.

2.1.2 Dynamic characteristic modeling

The force equation above expresses the muscle characteristics only in the static case. In dynamic sense, the muscle can be thought of as a variable spring and a parallel variable damper [10]. The total muscle force can be denoted as

$$F_{muscle}(p, L, \dot{L}) = F_{static}(p, L) + F_{damper}(p, \dot{L})$$

The damper component of the muscle force is calculated similarly to the normal mechanical damper. The damping coefficient C is additionally multiplied with the absolute muscle pressure p resulting in the following equation:

$$F_{damper}(p, \dot{L}) = -C * p * \dot{L}$$

The coefficient C is found with the help of experimental results.

Determining the dynamic behavior of the muscle the knowledge of the actual pressure inside the muscle must be known. The muscle pressure depends on the quotient amount of air in the muscle and volume of the muscle. It is necessary to calculate the volume of the muscle, which is correlated with the muscle length and the air in the muscle, which depends on the flow rate into the muscle. By assuming that the muscle has shape of a cylinder the approximated muscle volume can be calculated as

$$V = \frac{1}{4}\pi(d(L) - t)^2 L,$$

where *d(L)* is the diameter of the muscle as a function of the muscle length. The coefficient *t* is the thickness of the fiber and it is assumed to be constant during the contraction. The outer diameter and the length of the muscle were measured and the volume of the muscle was determined using the equation above.

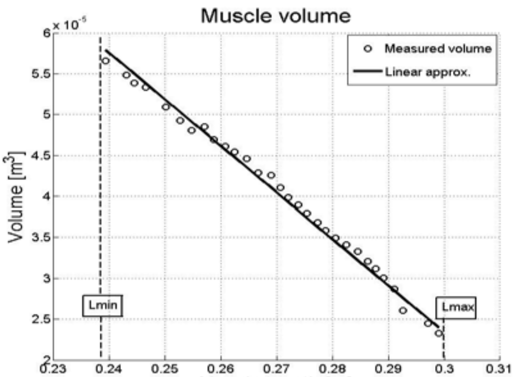

Figure 6. Muscle volume related to the muscle length.

The curve of the resulting volume in respect to the muscle length is presented in Figure 6. The volume shows a nearly linear behavior, so it is assumed that the volume can be approximated with

$$V_{mus} = aL + b$$

The coefficients *a* and *b* can be determined from the volume curve in Figure 6. The pressure in the muscle can be derived from the equation for ideal gases. Since the motion of the muscle is not so fast, we assumed isothermal change. Differentiation of the equation

$$p_{mus} = p_{amb} \frac{V_0}{V_{mus}}$$

where p_{amb} is the ambient pressure and V_0 is the volume of air in the muscle under ambient pressure, leads to the equation

$$\dot{p}_{mus} = p_0 \left(\frac{\dot{V}_0}{V_{mus}} - V_0 \frac{\dot{V}_{mus}}{V_{mus}^2} \right)$$

$$\dot{p}_{mus} = p_0 \frac{\dot{V}_0}{V_{mus}} - p_{mus} \frac{\dot{V}_{mus}}{V_{mus}}$$

The term $\dot{V}_0$ is the flow of air volume into the muscle through the high speed valve and it will be derived from the valve model.

2.2 High-speed valve model

The valve model is used to determine the volume flow rate through the valve into the muscle. The volume flow depends on the critical pressure relation *b*, which is typically between 0.3–0.5 for valves. The flow rate through a pneumatic valve is given in the following formula in an adiabatic process

$$\dot{V}_0 = C_q p_{in} \qquad , \frac{p_d}{p_u} \leq b \ (choked)$$

$$\dot{V}_0 = C_q p_{in} \sqrt{1 - \left(\frac{{p_d}/{p_u} - b}{1 - b} \right)^2} , \frac{p_d}{p_u} \quad b \ (notchoked)$$

If the ratio of downstream and upstream pressure p_d/p_u is below the critical pressure value, the flow rate is choked. Respectively, if the pressure ratio exceeds the critical value the volume is not choked. The flow coefficient C_q is obtained from the manufacturer's datasheet. The opening and closing time for this valve is approximately 2 ms and it is included in the model as a time delay.

2.3 Dynamic model verification

A step response test with a constant mass was executed by using the setup shown in Figure 7. A constant mass of 9.4 kg was attached to the muscle. A series of step response tests was executed for different supply pressure levels. The high speed on/off-valve was first closed and then opened to allow flow rate into the muscle. The data from the displacement and pressure sensors was recorded with the National Instruments DAQ card in order to get the muscle motion and the muscle pressure information.

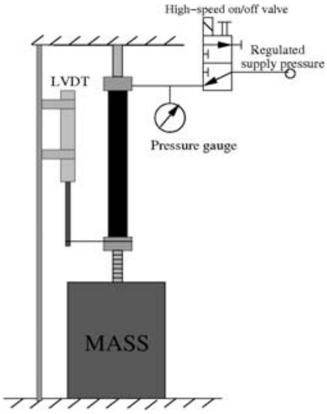

Figure 7. Dynamic test setup.

Similar tests were simulated with the dynamic model. Using the force balance on the mass, the equation of motion becomes

$$\ddot{x} = \frac{1}{M} \quad F_{static}(p,L) + F_{damper}(p,\dot{L}) - Mg$$

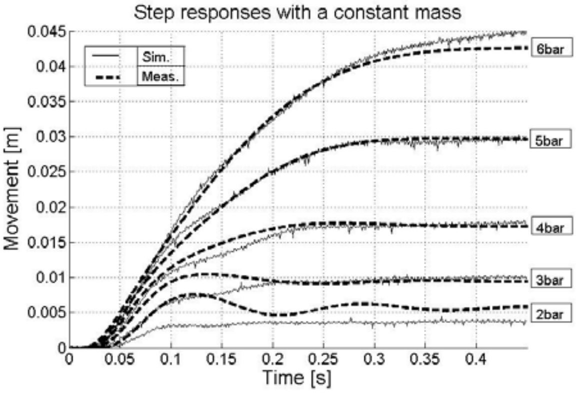

Figure 8. Step responses with a constant mass (model vs. measured).

The simulation and measurement results for different pressure step responses are compared in Figure 8. The y-axis indicates the load movement upwards. It can be noted that the model is quite accurate for high pressures. For low step pressures the load movement given by the model differs quite a lot from the real measurements. It shows that the muscle force model gives too much force for low pressure levels when the muscle is near its initial length. The possible reason for that might be the inaccuracies in the real force measurements. However, in the normal operating range the dynamic model predicts the load motion quite accurately.

2.4 Proportional pressure regulator

The pressure regulator (Festo MPPES-3-1/8-6-010) controls the system pressure for the muscle actuators. An integrated pressure sensor records the pressure at the working air connection. The electronic control compares the pressure value with the nominal value. An electrical signal proportional to the output pressure is then transmitted. If the nominal and actual values differ, the regulating valve will be actuated until the output pressure is the same as the nominal value.

A similar regulator was investigated and modeled by Cho et al [3]. They used the model to design a sliding-mode controller combining a PID scheme for the regulator. Their model was developed by defining the required parameters through analyzing geometrical and material data. In our case we do not need an exact model for the regulator. Instead, we can use a first order linear model approximation to describe the dynamics of the regulator and the constant volume after it.

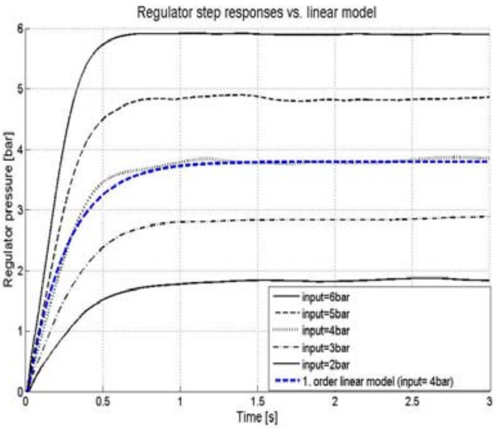

Figure 9. Open-loop step responses of the pressure regulator.

A set of step response tests was executed for the regulator. The control volume connected to the work port of the regulator consists of four hoses between the regulator and the multiplexer valves. In figure 9, output pressure signals are shown for a range of desired input pressures (2–6 bar). We can estimate the dynamic behavior of the regulator with a transfer function

$$G_p(s) = \frac{K}{\tau s + 1}$$

The parameters for the linear model were approximated from the open loop responses. We used the gain K=0.94 and time constant =0.25. An open loop response of the linear model for an input of 4 bar is also shown in figure 9. It should be noted that the open loop gain varies for a range of inputs and a steady state error exists in the responses. However, the linear model is accurate enough to approximate the dynamics of the regulator in our case. The pressure losses due to air flow in the hoses between the regulator and the high-speed on-off valves are included into a regulator model as an error term.

3 INDEPENDENT MUSCLE PRESSURE/FORCE CONTROL

In this chapter the independent force control of the muscles is examined first with simulations and then experimentally. First, the multiplexing concept is introduced. We also need to design a controller for the pressure regulator. At this stage we will settle for a traditional PID-scheme. When the controller is designed, we can simulate the system behavior.

3.1 Principle of multiplexing

In a multiplexed control, the actuators are actuated alternately and sequentially in such a manner that they are not simultaneously connected to the system pressure. The basic principle of multiplexing is shown in Figure 10. In our setup the high-speed on-off valves form the so-called multiplexer. The control cycle of the multiplexing can be expressed with the equation

$$t_{cycle} = n * (t_{act} + t_{gap})$$

The term n denotes the number of the muscles in the system. During the control cycle each muscle is connected once to the pressure line for a specific length of time. During the actuation time t_{act} the high-speed valve for a certain muscle is open. After the actuation time the valve is closed until its next actuation begins at the next cycle. In order to avoid simultaneous muscle actuations, there has to be a gap / un-actuation time between the controls of sequential actuators. During this gap time the previously activated valve has enough time to close. If the un-actuation time is kept short, the muscle is connected to the pressure line for approximately ¼ of the control cycle.

In our previous study [9], it was concluded that it is possible to increase the gap-time between the muscle actuations in the multiplexed control scheme. Due to the hermetic construction, the muscle can maintain the desired pressure level for quite a long time. This gives an opportunity to adjust the pressure regulator during the gap-time and thus supply a different pressure levels for the muscles. The gap-time should be long enough so that the regulator has time to reach its new target pressure value. The actuation time of the muscles should also be long enough that the regulator can adjust to the changes.

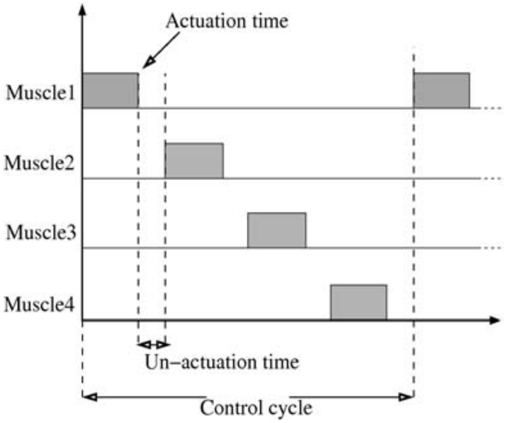

Figure 10. Principle of multiplexing.

3.2 PID-controller

As was done in Cho et al., a PID controller is adopted to improve both the transient and steady state performances. The transfer function of the PID-controller is

$$G_c(s) = P + I/s + Ds$$

The linear pressure regulator model was used to find the gains for the PID-controller. The PID-controller was implemented in the DSpace-hardware and used with the actual regulator. The measured closed-loop responses for a constant proportional gain P and integral gain I and different derivative gain D are shown in Figure 11. As a reference, also the regulator performance without a controller is shown. The results indicate that the PID-controller makes the operation of the regulator slightly faster and removes the steady state error. The best result is gained with the derivative term 0.1 (PID1). In order to improve the performance further, a sliding mode or another controller approach is needed

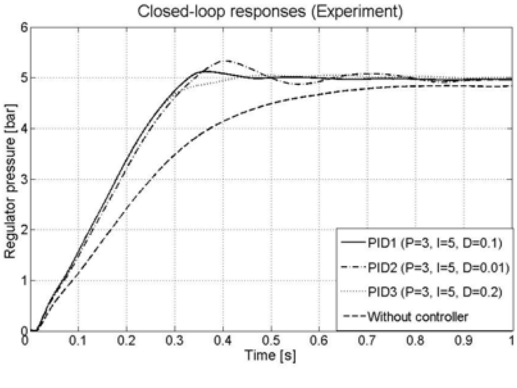

Figure 11. Closed-loop responses for a range of PID-controllers.

3.3 Simulation results

The independent pressure/force control of the muscles was first tested by simulations. Normally in force control applications like gripping and pressing the actuator first moves to a certain position to get in touch with a target object. When the actual gripping and pressing task begins the actuator position does not change much, naturally depending on the properties of the object. The multiplexed control system was studied in a static case where the muscles were locked into their nominal length. In the simulations and measurements we wanted the muscles to have different pressure levels from 2 bar to 5 bar. So, the input signal for the system was a continuous stair signal shown in Figure 12. The total time of a stair signal cycle is naturally the same as for the multiplexing cycle. The PID-controller gets this input signal as its reference signal and compares it to the regulator's actual pressure value. During the gap time the regulator should reach the target value required by the next muscle. Obviously, the gap time should be long enough that the action takes place before the connection between the control volume and the muscle opens. During the actuation time the muscle is connected to the control volume. If the system remains stable the actuation time could be quite short, because the muscle does not need substantial fluid flow to maintain its pressure. If there are external factors distracting the pressure balance inside the muscle, the actuation period should be long enough. Thus the regulator could react to changes in the system. It should be noted that our system configuration is actually an open-loop control unless the regulator is controlled with a closed-loop mode. That is, the controller does not get any feedback information of the muscle pressure levels. The purpose of these simulations is to investigate if the concept is at least workable. The simulation model can also be used to define the appropriate time parameters for the system.

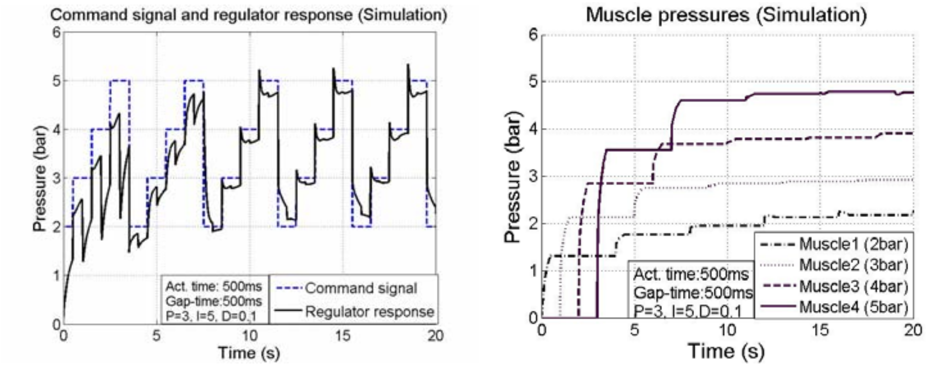

Figure 12. Simulated regulator response and muscle pressure curves for integral gain value 5.

The simulations were executed with quite a long actuation (500 ms) and gap (500 ms) times. The system was first simulated with the parameters of the PID1-controller. It can be seen in Figure 12 (left) that the regulator with the control volume can not reach its target values during the wanted gap time period. The worst case occurs when the regulator has to change its state from 5 to 2 bars. It can not reach either level. As a result there occurs a steady state error in the muscle pressures shown on the right side of Figure 12. The low performance of the system is mainly caused by the inaccurate regulator model. In order to achieve a better system performance we needed to speed up the controller action. It is done by increasing the integral gain of the PID-controller. The results for the integral gains of 10 and 20 are shown in Figures 13 and 14.

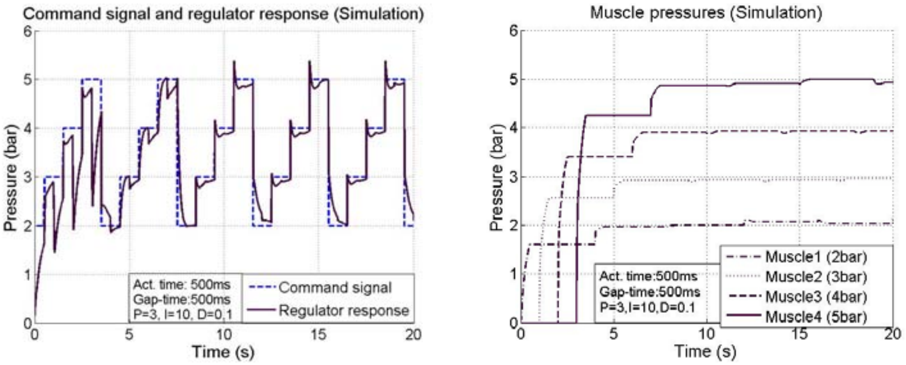

Figure 13. Simulated regulator response and muscle pressure curves for integral gain value 10.

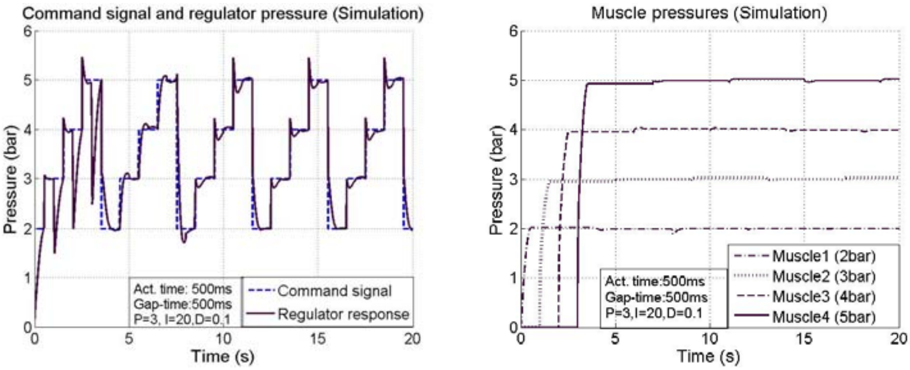

Figure 14. Simulated regulator response and muscle pressure curves for integral gain value 20.

The regulator pressure curves in Figures 13 and 14 show that the regulator can follow the command signal better with a faster controller. The best result is achieved with the integral gain 20 where the regulator response is already quite close to its target value after the gap time period. Then, during the muscle actuation time period the controller is able to correct the remaining error. As a result, the muscle pressure curves can gain their target pressure levels. They also show quite a stable and acceptable system behavior. It should be noted that the muscles were locked into their nominal lengths. The resulting forces as a function of respective muscle pressures depend highly on the muscle contractions/lengths. In our case only one muscle length case was studied. The force curves in Figure 15 are so a direct consequence of the muscle pressure curves.

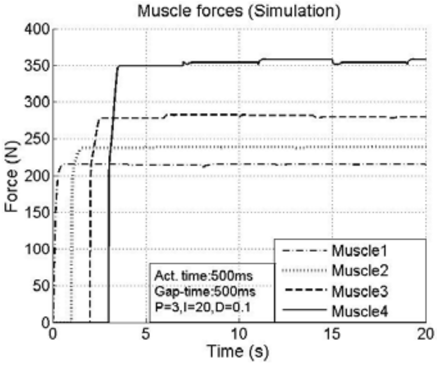

Figure 15. Simulated muscle force curves for integral gain value 20.

3.4 Experimental results

The simulation results were quite promising about the functionality of the independent force control of the muscles. The testing setup for this control method was introduced in Figure 2. The PID-controller was created in Matlab/Simulink and it controlled the system in real time via the DSpace hardware. The actual regulator pressure for the controller was transmitted by the regulator. Incrementing the integral gain above the value 5 as was done in simulations resulted in too much overshooting in the experiments. That is why the controller parameters of PID1 (Fig.11) were chosen for these system measurements.

In the first experiment the actuation and gap times of 500 ms were used. The regulator response in Figure 16 (left) shows quite a stable action. However, it does not reach its target values but gets quite close. The pressure curves shown in Figure 16 (right) indicate also a stable operation but there occur steady state errors between the measured and the target values. Despite of the inaccuracies the system works fast enough providing almost desired supply pressures for each of the muscles. In Figure 17 the force responses of the muscles are shown. Because the muscle lengths are constant during the operation the forces are almost a proportional result of the muscle pressures.

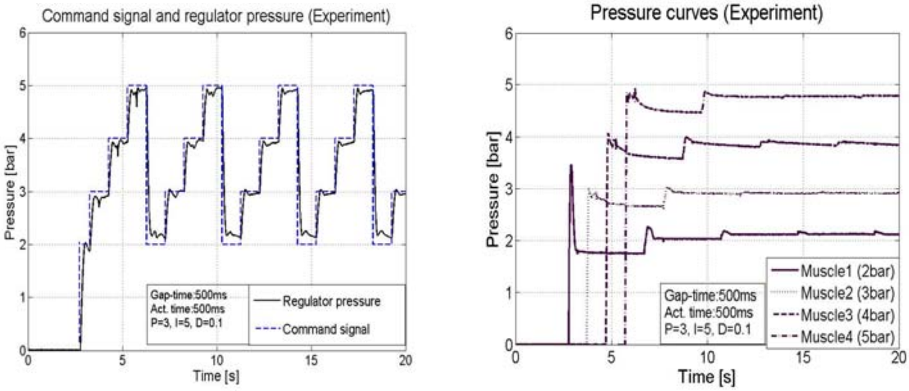

Figure 16. Experimental results for the regulator response and muscle pressures with the actuation and gap time 500 ms.

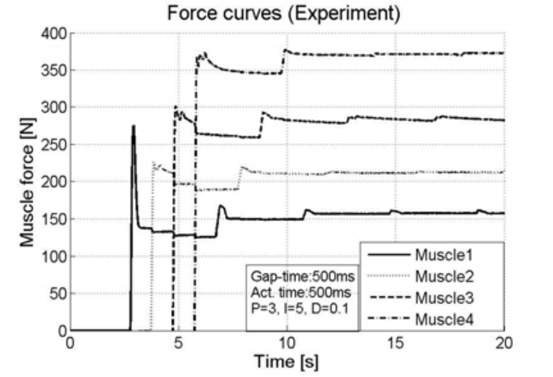

Figure 17. Experimental results for the muscle forces with the actuation and gap time 500 ms

In the second experiment the actuation and gap time was decreased to 250 ms. The regulator response and the muscle pressure and force curves introduced in Figures 18 and 19 indicate similar results as in the simulations. It can be noted that the regulator responds fast enough even for this gap period. The muscle pressure and force curves remain quite stable. There are slight steady state errors in the pressure curves but altogether they are quite near their target values (2, 3, 4 and 5 bars). The procentual steady state errors in the force curves are less than 7 %. The force levels are a direct consequence of the muscle pressure as was explained before. The resulting force levels for a specific pressure depend on the muscle length. In order to control the muscle forces accurately over the whole operational muscle motion range, displacement and force feedback for the controller would be needed. It would also need an advanced controller system. This would lead to a less robust system and costs of the system would increase due to the additional expensive sensors. The system is meant to work in static force applications (pressing, gripping) where the actuators have a specific work cycle. The independent pressure/force control enables the actuators to have different low dynamic force control tasks with low cost. However, further studies are needed to develop the control system and to implement it into the real system.

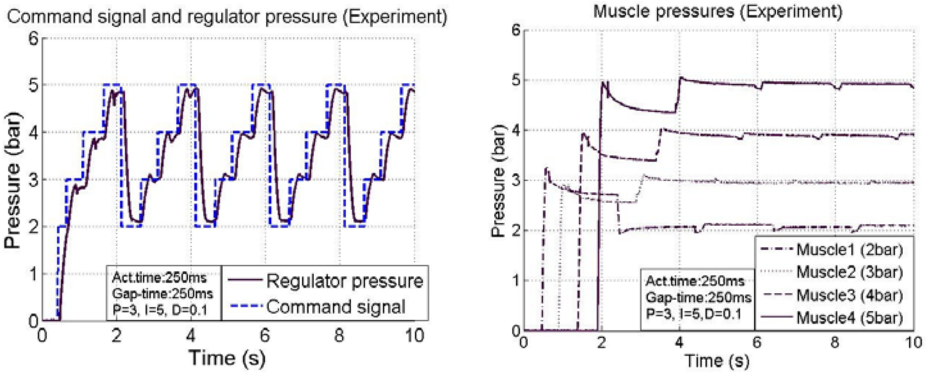

Figure 18. Experimental results for the regulator response and muscle pressures with the actuation and gap time 250 ms.

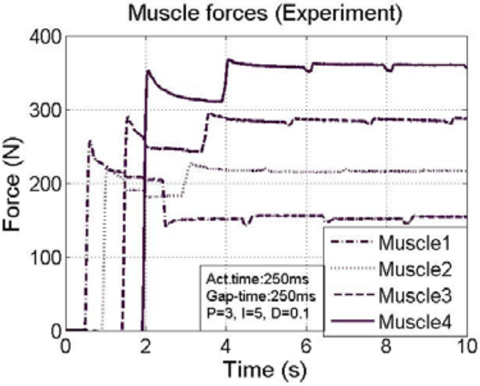

Figure 19. Experimental results for the muscle forces with the actuation and gap time 250 ms.

4 CONCLUSIONS

Recent improvements in valve technology providing low cost high-speed valves combined with digital technology can be used to develop new low cost control systems in pneumatics. In this paper, a possibility of controlling the pressure/force of multiple McKibben actuators independently was studied. The system exploits the control principle of multiplexing technique. The system simulations and experimental tests showed that in certain boundaries the control method is workable. However, due to the open-loop type muscle control, the system is sensitive to external disturbances. However, a closed-loop type control could be created so that during the actuation period the controller would get the real muscle pressure value to compare with the reference value. Of course, the system costs would increase due to the additional sensors and the operational reliability of the system would decrease. The gap and actuation periods are still quite long resulting in low dynamics for the system. To increase the dynamics a faster controller scheme such as sliding mode for the regulator is needed. The effects of the time parameters on the system behavior also need further investigations. In this configuration the system could be used in low dynamic and low cost applications where different force tasks of multiple actuators are required.

REFERENCES

[1] Caldwell, D.G., Medrano-Cerda, G.A, Goodwin, M.J., "Braided pneumatic actuator control of a multi-jointed manipulator", Proceedings of the IEEE International Conference on Systems, Man and Cybernetics, pp. 423–428, Le Touquet, 1993

[2] Caldwell D.G., Medrano-Cerda, G.A., Goodwin, M.J., "Control of Pneumatic Muscle Actuators", IEEE Control Systems Magazine, vol. 15, number 1, pp. 40–48, 1995

[3] Cho, S.H., Fiedler, M., Rudiger, F, Helduser, S. “Virtual-design-model-based pressure-tracking control of high-dynamic pneumatic valves using a sliding mode-controller

combined with a proportional-integral-derivative scheme", Proceedings of the Institution of Mechanical Engineers, Part I: Journal of Systems and Control Engineering, Vol. 220, Number 5/2006

[4] Chou, P. & Hannaford, B.. "Measurement and Modeling of a McKibben Pneumatic Artificial Muscles", IEEE TRANSACTIONS On Robotics and Automation Vol 12, No 1, Feb 1996.

[5] Colbrunn, R.W. "Design and control of a robotic leg with braided pneumatic actuators", Master Thesis, Department of Mechanical and Aerospace Engineering, Case Western Reserve University, May 2000

[6] Daerden, F., Lefeber, D., Verrelst, B., Van Ham, R. "Pleated pneumatic artificial muscles: actuators for automation and robotics" IEEE/ASME International Conference on Advanced Intelligent Mechatronics, Proceedings 8-12, Como, Italy, July 2001.

[7] Davis, S., and Caldwell, D. G."Enhanced dynamic performance in pneumatic muscle actuators. In IEEE Robotics and Automation Conf., Washington, USA, May.2002.

[8] Festo. Fluidic Muscle MAS. Festo Brochure.2002

[9] Jouppila, V. & Ellman, A."Multiplexed force control of pneumatic muscles", ASME International Mechanical Engineering Congress and Exposition, Chicago Illinois, USA, November 2006

[10] Kerscher, T., Albiez, J., Zöllner, J.M., Dillmann, R. "FLUMUT – Dynamic model of fluidic muscles using Quick-release", 3rd International Symposium on Adaptive Motion in Animals and Machines, Ilmenau, Germany, September 2005

[11] Medrano-Cerda, G.A., Bowler, C.J., Caldwell, D.G."Adaptive position control of antagonistic pneumatic muscle actuators", IEEE/RSJ International Conference on Intelligent Robots and Systems, vol. 1, pp.378-383, Pittsburgh, PA, USA, 1995.

[12] Tondu, B. & Lopez, P. " Modeling and Control of McKibben Artificial Muscle" IEEE Control Systems Magazine, pp. 15-38, April 2000.

[13] Tsagarakis, N., Caldwell, D.G.,"Improved modelling and assessment of pneumatic muscle actuators", ", In IEEE International Conference on Robotics and Automation, Vol. 4, pp. 3641–3646, San Francisco, CA, USA, 2000

[14] Wardle, J et al., "Multiplexed hydraulic control systems", U.S. patent EP 0438925, 1991

Fluid Dynamics and Noise

Vibroacoustic Load Reduction in Hydromechanical Systems by Use of Flow Oscillation Dampers

E.V. Shakhmatov, A.N. Kruchkov, A.B. Prokofiev, V.J. Sverbilov
Faculty of Flying Engines, Samara State Aerospace University, Russian Federation

ABSTRACT

Application of flow fluctuation dampers to increase hydraulic systems reliability is considered. The bases of the theory of damper characteristics calculation are presented. It is shown that in the field of low frequencies where it is possible to neglect the distribution of damper parameters for calculation of its characteristics the method of two-port network is preferable. In the field of high frequencies where the distribution of parameters is of great importance the usage of numerical methods is necessary. Examples of practical application of dampers are presented in paper. It is shown that inserting of fluctuation damper in hydraulic system allows lowering not only the level of pulsations of a fluid, but also vibration of mechanical elements.

1. INTRODUCTION

Development of aviation technology is connected to growth of capacity and profitability of power installations. At the same time functional problems of hydromechanical systems considerably extend and processes in system devices are intensified. Functional and parametrical reliability of hydromechanical systems especially of flying vehicles' power supply and engine control systems is appreciably reduced owing to an influence of working fluid pulsations on sensitive elements, actuators and pipelines. Pressure pulsations which amplitude in some cases reaches 50 % of static value are one of main causes of fatigue failures in hydromechanical systems.

An effective method of a vibroacoustic load reduction in hydromechanical systems is application of pressure fluctuation dampers or compensators. Their advantages consist not only in reduction of pressure pulsations' level, but also in reduction of vibration level caused by a pulsing working fluid. These devices are effectively applied in any hydromechanical system subjected to working fluid pulsations. It is explained by the following: the most of dampers have a simple construction and high reliability; their mounting does not complicate hydromechanical system and demands no significant alterations in it; oscillation dampers'

Power Transmission and Motion Control 2007 Edited by Dr D N Johnston and Professor A R Plummer
© With The Centre for Power Transmission and Motion Control

application provides a designer with a great freedom for optimizing project without taking pulsations into account.

The functioning of such corrective devices is based on two principles:

- on a principle of localization of fluctuations energy of a working liquid (devices of reactive type);
- on a principle of absorption of fluctuations energy (devices of dissipative type or dampers)

The devices of reactive type work like acoustic filters blocking fluctuations of a working fluid put into the hydraulic system. Structurally they represent serial connection of capacitor and inertial elements (figure 1). Restriction of downstream fluctuations intensity is reached simultaneously due to energy accumulation in chambers and inertial properties of the narrow passages.

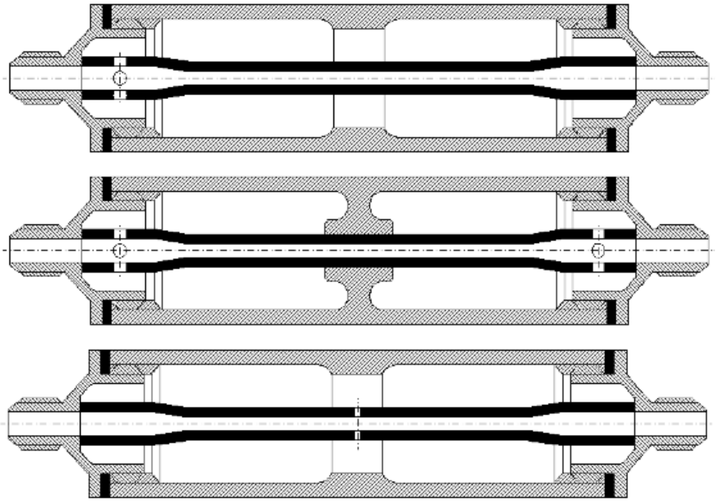

Figure 1. Constructive schemes of reactive pressure fluctuation dampers

In the dampers energy of fluctuations dissipates due to viscous friction. Diagrams of such devices are shown in Figure 2. In the design shown on Figure 2, a dispersion of energy is carried out on the throttles ***m*** , in the scheme shown on Figure 2,b - on a ring element ***k*** from a porous material.

To increase the fluctuations suppression efficiency as a rule the combined structures using both principles are applied.

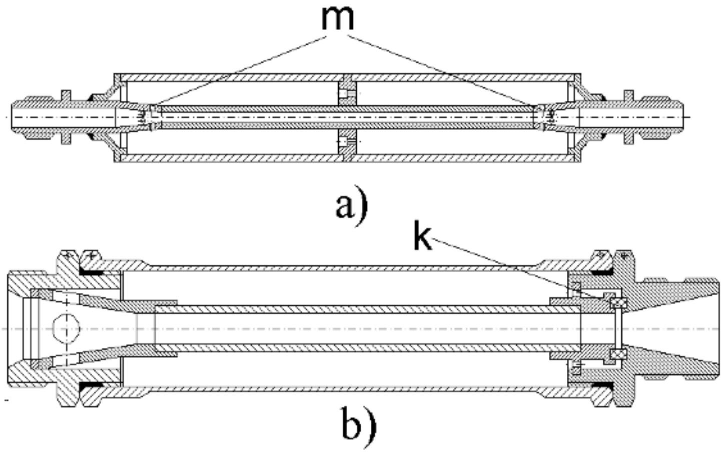

Figure 2. Dissipative pressure fluctuation dampers

2. BASIS OF THE THEORY

The analysis of oscillatory process in systems with corrective devices is carrying out with the use of multiterminal networks method well developed in the electrical engineering and the method of electro hydraulic analogies. The corrective devices can be described on the basis of the two-port network model. So the equations connecting complex amplitudes of pressure P_i and flow rate Q_i at the input $(i = 1)$ and at the output $(i = 2)$ of the device can be written as [1, 2, 3]:

$$\begin{bmatrix} P_1 \\ Q_1 \end{bmatrix} = \begin{bmatrix} A(\omega) B(\omega) \\ C(\omega) D(\omega) \end{bmatrix} \begin{bmatrix} P_2 \\ Q_2 \end{bmatrix},$$

where

$$A(\omega) = \sqrt{\frac{Z_{c1}}{Z_{c2}}} \cosh(q), B(\omega) = \sqrt{Z_{c1} Z_{c2}} \sinh(q), C(\omega) = \frac{1}{\sqrt{Z_{c1} Z_{c2}}} \sinh(q),$$

$D(\omega) = \sqrt{\frac{Z_{c2}}{Z_{c1}}} \cosh(q)$ - coefficients of the transfer matrix for the device,

ω - circular frequency,

Z_{C1} - the characteristic impedance from the input side;

Z_{C2} - the characteristic impedance from the output side;

q – the characteristic transfer constant;

$K_C = \left|e^q\right| = \left|\sqrt{A(\omega)\cdot D(\omega)} + \sqrt{B(\omega)\cdot C(\omega)}\right|$. - the inherent attenuation factor.

The inherent attenuation factor is equal to the ratio of pressure oscillation amplitudes at the input and the output of the device loading by the characteristic impedance. Generally the overall efficiency of the corrective network increases with K_C value.

An efficiency of corrective devices should be estimated separately for input and output parts of hydraulic system because there is no universal criterion. It is connected with various principles of devices action on these parts of the system. A significant drop in pulsations is usually only reached in the output part. In this part any degree of amplitude reduction is achievable with only restrictions on dimensions and weight of the devices. In this case the insertion attenuation factor K_i is used as criterion of efficiency being numerically equal to the ratio of amplitudes of pressure pulsations in certain sections of the output part of the pipe line before and after the damper introduction into the system:

$$K_i = K_C \left|\frac{Z_w}{\sqrt{Z_{C1}Z_{C2}}}\right| \left|\frac{(Z_{C1}+Z_s)(Z_{C2}+Z_l) - e^{-j2\varphi}(Z_s - Z_{C1})(Z_l - Z_{C2})\dfrac{1}{K_C^2}}{(Z_w+Z_s)(Z_w+Z_l) - e^{-j2\frac{\omega l}{\alpha}}(Z_s - Z_w)(Z_l - Z_w)}\right|,$$

where Z_w - pipe characteristic impedance;

Z_s - an impedance of a source;

Z_l - an impedance of a load;

$j = \sqrt{-1}$,

l - length of the damper;

$\varphi = arg\left(\sqrt{A(\omega)\cdot D(\omega)} + \sqrt{B(\omega)\cdot C(\omega)}\right)$ - the argument of the characteristic transfer constant.

A decrease of pulsations level in the input part between the source of oscillation and the corrective device is reached by acting on its reflecting ability. Here device opportunities are limited. Maximum decrease of pulsation level is restricted by the amplitudes in running wave which are defined by the source of oscillations. So criterion of the damper efficiency in the input part of the hydraulic system is a running wave factor K_r. It is numerically equal to the ratio of maximum of pressure pulsations amplitude in the system with damper to minimum value which is possible in running wave.

3. MODEL IN LUMPED PARAMETERS

The generalized structure of a single-stage corrective device is shown on Figure 3 from which all known structures can be derived only by variation of its parameters.

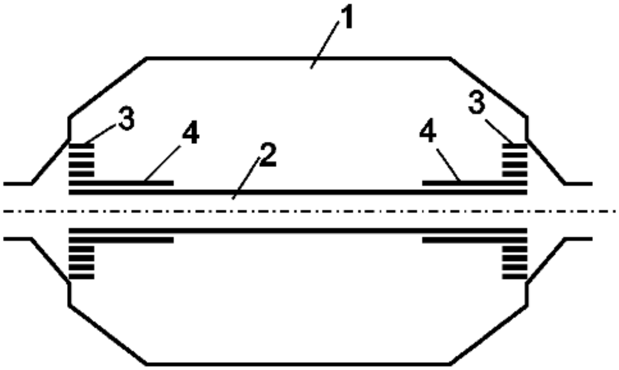

Figure 3. The generalized structure of a single-stage corrective device: 1 - expansion cavity; 2 - the central channel; 3 - throttles; 4 – inductive (resonance) tubes.

Coefficients of a transfer matrix for the generalized structure are:

$$\left.\begin{aligned}
A(\omega) &= \frac{L\left(1-\omega^2 cX_1\right)+X_1+X_2-\omega^2 cX_1X_2}{L+X_1+X_2-\omega^2 cX_1X_2}, \\
B(\omega) &= \frac{j\omega L\left(X_1+X_2-\omega^2 cX_1X_2\right)}{L+X_1+X_2-\omega^2 cX_1X_2}, \\
C(\omega) &= -\frac{1}{j\omega}\frac{\omega^2 Lc}{L\left(X_1+X_2-\omega^2 cX_1X_2\right)}\left(X_1+X_2-\frac{\omega^2 cLX_1X_2}{L+X_1+X_2-\omega^2 cX_1X_2}\right), \\
D(\omega) &= \frac{L\left(1-\omega^2 cX_2\right)+X_1+X_2-\omega^2 cX_1X_2}{L+X_1+X_2-\omega^2 cX_1X_2},
\end{aligned}\right\} \quad (1)$$

where $X_i = \dfrac{L_i R_i}{R_i + j\omega L_i}$, $i = 1,2;$

$\boldsymbol{L}$ - Inductance of the central channel 2;

$\boldsymbol{c} = \dfrac{\boldsymbol{V}}{\rho \boldsymbol{a}^2}$ - Capacity of expansion cavity 1 having volume $\boldsymbol{V}$;

$\boldsymbol{R}_i$ - Resistance of throttles 3;

$\boldsymbol{L}_i$ - Inductance of resonance tubes 4.

3. MODEL IN DISTRIBUTED PARAMETERS

The formulas (1) are received in the assumption that conditions for usage of lumped parameters of the device elements are satisfied, i.e. the length of the acoustic wave in the working fluid is much more than sizes of elements. On higher frequencies of fluctuations this condition ceases to be carried out first of all for the central channel 2 and expansion cavities 1. Taking into account the distribution of parameters of the central channel equations (1) should be copied as:

$$A(\omega) = \frac{Z_1 \cdot \frac{\rho a}{\pi r_1^2} \sinh \frac{j\omega l}{a} + Z \cdot \cosh \frac{j\omega l}{a}}{\frac{\rho a}{\pi r_1^2} \cdot \sinh \frac{j\omega l}{a} + Z}; \qquad D(\omega) = \frac{Z_2 \cdot \frac{\rho a}{\pi r_1^2} \sinh \frac{j\omega l}{a} + Z \cdot \cosh \frac{j\omega l}{a}}{\frac{\rho a}{\pi r_1^2} \cdot \sinh \frac{j\omega l}{a} + Z};$$

$$B(\omega) = \frac{Z \cdot \frac{\rho a}{\pi r_1^2} \cdot \sinh \frac{j\omega l}{a}}{\frac{\rho a}{\pi r_1^2} \cdot \sinh \frac{j\omega l}{a} + Z}; \qquad (2)$$

$$C(\omega) = \frac{\left(Z_2 \cdot \frac{\rho a}{\pi r_1^2} \cdot \sinh \frac{j\omega l}{a} + Z \cdot \cosh \frac{j\omega l}{a}\right)\left(Z_1 \cdot \frac{\rho a}{\pi r_1^2} \cdot \sinh \frac{j\omega l}{a} + Z \cdot \cosh \frac{j\omega l}{a}\right)}{\left(Z \cdot \frac{\rho a}{\pi r_1^2} \cdot \sinh \frac{j\omega l}{a}\right)\left(\frac{\rho a}{\pi r_1^2} \cdot \sinh \frac{j\omega l}{a} + Z\right)} - \frac{1}{\frac{\rho a}{\pi r_1^2} \cdot \sinh \frac{j\omega l}{a}} + j\omega c + \frac{(Z_1 Z_2)}{Z};$$

where

$$Z = j\omega\left(X_1 + X_2 - \omega^2 c X_1 X_2\right);$$

$$Z_1 = 1 - \omega^2 c X_1;$$

$$Z_2 = 1 - \omega^2 c X_2;$$

$$Y_1 = \frac{\rho a}{\pi r_1^2} \sinh \frac{j\omega l}{a}\ ;$$

a – speed of sound waves in fluid.

However the expressions (2) are derived without taking the distribution of parameters of expansion cavities into account because of difficulties of its analytical description.

For modeling characteristics of the corrective devices in the distributed parameters the technique based on a finite elements method is developed. The problem was solved in axisymmetric setting with use programming language APDL built in ANSYS software at the next assumptions: 1) a liquid is ideal; 2) on a border "liquid – structure" absorption of energy of sound waves is absent; 3) the case of damper and the central channel are absolutely rigid.

Frequency dependent factors ***A***, ***B***, ***C***, ***D*** of transfer matrix of the damper are defined by carrying out of three computing experiments using an element with known dynamic characteristics and defining complex amplitudes of pressure fluctuations in three sections of considered system (see fig. 4).

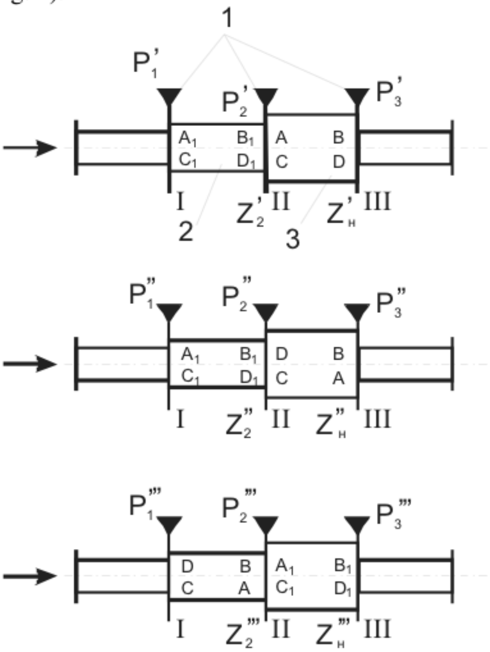

Figure 4. Illustration for technique of definition of dynamic characteristics of damper by results of 3 computing experiments: 1 - sections for which complex amplitudes of pressure are defined; 2 - an element with known frequency characteristics; 3 - investigated damper.

There are designated on Figure 4: $\boldsymbol{A_1}$, $\boldsymbol{B_1}$, $\boldsymbol{C_1}$, $\boldsymbol{D_1}$ - parameters of an element with known frequency characteristics; $\boldsymbol{A}$, $\boldsymbol{B}$, $\boldsymbol{C}$, $\boldsymbol{D}$ - searching parameters of the damper.

Let's write down for the set frequency:

$$\left.\begin{aligned}
&\frac{P'_1}{P'_2} = A_1 + \frac{B_1}{Z'_2}; \qquad \frac{P''_1}{P''_2} = A_1 + \frac{B_1}{Z''_2};\\
&\frac{P'_2}{P'_3} = A_1 + \frac{B}{Z'_1}; \qquad \frac{P''_2}{P''_3} = D + \frac{B}{Z''_1};\\
&\frac{P'_2}{P'_3 Z'_2} = C + \frac{D}{Z'_1}; \quad \frac{P''_2}{P''_3\, Z''_2} = C + \frac{A}{Z''_1};\\
&\frac{P'''_1}{P'''_2} = D + \frac{B}{Z'''_2};\\
&\frac{P'''_2}{P'''_3} = A_1 + \frac{B}{Z'''_1};\\
&\frac{P'''_2}{P'''_3 Z'''_2} = C_1 + \frac{D}{Z'''_1}
\end{aligned}\right\} \quad (3)$$

To lighten the calculations a boundary condition $Z'_1 = Z''_1 = Z'''_1 = \infty$ in spent computing experiments is accepted. Then for system (3) we shall receive the following decision:

$$A = \frac{P'}{P'_3}, \qquad B = \frac{P'''_1 - DP'''_2}{C_1 P'''_3}, \quad C = \frac{P'_1 - A_1 P'_2}{B_1 P'_3}, \quad C = \frac{P''_1 - A_1 P''_2}{B_1 P''_3}, \quad D = \frac{P''_2}{P''_3}.$$

One of estimations of definition accuracy of damper transfer matrix is based on comparison of factor $\boldsymbol{C}$ values within two computing experiments. Other accuracy estimation is definition of a transfer matrix determinant. For passive two-port networks the condition should be satisfied:

$$AD - BC = 1 .$$

A piece of rectilinear pipe with length $\boldsymbol{l}$ and radius $\boldsymbol{r_1}$ was accepted to an element with known dynamic characteristics. The transfer matrix of this pipe length in view of stated above assumptions can be written down in the form of:

$$\begin{bmatrix} \cosh\frac{j\omega l}{a} & \frac{\rho a}{\pi r_1^2}\sinh\frac{j\omega l}{a} \\ \frac{\pi r_1^2}{\rho a}\sinh\frac{j\omega l}{a} & \cosh\frac{j\omega l}{a} \end{bmatrix}.$$

In the paper its application is demonstrated on the example of corrective device which scheme is submitted on Figure 5.

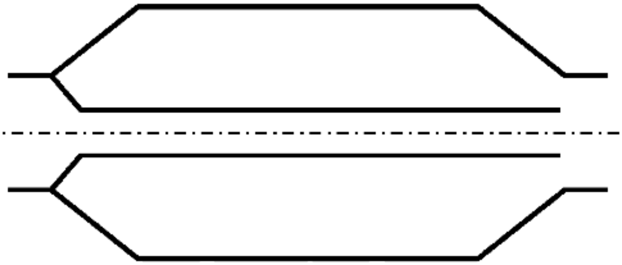

Figure 5. The structure of the damper which characteristics are investigated by a finite elements method.

It is derived from the generalized structure (Figure 3) at the following values of parameters: $L_1 = \infty$, $R_1 = \infty$, $L_2 = \infty$, $R_2 = 0$. The results of computation of the inherent attenuation factor, the characteristic impedances from the sides of inlet and outlet on the basis of the proposed technique are shown on Figure 5. In the same figure the results of calculation on analytical models in the lumped and distributed parameters using the method of two-port network are also presented, where the nondimensional parameters are

$$\varpi = \omega\sqrt{Lc},$$

$$\left|\bar{Z}_{C1}\right| = \frac{\left|Z_{C1}S\right|}{\rho a},$$

$$\left|Z_{C2}\right| = \frac{\left|Z_{C2}S\right|}{\rho a}.$$

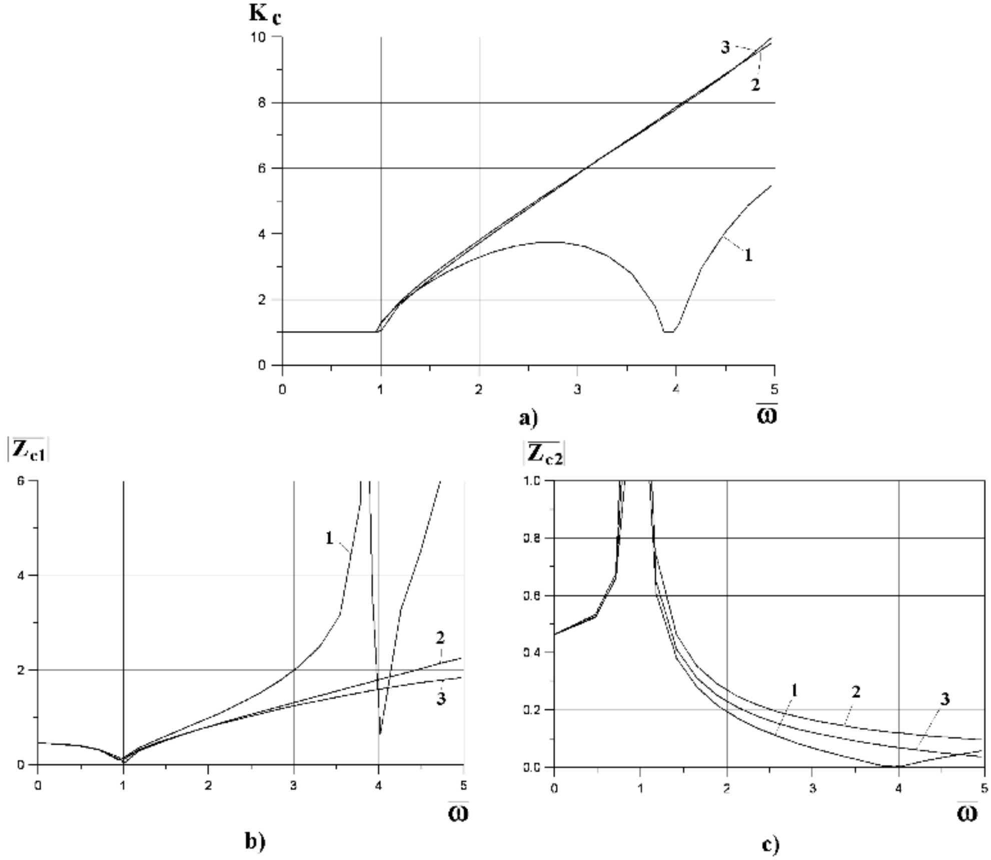

a)

b)

c)

Figure 6. Frequency dependences of damper characteristic complex: 1 - numerical model; 2 - analytical models in the lumped parameters; 3 - analytical model in the distributed parameters.

The distributed parameter analytical model (line 3 in figure 6) assumes lumped parameter theory for the expansion cavity. The results are very similar to the lumped parameter model (line 2).

The analysis of the graphs allows drawing a conclusion that distinction of the results of both models is insignificant till $\omega\langle 2$. However from $\omega\rangle 2$ there is their qualitative divergence. For analytical models $K_c(\overline{\omega})$ is monotonously growing at $\omega\rangle 1$, while for finite element model this function is characterized by a maximum at $\omega = 2,6...2,8$ and a minimum at $\omega = 3,9$. At $\omega \approx 4$ the inherent attenuation factor K_c comes nearer to unity and the range of frequencies $\varpi = 3{,}7...4{,}2$ is the device passband. Given device is referred to a type of acoustic filters of low frequencies. It provides restriction on intensity of fluctuations in hydraulic system due to reflection them. At that for an oscillatory component of a flow the cavity presents essentially smaller resistance in comparison with the narrowed central channel thus providing the localization of pressure pulsations in the input pipeline.

However the expansion cavity is spatially distributed element of a complex form in which (as it will be shown below) interference processes of acoustic waves are taken place. At $\varpi \approx 4$ because of interference the cavity begins to present essential resistance to an oscillatory component of a flow and pressure pulsations will penetrate through the inertial channel to the output of the device decreasing its inherent attenuation factor. With the further growth of frequency a new distribution of nodes and loops in the expansion cavities can lead to its effective work in the device structure again. At that the inherent attenuation factor grows.

The function $|Z_{c1}|(\varpi)$ also demonstrates a qualitative difference between an analytical and a finite element models at $\varpi \rangle 3$. For the analytical model at $\varpi \rangle 1$ the graph of this function is monotonously growing. For the finite element model at $\varpi \approx 3{,}8$ $|Z_{c1}| \to \infty$, i.e. the resonant increase of $|Z_{c1}|$ takes place.

Such distinction of results can be explained by not taking the distribution of the expansion cavity parameters into account in the analytical model. The length and diameter of the given cavity are values of a similar order so its analytical description as one-dimensional model is incorrect especially in the range of high frequencies. At the same time modeling of acoustic characteristics of hydraulic capacity as bidimensional object by analytical methods seems too difficult and labour-consuming.

The matrix of hydraulic capacity in the lumped parameters is [3]:

$$\begin{bmatrix} P_{in} \\ Q_{in} \end{bmatrix} = \begin{bmatrix} 1 & 0 \\ j\varpi c & 1 \end{bmatrix} \begin{bmatrix} P_{out} \\ Q_{out} \end{bmatrix}.$$

According to this the amplitude of pressure fluctuations at every point of the cavity should be identical. However due to the waves interference at their reflection from the walls of the cavity the above equation is invalid and the expansion cavity ceases to work as ideal hydraulic capacity. By way of illustration the distribution of pressure fluctuations amplitudes in the expansion cavities of the considered corrective device in longitudinal (a) and radial (b) directions is shown on Figure 7:

$$\bar{p} = f(\bar{l}),$$

where $p = \frac{p}{p_{max}}$, $l = \frac{l}{L}$, L - the characteristic geometrical size of a cavity in a considered direction, l - the current linear size.

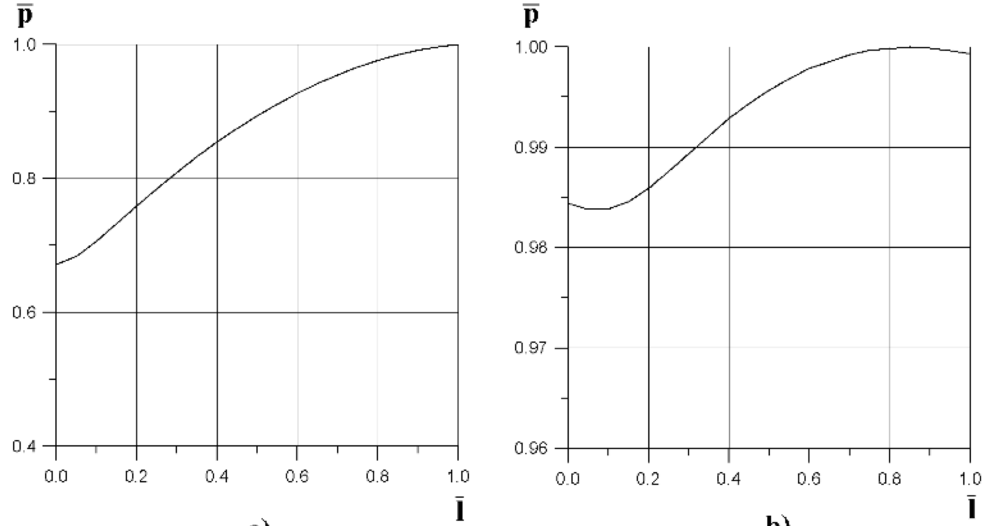

a) b)

Figure 7. Distribution of amplitudes of fluctuations in damper expansion cavity $\omega = 3,8$:

a) longitudinal direction; b) radial direction.

The analysis of Figure 7 shows that while the distribution of parameters of fluctuations in a radial direction is insignificant ($p_{min} \approx 0,984$) and it can be neglected, the distribution in a longitudinal direction is rather significant ($p_{min} \approx 0,67$). Thus representation of a corrective device cavity by the matrix equation (3) at high frequencies of fluctuations results in essential differences of the graphic results received by analytical and numerical models.

The expansion chamber has a large length/radial width ratio and so could be approximated using one-dimensional distributed parameter theory. It would be interesting to see how this model compared with the numerical model. This comparing will be developed in future researches.

The calculations make it clear that in the range of low frequencies $\frac{\omega l}{a} \leq 0,6$ (or $\frac{l}{\lambda} \leq 0,1$, where λ is wavelength) the analytical model is the most expedient. It allows easily enough analyzing dependence of characteristics of the devices from properties of elements included in their structure and realizing procedure of structure optimization. However in the range of high frequencies the efficiency of the devices calculated by analytical model is more optimistic than in reality because of difficulty taking distribution of parameters into account. Here the finite element model is more expedient for calculation of characteristics and optimum design of the device and for a proper choice of its application.

4. EXAMPLES OF DAMPERS APPLICATIONS

The developed theory of design corrective device and estimation of its efficiency has allowed introducing a number of pressure fluctuations dampers in the fluid power systems of airplanes (AN-124) and their engines (NK-86, NK-32, D18T) that have essentially lowered their vibroacoustic loading. The construction of the fluctuations damper installed in hydraulic system of plane AN-124 for decreasing of pressure pulsations generated by pump NP-107 [4] is submitted on Figure 8. The efficiency of this damper is illustrated by Figure 9. After damper installation pressure fluctuation amplitudes of a working liquid, both in a high-pressure cavity of pump NP-107, and in downstream system reduced in 5-15 times. Decrease in a level of pulsations of a working fluid has allowed reducing vibration load of accessory units too.

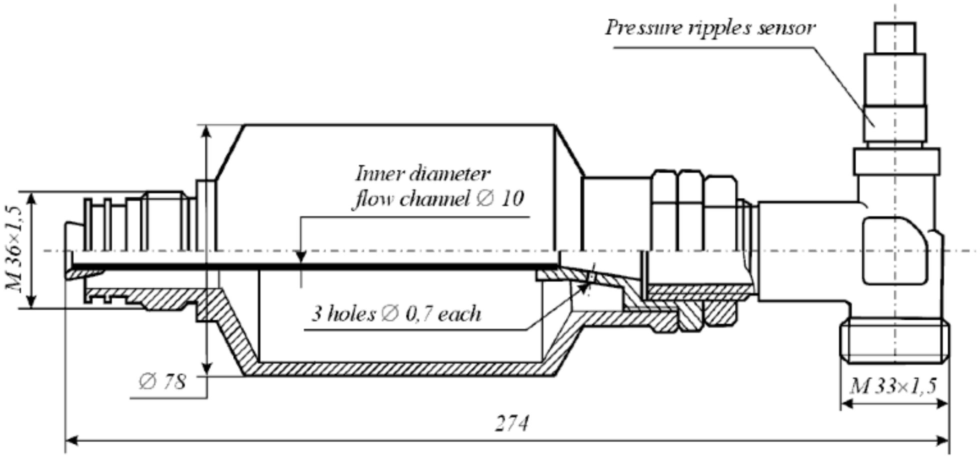

Figure 8. The constructive scheme of the fluctuation damper of plane AN-124 established in hydraulic system.

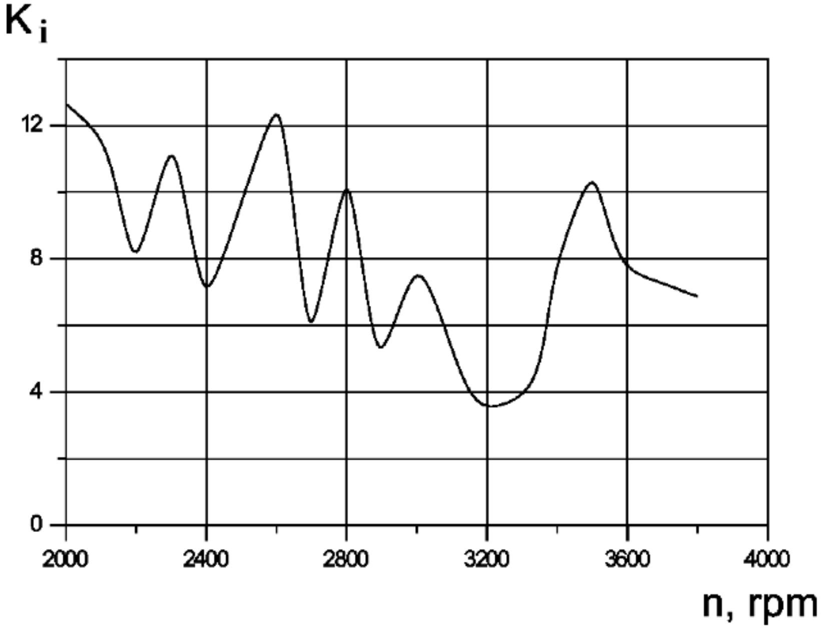

Figure 9. Dependence of insertion attenuation factor of fluctuation damper in hydraulic system of plane AN-124 from frequency of rotation of pump NP-107 rotor (experimental).

As it follows from the researches presented an introduction of flow fluctuations dampers has positive influence on a vibration load of hydromechanical system. At operation of the rig for ground tests for functioning of rocket steering machines the increased vibration of elements of the stand took place. Vibration led to formation of longitudinal cracks on high pressure pipelines and infringement of serviceability of the test rig was observed. The experimental researches have shown a high level of working fluid pressure pulsations in a high pressure line. The amplitude of pressure fluctuations on plunger frequency of the pump depending on average pressure in a line $(P_{av} = 14...20\ MPa)$ changed in a range of $2,9...4,0 MPa$. In a high pressure line directly on the pump output has been established developed fluctuations damper of capacitor type. Its application has lowered mean-square- root value of pressure pulsations of more than 30 times. Vibration measurements on the pipeline in a place of its former destruction have shown reduction in root-mean-square value of acceleration more than 6 times at almost all plunger harmonics. Some acceleration increasing has been registered at third plunger harmonic only. This shows that damper installation has changed elastic - mass characteristics of system, and modal frequency of a considered site of pipeline system is close to frequency of the third plunger harmonics.

5. CONCLUSIONS

According to this study the following conclusion can be made:

- in the range of low frequencies $\frac{\omega l}{a} \le 0{,}6$ (or $\frac{l}{\lambda} \le 0{,}1$) the analytical model is the most expedient. It allows easily enough analyzing dependence of characteristics of the dampers from properties of elements included in their structure and realizing procedure of structure optimization.
- in the range of high frequencies the efficiency of the devices calculated by analytical model is more optimistic than in reality because of difficulty taking distribution of parameters into account. Here the finite element model is more expedient for calculation of characteristics.
- inserting of fluctuation damper in hydraulic system allows lowering not only a level of pulsations of a fluid, but also vibration of mechanical elements.

Thus advantages of hydraulic damper applications for vibroacoustical characteristic correction in fluid power systems are shown in the paper.

6. REFERENCES

1. http://en.wikipedia.org/wiki/Acoustic_impedance#Characteristic_impedance
2. L.L.Beranek, I. L. Ver, Noise and vibration engineering, John Wiley and Sons, New York, 1992
3. Shorin V.P., Elimination of fluctuations in aircraft pipelines. - M.: Mechanical engineering, 1980. - 156 p.(in Russian)
4. Golovin A.N., Shorin V.P., Fluctuation dampers for hydraulic systems. - Samara: SSC of the Russian Academy of Science, 2005. - 168 p.(in Russian)

A New Method for Power Steering Hose Assembly Design and Acoustic Optimisation by means of Time Domain Hydraulic Line Simulation Models

Dr.-Ing. Heiko Baum
FLUIDON GmbH, Aachen, Germany
heiko.baum@fluidon.com

Dr.-Ing. Michael Hofmann
Continental ContiTech Fluid Technology, Caluire, France
michael.hofmann@fluid.contitech.fr

ABSTRACT

A known source of noise within the interior of a vehicle is from the hydraulically-assisted power steering system. Up to now the design and optimization of power steering hoses is mainly done by costly hardware tests. The method of power steering hose design and optimization presented in this paper implements a flexible wall model into distributed parameter time domain simulation models. During simulation significant design parameters such as tuner cable length and position or restriction dimension and position are automatically modified by a parameter variation algorithms.
This way the new method effectively evaluating various design alternatives at earlier stages in the development process and represents a key step in implementing innovative simulation methods that further increase the quality and performance of NVH development process.

1 INTRODUCTION

At all technological progress in the automotive industry, the purchase decision is finally influenced by subjective perceptions for a passenger car. In connection with this, the interior noise level of a vehicle represents a quite essential decision characteristic for the customer. To satisfy this consumer expectation, it is nowadays extremely important for auto-

Power Transmission and Motion Control 2007 Edited by Dr D N Johnston and Professor A R Plummer
© With The Centre for Power Transmission and Motion Control

motive manufacturers and suppliers that a potential source of noise, vibration or harshness (NVH) is identified, eliminated or at least minimised as early as possible in the development process.

A known source for noise which can lead to NVH problems within the vehicle is the fluid-borne noise, issued by the pump of the hydraulic power steering. Special flexible hose assemblies which must be adapted in their routing for every engine or at every platform change are the common remedy measure. Currently these modifications are carried out extensively by means of hardware prototypes and time-consuming test rig or vehicle tests.

The following contribution presents a development methodology to replace these hardware test by a virtual prototype. Based on a kit of conduction elements, the lay-out of the flexible hose with volumetric expansion as well as its acoustic optimisation is done automatically by means of computer simulation. With stepwise modification of the geometrical parameters a sensitivity and robustness analysis can very comfortably be carried out for the conduction design, e.g. by means of DoE techniques. As a consequence: early project phase optimization saves time and cost. Hardware prototypes for optimization can be avoided and customer prototype cars are earlier equipped with optimized solutions.

2 GENERAL INTRODUCTION

An excellent, comprehensive introduction in the topic "design of automotive hose lines" which also clarifies the complexity of the required work steps can be found in a patent of Visteon Global Technologies (Visteon, 2005).

> *„… A known source of noise within the interior of the vehicle is from a hydraulically-assisted power steering system. The power steering system includes a power steering pump that initiates a pressure ripple, which interacts with a hydraulic circuit and propagates throughout the power steering system as fluid-borne noise. Various noise reduction techniques are used to minimize the noise of the power steering system. For example, an attenuation device such as a flexible tuning cable is disposed within a power steering hose assembly, and in particular a high-pressure power steering hose assembly. The flexible tuning cable relies on a process of destructive interference to attenuate the pressure ripple. Through a series of reflections, the tuning cable induces a 180° phase difference in the pressure ripple, that ultimately reduces the amplitude of the pressure ripple. Advantageously, the length of the cable is adjustable to vary the attenuation ability of the tuning cable.*
>
> *Another example of a noise reduction technique is structural damping, whereby the hose assembly length is increased so that any expansion of the hose wall assists in absorbing the energy from the pressure ripple. In addition, the hose reduces the wave speed in the fluid, thus shortening the pressure ripple wavelength and increasing the effectiveness of the tuning cable.*
>
> *While these noise reduction techniques work well, it is advantageous to pre-*

> *dict the NVH characteristics of the power steering system, and the effectiveness of a noise reduction technique, early in the design process. In the past, the NVH characteristics of the power steering system, and in particular the power steering hose assembly were predicted using a combination of analytical, empirical, or experimental methodologies. An example of an experimental methodology is trial and error using a physical model. However, this methodology type is time consuming and costly. An example of an analytical methodology is a model of the power steering system represented by a set of equations resulting in a closed form solution. A closed form solution is an exact answer to a given set of equations. However, as power steering system models become increasingly complex, due to the nonlinear nature of the system, the complexity of the solution also increases. Therefore, analytical tools are not easy to use and are frequently constrained to analysis of simplified geometry and material properties. Thus, there is a need in the art for a method of power steering system hose assembly design and analysis that accurately and rapidly assesses the NVH characteristics of the system, including transfer loss, fluid flow characteristics, system vibration, and airborne noise prediction….*" (Visteon, 2005)

In contrast to the methodology of the Visteon patent at which the flexible hose model is built up in a finite element simulation system, the development methodology introduced in this contribution is based on the time domain calculation approach.

It is an essential advantage of the time domain based approach that the description of the hose boundary conditions pump and steering valve can be carried out via physically modelled component models. Moreover through this, the flexible hose models can also be used for detailed system simulations in which e.g. driving manoeuvres are examined (**Figure 1**).

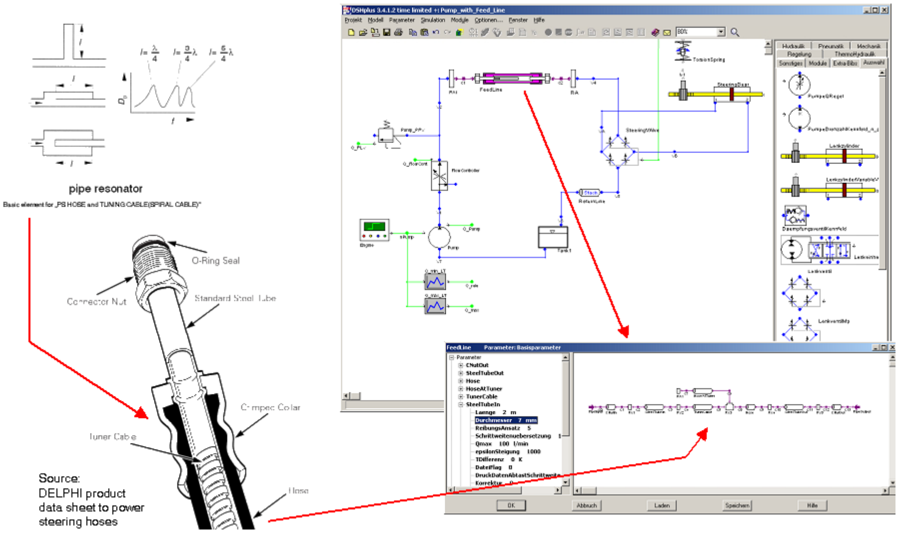
$l = \frac{\lambda}{4}$
$l = \frac{3}{4}\lambda$
$l = \frac{5}{4}\lambda$
D_p
f
l
pipe resonator
Basic element for „PS HOSE and TUNING CABLE(SPIRAL CABLE)"
O-Ring Seal
Connector Nut
Standard Steel Tube
Crimped Collar
Tuner Cable
Hose
Source:
DELPHI product
data sheet to power
steering hoses
DSHplus 3.4.1.2 time limited - [Pump_with_Feed_Line
Projekt Modell Parameter Simulation Module Optionen... Fenster Hilfe
FeedLine
SteeringGear
SteeringValve
Flow Controller
Pump
Tank
Hydraulik Pneumatik Mechanik
Regelung ThermoHydraulik
Sonstiges Module Extra-Bibs Auswahl
FeedLine Parameter: Basisparameter
OK
Abbruch
Laden
Speichern
Hilfe

Parameter
CNutOut
SteelTubeOut
Hose
HoseAtTuner
TunerCable
SteelTubeIn
Laenge 2 m
Durchmesser 7 mm
ReibungsAnsatz 5
Schrittweitenuebersetzung 1
Qmax 100 l/min
epsilonSteigung 1000
TDifferenz 0 K
Dateiflag 0
DruckDatenAbtastSchrittweite
Korrektur 0

Figure 1: Sub-model of a tuner hose line in a power steering simulation model

3 STATE OF THE ART IN HYDRAULIC LINE SIMULATION

However, the majority of available line simulation models are, as is in the case of Trikha (Trikha, 1975) built-up for a simulation in the frequency domain. Frequency domain based models are very fast. Because of the complex numeric boundary conditions they are in principle only usable for the description of linear connections with analysis of open and closed conduction ends. An application example of automotive hose simulations with pipe and hose models in frequency domain is the “Haus der Technik” (HDT) contribution of Eaton from the year 2003 (Zimpfer, 2003).

The modelling of time domain hose and pipe simulation elements, as base modules for the simulation supported development methodology of automotive power steering hoses, is a demanding task. In the field of hydraulic pipe simulation many models and works are known. Many of them confine themselves to the description of steel braided hoses with very low or no volumetric expansion and/or steel tube hydraulic circuits. Examples of concentrated and distributed parameter pipe models are found at Beater (Beater, 1999) or Theissen (Theissen, 1983) respectively.

Even if in the available numerical approaches the frequency dependent fluid friction is already taken into account (**Figure 2**), a detailed consideration of the viscous elastic behaviour of the tube material is missing in most of these models. However, this temperature and pressure -dependent viscous elastic quality of the hose material determines fundamentally the pulsation damping of an automotive flexible hose line. This hose material damping effect, as examined by Ehmann (Ehmann, 2000) or as described in the patent specification of Dana Corporation (Dana, 2006), is influenceable by the rubber compound and the braiding characteristics of the (textile) reinforcement of the hose, and moreover is also affected by the frequency of the pressure pulsation.

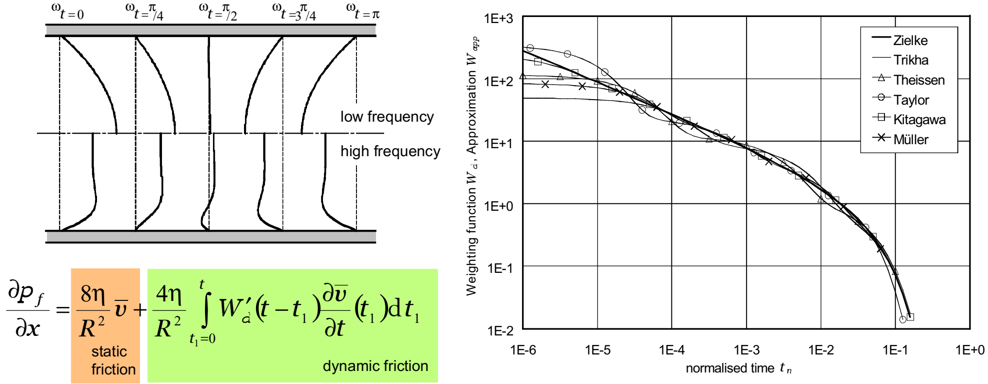

$$\frac{\partial p_f}{\partial x} = \underbrace{\frac{8\eta}{R^2}\bar{\upsilon}}_{\text{static friction}} + \underbrace{\frac{4\eta}{R^2}\int_{t_1=0}^{t} W_d'(t-t_1)\frac{\partial\bar{\upsilon}}{\partial t}(t_1)\,\mathrm{d}t_1}_{\text{dynamic friction}}$$

Figure 2: Oscillating flow profile and approximation of frequency dependent friction (Müller, 2002)

To the knowledge of the authors in numerical models for the simulation of hydraulic hose assemblies, these two influence parameters (rubber compound and braiding characteristics of the reinforcement) are not yet taken into account in a physically parameterizable form.

Nevertheless a lot of research work has been done to consider the hose material influence. A practicable attempt at the consideration of the material damping effect presents Müller (Müller, 2002) who, simplifying the approach of Bratland (Bratland, 1989), integrates the viscous elastic damping into the model description of the line elements in form of a phenomenological approach as a spring damper element unit (**Figure 3**).

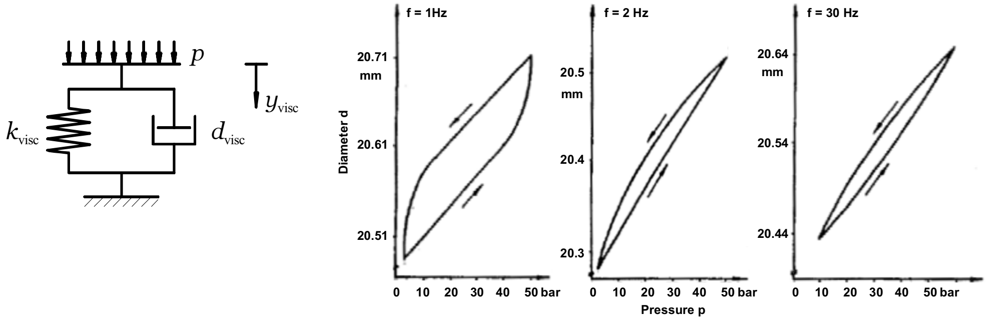

Replacement Wall Model of a Flexible Hydraulic Hose
(Diss Müller, IFAS, Aachen, 2002)

Hose Wall Dynamic at 1Hz, 2Hz, and 30 Hz
(Diss Sänger, IHP, Aachen, 1985)

Figure 3: Simple replacement model for the hose wall dynamics (Müller, 2002), and measured dynamic behaviour as shown by Sänger (Sänger, 1985)

The parameter setting of the Müller approach is made by identification from measurement results of the elastomer material based on the works of Kojima and Edge (Kojima, 1994). A similar approach was also introduced by Drew (Drew, 1997) in her frequency domain based hose model.

However, a comparison of transfer functions of different lines, computed from measurement and time domain based simulation results, shows that the known approaches meet the requirements for steel pipes and hydraulic hoses, which have a reinforcement from steel yarns (and consequently a low volumetric expansion), but are not sufficient for automotive hose assemblies for hydraulic power steering. These hoses have significantly higher volumetric expansion rates of about 15-35 cm³/m @100 bar and 23°C. With the exception of Drew‘s model effects of an interaction between natural frequency of the line and damping characteristics of the hose wall which can clearly be recognized in transfer function from the measurement result (**Figure 4**) are not shown in the simulation results.

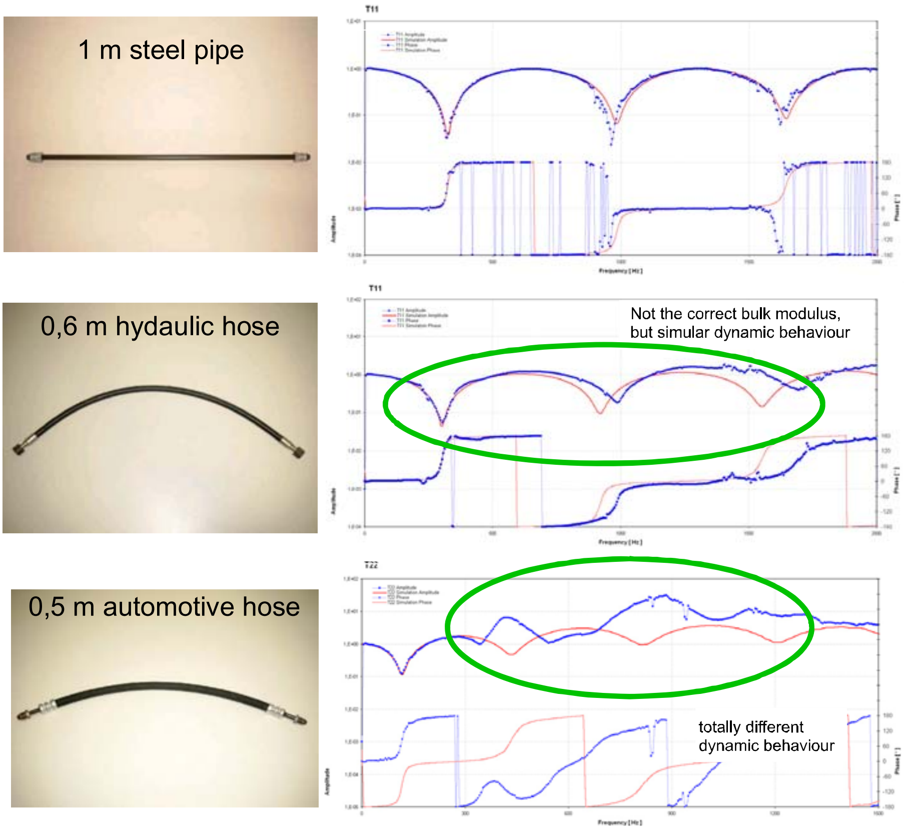

Figure 4: Transfer functions of different line types (inverse representation)

At frequencies that usually represent the second and higher orders of resonance of the lines under investigation, the measurements show a damping in the transfer functions. What causes this effect, that resembles somehow a parametric resonance between pressure pulsation and hose material dynamic, is not quite clear at the moment. Perhaps some day detailed scientific research work, which considers the flexible structure mix of rubber compound and polymeric yarn texture can explain this dynamic effect more clearly and can provide numerical models.

Unless such models are available a pragmatic approach shall be used to cover the hose wall dynamic in the flexible hose simulation models. The distributed parameter pipe elements, built-up by Müller, will be extended (**Figure 5**) by a set of time-discrete transfer functions, set in parallel to the existing spring-damper model.

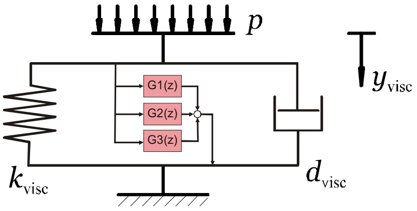

Wave characteristic in x-t plane

$$C^{+}: \frac{1}{\sqrt{\rho E'_{Fl}}}\frac{dp}{dt}+\frac{dv}{dt}+\frac{1}{\rho}\frac{\partial p_f}{\partial x}+\frac{2c}{Rd_{visc}}\left(G(z)+\left(p-k_{visc}y_{visc}\right)\right)=0$$

$$C^{-}: \frac{1}{\sqrt{\rho E'_{Fl}}}\frac{dp}{dt}-\frac{dv}{dt}-\frac{1}{\rho}\frac{\partial p_f}{\partial x}+\frac{2c}{Rd_{visc}}\left(G(z)+\left(p-k_{visc}y_{visc}\right)\right)=0$$

Figure 5: Extended characteristics equation used for the flexible hose simulation model

The parameters representing the hose wall dynamic in the time-discrete transfer function elements are identified from test rig measurements of the flexible hose material. Again the parameter setting is done by means of a phenomenological approach, similar to the existing models. This identification and the following parameter preparation procedure is displayed in detail in **Figure 6**.

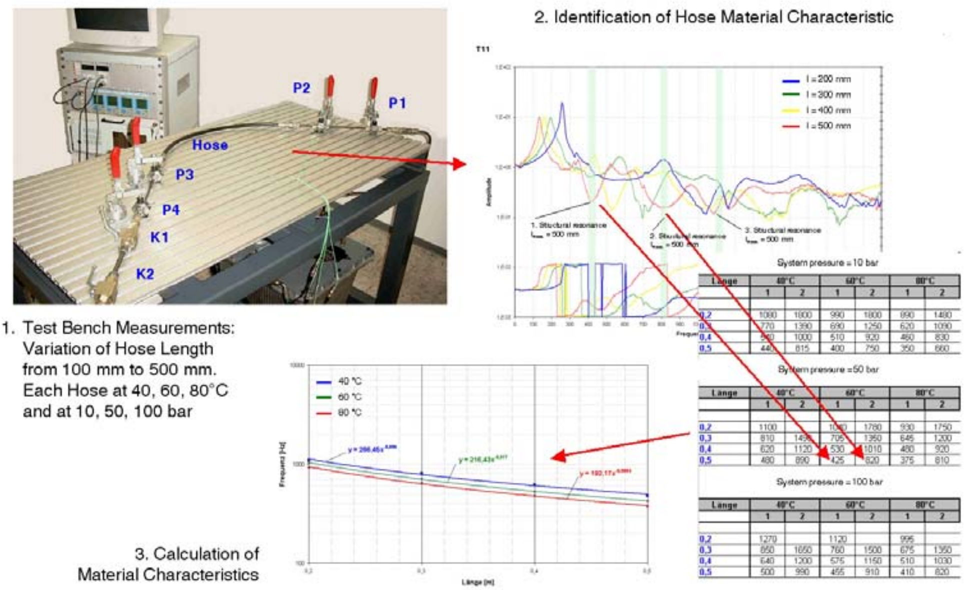

System pressure = 10 bar

Länge	40°C		60°C		80°C	
	1	2	1	2	1	2
0,2	1080	1800	990	1800	890	1480
0,3	770	1390	690	1250	620	1090
0,4	[illegible]	1000	510	920	460	830
0,5	[illegible]	815	400	750	350	660

System pressure = 50 bar

Länge	40°C		60°C		80°C	
	1	2	1	2	1	2
0,2	1100		[illegible]	1780	930	1750
0,3	810	[illegible]	705	1350	645	1200
0,4	620	1120	530	1010	480	920
0,5	480	890	425	820	375	810

System pressure = 100 bar

Länge	40°C		60°C		80°C	
	1	2	1	2	1	2
0,2	1270		1120		995	
0,3	850	1650	760	1500	675	1350
0,4	640	1200	575	1150	510	1030
0,5	500	990	455	910	410	820

Figure 6: Identification of pressure and temperature-depended hose material characteristic

In a first step hose line samples from 100 to 500 mm are measured on the FLUIDON line test rig at a pressure of 10, 50 and 100 bar and at temperatures of 40, 60 and 80 °C. In step two the characteristic frequencies of each line length are identified from the measurement and listed according to the measurement pressure and temperature. Objective is to identify a correlation of pressure pulsation frequency, line length, and fluid temperature to the parametric resonance of the hose wall material. Using the line length as x-axis scaling, the first characteristic frequency is then displayed in a graph at constant pressure or temperature (Step 3).

The coefficients of an exponential regression equation are later used in the model to compute the frequencies of the first three parametric resonances for a line length between the measured line lengths. Following this, gain and damping of time-discrete transfer functions that represent the parametric resonances in the numerical model are adjusted according to the measurement data. At the end of this parameter fitting all data is stored into a material data base which is later, in the simulation, assigned to the hose elements in the automotive hose assembly.

4 SETUP OF AN AUTOMOTIVE HOSE ELEMENT LIBRARY

A review of available patent publications shows that there is a wide range of possible configurations for the interior of automotive pressure lines. From this background an automotive hose element library needs to provide a set of elements that can be flexibly put together to represent these configurations. A good survey of possibly configurations can be found in a patent publication of Eaton Aeroquip GmbH (Aeroquip, 1992) that will be used as guideline to define the basic elements (**Figure 7**).

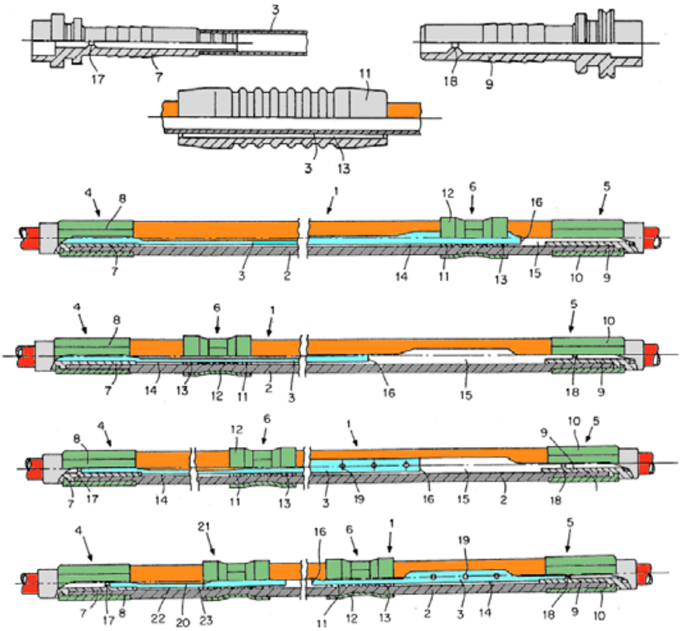

Figure 7: Examples for fittings and flexible hose elements according to (Aeroquip, 1992) (colorized for a better understanding)

In general there are two different types of mountings to connect hose material and steel tube. The first one is an empty straight connection (Figure 7, top right) the other one is a connection that also has either a nipple type extension or a socket to which a tuner cable can be mounted (Figure 7, top left). In addition to that there is also a restrictor that can be fixed somewhere inside the hose assembly (Figure 7, top middle). This restrictor can also hold the nipple or the socket to fix a tuner cable. Alternatively, the tuner cable is directly running through the restrictor, which in this case is separating the hose into two separate chambers. The diameters of all these elements are variable and it is possible to add additional elements like orifices etc.

In real life by means of these basic elements it is possible to create power steering hose assemblies that contain volume type, Helmholtz type or pipe type resonators. In case of a Helmholtz and pipe type resonator, the tuner cable can have one or more bore holes in order to achieve a fine tuning of the dynamic characteristic of the entire hose assembly.

Figure 8 gives an survey about the new flexible hose elements library and how the elements are represented in the simulation program. A distributed parameter pipe simulation model, as described by Müller (Müller, 2002), is the basic element of each single line segment. By means of special branch elements which allow a flexible parallel or series combination of the elements it is possible to model the required wide range of different power steering hose assemblies.

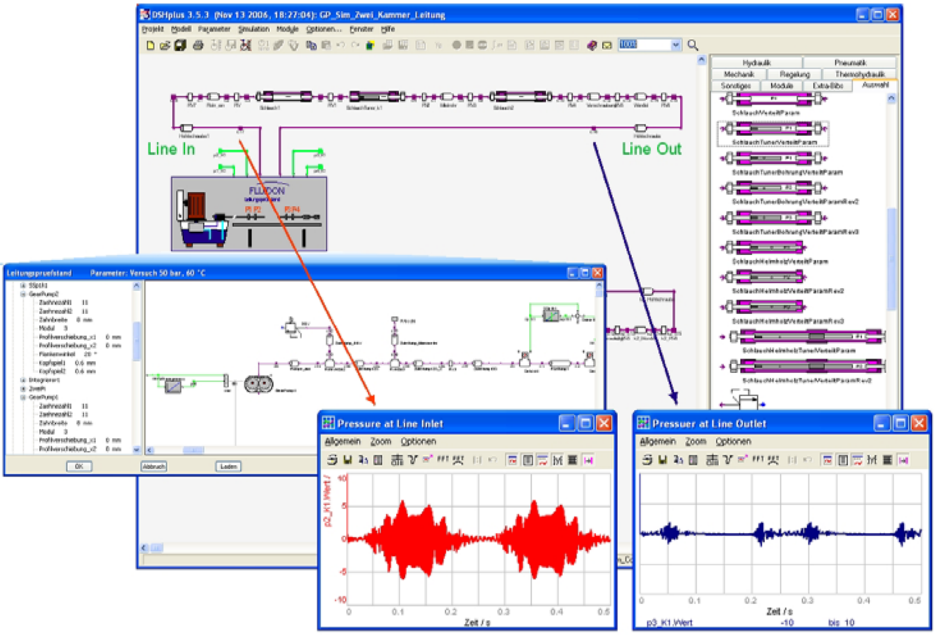
DSHplus 3.5.3 (Nov 13 2006, 18:27:04): GP_Sim_Zwei_Kammer_Leitung
Projekt Modell Parameter Simulation Module Optionen... Fenster Hilfe
Hydraulik
Pneumatik
Mechanik
Regelung
Thermohydraulik
Sonstiges
Module
Extra-Bibo
Auswahl
SchlauchVerteiltParam
SchlauchTunerVerteiltParam
SchlauchTunerBohrungVerteiltParam
SchlauchTunerBohrungVerteiltParamRev2
SchlauchTunerBohrungVerteiltParamRev3
SchlauchHelmholzVerteiltParam
SchlauchHelmholzVerteiltParamRev2
SchlauchHelmholzVerteiltParamRev3
SchlauchHelmholzTunerVerteiltParam
SchlauchHelmholzTunerVerteiltParamRev2
Line In
Line Out
FLUIDON
P1 P2
P3 P4
Leitungspruefstand
Parameter: Versuch 50 bar, 60 °C
OK
Abbruch
Laden
Pressure at Line Inlet
Allgemein Zoom Optionen
p2_K1.Wert /
10
5
0
-5
-10
0
0.1
0.2
0.3
0.4
0.5
Zeit / s
Pressuer at Line Outlet
Allgemein Zoom Optionen
0
0.1
0.2
0.3
0.4
0.5
Zeit / s
p3_K1.Wert
-10
bis 10

SSpth1
GearPump2
Zaehnezahl1 11
Zaehnezahl2 11
Zahnbreite 8 mm
Modul 3
Profilverschiebung_x1 0 mm
Profilverschiebung_x2 0 mm
Flankenwinkel 20 °
Kopfspiel1 0.6 mm
Kopfspiel2 0.6 mm
Integrierer1
ZweiPi
GearPump1
Zaehnezahl1 11
Zaehnezahl2 11
Zahnbreite 8 mm
Modul 3
Profilverschiebung_x1 0 mm
Profilverschiebung_x2 0 mm

Figure 8: Elements of the flexible hose element library

Only elements that represent sections of the outside of the automotive hose include the newly developed flexible hose model. The example in Figure 8 shows a simulation model of a two-chamber automotive hose line together with a simulation sub-model of the FLUIDON line test rig. This way the simulation results can be directly compared against available test rig measurement data.

5 DEVELOPMENT METHODOLOGY FOR AUTOMOTIVE PRESSURE LINES

It is not a new issue that more efficient and more compact systems have always to be developed at shorter and shorter product cycles by the development departments of the automotive industry suppliers. But in connection with this, the noise optimised design of automotive flexible hose assemblies almost already amounts to a quadrature of the circle. Without an amplified use of specialized CAE tools which, today, already are part of the standard in many other development areas of the automotive industry a cost optimized development on schedule of new hose lines is only very hard to reach in future.

What was missing for a CAE tool supported hose assembly design to this day were suitable flexible hose line simulation models which also represent the characteristic behaviour of the rubber hose with high volumetric expansion characteristics in a usable form. These flexible hose line models are available now as a result of the cooperation of FLUIDON GmbH and Continental ContiTech Fluid Technology. Consequently, a methodology could be developed for their use at the CAE tool based lay-out of automotive high pressure lines for power steering and chassis applications.

Figure 9 introduces the different procedure steps of the simulation supported development methodology for automotive pressure lines.

The customer boundary limits about the dynamic behaviour of the new hose assembly are start point of every development. It is the goal of the simulation to find an uncritical line design at specification of boundary conditions like losses of pressure, frequency responses or attenuation so that, in some cases, only a fine tuning must be carried out on the test rig or in the vehicle.

At first an initial line raw design is developed under consideration of experience knowledge from ancestor projects and from the available CAD data. In the next step this raw design is modelled with components of the DSH*plus* flexible hose library and integrated into the simulation model of the FLUIDON line test rig.

The parameter setting of line geometry is carried out extensively based on the drawing data. Merely the hose sections contained in the line are assigned the empirical data set describing the dynamic behaviour of the used tube material. The required parameter values for every used hose material must be identified once. They are stored in the DSH*plus* hose material database. Furthermore the used fluid is selected from the DSH*plus* fluid database and the temperature of the operation point to be simulated is finally adjusted.

For an automated calculation of different line geometries the geometry limit values to be taken into account are defined and adjusted in a parameter variation in the work step following now. The parameter variation modulus generates the parameter sets for the calculation of the single design variants. The processing of the parameter sets is carried out either on the producing PC or for the faster processing, distributed on several PCs simultaneously in the computer network. At the following analysis the results of the simulations are treated exactly like real measurements of the FLUIDON line test rig. The series evaluator of the

DSH*plus* two-port analysis now calculates the two-port transfer functions of all simulated design variants and saves them as ASCII and BMP file.

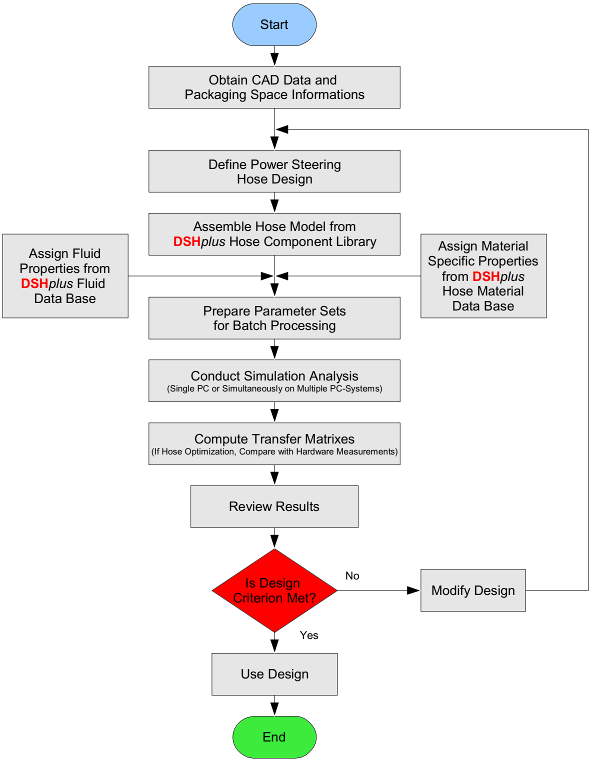
Start
Obtain CAD Data and Packaging Space Informations
Define Power Steering Hose Design
Assemble Hose Model from DSHplus Hose Component Library
Assign Fluid Properties from DSHplus Fluid Data Base
Assign Material Specific Properties from DSHplus Hose Material Data Base
Prepare Parameter Sets for Batch Processing
Conduct Simulation Analysis (Single PC or Simultaneously on Multiple PC-Systems)
Compute Transfer Matrixes (If Hose Optimization, Compare with Hardware Measurements)
Review Results
Is Design Criterion Met?
No
Modify Design
Yes
Use Design
End

Figure 9: Simulation supported development methodology for automotive hose assemblies

If the simulation task is the optimisation of an already available stretching hose line, at first the simulation model is tuned to represent the existing line. To do so the two-port analysis processes the simulation data together with the measurements of the line and represents both transfer functions in a common result diagram. About an additional function the two-port evaluation calculates, for a frequency range specified by the user, the deviation between measurement and simulation. The calculated quality value is then used to control the parameter variation or in a design of experiment (DoE) analysis, through which the comparison between simulation and measuring is considerably accelerated.

If a result which meets the formulated requests is under the analysed design variants, then a first hardware prototype of the automotive hose line is derived from it. If none of the examined designs fulfils the requests, a re-entry at the beginning of the development methodology is necessary to modify the initial raw design of the line or to define the bounds of the parameter variation newly.

6 PRESENTATION OF TWO SAMPLE LINES

Following the results of the development methodology will be presented at the example of a two-chamber automotive hose line (**Figure 10**) with PTFE tuners and a one-chamber automotive hose line (**Figure 11**) with a flexible steel tuner.
Both lines are existing automotive lines which were rebuilt in the simulation model for design parameter studies, like e.g. length of the tube quotas, tuner length and position or nipple inner diameter.

By means of the DSH*plus* two-port analysis the pressure and flow dependent transfer functions of the pipe are calculated from time domain result data of measurement and simulation. The result graphics of the transfer functions are represented in the frequency representation as a network matrix.

Gl. 1: $$\begin{pmatrix}\hat{p}_1\\ \hat{Q}_1\end{pmatrix}=\mathbf{T}\begin{pmatrix}\hat{p}_2\\ \hat{Q}_2\end{pmatrix}=\begin{bmatrix}T_{11} & T_{12}\\ T_{21} & T_{22}\end{bmatrix}\begin{pmatrix}\hat{p}_2\\ \hat{Q}_2\end{pmatrix}$$

The individual terms T_{ij} of the transfer matrix **T** (**Gl. 1**) represent functions in the frequency domain which arise from the behaviour of the component. In the notation on hand the vector of the state quantities $\hat{p}_1$ and $\hat{Q}_1$ at the input arises from the multiplication of the vector of the state quantities $\hat{p}_2$ and $\hat{Q}_2$ at the output by the transfer matrix **T**. A detailed description of the measuring and the analysis procedure can be found by Müller (Müller, 2002). At this form of representation the graphic T11 represents in principle the pressure transfer function from pump side to steering side and the graphic T12 the transfer function between flow at pump side and pressure at steering side.

The blue graph in **Figure 10** represents the transfer function calculated from the measurement. The red graph represents the transfer function calculated from the simulation data.

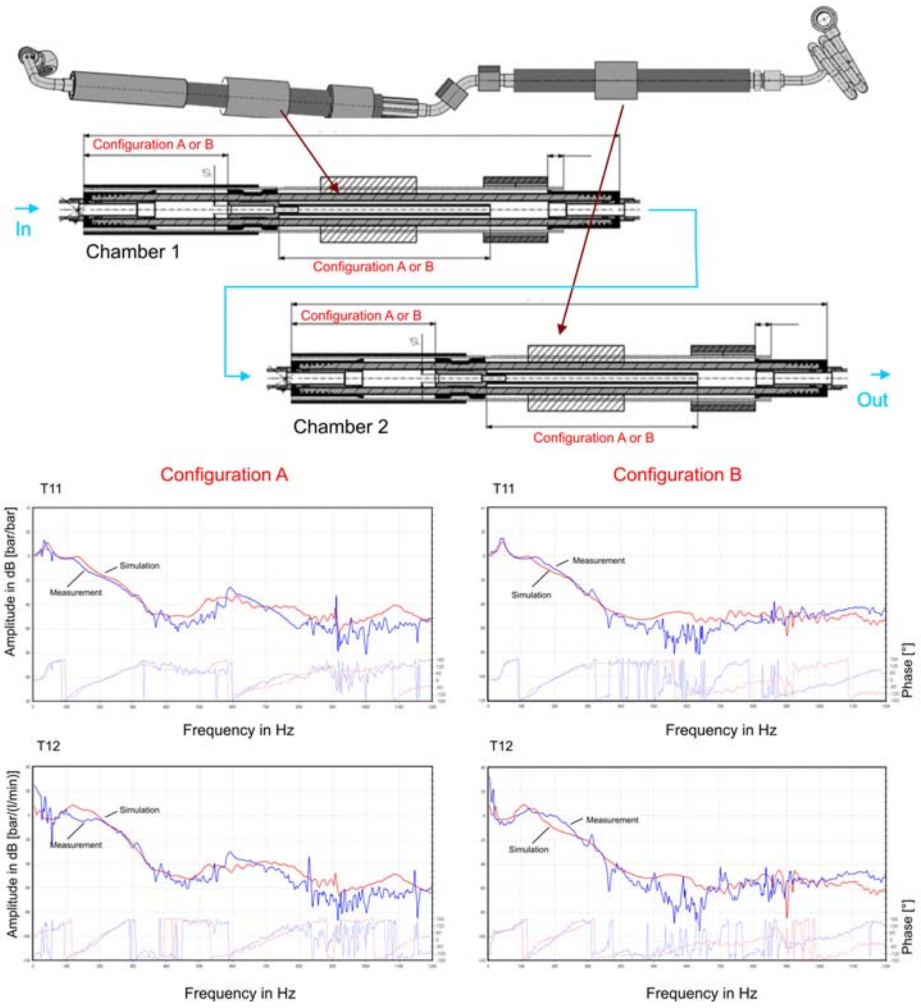

Figure 10: Measuring and simulation of a two-chamber automotive line

The comparison of configuration A and B indicates that the clearly visible reduction in damping between 500 Hz and 700 Hz in configuration A can be eliminated simply by changing the position of the internal restrictors and the length of the tuner cables. Like the results of configuration B point out will the overall damping performance of the line not be influenced by these changes.

Figure 11 shows the measurement (blue) and the simulation (red) of an automotive pressure line with flexible steel tuner. At first the simulation was carried out with the exact drawing measures (red graph). With the help of an automatic parameter variation the essential geometry values of the conduction were then changed according to the tolerant values listed in the drawing. The grey graphs show the results of these simulations, which envelope the red graph of the exact geometry. This way it is possible to check the robustness of the initial line outline and to identify sensitive geometry measures already at a very early development stage.

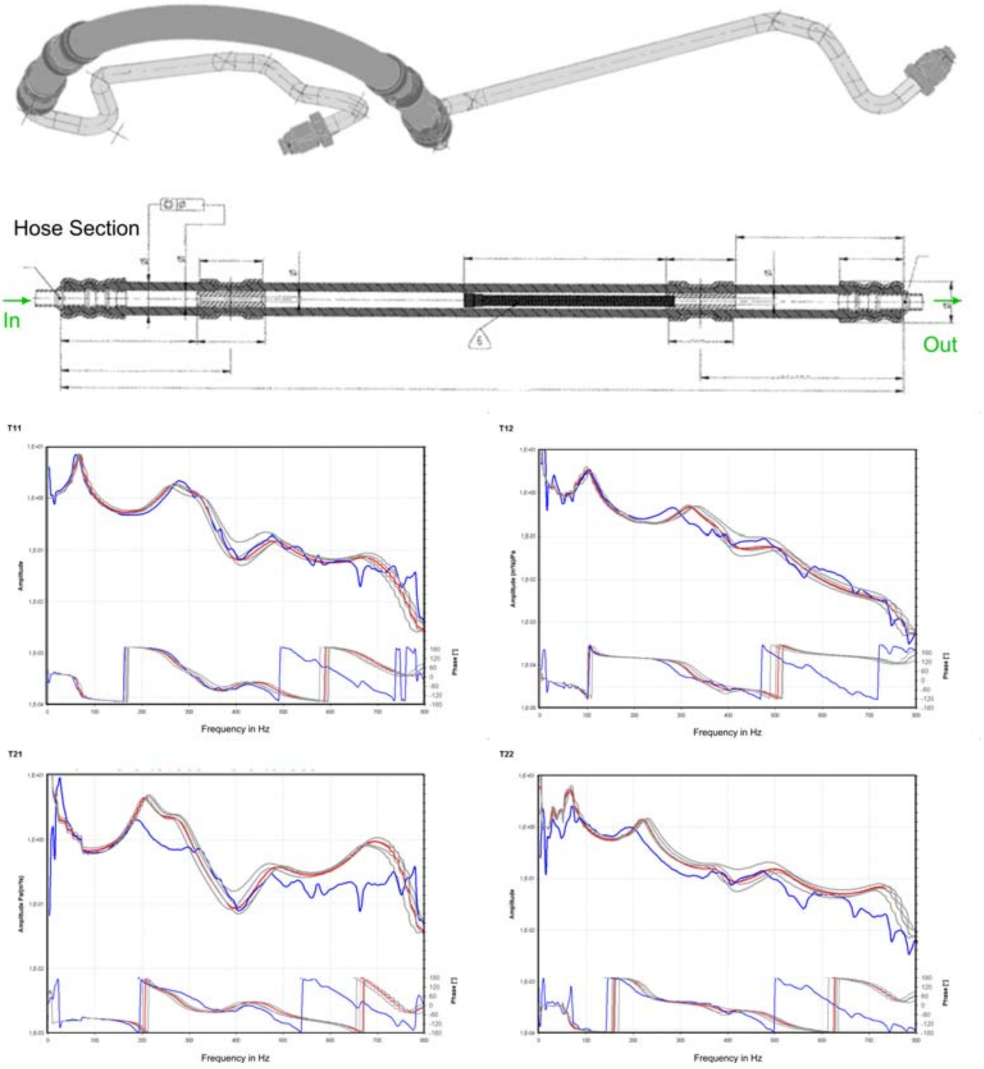

Figure 11: Measurement and simulation of an automotive hose line with flexible steel tuner

7 SUMMARY

A known source of noise within the interior of a vehicle is caused by the hydraulically-assisted power steering system. Pressure ripples, initiated by the power steering pump, interact with the hydraulic circuit and propagate throughout the power steering system as fluid-borne noise.

The most efficient noise reduction technique is still a flexible hose assembly having various installations such as restrictors or flexible tuning cables. Up to now the design and optimization of power steering hoses was mainly done by costly hardware tests. If simulation techniques are used at all, most of these approaches are based on frequency domain simulation models.

The presented method of power steering hose design and optimization is based on distributed parameter time domain simulation models. The characteristic behavior of the hose material is implemented into a flexible wall model. The hose materials individual characteristics are identified once on a test rig and stored into a data base.

A component library comprising the most basic hose elements is used to create hose assembly models merely based on the geometrical description of the hose assembly. Hose material characteristics are taken from the material data base. During simulation significant design parameters such as tuner cable length and position or restriction dimension and position are automatically modified by a parameter variation algorithm. Using this method, the design engineer can effectively evaluate various design alternatives at early stages in the development process.

The new design and optimization method represents a key step in implementing innovative simulation methods that further increase the quality and performance of the vehicle NVH development process. Moreover the hose simulation models can directly be implemented into a detailed power steering simulation model increasing the quality of dynamic system simulation.

8 REFERENCES

(Visteon, 2005) Method of power steering hose assembly design and analysis
Visteon Global Technologies, Inc. (Van Buren Township, MI)
United States Patent 6917907, Publication Date: 2005-07-12

(Trikha, 1975) A. K. Trikha: An Efficient Method for Simulating Frequency-Dependent Friction in Transient Liquid Flow
Transactions of ASME, Journal of Fluids Engineering, March, S. 97-105, 1975.

(Zimpfer, 2003) M. Zimpfer: Einfluss von Schläuchen und Einbauten auf das Geräuschverhalten in Servolenkungen und aktivem Fahrwerk.
Vortag der Eaton Fluid Power GmbH im Haus der Technik Essen, 12-13.11.2003

(Ehmann, 2000) W. Ehmann: Untersuchung des Übertragungsverhaltens von textilverstärkten Hochdruck-Hydraulikschlauchleitungen
Diss. Universität Stuttgart, 2000

(Dana, 2006) Fluid-borne noise suppression in an automotive power steering system
Dana Corporation (Ottawa Lake, MI)
United States Patent 7063181, Publication Date: 2006-06-20

(Kojima, 1994) E. Kojima, K. A. Edge: Experimental determination of hydraulic silencer matrices and assessment of the method for use as a standard test procedure,
Seventh Bath International Fluid Power Workshop, Bath, 1994.

(Müller, 2002) B. Müller: Einsatz der Simulation zur Pulsations- und Geräuschminderung hydraulischer Anlagen [Using simulation to reduce pulsation and noise in hydraulic systems], Diss. RWTH Aachen, 2002

(Beater, 1999) P. Beater: Entwurf hydraulischer Maschinen - Modelbildung, Stabilitätsanalyse und Simulation hydraulischer Antriebe und Steuerungen
VDI Verlag, 1999, Seite 34 – 52

(Theissen, 1983) H. Theissen: Die Berücksichtigung instationärer Rohrströmungen bei der Simulation hydraulischer Anlagen [Allowing for unsteady pipe flow in the simulation of hydraulic systems], Diss. RWTH Aachen, 1983.

(Aeroquip, 1992) Expandable hose that reduces the hammering produced in hydraulic system by pumps
Aeroquip GmbH
United States Patent 5094271, Publication Date: 1992-03-10

(Drew, 1997) J. E. Drew: The use of flexible hose to reduce pressure ripple in power steering, PhD University of Bath, 1997

(Sänger, 1985) J. Sänger: Hydraulikschlauchleitungen. Berechnung der Geflechte und Simulation des Übertragungsverhaltens, Diss. RWTH Aachen, 1985

(Bratland, 1989) O. Bratland: Determination of the damping characteristics of a hydraulic hose, JHPS. International Symposium on Fluid Power, Tokyo, 1989

Numerical Simulation of Pulsating Flow in Resonator Hose Based on Measured Data of Wave Speed

I-Y Lee, M-G Kang and J-W Kim
Pukyong National University, Korea

Abstract

In this study, a new method for analyzing pulsating flow in hose based on wave speed data in hose is suggested. Then a new method to measure wave speed in hose(viscoelastic pipe) 'closed-end-conduit with three transducer method' proposed by the authors is explained in detail. Using the proposed wave speed measuring method, wave speed data in each component of the object resonator hoses are measured through preliminary experiments. Finally, with several object resonator hoses, pressure attenuation characteristics are investigated by experiments and simulations, to show the validity of the suggested method for analyzing pulsating flow in resonator hose.

1 INTRODUCTION

To reduce fluidborne noise in automotive HPS(hydraulic power steering) systems, a "resonator hose" originally proposed by Klees[1] is usually used in power steering high pressure lines. The resonator consists of hydraulic hose(s) and flexible metal pipe(s) called "spiral pipe" or "tuning cable". The resonator hose is fabricated by placing spiral pipe(s) inside sections of hose coaxially. Some researchers investigated the pulsation attenuation characteristics and effectiveness of the resonator hose. For instance, Hastings and Chen[2] proposed a mathematical model of it by treating the hose wall as elastic substance. In the analysis by Nagata *et al.* [3] and Kojima *et al.* [4], the circumferential motion of the hose was assumed to be viscoelastic while the stiffness of longitudinal motion of the hose to be rigid. In these studies, the accuracy of the theoretical models was confirmed only in quite low frequency regions, and so the confirmation is not enough for the full understanding of the pulsation attenuation in resonator hoses.

In this study, the authors survey former researches on hose(viscoelastic pipe) modeling in advance. Then, suggest a new method for analyzing pulsating flow in hose based on wave speed data measured through a preliminary test. Measurement of wave speed in hose as frequency series data has been a technical problem to be solved. A new method to measure wave speed in hose 'closed-end-conduit with three transducer method' is proposed and explained in detail. Using the proposed wave speed measuring method, wave speed data in each component of the object resonator hoses are measured through preliminary experiments. Finally, with several object resonator hoses, pressure attenuation characteristics are investigated by experiments and simulations. For the simulation, the measured wave speed data are utilized. The simulation results are compared with the experimental ones, and the validity of the suggested method for analyzing pulsating flow in

---

Power Transmission and Motion Control 2007 Edited by Dr D N Johnston and Professor A R Plummer
© With The Centre for Power Transmission and Motion Control

resonator hose is confirmed.

2 METHODS FOR ANALYSING PULSATING FLOW IN HOSES (VISCOELASTIC PIPES)

2.1 Former researches on hose(viscoelastic pipe) modeling

By many researchers, efforts have been contributed to the analyses of wave propagation characteristics in hoses(viscoelastic fluid pipes). For instance, in the theoretical analyses presented by Morgan and Kiely[5], Klip *et al.*[6], and Cox[7], both longitudinal and circumferential motions of the pipe wall were considered, but the fluid was assumed to be incompressible. In the studies on wave propagation in compressible fluid through viscoelastic pipes shown by Nakano *et al.*[8], Gally *et al.*[9], Rieutord[10], and Suo and Wylie[11], they just considered the circumferential motions of pipe under stiff longitudinal constraint of the pipe wall. Longmore and Schlesinger[12], and Nakano and Abo-Ismail[13, 14] have tried to include the fluid compressibility and both the longitudinal and circumferential motion of the pipe wall in their theories, but their experimental investigation was limited to a low frequency of about 0~400 Hz.

With regard to the coupled vibrations of a hose and the fluid in the hose, Wiggert *et al.*[15] considered the effect of pipe elbow restraint on the pressure transients in the elbow. Yu and Kojima modeled hoses considering the anisotropic viscoelasticity of the hose wall and including both the radial and longitudinal motions of the hose wall[16, 17], and they extended their research to the practical situation of a finite-length hose under anchored end conditions, trying to develop a more accurate model which even may predict the effect of longitudinal resonances of the hose[18].

Among the former researches mentioned above, Yu and Kojima's works are understood to be an extensive research considering almost all the meaningful physical items in hoses. In the view point of applicability of the model[18] to practical hoses, however, the followings could be pointed out; (1) As physical parameters for the model[18], the components of normal strain in the circumferential and longitudinal directions are measured by strain gauges. But these kinds of measurements could be performed with comparatively stiff hoses for industrial uses(not for automobile power steering uses). (2) The retardation and relaxation time constant of a hose wall are evaluated by an optimization method with the measured transfer matrix parameters of hose. This procedure would require very precise measurements and computing process. (3) The model[18] is applied to hoses for comparatively high pressure (over 21 MPa) uses, where physical parameters of hoses remain constants over wide range of frequency. Conclusively speaking, it seems that the model[18] requires a quite complex procedure to apply it to practical hoses. And also, the model[18] seems not appropriate to soft hoses like ones for automobile power steering uses.

2.2 Suggestion of a new method for analyzing pulsating flow in hoses(viscoelastic pipes)

We will denote the Laplace transformed variables of pressure and flowrate in arbitrary two positions #1 and #2 on a hose as (P_1, Q_1) and (P_2, Q_2). The relation between the variables is represented as following transfer matrix equation, on the assumption that the hose wall does not encounter the dynamic longitudinal deformation due to a longitudinal resonance of a hose.

$$\begin{bmatrix} P_1 \\ Q_1 \end{bmatrix} = \begin{bmatrix} \cosh(\lambda_h l) & Z_h \sinh(\lambda_h l) \\ 1/Z_h \sinh(\lambda_h l) & \cosh(\lambda_h l) \end{bmatrix} \begin{bmatrix} P_2 \\ Q_2 \end{bmatrix} \tag{1}$$

where, l is hose length between position #1 and #2, and Z_h is the characteristic impedance of a hose and described as

$$Z_h = \frac{\rho \lambda_h c_h^2}{A_h s} \tag{2}$$

In equation (2), ρ is the density of fluid in a hose, c_h is wave speed in a hose, A_h is cross-sectional area of a hose, and s is Laplace operator and λ_h is wave propagation coefficient of a hose. λ_h in equations (1) and (2) is written as equation (3) with an approximate form[19].

$$\lambda_h \approx \frac{s}{c_h}\left[1 + \left(\frac{\nu}{R^2 s}\right)^{0.5} + \left(\frac{\nu}{R^2 s}\right) + \frac{7}{8}\left(\frac{\nu}{R^2 s}\right)^{1.5}\right] \tag{3}$$

where, ν is kinematic viscosity of fluid, R is radius of a hose(pipe). As we see in equations (1) ~ (3), if c_h $[= f(j\omega)]$ is known, the pulsation transfer characteristics in a hose can be computed.

In this study, the authors suggest a new method of pulsating flow analyzing in hoses not by using any mathematical models on wave speed, but by using frequency series wave speed data measured through a preliminary test. Wave speed measuring methods are described in detail in the next section of this paper.

3 A METHOD FOR MEASURING FREQUENCY SERIES WAVE SPEED IN HOSES

3.1 Introductory note

It has been a technical problem to be solved to measure wave speed in hoses (viscoelastic pipes) as frequency series data with precise frequency resolution. The authors propose a wave speed measuring method in hoses that enable us to obtain wave speed data with frequency series form through just a single process of test. The proposed wave speed measuring method is explained in detail in the next sub-section. To help understanding the proposed method for wave speed measuring, former researches on wave speed measurement in pipes are summarized in the appendix of this paper.

3.2 Suggestion of a new wave speed measuring method "closed-end-conduit with three transducer method"

In oil hydraulic systems, generally hoses(viscoelastic pipes) are connected with other components through metal fittings. Hence, pressure measuring in the end point of a test hose is not easy work. Yu and Kojima proposed a method for wave speed measurement in hoses. The principle of it is summarized in Appendix A.3[A2]. When we use the method[A2], we can obtain wave speed in a hose without direct measurement of pressures in the end point of a test hose. However, the method[A2] has some drawbacks as explained in Appendix A.3. The authors propose "closed-outlet-conduit with three transducers" method shown in Fig. 1 as a wave speed measuring method in hoses as stated in detail below.

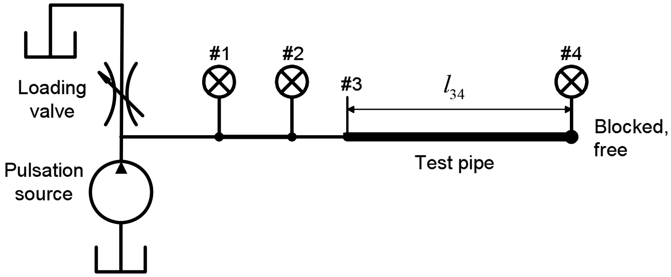

Fig. 1 "Closed-outlet-conduit with three transducers" method

In the pipe system shown in Fig. 1, three pressure transducers are installed in position #1, #2 and #4. The pipe system consists of a metal pipe between position #1 and #2, a metal pipe(including metal fitting in the upstream end of a test hose) between position #2 and #3, and a test hose between position #3 and #4. A specially designed metal fitting shown in Fig. 2 is attached to the downstream end of the test hose.

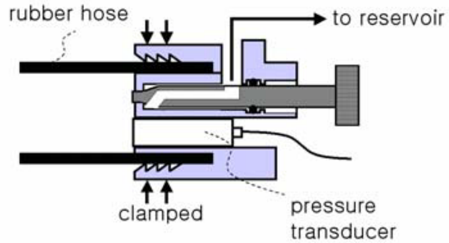

Fig. 2 Detailed drawing of the metal fitting in position 4 of Fig. 1

In the metal fitting(Fig. 2), a small-diameter piezo-electric type pressure transducer and a small-sized air purge valve are inserted together. With a piezo-electric type pressure transducer installed in the fitting in Fig. 2, the pressure at the position #4(the downstream end of the test hose) can be directly measured. Entrained air in oil can be drawn out through the air purge valve in the stage of test preparation.

We will define the Laplace transformed variables on pressure and flowrate in the position #1, #2, #3 and #4 in the pipe system of Fig. 1 as (P_1, Q_1), (P_2, Q_2), (P_3, Q_3) and (P_4, Q_4) respectively. Then, following transfer matrix equations describing relations between (P_1, Q_1) and (P_2, Q_2), between (P_2, Q_2) and (P_3, Q_3), between (P_3, Q_3) and (P_4, Q_4) are obtained.

$$\begin{bmatrix} P_2 \\ Q_2 \end{bmatrix} = \begin{bmatrix} \cosh(\lambda l_{12}) & -Z_c \sinh(\lambda l_{12}) \\ -\frac{1}{Z_c} \sinh(\lambda l_{12}) & \cosh(\lambda l_{12}) \end{bmatrix} \begin{bmatrix} P_1 \\ Q_1 \end{bmatrix} \tag{4}$$

$$\begin{bmatrix} P_3 \\ Q_3 \end{bmatrix} = \begin{bmatrix} \cosh(\lambda l_{23}) & -Z_c \sinh(\lambda l_{23}) \\ -\frac{1}{Z_c} \sinh(\lambda l_{23}) & \cosh(\lambda l_{23}) \end{bmatrix} \begin{bmatrix} P_2 \\ Q_2 \end{bmatrix} \tag{5}$$

$$\begin{bmatrix} P_3 \\ Q_3 \end{bmatrix} = \begin{bmatrix} \cosh(\lambda_h\, l_{34}) & Z_c \sinh(\lambda_h\, l_{34}) \\ \frac{1}{Z_c} \sinh(\lambda_h\, l_{34}) & \cosh(\lambda_h\, l_{34}) \end{bmatrix} \begin{bmatrix} P_4 \\ 0 \end{bmatrix} \tag{6}$$

Equation (6) is effective on the condition that the wall of a test hose does not receive the dynamic longitudinal deformation due to a longitudinal resonance of a hose. In above equations (4) ~ (6), λ_h is already defined in equation (3), and λ is defined as follows.

$$\begin{aligned} \lambda &\approx \frac{s}{c}\left[1+\left(\frac{\nu}{R^2 s}\right)^{0.5}+\left(\frac{\nu}{R^2 s}\right)+\frac{7}{8}\left(\frac{\nu}{R^2 s}\right)^{1.5}\right] \\ &= \frac{s}{c}[f(j\omega)] \end{aligned} \tag{7}$$

where, c is wave speed in metal pipes. When determining pipe length l_{12} between position #1 and #2, and pipe length l_{23} between position #2 and #3, as the same value, we have equations on P_2, P_3 and Q_2 as follows.

$$P_2 = \cosh(\lambda l_{12})P_1 - Z_c \sinh(\lambda l_{12})Q_1 \tag{8}$$

$$P_3 = \cosh(\lambda l_{12})P_2 - Z_c \sinh(\lambda l_{12})Q_2 \tag{9}$$

$$Q_2 = \cosh(\lambda l_{12})Q_1 - 1/Z_c \sinh(\lambda l_{12})P_1 \tag{10}$$

Combining equations (8), (9) and (10) yields the following equation on P_3.

$$P_3 = 2\cosh(\lambda l_{12})P_2 - P_1 \tag{11}$$

From equation (6), P_4 is given as

$$P_4 = P_3 / \cosh(\lambda_h\, l_{34}) \tag{12}$$

From equations (11) and (12), we have

$$\frac{2\cosh(\lambda l_{12})P_2 - P_1}{P_4} = \cosh(\lambda_h\, l_{34}) \tag{13}$$

From equation (13), wave speed c_h in a test hose can be denoted as

$$c_h = \frac{s \cdot f(j\omega) \cdot l_{34}}{\cosh^{-1} \dfrac{2\cosh(\lambda l_{12})P_2 - P_1}{P_4}} \tag{14}$$

Equation (14) on c_h is effective in a frequency range except near the resonance frequency of a hose to the longitudinal direction.

In the test to have wave speed data, we record pressure signals in time domain $P_1(t)$, $P_2(t)$, and $P_4(t)$ in the pipe system shown in Fig. 1. The pressure signals are recorded while the hydraulic pump is driven with continuously varying speed from 0 to maximum by a servo motor. The recorded pressure data are FFT transformed, and the obtained frequency domain pressure data are substituted to equation (14). Through this test and computation process, we can obtain frequency series wave speed data in a wide band frequency range for a hose.

4 THE RESONATOR HOSE

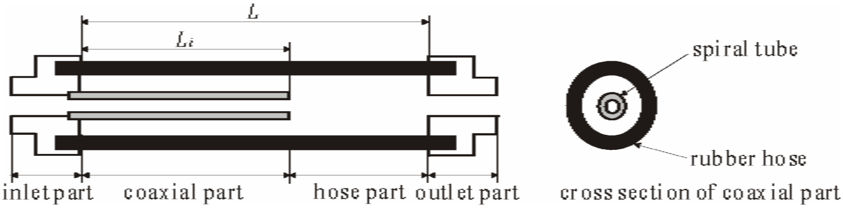

Fig. 3 Structure of the resonator hose

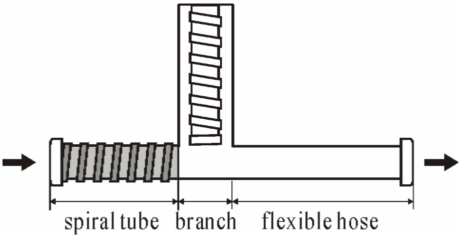

Fig. 4 Equivalent pipe model for the resonator hose shown in Fig. 3

For the resonator hose shown in Fig. 3 and Fig. 4, the following transfer matrix equation can be written

$$\begin{bmatrix} P_1 \\ Q_1 \end{bmatrix} = T \begin{bmatrix} P_2 \\ Q_2 \end{bmatrix} \tag{15}$$

The total transfer matrix T in equation (15) is denoted as equation (16), that is the multiplication of the transfer matrices of the spiral pipe part, the branch part(the coaxial part) and hose part.

$$T = M_{spiral} \cdot M_{branch} \cdot M_{hose} \tag{16}$$

In equation (16), M_{hose} is the same matrix as shown in the right side of equation (1). M_{spiral} has the same in the form of matrix as M_{hose}, except that λ_h in M_{hose} is replaced by λ. M_{branch}, the transfer matrix of the branch part(= the coaxial part, see Fig. 4) is described as

$$M_{branch} = \begin{bmatrix} 1 & 0 \\ 1/Z_{cb}\ \tan(\lambda_b l_b) & 1 \end{bmatrix} \tag{17}$$

where λ_b, Z_{cb} are described as [20]

$$\lambda_b = \frac{s}{c_b}\left(1 + \frac{1}{(1-m)z} + \frac{1}{2(1-m)^2 z^2} - \frac{1-22m+m^2}{8m(1-m)^3 z^3} \right) \tag{18}$$

$$Z_{cb} = \frac{\rho\, {c_b}^2}{A_b s}\lambda_b \tag{19}$$

where c_b: wave speed in a coaxial hose, l_b: length of a coaxial hose, $m = r_2/r_1$, r_2: inside radius of a hose, r_1: outside radius of spiral pipe, $z = \sqrt{{r_2}^2\, s/v}$.

In equation (15) and (16), unknown parameters are wave speed data in each components of the resonator hose. Therefore, if we have wave speed data in the components, we can analyse the pulsation flow characteristics in the resonator hose.

5 PRELIMINARY EXPERIMENTS USING THE RESONATOR HOSE

5.1 Introductory note

In section 2.2 of this paper, the authors suggested a new method to analyse pulsating flow in hoses by using frequency series wave speed data in hoses. This concept to analyse pulsating flow in hoses will be applied to the other components like the spiral pipe part and the coaxial part in the resonator hose(refer to Fig. 3 and 4), to analyse the pulsating flow in the whole resonator hose. To use this method to analyse pulsating flow in resonator hose, in this section, wave speed data in each component of the resonator hose shall be evaluated through preliminary experiments.

5.2 Wave speed in a metal pipe and a hose

A metal pipe(internal diameter : 6 mm, length : 0.5 m, steel pipe) was applied as a test pipe to the wave speed measuring system shown in Fig. 1. The pump for pulsating flow generation in the test system was a variable displacement type piston pump with 9 pistons, 14 cm^3/rev capacity, and a regulator having constant pressure control function. The test was carried out by recording pressure signals for about 10 seconds while the pump was driven with continuously varying speed from 0 to 3000 rpm by a servo motor. The measured pressure signals were FFT transformed and substituted to the equation (14) to obtain frequency series wave speed data. Fig. 5 shows the measured result of wave speed, almost constant wave speed of 1360 m/s in the frequency range 100 ~ 1000 Hz.

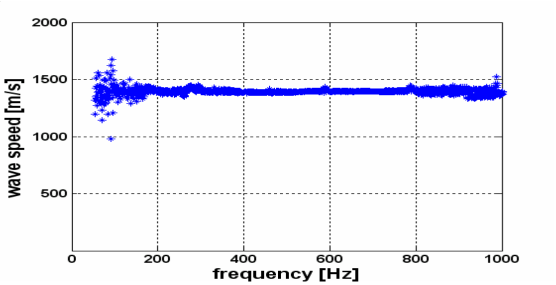

Fig. 5 Frequency series wave speed in a rigid pipe (0.5m)

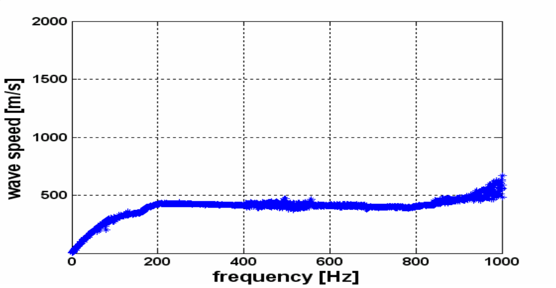

Fig. 6 Frequency series wave speed in a hose (0.2m)

Fig. 6 shows a result of wave speed measurement when a hose(inside diameter : 9.8 mm, length : 0.2 m, material : NBR/CR) was applied to the test system in Fig. 1. The same test system and the same test procedure used to obtain Fig. 5 were applied to obtain the test result in Fig. 6. The wave speed in the test hose shown in Fig. 6 appeared about 415 m/s in the frequency range of 200 ~ 700 Hz.

5.3 Wave speed in a spiral pipe and a coaxial conduit

Particular conduit structures shown in Fig. 7 were designed and fabricated to measure wave speed in a spiral pipe(inside diameter : 4 mm, length : 0.2 m)and a coaxial conduit(inside diameter of hose : 9.8 mm, outside diameter of spiral pipe : 6.3 mm).

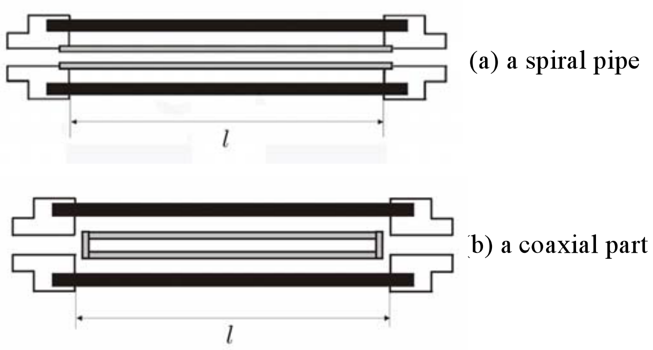

Fig. 7 Test conduits to measure wave speed

The conduit structure in Fig. 7(a) enables us to apply a spiral pipe to the wave speed measuring system shown in Fig. 1 without any worry about oil leakage to outside. The same test system and the same test procedure as the ones in 2.2 were applied to obtain the test results in Fig. 8 and Fig. 9. When comparing Fig. 6 and Fig. 9, wave speed in the coaxial conduit appeared to be a little lower than that in hose.

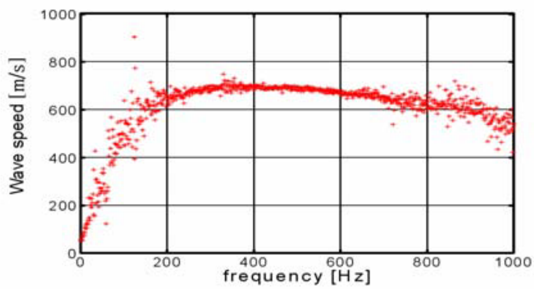

Fig. 8 Wave speed in a spiral pipe

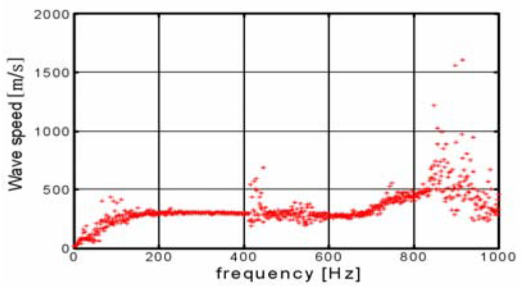

Fig. 9 Wave speed in a coaxial part

6 PRESSURE PULSATION ATTENUATION THROUGH RESONATOR HOSE(EXPERIMENT & SIMULATION)

6.1 Introductory note

To confirm the validity of the suggested analyzing method of pulsating flow in hoses, the authors investigated pressure attenuation characteristics for some resonator hoses by experiments and simulations. Fig. 10 shows the structure of the resonator hoses used in the experiment.

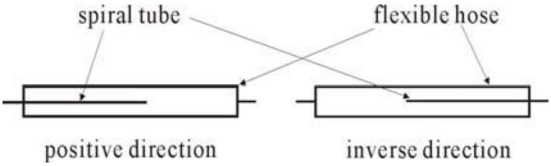

Fig. 10 Resonator hoses with spiral pipes

Of the test hoses shown in Fig. 10, one has a spiral pipe with positive direction and another with inverse direction. In both resonator hoses, the hose material(NBR/CR) and the hose length(0.3 m)are same. Physical parameters' values related to the test resonator hose and test conditions are summarized in Table 1.

Table 1 Physical constant in the test system

mean pressure	70 bar	inside diameter of spiral pipe	4.2 mm
mean flowrate	0 1/m	inside diameter hose	9.8 mm
length of resonator hose	0.3 m	outside diameter of spiral pipe	6.3 mm
length of spiral pipe		sample 1	0.25 m
		sample 2	0.2 m
		sample 3	0.4 m

6.2 Pressure attenuation characteristics in resonator hoses with spiral pipe

Fig. 11, 12 and 13 show experiment and simulation results for resonator hoses(length : 0.3 m) with spiral pipes(length : 0.25, 0.2, 0.1 m respectively) positioned positively.

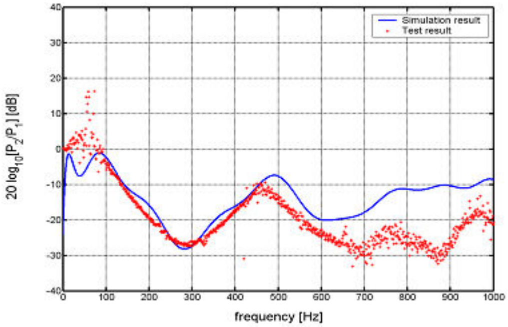

Fig. 11 $|P_2 / P_1|$, spiral pipe positioned positively(hose: 0.3, spiral pipe: 0.25 m)

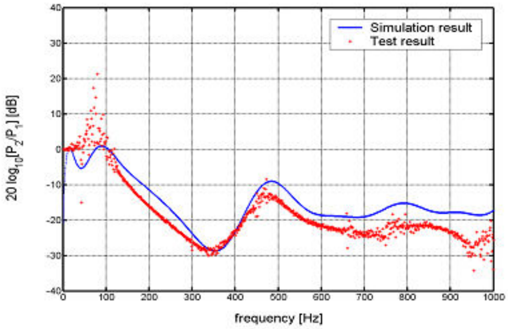

Fig. 12 $|P_2 / P_1|$, spiral pipe positioned positively(hose: 0.3, spiral pipe: 0.2 m)

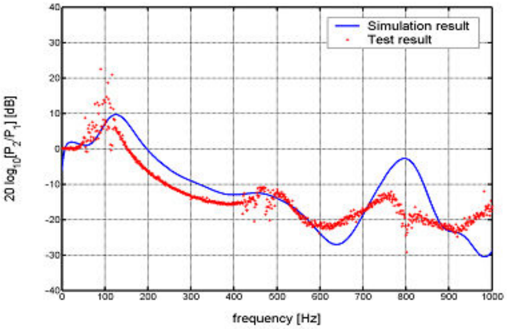

Fig. 13 $|P_2 / P_1|$, spiral pipe positioned positively(hose: 0.3, spiral pipe: 0.1 m)

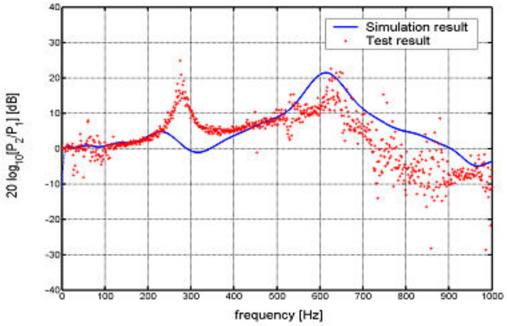

Fig. 14 $|P_2 / P_1|$, spiral pipe positioned inversely(hose: 0.3, spiral pipe: 0.25 m)

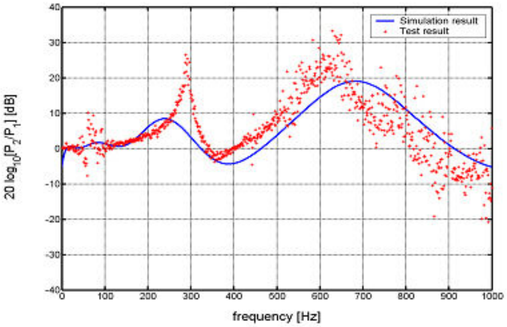

Fig. 15 $|P_2 / P_1|$, spiral pipe positioned inversely(hose: 0.3, spiral pipe: 0.2 m)

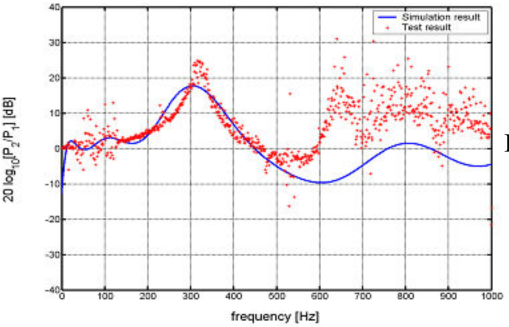

Fig. 16 $|P_2 / P_1|$, spiral pipe positioned inversely(hose: 0.3, spiral pipe: 0.1 m)

Fig. 14, 15 and 16 are results for resonator hoses(length : 0.3 m) with spiral pipes(length : 0.25, 0.2, 0.1 m respectively) positioned inversely.
In Fig. 11~16, there were comparatively good agreements between the experimental results and the simulated results in the frequency range lower than 600 Hz. From these results, the validity of the analyzing method for pulsating flow in resonator hoses was confirmed.

CONCLUSIONS

In this study, the authors surveyed former researches on hose(viscoelastic pipe) modeling in advance. Then, suggested a new method for analyzing pulsating flow in hose based on wave speed data measured through a preliminary test. Also, a new method to measure wave speed in hose 'closed-end-conduit with three transducer method' was proposed and explained in detail. Using the proposed wave speed measuring method, wave speed data in each component of the object resonator hoses were measured through preliminary experiments. Finally, with several object resonator hoses, pressure attenuation characteristics were investigated by experiments and simulations. For the simulation, the measured wave speed data were utilized. There were comparatively good agreements between the experimental results and the simulated results in the frequency range lower than 600 Hz. From these results, the validity of the analyzing method for pulsating flow in resonator hoses was confirmed.

The newly suggested method for analyzing pulsating flow in resonator hoses based on wave speed data measured in each component of a resonator hose could be used for computing the pulsation flow, evaluating the transmission loss of resonator hoses, and eventually for optimum design of resonator hoses.

REFERENCES

[1] G. T. Klees, "Attenuation Device", United States Patent No. 3,323,305, 1967-6.
[2] M. C. Hastings and C. C. Chen, "Analysis of Tuning Cables for Reduction of Fluidborne Noise in Automotive Power Steering Hydraulic Lines", SAE Paper 931295, pp. 277～282, 1993.
[3] K. Nagata, K. Takahashi and T. Nonoshima, "Analysis of a Hydraulic Hose Used for Pulsation Damping", Journal of Japanese Hydraulics and Pneumatics Society, Vol. 27, No. 7, pp.94～103, 1996.
[4] E. Kojima. T. Ichiyanagi and Y. Kimura, "Analysis of Flexible Hoses with Spiral Tubular Inserts for Reduction in the Fluidborne Pressure Pulsation in an Automotive Power Steering Hydraulic System", Journal of Japanese Hydraulics and Pneumatics Society, Vol. 27, No. 6, pp.98～105, 1996.
[5] G. W. Morgan and J. P. Kiely, J. Acoust. Soc. Am. 26, 323-328, 1954.
[6] W. Klip, P. Van Loon, and D. A. Klip, J. Appl. Phys. 38, (9), 3745-3755, 1967.
[7] R. H. Cox, Biophys. J. 8, pp.691～709, 1968.
[8] K. Nakano, M. Yoshimoto, and N. Okazaki, Bulletin of the Tokyo Institute of technology, Vol. 99, pp.123～142, 1970.
[9] M. Gally, M. Guney, and E. Rieutord, J. Fluids Eng. 101(4), pp.495～499, 1979.
[10] E. Rieutord, J. Fluids Eng. Vol. 104, pp.335～341, 1982.
[11] L. Suo and E. B. Wylie, J. Fluids Eng. Vol. 112, pp.496～500, 1980.
[12] D. K. Longmore and A. Schlesinger, Journal of Systems and Control Engineering, Proc.

Inst. Mech. Eng. Part 1 Vol. 205, pp.97～104, 1991.

[13] K. Nakano and A. Abo-Ismail, Hydraulics & Pneumatics Vol. 7, No. 3, pp.155～162 , 1976(in Japanese).

[14] A. Abo-Ismail and K. Nakano, Hydraulics & Pneumatics, Vol. 10, No.7, pp.450～427, 1979, (in Japanese).

[15] D. C. Wiggert, R. S. Otwell, and F. J. Hatfield, J. Fluids Eng. Vol. 107, pp.402～406, 1985.

[16] J. Yu and E. Kojima, "Dynamic Response of Unhomogeneously Viscoelastic Fluid Lines", Proceedings of the 1995 American Control Conference, Seattle, Washington, pp. 1821～1825, 1995,

[17] J. Yu and E. Kojima, "Transmission of Fluidborne Pressure Ripples in Fluid Power Flexible Hoses with Relatively Long Length", Proceedings of the 2nd International Symposium on FPTC, edited by Z. Chen *et al,* Shanghai, pp.596～601, 1995.

[18] J. Yu and E. Kojima, "Wave Propagation in Fluids Contained in Finite-Length Anisotropic Viscoelastic Pipes", J. Acoust. Soc. Am. Vol. 104, No. 6, pp.3227-3228, 1998.

[19] F. T. Brown, Trans. ASME, Ser. D, Vol. 84, No. 4, pp.547～553, 1962.

[20] S. Washio and T. Konishi, Trans. of JSME, Vol. 50, No. 459, pp.2569～2576, 1984.

APPENDIX
SUMMARY OF WAVE SPEED MEASURING METHODS IN PIPES

A.1 Three transducer method[A1]

This is a wave speed measuring method which utilizes pressure data acquired from the three pressure transducers on the test pipe shown in Fig. A.1, and a computing process. This is one of the wave speed measuring methods registered in ISO 15806-2. This method is only effective in wave speed measurement in metal(almost rigid) pipes, not applicable to hoses(viscoelastic pipes). Also, the equation for computing wave speed in this method are described as an implicit function, hence the computing process is complex and requires comparatively long computation time.

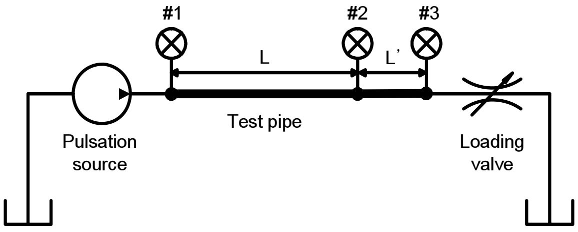

Fig. A.1 Three transducer method[A1]

A.2 Anti-resonance method[A1]

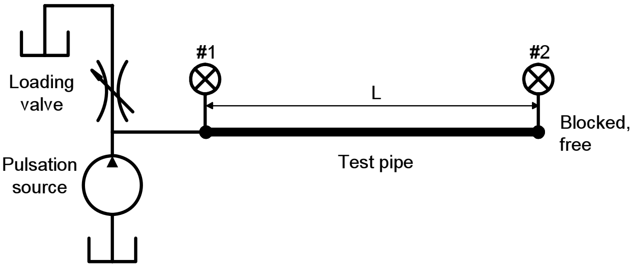

Fig. A.2 Anti-resonance method[A1]

As shown in Fig. A.2, the anti-resonance method uses a metal pipe with closed outlet(the outlet flowrate Q_2=0). Therefore, the test system configuration is simpler than that of the three transducer method. This anti-resonance method is also one part of ISO 15806-2. In the same way as the three transducer method, the equation for computing wave speed in the anti-resonance method has form of an implicit function, so using it in the wave speed computing process is inconvenient.

A.3 Four transducer method[A2]

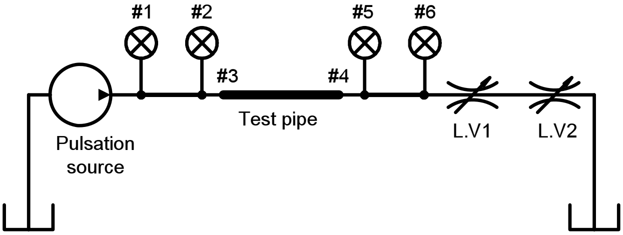

Fig. A.3 Four transducer method[A2]

This method uses four pressure transducers and two valves on the test pipe system as shown in Fig. A.3. This method is available not only for test pipes made of metal material but also hoses(viscoelastic pipes). However, in the same way as the three transducer method and the anti-resonance method, the equation for computing wave speed in the four transducer method has form of an implicit function, hence using it in wave speed computation is inconvenient.

REFERENCES IN APPENDIX

[A1] ISO 15086-2, "Hydraulic fluid power - Determination of fluid-borne noise characteristics of components and systems -part2: Measurement of speed of sound in a fluid in a pipe", 2000.

[A2] J. Yu and E. Kojima, "Methods for Measuring the Speed of Sound in the Fluid in Fluid Transmission Pipes", Society of Automotive Engineers, 2000.

High Performance Valves

Dynamical Performance of a Fast Magnetorheological (MR) Valve

Jari Kostamo, Esa Kostamo, Jyrki Kajaste, Matti Pietola
Helsinki University of Technology, Laboratory of Machine Design

Abstract:
Magnetorheological (MR) fluid belongs to the group of smart materials whose rheological properties can be varied by application of a magnetic field. The response time of magnetorheological technology is generally considered fast. In a recent study the response time of the MR fluid was estimated to be approximately 0.5 milliseconds. However, there is remarkable variation in measured response times of magnetorheological devices in different studies. In this paper some design considerations of a fast magnetorheological valve are discussed and a response time of less than 1 millisecond is demonstrated with an experimental valve.

1 Introduction

The functional principle of magnetorheological fluid is based on micron sized ferromagnetic particles mixed into a base fluid. In consequence of an external magnetic field the ferromagnetic particles align parallel to the magnetic field lines and the shear stress of the fluid is increased and the fluid flow is resisted or restricted. This state transition of MR fluids can be used to implement various types of controllable dampers, valves, brakes or squeeze film devices (1). The advantage of the magnetorheological devices is no moving parts are needed for the valve function. This feature enables novel designs compared to traditional hydraulic valves and makes the structure of the devices simpler. Because no moving parts are needed in the valve, the dynamical performance of MR devices is ultimately limited by the response time of the MR fluid or by the fluid dynamics.

During the past ten years magnetorheological technology has been applied widely in different industrial areas. The response time of the MR devices is fast and real time tuning of the damper parameters can be done (1, 2). Many papers have been published evaluating the performance of magnetorheological dampers, valves and MR brakes. Most of the studies seem to have examined magnetorheological dampers because it is perhaps the most attractive application of this technology. This is due to the fact that the construction of a linear MR fluid damper is simple and similar to conventional viscous fluid damper. The

Power Transmission and Motion Control 2007 Edited by Dr D N Johnston and Professor A R Plummer
© With The Centre for Power Transmission and Motion Control

damping oil is replaced with MR fluid and active fluid is led from one side of the moving piston to another through annular flow channels in which the MR fluid can be activated by magnetic field. MR fluid dampers are typically characterized by large damping force and low power consumption. See e.g. (3-7).

The similar technology comparable to magnetorheological fluid is electrorheological fluids. The functional principle is quite similar but instead of magnetic field the fluid is activated with electric field. The applications of the electrorheological technology are mainly in the same areas with the MR technology and they can be seen as competing technologies. Quite recently some papers have been published in which the applicability of the electrorheological technology in implementing servo systems has been evaluated (8, 9). A valve capable of controlling a pressure difference of 1.6MPa in one millisecond has been reported.

Recent studies presented by (10, 11) suggest that the response time of MR fluids is about 0.5 milliseconds. The measurement method used in these papers is based on measuring the pressure difference over the MR fluid gap with different flow velocities. By increasing the flow velocity the dwell time of the fluid in the valve can be reduced until no MR effect is observed. Using this method the pressure difference developed in the valve can be measured as a function of the dwell time and the response time of the fluid can be estimated.

Based on these research results it should be possible to develop highly dynamical magnetorheological valves. However, there are only few studies demonstrating MR devices with response times in the scale of few milliseconds. This is probably mainly caused by the fact that the design process of an MR valve is a multidisciplinary task combining the design of control electronics, the design of power electronics, the magnetic design, the hydraulic design and the design of the MR fluid. Failure in any of these tasks will limit the performance of the valve on a modest level even though other areas would work perfectly well. For example: It can easily be understood if the response time of the coils used for generating magnetic field is slow, it is not possible to measure any faster effects caused by the MR effect from the hydraulic circuit. On the other hand if the hydraulic circuit is designed poorly and its natural frequency is low, the response of the hydraulic will not tell much about the dynamics of the MR effect. When the response of the magnetic circuit and the dynamics of the MR fluid are combined it makes it considerably more difficult to decide which part of the valve works well and which part is the bottle neck.

In this study some basic design criteria related to designing a fast magnetorheological valve are discussed. Based on these criteria an experimental valve was built and the performance was measured. More emphasis is put on the analysis of the results and discussion of the dynamical performance. It will be shown that the response time of the magnetorheological valve can be less than 1 millisecond.

2 Design considerations of a high dynamic MR valve

In this chapter the starting points for the design process are discussed. It was pointed out in the previous chapter that the design process of an MR valve is a multidisciplinary task. The factors related to the performance of the valve are listed here and some of them are discussed in more detail. It is, however, well beyond the scope of this paper to describe the entire design process of an optimal high frequency valve.

Factors affecting the performance of a magnetorheological valve are:

- Properties and response time of the MR fluid
- Design of flow channels and the hydraulic circuit.
- Mechanical design and stiffness of the structure
- Magnetic circuit: the coil, magnetic core material and geometry
- Power electronics
- Control circuit

Each of these can be divided into subcategories if they are examined more closely. In addition the demands for the performance of the MR valve vary in different applications. Usually it is more expensive and more difficult to design the performance of the valve to be very good on any aspect and therefore the required performance criteria should be kept in mind from the beginning of the design process.

2.1 Hydraulic design

The behavior of a magnetorheological valve differs significantly from a traditional hydraulic valve. If an MR valve is compared with traditional hydraulic components it is more like a rapidly controllable pressure relief valve rather than a traditional servo or a proportional valve. This is caused by the fact that the functional principle of the MR valve relies on the increase of the yield stress of the MR fluid in the fluid gaps. When the maximum pressure difference defined together by the yield stress of the fluid and the construction of the valve is exceeded the valve will pass fluid flow.

The requirements for the hydraulic power controlled by the valve and the properties of the MR fluid define the possible geometries of the fluid gaps. In MR valve applications the geometry of the flow channel is mainly defined by the desired maximum pressure difference over the valve and the maximum volume flow rate needed. In general, the hydraulic power P can be expressed as a function of the flow rate Q and the pressure difference Δp and it gives the starting point for deciding the dimensions of the valve.

$$P = Q\Delta p \tag{1}$$

The magnetic field induced yield stress of the MR fluid is often represented as a Bingham plastic having magnetic field dependent yield strength. For stresses τ above the field dependent yield stress τ_0, the flow is governed by Bingham's equation. In the Bingham model the total shear stress is given by

$$\tau = \tau_0(H)\,\mathrm{sgn}(\dot{\gamma}) + \eta\dot{\gamma} \qquad |\tau| > |\tau_0| \tag{2}$$

$$\dot{\gamma} = 0 \qquad |\tau| < |\tau_0|, \tag{3}$$

where τ_0 is the yield stress caused by the magnetic field; $\dot{\gamma}$ is the shear rate and η is the field-independent viscosity. (2)

When MR fluids are used in a valve application and the Bingham plastic model of the behaviour is adopted the pressure difference over the valve can be approximated with the following equation.

$$\Delta p = \frac{12\eta QL}{d^3 w} + 2.5\frac{\tau_0 L}{d}, \tag{4}$$

where L is the length of the flow channel, w is the width of the fluid channel and d is the height of the fluid gap. It can be seen from equation (4) that the pressure difference is a sum of two terms. The first term describes the pressure difference caused by the viscous flow of the fluid and the second term is the pressure difference caused by the field dependent yield stress. If the pressure difference caused by the second term is not exceeded, there will be no flow through the valve. It is usually desired in MR valve applications that the fluid flow can be stopped by switching on the magnetic field. In this case Q=0 and the second term of the equation (4) defines the maximum pressure difference. When the magnetic field is switched off τ_0 approaches zero and the flow rate can be estimated by using the first term in the equation (4). When the pressure difference and the flow rate are know, equation (1) can be used to calculate the maximum hydraulic power which can be controlled with the MR valve.

The field dependent yield stress for the MR fluid used in this study is presented in figure (1). The value for the dynamic viscosity of the fluid is 0.09 ± 0.02Pa-s.

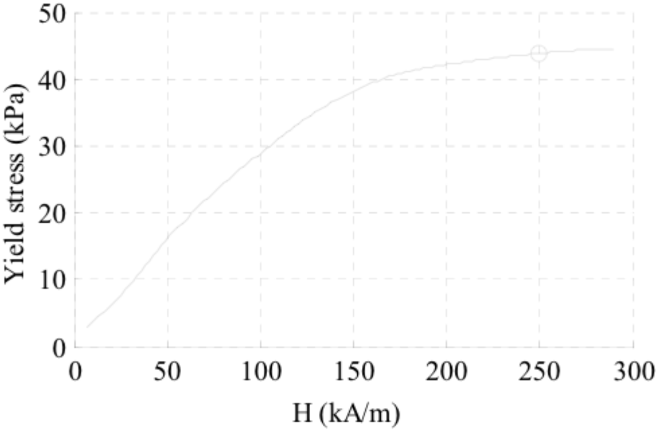

Figure 1: Yield stress of MRF-132DG as a function of magnetic field (12)

2.2 Magnetic design

In general, magnetic circuits are easy to construct and a simple electromagnet can be built in almost any laboratory. The basic parts of an electromagnet are a coil and an iron core. The iron core acts as a low reluctance flux conduit and it is used to guide the magnetic field to the air gap. In the case of the MR valve the air gap is filled with MR fluid.

Usually more than 250kA/m magnetic field strengths are required to achieve the full performance of the MR fluid. This requirement is not exceptional in the magnetic devices but it can not be achieved without proper design. If the valve is operated at higher frequencies the design of the magnetic circuit becomes more complex and more knowledge about choosing the right core material is needed. (13)

When the geometry of the fluid gap is calculated based on the performance requirements defined by the hydraulic power, magnetic circuit must be designed so that the desired operation point of the fluid can be achieved. The geometry of the fluid gap and the magnitude of the magnetic field needed to activate the fluid define the requirements for the iron core and the coil. It is essential to ensure the electro magnet is strong enough and the magnetic core does not saturate. In next chapters basic design criteria of the magnetic circuit are discussed.

2.2.1 Model of the magnetic circuit

A simple model for the magnetic circuit of the MR valve can be formed by using circuit equations. The magnetic flux Φ and magnetomotive force U_{m} of the magnetic circuit behave similarly as the electric current I and voltage U of the electric circuit. The magnetomotive force can be expressed as a function of magnetic field strength H and distance l.

$$U_{\mathrm{m}} = Hl\,. \tag{5}$$

If a coil is used to generate the magnetomotive force it can be expressed as shown in equation (6).

$$U_{\mathrm{m,coil}} = NI \tag{6}$$

Where N is the number of Ampere turns in the coil. The magnetic flux can be expressed as a function of flux density B and area A.

$$\Phi = BA \tag{7}$$

In magnetic circuits reluctance R_{m} is equivalent to resistance in the electric circuits. Reluctance for magnetic material is given by

$$R_{\mathrm{m}} = \frac{U_{\mathrm{m}}}{\Phi} = \frac{l}{\mu A}\,, \tag{8}$$

where μ is the permeability of the material, A is the area of the cross section of the magnetic path. The permeability of the material relates the magnetic field strength with the magnetic flux density.

$$B = \mu H \tag{9}$$

If the magnetic circuit is assumed to be ideal and no flux fringing is taken into account a circuit equation can be written as

$$U_{\mathrm{m,coil}} = (R_{\mathrm{m,Fe}} + R_{\mathrm{m,MR}})\Phi\,, \tag{10}$$

where $R_{\mathrm{m,Fe}}$ is the reluctance of the iron core and $R_{\mathrm{m,MR}}$ is the reluctance of the MR fluid in the fluid gap. If the magnitude of the magnetic flux is assumed to be constant through the circuit, equation (10) can be simplified to a following form

$$U_{\mathrm{m,coil}} = H_{\mathrm{Fe}} l_{\mathrm{F}e} + H_{\mathrm{MR}} d\,, \tag{11}$$

where H_{Fe} is the magnetic field in the iron core, l_{Fe} is the length of the magnetic path in the iron core and H_{MR} is the magnetic field in the MR fluid. By substituting equation (6) into equation (11) and solving for N we get the number of Ampere turns needed in the coil.

$$N = \frac{H_{\mathrm{Fe}} l_{\mathrm{Fe}} + H_{\mathrm{MR}} d}{I} \qquad (12)$$

This approach for evaluating the number of Ampere turns is simple and it gives reasonably good results with simple geometries.

Real magnetic materials can not amplify the magnetic flux infinitely and typical ferromagnetic materials saturate at flux densities of 1-2T. When designing the magnetic circuit it should be kept in mind that the cross section of the magnetic core is not too small in any part of the magnetic circuit and the core does not saturate before the desired operation point of the valve is achieved. (13, 14)

Finite element programs can be used to model the magnetic circuit more precisely. FE modeling of the magnetorheological valve has been presented e.g. in (15-17). Numerical methods are especially useful when more complex magnetic circuit geometries are designed.

2.2.2 Magnetic core material

As suggested in the previous chapter the magnetic material should be chosen so that the material does not saturate until the desired operation point of the fluid is achieved. The BH curve of the MR fluid shown in figure (2) can be used to evaluate the magnetic flux density in the fluid when the operating point of e.g. 250kA/m is required. This approximately 0.8T flux density is also the minimum saturation flux density required for the core material. The BH curve for the core material used in this study is shown in figure (3) and it can be seen that this material saturates at approximately 1.5T flux density. The operation points of MR fluid and iron core used in this study are plotted in figures (2) and (3) with red circles.

If MR fluid device is designed to be used in an application requiring fast response, more attention should be paid to selection of proper core material. The eddy currents in the magnetic core will limit the dynamical performance of the valve if the core material is not suitable for high frequency applications. Eddy currents can be reduced by selecting a core material with high resistance e.g. ferrites or by manufacturing the core of laminated transformer steel.

There are many different types of commercial magnetic materials available for high frequency applications. However, getting specially made magnetic cores is expensive and difficult in general. To be able to build inexpensive prototypes of the valves the design should be based on commercially available stock products. Unfortunately the desired valve geometry does not usually enable utilization of all stock magnetic cores. Therefore the design is a tradeoff between the available parts and the optimal geometry.

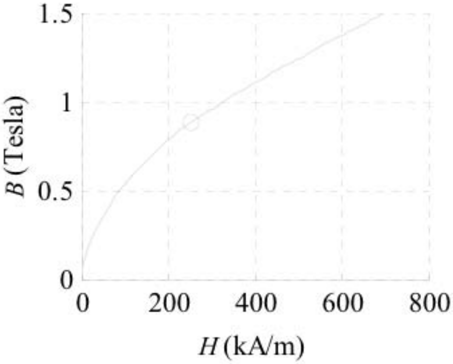

Figure 2: BH curve of MRF-132AD (12)

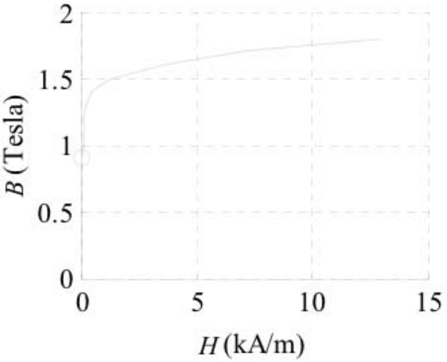

Figure 3: BH curve for the core material used in this study (18)

3 Construction of the magnetorheological valve

The valve presented in this paper is a rectangular shaped magnetorheological valve and it is specially designed for high dynamic applications. The MR valve consists of an aluminum body, laminated iron cores and coils and it has two separately controlled edges. The magnetic circuit of the valve is designed so that the magnetic field can be switched on and off rapidly. Figure (4) shows the MR valve without cover plates.

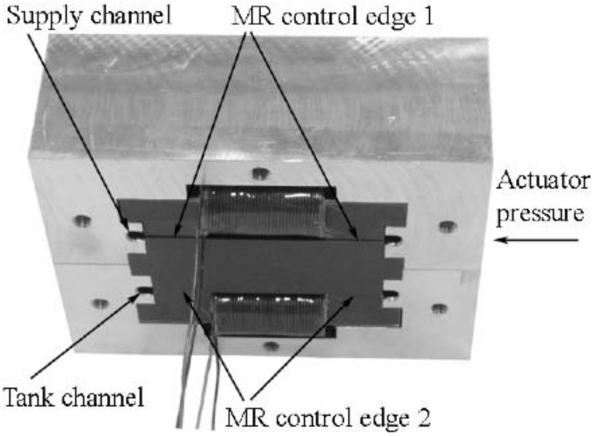

Figure 4: Measured MR valve without side covers

When the valve is assembled the pressure supply line will be attached to the cover plate. MR fluid flows through the cover plate to the supply channel which distributes the volume flow equally over the width of the MR control edge 1. Next the MR fluid changes its direction and flows through the MR control edge 1.

After the first control edge the MR fluid flows to the actuator pressure measurement and continues to the supply of the second control edge. After the MR control edge 2 MR fluid ends up to the tank channel from which it is lead through the cover plate to the tank line.

The dimensions of the MR valve are listed in table (1).

Dimension	Value
Length of the fluid gap, *L*	2*15mm
Width of the fluid gap, *w*	36mm
Height of the fluid gap, *d*	0.35mm
Length of the valve (outside)	110mm
Height of the valve (outside)	87mm
Width of the valve (outside)	54mm

Table 1: Dimensions of the MR valve

The performance of the valve can be estimated based on these parameters. Equation (4) can be used to calculate the maximum pressure difference with zero flow rate. In this case Q=0, τ_0 can be assumed to be 40Pa-s, d=0.35mm and L=30mm. With these parameters pressure difference will be about 8.5MPa. When the magnetic field is off τ_0 can be roughly assumed to be zero and the maximum flow rate can be solved from equation (4). With given values flow rate will be $4.1*10^{-4}m^3/s$. Finally the hydraulic power can be calculated using equation (1) giving a result P=3.5kW.

4 Experimental setup for testing the MR valve

An experimental setup was designed and built to measure the performance of the MR valve presented in previous chapters. The setup consisted of a hydraulic circuit and a control and measurement setup. In addition some devices were developed to evaluate the magnetic properties of the MR valve.

4.1 Hydraulic setup

The MR hydraulic setup was developed and built to provide the hydraulic circuit needed in the application and to generate the hydraulic power needed to pressurize the MR valve. Extra attention was paid to the reliability of the hydraulic setup because small particles in the MR fluid can cause problems for regular components used in conventional hydraulic systems. The setup was also designed to be modular so that the MR valve can be replaced easily with other MR valve prototypes. The hydraulic circuit is shown in figure (5).

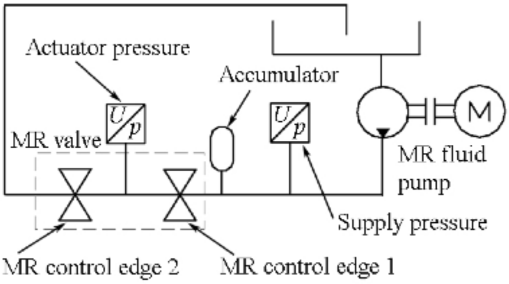

Figure 5: Hydraulic circuit

The main parts of the hydraulic circuit are a tank, a pump for the MR fluid, pressure sensors, an accumulator and the experimental valve. A high dynamic accumulator was attached to the pressure supply line to compensate for the pressure fluctuations during the measurements.

The performance of the MR valve was evaluated by conducting step response measurements. The two control edges of the valve were switched on and off in reversed phase and the step response of the actuator pressure was measured. The actuator pressure sensor was attached directly to the valve to minimize the fluid volume and fluid compression.

4.2 Control and measurement setup

The control and measurement setup used in these experimental measurements consisted of a measurement computer, a microcontroller, two current amplifiers, two current measurement devices, pressure sensors, signal filtering components, and a data acquisition device. The setup is shown in figure (6).

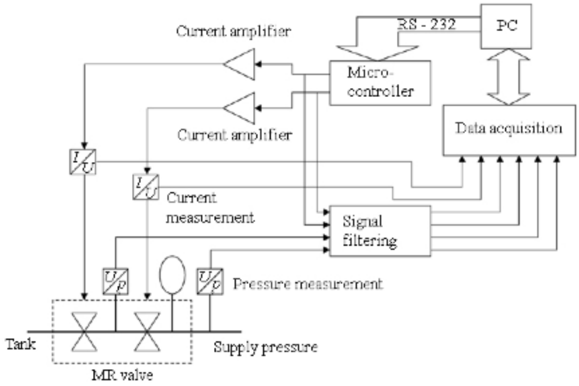

Figure 6: Measurement setup

The microcontroller was used to generate the reference signals for current amplifiers and the signals could be modified with LabView user interface programmed to the measurement computer. The reference signals were measured from the output of the microcontroller and they were wired to the signal conditioning box. Supply and actuator pressure levels of the MR valve were measured with two Keller pressure sensors with a pressure range from 0 to 20MPa.

4.3 Measurement setup for the magnetic response of the valve

A measurement setup was designed to verify the performance of the magnetic parts of the MR valve. To be able to measure the magnetic flux in the fluid gaps a thin coil was manufactured. The coil had 10 turns and it was small enough to fit in the fluid gap of the valve. The cross section of the coil was slightly larger than the cross sectional area of the magnetic circuit in the fluid gap. Therefore it can be assumed with sufficient accuracy that all of the magnetic flux goes through the coil.

According to Faraday's law the electromotive force induced in the closed loop is given by the equation (13)

$$U = -N\frac{d\Phi}{dt}, \tag{13}$$

where U is the electromotive force (voltage), N is the number of turns in the coil and Φ is the magnetic flux. Faraday's law can be used to determine the magnetic flux in a magnetic circuit if the voltage of a sensor coil is measured. Solving equation (13) for $d\Phi$ and integrating gives

$$\Phi = \frac{1}{N}\int U dt \tag{14}$$

Now the magnetic flux can be approximated by integrating the measured voltage. The cross sectional area of the magnetic circuit is known from the design parameters of the valve and equation (7) can be used to solve the magnetic flux density in the fluid gap. (14)

5 Measurements of the prototype MR valve

The measured results of the experimental MR valve are presented in this chapter. The results include the measurements of the magnetic circuit, static pressure measurements with constant coil current and dynamic step response measurements.

5.1 Measurements of the magnetic circuit

At first the response of the magnetic circuit was measured. This is important because the response of the MR effect in the hydraulic circuit will not be any faster than the response magnetic flux. The voltage of the sensor, specially developed for this purpose, was measured and the result was integrated using equation (14). Magnetic flux was divided by the area of the fluid gap and the result is the magnetic flux density plotted in figure (7). It can be seen that the magnetic flux can be switched on in 0.3ms. The same response time was also verified for turning the magnetic field off.

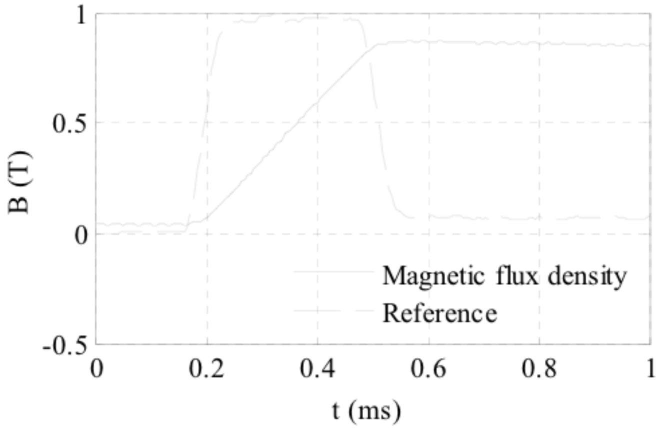

Figure 7: Step response of the magnetic circuit

5.2 Static pressure measurements

The pressure difference over the MR control edges was measured with different current values and during the measurement a constant, small fluid flow was forced through the valve. It was noticed that if there is no fluid flow before coil current is increased, MR fluid can form a 'plug' in the inlet of the valve. Therefore pressure will increase more than the model predicts and in addition the measurements will not be repeatable.

In figure (8) two repeated static pressure measurements are plotted in the same figure. It can be seen that the measurements are repeatable and the magnetorheological valve can create a pressure difference of over 7.5MPa with 4A coil current.

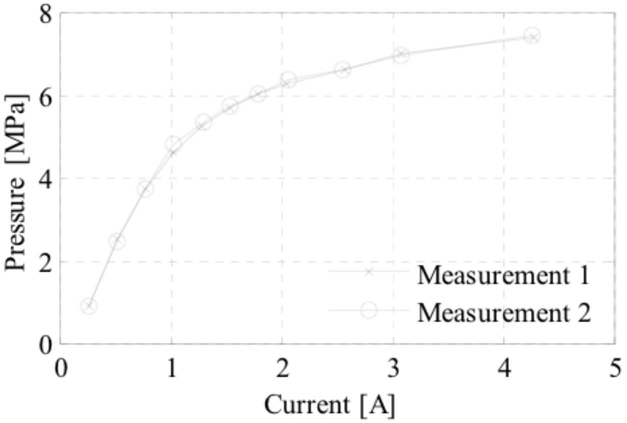

Figure 8: Static pressure measurements

5.3 Dynamic pressure measurements

The maximum supply pressure level was set to about 8.0MPa when the dynamic pressure measurements were done. The frequency of the square wave reference was 40Hz in order to measure the step responses of the MR valve. Figure (9) shows one period of the step response experiment.

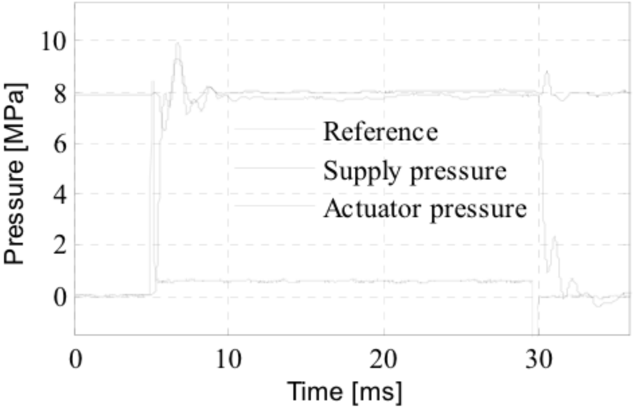

Figure 9: Pressure step response

It can be seen from figure (9) that the valve can be used to control the pressure in about 7.7MPa pressure range. It can also be noted that there occurs some oscillation in the pressure during the rise period and fall period. The cause of the pressure oscillations was not fully clarified but one likely explanation could be the pressure shock and the flexibility of the structure of the valve.

The rising edge of the step response is investigated in more detail in figure (10). Some interesting points are marked in this figure and the coordinates of the corresponding points are given in table (2). The reference point of step response is plotted with square, the point where the pressure starts to rise is plotted with circle and the maximum operating pressure point is plotted with diamond.

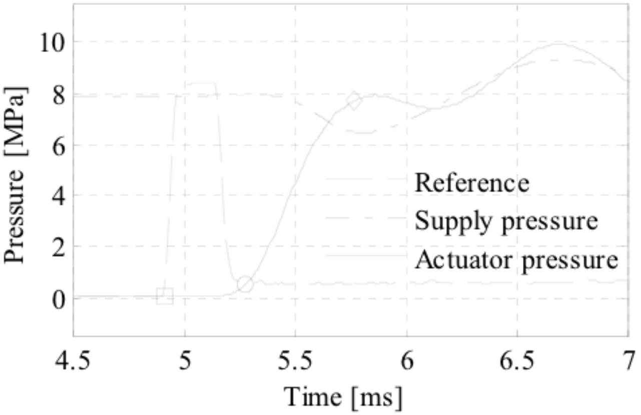

Figure 10: Rising edge of the step response

Symbol	Time [ms]	Pressure [Mpa]
□ Square	4,91	0,041
○ Circle	5,28	0,524
◊ Diamond	5,77	7,719

Table 2: Symbol coordinates from the figure (10)

The delay time for the MR valve can be evaluated by measuring the time difference between square and circle symbols. The delay time was measured to be 0,37ms. Another interesting feature which can be evaluated from the figure (10) is the rate of the pressure change. The rise rate can be evaluated between circle and diamond or square and diamond whether the delay time is neglected or not. If the delay time of the valve is neglected, the pressure difference can be calculated to rise with the rate of 14.7MPa/ms. When the delay is taken into account, the pressure rises with the rate of 8.9MPa/ms. The full pressure difference was achieved in 0,86ms.

It can be seen from figure (10) there is a gap in the supply pressure during the rise period of the actuator pressure. The drop of the supply pressure was tried to be compensated with a small high dynamic accumulator but it could not be avoided completely.

6 Conclusions

Performance of an MR valve for high dynamic applications was investigated in this study. It was pointed out that the design process of a fast MR valve is a multidisciplinary task and every area of the valve design must succeed in order to gain a good performance. All these factors together will establish an interaction chain which will define the dynamic range and the performance of the MR valve. Generally a satisfactory solution will be found even if some compromises are made. However, if the objective of the MR valve design is to strive for the best possible performance, it means all the functional parts have to be optimized.

An experimental valve was built to demonstrate the fast response time of MR technology. It was shown a pressure difference of 7.7Mpa with response time of 0.86 milliseconds can be achieved with a magnetorheological valve. The maximum slope of the pressure increase was 14,7MPa/ms. The results of dynamic measurements are in accordance with the results published in (10, 11). If the response time of the MR fluid is less than one millisecond the response time of the valve should be in approximately same scale.

The performance of the valve was not optimal but it shows that rapid pressure differences can be created with MR technology. Controlling over 3kW of hydraulic power with response time of less than 1 millisecond offers some interesting possibilities in designing servo actuators based on MR technology. In addition this technology scales up and it would be almost trivial to double the hydraulic power delivered by the valve presented here.

The dynamic modeling of the fluid flow was left out of the scope of this paper even though it obviously is an important factor. The dynamical modeling of the fluid flow could offer better understanding for some of the observed oscillations and therefore dynamics of the fluid flow should be investigated in more detail in the future work. Future work is also planned in applying the MR valve for actuator applications and its applicability in e.g. active vibration damping applications will be investigated.

References

(1) Jolly, M.R., Bender, J.W. & Carlson, J.D. 1999, "Properties and Applications of Commercial Magnetorheological Fluids", Journal of Intelligent Material Systems and Structures, vol. 10, no. 1, pp. 5-13.

(2) Goncalves, F.D., Koo, J.H. & Ahmadian, M. 2006, "A Review of the State of the Art in Magnetorheological Fluid Technologies -- Part I: MR fluid and MR fluid models", Shock & Vibration Digest, vol. 38, no. 3, pp. 203.

(3) Koo, J.H., Goncalves, F.D. & Ahmadian, M. 2006, "A comprehensive analysis of the response time of MR dampers", Smart Materials and Structures, vol. 15, no. 2.

(4) Lindler, J.E., Dimock, G.A. & Wereley, N.M. 2000, "Design of a magnetorheological automotive shock absorber", SPIE-Int. Soc. Opt. Eng, pp. 426.

(5) Xinchun, G., Jinhai, L. & Jinping, O. 2005, "Experiment study of large-scale magnetorheological fluid damper", SPIE-Int. Soc. Opt. Eng, pp. 588.

(6) Ericksen, E.O. & Gordaninejad, F. 2003, "A magneto-rheological fluid shock absorber for an off-road motorcycle", International Journal of Vehicle Design, vol. 33, no. 1-3.

(7) Milecki, A. 2002, "Investigation of Dynamic Properties and Control Method Influences on MR Fluid Dampers' Performance", Journal of Intelligent Material Systems and Structures, vol. 13, no. 7-8, pp. 453-458.

(8) Zaun, M. 2006, "Design of Cylinder Drives Based on Electrorheological Fluids", International Journal of Fluid Power, vol. 7, no. 1, pp. 7-13.

(9) Zaun, M. 2006, "Design Concept for the Development of Cylinder Drives based on Electrorheological Fluids", Journal of Intelligent Material Systems and Structures, vol. 17, no. 4, pp. 303-307.

(10) Goncalves, F.D. 2005, "A study on MR fluids subjected to high shear rates and high velocities", SPIE--the International Society for Optical Engineering, Bellingham, Wash., pp. 46.

(11) Goncalves, F.D. 2006, "Investigating the magnetorheological effect at high flow velocities", Smart materials structures, vol. 15, no. 1, pp. 75.

(12) Lord Co. ,"Magnetorheological fluid MRF-132AD", product specification, Available from: www.mrfluid.com. [10.6.2006].

(13) Lord Co. ,1999, "Magnetic Circuit Design", Engineering note, Available from: http://www.lord.com/Portals/0/MR/Magnetic_Circuit_Design.pdf. [23.5.2007].

(14) Halliday, D., Resnick, R. & Walker, J. 2001, Fundamentals of Physics, John Wiley & Sons, Singapore.

(15) Kostamo, J.T. & Kajaste, J.T. 2006, "Finite element modeling and simulation of a magnetorheological (MR) valve", The 2nd International Conference on Computational Methods in Fluid Power FPNI'06, Aalborg, Denmark, pp. 8.

(16) Li, W.H., Du, H. & Guo, N.Q. 2003, "Finite element analysis and simulation evaluation of a magnetorheological valve", International Journal of Advanced Manufacturing Technology, vol. 21, no. 6, pp. 438-445.

(17) Szelag, W. 2004, "Finite element analysis of the magnetorheological fluid brake transients", COMPEL The International Journal for Computation and Mathematics in Electrical and Electronic Engineering, vol. 23, no. 3, pp. 758-766.

(18) Surahammars Bruk AB ,Box 201, SE-735 23 Surahammar, Sweden, Available from: http://www.sura.se/. [12.02.2007].

Design optimization of a special relief valve with Response Surface Methodology

Paolo Casoli, Andrea Vacca
Department of Industrial Engineering – University of Parma (Italy)

ABSTRACT

This paper describes the utilize of a numerical procedure for the analysis and the optimization of an hydraulic component, namely a particular direct acting relief and anti-cavitation cartridge valve. The element taken as reference is usually connected to a hydraulic line with the aim of keeping the circuit pressure between two different set values; moreover it can work as anti-shock valve, avoiding pressure peaks.

The developed procedure is based on *Response Surface Methodology* techniques, adopting the path search method known as *Steepest Descent*. For this purpose, the valve behaviour is analytically described by means of a properly defined objective function. The procedure approximates this objective function with a simple model whose coefficients are evaluated using the predictions performed by a AMESim® model of the valve, developed in C++ language by the authors. The sets of simulations for the fitting model are planned according to *Design Of Experiments* techniques. The entire optimization algorithm has been developed with MATLAB® scripts, which are able to plan the simulation with the AMESim® model of the valve, automatically execute the simulations, post process the results and finally establish the optimal configuration of the component taken as reference.

The considered starting point for the optimization process is given by a stock configurations of the valve, considered also for the experimental validation of the AMESIM® model in previous works. Three different optimal configurations of the valve, for different values of the preset pressure, have been proposed, and prototypes of the new designs have been realized. Experimental investigations point out the improved performance of the proposed designs, highlighting the potentials of the developed optimization methodology.

1. INTRODUCTION

Potentials reached by the latest simulation techniques are becoming more and more reliable and efficient, as concerns the capability of developing numerical models predictive of the behavior of components or complete systems, and the possibility of implementing mathematical algorithm for design optimization. However, although the literature on fluid power presents innumerable examples of advanced simulation tools developed for the

Power Transmission and Motion Control 2007 Edited by Dr D N Johnston and Professor A R Plummer
© With The Centre for Power Transmission and Motion Control

analysis of both elements and circuits, in the hydraulics field the adoption of sophisticated optimization techniques remains nowadays uncommon. This is often due to the mathematical formulation of optimization algorithms, that requires a well-posed definition of the problem in terms of inputs, constraints and goals, often considered unsuitable for hydraulic applications. Nevertheless, few works demonstrate the efficacy of different methodologies for the design of hydraulic components: for example, in [1] a Sequential Quadratic Programming was employed as algorithm for the selection of an optimal electrohydraulic component; in [2] the method of moving asymptotes is used for the optimization of the design of a distributor valve; in [3] a genetic algorithm was utilized to develop a new variable ratio flow divider valve. In addition to the methods used in the mentioned works, the literature propose many other evolutionary or combinatorial algorithms, as described in [4-7], just to quote some of the many books on this topic.

A relevant aspect that characterizes many optimization studies, such as [1-3], is given by the prerequisite of the initial definition of the input variables (whose values need to be optimized): many mentioned algorithms work well with a limited number of parameters and the number of steps required by the numerical procedure can became excessive if the number of variables is too elevated. Unfortunately, the latter is the case that typically characterizes most optimization problems in hydraulics. This implies the importance of the criteria for the variable selection, often based on the designer's experience. A high degree of subjectivity, at this phase, can inevitably affects the whole procedure, and – in most cases – the entire optimization process (in both the experimental or numerical optimization fields) is based on simple evaluations founded on the designer's intuition. Basing on this consideration, a fundamental prerogative of a numerical tool for component optimization is given by the possibility of adopting a module for the impartial variable selection, at the beginning of the optimization process. Following this idea, the authors have been developed a numerical procedure based on Design Of Experiments (DOE) and RSM (Response Surface Methodology) for the analysis and the optimization of different typologies of components. Despite the generality of the procedure, this work presents its application for the optimization of a particular relief cartridge valve.

In detail, the present study aims to optimize the design of a stock version of the valve, improving its behavior in steady conditions, by means of modifications that do not radically change its design. In addition, respect to the requirements that characterize the stock version, in this work higher flow rates values have been considered as a target of the optimized valve.

The optimization procedure accounts of the geometrical requirements that characterize the valve design and takes advantage of the results provided by a numerical model of the valve previously developed by the authors and discussed in [8]. This model has been developed in the AMESim® environment and its results have been verified through comparisons with the experimental data reported in [9].

The methodology used for the optimization consists of different phases: the *screening* analysis, that allows to identify the design parameters characterized by a great degree of influence on the component behavior, and the pure *optimization*. The *screening* is a very useful phase that allows a better understanding of the optimization problem and permits to select the set of factors whose value needs improvements. *Optimization* follows the *screening* phase and permits to find the optimal set of values for the factors considered as input. This problem is expressed in terms of minimization (or maximization) of a proper objective function (OF), representative of the component behavior. In this work both the phases (*screening* and *optimization*) have been performed through MATLAB® scripts, as represented in fig. 1. In particular, DOE techniques are utilized for the screening phase, while a combination of DOE and RSM-*Steepest Descent* method is adopted for the pure optimization process.

The developed procedure is fast and versatile, as highlighted by the optimizations performed in this work. As a matter of facts, different optimal configurations, varying the value of the preset pressure, have been proposed and prototypes have been realized and tested. The comparison between the ($Q \div \Delta p$) measured characteristics, for the prototypes and stock versions of the valve point out the improvements obtained thank to the developed procedure.

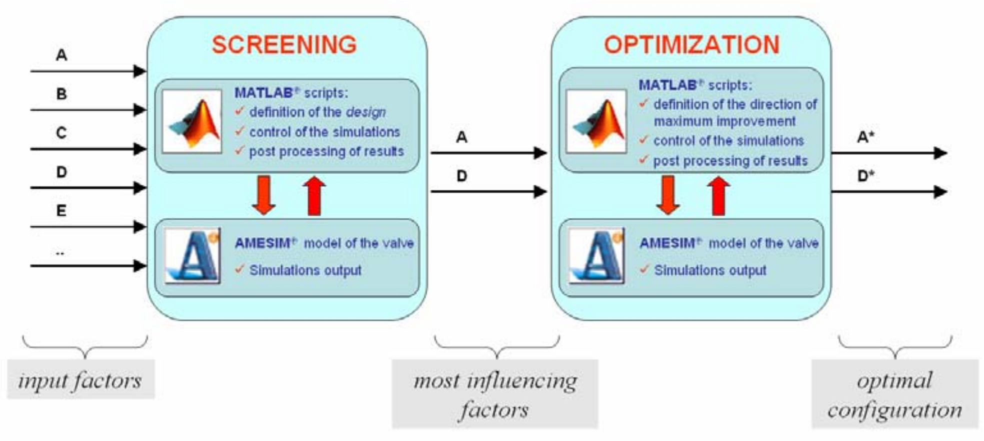
SCREENING
A
B
C
D
E
..
MATLAB® scripts:
✓ definition of the design
✓ control of the simulations
✓ post processing of results
AMESIM® model of the valve
✓ Simulations output
A
D
OPTIMIZATION
MATLAB® scripts:
✓ definition of the direction of maximum improvement
✓ control of the simulations
✓ post processing of results
AMESIM® model of the valve
✓ Simulations output
A*
D*
input factors
most influencing factors
optimal configuration

Figure 1 – Scheme of the procedure used for the valve optimization

2. THE VALVE AND ITS REQUIREMENTS

The component concerned in this work is a relief-shock and anti-cavitation cartridge valve (fig. 2): in a single unit it combines two direct acting relief valves, thus realizing the functions of relief and preventing the circuit from cavitation. The fast dynamic of the valve allows its use as shock suppressor. For all these reasons, the valve is typically used for two-directional users (i.e. double effect cylinders, motors, etc.) - where the pressure can suddenly rise or collapse - and placed close as much as possible to the load. Fig. 3 describes the features and the working principles of the valve. The values of the two opening pressures depend only on the spring preloads; in particular the maximum pressure level can be set adjusting the position of the calibration element highlighted in fig. 3*b*, taking advantage of the thread realized on the stem.

As well known, a actual direct acting relief valve is characterized by a significant dependence between the flow rate and the value of pressure kept at the inlet port. The inconstancy of the maximum pressure level kept by the valve is determined by the variability of the force due to the spring and by the effects of flow forces [10], and represents an undesired feature of the component, especially when it has to face with elevated flow rates. Typically, this does not happen for unsteady conditions (such as shock suppressions), but in the normal operating as pressure limiter. Moreover, in many cases – in order to reduce the costs of the circuit – the considered valve is used as single element for limiting the maximum pressure reached by the user.

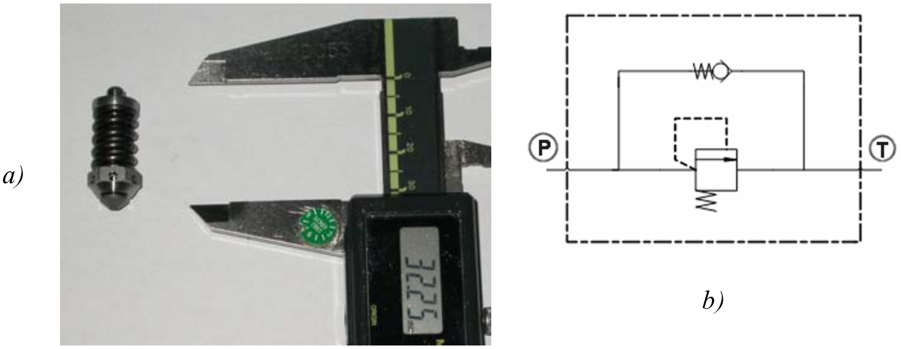

a) *b)*

Figure 2 – Picture of a stock version of the valve (*a*) and ISO equivalent circuit (*b*)

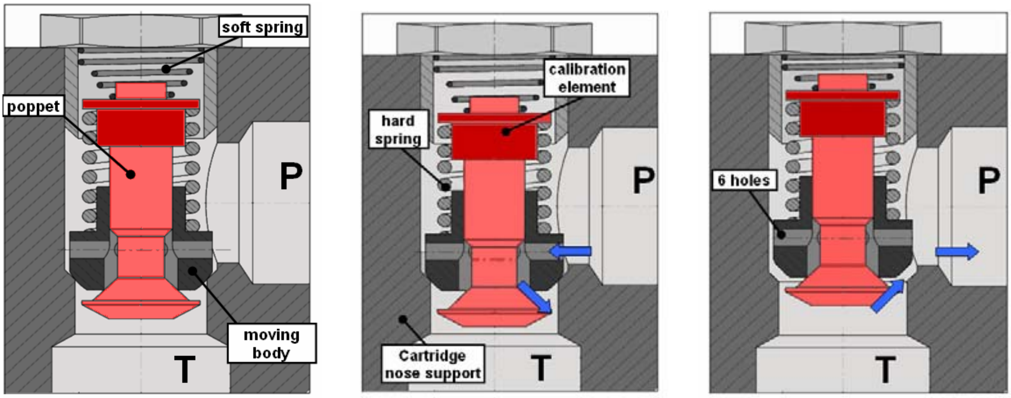

a) *b)* *c)*

Figure 3 – Elements of the valve and description of its operation:
a) condition of equilibrium (no working);
b) control of maximum pressure (relief);
c) control of minimum pressure (anti cavitation)

These premises highlight the importance of the behaviour of the valve when it works as relief valve. For this purpose this work considers an optimization of the component in the latter condition, neglecting both the functions as anti-shock and as anti-cavitation. In particular, the procedure aims to optimize the steady characteristic ($Q \div \Delta p$), limiting as much as possible the dependence between pressure and flow rate and – at the same time - avoiding courses of Δp that can compromise the circuit stability (fig. 4). Previous studies [8,9] point out how thorough a proper design of the cap (the terminal part of the poppet, fig. 3), it is possible to improve the ($Q \div \Delta p$) characteristic. In this work, all the main parameters that characterizes the valve design are taken into account for the optimization of its design.

The goal of this study consist in the definition of an optimal design of a valve suitable for 80 l/min, with different values of the nominal preset pressure. The stock valve taken as reference can operate in a pressure range from 50 to 380 bar, with a maximum flow rate of 60 l/min [11].

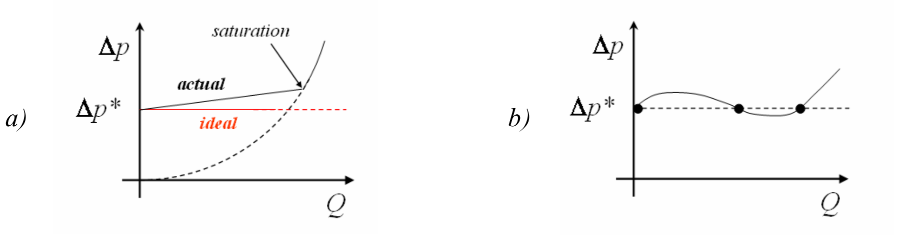

Figure 4 – *a)* Ideal and actual steady characteristic of the relief valve
b) Example of characteristic critical for the dynamic stability of the circuit

3. THE AMESIM® MODEL OF THE VALVE

The optimization algorithm is based on simulation results provided by a AMESim® model of the valve, shown in fig. 1, originally presented in [8]. Respect to the model discussed in the mentioned work, slight improvements on its implementation and concerning the prediction of valve dynamics have been carried out, as pointed out in the detail of fig. 5.

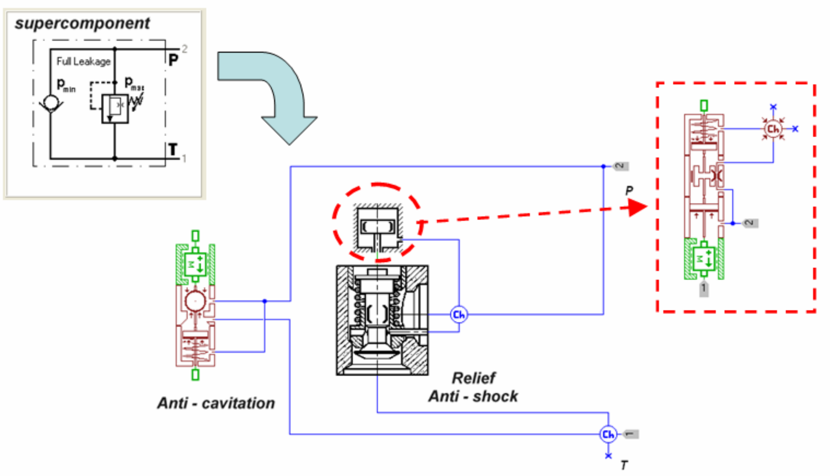

Figure 5 – Model of the valve: the AMESim® sketch

The relevant difference between the stiffness of the two spring (fig. 3) permits to consider the two possible operating conditions of the valve, described in figs. 3*b* and 3*c*, independent; as shown in fig. 5 the model is founded on this hypothesis. Simulation results utilized in the present study regards the part of the model conceived for the simulation of the relief and anti-shock conditions. Substantially, this part – developed in the C++ language – consists in two lumped parameter sub-models in strict interaction: the flow dynamic module and the model of stem dynamics.

3.1 Fluid dynamic model

The fluid dynamic model is based on the evaluation of the flow rate through the valve, according to the orifice equation:

$$Q = \Omega_{12}(x) \cdot c_{eq}(x) \sqrt{\frac{2(p_{t,u} - p_d)}{\bar{\rho}}} \tag{1}$$

in eq. (1) both Ω_{12} and c_{eq} are function of the stem lift[1], x; in particular Ω_{12} is null if the value of $\Delta p = (p_{t,u} - p_d)$ is lower than Δp^*. While Ω_{12} is evaluated accounting of the actual geometry of both stem and seal, according to calculations explained in [13], c_{eq} can be assumed following the results discussed in [12,14]. However, in this work, to improve the accuracy of results the values of c_{eq} come from measurements carried out on stock valves, deeply explained in [9].

Once the instantaneous value of Q is determined, the model evaluates the velocities w_1, w_{12}, w_2 respectively at the sections Ω_1, Ω_{12}, Ω_2 (fig. 6*a*), considering a proper value of discharge coefficient at every section (c_1, c_{12}, c_2) and the presence of a deviation expressed by the angles γ_1 and γ_2. As discussed in [8], these latter values (coefficients c_i and angles γ_i) are assumed with the aid of CFD simulations carried out on purpose and on the basis of data reported in [12,15].

The calculation of the velocities w_i allows the description of the pressure drop Δp with the following equation (fig. 6*a*):

$$\Delta p = \Delta p_1 + \Delta p_{12} + \Delta p_2 + \Delta p_3 \tag{2}$$

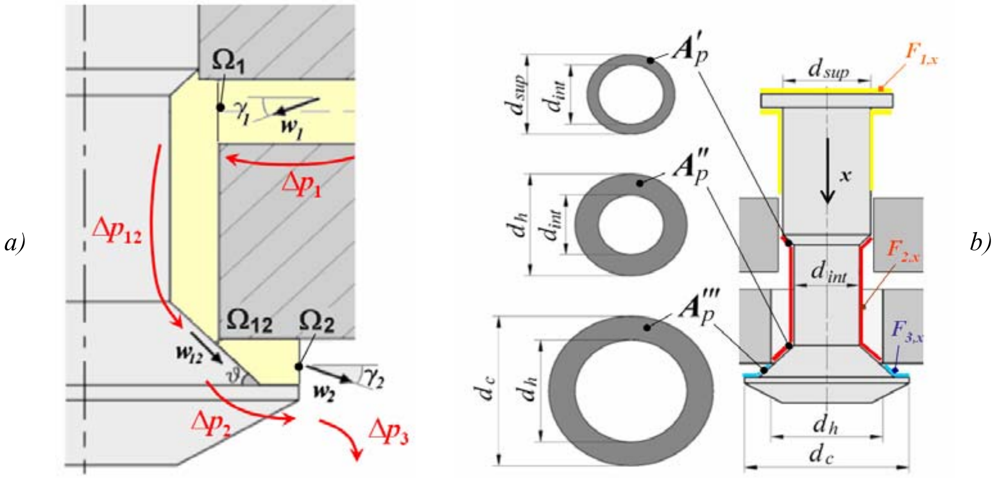

Figure 6 – *a)* Fluid dynamic model; *b)* Forces acting on the stem in the *x* direction

where:

---

[1] Actually $c_{eq} = c_{eq}(x,\mathrm{Re})$. The dependence of c_{eq} on flow conditions, through the Reynolds number (Re) is accounted providing the value for fully turbulent condition (saturated discharge coefficient), then evaluating the actual coefficient of discharge as described in [12,13].

$$\Delta p_1 = \rho \xi_1 \frac{w_1^2}{2}\,;\; \Delta p_{12} = \rho \xi_{12} \frac{w_{12}^2}{2}\,;\; \Delta p_2 = \rho \xi_2 \frac{w_{12}^2}{2}\,;\; \Delta p_3 = \rho \xi_3 \frac{w_2^2}{2} \tag{3}$$

The terms ξ_i, in eq. (3), represent loss coefficients whose value can be estimated according to indications given in [15] for similar geometries, with the exception of ξ_{12}. This latter pertains to the divergence from Ω_{12} to Ω_2, that is peculiar of the analyzed kind of valves. Notwithstanding this, the value of ξ_{12} can be evaluated through the relationship between c_{eq} and the terms c_i and ξ_i :

$$c_{eq} = \frac{c_{12}}{\sqrt{\xi_1 \left(\frac{c_{12}}{c_1} \frac{\Omega_{12}}{\Omega_1} \right)^2 + \xi_{12} + \xi_2 + \xi_3 \left(\frac{c_{12}}{c_2} \frac{\Omega_{12}}{\Omega_2} \right)^2}} \tag{4}$$

3.1 Model of stem dynamics

This module calculates the position and the velocity of stem (along the x axis, fig. 6*b*) integrating the Newton's law. The forces acting on the stem can be summarized as follows:

- $\vec{F}_s$: spring force.
- $\vec{F}_{hs}$: hydrostatic force, due to fluid pressure. Its projection on the x axis, $F_{hs,x}$, can be expressed with the three terms $F_{1,x}$, $F_{2,x}$, $F_{3,x}$ (fig. 6*b*)[2], that are easy to evaluate from the results provided by the fluid dynamic model:

  $$F_{1,x} = p_{sup} A_{sup}\,;\; F_{2,x} = p_{12} A_p^{''} - p_1 A_p^{'}\,;\; F_{3,x} = \hat{p} A_p^{'''} - p_d A_c \tag{5}$$

  where $A_c = \pi \frac{d_c^2}{2}$, $A_{sup} = \pi \frac{d_{sup}^2}{2}$ while $\hat{p}$ is representative of the pressure acting on the surface $A_p^{'''}$:

  $$\hat{p} = \frac{8}{\left(d_c^2 - d_h^2\right)} \int_{\frac{1}{2}d_h}^{\frac{1}{2}d_c} y\, p(y)\, dy = p_{12} - \frac{\left(p_{12} - p_2\right)}{\left(d_c - d_h\right)} \left[\frac{2\left(d_c^3 - d_h^3\right)}{3\left(d_c^2 - d_h^2\right)} - d_h \right] \tag{6}$$

- $\vec{F}_{hd}$: hydrodynamic forces, estimated with (for details see [8]):

  $$F_{hd,x} = \rho \Omega_1 w_1^2 \sin\gamma_1 - \rho \Omega_2 w_2^2 \sin\gamma_2 \tag{7}$$

  Eq. (7) put in evidence the reduction of the x component of the hydrodynamic force, achieved by the cap at the end of the stem.

- $\vec{F}_f$: friction forces. The contribution given by $\vec{F}_f$ can be considered negligible in steady conditions. However, in order to permit reliable unsteady simulations, the model carefully evaluates $F_{f,x}$, adopting the formulation described in [16], implemented in the AMESim® standard submodels [13].

---

[2] The latest version of the AMESim® model of the valve (fig. 5), respect to the one discussed in [8], allows to distinguish p_{sup} from $p_{t,u}$. However, in steady conditions, $p_{sup} = p_{t,u}$.

4. THE OPTIMIZATION PROCEDURE

The valve design parameters considered for the study and the optimization of the valve (utilizing the procedure synthesized in fig. 1) are reported in tab. 1 and displayed in fig. 7.

factor	description	unit	lower value	upper value
A	Internal diameter of stem	[mm]	2,5	3
B	Diameter of hole (moving element)	[mm]	4,5	5.75
C	External cap diameter	[mm]	6.99	8,2
D	Angle of poppet cone	[°]	45	155
E	Diameter of inlet holes (moving element)	[mm]	1.5	2.5
F	Initial height for exiting flow	[mm]	0.4	1.5
G	Spring stiffness	[N/m]	45750	223000

Table 1 – Factors considered for the analysis and the optimization of valve design

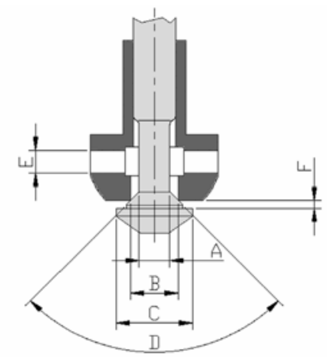

Figure 7 – Representation of the geometrical parameters of tab. 1

The set pressure of the valve, as well as the maximum flow rate, represents a boundary condition of the optimization problem. Therefore, once Δp^* is establishes, it is possible to calculate the spring preload F_0, and the initial length of the spring L_0 (when the valve is closed, $x = 0$):

$$F_0 = K_s\left(L_f - L_0\right) = \frac{\pi}{4} d_h^2 \, \Delta p^* \tag{8}$$

Another parameter related to the spring is the length of maximum compression, $L_{\min}$ ($<L_0$) that should never be exceeded during the valve operating. For the cases taken as reference in this study the authors have individuate a set of possible springs (whose stiffness spam into the interval specified in tab. 1), that allows to impose a relationship between K_s and $L_{\min}$. The knowledge of $L_{\min}$ permits to define a constraint for the maximum stem lift, $x_{\max}$. This latter is related to the flow rate Q, according to eq. (1). An accurate evaluation of $x_{\max}$ for each configuration of the valve can be performed with the AMESim® model of the valve. From these considerations, it is possible to define a further constraint as concerns the value of d_h:

$$x_{\max} \le L_0 - L_{\min} = \left(L_f - \frac{\pi}{4} d_h^2 \frac{\Delta p^*}{K_s} \right) - L_{\min} \quad \rightarrow \quad d_h \le \sqrt{\frac{4}{\pi} \frac{K_s}{\Delta p^*} \left(L_f - L_{\min} - x_{\max} \right)} \tag{9}$$

The study of the valve, with the procedure of fig. 1, requires the definition of an analytical objective function (OF), that permits to quantify the behavior, in terms of its ($\Delta p \div Q$) steady characteristic. The optimal design of the component is reached when its design parameters allow the minimization of the defined OF. For this purpose, a OF suitable for the analyzed valve needs to account of two different aspects:

- during its working the valve should maintain the pressure at the upstream circuit on a value close as much as possible to the preset value, Δp^*;

- an increasing monotonic course, for the characteristic ($\Delta p \div Q$) is preferable in order to avoid more than one possible flow rate value for any given Δp. In this way, the valve cannot cause instabilities on the circuit where it is placed.

For these purposes, a OF that considers two sub-OFs based on the derivative of the ($\Delta p \div Q$) characteristic has been taken into account:

$$\mathrm{OF}_1 = \int_0^{Q_{\max}} \left| \frac{\partial p}{\partial q} \right| dq; \quad \mathrm{OF}_2 = \int_0^{Q_{\max}} \left| \frac{\partial p}{\partial q} \right|_{\frac{\partial p}{\partial q}<0} dq; \quad \mathrm{OF}_{tot} = z_1 \cdot \mathrm{OF}_1 + z_2 \cdot \mathrm{OF}_2 \qquad (10)$$

an optimal OF_1 pertain to a flat characteristic, while OF_2 permits to separate the contribution given by the negative gradients (fig. 8). The valve optimization has been made on function OF_{tot}, in which, for weights z_1 and z_2, it has been assumed z_1=0.4 and z_2=0.6.

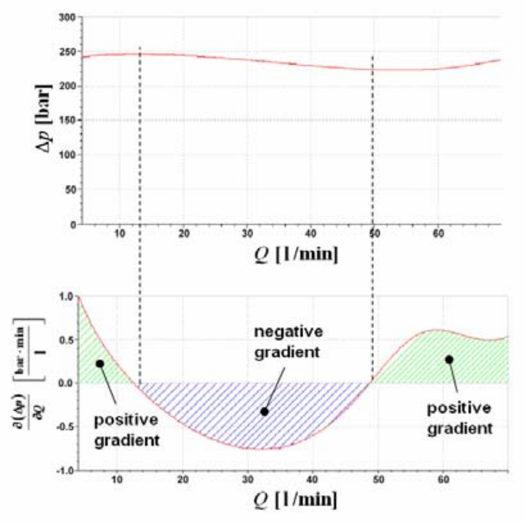

Figure 8 – Example of calculated steady characteristic of the relief valve. Detail on the gradients

The *screening* analysis about the influence of the parameters listed in tab. 1 on the function $\mathrm{OF}_{\mathrm{tot}}$ can be performed with a two-level factorial design [17], that is based on the evaluation of $\mathrm{OF}_{\mathrm{tot}}$ in the configurations of the valve given by all the possible combinations of levels displayed in tab. 1. The set of configurations involved by the full factorial approach is acceptable (2^7 configurations), being the evaluation of $\mathrm{OF}_{\mathrm{tot}}$ performed through fast simulations with the described AMESim® model, as represented in fig. 1. Notwithstanding, DOE methodologies, that are conceived for experiments conducting and planning, allow several possibilities as concerns the reduction of the number of configurations required for the analysis (i.e. fractional factorial designs) [17]. For example, a *screening* analysis based on a procedure similar to the one adopted in this work is discussed in [18], where the elevated number of initial parameters led to a reduction of the set of configurations by means of a proper fractional strategy. However, to avoid aliasing effects [17] (in other terms parameters – or interaction between them – whose effect is confused with interactions of superior order), in this work the full factorial approach has been preferred.

After the evaluation of OF_{tot}, the subsequent step of the *screening* consists in the evaluation of the effects of the parameters adopting the Yates algorithm [19] (originally proposed by F. Yates in 1937 [20]). A graphical representation of the *screening* results is useful for a better understanding of the component behaviour and can suggest considerations about its design. Typical plots used in this ambit are the diagnostic plots of residuals, square and cube plots, surface and contour plots, normal probability plot of effects and Pareto chart of effects [17,21]. These two latter are widely diffuse – and probably the most effective – for communicating the screening results. In particular, *normal probability plots* represent the effect estimates (rank ordered) related to each of the factors (and of the main interactions) against the normal probability; the effects that are negligible are normally distributed and will tend to fall along a straight line (representative of a normal distribution), whereas significant effects will have nonzero means and will not lie along the straight line. In the Pareto charts the effect estimates (provided by the analysis of variance) are sorted from the largest absolute value to the smallest absolute value.

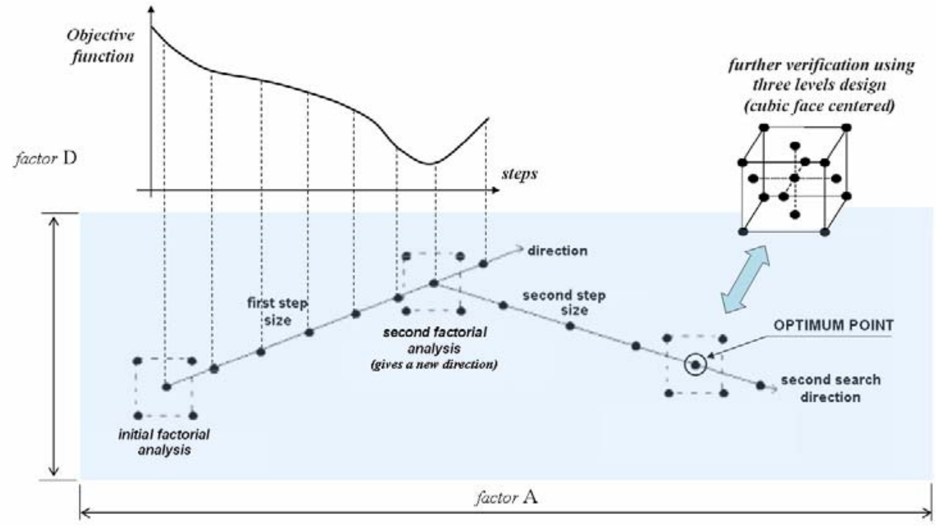
Objective function
steps
factor D
further verification using three levels design (cubic face centered)
direction
first step size
second step size
second factorial analysis (gives a new direction)
OPTIMUM POINT
second search direction
initial factorial analysis
factor A

Figure 9 – The optimization process with the RSM-Steepest Descent technique

Although *screening* results can provide useful information for design improvements, they are strongly affected by the initial assumptions made on the intervals assumed for the considered parameters. A factor may assume a different relevance on the same OF in function of the value of levels assigned to it, respect to the amplitude of the intervals considered for the other design parameters. As described in [17,21,22], many techniques, in the RSM discipline, overcome this aspect. In this work a particular RSM technique, named *Steepest Descent*, has been chosen for the valve optimization. This approach aims to find the minimum of the OF reproducing its shape iteratively. In detail, the OF is locally approximated with a first-order polynomial:

$$\hat{y} = b_0 + Y'b \tag{11}$$

where, in eq. (11), Y is the vector (Y' its transposition) of input variables (factors of tab. 1), b the vector of fitting coefficients and b_0 the mean value of $\hat{y}$.

Fig. 9 describes the path search method implemented according to the *Steepest Descent* methodology: by means of a DOE full factorial analysis, considering small intervals of the parameters of tab. 1, the fitting coefficient of eq. (1) are evaluated. These coefficient represent a local approximation of the considered OF, around the starting point. Similarly to the screening analysis, the described process is based on simulation results, utilizing the AMESim® model of the valve, as indicated in fig. 1. Then, the function OF_{tot} is approximated by the eq. (11), calculating the *b* coefficients with the Ordinary Least Square method.

Once the first expression for $\hat{y}$ is determined, the local gradient of the fitted model is used for the evaluation of the first direction of maximum improvement. According to this direction and selecting a proper step size, the OF is calculated until a minimum is found (or until a border of the region of interest is reached). The procedure starts again from this new point, evaluating a new fitting model $\hat{y}$ and a new direction of maximum improvement. The search sequence is continued until there is no evidence of further improvements. The literature reports many consideration and criteria about the evaluation of the direction of maximum improvement and the selection of a suitable step size [17,21-23]. The MATLab® procedure utilized in this work implements a basilar *Steepest Descent*, that is effective for the case considered because of the following considerations:

- the tiny intervals assigned to the parameters, for the full factorial analysis required at each change of direction, assure the adequacy of the first-order model given by eq. (11), for the local description of OF_{tot}. This has been verified through method of Least Square Estimators [17,19], that involves additional runs (evaluations of OF_{tot}) at the centers of the intervals considered for the full factorial design.
- adopting a fixed and small value for the step size it is possible to perform the path search algorithm of fig. 9 without using complex criteria based on the value of the parameters estimated, as suggested in [21-23], keeping acceptable the time required for executing the optimization procedure (about 3 hours, with a common Pentium IV PC).

Hence, the developed procedure can be improved, as concern the overall number of evaluations of the OF, that is a primary necessity for experimental optimization processes; however, it yields to a simple and robust algorithm, and it is suitable for fast simulation models, like the one described in the previous paragraph.

At each search, the direction of maximum improvement is determined calculating the negative gradient of $\hat{y}$:

$$\vec{g} = \left(\frac{\partial \hat{y}}{\partial X_1}, \frac{\partial \hat{y}}{\partial X_2}, \ldots, \frac{\partial \hat{y}}{\partial X_n} \right) \tag{12}$$

where, in eq. (12) the symbol X_i indicates the coded factor (each factor of tab. 1). For example, for factor A:

$$X_i = \frac{A_i - (A_{\min} + A_{\max})/2}{(A_{\min} - A_{\max})/2} \tag{13}$$

The convention for coded factors has been introduced in order to obtain parameter estimates scale independent, leading to a most effective search direction.

In order to optimize the valve behaviour, the procedure of fig. 9 approximates both functions OF$_1$ and OF$_2$, finding out two directions of maximum improvement, $\vec{g}_{\mathrm{OF}_1}$ and $\vec{g}_{\mathrm{OF}_2}$. Then, the direction of maximum improvement of OF$_{\mathrm{tot}}$, $\vec{u}$, is found applying the weighs z_1 and z_2 to the versors $\vec{u}_{\mathrm{OF}_1}$ and $\vec{u}_{\mathrm{OF}_2}$:

$$\vec{u} = z_1 \cdot \vec{u}_{\mathrm{OF}_1} + z_2 \cdot \vec{u}_{\mathrm{OF}_2} \tag{14}$$

where $\vec{u}_{\mathrm{OF}_1} = \dfrac{\vec{g}_{\mathrm{OF}_1}}{\left|\vec{g}_{\mathrm{OF}_1}\right|}$; $\vec{u}_{\mathrm{OF}_2} = \dfrac{\vec{g}_{\mathrm{OF}_2}}{\left|\vec{g}_{\mathrm{OF}_2}\right|}$.

5. RESULTS

A *screening* analysis of the component taken as reference, when it operates as a relief valve, has been carried out in order to investigate the influence of the parameters summarized in tab. 1 on OF$_{\mathrm{tot}}$. Similarly to the analysis performed in [18], results are strongly influenced by the assumptions made as regards: the amplitude of the interval (lower and upper values of the two level analysis) defined for each parameter of tab. 1; the value of the preset pressure Δp^*; the interval of flow rate through the valve. Therefore, an exhaustive discussion of *screening* results should consider a variety of cases representative of different operating conditions and various possible regions of interest of the parameters listed in tab. 1. Figure 10 shows a normal probability plot obtained assuming – for the factors of tab. 1 – a small interval (±5%) around the value pertinent to a stock valve [11] (such interval is included in the region of interest specified in tab. 1).

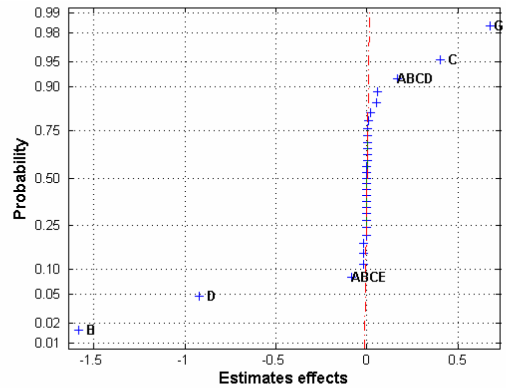

Figure 10 – Normal probability plot for a stock valve (parameters varied up to ±5%; Q_{max} = 85 l/min, Δp^* = 300 bar)

Results displayed in fig. 10 are representative of the majority of the conditions considered: the hole diameter of the moving element (parameter B, fig. 7) always assumes the highest importance on valve behaviour. Moreover, also the angle of poppet cone, the spring stiffness and the external cap diameter (parameter D, G, C) have a great influence on function OF$_{\mathrm{tot}}$, although their importance strongly depends on the boundary conditions assumed for the analysis.

Step		path details						
from	to	A	B	C	D	E	F	G
1	343	↑	↑	↓	↓	↑	↑↑	↑
344	511	↓	↑	↑	-	↓	↓	↓

Table 2 – Modifications of parameters during the optimization process of fig. 11

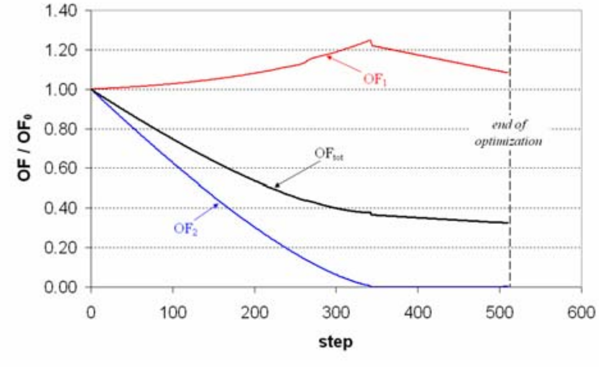

Figure 11 – Courses of OF_1, OF_2 and OF_{tot} during the optimization process (case of $\Delta p^* = 180$ bar)

The parameters highlighted by the *screening* phase can be considered as selected variables for the following optimization phase, according to the scheme of fig. 1. However, considering the restricted number of parameters of tab. 1 and the simulation swiftness of the developed procedure, all the parameters A to F can be considered for the valve optimization. In particular, the *Steepest Descent* process has been applied to three different cases, varying the value of the preset pressure Δp^* (60 bar, 180 bar, 300 bar). Fig. 11 and tab. 2 provide details concerning the path search process for the case $\Delta p^* = 180$ bar, assuming a stock configuration of the valve (described in [11]) as starting point. Obviously, the initial choice on the starting point affects the path followed by the procedure, but does not alter the final result (optimal configuration). Tab. 2 points out the two directions followed by the procedure for the considered case; a third direction does not yield to further improvement on OF_{tot}. Fig. 11 shows the values of the OFs defined in eq. (10): during the first search OF_{tot} reduces its value while only OF_2 decrease. This is caused by the assumptions made on the weight coefficients $z_1$and z_2. Similar results, assuming the same starting point, have been found for the cases Δp^*=60 bar and Δp^*=300 bar (in this latter condition three changes of direction have been occurred). At each step of the search process, the set of values assumed by the input parameters is checked in order to guarantee that the values are included into the interval specified in the tab. 1 and respect the constraint given by eq. (9).

In all the cases the reduction of function OF_{tot} is mainly caused by the parameter B and D; significant variations respect to the nominal configuration (the stock valve, normally employed in a wide pressure range - up to 300 bar – only adopting different springs) also occur in the values of the angle of the poppet cone (D) and of the cap diameter (C). This is consistent with the results of fig. 10. As evident observing tab. 2, the optimization process involves also the values of the remaining parameters of tab. 1, that have a secondary influence on OF_{tot}.

Tab. 3 summarizes, in dimensionless form, the results obtained for the three performed optimizations. Prototypes of the three optimized valves have been realized and a test campaign has been carried out at the laboratory of the Dept. of Industrial Engineering at the University of Parma (Italy). Tests have been conducted with the aim of verifying the improved performance of the prototypes, respect to the analogous stock valves taken as reference. Moreover, experimental results are useful for a further verification of the potential of the AMESim® model as a predictive tool.

	Optimization (Δp^*)		
Factor	60 bar	180 bar	300 bar
A	98	100	100
B	116	100	99
C	101	100	101
D	135	100	118
E	101	100	93
F	141	100	138
G	48	100	181
H	47	100	166

Table 3 – Percentages of values for the considered design parameters for the optimized valves, respect to the case Δp^*=180 bar

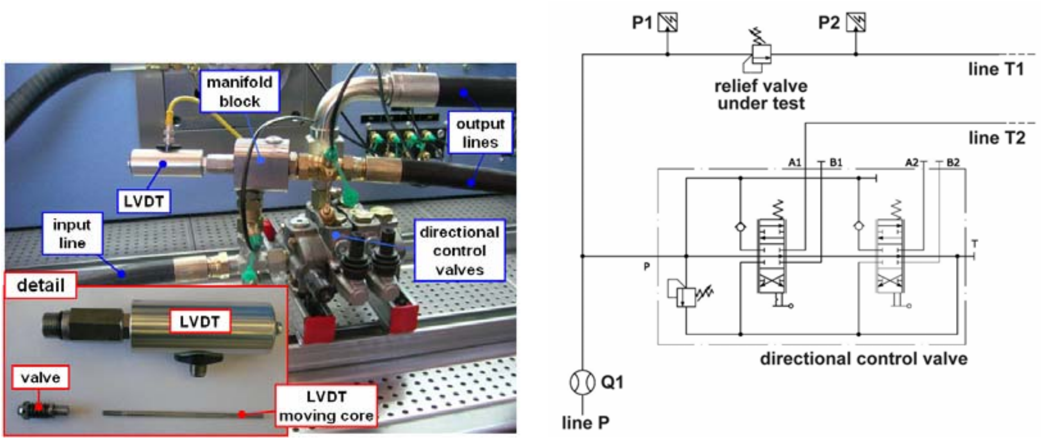

a) *b)*

Figure 12 – *a)* Image of the apparatus utilized for the test campaign
b) Simplified sketch of the hydraulic circuit used for testing the valves

As noticeable observing fig. 12*a*, a manifold block with a conventional SAE cavity includes the cartridge valve. A four-way directional valve is used to permits the circuit upstream the valve to be discharged after each test (see also fig. 12*b*). The apparatus allows the measurement of the pressure upstream and downstream the valve, controlling the value of the flow rate through it, into the range 0÷85 l/min (line P in fig. 12*b*). A linear variable differential transformer (LVDT) has been utilized in order to measure the stem lift. For this purpose the valves used for the test campaign have been slightly modified as to permit the same movement for the poppet and the moving core of the LVDT.

Tests were performed in steady conditions, for different values of Δp^* (obtained changing the spring and varying the initial preload, F_0, acting on the calibration element, fig. 3). The stem lift measurements have permitted the evaluation of the equivalent saturated coefficient of discharge c_{eq} of each valve, as a function of the stem lift. These courses – not reported here for brevity – are close to the one found in [9], initially assumed for the simulations performed during the optimization processes.

Finally, the fig. 13 reports some comparisons between measured data and simulated results obtained for the stock valve and the prototype obtained assuming Δp^* = 60 bar. The stock valve adopts the spring suggested by the manufacturer [11], while for the prototype the set of values of tab. 3 has been adopted. The same figure reports also the comparisons between the experimental courses and the ones predicted by the AMESim® model of the valve. The good agreement between the experimental and simulated courses, highlighted by the figure, confirms the potentials of the numerical tools utilized:

- the AMESim® model of the valve, as concern the prediction of its ($Q \div \Delta p$) characteristic;
- the RSM optimization procedure, implemented in MATLAB, as a tool for design optimization.

Similar results have been obtained considering the comparison between the stock valve and the optimal design for the other cases considered in this work ($\Delta p^* = 180$ bar and $\Delta p^* = 300$ bar).

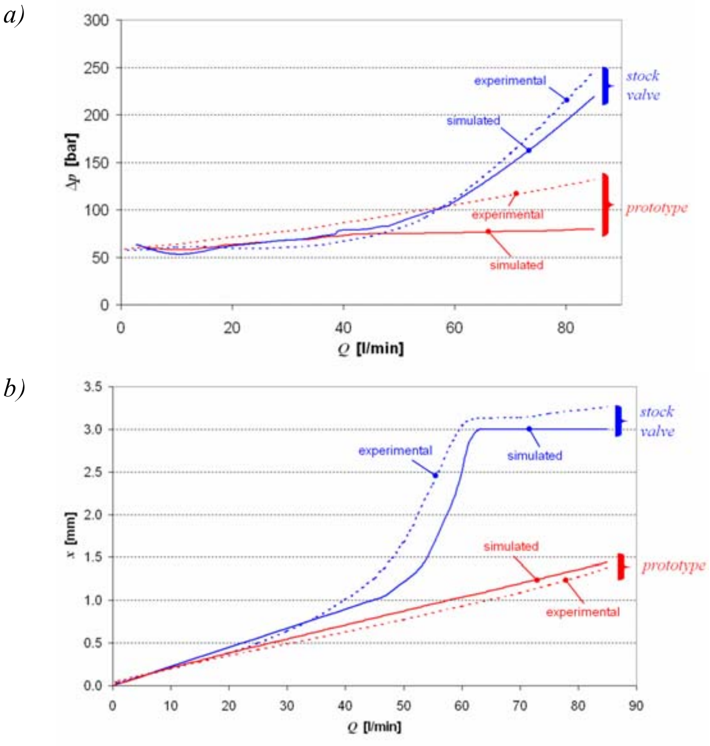

Figure 13 – Comparisons between simulation results and experimental data (case $\Delta p^* = 60$ bar):

a) characteristics ($Q \div \Delta p$) of the relief valve;

b) stem lift

6. CONCLUSIONS

This paper focuses in the optimization of the design of a particular cartridge direct acting relief valve, following a numerical procedure based on Response Surface Methodology. In particular, MATLAB® scripts have been developed in order to implement a simple Steepest Descent path search algorithm. The calculations are performed using a AMESim® model of the valve, written in C++ by the authors, evaluating a proper objective function representative of the valve behaviour, in steady conditions. In order to minimize the number of simulations, and to study the influence of each design parameter on the considered objective function (*screening* phase), Design Of Experiments techniques have been utilized for planning the simulation and for post processing the resulting data.

Results proposed in the paper point out the importance of some design parameters of the valve, namely the diameter of the main hole in the moving element, the spring parameters, the angle of the cone and finally the cap diameter. Three different optimizations have been carried out, defining three different optimal configurations for various values of the preset pressure (Δp^* = 60 bar, 180 bar and 300 bar). A different combinations of design parameters has been found for each case, in particular a different spring and a different value of the hole diameter pertains to each optimal configuration.

Prototypes of the optimal valves have been realized and a test campaign performed at the laboratories of the dept. of Industrial Engineering (University of Parma, Italy) has permitted to verify the improvements achieved through the optimized valve designs, respect to the stock versions. The results highlight also the potential of the AMESim® model of the valve as concerns the prediction of the valve operating and as a tool useful for design.

7. NOMENCLATURE

A	Area
A..G	Valve design parameter
F	Force
F_0	Spring preload
K_s	Spring stiffness
L	Length
L_f	Free length of spring
L_0	Initial spring length
Q	Volumetric flow rate
X	Coded factor
Y	Vector of input variables
b	Vector of fitting coefficient
c	Discharge coefficient
d	Diameter
g	Gradient function
u	Unit vector
p	Pressure
w	Fluid velocity
x	Stem lift
$\hat{y}$	Fitting model
z	Weight

Abbreviations

DOE	Design of Experiments
OF	Objective Function
RSM	Response Surface Methodology

Greek letters

Δp^*	Preset pressure
Ω	Flow area
γ	Angle
ρ	Fluid Density
ξ	Loss coefficient

Subscripts

c	Valve cap
d	Downstream
eq	Equivalent
f	Friction
h	Hole
hd	Hydrodynamic
hs	Hydrostatic
max	Maximum
min	Minimum
u	Upstream
s	Spring
t	Stagnation
tot	Total
x	x-axis projection
0	Initial

8. ACKNOWLEDGEMENTS

The authors would like to thank the R&D division of Walvoil Group for providing founding and supporting this research. Special acknowledgements are due to Professor G.L. Berta (University of Parma) and Mr. Denti (Walvoil Group) for their insight and advice throughout.

9. REFERENCES

[1] Papadopulos E., Davliakos I., 2004, *A systematic methodology for optimal component selection of electrohydraulic servosystems*, Int. Journal of Fluid Power, vol. 5, n. 3, November 2004.
[2] Dahlén L., Carlsson P., 2003, *Numerical optimization of a distributor valve*, Int. Journal of Fluid Power, vol. 4, n. 3, November 2003.
[3] Wiens T., Burton R., Schoenau G., Ruan J., 2005, *Optimization and experimental verification of a variable ratio flow divider valve*, Int. Journal of Fluid Power, vol. 6, n. 3, November 2005.
[4] Cohon J. L., 1978, *Multiobjective programming and planning*, Academic Press, New York, USA.
[5] Eschenauer H., Koski J., Osyczka A., 1990, *Multicriteria Design Optimization*, Berlin, Springer Verlag.
[6] Cook W.J., Cunningham W.H., Pulleyblank W.R., Schrijver A., 1997, *Combinatorial Optimization*, J. Wiley & Sons.
[7] Papadimitriou C.H., Steiglitz K., 1998, *Combinatorial Optimization: Algorithms and Complexity*, Dover Pub.
[8] Franzoni G., Vacca A., Casoli P., 2004, *A numerical model for the simulation of a special poppet valve*, 3rd Fluid Power Net Int. PhD Symposium, Tech. Univ. of Catalonia, Terrassa – Spain, 30th June – 2nd July 2004.
[9] Vacca A., Franzoni G., Casoli P., 2004, *Experimental investigation on a hydraulic special poppet valve*, 3rd Fluid Power Net Int. PhD Symposium, Tech. Univ. of Catalonia, Terrassa – Spain, 30th June – 2nd July 2004.
[10] Nervegna N., 2003, *Oleodinamica e Pneumatica*, Politeko, Tourin Italy
[11] Walvoil Standard Products Catalogue – SDS100 relief and anti-cavitation valves – (www.walvoil.com).
[12] Blackburn J. F., Reethof G., Shearer J. L., 1966, *Fluid Power Control*, USA: MIT Press.
[13] IMAGINE S.A., AMESim 4.3.0 Manual, Roanne, France, September 2004.
[14] McCloy D., Martin H. R., 1980, *Control of Fluid Power*, J. Wiley & Sons.
[15] Idel'Cik E., 1986, *Memento del Pertes de Charge, Coefficients de Pertes de Charge Singulières et de Pertes de Charge par Frottement*, Ed. Eyrolles.
[16] Karnopp D., 1985, *Computer simulation of stick slip friction in mechanical dynamic systems*, Transaction ASME, J. of Dynamic Systems, Measurement and Control, vol. 107, March 1985, pp. 100-103.
[17] Montgomery D.C., 1997, *Design and analysis of experiments*, J. Wiley & Sons.
[18] Vacca A. 2006, *Proposal of a Load Sensing two-way valve model, applying "Design of Experiments" techniques to simulations*, Proc. of IMECE2006, 2006 ASME Int. Mech. Engineering Congress and Expo., November 5-10, 2006 Chigago Illinois, USA.
[19] Montgomery D.C., 2000, *Introduction to Statistical Quality Control*, J. Wiley & Sons
[20] Yates F., 1937, *Design and Analysis of Factorial Experiments*, Tech. Comm. No. 35, Imperial Bureau of Soil Sciences, London.
[21] Box G.E.P., Draper N.R., 1987, *Empirical model building and response surfaces methodology*, J. Wiley & Sons.
[22] Myers R.H., Montgomery D.C., 2002, *Response Surface Methodology: process and product optimization using designed experiment*, J. Wiley & Sons.
[23] Kleijnen J.P.C., Hertog D., Angün E., 2002, *Response Surface Methodology's Steepest Ascent and Step Size Revisited*, Proceedings of the 2002 Winter Simulation Conference, eds. E. Yucesan et al., pp. 377-383.

A proposal to compare electro-pneumatic continuous control valves: required main characteristics

S. Sesmat*, R. de Giorgi*, E. Bideaux*, D. Thomasset*, D. Hubert, J.P. Lecerf*****
* Ampere, INSA-Lyon, F-69621, France
** ASCO-Joucomatic, France
*** CETIM, France

ABSTRACT

Comparative characteristics of components are required to make the adequate choice according to the desired performances or requirements of the system to be designed. This paper proposes to define a set of characteristics, which constitute the needed data for comparing the performances of electro-pneumatic continuous control valves including pressure or flow control valves. These static and dynamic characteristics correspond to the essential information required by users to make a proper choice at the design stage. The associated experimental test rig and procedures for determining these characteristics are also shortly described.

1. INTRODUCTION

When designing or implementing a pneumatic system or a pneumatic circuit, comparative characteristics are required to make the adequate choice of components according to the desired performances or design requirements. Whereas functionalities and reliability of the designed system are more affected by the chosen architecture, the physical performances of pneumatic circuits are mainly related to the components characteristics.

Up-to-now, much attention has been paid to the determination of mass flow rate characteristics of components that are considered as fixed orifices [1]. Several works deal with the mass flow rate characteristics of more complex components [2] such as silencers, valve manifolds, or combined systems with an inlet and an exhaust ports such as solenoid valves but in this last case, the mass flow rate is given according to the maximum valve opening [3].

An electro-pneumatic continuous control valve is a control valve which continuously modulates the transmitted pneumatic power in response to an electrical continuous input signal. These components must be classified into two types according to their function since the electrical control signal can be related to a pressure value (pressure control valves)

Power Transmission and Motion Control 2007 Edited by Dr D N Johnston and Professor A R Plummer
© With The Centre for Power Transmission and Motion Control

or to an effective variable section of each port of the flow rate stage (flow rate control valves). These control valves include electrically modulated pneumatic proportional valves, proportional control valves and servo valves. In this paper only devices with exhaust port to atmosphere are considered.

Pressure regulators and servo valves, which are electro-pneumatic continuous control valves, are complex components since their internal circuit is composed of several restrictions with variable flow areas. For these components, the static mass flow rate characteristics must be completed by other static characteristics and by dynamic characteristics to make the comparison between components possible.

Several works have been done on the modelling of these types of components in order to define simulation models, and some others have been conducted on the determination of different characteristics, for example static characteristics obtained by tests in stationary or in transient conditions [4, 5], or also, dynamic characteristics of valves [6]. But, none presents a global testing and characterizing procedure that could be used as a basis for comparing such components. Therefore, the purpose of this paper proposes to define a set of characteristics, which constitute the needed data for comparing the performances of electro-pneumatic continuous control valves and the associated experimental procedures for determining these characteristics. For each type of control valve, this paper will justify the essential information required for an objective comparison before developing on one side, the static characteristics and on the other side, the dynamic characteristics.

2. ELECTRO-PNEUMATIC PRESSURE CONTINUOUS CONTROL VALVES

The electro-pneumatic pressure continuous control valves are generally used to provide rapidly a flow in open or closed pneumatic circuits in order to reach a desired operating pressure, and then to keep this pressure in despite of perturbations in the working conditions. The choice of such a component is consequently guided by performances related to static and dynamic characteristics. Several aspects are required for an adequate choice:

- the performances of the pressure regulation in stationary conditions: precision according to perturbations in working conditions, saturation, sensitivity, and dead zone,
- the dynamic performances according to changes in the control value: response time, time delay, overshoot, bandwidth.

Due to the complexity of these components and the different existing technologies, the use of a single and general model is not conceivable. The performances must be deduced from a set of characteristics, which can be obtained for any components in the most objective manner. Therefore, our proposal consists in defining a minimal set of data or characteristics evaluating the quality of the relation between the electrical signal (input) and the operating pressure (output), which are sufficient to make a proper choice:

- the control-pressure characteristics at null operating flow rate give the precision and the regularity of the pressure regulation for a closed circuit.

- the flow-pressure characteristics correspond to the admissible working domain of the component at a given inlet pressure. This information is useful for open circuits. It can be also interpreted as the component performance in pressure regulation according to the operating flow.

- the pressure regulation characteristics show complementary information about the component performance in pressure regulation according to the inlet pressure. This is of interest to select the right inlet pressure or the sizing of the upstream circuit.

- Finally, the dynamic characteristics give some indication on the component response to changes in the control value for different magnitudes. These data, limited here to closed circuit, are naturally not sufficient to fully characterize the dynamic of the component, but it seems sufficient for most of the applications. Due to the highly non linear behaviour of these components and the asymmetry of their architecture, a full characterisation would have required too many measurements.

For all the tests, the pressure measurements have to be done using external sensors even if the device has an internal pressure sensor. The use of an external sensor leads to a more objective comparison of components as the evaluation does not depend on the internal pressure sensor characteristic.

2.1 Static characteristics

2.1.1 Control-pressure characteristics at null operating flow rate

The control-pressure characteristics are deduced from the hysteresis curve describing the measured operating pressure versus the electrical control signal varying in both directions on its full scale, while the operating flow rate is null, for a constant inlet pressure as shown schematically in Figure 1b.

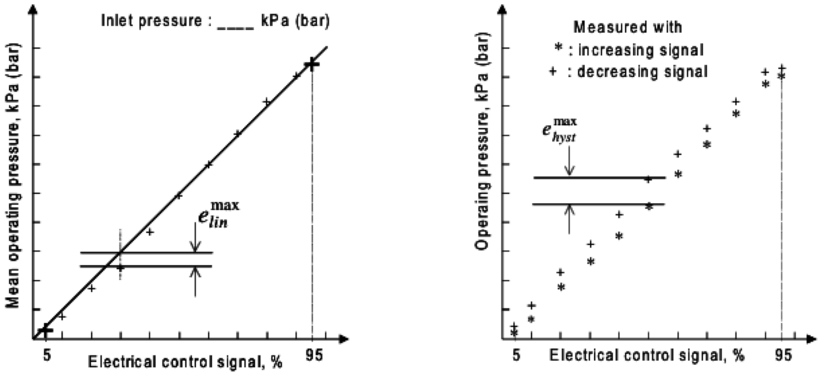

a) Maximal linearity difference **b) Maximal hysteresis difference**

Figure 1 Determination of characteristic parameters on a schematic example of control-pressure characteristic curve at null operating flow rate

This characteristic curve is obtained using the test rig shown on Figure 2. The inlet and operating pressure sensors are external sensors plugged on measurement tubes according to the ISO 6358 standard [1].

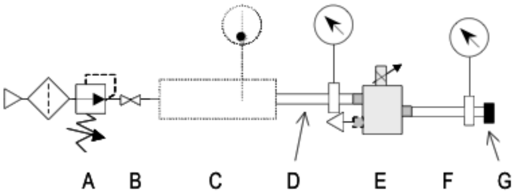

A	Supply pressure regulator	E	Device to be characterized
B	Shut-off valve	F	Downstream measurement tube
C	Temperature measurement tube	G	Plug
D	Upstream measurement tube		

Figure 2 Test rig for control-pressure characterisation

To build an objective comparison of components based on the obtained characteristic curve, three complementary characteristic values have to be determined: the linearity, the control-pressure hysteresis and the threshold. These values quantify the precision, the regularity and the sensitivity of the pressure control valve for a closed circuit. Figure 1 shows respectively the determination of graphical data necessary to calculate the linearity (Eq. 1) and the hysteresis (Eq. 2). The linearity is obtained by comparing the measured pressures to the component gain defined as the straight line between the operating pressure values obtained for 5% and 95% of the control signal full scale.

$$lin = \frac{\left|e_{lin}^{\max}\right|}{\max(poper)} \times 100 \tag{1}$$

$$hyst = \frac{\left|e_{hyst}^{\max}\right|}{\max(poper)} \times 100 \tag{2}$$

The threshold is corresponding to the sensibility near the null control signal. It is defined for the null operating flow and corresponds, on the control-pressure curve, to the minimal value of the control signal at which the operating pressure starts to change from the value reached at the null control signal. It can be determined in two ways:

- either by the smallest control signal value at which the mean of the measured operating pressures starts to change from the value reached at the minimal control signal (case a),
- or by the control signal value at which the characteristic curve intersects the abscissa axis (case b).

The threshold value, defined as a percentage of the control signal full scale, is then chosen as the maximal value of these two previous values as shown in Figure 3.

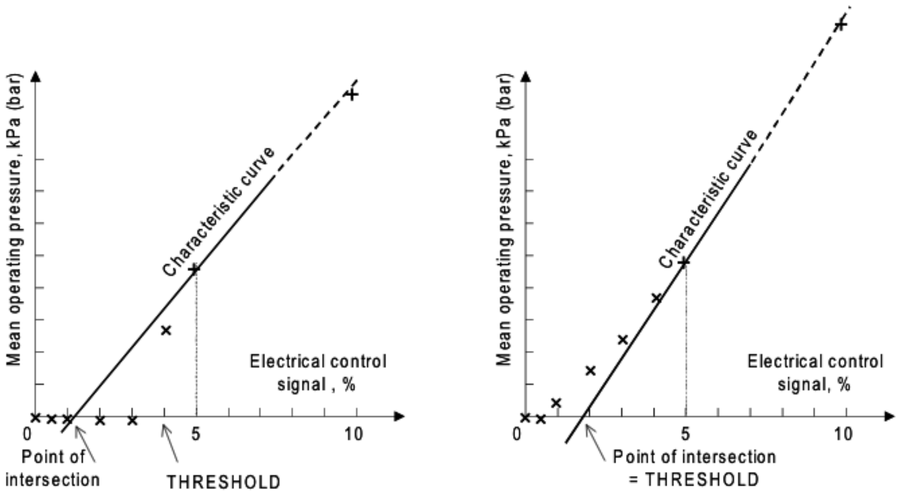

Case a Case b

Figure 3 Graphical determination of the threshold value

2.1.2 Flow-pressure characteristics

The flow-pressure characteristic curve shows the evolution of the operating pressure according to the operating flow rate that can be considered as a perturbation while the control signal and the inlet pressure are kept constant. Due to the non linear behaviour of the component it is interesting to plot this curve for at least four different settings of the electrical control signal according to the Renard series : 25%, 40%, 63% and 80% of the control signal full scale as shown in Figure 4. These curves indicate the pressure static error for a given control signal value according to the flow rate passing through the component.

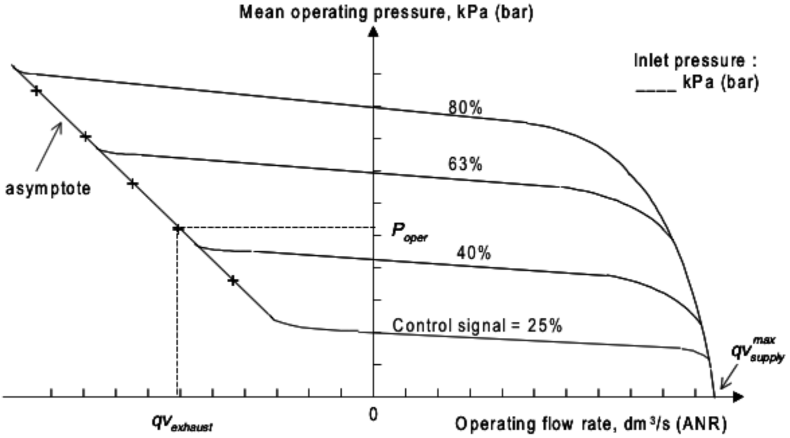

Figure 4: Flow-pressure characteristic curves

Due to the application ranges, the electro-pneumatic pressure continuous control valves have to be characterized for supply flow rates as well as for exhaust flow rates, for both increasing and decreasing flow values. It requires two test rigs using a mass flow meter, modified from the ones of the ISO 6358 standard as shown in Figure 5. In both cases, the component inlet port has always to be connected to the supply circuit with the inlet pressure kept constant, and the exhaust port must always be connected to the atmosphere. These requirements are important since the component has to be characterized according to its normal use. Therefore the flow-meter has to be located at the operating port, in order to measure the useful operating flow rate.

Since the aim of this type of characterisation is the evaluation of the quality of the pressure regulation according to the operating flow rate, it is essential that the pressure regulation is well established. Stationary measurements are thus the most convenient even if some works [5, 7] have shown that alternative methods for measuring the supply flow rate using the charge of an isothermal tank can be used. It can be noticed that using this type of characterisations, it is not possible to measure the flow-pressure hysteresis.

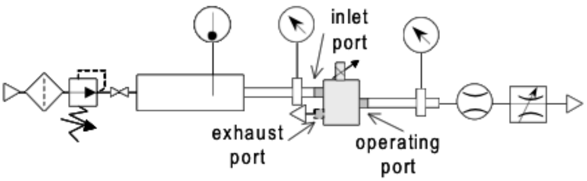

a) Supply flow rate-pressure characterization and pressure regulation test circuit

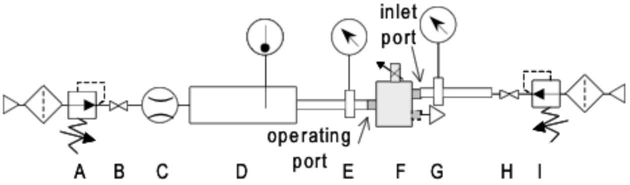

b) Exhaust flow rate-pressure characterisation

A	Operating pressure regulator (upstream)	E	Upstream measurement tube (operating)
B	Upstream shut-off valve	F	Device to be characterized
C	Operating flow-meter	G	Inlet measurement tube
D	Upstream temperature measurement tube (operating)	H	Supply shut-off valve
		I	Supply pressure regulator

Figure 5 Test circuits for flow-pressure characterisation

Three quantitative parameters can be determined from this characterization: the flow-pressure hysteresis determined in a similar manner as in Figure 1b using equation (2), and the supply and the exhaust maximum sonic conductances.

The maximal sonic conductances values, corresponding to the maximal supply or exhaust areas of the control valve, are obtained from equations (3) and (4). These values enable a quick comparison of the maximal flows and consequently the range of the admissible working domain of the pressure control valves. The flow rates values, which are needed for the computation of these parameters, can be identified from the flow-pressure characterisation as shown in Figure 4. The maximal sonic conductance in the exhaust conditions is then determined by the average value of 5 sonic conductances obtained from Eq. (4) using 5 points all over the asymptote of the exhaust flow rate-pressure curves (Figure 4).

$$C_{supply}^{max}=\frac{qv_{supply}^{max}}{P_{inlet}}\sqrt{\frac{T_{inlet}}{T_0}} \tag{3}$$

$$C_{exhaust}=\frac{qv_{exhaust}}{P_{oper}}\sqrt{\frac{T_{oper}}{T_0}} \tag{4}$$

2.1.3 Pressure regulation characteristic

The effects of the inlet pressure on the operating pressure can be measured with the previous test rig (Figure 5a). Each curve, as shown in Figure 6, describes the rate of change of the operating pressure versus the inlet pressure, for a nearly steady operating flow rate as referenced on Figure 6. These characteristics give for several mass flow rates the influence of the inlet pressure on the pressure static error.

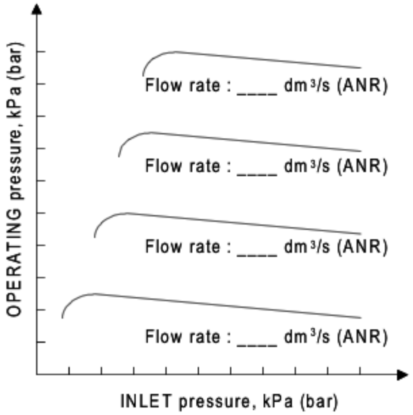

Figure 6 Pressure regulation characteristic curves

Note that the previous flow-pressure characteristics and pressure regulation characteristics are similar to those proposed by the ISO 6953 standard concerning the compressed air regulators and filter-regulators [8].

2.2 Dynamic characteristics

Since the position of the mobile part of the mechanical elements of the pressure continuous control valve can hardly and rarely be measured, two indirect and global tests can be done to characterize the global dynamic behaviour of the component under study: tank charges and discharges, using the test rig shown in Figure 7. Due to the non linear behaviour of the system and in order to give significant information about the valve dynamic, three different sizes of test tank have to be chosen according to the maximal sonic conductance obtained from Eq. 3. The curves, corresponding to the measure of the tank pressure versus time

(Figure 8) for steps of the electrical control signal on its full scale, give then an indication of the valve dynamic performance in different conditions of use. The time response at 95% of amplitude can be determined in ech case.

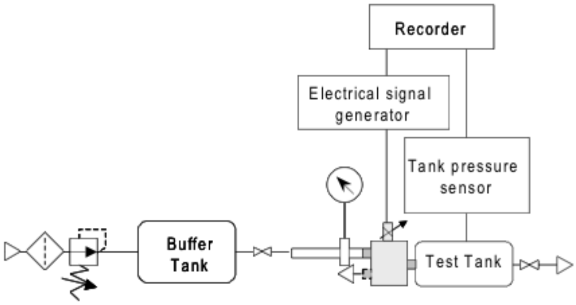

Figure 7 Test circuit for dynamic characterization

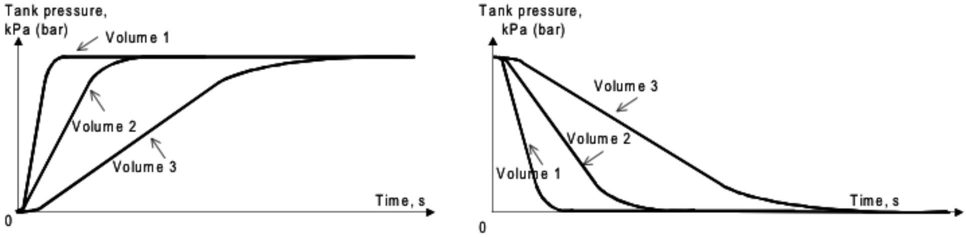

a) Charge characteristics b) Discharge characteristics

Figure 8 Dynamic characteristics

3. ELECTRO-PNEUMATIC FLOW RATE CONTINUOUS CONTROL VALVES

It is important to note that in the case of the electro-pneumatic flow continuous control valves, to the electrical control signal (input control) corresponds the position of the moving mechanical part, which defines the effective variable section of each port of the flow rate stage (output). In order to compare different flow components, their characterisation should consist in evaluating the quality of the relation between these input and output.

But unlike pressure control components, the operating mass flow rate, which is here the output of interest at the user level, is not directly controlled. It results from a superposition of different flows in the valve and it varies with the effective sections reached for a control signal and with the upstream and downstream pressures of each flow path. Moreover the effective variable section of each port (depending on the position of the moving part) is not easily measurable. Several works using stationary flow tests [9] or transitory tests [6] have obtained some results concerning the evolution of the equivalent effective areas of the control valve (for supply flows and for exhaust flows). But these methods are identification procedures, in which the equivalent effective areas is computed using flow measurement and mathematical expressions of the flow issued either from the fluid mechanics theory [9] or from the mathematical approximation of the ISO 6358 standard [1].

Since the main applications of flow continuous control valves are flow regulations, electro-pneumatic positioning systems or force control system, there are advantages to directly measure the operating mass flow rate, the significant output. In a first way to compare different control valves, we propose the use of static flow characterizations. Even if it is easier to characterize only one port, the other one being plugged [10], we propose to measure the global operating flow. This global flow is indeed the real outgoing (supply) or ingoing (exhaust) operating flow through the component. It has to be measured at the operating port, the inlet port respectively the exhaust port being always connected to the supply circuit respectively to the atmospheric pressure according to the normal use of the control valve.

As the operating mass flow rate depends not only on the control input (the electrical control signal) but also on the operating pressure when the inlet and exhaust pressures are kept constant, the static flow characteristics should consist in a 3D-map showing the evolution of the global flow rate according to the electrical control signal and to the operating pressure as shown in Figure 9 [11].

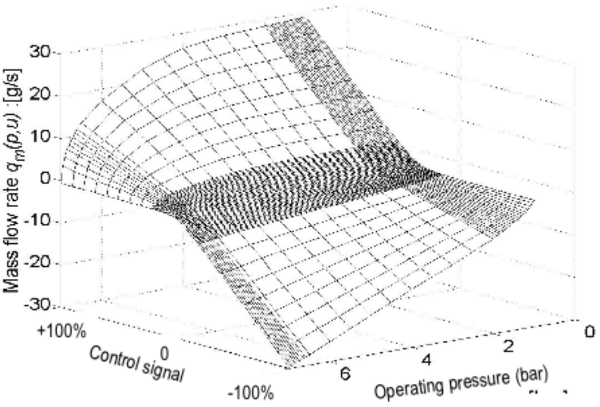

Figure 9 3D-map of the flow rate global characteristic

Such a map is naturally useful for modelling purposes [11, 12, 13], but is not well-adapted when the goal is only the comparison of several components. It is the reason why our proposal is to use two types of flow characteristics corresponding to planar projections of this 3D-map: the first one is the global flow gain characteristic curves and the second one is the pressure-flow global characteristics. These informations give the evolution of the global mass flow rate according to the electrical control signal respectively to the operating pressure when the other variable is kept constant.

It can be noticed that the third planar projection of the 3D-map (Figure 9), which gives the evolution of the operating pressure according to the electrical control signal for different constant mass flow rates can have an interest for flow control valve applications at constant flow rate. The simplest case is obtained for a null flow rate and is interesting when flow control valves are used to control the position of a double acting cylinder with no leakage between the two chambers. Furthermore this particular characteristic called pressure gain characteristic at null operating flow presents the advantage to be very easily obtained experimentally.

Similarly to the static characterization, the dynamic performances of flow control valves should be obtained using the operating flow rate as the output, but up to now, mass flow rates cannot be measured by flow meters at high frequencies. Kawashima et al. [6, 7, 15] have proposed to identify the instantaneous flows from pressure measurements during the charge or the discharge of an isothermal chamber. This method enables the identification of the frequency characteristics of the effective area of the flow path. The presented results are naturally very interesting even if their application to frequency characteristics of the global operating flow rate seems to be more difficult to obtain. Actually, to be fully usable, it would require the stabilisation of the flow (and therefore, of the pressure) for any sinusoidal control signal. We propose then to compare the dynamic characteristics of the flow components using the output, which is directly linked to the control signal that is to say generally the position of the moving part.

In conclusion, our proposal for evaluating the quality of the flow control valve consists in the following minimal set of data or characteristics:

- the pressure gain characteristics at null operating flow. The shape of the characteristic curve (linear or not), its hysteresis value and its slope are relevant parameters for applications such as positioning systems. They have actually a direct influence on the static positioning performances, and especially on the stability of the steady state of the positioning system [16, 17].

- The leakage flow characteristic curve at null operating flow. Its shape and particularly its maximal value give information concerning the air consumption of the component at null operating flow.

- The global flow gain characteristic curves. The two curves, measured for an operating pressure equal to the atmospheric pressure respectively to the inlet pressure, define the admissible working domain of the component at a given inlet pressure when the operating pressure varies between inlet and exhaust pressure values. A third curve obtained for the operating pressure equal to the inlet pressure minus 100kPa enables the eventual non linearity of the flow rate to be pointed out according to the control signal (due mainly to a non linear evolution of the equivalent effective area along the flow path).

- The network of pressure-flow global characteristic curves. These curves show the influence of the control signal on the flow parameters determined according to the ISO 6358 [1], i.e. on the sonic conductance corresponding to the equivalent effective area and on the critical pressure ratio.

- Finally, the dynamic characteristics, consisting in both frequency responses and step responses. They are useful to compare the component responses to changes in the control value. These characteristics are obtained from the measurement of the position of the moving part (using internal or external sensor) for different magnitudes due to the high non linearity of the component behaviour.

We will limit here our proposal to three-port flow continuous control valves, but it can be obviously extended to five-port components.

3.1 Static characteristics

3.1.1 Pressure gain and leakage flow characteristics at null operating flow rate

The pressure gain characteristic corresponds to the hysteresis curve (Figure 10a), which gives the measured operating pressure, at null operating flow rate and constant inlet pressure, versus the electrical control signal when this last one is varying in both directions on its full scale. The hysteresis value is calculated identically as in Fig. 1b using Eq. 2. The used test rig (Fig. 11) is identical to the rig previously presented in Fig. 2, except for the additional flow meter placed upstream the supply line in order to measure the component leakage. This means that the evolution of the leakage flow rate at the inlet port according to electrical control signal can be measured simultaneously to the pressure gain characteristic at null operating flow rate.

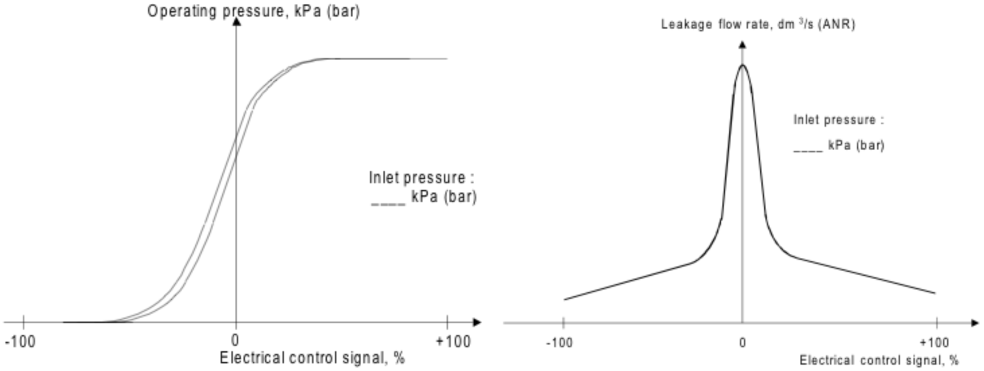

a) Pressure gain characteristic curve **b) Leakage characteristic curve**

Figure 10 Static characteristic curves at null operating flow rate

3.1.2 Global flow characteristics

The global flow characteristics can be obtained by stationary measurements, using the same test rigs as in the case of pressure control valves: Figure 5a for the supply flow rates and Figure 5b for the exhaust flow rates. The convention is to have supply flows corresponding to positive values of the operating flow and exhaust flows to negative values as shown on Figures 11 and 13.

A global flow gain characteristic curve shows the evolution of the operating flow rate when the electrical control signal is changed in both directions on its full scale, for given operating and inlet pressures. We propose here to determine experimentally the two curves delimiting the operating flow range according to the minimum and the maximum operating pressures, i.e. from the exhaust pressure (Pe) to the inlet pressure (Pi). A third curve has to be measured for an intermediary operating pressure equal to the inlet pressure minus 100 kPa (usual conditions for determining the nominal flow rate [18]). Note that when the flow gain curve is measured for an operating pressure equal to the exhaust pressure, a simplified test rig (Figure 12) is used.

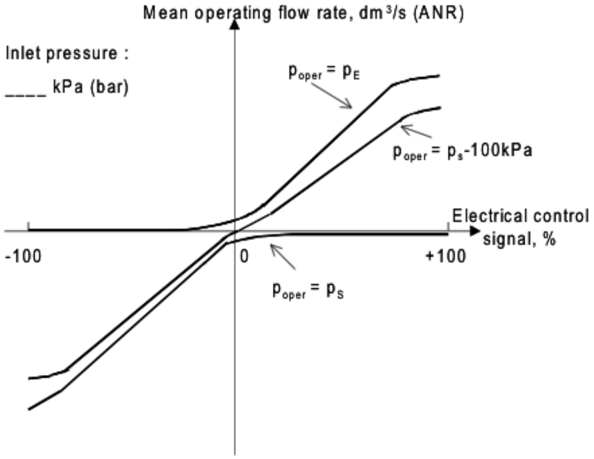

Figure 11 Global flow gain characteristic curves

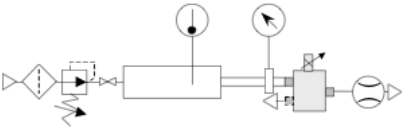

Figure 12 Test circuit for characterising flow rate gain with operating port connected to atmosphere

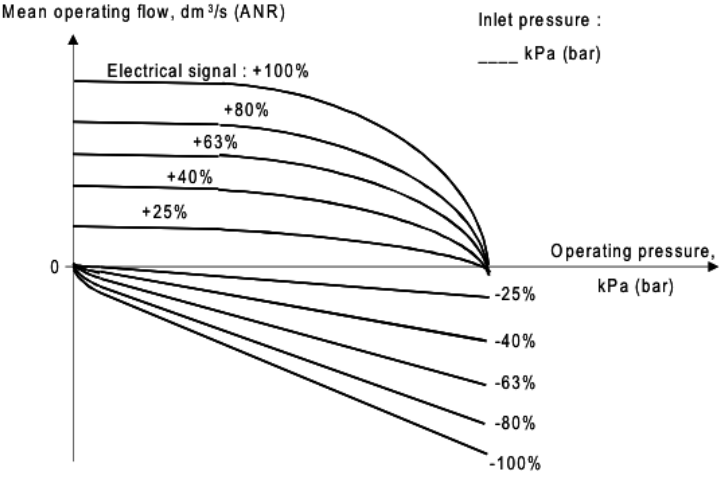

Figure 13 Pressure-flow global characteristics

A pressure-flow global characteristic curve describes only the operating flow rate evolution according to the operating pressure, for a given constant electrical control signal. To determine the influence of the control signal, a network of curves is required. It can be obtained by making the measurements for several electrical control signal values, as referenced in Figure 13. Because the flow path corresponding to a given control value does not correspond to a single restriction but to a complex network of restrictions, it is generally difficult to determine the flow parameters (sonic conductance C, critical pressure ratio b) according to the ISO 6358 standard [1]. However, with the extension of the mathematical flow expression proposed by Kagawa et al. [19], and particularly with the flow parameter m, and eventually with the cracking ratio parameter a, the determination of the 4 flow parameters (b, C, a, m) as a function of the control signal is easier. But this can be used only for high control signal values (greater than 20% of the maximal value) for which one restriction along the flow path becomes predominant compared to the others.

Note that these pressure-flow global characteristic curves could be obtained using transitory tests through the charge or a discharge of a tank of an adequate volume to be sure that the flow is well-established at each sampling time. However the global flow gain characteristic curves cannot be obtained from transitory tests since the three port pressures has to be kept constant.

3.2 Dynamic characteristics

For the dynamic characterization of electro-pneumatic flow rate continuous control valves, the position measurement can be given by the internal position sensor of the component, if it owns one, otherwise, it will be necessary to add an external position sensor, taking care that the implementation of such a sensor does not modify the dynamic characteristics.

A typical test circuit for the dynamic characterization of electro-pneumatic flow rate three-port continuous control valve is described in Figure 14. The buffer tank is used to limit inlet pressure fluctuations and it has to be placed as close as possible to the device inlet port.

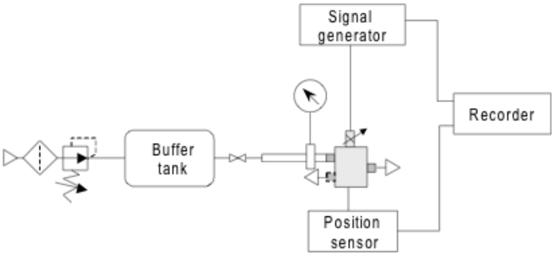

Figure 14 Test circuit for dynamic characterization

Dynamic characterization consists on one hand in classical frequency responses as shown in Figure 15 and on the other hand in step time responses as shown in Figure 16.

Due to the non linearity of the system, it is necessary to determine the frequency responses for at least 3 different control signal amplitudes (± 5%, ± 50%, ± 90%) plotted in bode diagrams as shown in Figure 15. From these curves, the cut frequencies at –3dB and at –90° are identified enabling the comparison of flow control valves.

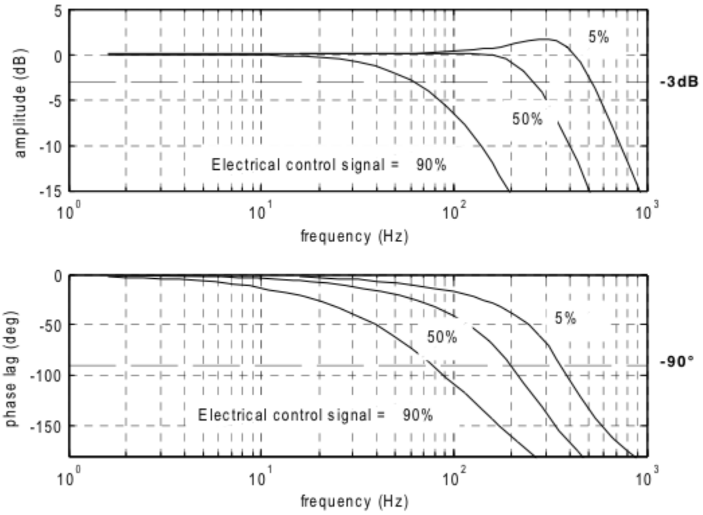

Figure 15 Frequency responses

In order to compare dynamic characteristics of control valves, it is also possible to record the time response of the position of the moving part to electrical signal steps. As the electromechanical system is non linear, a complete comparison requires several step responses for at least 3 sets of control signals on each side of the median value (0%): 5%, 50% and 90%. They can be classified in 3 groups where:

- Step responses shown in Figure 16a are corresponding to control signal steps centred on the median value of the signal,

- Step responses shown in Figure 16b are corresponding to control signal steps from the median value of the signal,

- Step responses shown in Figure 16c, corresponding to control signal steps towards the median value of the signal.

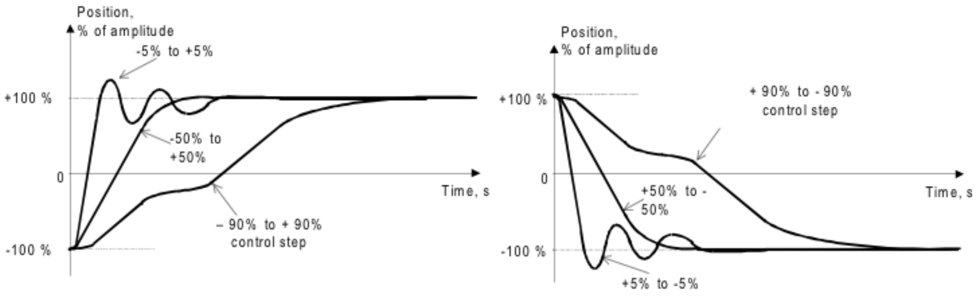

a) Step responses to control steps on both side of the control signal median value

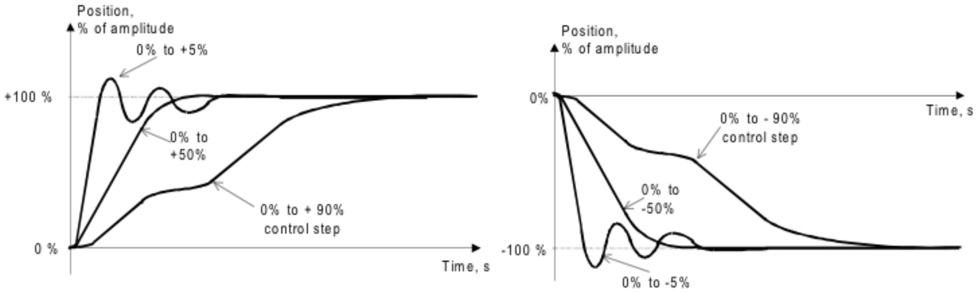

b) Step responses to control steps from the control signal median value

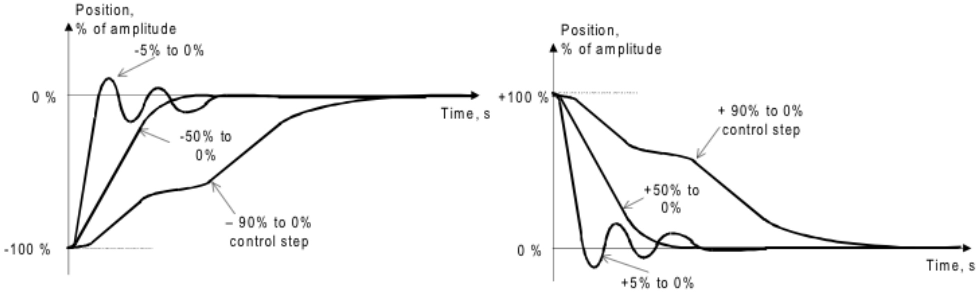

c) Step responses to control steps from the control signal median value
Figure 16 Dynamic characteristics

4. CONCLUSION

The aim of this work was to set up a proposition pointing out characteristic data useful to compare electro-pneumatic continuous pressure and flow control valves in order to help user choice at the design stage of a pneumatic system. As it is usually the user main concern, this proposal focused on the evaluation of the quality of the relation between the input (the electrical signal) and the useful output of the component (operating pressure or global operating flow rate) using static characteristics as well as dynamic ones.

Another purpose of this work was also the definition of the experimental procedures to apply in order to obtain the different characteristics. Our main goal was also here to simplify and to limit the required equipment. Although other procedures are available, we have preferred to use procedures based on the ISO6358, in which static characteristics are obtained using stationary measurements. Some remarks have been introduced in the paper when other methods can be applied, such as measurements in transient conditions. It is surely conceivable, that, shortly, this last procedure can be adapted to fasten the component characterisation, to make easier the measurement of large flow components, or to obtain directly flow frequency characteristics.

Acknowledgment

The authors wish to thank the French Technical Centre of Mechanical Industries (CETIM) for its financial support and its collaboration during this work. This work has led to the proposal at the International Standard Office (ISO) of a standard project in 6 parts that is followed through by the French Standardization Office for the mechanical engineering and rubber industries (UNM).

REFERENCES

1. International Standard ISO 6358. Pneumatic Fluid Power - Components using Compressible Fluids – Determination of Flow-rate Characteristics, 1989. 15p.
2. Oneyama, N., Takahashi, T., Terashima, Y., Kuroshita, K. and Kagawa, T., Study and suggestions on flow-rate characteristics of pneumatic components,7th Symposium on Fluid Control, Measurement and Visualization, 2003
3. K. Kawashima, Y. Ishii, T. Funaki, and T. Kagawa. Determination of flow-rate characteristics of pneumatic solenoid valves using an isothermal chamber. Transaction of the ASME, Journal of fluids Engineering, vol. 126, March 2004, pp 273-279
4. Sesmat, S., Scavarda, S. Static characteristics of a three way servovalve. In: 12th Aachen Conference on Fluid Power Technology, Aachen, Allemagne, March 12-13, 1996, p 643-652.
5. Peng G., Chai, X., Fan, W., A new measurement method of the flow-rate characteristics of the regulator, Proceedings of the 6th JFPS International Symposium on Fluid Power, Tsukuba 2005, November 7-10, 2005, Paper 3C2-4, pp 766-770
6. Kawashima, K., Fujita, T., Kagawa, T., and Jang, J., Characteristic measurement of pneumatic flow control valves using isothermal chamber. 10th Bath International Fluid Power Workshop, Challenges and Solutions, 10-12 september 1997
7. Kawashima, K., Fujita, T., Kagawa, T., Jang, J. Characteristics measurement of pneumatic elements using isothermal chamber. Proceedings of the 3rd JHPS Int. Symposium on Fluid Power, Yokohama'96, Paper n°204, pp 253-258
8. International Standard ISO 6953-1. Pneumatic Fluid Power – Compressed air regulators and filter-regulators, Part 1: Main characteristics to be included in literature from suppliers and product-marking requirements, 2000.
9. Det, F., Scavarda, S., Richard, E. Simulation of an electropneumatic servovalve to study the feasability of a position control loop. In: Fluid power Transmission and Control, proceeding of the 2nd int. Conf., Hangzhou (China), March 20-22, 1989, Beying : International Academic, pp 505-510
10. Fernandez Jiménez, A., Pérez Garcia, J., Compressible bench flow adaptations to the experimental characterization of pneumatic components. Application to the determination of flow-rate characteristics of a MPYE-5-3/8-010-B proportional valve, Proceedings of the 3rd FPNI-PhD Symposium on Fluid Power, Terrassa, Spain, June 30-July 2, 2004
11. Belgharbi, M., Thomasset, D., Scavarda, S., Sesmat, S., Analytical model of the flow stage of a pneumatic servo-distributor for simulation and nonlinear control, in the Sixth Scandinavian International Conference on Fluid Power, SICFP'99, Tampere, Finland, May 26-28, 1999, pp847-860.

12. Kaasa, G. O., Chapple, P. J., Lie, B. Modeling of an electro-pneumatic cylinder actuator for non linear and adaptive control, with application to clutch actuation in heavy-duty trucks, Proceedings of the 3rd FPNI-PhD Symposium on Fluid Power, Terrassa, Spain, June 30-July 2, 2004, pp255-273
13. Sorli, M., Figliolini, G., Pastorelli, S., Rea, P., Experimental identification and validation of a pneumatic positioning servo-system, In Power Transmission and Motion Control, PTMC'05, Sept. 2005, pp 365–378.
14. Olaby, O., Brun, X., Sesmat, S., Redarce, T., Bideaux, E., Characterization and modeling of a proportional valve for control synthesis, in the 6th JFPS International Symposium on Fluid Power, Tsukuba , Japan, November 7-10, 2005, pp 771-776.
15. Kawashima, K., Kagawa, T., and Fujita, T., Instantaneous Flow Rate Measurement of Ideal Gases, Transaction of ASME, Journal of Dynamic Systems, Measurement and Control, vol. 122, march 2000, pp 174-178
16. Sesmat, S., Scavarda, S., Study of the behaviour of an electropneumatic positioning system near the equilibrium state. 1 Int. Fluid. Kolloq. in Aachen, Aachen, 17-18 Marz, 1998, vol. 2, p 321-334.
17. Brun, X., Sesmat, S., Thomasset, D., Scavarda, S., Study of sticking and restarting phenomenon in electropneumatics, Journal of Dynamic Systems Measurements and Control, Vol 127,N°1, March 2005, pp 173-184.
18. Scholz, D., Auslegung servopneumatisher Antriessysteme. Dissertation RWTH, Aachen, 1990, 231p.
19. Kagawa, T., Cai, M., Kawashima, K., Wang, T., Nagaki, T., Hasegawa, T., and Oneyama, N.. Extended representation of flow-rate characteristics for pneumatic components and its measurement using isothermal discharge method. In Power Transmission and Motion Control, PTMC'04, pages 271–282, Sept. 2004.

Flow characteristics measurement of large valves

Bernhard Manhartsgruber[1], **Bernd Winkler**[2]
[1)]Institute of Machine Design and Hydraulic Drives
Johannes Kepler University, Altenbergerstr. 69, 4040 Linz, Austria
[2)]Linz Center of Mechatronics GmbH
Altenbergerstr. 69, 4040 Linz, Austria

ABSTRACT

The functional relationship between the flow rate through a hydraulic resistance and the occuring pressure drop is fundamental for the design and analysis of fluid power systems. In the case of valves, a standardized procedure for the measurement of the flow rate vs. pressure drop characteristics is given in ISO 4411. However, the test rig for an experiment according to this standard is quite expensive in the case of large valves. The largest commercially available cartridge valves have a flow capacity of 25000 l/min. In order to measure their flow characteristics according to ISO 4411, the test rig has to deliver this flow rate over some period of time. The second problem is the cost for a flow meter of this size. Typically, valve test rigs are only available up to flow rates of a few hundred litres per minute. If the flow capability of the valve to be tested is in the thousands of litres per minute, valves can often only be tested in the application but not in a laboratory.

This paper describes a new approach for the measurement of the flow characteristics of large valves by the use of a pressurized column of oil in a pipeline. During an opening instant of the device under test, several pressure signals are recorded and used for an analysis based on the Joukowsky relation between pressure and flow rate. This valve opening experiment can be repeated at different pressure levels resulting in a pointwise determination of the pressure drop vs. flow rate function. The method has experimentally been checked against the conventional flow-meter approach with a cartridge valve of nominal size 16 mm at flow rates up to 150 l/min. A large scale test rig for flow rates up to 4000 l/min is under consideration.

1 INTRODUCTION

The basic function of hydraulic valves is to control the flow of a hydraulic fluid by opening, closing or partially obstructing various passageways. For a given position of the control element, a valve is simply a hydraulic resistance providing a certain flow rate at a given pressure differential across the passageway. The resulting relationship between pressure drop and flow rate is nonlinear. Starting from zero flow at a zero pressure drop a laminar flow region with a linear flow rate vs. pressure drop characteristics exists. This linear region corresponds to a small Reynolds number of the flow in the passageway. At high flow rates the behaviour of the flow in the valve is dominated by the mass inertia of the fluid. The

Power Transmission and Motion Control 2007 Edited by Dr D N Johnston and Professor A R Plummer
© With The Centre for Power Transmission and Motion Control

flow is turbulent and the flow rate is approximately proportional to the square root of the pressure drop for this high Reynolds number situation. A transition region with complicated flow behaviour exists in between the laminar and the trubulent flow regime. For fluid power systems design, analysis, and simulation it is normally sufficient to combine a square root law for large pressure differentials and a polynomial approximation around the zero flow point into a continuously differentiable function [1]. For a given valve, the parameters for this function can either be found in the manufacturers data sheet or they must be measured. Some data sheets only give a flow rating at a certain pressure drop while others contain a graphical representation of the flow rate vs. pressure drop function. For small valves the measurement of this graph can be done directly on a laboratory test rig using a flow meter and at least two pressure sensors. Standardized guidelines both for the design of the test rig and its operation are given for instance in ISO 4411.

To the authors knowledge, the largest hydraulic valves available from stock are rated at 25000 l/min at a pressure drop of 10 bar (e. g. size 160 BOSCH Rexroth LC cartridge). The construction of an ISO 4411 conformal test rig for a flow rate in this order of magnitude is a very expensive task. In order to measure the flow rate vs. pressure drop characteristics up to the limit point with 25000 l/min at 10 bar the flow rate has to be continuously delivered by the supply unit. The power consumption of approximately 420 kW may be manageable but the installation of a pump station capable of 25000 l/min is a big problem in a laboratory environment. Another expensive component is the flowmeter.

This paper describes an idea and first experimental results towards a novel method for the measurement of the pressure drop vs. flow rate characteristics. Section 2 describes the basic idea - a measurement principle based on the Joukowsky relation [3]. The basic idea has to be adapted in some ways in order to get a practicable approach. These modifications are described in section 3. Section 4 gives first experimental results in the range of 0 to 150 l/min. Section 5 concludes the paper.

2 THE BASIC IDEA

The roots of what is nowadays known as fluid transmission line theory lie in Nikolai E. Joukowsky's work on the explanation of pressure transients following sudden valve closure in the St. Petersburg imperial water works [3]. For a circular pipe of inner radius R filled with a fluid of mass density ρ and effective bulk modulus of compressibility E', the characteristic impedance is defined as

$$Z_0 = \frac{\sqrt{E' \rho}}{R^2 \pi}.$$

The Joukowsky equation

$$dp = Z_0 \cdot dQ \tag{1}$$

describes the relationship between a variation of the pressure p and the flow rate Q at the end of a transmission line.

Figure 1 shows a transmission line with an ideal pressure boundary condition $p = p_s = const.$ at the right end and a 2/2-valve at the left end. Upon opening of this valve, the left end of the transmission line is connected to the tank pressure p_0. A simulation model using

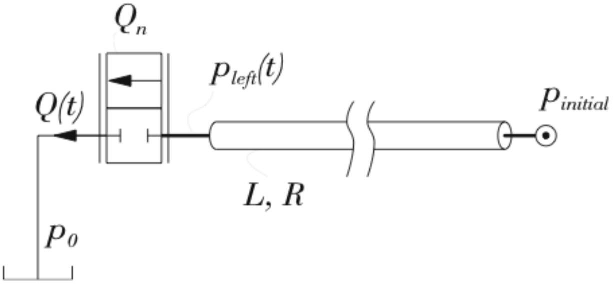

Figure 1: A simple example.

Table 1: Example parameter set.

E'	$1.4 \cdot 10^9$	Pa	effective bulk modulus of compressibility
ρ	860	$\frac{\mathrm{kg}}{\mathrm{m}^3}$	mass density of the fluid
ν	$32 \cdot 10^{-6}$	$\frac{\mathrm{m}^2}{\mathrm{s}}$	kinematic viscosity of the fluid
L	25	m	transmission line length
R	14	mm	transmission line internal radius
$p_{initial}$	200	bar	initial line pressure
p_0	1	bar	tank pressure
Q_n	200	l/min	nominal valve flow rate
Δp_n	5	bar	nominal pressure drop

a Zielke-Suzuki method of characteristics [5, 4] accounting for the wave propagation effects in the transmission line and a simple valve flow model

$$Q\left(t\right) = y\left(t\right)\ Q_n \sqrt{\frac{p_{left}\left(t\right) - p_0}{\Delta p_n}}$$

is set up in MATLAB/Simulink. A ramp function

$$y\left(t\right) = \begin{cases} 0 & t < 0 \\ \dfrac{t}{T_v} & 0 \leq t \leq T_v \\ 1 & t > T_v \end{cases}$$

with a valve opening time T_v is assumed for the valve opening function $y\left(t\right)$. Trivial initial conditions with zero flow rate and constant pressure p_s everywhere along the transmission line are used for a simulation with parameters according to Table 1.

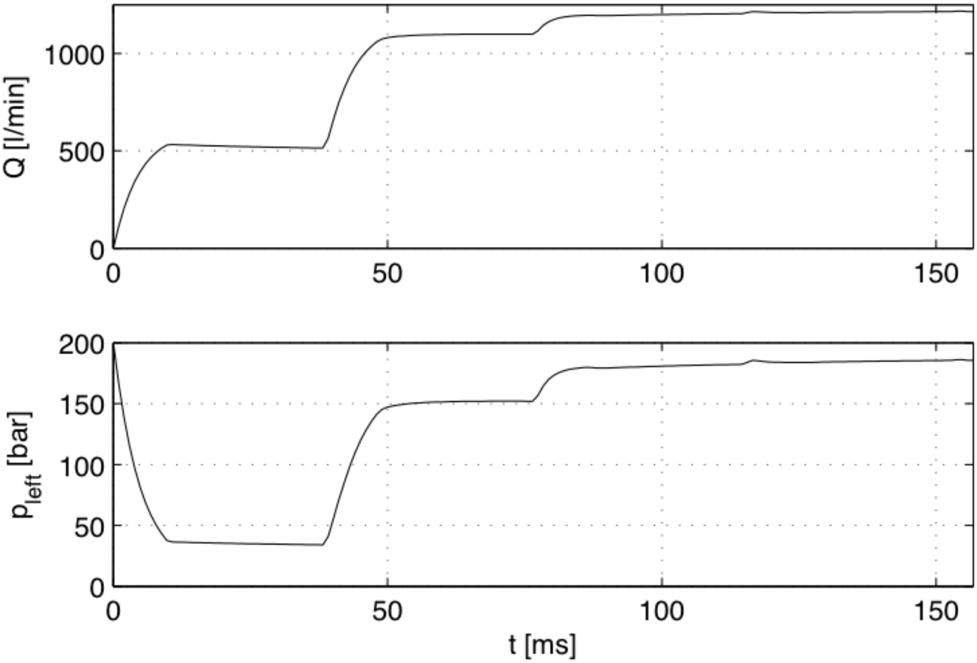

Figure 2: Simulation result over eight wave travel times.

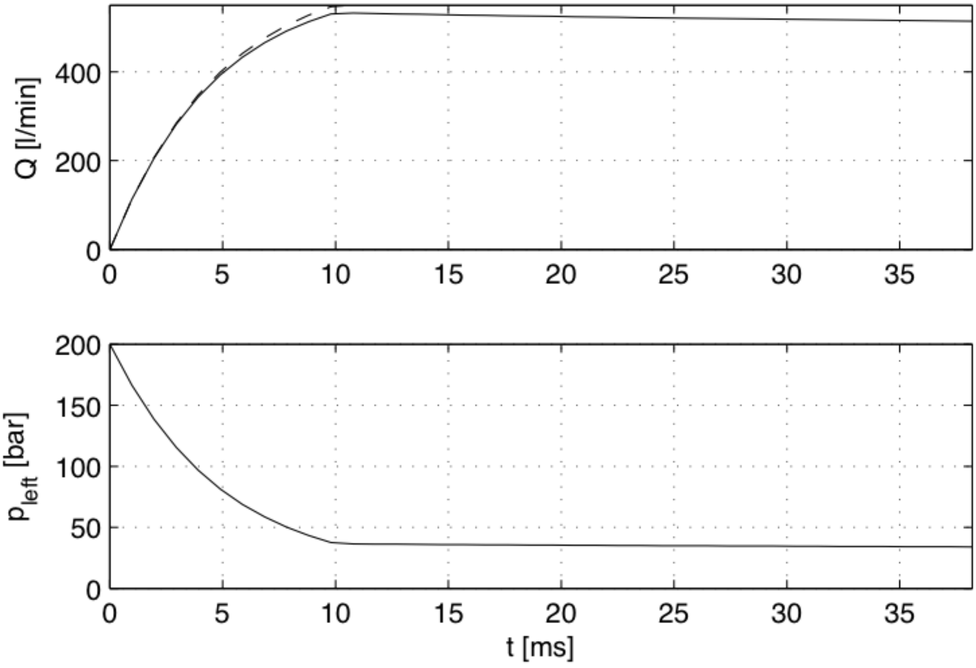

Figure 3: Reflexion-free interval: two wavel travel times.

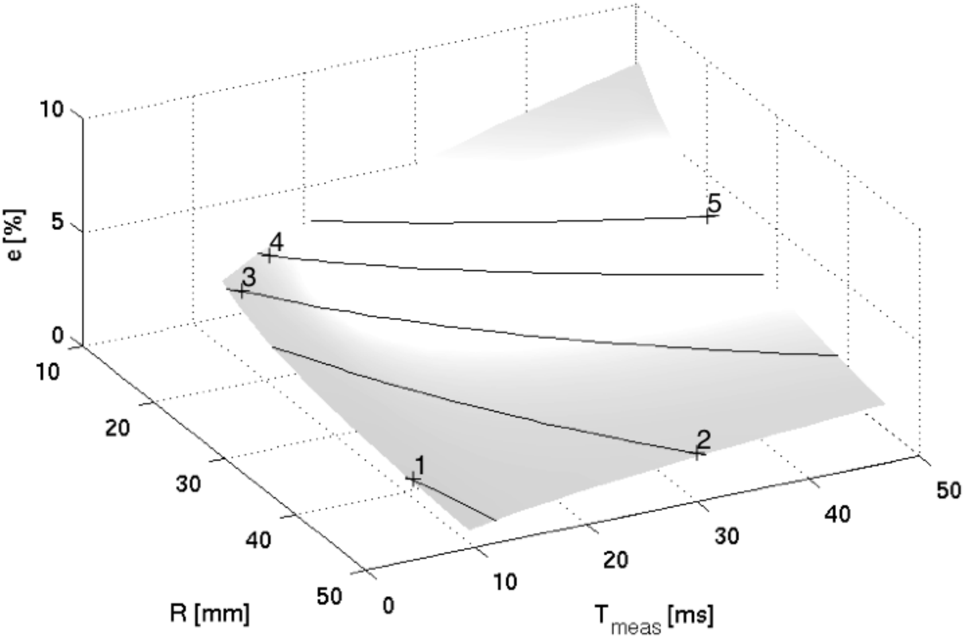

Figure 4: Relative errors in the flow rate estimation.

After the valve is opened, a wave travels along the transmission line towards the boundary condition at the far end. With the speed of sound given by

$$c_0 = \sqrt{\frac{E'}{\rho}}$$

the wave travel time is

$$T_{travel} = \frac{L}{c_0} = L\sqrt{\frac{\rho}{E'}}. \tag{2}$$

The wave is reflected at whatever boundary condition it meets at the far end. As the reflected wave needs again a time of T_{travel} to travel back to the valve under test, a time span of two wave travel times is available for reflection free conditions. This is defined as the available measurement time

$$T_{meas} = 2\,T_{travel} = 2L\sqrt{\frac{\rho}{E'}}. \tag{3}$$

Figure 2 shows the simulation results for the pressure p_{left} at the valve side of the transmission line and the flow rate Q discharging over the valve under test. A simulation time of four times the reflection free time span T_{meas}, i.e. eight wave travel times, has been used to show the influence of waves travelling back and forth along the transmission line.

Figure 3 shows the same simulation results restricted to the reflection free measuring time. According to eq. (1), starting at the trivial initial condition with the fluid in the transmission line at rest, the variation of the flow rate Q should be related to the variation of the pressure p_{left}. Using

$$Q_{th}\left(t\right)=\frac{p_{initial}-p_{left}\left(t\right)}{Z_0},$$

the theoretical flow rate according to the Joukowsky relation can be computed. The result is shown as a dashed line in Fig. 3. Obviously, the theoretical flow rate significantly deviates from the flow rate computed by the Zielke-Suzuki transmission line model. The reason is to be found in the viscous friction effects. While the Zielke-Suzuki model accounts for those effects in detail, the use of the Joukowsky relation over the whole measurement time is only valid in the inviscid case. For a viscous fluid it is only an approximation. The increase of the flow rate estimation error over time can be explained by the increasing influence of viscous friction effects. For the initial time instant, the Joukowsky relation is exact even if viscous friction is present. With increasing time, more and more fluid starts to move along the transmission line resulting in a more pronounced friction loss.

In order to quantify the error in the flow rate estimation and to gain some insight into the role of system parameters like transmission line length and diameter, a series of simulations has been performed. Due to the linearity of laminar pipe flow, the parameter influence is easy to characterise. If the estimation error is measured in terms of a relative error taken as the maximum deviation between the flow rate from the detailed model and the Joukowsky estimation scaled by the maximum flow rate occuring in the simulation, i. e.

$$e=100\%\cdot\frac{\max\left|Q\left(t\right)-Q_{th}\left(t\right)\right|}{\max\left|Q\left(t\right)\right|},$$

the error e depends only on the fluid properties and the geometric dimensions of the transmission line. Fig. 4 shows the error as a function of the transmission line internal radius R and the desired measurement time T_{meas}. Clearly, the fluid viscosity has a strong influence too. With increasing viscosity the estimation error increases. The transmission line length L is coupled to T_{meas} by equation (3). The viscous damping of transmission lines can be characterised by a dimensionless dissipation number [2]

$$D_n=\frac{\nu L}{c_0 R^2}$$

containing the kinematic viscosity ν. With eqs. (2) and (3) the dissipation number can be rewritten as

$$D_n=\frac{T_{meas}\nu}{2\,R^2}.$$

The damping responsible for the estimation error increases with the measurement time T_{meas} and decreases with a larger pipe radius. This behaviour is confirmed by the results shown in Fig. 4.

Besides the estimation error analysis the sizing of the transmission line diameter with respect to the desired flow rate over the valve to be tested is important. The discharge flow depends on the internal pipe diameter and the initial pressure. The maximum possible flow is generated if the pressure p_{left} is lowered to approximately zero by a large valve under test while the initial pressure $p_{initial}$ in the transmission line was at the allowable upper limit

p_{max} defined by the strength of the pipe wall. In this case the remaining pressure p_{left} will be negligibly small compared to $p_{initial} = p_{max}$ and the discharge flow is approximately

$$Q = \frac{p_{max}}{Z_0} = R^2 \pi \frac{p_{max}}{\sqrt{E' \rho}}.$$

For a given maximum flow rate Q_{max} to be generated, the requirement for the internal pipe radius is

$$R > \sqrt{\frac{Q_{max} \sqrt{E' \rho}}{\pi \, p_{max}}}.$$

For the bulk modulus and density given in Table 1 and a maximum working pressure of 250 bar, the following table gives minimum pipe dimensions for a number of maximum flow rates.

flow rate	Q_{max} [l/min]	1000	2000	5000	10000	25000
internal diameter	$2R$ [mm]	30.5	43.2	68.2	96.5	152.6

3 A PRACTICABLE APPROACH

The computations described in the previous section are built upon the assumption of a constant bulk modulus of compressibility and negligible variations of fluid density. Both assumptions are violated in the low pressure region due to the effect of entrained air in the hydraulic fluid. If the pressure remains sufficiently high – the sufficient pressure levels depend on the amount of air in the hydraulic fluid – the influence of entrained air can be neglected. For moderate air entrainment levels of about 1 $\%$ air volume at atmospheric pressure a lower pressure limit of 100 bar will be sufficient.

However, even without air in the hydraulic fluid, the adiabatic bulk modulus of mineral oil is not constant. It depends on both pressure and temperature. The temperature effect can be accounted for by measuring the speed of sound in the transmission line immediately before the experiment. As the temperature varies slowly, this will allow for cancelling out temperature related errors.

Pressure related variations of the bulk modulus and the fluid density end up as estimation errors in the flow rate calculation according to the Joukowsky relation (1). An upper limit for the pressure is given by the allowable working pressure p_{max} of the transmission line. Keeping the assumption of $p_{max} = 250$ bar results in a pressure range between the lower limit of 100 bar to avoid excessive air influence and the upper limit of 250 bar due to limited pipe wall strength.

At a bulk modulus of $E' = 14000$ bar the remaining pressure variation of 150 bar results in a density variation of approximately 1 $\%$. The variation of the effective bulk modulus for mineral oil will be in the order of 10 % for a 150 bar pressure variation. Both variations enter the Joukowsy relation as a product under a square root. Thus the effect on the estimation error will be $\sqrt{1.01 \cdot 1.1} \approx 1.054$ or an error of 5 $\%$ for the maximum flow rate. At lower flow rates the pressure variations and thus the error will be smaller.

For the measurement of the flow rate vs. pressure drop characteristics not only the flow rate estimation but also a precise measurement of the pressure drop across the valve under test is needed. In the first experiments for the verification of the proposed method a problem with the measurement of the tank pressure at the valve occurred. While this pressure is assumed constant in the basic principle shown in Fig. 1, even a short piece of pipe or hose between the valve and the reservoir will result in considerable back pressure when the column of oil is accelerated during the valve opening. The possibility of mounting the device under test directly to the reservoir in order to discharge freely at atmospheric pressure was disapproved because the pressure at the discharge side of the valve under test is then always fixed at the atmospheric pressure level. In some cases a controllable amount of back pressure at the valve is highly desirable, for instance when studying the dynamic behaviour of cartridge valves.

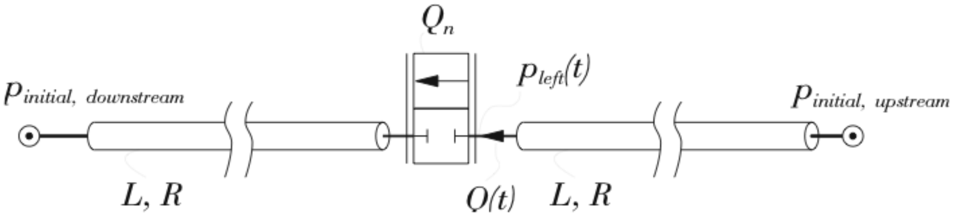

Figure 5: The symmetrical circuit.

Most of the problems described above can be solved by using a symmetrical test rig with an equal transmission line length on both sides of the valve under test: Both sides are now free of reflection for the measurement time according to eq. (3). For measuring the flow characteristics of a valve, the graph of flow rate vs. pressure drop is measured point by point. With the valve closed both transmission lines are kept at a certain pressure level. For the maximum flow rate point, the discharge line will be at atmospheric pressure and the upstream line will be at the maximum pressure p_{max}. Assuming equal transmission line dimensions, the minimum pressure in the upstream line will never fall below $p_{max}/2$. For smaller flow rates the difference between the two line pressures before the valve opening instant must be lowered. This can be done either by decreasing the upstream initial pressure or by increasing the downstream intial pressure. The latter choice offers a possibility to keep the upstream pressure sufficiently high in order to prevent entrained air from affecting the measurement results. This is bought at the expense of a coupling between the back (downstream) pressure at the valve and the generated flow rate.

Furthermore, the use of two transmission lines makes the test rig more expensive due to the doubled pipeline length and a larger diameter required for the same flow rate: Only half of the maximum allowable working pressure p_{max} can now be transformed into a flow rate according to eq. (1).

4 A FIRST EXPERIMENT

A test rig with a steel pipe of 38 mm outer diameter and a wall thickness of 5 mm was built in the laboratory. As there was no space for a straight pipe of 25 m length, the transmission line was rolled in as shown in Fig. 6. For a verification of the proposed method, a hydraulic valve was measured both in the conventional setup with two pressure transducers and a turbine flow-meter as well as using the proposed method. The result is shown in Fig. 7. The match

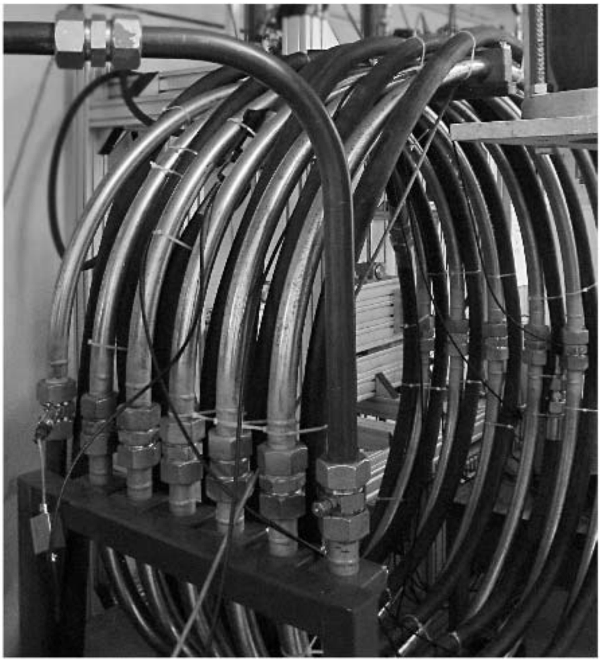

Figure 6: Helical transmission line.

between the conventional method and the proposed approach is good and errors are found to be within the discussed error margins.

5 CONCLUSIONS AND OUTLOOK

A method for the measurement of the flow-rate vs. pressure drop charactersitics of large valves has been proposed and experimentally verified. In its current version, the method is a direct application of the Joukowsky relation under the assumption of a constant bulk modulus of compressibility. Depending on the degree of utilisation of the available test rig size, a flow rate error margin between 1% and 5% can be achieved for typical material parameters of mineral oil and moderate working pressure ranges up to 250 bar.

A patent covering the basic idea and some details of the experimental setup has been filed at the Austrian patent office.

Further research is needed for a refinement of the method towards a nonlinear computation of the flow rate taking into account the variation of the bulk modulus with the hydrostatic pressure. A test rig with a much bigger pipe dimension of 97 mm outer diamter and a wall thickness of 12 mm is currently designed for future experiments with large flow rates.

Acknowledgement

The authors gratefully acknowledge the sponsoring of this work by the *Linz Center of Mechatronics* in the framework of the Kplus program of the Austrian government. This program is

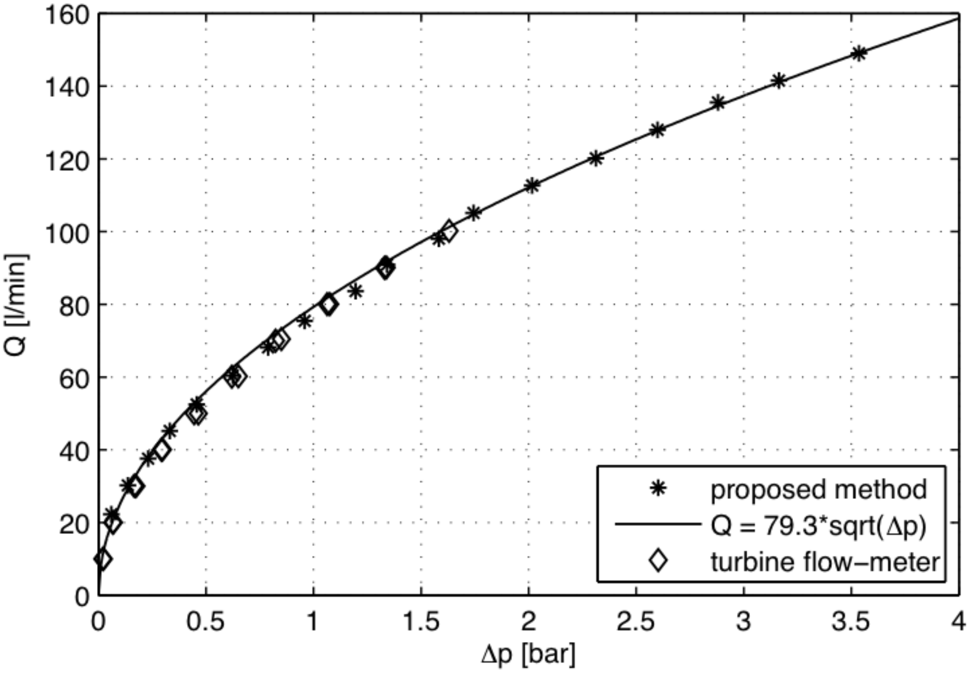

Figure 7: Experimental results.

funded by the Austrian government, the province of Upper Austria and the Johannes Kepler University Linz.

References

[1] A.K. Ellman and R.A. Piche. A modified orifice flow formula for numerical simulation. *Journal of Dynamic Systems, Measurement, and Control*, 121(4):721–724, 1996.

[2] R. E. Goodson and R. G. Leonard. A survey of modeling techniques for fluid transients. *Transactions of the ASME - Journal of Basic Engineering*, 94(2):474–482, 1972.

[3] N. E. Joukowsky. Über den hydraulischen Stoß in Wasserleitungsrohren. *Memoires de 1 Academie Imperiale des Sciences de St. Petersbourg*, 8, 1900.

[4] K. Suzuki, T. Taketomi, and S. Sato. Improving Zielke's method of simulating frequency dependent friction in laminar liquid pipe flow. *J Fluids Eng - Trans ASME*, 113(4):569–573, 1991.

[5] W. Zielke. Frequency-dependent friction in transient pipe flow. *Trans ASME, J Basic Engng*, 90(1):109–115, 1968.

Authors' Index

A
Almondo, A 269

B
Baum, H 367
Beierer, P 159
Bideaux, E 431
Bitner, D 175
Burton, R 175

C
Calinoui, C 189
Casoli, P 413
Cline, O 283

D
Dyminski, D 83

E
Ellman, A 331
Ericson, L 103

F
Fales, R 283
Fritz, S 27

G
Gasparov, M 117
de Giorgi, R 431

H
Haas, R 217
Harms, H-H 201
Harvey, C 283
Helduser, S 245
Hofmann, M 367
Hubert, D 431
Huhtala, K 159
Huova, M 67
Huvila, T 15

I
Ivantysynova, M 83

J
Jacazio, G 269
Jouppila, V 331

K
Kajaste, J 399
Kang, M-G 383
Karam, W 145
Kim, J-W 383
Klop, R 83
Kogler, H 217
Kostamo, E 399
Kostamo, J 399
Kruchkov, A 117, 351

L
Lecerf, J 431
Lee, I-Y 383
Li, L 175
Liermann, M 315
Linjama, M 67, 297

M
Mäkinen, E 15, 53
Manhartsgruber, B 217, 449
Mare, J-C 145
Murrenhoff, H 27, 129, 231, 315

O
Ölvander, J 103

P
Palmberg, J-O 103
Pietola, M 399
Prokofiev, A 351
Prust, D 231

Power Transmission and Motion Control 2007 Edited by Dr D N Johnston and Professor A R Plummer
© With The Centre for Power Transmission and Motion Control

R

Rodionov, L 117

Räcklebe, S 245

S

Schoenau, G 175

Schumacher, A 201

Sesmet, S 431

Sethson, M 41

Shakhmatov, E 117, 351

Siivonen, L 67

Stammen, C 315

Sun, W 255

Sverbilov, V 351

T

Thomasset, D 431

V

Vacca, A 413

Vasiliu, D 189

Vasiliu, N 189

Vilenius, M 159, 297

Virvalo, T 53, 255

W

Williams, K 83

Winkler, B 449

Wohlers, A 129

Z

Zachrison, A 41